Complexes of Pt(II), Pd(II) and Ni(II) with Ring-Expanded Tridentate Cyclometalated Ligands

Inaugural Dissertation
for the attainment of the
Doctoral Degree (Dr. rer. nat. / Ph.D.)

University of Cologne
Department of Chemistry
Institute for Inorganic and Materials Chemistry
Research Group of Prof. Dr. Axel Klein

submitted by

Leo Michel David Payen (M. Sc.)

Accepted in the year 2025

Abstract

In this work, square-planar complexes [M(L)X] of Pt(II), Pd(II) and Ni(II) with L = tridentate, cyclometalated, so-called ring-expanded ligands were studied. In a first approach, the 8-quinolinyl moiety was used to achieve the ring-expanded, six-membered metallacycle. The complexes with N^C^N or C^N^N binding motives (N = pyridyl or quinolinyl) for the tridentate ligands revealed strong geometric distortions as indicated by single crystal X-ray diffraction. This leads to nearly perfect square planar coordination at the cost of coplanarity and conjugation of the ligand backbones. Spectroscopic data, supported by DFT-calculations revealed a strong influence of the ring-expansion on MLCT absorptions. Preliminary investigations showed promising luminescence results, especially for Ni(II) compounds.

Introduction of further chromophore moieties such as carbazolyl and fluorenyl resulted in even stronger structural distortions of the ligand backbone. UV/Vis-absorption spectroscopy and cyclic voltammetry confirmed carbazole-containing complexes to exhibit strong shifts of MLCT transitions as well as electrochemical potentials, due to the strong σ-donor character of the ligands. Fluorene-containing complexes showed broad UV/Vis-absorptions, but the introduction of the fluorene moiety had little impact on electrochemistry.

Introduction of sulphur and oxygen into the ligand backbones expanded the scope to N^C^S and N^C^O systems. Their complexes feature interesting oxidations of the sulphur-atoms in the ligand backbone and weak coordination of oxygen-donors, prone to exchange with solvent molecules.

Systematic coligand (X) exchange reactions of the [M(L)X] complexes were carried out using the nitrato derivatives [M(L)NO_3] as key intermediates. This NO_3-coligand was exchanged under very mild conditions, allowing for a wide range of anionic, pseudo-halogenide coligands to be introduced. This method was further adapted to introduce acetylide- or pyrrole-derived coligands, that are strong σ-donors with potential for π-backbonding. These coligands have a large impact on optical and electrochemical properties and the systematic exchange is a potent method for adjusting complex properties.

Overall, this work broadens the portfolio of tridentate ligands for cyclometalated complexes, with ring-expansion opening the way to many new complex species. Their properties can be tailored to specific applications through ligand design with various donors or further tuned by coligand exchange reactions. Future work could see these methods applied towards complexes in luminescent materials and optoelectronic devices.

Table of Contents

1 Introduction

1.1 Tridentate Cyclometalated Complexes

Many cyclometalating ligands contain three (hetero) aromatic units, in the simplest case either phenyl or pyridyl, connected via a single bond. Structurally, they are derivatives of the prototypical tridentate N^N^N ligand 2,2′:6′,2′′-terpyridine (terpy, see Figure 1).[1, 5] The carbanionic phenyl in such ligands can be replaced by extended aromatic systems like naphthalene[6] or anthracenes[7] but also by C-bond thiophenyl[6, 8], furanyl[9] and more. Pyridyl groups can be replaced by any heteroaromatic moieties containing at least one N-function. Examples are pyrazoles[10], thiazoles[11, 12], pyrimidines[13] and more. Beyond nitrogen-binding aromats systems with oxygen[14, 15], sulphur[8, 16] or phosphorous[17] have been reported but are far less common compared to nitrogen.[1, 14, 16-19]

These tridentate cyclometalating ligands are useful because of their ease of synthesis and the possibility of derivatisation with the large range of aromats previously mentioned. Their chelation and meridional coordination usually results in strong ligand field splitting, desirable for many applications such as catalysis, photophysical appliances and photoluminescence.[13, 17, 18, 20-24]

The group ten metals Ni(II), Pd(II) and Pt(II) are among the most commonly complexated metals featuring these tridentate cyclometalating ligands.[1, 15-18, 20-27] While less frequent, many different metals have been reported with these ligands, such as Au(III) [28], Rh(III) [29, 30], Ru(II)[29, 30], Ir(III)[31, 32], Co(II)[33], Fe(II)[34] and Os(IV)[31].

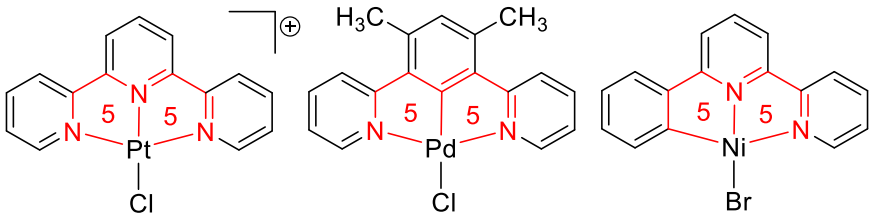

Figure 1 Different cyclometalated complexes bearing five-membered metallacycles (marked red). From left to right: [Pt(terpy)Cl]+, [Pd(PyMe2PhPy)Cl], [Ni(PhPyPy)Br]. [1-4]

Looking at the example of the Pt(II) complex of the pyridine-phenyl-pyridine protoligand, [Pt(PyPhPy)Cl] (Figure 2, left), a square planar geometry is obtained, as is to be expected of d^8-metals.[35] The *Hückel*-aromatic nature of the sp^2-hybridized rings dictates angles of 120°, including the nitrogen lone pairs.[36] This opposes the energetically favoured square planar geometry of Pt(II) with an ideal N–Pt–N angle of $\gamma_i = 180°$ and N–M–C angles of $\beta_i = 90°$ (see Figure 2, right). The Pt–C bond length of 1.907(8) Å (compared to Pt–N_1 2.033(6) Å, Pt–N_2 2.041(6) Å) further ensures the Pt(II) ion cannot achieve its ideal square planer geometry.[1] Instead, distortion takes place, resulting in an N–Pt–N angle of $\gamma = 161.1(2)$.[1]

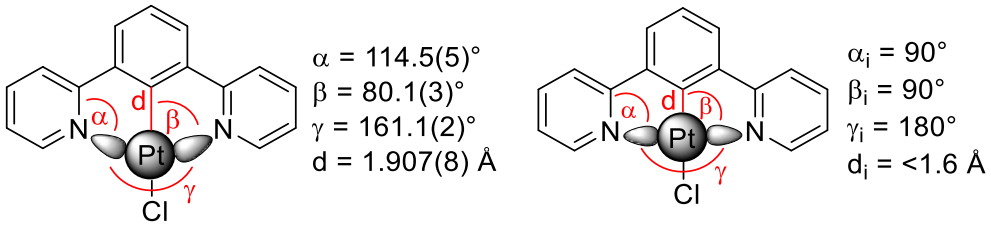

Figure 2 Experimental bond lengths and angles surrounding Pt(II) determined by SC-XRD of [Pt(PyPhPy)Cl] (left) and hypothetical "ideal" square planar geometry (right).[1]

This results in a weakened ligand field splitting for these complexes. This can be severely detrimental to applications of such complexes in optical appliances. High ligand field splitting is generally attributed to raising of the metal centred (MC) excited d-d states.[37] In addition to this, the strength of geometrical distortion of the excited triplet state of these complexes can be directly linked to an increase of luminescence quenching.[38-41] For example, the N^C^N type complex [Pt(PyPhPy)Cl] retains its rigid coplanar ligand backbone even upon excitation. [38] In contrast, the C^N^N type complex [Pt(PhPyPy)Cl] exhibits a distortion of its excited triplet state out of plane, caused by population of the antibonding $dx^2–y^2$ orbital.[42] This results in nonradiative decay pathways being more accessible, by vibronic coupling of the excited triplet and the singlet ground state.[39] The distortion of the excited states is much less pronounced for the N^C^N counterpart, making it a much more efficient luminophore.[38, 42] Therefore, rigidification of the ligand backbone is a useful method to supress non-radiative decay and increase lifetimes and quantum yields.[38, 40, 43-46]

1.2 Complexes with Ring-Expanded Tridentate Ligands

These ligand design challenges stemming from systems with five-membered metallacycles can be addressed by expanding said ligand systems to six-membered metallacycles.[18, 47] These ligands can be based on larger aromatic ring systems or of smaller aromatic systems that are linked by suitable spacer groups (see Figure 3). For example, exchanging the ubiquitous 2-pyridine donor for 8-quinoline, results in the formation of the larger metallacycles (see Figure 3).[18, 47]

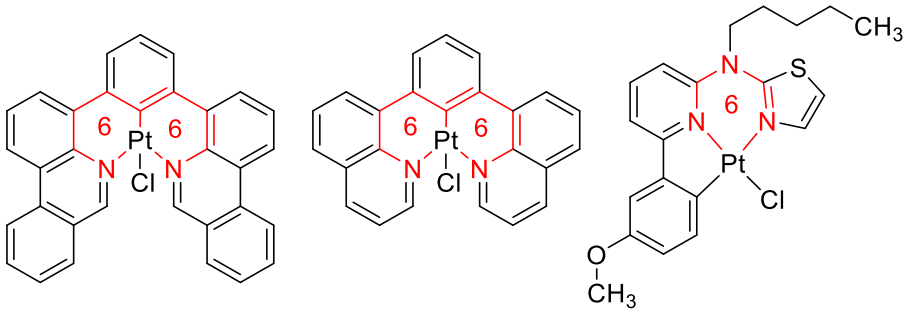

Figure 3 Examples of Pt(II) complexes with tridentate ligands forming six-membered metallacycles (chelates, marked in red).[18, 47, 48]

The geometries of complexes with such larger six-membered metallacycles differ from the five-membered ones previously discussed. The larger metallacycle would result in very small

binding pockets if the aromatic rings were to remain coplanar. However, the rotational degree of freedom around the single bond connecting the different aromats causes distortions of the ligand backbone. They twist to angles that best accommodate the metal ions, resulting in bonding angles close to the ideal 180° (see Figure 4).[18, 49]

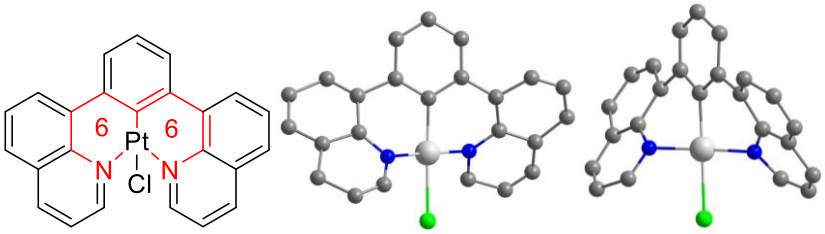

Figure 4 Lewis structure of [Pt(QPhQ)Cl) (left) and molecular structure from SC-XRD (middle, right), showing distortion of the ligand backbone and loss of coplanarity.[18, 49]

This generally results in stronger ligand field splitting, which could make d-d states less accessible for deactivation pathways.[18, 50] However, a significant amount of distortion of the ligand backbone is caused, leading to loss of coplanarity and conjugation.[18, 50] Upon excitation these distortions and the resulting angle strain then promote population of radiationless d-d excited states.[50]

However, previous studies have found that this fine balance can be struck. *Williams et al.* reported the N^N^N type six-membered derivative of the Pt(II) terpyridine complex, [Pt(QPyQ)Cl]Cl to be more luminescent with higher lifetimes and quantum yields that its counterpart with five-membered metallacycles.[18] (see Figure 5) However, the opposite is the case for the N^C^N derivatives, while the lifetime remains longer, the quantum yield is drastically diminished for the ring-expanded species [Pt(QPhQ)Cl].[18] This is surprising, since the carbanion of the later should be a much stronger σ-donor, resulting in a stronger ligand field splitting, thus inhibiting radiationless MC d-d exited states.[37, 43]

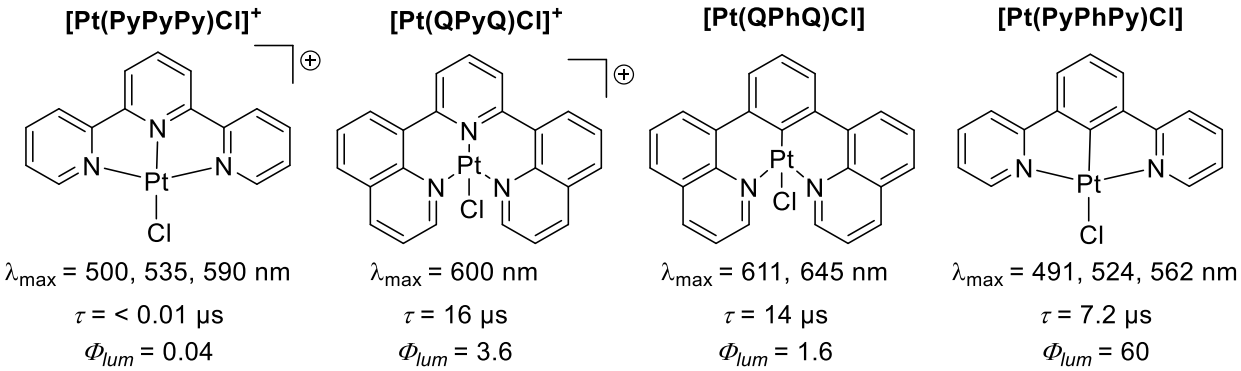

Figure 5 Comparison of structurally related N^N^N and N^C^N type Pt(II) complexes with differing five- and six-membered metallacycles and their emission maxima and lifetimes (r.t., degas. CH_2Cl_2, Φ_{lum} values $x10^2$).[18, 51]

The structures of these complexes were not investigated by single crystal x-ray diffraction. Instead DFT-calculations were carried out for structure elucidation, revealing a strong

distortion of the ligand backbone, with interplanar angles as high as 38.5° for the N^N^N type [Pt(QPyQ)Cl]Cl complex.[18]

The beneficial influence of ring-expansion on luminescence properties is not limited to symmetric and rigid aromatic ring systems. Ring-expansion can also be achieved by bridging ligand systems with donor such as amine, ether or sulphur moieties (see Scheme 1 and 2).[42, 48, 50, 52-54]

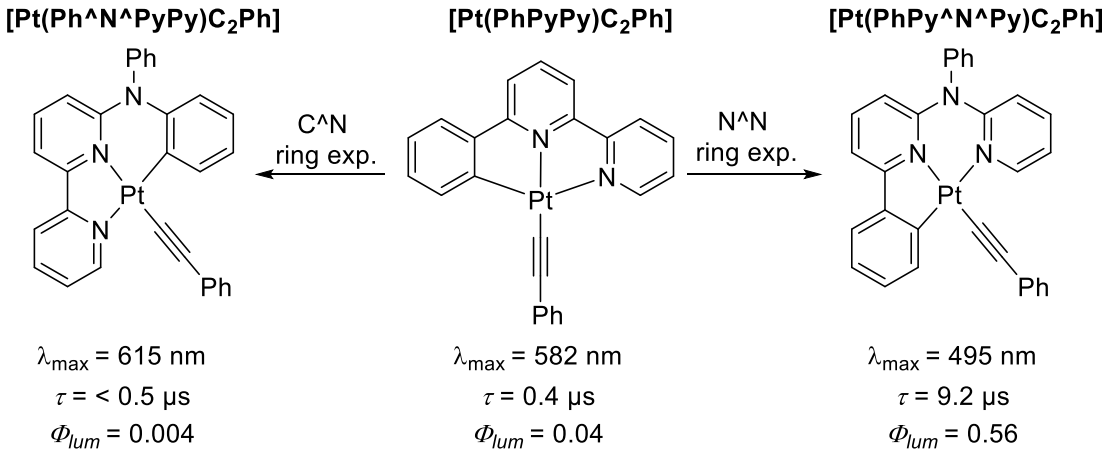

Scheme 1 Site-selective ring expansion of [Pt(PhPyPy)Cl] drastically impacts luminescent properties.[42, 43, 52, 53]

Such ring expansion of [Pt(PhPyPy)C_2Ph] lead to interesting, diverging results.[42, 43, 52] Expansion of the ligand backbone between the phenyl- and bipyridine subunits lead to red-shifted emissions with equally short lifetimes and much lower quantum yields than exhibited by the parent compound ([Pt(PhPyPy)C_2Ph], see Scheme 1, left).[42, 53] The opposite is the case when the ring-expansion is introduced in between the two pyridine units (Scheme 1, right). For the [Pt(PhPy^N^Py)C_2Ph] complex, the emission is strongly blue-shifted, with much longer lifetime and higher quantum yield.[42, 52]

This major difference is attributed to different composition of the triplet excited states. For [Pt(PhPy^N^Py)C_2Ph] (Scheme 1, right), the triplet state is of $^3\pi$–π^*(C^N) character mixed with MLCT ^{3}[dπ(Pt)→π^*(C^N)] components.[43] These transitions are not accessible for [Pt(Ph^N^PyPy)C_2Ph] (Scheme 1, left), since the amine bridge affects conjugation and the rings are geometrically distorted. This geometrical distortion of both the singlet and especially the triplet excited state of the complex [Pt(PhPy^N^Py)C_2Ph] seems to be beneficial for the quantum yields and lifetimes of the luminescence.[52]

Similar detrimental effects of ring-expansion on luminescence like exhibited by ([Pt(Ph^N^PyPy)C_2Ph] (see Scheme 1) were found in complexes with bridging sulphur and methylamine moieties (see Figure 6).[50]

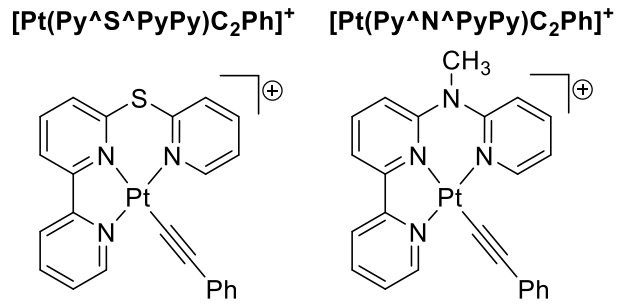

Figure 6 Sulphur- and methylamine-bridged ring-expanded Pt(II) complexes bearing phenylacetylene coligands.[50]

While the ring-expansion on these systems did increase the bite-angles around the metal as intended, a strong distortion of the overall geometry of the complex was the result. The adoption of a pseudo-tetrahedral conformation then lead to promotion of non-emissive d–d excited states.[50]

The bridging ring-expanded complexes discussed show that, case-dependent, site-selective, asymmetric ring-expansion can have a large impact on the properties of the resulting complex.[42, 43, 50, 52, 53]

Further ring-expanded systems with azaindole-based ligands (Bab) were reported containing both Pt(II) and Pd(II) metal ions (see Figure 7).[55, 56]

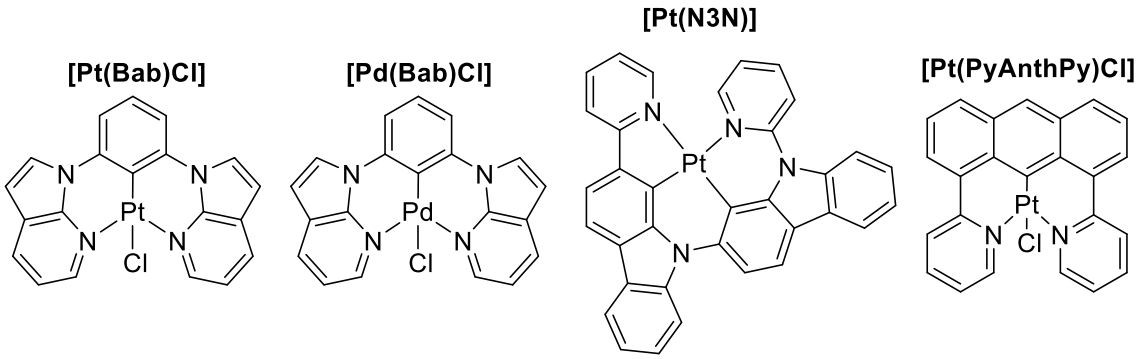

Figure 7 Examples of complexes with different ring-expanded ligands and metal ions Pt(II) and Pd(II).[7, 55-58]

Both complexes [Pt(Bab)Cl] and [Pd(Bab)Cl] also exhibit luminescence at low temperature (77 K, glassy frozen CH_2Cl_2), reported to be of $^3\pi$–π^*(L) character with ^{3}[dπ(M)→π^*(L)] contributions similar to the amine-bridged complexes previously discussed.[43, 55] As was the case for the structurally related [Pt(QPhQ)Cl], the complexes [M(Bab)Cl] feature strong distortion of the ligand backbone in the crystal structures, in favour of more square-planar geometries. The interplanar angles of the two azaindole units of [Pd(Bab)Cl] are 78.0° with N–Pd–N angles of perfectly 180.0(1)°, while for [Pt(Bab)Cl] an interplanar angle of 72.9° with N–Pt–N angles of 178.69(2)° were found.[55]

Next to the various applications of ring-expanded systems in luminescence applications, they have also been used in bio-inorganic applications.[59] For example, the luminescent properties of [Pt(QPhQ)Cl] (see Figure 5) can be applied for switchable sensing of G-quadruplex DNA.[59] This specific type of DNA secondary structure forms in guanine-heavy DNA strands and can form different morphologies.[60] The complex [Pt(QPhQ)Cl] shows selective binding and in such G-quadruplex DNA as opposed to duplex DNA. The reported luminescence of the platinum complex can then be used to selectively detect G-quadruplex DNA.[59]

Next to ring-expansion by the introduction of larger aromatic systems like quinoline or azaindole ([Pt(QPhQ)Cl], Figure 5, [Pt(Bab)Cl], Figure 7), larger metallacycles can also be built up by expansion of the central aromatic ring, moving away from phenyl moieties.

For example, carbazole moieties have been incorporated into ring-expanded tetradentate ligand systems of Pt(II) complexes ([Pt(N3N)], Figure 7). These complexes were successfully applied in OLEDs.[57, 58]

Anthracene-based protoligands have also been complexated with platinum ([Pt(PyAnthPy)Cl], Figure 7).[7] The structure of the resulting complex shows nearly perfect square planar geometry around the metal ion, with angles of 178.16(7)° for N–Pt–N and 178.58(6)° for C–Pt–Cl. In that regard the structure is very similar to that of [Pt(QPhQ)Cl].[7] However, it differs in a pronounced distortion of the anthracene substructure, which, as an aromatic system, should be fully planar. This indicates that the tendency to form square planar geometries is much more energetically favoured than other structural features like coplanarity of the aromatic rings (as seen for five-membered metallacycles, e.g. [Pt(PyPhPy)Cl] or even the aromatic character of the anthracene itself.

These complexes are good examples of the synthetic flexibility regarding ligand design possible by ring-expansion.

Complex with mixtures of five- and six-membered N^C^N type ligands have been reported with ruthenium as metal ion (see Figure 8).

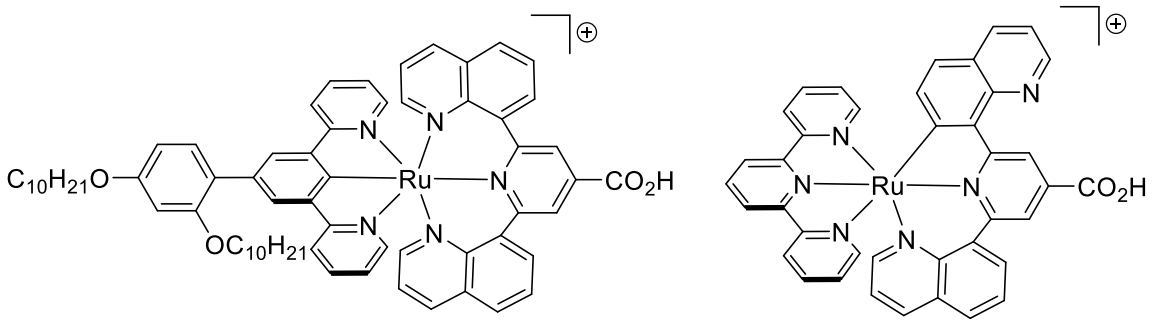

Figure 8 Ruthenium complexes with mixed five- and six-membered metallacycles. Ruthenium favours cyclometalation forming five-membered metallacycles. Roll-over metalation is observed, if no suitable ligand N^C^N is present (right side).[61]

During synthesis, the [Ru(QPyQ)Cl$_3$] complex is reacted with the PyHPhPy derivative, undergoing cyclometalation and yielding the desired product. However, a reaction with the ring-expanded analogue, QHPhQ, does not yield the desired product and no conversion was observed. When reacting [Ru(QPyQ)Cl$_3$] with terpyridine, a rollover cyclometalation of one of the quinoline-rings was observed, featuring a five-membered metallacycle.[61] These ruthenium complexes have found application towards dye-sensitized solar cells (DSC) because of their promising luminescent properties.[61]

Structurally similar ruthenium complexes, featuring the ring-expanded N^N^N-type protoligand QPyQ have been reported for applications in polymer chemistry (see Figure 9). [62]

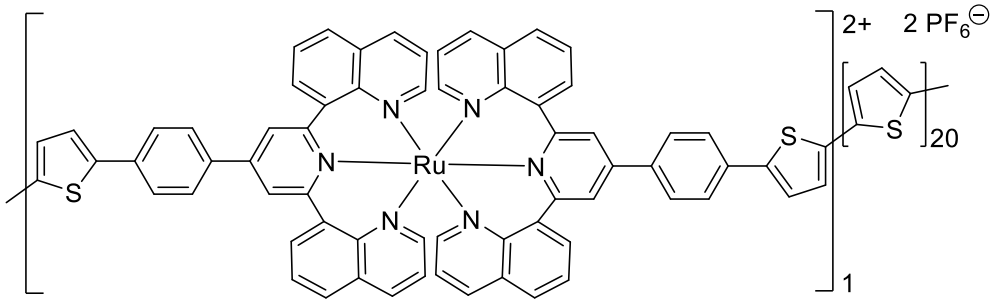

Figure 9 Example of thiophene based polymer including [Ru(QPyQ)]$^{2+}$ complexes.[62]

The introduction of the ruthenium complex units into thiophene based polymers lead to increased luminescence. Additionally, their electrochemistry featured remarkable stability upon oxidation. Additionally, polymers of high ruthenium-complex content also featured reversible switching of polymer conductivity based on this oxidative stability.[62] These properties are useful applied in solar cells like the cyclometalated complexes discussed earlier, or potentially in light- and redox-driven sensoring.[61, 62]

1.3 Methods for the Synthesis of Pt(II), Pd(II) and Ni(II) Complexes with Tridentate Cyclometalating Ligands

1.3.1 C–H-Activation for Pt(II) Complexes

The complexation of Pt(II) towards ring-expanded systems (e.g. [Pt(QPhQ)Cl]) was carried out under conditions previously reported for complexes with five-membered metallacycles. [18, 52] Generally, these ring-expanded complexes seem to follow the same reactivity for both Pt(II) and Pd(II). [18, 55]

The first direct C–H-activation synthesis of complexes with tridentate cyclometalated N^C^N-type ligands was reported in 1999. [1] The protoligand, (pyridine-phenyl-pyridine, PyHPhPy) was reacted with potassium tetrachloroplatinate in acetic acid at reflux temperature, yielding the desired product (see Scheme 2).[1]

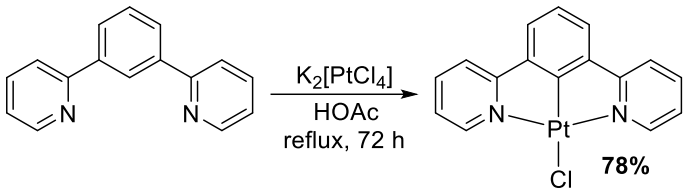

Scheme 2 Synthesis of [Pt(PyPhPy)Cl], as first reported by *Cardenas et al. in 1999*.[1]

Since then, this method has found application for a vast range of cyclometalated platinum complexes, proving its reliability and versatility.[52, 54, 63-73]

1.3.2 C–H-Activation for Pd(II) Complexes

The same conditions can be extended to Pd(II), which undergoes cyclometalation under similar conditions.[55, 74-77] However, when the protoligand PyHPhPy (see Scheme 3) is reacted under the same conditions, a different product then the intended cyclometalated product is obtained.

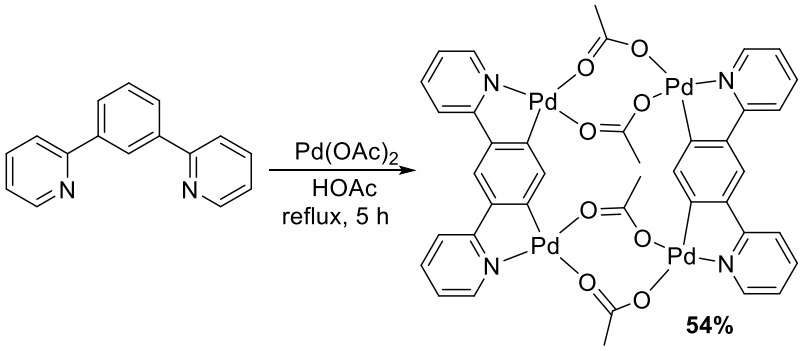

Scheme 3 Reacting PyHPhPy with a palladium precursor under acidic C–H-activation conditions leads to a dimeric species instead of the desired complex.[1]

Instead, the pyridine rings rotate around their connecting single bond and C–H-activation takes place not in the intended tridentate binding pocket but on both sides of the phenyl rings in a bidentate fashion. The result is a bridged structure featuring two protoligands with a total of four cyclometalated palladium centres, bridged by acetate-ligands (see Scheme 3).[1] This behaviour is not limited to the PyHPhPy protoligand and can occur for all protoligand that allow for ring rotation.[73] To circumnavigate this, the exterior activation cites can be blocked by substitution. The complex [Pd(PyMe2PhPy)Cl] undergoes base-assisted C–H-activation, resulting in the intended N^C^N type coordination (see Scheme 4).[2]

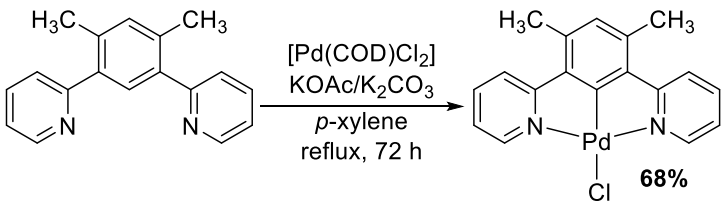

Scheme 4 Synthesis of [Pt(PyMe2PhPy)Cl], as reported by *Kletsch et al*. in 2021.[2]

Studies of the role of palladium in C–H-functionalisation and cross-coupling catalysis also suggest a direct involvement of acetate groups, as present in the commonly used catalyst $Pd(OAc)_2$.[78-80] The bidentate acetate coordinates to the metal ion and can then interact with the C–H bond. This weakens it and facilitates subsequent, formally base assisted, C–H-activation.[78-80] The same mechanism is feasible for acetate-species generates *in situ* from metal precursors in acetic acid solution.

C–H-activation of C^N^N type ligands (e.g. HPhPyPy) with $K_2[PdCl_4]$ was reported in a solvent mixture of acetonitrile and water under reflux.[81] These complexes can also be synthesized by oxidative addition, reacting halogenide-bearing protoligands with suitable Pd(0) precursors (e.g. $[Pd_2(dba)_3]$).[81]

1.3.3 C–H-Activation for Ni(II) Complexes

Nickel(II) requires different conditions to achieve cyclometalation compared to Pd(II) and Pt(II). Instead of direct C–H-activation in solvents, base-assistance is needed.[17, 26]

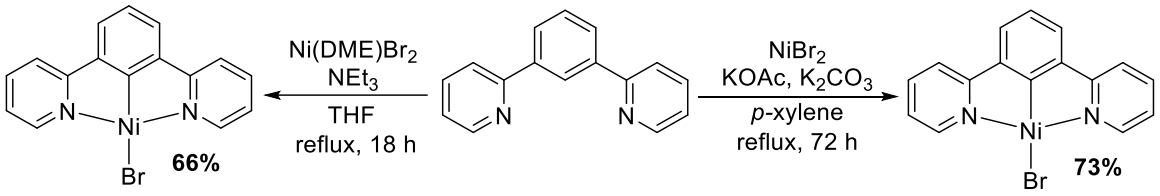

Scheme 5 Different conditions of base-assisted C–H-activation of PyHPhPy with Nickel-precursors.[17, 26]

This can either be achieved by using triethylamine and $Ni(DME)Br_2$ as a soluble nickel precursor in THF, or $NiBr_2$ alongside a mixture of KOAc and K_2CO_3 in *p*-xylene at reflux temperature under strict exclusion of moisture.[17, 26] These methods have proven versatile for the preparation of various cyclometalated nickel systems since their first publication in 2020.[2, 12, 13, 49, 77, 82-89]

While Ni(II) can undergo C–H-activation reactions similar to Pd(II) and Pt(II) it does so at much harsher conditions, even with the assistance of base (see Scheme 5).[17, 26] This need for much higher activation energy shows the lower driving force nickel has towards C–H-activation compared to its heavier analogues. Paired with the much higher susceptibility of nickel complexes to hydrolysis and solvolysis, the preparation of nickel complexes is more challenging overall.[13, 49] Alternatively, transmetallation using organo-mercury compounds or oxidative addition of halogenated protoligands and Ni(0) can be employed to obtain the corresponding complexes.[3, 24]

While the C–H-activation conditions discussed were applied to the complexation of Pt(II) with ring-expanded protoligands in the past, the same has not been done yet for nickel and only in a limited way for Pd(II).[18, 52, 55]

2 Scientific Objectives

2.1 Complexes with Ring-Expanded Tridentate Cyclometalated Ligands

The main scientific objective of this work is the synthesis of new cyclometalated, tridentate complexes of Ni(II), Pd(II) and Pt(II). These complexes should feature at least one six-membered cyclometalated ring system and can encompass various donor atoms. To retain a neutral complex, a donor motif of either N^C^N or C^N^N was chosen for the first target protoligands. This leaves various combinations of either 5^6, 6^5 or 6^6-type cyclometalated ring systems (see Figure 10).

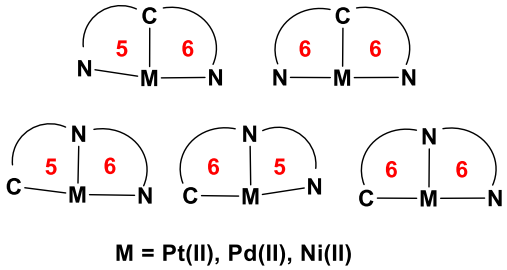

Figure 10 Overview of possible cyclometalated complexes with tridentate cyclometalated ligands of N^C^N and C^N^N type, bearing five- or six-membered metallacycles (red numbers). The coligands are omitted for clarity.

Various coupling methods are suitable to synthesize these different protoligands. The most approachable and widely applicable method would be coupling under *Suzuki*-conditions.[90, 91] Using this method, symmetric protoligands could be synthesized in one step with suitable building blocks (see Scheme 6).

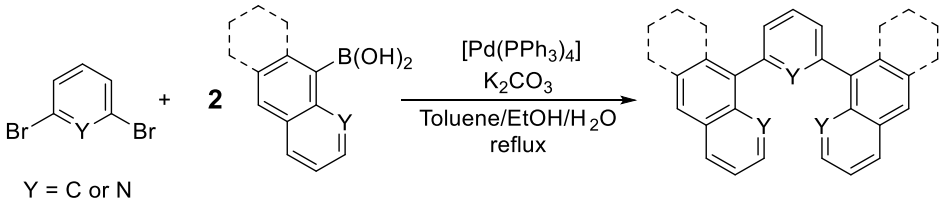

Scheme 6 General synthetic procedure towards the synthesis of symmetrical 6^6-membered protoligands via *Suzuki*-coupling.

These building blocks should contain the donor, nitrogen, and be an aromatic system. This way the rigidity of the individual rings can be guaranteed and the binding pocket can be approximated before complexation, to insure cyclometalation at the desired position, if possible. [1] For the six-membered cyclometalated rings, 8-quinolinyl boronic acid is a very useful building block, ensuring the desired protoligand properties.

A problem arises for the synthesis of asymmetric protoligands, of mixed 5^6-membered ring sizes. The essential building block for 5-membered cyclometallacycles is the 2-pyridinyl-moiety. However, 2-pyridinyl-boronic acid, as well as its pinacol ester, are both highly susceptible to solvolysis and decompose fairly rapidly in solution, even without

addition of other reactants.[92] While these building blocks can be synthesized, and therefore are commercially available, they are expensive and difficult to handle. This leads to poor yields and renders them unattractive for synthesis. Therefore, care should be taken to plan protoligand synthesis accordingly, avoiding the need for a pyridine-boronic acid moiety. Instead, aryl-bromides can be used, coupling them to boronic acids (see Scheme 7).

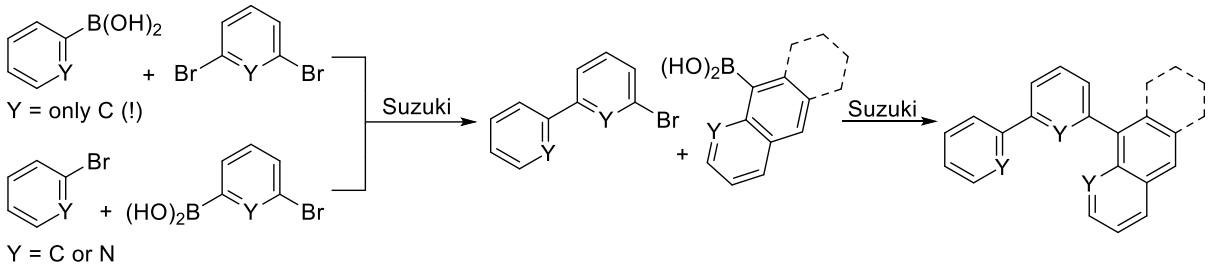

Scheme 7 General synthetic procedure towards the synthesis of asymmetrical 5^6-membered protoligands via *Suzuki*-coupling.

This general approach can be applied to build up various protoligand systems of both C^N^N and N^C^N type. If needed, different reaction conditions can be used to couple already built-up ring systems with building blocks requiring different conditions like other cross-coupling reactions (e.g. *Negishi*) or condensation reactions.

Using the same methodology, aromatic rings bearing donor atoms other than nitrogen can be introduced. This way, protoligands with potential N^C^S-, N^C^O- or even S^C^S-binding are obtained (see Figure 11).

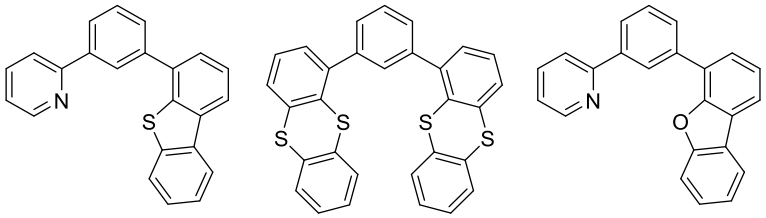

Figure 11 Examples of target protoligands with sulphur or oxygen donor moieties.

The precoordination typical for N^C^N and C^N^N type ligands should be less strong for sulphur and especially oxygen donors.[26] [93] This could be reflected both in the reactivity of the protoligands towards complexation, as well as in the stability of the resulting complexes. These ligands could exhibit different reactivity, sulphur donors showing stronger bonding with Pt(II) and Pd(II) and oxygen donors with Ni(II), according to HSAB theory.[94]

2.2 Synthesis of Pt(II), Pd(II) and Ni(II) Complexes with Ring-Expanded Tridentate Cyclometalated Ligands

With the protoligands in hand, cyclometalation can be achieved by applying previously reported C–H-activation conditions (see Scheme 8). Heating the protoligands with suitable metal precursors in acetic acid is a suitable method for the metals Pd(II) and Pt(II).[18, 25] For Ni(II), a base assisted method must be used, heating the protoligands with nickel bromide, potassium acetate and potassium carbonate in *p*-xylene at reflux temperature (see Scheme 8).[26]

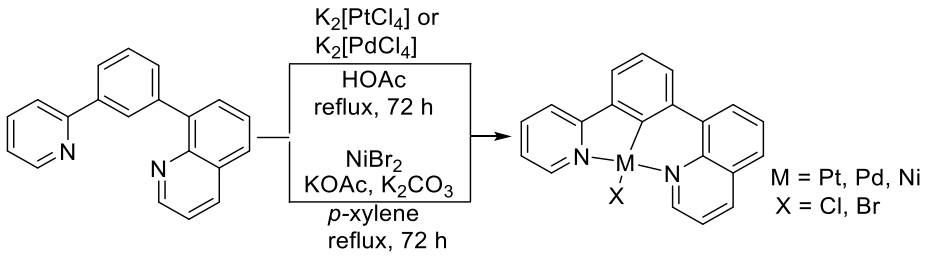

Scheme 8 Reactions conditions for C–H-activation of Ni, Pd and Pt using a model protoligand (pyridine-phenyl-quinoline, PyPhQ).[25, 26]

If C–H-activation under the discussed conditions cannot be achieved, other C–H-activation methods need to be screened for. Alternatively, oxidative addition approaches can be used. This would need adaptation of the protoligands, introducing halogen-bearing building blocks early on.

2.3 Coligand Exchange Reactions

To further change and fine-tune the properties of obtained complexes at a late stage, coligand exchange reactions will be carried out. While many reaction conditions have been reported for such reactions, often a case-by-case approach is necessary to screen for ideal conditions (see Scheme 9).[9, 95]

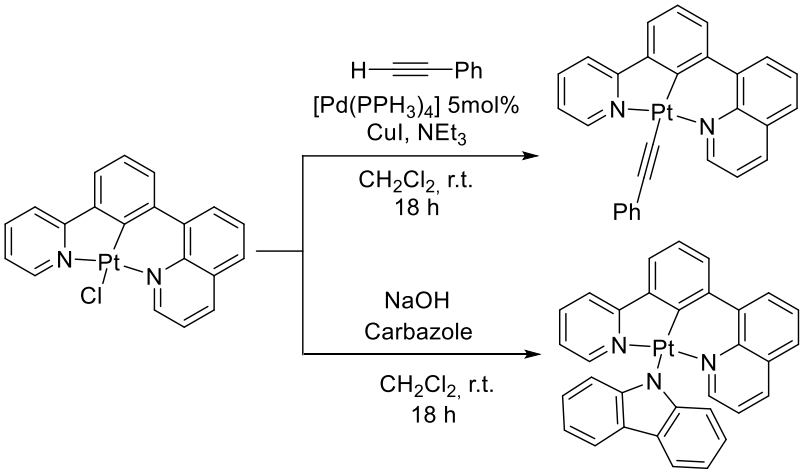

Scheme 9 Potential reaction conditions for coligand exchange reactions on the complex [Pt(PyPhQ)Cl].[9, 95]

With optimal conditions found, coligand exchanged complexes can be compared to establish a portfolio of suitable coligands to influence optical and electronical properties.

With the desired complexes in hand, their optical and electrochemical properties will be studied in detail using suitable methods, with a special focus on the effect of the ring-expansion on the structure and properties. To this end, structural analysis by single crystal X-ray diffraction will be used if possible. Additionally, luminescence spectroscopy and DFT-calculations will be carried out.

3 Results and Discussion

3.1 Publication: Pt(II), Pd(II), and Ni(II) Complexes with Tridentate Cyclometalating Five- and Six-Ring Chelating N^C*N, C^N*N and N*C*N Quinolinyl Ligands

The structural motif of complexes with ring-expanded ligands was explored by altering previously reported tridentate cyclometalated complex systems by addition of quinoline moieties replacing pyridines. The resulting complexes with N^C^N and C^N^N binding where fully characterized by NMR spectroscopy and mass spectrometry. Their properties were investigated in detail by UV/Vis-absorption spectroscopy, luminescence spectroscopy and cyclic voltammetry, validated by DFT-calculations. The structure of the complexes was elucidated by single crystal XRD.

The findings of these investigations were published in Organometallics 2025, 44, 7, 847–857 (https://doi.org/10.1021/acs.organomet.4c00500).[49] More detailed data is provided in the supplementary information.[49]

ORGANOMETALLICS

pubs.acs.org/Organometallics Article

Pt(II), Pd(II), and Ni(II) Complexes with Tridentate Cyclometalating Five- and Six-Ring Chelating N^C*N, C^N*N, and N*C*N Quinolinyl Ligands

Leo Payen, Tobias Lapić, Mathias Wickleder, and Axel Klein*

Cite This: Organometallics 2025, 44, 847−857 Read Online

ACCESS | Metrics & More | Article Recommendations | Supporting Information

ABSTRACT: Nine cyclometalated Ni(II), Pd(II), and Pt(II) complexes of the type [M(NCN)Cl] and [M(CNN)X] (X = Cl for Pt and Pd, or Br for Ni) containing 8-quinolinyl (Q), 2-pyridyl (Py), and phenyl (Ph) moieties are presented. The introduction of Q leads to six-ring chelates (N*C or N*N) compared with five-ring chelates (C^N or N^N) for 2-pyridyl-containing systems in the $PyPhQ^-$ (N^C*N), $QPhQ^-$ (N*C*N), and $PhPyQ^-$ (C^N*N) ligands. Single-crystal X-ray diffractometry showed the six-ring chelate units with angles around 90° compared with 80° for the five-ring chelates. Marked tilts of the planar Q systems toward the central Py or Ph core (up to 37°) were observed. Cyclic voltammetry showed first reduction potentials varying from −1.8 to −2.2 V vs ferrocene/ferrocenium and oxidations at around 0.45 V for Pt, 0.75 V for Pd, and 0 V for Ni complexes. DFT-calculated energies and compositions of the frontier molecular orbitals allowed assigning reductions to ligand-centered processes and oxidations to processes with mixed X(p)/M(d)/Ph(π) contributions. Long-wavelength UV−vis absorption maxima ranging from 400 to 430 nm were assigned to mixed ligand-centered(π−π^*)/metal(d)-to-ligand(π^*) transitions. The new complex [Pt(PyPhQ)Cl] showed very long-wavelength photoluminescence (>600 nm), similar to that of the previously reported [Pt(QPhQ)Cl] derivative.

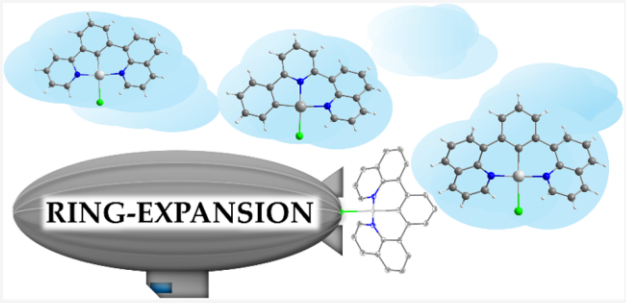

INTRODUCTION

Cyclometalated Pt(II), Pd(II), and Ni(II) complexes have been extensively studied in the last 20 years for their interesting photophysical and catalytic properties,[1−7] with a particular focus on photoluminescence of Pt(II) and Pd(II) complexes[1,2,7−12] and catalysis of Pd(II) and Ni(II) derivatives.[3−6,13−17] For these square planar configured M(II) complexes, bi-, tri-, or tetradentate[7−12] cyclometalating *N*-heteroaromatic ligands have been frequently used. Among them are many tridentate ligands with either C^N^N, N^C^N, or C^N^C coordination,[7−11,15−28] which can be traced to the parent systems containing benzene units for the C moieties and pyridine groups as N moieties (Chart 1). These parent systems including 6-phenyl-2,2′-bipyridine (HPhbpy), 1,3-di(2-pyridyl)benzene (Hdpb), and 2,5-diphenyl-pyridine (H_2dpp) have been reported for all three metals and have been studied mainly for their photophysical properties, in particular, their ability for triplet luminescence.[7−12,19−25]

An obvious disadvantage of these tridentate ligands is their double five-ring chelated binding to the metal (Chart 1), which leads to angles markedly below 90° for the adjacent (*cis*-positioned) C or N groups and values markedly below 180° for the *trans*-positioned C or N groups of these ligands. It is easy to understand that for a square planar coordination of d^8 configured metals such as Pt(II), Pd(II), and Ni(II), such distortion leads to decreased ligand strength compared with a perfect square planar coordination close to 90 and 180° geometries.[29,30] The introduction of the N*C*N coordinating

Chart 1. Parent C∧N∧N, N∧C∧N, and C∧N∧C Ligands Based on Phenyl and Pyridyl Units[a]

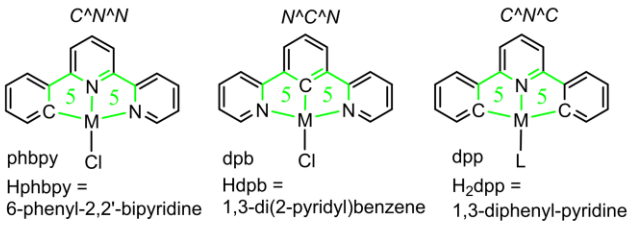

[a]The double five-ring chelate binding is depicted in green.

Received: December 13, 2024
Revised: March 7, 2025
Accepted: March 13, 2025
Published: March 26, 2025

Chart 2. Herein Studied Pt, Pd, and Ni Complexes[a]

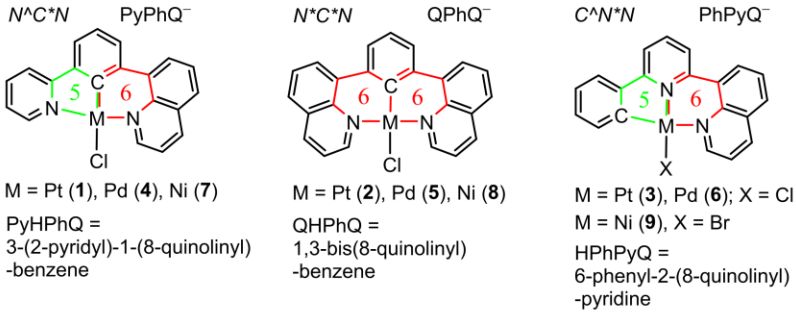

[a]With numbering from **1** to **9**. ^ and * denote five- and six-ring chelate coordinations. Five-ring chelates are colored in green and six-ring chelates in red. Complex **2** was previously reported.[31,34]

bis-1,3-bis(8-quinolyl)benzene (QHPhQ) ligand scaffold (Chart 2) allowed the generation of two six-ring chelates adopting far better the ideal 90 and 180° angles around Pt.[31−35] Indeed, [Pt(QPhQ)Cl] complexes showed geometries far closer to the perfect square planar configuration,[31−35] but the photoluminescence properties were not superior to the established five-ring chelate-containing derivatives.[31,32] Nevertheless, further cyclometalating ligands allowing six-membered chelates with Pt(II) have been developed such as the NR-bridged Py*Py∧Ph systems,[36−43] the recently reported [Pt(N*C*N)Cl] complexes containing the benzannulated 1,3-di(4-phenanthridinyl)benzene ligand[44,45] or the 1,8-bis(2-pyridyl)anthracene ligand.[32] The approach of using 8-quinolinyl units for N*C^N and C∧N∧N in cyclometalated complexes has been pursued in the $[Ru(L)_2]$ complexes containing the $QPhQ^-$ and $QPy(arene)^-$ ligands with arene = phenyl, naphthyl, and anthracenyl, thus representing N*C*N, N*N^C (C = phenyl), and N*N*C (C = naphthyl and anthracenyl) cyclometalating systems.[46]

Herein, we report a study of Pt(II), Pd(II), and Ni(II) complexes containing cyclometalating C^N*N, N^C*N, and N*C*N ligands bearing the 8-quinolinyl (*N) unit. The quinolinyl (Q) unit generates one (PhPyQ or PyPhQ; Py = pyridyl, Ph = phenyl) or two six-membered chelates (QPhQ) in the corresponding complexes (Chart 2). The coordination chemistry of the QPhQ ligand has been established only for Pt(II),[31−35] while it is completely missing for Pd(II) and Ni(II). Pt(II), Pd(II), and Ni(II) complexes of the PhPyQ and PyPhQ ligands are yet unknown. We expected a strengthening of the ligand field in the quinolinyl-containing complexes [M(PyPhQ)X], [M(QPhQ)X], and [M(PhPyQ)X] (M = Pt, Pd, or Ni, X = Cl or Br) (Chart 2) through the superior geometry of the six-membered rings (C*N or N*N) in them, compared with those of the established pyridyl-containing Phbpy and dpb derivatives that exhibit exclusively five-membered ring chelates (C^N or N^N). We studied the effects of the introduction of the six-ring chelates on the molecular and electronic structures in comparison with Phbpy and dpb derivatives (Chart 1). The electronic structures were investigated through electrochemical measurements and UV−vis absorption and photoluminescence spectroscopy in combination with (time-dependent) density functional theory ((TD)DFT) calculations.

RESULTS AND DISCUSSION

Synthesis and Characterization. For the cyclometalation reactions of Pt(II) and Pd(II), the protoligands (ligands before C−H metalation) PyHPhQ, QHPhQ, and HPhPyQ were synthesized using established Suzuki-type C−C cross-coupling methods (see Experimental Section in the Supporting Information, SI). The three Pt(II) complexes [Pt(PyPhQ)Cl] (**1**), [Pt(QPhQ)Cl] (**2**), and [Pt(PhPyQ)Cl] (**3**) were obtained from reactions with K_2PtCl_4 and the protoligands in glacial acetic acid under reflux in good yields of 95%, 80%, and 66%, respectively. Complex **2** has previously been synthesized from QHPhQ and K_2PtCl_4 in $MeCN/H_2O$ under reflux conditions in 56% yield, described as a yellow−green solid,[34] and in 14% yield, described as a gray−green solid.[31] We obtained a bright orange material with an 80% yield, pointing to a superior preparation method compared to those reported. The reported NMR data in $CDCl_3$[31,34] agrees qualitatively with our data recorded in DMSO-d_6 (page 4, SI).

The three Pd(II) derivatives [Pd(PyPhQ)Cl] (**4**), [Pd(QPhQ)Cl] (**5**), and [Pd(PhPyQ)Cl] (**6**) were synthesized under similar conditions with good yields of 92%, 49%, and 47%. This is remarkable because the same reaction using the well-established simplest heteroaromatic protoligand 1,3-dipyridyl-benzene (Hdpb) did not lead to the [Pd(dpb)Cl] complex right away. The noncyclometalated dinuclear complex $[Pd_2Cl_2(\mu\text{-}\kappa^2N,N\text{dpbH})]$ was obtained when starting from $PdCl_2$ or K_2PdCl_4, whereas the use of $Pd(OAc)_2$ gave the cyclometalated tetranuclear $[Pd_4(\mu\text{-}\kappa^2,\kappa^2\text{dpb})_2(\mu\text{-}\kappa^1,\kappa^1\text{-OAc})_4]$ species.[21,47] The high acidity in the 3,5-C−H functions at the central benzene moiety leads to double $N_{py}\text{^}C_{benzene}$ cyclometalation and tetranuclear complexes. This can only be prevented by the substitution of the benzene-1,3-positions as in the 3,5-Me_2-dpb derivative for which the complex [Pd(Me_2dpb)Cl] was previously obtained using this method.[21] We assume that the precoordination of Pd to the quinoline N atom leads to the preferred metalation of the central 2-CH benzene function, explaining our success.

For the nickelation reaction, we first tried the base-assisted C−H nickelation starting from the protoligands HPhPyQ, QHPhQ, or PyHPhQ and $NiBr_2$ using $KOAc/K_2CO_3$ as base and xylene as solvent in the same way as previously for the established N^HC^N = 1,3-dipyridyl-benzene (dpb)[16,21,47] or HC^N^N 6-phenyl-2,2′-bipyridine (Phbpy) protoligands.[48,49] Thus, we synthesized [Ni(PyPhQ)Br] (**7**) in 51% yield and [Ni(PhPyQ)Br] (**9**) in 24% yield. As this reaction failed for the QHPhQ protoligand, we synthesized the chlorinated ligand precursor QClPhQ and reacted it with $[Ni(COD)_2]$ (COD = 1,5,cyclooctadiene) in an oxidative addition approach,[17] forming [Ni(QPhQ)Cl] (**8**) in 43% yield.

https://doi.org/10.1021/acs.organomet.4c00500
Organometallics 2025, 44, 847−857

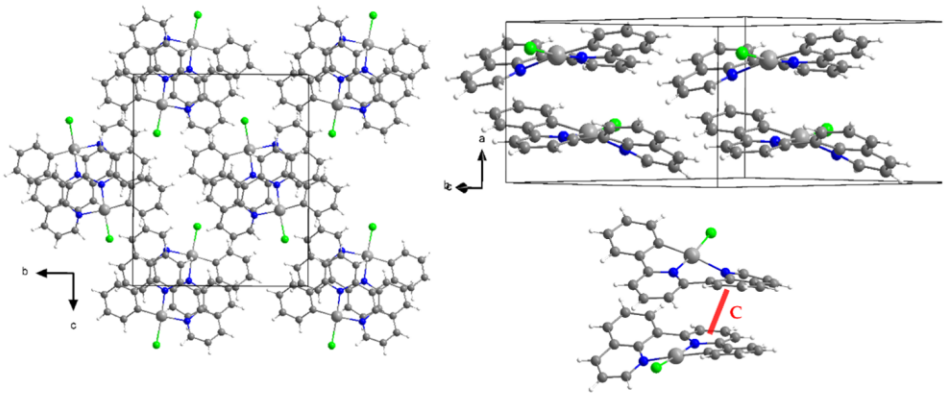

Figure 1. Views on the crystal structure of [Pt(PhPyQ)Cl] (**3**) along different axes from single-crystal X-ray diffraction (left and top right). Bottom right: the red bar **C** marks a π-stacking interaction with a centroid···centroid distance of about 3.82 Å.

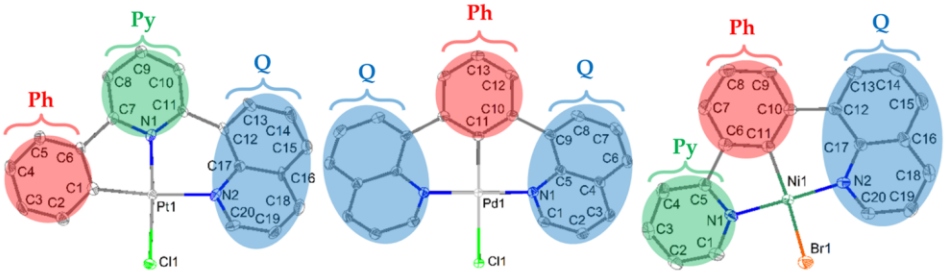

Figure 2. Molecular structures of [Pt(PhPyQ)Cl] (**3**) (left), [Pd(QPhQ)Cl] (**5**) (central), and [Ni(PyPhQ)Br] (**7**) (left) from single-crystal X-ray diffraction (ORTEP plots with displacement ellipsoids at 50% probability; H atoms not shown).

Table 1. Selected Metrics of the Molecular Structures of Complexes 1 to 5, 7, and 8[a]

	1	2	3	4	5	7	8
ligand motive	N^C*N	N*C*N	C^N*N	N^C*N	N*C*N	N^C*N	N*C*N
bond lengths (Å)							
M−C1	1.957(4)	1.958(5)	1.986(7)	1.948(1)	1.962(4)	1.855(4)	1.857(1)
M−N1	2.024(3)	1.990(3)	1.984(5)	2.045(1)	1.985(2)	1.925(3)	1.910(3)
M−N2	2.029(3)	2.050(3)	2.116(6)	2.039(1)	2.092(2)	1.909(3)	1.930(3)
angles (°)							
C/N−M−C/N (^)	82.0(1)	93.8(1)	82.30(2)	82.47(4)	90.63(6)	84.7(2)	90.2(1)
C/N−M−C/N (*)	93.1(1)	88.0(1)	92.7(2)	91.77(4)	89.00(1)	92.2(2)	89.9(1)
cis-C/N−M−X	91.9(9)	87.7(6)	93.7(2)	91.93(3)	90.27(6)	93.50(2)	91.3(8)
cis-N2−M−X	94.3(9)	90.5(6)	91.52(2)	95.50(3)	90.20(6)	94.69(2)	88.6(8)
trans C/N−M−N2	170.6(1)	177.9(1)	173.6(3)	169.2(4)	179.0(7)	165.5(2)	178.0(2)
trans C/N−M−X	168.1(1)	178.4(9)	174.6(2)	167.0(3)	179.2(1)	157.5(2)	178.4(1)
τ_4	0.148	0.024	0.081	0.166	0.010	0.260	0.023
interplanar angles (°)							
Ph/Py	5.2(2)		10.8(2)	4.9(6)		4.4(2)	
Py_{cent}/Q or Ph_{cent}/Q	12.9(3)	33.3(5)	28.9(2)	14.3(4)	33.9(6)	17.6(2)	36.9 (5)
Ph_{peri}/Q or Py_{peri}/Q	20.1(1)		37.9(2)	19.1(5)		21.4(2)	
Q/Q		66.7(8)			68.1(6)		73.3(7)

[a]From single-crystal X-ray diffraction (full data in Tables S1−S3), single crystals of **6** and **9** were not obtained. DFT-calculated structural data is available in Tables S5, S6, respectively.

In contrast to the complexes **1** to **6** and **8**, the Ni(II) complexes **7** and **9** showed very high reactivity toward hydrolysis, forming QHPhQ and HPhPyQ, respectively. While single crystals of **7** were feasible for X-ray diffractions and we were able to carry out basic measurements such as nuclear magnetic resonance (NMR), mass spectrometry (MS) and cyclic voltammetry (CV), we completely failed to study complex **9** [Ni(PhPyQ)Br] by experimental methods. All complexes were soluble in common organic solvents, such as $CHCl_3$, CH_2Cl_2, tetrahydrofuran (THF), acetone, and dimethyl sulfoxide (DMSO). Protic solvents must be avoided due to a high tendency of the complexes to undergo hydrolysis reactions, yielding protonated ligands (protoligands).

Crystal and Molecular Structures from Single-Crystal X-ray Diffraction and DFT. Single crystals of compounds **1** to **5**, **7**, and **8** were submitted to an X-ray diffraction study (data of structure solution and refinement in Tables S1−S3). The crystal structures (Figures 1, S1 and S15) show a head-to-

https://doi.org/10.1021/acs.organomet.4c00500
Organometallics 2025, 44, 847−857

tail orientation of the molecules within the unit cell. The packing of the molecular units is supported by the π-stacking of heteroarene rings in the chelate ligands (Figure 1, bottom right). However, due to the distortion of the peripheral Q moieties toward the central Ph or Py rings (see also later), the π-stacking is generally far less pronounced than in the complexes containing the almost completely coplanar PyPhPy or Phbpy ligand systems.[1,16−22,25,49−51]

The molecular structures (examples shown in Figure 2) show the distorted square planar coordination of the central metal. The τ_4 values representing the overall distortion (τ_4 = 0 for perfect square planar, τ_4 = 1 for tetrahedral geometry)[50] range from 0.010 to 0.260 (Table 1). The largest distortions for complexes **1**, **4**, and **7** result from the *trans* N/C−M−N angles around or even below 170° and the *trans* N/C−M−X angles ranging from 158 to 168°, thus deviating markedly from the ideal 180°. For the symmetric QPhQ complexes **2**, **5**, and **8**, showing very low τ_4 values of 0.01 to 0.024, these values are around 180° in keeping with a perfect square planar coordination for the six-ring N*C*N chelate coordination. Accordingly, perfect chelate bite angles around 90° are found for the N*N and C*N parts in all complexes compared with the C^N and N^N moieties showing typical bite angles of 82 to 84°.

As another consequence of the introduction of N*C and N*N six-ring chelates, the ligand scaffolds PhPyQ, QPhQ, and PyPhQ in the complexes deviate markedly from the coplanar arrangements of Ph and Py groups that are usually found for the tridentate N^C^N, C^N^N, or C^N^C ligands with five-membered chelates binding to Pt(II), Pd(II), or Ni(II).[15−17,20,21,37,47−54] A closer look reveals that **3**, **5**, and **8** show large Q/Q interplanar angles of 67° to 73° (Table 1). Interplanar angles from neighboring Q/Ph or Q/Py combinations range from 13 to 38°, while all Py/Ph combinations come with typically low angles of a few degrees.

DFT-calculated metrics for complexes **1** to **5**, **7**, and **8** agree very well with the experimentally observed values (Tables S5−S7). Therefore, we are confident that our calculated structures for **6** and **9** represent a good approach for the metrics of these molecules. The DFT-calculated molecular structure of complex **2** has been previously reported with a QPhQ interplanar angle of 38.5° and a *trans* N−Pt−N angle of 178.8°.[31] These values agree quite well with our experimental and DFT-calculated values. The same is true for the recently reported experimental crystal structure of the 3,5-dimethyl-phenide derivative of **2** that crystallized in the space group $P\bar{1}$ and shows *trans* angles N−Pt−N and C−Pt−Cl of 177.8(2) and 180.0, respectively.[32]

Electrochemistry and DFT-Calculated Frontier Molecular Orbitals. The complexes show multiple reduction waves in cyclic voltammetry (CV) in THF solution at 298 K (Figures 3, 4; CV plots in Figures S18−S21), which were also found for the protoligands (CV plots in Figures S16 and S17, data in Table S8). They can thus be provisionally assigned to ligand-centered processes. For the C^N*N coordinated PhPyQ complexes with a central pyridine unit, the first reduction occurring at around −2 V vs ferrocene/ferrocenium is reversible in keeping with our observations for related [M(C^N^N)X] complexes (M = Pt, Pd, Ni).[15−17,20,38,49,51,52]

For the N*/^C*N coordinated PyPhQ and QPhQ derivatives, this wave occurs irreversible, in line with related [M(N^C^N)X] complexes (M = Pt, Pd, Ni).[16,21,47,48,50,53,54] For the PhPyQ complexes, the first wave is followed by further irreversible reduction waves at around −2.5, −3.0, and −3.2 V,

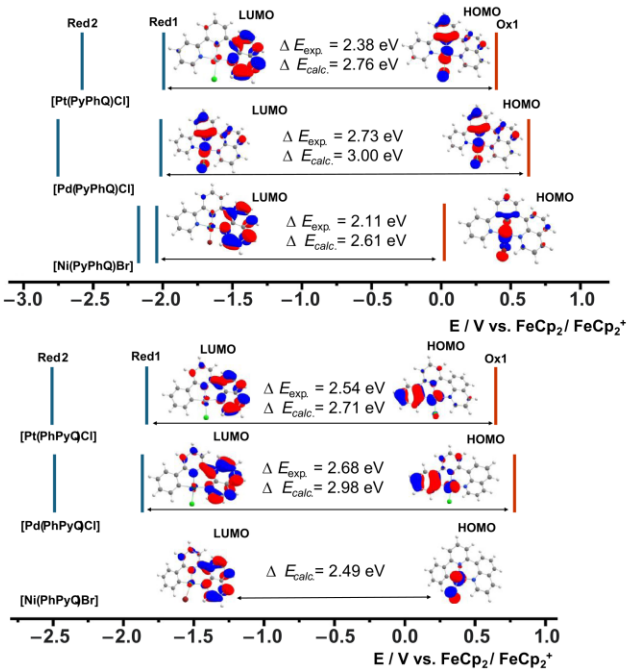

Figure 3. Redox potentials of [M(PyPhQ)Cl] (**1**, **4**, and **7**) (top) and [M(PhPyQ)X] (**3**, **6**, and **9**) (bottom) complexes from cyclic voltammetry presented as bars, with electrochemical gaps $\Delta E_{exp.}$ = E_{ox}−E_{red}, DFT-calculated HOMO−LUMO gaps $\Delta E_{calc.}$ (= E_{HOMO}−E_{LUMO}), and frontier molecular orbital surfaces of the HOMO (highest occupied molecular orbitals) and LUMO (lowest unoccupied molecular orbitals).

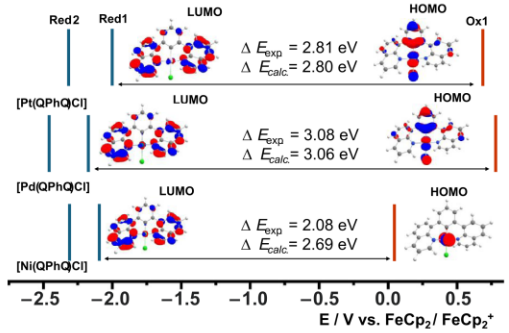

Figure 4. Redox potentials of [M(QPhQ)Cl] complexes (**2**, **5**, and **8**) from cyclic voltammetry presented as bars, with electrochemical gaps $\Delta E_{exp.}$ (= E_{ox}−E_{red}), DFT-calculated HOMO−LUMO gaps $\Delta E_{calc.}$ = E_{HOMO}−E_{LUMO}, and frontier molecular orbital surfaces of the HOMO (highest occupied molecular orbitals) and LUMO (lowest unoccupied molecular orbitals).

while the PyPhQ derivatives show one further partially reversible wave at around −2.8 V. The QPhQ complexes show two consecutive waves at −2.3 and −2.8 V (Figure 4; data in Table S9). The reported electrochemical data of complex **2** with Ox = 0.62 V, Red1 = −1.57 V, and Red2 = −2.26 V match those previously reported.[31] However, the MeCN solvent used in this study obviously causes marked differences for the potentials (compare 0.73, −2.08, and −2.32 V in THF; Table S9).

When comparing different ligand systems for the same metal, we found increasing (less negative) reduction potentials along the series dpb < QPhQ < PyPhQ < PhPyQ < Phbpy when including the double five-ring N^C^N (dpb) and

https://doi.org/10.1021/acs.organomet.4c00500
Organometallics 2025, 44, 847−857

Table 2. Selected Electrochemical and Photophysical Data of the Pt, Pd, and Ni Complexes

	X	M (no.)	$\Delta E_{ox1-red1}$ (eV)[a]	$\Delta E_{HOMO-LUMO}$ (eV)[b]	λ_{max} (nm)[c]	ΔE_{opt} (eV)[d]	reference
NCN							
PyPhQ	Cl	Pt (**1**)	2.38	3.384	418	2.97	this work
	Cl	Pd (**4**)	2.73	3.657	381	3.25	this work
	Br	Ni (**7**)	2.11	3.491	436	2.84	this work
QPhQ	Cl	Pt (**2**)	2.81	3.412	426	2.91	this work
	Cl	Pd (**5**)	3.04	3.701	388	3.20	this work
	Cl	Ni (**8**)	2.08	3.672	474	2.62	this work
dpb	Cl	Pt	2.58		401[e]	3.09	ref50,53
Me_2dpb	Cl	Pd	3.08	3.39	375	3.31	ref 21
dpb	Cl	Ni	2.39	3.08	437	2.84	ref 48
CNN							
PhPyQ	Cl	Pt (**3**)	2.54	3.343	367	3.38	this work
	Cl	Pd (**6**)	2.68	3.879	330	3.76	this work
Phbpy	Cl	Pt	2.23		430	2.88	ref48,51
	Cl	Pd	2.72	3.58	342	3.63	ref 51
	Br	Ni	1.98	2.717	506	2.45	ref 17

[a]From cyclic voltammetry (data, see Table S9). [b]DFT calculated. [c]From UV−vis absorption spectroscopy in THF (data, seeTable S11). [d]Taking the long-energy-maximum of the intense band system from 350 to 450 nm. [e]Further weak absorptions are found at 454 and 485 nm for this complex.

C^N^N (Phbpy) derivatives (Table S9). This means that the new quinoline-containing ligands fill the gap between the two established N^C^N ligands dpb and C^N^N ligand Phbpy. Assuming that a quinoline moiety has superior electron-accepting properties compared with those of a pyridyl group, several positions in this series are remarkable. The most prominent is the easiest reduction found for the Phbpy systems, while all quinoline-containing systems are seemingly poorer electron-acceptors. However, in Phbpy, all three rings are coplanar, and the ligand thus provides an extended bpy (2,2′-bipyridine) system for electron uptake. In contrast to this, PyPhQ and PhPyQ contain both the poorer electron-accepting unit PyPh as a coplanar two-ring π-system. The Q moieties are tilted from the central Py or Ph moiety by 12 to 18° for PyPhQ, 29 to 32° for PhPyQ, and 32 to 37° for QPhQ (Figures S10−S12), meaning that the quinoline moieties have only small (PyPhQ) or no (PhPyQ and QPhQ) contributions to an extended two-ring π system for electron uptake. QPhQ has no coplanar extended π-system, but its superior electron-accepting properties compared with dpb confirm the initial assumption that Q is a better acceptor compared with Py.

DFT-calculated LUMO energies agree with this idea as they see the QPhQ complexes at around −2.3 eV, the PyPhQ derivatives at around −2.4 eV, and the PhPyQ homologues at less than −2.5 eV. A perfect fit of the calculated data with the experimental data is probably impeded, as the DFT calculations underestimate the tilt angles and thus overestimate conjugation in the near-coplanar PhPy units.

The DFT-calculated compositions of the lowest unoccupied molecular orbitals (LUMO) essentially confirm our assumptions regarding the electron-accepting moieties. For the nonsymmetric PyPhQ complexes **1**, **4**, and **7**, the LUMOs are essentially localized on the quinoline moiety (Figures 3 and S22). The LUMO+1 is dominated by the PyPh unit. The LUMO+2 for the Ni complex **7** shows marked contributions of the antibonding $d_{x^2-y^2}$ orbital, while for the Pd (**4**) and Pt (**1**) derivatives, this orbital lies far higher in energy, in line with the larger ligand field splitting of the heavier elements. For **1** and **4**, LUMO+2 is essentially a π^* orbital localized in the Py moiety. For the PhPyQ complexes, the situation is very similar, with quinoline-centered LUMOs, PhPy dominating the LUMO+1, and the antibonding $d_{x^2-y^2}$ orbital representing the LUMO+2 of the Ni(II) complex **9** (Figure S24). For the symmetric QPhQ complexes **2**, **5**, and **8**, the first three LUMOs are dominated by quinoline π^* orbitals (Figure S23). Interestingly, this included LUMO+2 for the Ni(II) derivative **8**. The orbital with a marked contribution from the antibonding $d_{x^2-y^2}$ orbital is found as LUMO+6 at −1.138 eV and thus lies much higher than the LUMO+2 in the PyPhQ complex **7** (−1.831 eV, Figure S22) and the PhPyQ derivative **9** (−2.158 eV, Figure S24) in keeping with the strongest ligand field expected for the superior 2 × six-ring chelate metal−ligand binding of the QPhQ ligand.

The oxidation waves are irreversible for the Pt and Pd complexes, and the potentials range from 0.45 to 0.83 V. In contrast to this, they are reversible for Ni and occur at markedly lower potentials around 0 V. This is in line with observations for related N^C^N or C^N^N complexes of the three metals.[15−17,20,21,38,48−54] Within the series of Pt complexes, the potentials increase along the series dpb < Phbpy < PyPhQ < QPhQ = PhPyQ (Table S9), placing the six-ring chelate-containing ligands on top in keeping with a stronger ligand field. The DFT-calculated highest occupied molecular orbitals (HOMO) for the PhPhQ and QPhQ complexes are found in the central part and comprise Cl or Br p-orbitals, metal d_{xz} orbitals, and parts of the Ph π system (Figures S22, S23). For the PhPyQ Pt (**3**) and Pd (**6**) derivatives, a combination of Cl p and metal d_z^2 is found as HOMO−1 (Figure S24). Interestingly, for the PhPyQ Ni(II) complex (**9**), the HOMO has main contributions from Ni d_z^2 and Br p-orbitals, while the HOMO−1 looks like the HOMO of the Pt and Pd derivatives.

Thus, the electrochemical oxidations can overall be assigned to metal-centered redox-pairs M(II)/M(III) with contributions from the halido coligand and the phenyl groups, regardless of whether they reside in the central or the peripheral position of the tridentate ligands.

The experimental electrochemical gaps $\Delta E_{ox1-red1}$ decrease in each series of ligands along the series Pd > Pt > Ni. This is in keeping with the previously reported series of isoleptic

https://doi.org/10.1021/acs.organomet.4c00500
Organometallics 2025, 44, 847−857

complexes of the nickel group.[16,20,21,54−60] In agreement with Koopmans' and Janak's theorems,[61−63] we compared the DFT-calculated HOMO−LUMO gaps ($\Delta E_{HOMO-LUMO(calc)}$) with the electrochemical gaps. However, our DFT-calculated HOMO−LUMO gaps show the lowest values for the Pt complexes, reversing the series to Pd > Ni > Pt (Table 2).

When comparing the different ligand systems for the Pt complexes, the experimental gaps decrease along the series QPhQ > dpb > PhPyQ > PyPhQ > Phbpy (Table 2), which differs from the series for the reduction potentials (dpb < QPhQ < PyPhQ < PhPyQ < Phbpy) in that QPhQ and dpb as well as PyPhQ and PhPyQ have changed positions. The very high position of the QPhQ systems underlines that the ligand field splitting is highest for this double-ring-extended system, which stabilizes the HOMO through strong metal−ligand bonding and destabilizes the LUMO through hampering the formation of an extended two-ring π system.

The above-discussed differences of the reported electrochemical potentials for complex **2** with an electrochemical gap $\Delta E_{ox1-red1}$ of 2.30 eV in MeCN solution compare well to the reported calculated HOMO−LUMO gap of 2.61 eV,[31] confirming the marked impact of the solvent.

UV−Vis Absorption Spectroscopy. The eight complexes show very intense absorption bands in the UV range from 200 to 270 nm and a bit less intense bands in the range from 270 to 350 nm (Figures 5, 6; spectra for the QPhQ complexes **2**, **5**,

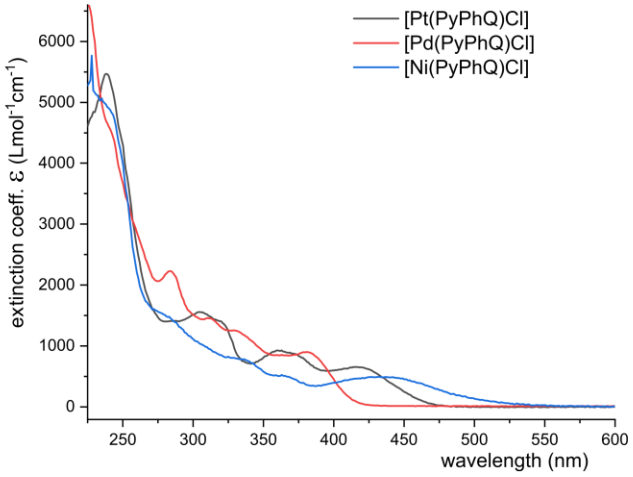

Figure 5. UV−vis absorption spectra of [Pt(PyPhQ)Cl] (**1**) (black), [Pd(PyPhQ)Cl] (**4**) (red), and [Ni(PyPhQ)Cl] (**7**) (blue) in THF at room temperature.

and **8** in Figure S29). They are also found for the protoligands PhHPhQ, QHPhQ, QClPhQ, and HPhPyQ (Figures S25 and S28, data in Table S10) and can be assigned to ligand-centered (LC) $\pi-\pi^*$ transitions. Long-wavelength bands are observed in the range from 300 to 500 nm depending on the ligands and the metal (Table 2, full data in Table S11). They are the highest in energy for the Pd(II) complexes, while Pt(II) and Ni(II) derivatives are red-shifted. Such Pd(II) > Pt(II) > Ni(II) series for absorption energies have been observed previously for other series of isoleptic complexes of the nickel group[16,20,21,55−60,64] and is in line with our observed electrochemical gaps $\Delta E_{ox1-red1}$ (Table 2).

When taking the Pt complexes, the long-wavelength absorption energies for the different ligand systems decrease

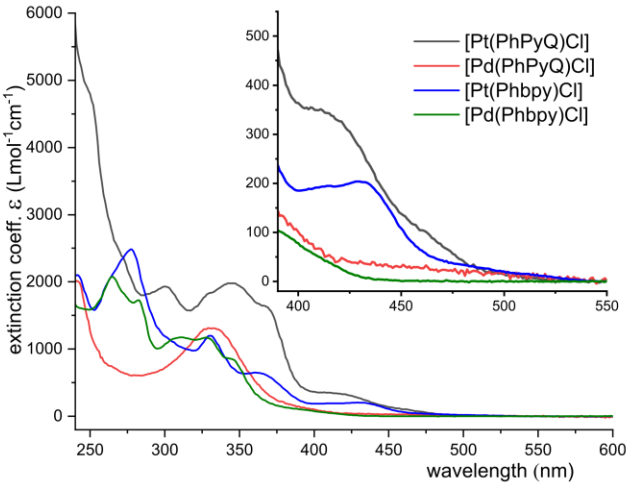

Figure 6. UV−vis absorption spectra of [Pt(PhPyQ)Cl] (**3**) (black), [Pd(PhPyQ)Cl] (**6**) (red), [Pt(Phbpy)Cl] (blue), and [Pd(Phbpy)-Cl] (green) in THF at room temperature.

along the series PhPyQ > dpb > PyPhQ > QPhQ > Phbpy (Table 2; full data in Table S11).

The reported absorption spectrum of complex **2** in CH_2Cl_2 shows maxima at 320, 356, and 420 nm,[31] which reveals a slight blue shift of the long-wavelength band at 420 nm compared to that in THF at 426 nm while the other maxima are conserved (Table S11). The DFT-calculated excited S_1 state lies at 475 nm.[31]

Photoluminescence Spectroscopy. The photoluminescence spectrum of the previously reported [Pt(QPhQ)Cl] (**2**)[31] shows a broad, partially structured emission with the main maximum lying at 640 nm and a high-energy shoulder at 605 nm when irradiated at 430 nm in THF solution at 293 K (Figure 7). For the new complex [Pt(PyPhQ)Cl] (**1**), the spectrum looks very similar, with the difference that the main maximum lies at 610 nm, in addition to a second maximum at 647 nm, when exciting at 445 nm (Figure 7). The excitation spectrum shows a long-wavelength excitation peak at 450 nm (Figure S31) in keeping with the long-wavelength shoulder in

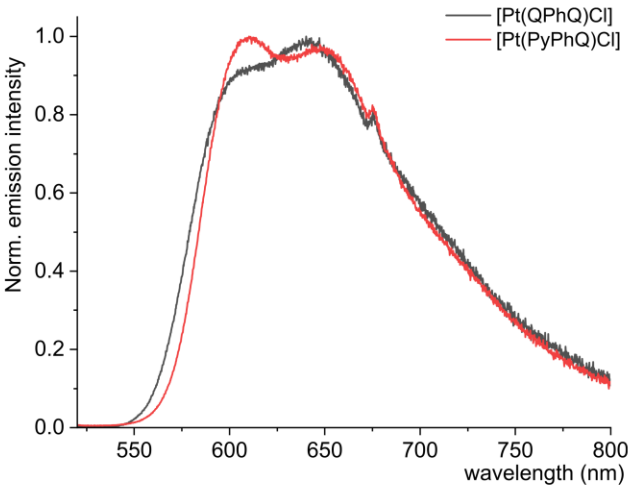

Figure 7. Photoluminescence spectrum of [Pt(QPhQ)Cl] (**2**) (black) at 293 K in a THF solution, λ_{exc} = 430 nm, and photoluminescence spectrum of [Pt(PyPhQ)Cl] (**1**) (red) at 293 K in a THF solution, λ_{exc} = 445 nm.

https://doi.org/10.1021/acs.organomet.4c00500
Organometallics 2025, 44, 847−857

the absorption spectrum (Figures 5 and S32). As for **1**, the excitation spectrum of **2** coincides with the long-wavelength absorptions (Figures S33, S34). In contrast to this, the C^N*N complex [Pt(PhPyQ)Cl] (**3**) fails to show photoluminescence under the same conditions. The same is true for Pd derivatives **4**, **5**, and **6**.

Irradiation of the complex [Ni(PyPhQ)Br] (**7**) at 360 nm leads to a broad emission band peaking at 480 nm and tailing down to about 700 nm (Figure S35). The bands in the corresponding excitation spectrum (Figures S35, S36) are merged with the Raman peak of THF at 355 nm, indicative of a very weak emission. Upon irradiation at 435 and 465 nm which coincides with the long-wavelength absorption band of the complex, no emission was observed. The protoligand PyHPhQ did not show any photoluminescence when irradiated at wavelengths ranging from 260 to 340 nm. Thus, we can rule out that the 480 nm emission is due to the protoligand occurring either as an impurity in the material of the complex or stemming from the hydrolysis of the complex. For the symmetric complex [Ni(QPhQ)Cl] (**8**), very similar photoluminescence behavior is found, with a very weak emission peaking at 540 nm and tailing until 700 nm when irradiating at 416 nm (Figure S37). The bands of the corresponding excitation spectrum coincide approximately with the absorption spectrum of the complex (Figure S38). The broad emission band is remarkable, as protoligands QHPhQ and QClPhQ did not show any emission when irradiated at wavelengths ranging from 250 to 350 nm under otherwise identical conditions.

For complex **2**, triplet luminescence (phosphorescence) was previously reported in a fluid CH_2Cl_2 solution at 298 K with maxima λ_{em} at 611(sh) and 645 nm,[31] fully in line with our results. This is markedly red-shifted compared with the N^C^N coordinated [Pt(dpb)Cl] complex with λ_{em} = 491, 524, and 562 nm at $\lambda_{ex} \sim$ 400 nm.[31,52−54,65] The photoluminescence quantum yield of **2** of 1.6% is drastically reduced compared with that of [Pt(dpb)Cl] (60%), while the lifetime lies in the same range (14 vs 7.2 μs).[31] A study of the 3,5-dimethyl-phenide derivative of **2** reported very similar data.[32] The difference observed between the N*C*N cyclometalated complex **2** and the N^C^N coordinated [Pt(dpb)Cl] was explained mainly through the difference in the radiative rate constant of **2** of 1.1×10^3 s^{-1} compared with 83×10^3 s^{-1} for [Pt(dpb)Cl], while the nonradiative decay is of a similar order in the two complexes (70 vs 56×10^3 s^{-1}). Furthermore, the authors assumed lower spin−orbit coupling for **2**.[31] In other words, the "triplet radiative transition is less allowed for **2** than that for [Pt(dpb)Cl]". In a recent study, a similar [Pt(N*C*N)Cl] complex with a Py*anthracenyl*Py ligand was reported to show no emission at ambient T in a fluid solution.[32]

Thus, for PtCl complexes, the N^C^N ligand dpb^- is largely favored over the N*C*N ligand $QPhQ^-$ and the overall photoluminescence performance of the N^C*N coordinated PyPhQ complex **1**, which is very similar to that of **2**, and the complete failure of the C^N*N coordinated PhPyQ complex **3** lets us conclude that the six-ring chelates decrease the probability of emission from an excited triplet state. The same seems to be true for PdCl derivatives. The reason for this is probably connected to the distortion of the peripheral Q moieties toward the central Py or Ph units in the complex geometries hampering the emission. However, the distortion might as well lead to a lower population of the emissive state.[64] Therefore, the nature of this correlation is far from being clear, which calls for detailed DFT calculations on the excited states.

Furthermore, the weak green photoluminescence of Ni(II) complexes **7** and **8** suggests that N*C*N ligands, although detrimental to the luminescence of PtCl and PdCl complexes, might be favorable for NiX systems. Additionally, we are confident that the exchange of the halide coligands to more suitable derivatives might also help pave the way to phosphorescent Ni(II)(N*C*N) complexes. Recently, the [Ni(dpb)(carbazolate)] complex was reported as the first phosphorescent Ni(II) of this structure type.[22] In this study, the coligand exchange from Cl^- to carbazolate was decisive.

CONCLUSIONS

The introduction of 9-quinolinyl (Q) moieties instead of pyridyl (Py) in the established tridentate cyclometalating ligands 1,3-dipyridylbenzene (Hdpb) with an N^C^N motive and 6-phenyl-2,2′-bipyridine (HPhbpy) offering a C^N^N motive leads to six-membered chelate moieties Py*Q or Ph*Q in corresponding complexes with tridentate C^N*N, N*C*N, and N^C*N ligands. In this initial study, we synthesized nine complexes resulting from the combination of Pt(II), Pd(II), and Ni(II) with the three ligands 1-(8-quinolinyl)-3-(2-pyridinyl)-phenide ($PyPhQ^-$; N^C*N motive), 1,3-diquinolino-phenide ($QPhQ^-$; N*C*N motive), and 2-phenide-6-(8-quinolinyl)-pyridine ($PhPyQ^-$; C^N*N motive), with * denoting binding moieties firming six-ring chelates and ^ binding sites forming five-membered chelate rings with these metals. We studied structures and electrochemical and basic photophysical properties to probe for the impact of this variation in chelate-binding sites.

As expected, the introduction of the six-ring chelates N*N or N*C optimized the chelate bites toward 90° compared with around 80° for five-ring chelates N^C and N^N, leading to increased ligand field splitting as could be observed from electrochemical data and DFT-calculated energies and compositions of frontier orbitals. For the Ni complexes, the QPhQ derivative shows the highest DFT-calculated energy for the antibonding $d_{x^2-y^2}$ orbital in line with this. On the other hand, the marked tilts of the Q systems toward the central Py or Ph core (up to 37°) hamper or disable the formation of two-ring-extended π systems, and the remaining PhPy moieties in PyPhQ and PhPyQ are poorer electron-acceptors as the bpy system in Phbpy as can be seen in lower (more negative) reduction potentials and blue-shifted UV−vis absorptions. The double six-ring chelate QPhQ system thus contains two isolated electron-accepting Q units, but the individual superior electron-accepting property of Q compared with Py allows easier reduction, smaller electrochemical gaps ΔE_{exp}. (= $E_{ox}-E_{red}$), and red-shifted absorptions for Q-containing complexes when compared with the double five-ring Py^Ph^Py system dpb.

On the other hand, the (partially) new Q-containing ligands fill the gap between the established N^C^N ligand dpb and C^N^N ligand Phbpy concerning its electronic inventory and thus allow fine-tuning for applications in catalysis or photoluminescence. As a first step toward applications, we found the new Pt(II) complexes [Pt(QPhQ)Cl] and its previously reported derivative [Pt(PhPhQ)Cl] photoluminescent at ambient temperature with broad bands peaking at around 630 nm. For the Ni(II) derivatives [Ni(QPhQ)Cl] and [Ni(PyPhQ)Br], we found weak and broad photoluminescence bands peaking at 540 and 490 nm, respectively. So, for

https://doi.org/10.1021/acs.organomet.4c00500
Organometallics 2025, 44, 847−857

Pt and Pd, the introduction of the six-ring chelates N*C and N*N seems to be detrimental to efficient photoluminescence, and for Ni, this seems to be different.

The green luminescence of these two Ni(II) complexes makes us confident that in future investigations, the variation of the coligands and the application of low temperatures combined with the use of rigid matrices will allow us to substantiate this very interesting observation.

EXPERIMENTAL SECTION

Materials and Synthesis. See Supporting Information.

Instrumentation. ^{1}H and ^{13}C spectra were recorded on a Bruker Avance II 300 MHz (^{1}H: 300 MHz, ^{13}C: 75 MHz) equipped with a double resonance (BBFO) 5 mm observe probe head with a z-gradient coil, Bruker Avance III 500 MHz (^{1}H: 500 MHz, ^{13}C: 125 MHz), and Bruker Avance II 600 MHz spectrometer (^{1}H: 600 MHz, ^{13}C: 150 MHz, ^{195}Pt: 54 MHz) with a triple resonance (TBI) 5 mm inverse probe head with a z-gradient coil using a triple resonance (Bruker, Rheinhausen, Germany). The unambiguous assignment of the ^{1}H and ^{13}C resonances was obtained from ^{1}H COSY, ^{1}H ^{13}C HSQC, and ^{1}H ^{13}C HMBC experiments. All 2D NMR experiments were performed by using standard pulse sequences from the Bruker pulse program library. Chemical shifts were measured relative to TMS (^{1}H, ^{13}C). UV−vis absorption spectra were recorded on a Varian Cary 05E spectrophotometer (Varian Medical Systems, Darmstadt, Germany). Elemental analyses were obtained using a HEKAtech CHNS EuroEA 3000 analyzer (HEKAtech, Wegberg, Germany). HR-ESI-MS(+) spectra in positive mode were measured on a Thermo Scientific LTQ OrbitrapXL mass spectrometer with electron spray ionization and an FTMS Analyzer. EI-MS spectra in positive mode were measured using a Finnigan MAT 95 mass spectrometer. Simulations were performed by using ISOPRO 3.0. Electrochemical measurements were carried out in 0.1 M n-Bu_4NPF_6 solution in THF (tetrahydrofuran) using a three-electrode configuration (glassy carbon electrode, Pt counter electrode, Ag/AgCl reference) and a Metrohm Autolab PGSTAT30 or μStat400 potentiostat (Metrohm, Filderstadt, Germany). The potentials were referenced against the ferrocene/ferrocenium redox couple as an internal standard.

Single-Crystal X-ray Diffraction. Single crystals of the complexes were grown either from layering of saturated solutions in CH_2Cl_2 with Et_2O or slow evaporation of saturated CH_2Cl_2 solutions. All measurements were carried out at 100(2) K, employing a Bruker D8 Venture, including a Bruker Photon 100 CMOS detector using Mo Kα radiation (λ = 0.71073 Å; Bruker, Rheinhausen, Germany). The crystal data was collected using using APEX4 v2021.10−0.[66] The structures were solved by dual space methods using SHELXT (Sheldrick 2015),[67] and the refinement was carried out with SHELXL 2017 employing full-matrix least-squares methods on $F_0^2 \geq 2\sigma(F_0^2)$.[68] The nonhydrogen atoms were refined with anisotropic displacement parameters without any constraints. The hydrogen atoms were included by using appropriate riding models.

DFT Calculations. The DFT calculations were performed using the Gaussian 16 suite of programs.[69] Def2-TZVP basis sets were used for all atoms including Ni, while for Pt and Pd, corresponding def2-ECPs (ecp-46 and ecp-28) were used for the core electrons.[70,71] The S_0 geometries of all compounds were optimized with the hybrid functional TPSSh using *Grimm's* D3 dispersion correction and the conductor-like polarizable continuum model (CPCM) parametrized for THF as an approximate solvation model.[72−74] Geometry optimization of all complexes was followed by frequency calculations and yielded no imaginary modes, thus confirming the energetically minimal nature of the stationary points. Molecular orbitals and electronic properties were extracted from the single-point calculations.

ASSOCIATED CONTENT

Data Availability Statement

Data of the structure solutions and refinements can be obtained for [Pt(PyPhQ)Cl] (CCDC: 2382070), [Pd(PyPhQ)Cl] (CCDC: 2382071), [Ni(PyPhQ)Br] (CCDC: 2382072), [Pt(QPhQ)Cl] (CCDC: 2382074), [Pd(QPhQ)Cl] (CCDC: 2382082), [Ni(QPhQ)Cl] (CCDC: 2382081), and [Pt(PhPyQ)Cl] (CCDC: 2382073) free of charge at https://summary.ccdc.cam.ac.uk/structure-summary-form or from the Cambridge Crystallographic Data Centre, 12 Union Road, Cambridge, CB2 1EZ UK (fax: + 44−1223 336033 or e-mail: deposit@ccdc.cam.ac.uk; www.ccdc.cam.ac.uk/structures).

Supporting Information

The Supporting Information is available free of charge at https://pubs.acs.org/doi/10.1021/acs.organomet.4c00500.

Materials and syntheses including NMR and MS data; supporting figures with crystal and molecular structures from single-crystal X-ray diffraction, cyclic voltammograms, DFT-calculated energies and orbital compositions, UV−vis absorption spectra, and photoluminescence spectra; supporting tables with crystal and molecular structure data, DFT-calculated metrics, experimental redox potentials, and experimental UV−vis absorption data (PDF)

DFT-calculated coordinates of the singlet ground state S_0 structures (XYZ)

Accession Codes

Deposition Numbers 2382070−2382074 and 2382081−2382082 contain the supplementary crystallographic data for this paper. These data can be obtained free of charge via the joint Cambridge Crystallographic Data Centre (CCDC) and Fachinformationszentrum Karlsruhe Access Structures service.

AUTHOR INFORMATION

Corresponding Author

Axel Klein − *University of Cologne, Faculty for Mathematics and Natural Sciences, Department of Chemistry and Biochemistry, Institute for Inorganic and Materials Chemistry, 50939 Koeln, Germany;* orcid.org/0000-0003-0093-9619; Phone: +49-221-470-4006; Email: axel.klein@uni-koeln.de

Authors

Leo Payen − *University of Cologne, Faculty for Mathematics and Natural Sciences, Department of Chemistry and Biochemistry, Institute for Inorganic and Materials Chemistry, 50939 Koeln, Germany*

Tobias Lapić − *University of Cologne, Faculty for Mathematics and Natural Sciences, Department of Chemistry and Biochemistry, Institute for Inorganic and Materials Chemistry, 50939 Koeln, Germany*

Mathias Wickleder − *University of Cologne, Faculty for Mathematics and Natural Sciences, Department of Chemistry and Biochemistry, Institute for Inorganic and Materials Chemistry, 50939 Koeln, Germany*

Complete contact information is available at: https://pubs.acs.org/10.1021/acs.organomet.4c00500

Notes

The authors declare no competing financial interest.

ACKNOWLEDGMENTS

We thank the Deutsche Forschungsgemeinschaft [DFG Priority Programme 2102 "Light-controlled Reactivity of Metal Complexes" KL1194/16-1 and 16-2 (A.K.)] for funding

of this project. We also like to thank the Regional Computing Center of the University of Cologne (RRZK) for providing computing time on the DFG-funded High Performance Computing (HPC) system CHEOPS as well as for the support.

REFERENCES

(1) Herbert, D. E. When is a pyridine not a pyridine? Benzannulated *N*-heterocyclic ligands in molecular materials chemistry. *Can. J. Chem.* **2023**, *101*, 892−902.
(2) Haque, A.; El Moll, H.; Alenezi, K. M.; Khan, M. S.; Wong, W.-Y. Functional Materials Based on Cyclometalated Platinum(II)-Diketonate Complexes: A Review of Structure−Property Relationships and Applications. *Materials* **2021**, *14*, 4236.
(3) Campillo, D.; Escudero, D.; Baya, M.; Martín, A. Heteropolymetallic Architectures as Snapshots of Transmetallation Processes at Different Degrees of Transfer. *Chem. - Eur. J.* **2022**, *28*, e202104538.
(4) Zucca, A.; Pilo, M. I. Rollover Cyclometalation as a Valuable Tool for Regioselective C−H Bond Activation and Functionalization. *Molecules* **2021**, *26*, 328.
(5) Ryabov, A. D. The Exchange of Cyclometalated Ligands. *Molecules* **2021**, *26*, 210.
(6) Jain, V. K. Cyclometalated group-16 compounds of palladium and platinum: Challenges and opportunities. *Coord. Chem. Rev.* **2021**, *427*, 213546.
(7) Yam, V. W.-W.; Law, A. S.-Y. Luminescent d^8 metal complexes of platinum(II) and gold(III): From photophysics to photofunctional materials and probes. *Coord. Chem. Rev.* **2020**, *414*, 213298.
(8) Koshevoy, I. O.; Krause, M.; Klein, A. Non-Covalent Intramolecular Interactions through Ligand-Design Promoting Efficient Photoluminescence from Transition Metal Complexes. *Coord. Chem. Rev.* **2020**, *405*, 213094.
(9) To, W.-P.; Wan, Q.; Tong, G. S. M.; Che, C.-M. Recent Advances in Metal Triplet Emitters with d^6, d^8, and d^{10} Electronic Configurations. *Trends Chem.* **2020**, *2*, 796−812.
(10) Cebrián, C.; Mauro, M. Recent advances in phosphorescent platinum complexes for organic light-emitting diodes. *Beilstein J. Org. Chem.* **2018**, *14*, 1459−1481.
(11) Yam, V. W.-W.; Au, V. K.-M.; Leung, S. Y.-L. Light-Emitting Self-Assembled Materials Based on d^8 and d^{10} Transition Metal Complexes. *Chem. Rev.* **2015**, *115*, 7589−7728.
(12) Li, K.; Tong, G. S. M.; Wan, Q.; Cheng, G.; Tong, W.-Y.; Ang, W.-H.; Kwong, W.-L.; Che, C.-M. Highly phosphorescent platinum(II) emitters: photophysics, materials and biological application. *Chem. Sci.* **2016**, *7*, 1653−1673.
(13) Budnikova, Y. H. Electrochemical Insight into Mechanisms and Metallocyclic Intermediates of C−H Functionalization. *Chem. Rec.* **2021**, *21*, 2148−2163.
(14) Dudkina, Y. B.; Fayzullin, R. R.; Lyssenko, K. A.; Gubaidullin, A. T.; Kholin, K. V.; Levitskaya, A. I.; Balakina, M. Y.; Budnikova, Y. H. Cyclometalated Nickel Complexes as Key Intermediates in $C(sp^2)$−H Bond Functionalization: Synthesis, Catalysis, Electrochemical Properties, and DFT Calculations. *Organometallics* **2019**, *38*, 1254−1263.
(15) Klein, A.; Sandleben, A.; Vogt, N. Synthesis, Structure and Reactivity of Cyclometalated Nickel(II) Complexes: A Review and Perspective. *Proc. Natl. Acad. Sci., India, Sect. A* **2016**, *86*, 533−549.
(16) Payen, L.; Kletsch, L.; Lapíc, T.; Wickleder, M.; Klein, A. C−H Metalation of Terpyridine Stereoisomers with Ni(II), Pd(II), and Pt(II). *Inorganics* **2023**, *11*, 174.
(17) Vogt, N.; Sandleben, A.; Kletsch, L.; Schäfer, S.; Chin, M. T.; Vicic, D. A.; Hörner, G.; Klein, A. Role of the X Coligands in Cyclometalated [Ni(Phbpy)X] Complexes (HPhbpy = 6-phenyl-2,2′-bipyridine). *Organometallics* **2021**, *40*, 1776−1785.
(18) McEllin, A. J.; Goult, C. A.; Whitwood, A. C.; Lynam, J. M.; Bruce, D. W. On the mercuration, palladation, transmetalation and direct auration of a C^N^C pincer ligand. *Dalton Trans.* **2023**, *52*, 872−876.
(19) De Soricellis, G.; Fagnani, F.; Colombo, A.; Dragonetti, C.; Roberto, D. Exploring the potential of N^C^N cyclometalated Pt(II) complexes bearing 1,3-di(2-pyridyl)benzene derivatives for imaging and photodynamic therapy. *Inorg. Chim. Acta* **2022**, *541*, 121082.
(20) Eskelinen, T.; Buss, S.; Petrovskii, S. K.; Grachova, E. V.; Krause, M.; Kletsch, L.; Klein, A.; Strassert, C. A.; Koshevoy, I. O.; Hirva, P. Photophysics and Excited State Dynamics of Cyclometalated [M(Phbpy)((CN)] (M = Ni, Pd, Pt) Complexes: A Theoretical and Experimental Study. *Inorg. Chem.* **2021**, *60*, 8777−8789.
(21) Kletsch, L.; Jordan, R.; Köcher, A. S.; Buss, S.; Strassert, C. A.; Klein, A. Photoluminescence of Ni(II), Pd(II), and Pt(II) Complexes [M(Me_2dpb)Cl] Obtained from C−H Activation of 1,5-Di(2-pyridyl)-2,4-dimethylbenzene (Me_2dpbH). *Molecules* **2021**, *26*, 5051.
(22) Wong, Y.-S.; Tang, M.-C.; Ng, M.; Yam, V. W.-W. Toward the Design of Phosphorescent Emitters of Cyclometalated Earth-Abundant Nickel(II) and Their Supramolecular Study. *J. Am. Chem. Soc.* **2020**, *142*, 7638−7646.
(23) Garbe, S.; Krause, M.; Klimpel, A.; Neundorf, I.; Lippmann, P.; Ott, I.; Brünink, D.; Strassert, C. A.; Doltsinis, N. L.; Klein, A. Cyclometalated Pt Complexes of CNC Pincer Ligands: Luminescence and Cytotoxic Evaluation. *Organometallics* **2020**, *39*, 746−756.
(24) Haque, A.; Xu, L.; Al-Balushi, R. A.; Al-Suti, M. K.; Ilmi, R.; Guo, Z.; Khan, M. S.; Wong, W.-Y.; Raithby, P. R. Cyclometallated tridentate platinum(II) arylacetylide complexes: old wine in new bottles. *Chem. Soc. Rev.* **2019**, *48*, 5547−5563.
(25) Williams, J. A. G. The coordination chemistry of dipyridylbenzene: N-deficient terpyridine or panacea for brightly luminescent metal complexes? *Chem. Soc. Rev.* **2009**, *38*, 1783−1801.
(26) Kergreis, A.; Lord, R. M.; Pike, S. J. Influence of Ligand and Nuclearity on the Cytotoxicity of Cyclometallated C^N^C Platinum(II) Complexes. *Chem. - Eur. J.* **2020**, *26*, 14938−14946.
(27) Soro, B.; Stoccoro, S.; Minghetti, G.; Zucca, A.; Cinellu, M. A.; Manassero, M.; Gladiali, S. The first pincer-aryl [M−(NCN)] complexes {M = Pd(II); Pt(II)} with chiral pyridine donors: Synthesis and catalytic activity in C−C bond formation. *Inorg. Chim. Acta* **2006**, *359*, 1879−1888.
(28) Soro, B.; Stoccoro, S.; Minghetti, G.; Zucca, A.; Cinellu, M. A.; Gladiali, S.; Manassero, M.; Sansoni, M. Synthesis of the First C-2 Cyclopalladated Derivatives of 1,3-Bis(2-pyridyl)benzene. Crystal Structures of [Hg(N-C-N)Cl], [Pd(N-C-N)Cl], and [Pd_2(N-C-N)$_2$(μ-OAc)]$_2$[Hg_2Cl_6]. Catalytic Activity in the Heck Reaction. *Organometallics* **2005**, *24*, 53−61.
(29) Omae, I. Applications of six-membered ring products from cyclometalation reactions. *J. Organomet. Chem.* **2017**, *848*, 184−195.
(30) Natoli, S. N.; Hight, L. M.; Zeller, M.; McMillin, D. R. Photophysical Properties of Pt(II) Polypyridines with Five- versus Six-Membered Chelate Rings: Trade-Offs in Angle Strain. *Inorg. Chem.* **2018**, *57*, 6521−6529.
(31) Garner, K. L.; Parkes, L. F.; Piper, J. D.; Williams, J. A. G. Luminescent Platinum Complexes with Terdentate Ligands Forming 6-Membered Chelate Rings: Advantageous and Deleterious Effects in N^N^N and N^C^N-Coordinated Complexes. *Inorg. Chem.* **2010**, *49*, 476−487.
(32) Wood, E. A.; Gildea, L. F.; Yufit, D. S.; Williams, J. A. G. Synthesis, structures and luminescence properties of N^C^N-coordinated platinum(II) complexes based on an anthracene core: A red shift and a twist. *Polyhedron* **2021**, *207*, 115401.
(33) Saini, M.; Keyes, T. E. Cyclometalated platinum(II) complex as a selective light switch for G-quadruplex DNA. *Dalton Trans.* **2023**, *52*, 7787−7791.
(34) Wekesa, I. M.; Jaganyi, D. The deleterious effect of pyrollic-nitrogen on the substitution reactivity of tridentate N^C^N platinum(II) complexes. A kinetic and mechanistic study. *J. Coord. Chem.* **2016**, *69*, 389−403.
(35) Wekesa, I. M.; Jaganyi, D. The electronic effect of quinoline moieties on the lability of platinum(II) complexes of tridentate

https://doi.org/10.1021/acs.organomet.4c00500
Organometallics 2025, 44, 847−857

N^N^N and N^C^N ligands: a kinetic, mechanistic and theoretical analysis. *Transition Met. Chem.* **2021**, *46*, 363−371.
(36) Ravindranathan, D.; Vezzu, D. A. K.; Bartolotti, L.; Boyle, P. D.; Huo, S. Improvement in Phosphorescence Efficiency through Tuning of Coordination Geometry of Tridentate Cyclometalated Platinum-(II) Complexes. *Inorg. Chem.* **2010**, *49*, 8922−8928.
(37) Vezzu, D. A. K.; Deaton, J. C.; Jones, J. S.; Bartolotti, L.; Harris, C. F.; Marchetti, A. P.; Kondakova, M.; Pike, R. D.; Huo, S. Highly Luminescent Tetradentate Bis-Cyclometalated Platinum Complexes: Design, Synthesis, Structure, Photophysics, and Electroluminescence Application. *Inorg. Chem.* **2010**, *49*, 5107−5119.
(38) Khistiaeva, V. V.; Buss, S.; Eskelinen, T.; Hirva, P.; Kinnunen, N.; Friedel, J.; Kletsch, L.; Klein, A.; Strassert, C. A.; Koshevoy, I. O. Cyanido-bridged diplatinum(II) complexes: ligand and solvent effect on aggregation and luminescence. *Chem. Sci.* **2024**, *15*, 4005−4018.
(39) Li, W.; Wang, J.; Yan, X.; Zhang, H.; Shen, W. Electronic structures and photophysical properties of phosphorescent platinum-(II) complexes with tridentate C^N*N cyclometalated ligands. *Appl. Organomet. Chem.* **2018**, *32*, e3929.
(40) Jing, J.; Yu, M.; Pan, L.; Zhao, Y.; Xu, G.; Zhang, H.-H.; Li, C.; Zhang, X.-P. Synthesis and Biological Activities of Luminescent 5,6-Membered Bis(Metallacyclic) Platinum(II) Complexes. *Molecules* **2023**, *28*, 6369.
(41) Knedel, T.-O.; Buss, S.; Maisuls, I.; Daniliuc, C. G.; Schlüsener, C.; Brandt, P.; Weingart, O.; Vollrath, A.; Janiak, C.; Strassert, C. A. Encapsulation of Phosphorescent Pt(II) Complexes in Zn-Based Metal−Organic Frameworks toward Oxygen-Sensing Porous Materials. *Inorg. Chem.* **2020**, *59*, 7252−7264.
(42) Buss, S.; Cappellari, M. V.; Hepp, A.; Kösters, J.; Strassert, C. A. Modification of the Bridging Unit in Luminescent Pt(II) Complexes Bearing C^N*N and C^N*N^C Ligands. *Chemistry* **2023**, *5*, 1243−1255.
(43) Buss, S.; Geerkens, L.; Jordan, R.; Kletsch, L.; Hepp, A.; Kösters, J.; Klein, A.; Strassert, C. A. Tuning the terminal N* and C^ moieties towards tailored Pt(II) complexes with thiazole-based N*N^C luminophores. *Organometallics* **2025**, *44*, 487−501.
(44) Huo, S. Platinum in Chemistry: An Adventure from Phosphorescent Materials to Catalytic C−H Functionalization. *Chem. Rec.* **2018**, *18*, 1583−1595.
(45) Ortiz, R. J.; Braun, J. D.; Williams, J. A. G.; Herbert, D. E. Brightly Luminescent Platinum Complexes of N^C^N Ligands Forming Six-Membered Chelate Rings: Offsetting Deleterious Ring Size Effects Using Site-Selective Benzannulation. *Inorg. Chem.* **2021**, *60*, 16881−16894.
(46) Schlotthauer, T.; Parada, G. A.; Görls, H.; Ott, S.; Jäger, M.; Schubert, U. S. Asymmetric Cyclometalated Ru^{II} Polypyridyl-Type Complexes with π-Extended Carbanionic Donor Sets. *Inorg. Chem.* **2017**, *56*, 7720−7730.
(47) Cárdenas, D. J.; Echavarren, A. M.; Ramirez de Arellano, M. C. Divergent Behavior of Palladium(II) and Platinum(II) in the Metalation of 1,3-Di(2-pyridyl)benzene. *Organometallics* **1999**, *18*, 3337−3341.
(48) Kletsch, L.; Hörner, G.; Klein, A. Cyclometalated Ni(II) complexes [Ni(N^C^N)X] of the tridentate 2,6-di(2-pyridyl)-phen-ide ligand. *Organometallics* **2020**, *39*, 2820−2829.
(49) Vogt, N.; Sivchik, V.; Sandleben, A.; Hörner, G.; Klein, A. Direct Base-Assisted C−H Cyclonickelation of 6-Phenyl-2,2′-bipyridine. *Molecules* **2020**, *25*, 997.
(50) Niazi, M.; Maisuls, I.; Strassert, C. A.; Klein, A. Molecular Rigidification of Cyclometalated N^C^N Pt(II)- and Pd(II)-based Triplet Emitters. *Organometallics* **2024**, *43*, 1547−1556.
(51) Von der Stück, R.; Schmitz, S.; Klein, A. C−X vs. C−H activation for the synthesis of the cyclometalated complexes [Pd(YPhbpy)X] (HPhbpy = 6-phenyl-2,2′-bipyridine; X/Y = (pseudo)halides). *Inorg. Chem. Res.* **2021**, *5*, 173−192.
(52) Krause, M.; von der Stück, R.; Brünink, D.; Buss, S.; Doltsinis, N. L.; Strassert, C. A.; Klein, A. Platinum and palladium complexes of tridentate $^{-}$C^N^N (phen-ide)-pyridine-thiazol ligands—A case study involving spectroelectrochemistry, photoluminescence spectroscopy and TD-DFT calculations. *Inorg. Chim. Acta* **2021**, *518*, 120093.
(53) Williams, J. A. G.; Beeby, A.; Davies, E. S.; Weinstein, J. A.; Wilson, C. An Alternative Route to Highly Luminescent Platinum(II) Complexes: Cyclometalation with N^C^N-Coordinating Dipyridylbenzene Ligands. *Inorg. Chem.* **2003**, *42*, 8609−8611.
(54) Wang, Z.; Turner, E.; Mahoney, V.; Madakuni, S.; Groy, T.; Li, J. Facile Synthesis and Characterization of Phosphorescent Pt-(N^C^N)X Complexes. *Inorg. Chem.* **2010**, *49*, 11276−11286.
(55) Niazi, M.; Klein, A. DFT Investigation of the Molecular Properties of the Dimethylglyoximato Complexes $[M(Hdmg)_2]$ (M = Ni, Pd, Pt). *Inorganics* **2021**, *9*, 47.
(56) Haseloer, A.; Jordan, R.; Denkler, L. M.; Reimer, M.; Olthof, S.; Schmidt, I.; Meerholz, K.; Hörner, G.; Klein, A. Ni, Pd, and Pt complexes of a tetradentate dianionic thiosemicarbazone-based O^N^N^S ligand. *Dalton Trans.* **2021**, *50*, 4311−4322.
(57) Poirier, S.; Lynn, H.; Reber, C.; Tailleur, E.; Marchivie, M.; Guionneau, P.; Probert, M. R. Variation of M···H−C Interactions in Square-Planar Complexes of Nickel(II), Palladium(II), and Platinum-(II) Probed by Luminescence Spectroscopy and X-ray Diffraction at Variable Pressure. *Inorg. Chem.* **2018**, *57*, 7713−7723.
(58) Manar, K. K.; Gupta, A. N.; Gupta, A. K.; Prasad, L. B.; Srivastava, P.; Drew, M. G. B.; Singh, N. Synthesis, Crystal Structures and Photosensitizing Activities of Ni(II) and Pd(II) Heteroleptic Dithiolate−dppf Complexes. *ChemistrySelect* **2017**, *2*, 2655−2664.
(59) Pilia, L.; Espa, D.; Barsella, A.; Fort, A.; Makedonas, C.; Marchio, L.; Mercuri, M. L.; Serpe, A.; Mitsopoulou, C. A.; Deplano, P. Combined Experimental and Theoretical Study on Redox-Active d^8 Metal Dithione−Dithiolato Complexes Showing Molecular Second-Order Nonlinear Optical Activity. *Inorg. Chem.* **2011**, *50*, 10015−10027.
(60) Shimazaki, Y.; Stack, T. D. P.; Storr, T. Detailed Evaluation of the Geometric and Electronic Structures of One-Electron Oxidized Group 10 (Ni, Pd, and Pt) Metal(II)-(Disalicylidene)diamine Complexes. *Inorg. Chem.* **2009**, *48*, 8383−8392.
(61) Koopmans, T. Über die Zuordnung von Wellenfunktionen und Eigenwerten zu den Einzelnen Elektronen Eines Atoms. *Physica* **1934**, *1*, 104−113.
(62) Janak, J. F. Proof that $\partial E/\partial n_i = \varepsilon$ in density-functional theory. *Phys. Rev. B* **1978**, *18*, 7165−7168.
(63) Tsuneda, T.; Song, J.-W.; Suzuki, S.; Hirao, K. On Koopmans' theorem in density functional theory. *J. Chem. Phys.* **2010**, *133*, 174101.
(64) Frei, F.; Rondi, A.; Espa, D.; Mercuri, M. L.; Pilia, L.; Serpe, A.; Odeh, A.; Van Mourik, F.; Chergui, M.; Feurer, T.; Deplano, P.; Vlček, A., Jr.; Cannizzo, A. Ultrafast electronic and vibrational relaxations in mixed-ligand dithione−dithiolato Ni, Pd, and Pt complexes. *Dalton Trans.* **2014**, *43*, 17666−17676.
(65) Rausch, A. F.; Murphy, L.; Williams, J. A. G.; Yersin, H. Probing the Excited State Properties of the Highly Phosphorescent Pt(dpyb)Cl Compound by High-Resolution Optical Spectroscopy. *Inorg. Chem.* **2009**, *48*, 11407−11414.
(66) APEX4. *Software Suite for Crystallographic Programs*; Bruker AXS, Inc.: Madison, WI, USA, 2021.
(67) Sheldrick, G. M. Crystal Structure Refinement with SHELXL. *Acta Crystallogr., Sect. C:Struct. Chem.* **2015**, *71*, 3−8.
(68) Sheldrick, G. M. A short history of SHELX. *Acta Crystallogr., Sect. A: Found. Crystallogr.* **2008**, *64*, 112−122.
(69) Frisch, M. J.; Trucks, G. W.; Schlegel, H. B.; Scuseria, G. E.; Robb, M. A.; Cheeseman, J. R.; Scalmani, G.; Barone, V.; Petersson, G. A.; Nakatsuji, H.; Li, X.; Caricato, M.; Marenich, A. V.; Bloino, J.; Janesko, B. G.; Gomperts, R.; Mennucci, B.; Hratchian, H. B.; Ortiz, J. V.; Izmaylov, A. F.; Sonnenberg, J. L.; Williams-Young, D.; Ding, F.; Lipparini, F.; Egidi, F.; Goings, J.; Peng, B.; Petrone, A.; Henderson, T.; Ranasinghe, D.; Zakrewski, V. G.; Gao, J.; Rega, N.; Zheng, G.; Liang, W.; Hada, M.; Ehara, M.; Toyota, K.; Fukuda, R.; Hasegawa, J.; Ishida, M.; Nakajima, T.; Honda, Y.; Kitao, O.; Nakai, H.; Vreven, T.; Throssell, K.; Montgomery, J. A.; Peralta, J. E.; Ogliaro, F.; Bearpark, M. J.; Heyd, J. J.; Brothers, E. N.; Kudin, K. N.; Staroverov, V. N.;

https://doi.org/10.1021/acs.organomet.4c00500
Organometallics 2025, 44, 847−857

Keith, T. A.; Kobayashi, R.; Normand, J.; Raghavachari, K.; Rendell, A. P.; Burant, J. C.; Iyengar, S. S.; Tomasi, J.; Cossi, M.; Millam, J. M.; Klene, M.; Adamo, C.; Cammi, R.; Ochterski, J. W.; Martin, R. L.; Morokuma, K.; Farkas, O.; Foresman, J. B.; Fox, D. J. *Gaussian 16, Rev. A.03*; Gaussian, Inc.: Wallingford, CT, 2016.

(70) Weigend, F.; Ahlrichs, R. Balanced basis sets of split valence, triple zeta valence and quadruple zeta valence quality for H to Rn: Design and assessment of accuracy. *Phys. Chem. Chem. Phys.* **2005**, *7*, 3297−3305.

(71) Andrae, D.; Häußermann, U.; Dolg, M.; Stoll, H.; Preuss, H. Energy-adjusted ab initio pseudopotentials for the second and third row transition elements. *Theor. Chim. Acta* **1990**, *77*, 123−141.

(72) Staroverov, V. N.; Scuseria, G. E.; Tao, J.; Perdew, J. P. Comparative Assessment of a New Nonempirical Density Functional: Molecules and Hydrogen-bonded Complexes. *J. Chem. Phys.* **2003**, *119*, 12129−12137.

(73) (a) Grimme, S.; Antony, J.; Ehrlich, S.; Krieg, H. A consistent and accurate ab initio parametrization of density functional dispersion correction (DFT-D) for the 94 elements H-Pu. *J. Chem. Phys.* **2010**, *132*, 154104. (b) Grimme, S.; Ehrlich, S.; Goerigk, L. Effect of the damping function in dispersion corrected density functional theory. *J. Comput. Chem.* **2011**, *32*, 1456−1465.

(74) (a) Cossi, M.; Rega, N.; Scalmani, G.; Barone, V. Energies, Structures, and Electronic Properties of Molecules in Solution with the C-PCM Solvation Model. *J. Comput. Chem.* **2003**, *24*, 669−681. (b) Barone, V.; Cossi, M. Quantum Calculation of Molecular Energies and Energy Gradients in Solution by a Conductor Solvent Model. *J. Phys. Chem. A* **1998**, *102*, 1995−2001.

https://doi.org/10.1021/acs.organomet.4c00500
Organometallics 2025, 44, 847−857

Supporting Information
for
Pt(II), Pd(II), and Ni(II) Complexes with Tridentate Cyclometalating Five- and Six-Ring Chelating N^C*N, C^N*N, and N*C*N Quinolinyl Ligands

Leo Payen, Tobias Lapić, Mathias Wickleder and Axel Klein*

University of Cologne, Faculty for Mathematics and Natural Sciences, Department of Chemistry and Biochemistry, Institute for Inorganic and Materials Chemistry, Greinstraße 6, D-50939 Köln, Germany
*Correspondence: axel.klein@uni-koeln.de; ORCID: 0000-0003-0093-9619; Tel.: +49-221-470-4006 (A.K.)

Contents

Experimental Section

1. Materials and Syntheses

1.1 Materials

All chemicals were purchased from ACROS, ABCR, Alfa Aesar, BLD Pharm or Sigma Aldrich and used without any further purification. Reactions sensitive to oxygen or water were carried out under argon gas by Linde (99.998%) using *Schlenk*-technique. Dry THF was distilled over Na/K (alloy 3:7) before use. Dry *p*-xylene was freshly distilled over sodium. Other solvents were obtained by Fischer chemical (HPLC grade) and used without any additional drying.

1.2 Syntheses of ligand precursors – General procedure:

Under inert conditions, the aryl bromide (1 eq.), the boronic acid (1 eq.) and Na_2CO_3 (10 eq.) were suspended in a degassed mixture of toluene, EtOH and distilled water (1:1:1 vol., adjusted to give a 2 M concentration of Na_2CO_3 in water). The catalyst [$Pd(PPh_3)_4$] (5 mol%) was added and the reaction mixture was heated under reflux for 18 h. After cooling to room temperature, the mixture was extracted three times using CH_2Cl_2 and the solvent evaporated. The crude product was purified by column chromatography.

2-phenyl-6-bromopyridine: 6 g 1,3-dibromopyridine (25.3 mmol, 1 eq.), 3.08 g phenylboronic acid (25.3 mmol, 1 eq.), 26.8 g Na_2CO_3 (253 mmol, 10 eq.) and 1.46 g [$Pd(PPh_3)_4$] (1.27 mmol, 5 mol%) were added to the solvent mixture and the reaction mixture was heated under reflux for 48 h. The obtained yellow crude oil was purified by column chromatography (SiO_2, *c*-hexane/EtOAc 50:1). The product was obtained as colorless oil (2.80 g, 11.9 mmol, 47%). ^{1}H NMR ($CDCl_3$, 300 MHz): δ [ppm] = 8.21–8.15 (m, 1H), 8.05–7.97 (m, 1H), 7.75–7.68 (m, 1H), 7.55–7.40 (m, 4H). GC-MS: 235.00 $[M+H]^+$.

1-(2-pyridinyl)-3-bromobenzene: From 1-bromobenzene-3-boronic acid (3.55 g, 17.7 mmol, 1 eq.), 2-bromopyridine (2.80 g, 1.72 mL, 17.7 mmol, 1 eq.), Na_2CO_3 (18.8 g, 177 mmol, 10 eq.) and [$Pd(PPh_3)_4$]

(1.03 g, 0.89 mmol, 5 mol%) were added to the solvent mixture and heated under reflux for 19 h. The obtained yellow crude oil was purified by column chromatography (SiO_2, *c*-hexane/EtOAc 40:1). The product was obtained as colorless oil (3.46 g, 14.7 mmol, 83%). ^{1}H NMR ($CDCl_3$, 300 MHz): δ [ppm] = 8.70 (d, ^3J = 4.8 Hz, 1H), 8.18 (t, ^3J = 1.8 Hz, 1H), 7.91 (d, ^3J = 7.8 Hz, 1H), 7.76 (dd, ^3J = 7.3 Hz, ^4J = 1.7 Hz, 1H), 7.70 (d, ^3J = 7.9 Hz, 1H), 7.58–7.51 (m, 1H), 7.34 (t, ^3J = 7.9 Hz, 1H), 7.30–7.23 (m, 1H). GC-MS: 235.00 $[M+H]^+$.

1.3 Syntheses of the protoligands

Synthesis of 1-(8-quinolinyl)-3-(2-pyridinyl)-benzene (PyHPhQ): Following general procedure A, 1-(2-pyridinyl)-3-bromobenzene (1 g, 4.27mmol, 1 eq.), quinoline-8-boronic acid (739 mg, 4.27 mmol, 1 eq.), Na_2CO_3 (4.52 g, 42.7 mmol, 10 eq.) and $[Pd(PPh_3)_4]$ (243 mg, 0.21 mmol, 5 mol%) were added to the solvent mixture and the reaction mixture was heated under reflux for 72 h. The obtained crude oil was purified by column chromatography (SiO_2, *c*-hexane/EtOAc 2:1). The product was obtained as light-yellow oil (1.14 g, 4.04 mmol, 95%). ^{1}H NMR ($CDCl_3$, 500 MHz): δ [ppm] = 8.93 (d, ^3J = 4.8 Hz, 1H, H1), 8.68 (d, ^3J = 4.8 Hz, 1H, H13), 8.31 (s, 1H, H16), 8.14 (d, ^3J = 8.3 Hz, 1H, H3), 8.05 (d, ^3J = 7.8 Hz, 1H, H9), 7.81–7.73 (m, 3H, H4, H7, H10), 7.67 (t, ^3J = 7.5 Hz, 1H, H11), 7.58 (dt, 2H, ^3J = 15.1 Hz, 7.7 Hz, H5, H8), 7.35 (dd, ^3J = 8.3 Hz, 4.2 Hz, 1H, H2), 7.16 (dd, ^3J = 7.5 Hz, 4.8 Hz, 1H, H12). ^{13}C NMR ($CDCl_3$, 125 MHz): δ [ppm] = 157.6 (Cq, C14), 150.3 (CH, C1), 149.6 (CH, C13), 146.1 (Cq), 140.7 (Cq, C18), 140.1 (Cq, C15), 139.2 (Cq, C17), 136.7 (CH, C10), 136.3 (CH, C3), 131.4 (CH, C7), 130.4 (CH, C6), 129.2 (CH, C16), 128.7 (Cq, C20), 128.4 (CH, C11), 127.7 (CH, C4), 126.3 (CH, C5) 126.0 (CH, C9), 122.0 (CH, C12), 121.0 (CH, C2), 120.7 (CH, C8). HR-EI-MS: 282.11 $[M]^+$.

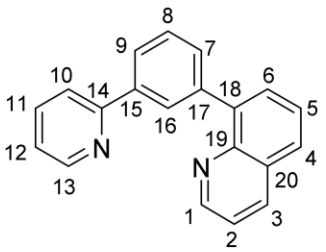

Synthesis of 1,3-diquinolino-benzene (QHPhQ): Following general procedure A, 8-bromoquinoline (6.28 g, 30.2 mmol, 2 eq.), benzene-1,3-diboronic acid pinacol ester (5 g, 15.1 mmol, 1 eq.), Na_2CO_3 (16.0 g, 151 mmol, 10 eq.) and $[Pd(PPh_3)_4]$ (697 mg, 0.6 mmol, 4 mol%) were added to the solvent mixture which was heated under reflux for 20 h. The obtained crude oil was purified by column chromatography (SiO_2, *c*-hexane/EtOAc 5:1). The product was obtained as light-yellow solid (1.88 g, 5.65 mmol, 37%). ^{1}H NMR (CD_2Cl_2, 500 MHz): δ [ppm] = 8.91 (dd, ^3J = 4.1 Hz, ^4J = 1.8 Hz, 2H, H1), 8.22 (dd, ^3J = 8.3 Hz, ^4J = 1.7 Hz, 2H, H3), 7.92 (t, ^4J = 1.5 Hz, 1H, H13), 7.84 (ddd, ^3J = 10.6 Hz, 7.7 Hz, ^4J = 1.3 Hz, 4H, H5, H7), 7.72 (dd, ^3J = 7.7 Hz, ^4J = 1.7 Hz, 2H, H11), 7.64–7.60 (m, 2H, H6), 7.58 (t, ^3J = 7.6 Hz, 1H, H12), 7.42 (dd, ^3J = 8.3 Hz, ^4J = 4.1 Hz, 2H, H2). ^{13}C NMR (CD_2Cl_2, 125 MHz): δ [ppm] = 150.7 (CH, C1), 146.8 (Cq, C9), 141.5 (Cq, C8), 139.9 (Cq, C10), 136.7 (CH, C3), 133.4 (CH, C13), 130.7 (CH, C5), 130.3 (CH, C11), 129.3 (Cq, C4), 128.1 (CH, C7), 127.6 (CH, C12), 126.8 (CH, C6), 121.6 (CH, C2). GC-MS: 332.10 $[M]^+$.

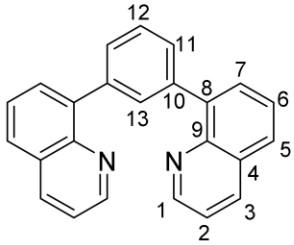

Synthesis of 2-phenyl-6-(8-quinolinyl)-pyridine (HPhPyQ): Following general procedure **A**, 2-phenyl-6-bromopyridine (2.2 g, 9.4 mmol, 1 eq.), quinolinyl-8-boronic acid (1.63 g, 9.4 mmol 1 eq.) Na_2CO_3 (9.96 g, 94 mmol, 10 eq.) and $[Pd(PPh_3)_4]$ (543 mg, 0.47 mmol, 5 mol%) were added to the solvent mixture which was heated under reflux for 72 h. The obtained brown crude oil was purified by column chromatography (SiO_2, *c*-hexane/EtOAc 20:1). The product was obtained as yellow solid (1.81 g, 6.41 mmol, 68%). Yield: 1.81 g, 6.41 mmol, 68%. ^{1}H NMR ($CDCl_3$, 300 MHz): δ [ppm] = 8.98 (dd, ^3J = 4.1 Hz, ^4J = 1.8 Hz, 1H, H1), 8.34 (dd, ^3J = 7.2 Hz, ^4J = 1.4 Hz, 1H, H6), 8.22 (dd, ^3J = 8.3 Hz, ^4J = 1.7 Hz, 1H, H3), 8.12 (d, ^3J = 7.4 Hz, 3H, H9, H10), 7.88 (t, ^3J = 7.9 Hz, 1H, H8), 7.75 (d, ^3J = 7.4 Hz, 1H, H7), 7.72–7.67 (m, 1H, H5), 7.48 (t, ^3J = 7.5 Hz, 2H, H11), 7.44–7.38 (m, 2H, H2, H12). ^{13}C NMR ($CDCl_3$, 75 MHz): δ [ppm] = 157.2 (Cq, C14), 156.6 (Cq, C15), 150.3 (CH, C1), 146.0 (Cq, C17), 139.9 (Cq, C13), 136.5 (CH, C3), 136.2 (CH, C8), 131.6 (CH, C6), 128.8 (CH, C4), 128.73 (CH, C2), 128.7

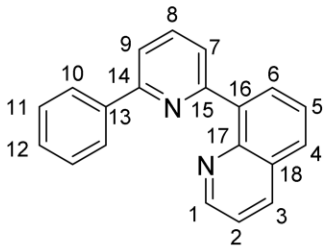

(Cq, C18), 127.1 (CH, C10), 126.6 (CH, C5), 125.6 (CH, C9), 121.0 (CH, C2), 119.0 (CH, C7). HR-EI-MS (70 eV): 282.11 $[M]^+$.

Synthesis of 1,3-diquinolino-2-chloro-benzene (QClPhQ): Following general procedure A, quinolinyl-8-boronic acid (1.36 g, 7.84 mmol, 2.2 eq.), 1,3-dibromo-2-chloro-benzene (962 mg, 3.56 mmol, 1 eq.), Na_2CO_3 (8.3 g, 78.4 mmol, 10 eq.) and $[Pd(PPh_3)_4]$ (452 mg, 0.39 mmol, 5 mol%) were added to the solvent mixture which was heated under reflux for 21 h. The obtained crude oil was purified by column chromatography (SiO_2, *c*-hexane/EtOAc 4:1). The product was obtained as light-yellow solid (302 mg, 0.82 mmol, 23%). ^{1}H NMR ($CDCl_3$, 500 MHz): δ [ppm] = 8.95 (s, 2H, H1), 8.20 (d, ^3J = 7.1 Hz, 2H, H3), 7.90–7.83 (m, 4H, H5, H7), 7.72 (d, ^3J = 6.7 Hz, 1H, H12), 7.64–7.60 (m, 2H, H6), 7.52–7.47 (m, 2H, H11), 7.40 (dd, ^3J = 7.9 Hz, 4.0 Hz, 2H, H2). ^{13}C NMR ($CDCl_3$, 125 MHz): δ [ppm] = 150.4 (CH, C1), 146.5 (Cq, C9), 139.4 (Cq, C8), 139.3 (Cq, C13), 139.2 (Cq, C10), 136.2 (CH, C3), 131.5 (CH, C11), 131.3 (CH, C7), 130.5 (CH, C12), 128.4 (Cq, C4), 128.0 (Cq, C5), 126.0 (CH, C6), 121.0 (CH, C2).

1.4 Syntheses of the Platinum Complexes – General Procedure

The ligand (1.2 eq.) and K_2PtCl_4 (1 eq.) were mixed with glacial HOAc in a round bottom flask and heated under reflux. After completion of the reaction the mixture was cooled to room temperature. The precipitate was filtered off over a glass frit and washed with de-mineralized water and diethyl ether. The complex was re-dissolved in CH_2Cl_2 and the solvent removed to yield the target complex.

[Pt(PyPhQ)Cl] (1): PyHPhQ (800 mg, 2.82 mmol, 1 eq.) and K_2PtCl_4 (1.17 g, 2.82 mmol, 1 eq.) were heated under reflux in glacial HOAc for 72 h. The complex was isolated as orange powder (1.38 g, 2.69 mmol, 95%). ^{1}H NMR ($CDCl_3$, 600 MHz): δ [ppm] = 10.88 (dd, $J_{Pt\text{-}H}$ = 39.7 Hz, ^3J = 5.5 Hz, ^4J = 1.7 Hz, 1H, H1), 9.98 (ddd, $J_{Pt\text{-}H}$ = 37.7 Hz, ^3J = 5.9 Hz, ^4J = 1.5 Hz, 0.6 Hz, 1H, H13), 8.50 (dd, ^3J = 8.1 Hz, ^4J = 1.6 Hz, 1H, H3), 8.47 (dd, ^3J = 7.6 Hz, ^4J = 1.2 Hz, 1H, H4), 7.92–7.88 (m, 3H, H5, H7, H11), 7.80–7.74 (m, 2H, H6, H10), 7.59 (dd, ^3J = 7.5 Hz, ^4J = 0.9 Hz, 1H, H9), 7.50 (dd, ^3J = 8.0 Hz, 5.5 Hz, 1H, H2), 7.38 (t, ^3J = 7.7 Hz, 1H, H8), 7.26 (ddd, ^3J = 7.4 Hz, 5.9 Hz, ^4J = 1.5 Hz, 1H, H12). ^{13}C NMR ($CDCl_3$, 125 MHz): δ [ppm] = 158.8 (CH, C1), 152.4 (CH, C13), 144.8 (Cq, C16), 141.3 (Cq, C18), 140.6 (CH, C3), 139.2 (Cq, C19), 138.8 (CH, C5), 137.4 (Cq, C15), 131.4 (Cq, C17), 130.5 (CH, C4), 130.3 (Cq, C20), 129.2 (CH, C11), 127.4 (CH, C7), 127.1 (CH, C10), 124.5 (CH, C8), 123.2 (CH, C9), 122.3 (CH, C12), 121.2 (CH, C2), 118.4 (CH, C6). ^{195}Pt NMR ($CDCl_3$, 54 MHz): δ [ppm] = −3656.5. HR-ESI-MS (70 eV): 475.07 $[M–Cl]^+$.

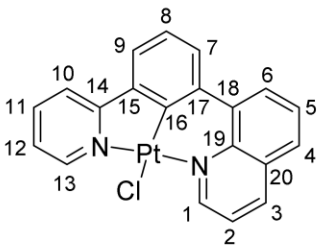

[Pt(QPhQ)Cl] (2): QHPhQ (60 mg, 0.18 mmol, 1.2 eq.) and K_2PtCl_4 (62.3 mg, 0.15 mmol, 1 eq.) were heated under reflux in glacial HOAc for 72 h. The complex was isolated as orange powder (66.1 mg, 0.12 μmol, 80%). ^{1}H NMR (DMSO-d_6, 500 MHz): δ [ppm] = 9.54 (dd, ^3J = 5.3 Hz , ^4J = 1.4 Hz, 2H, H1), 8.78 (dd, ^3J = 8.2 Hz, ^4J = 1.3 Hz, 2H, H3), 8.48 (d, ^3J = 6.6 Hz, 2H, H7), 8.14 (d, ^3J = 7.6 Hz, 2H, H5), 7.85 (t, ^3J = 7.7 Hz, 2H, H6), 7.63–7.55 (m, 2H, 4H), 7.32 (t, ^3J = 7.7 Hz, 1H, H12). ^{13}C NMR (DMSO-d_6, 125 MHz): δ [ppm] = 157.6 (CH, C1), 141.7 (Cq, C9), 140.5 (Cq, C8), 140.1 (CH, C3), 134.6 (Cq, C10), 129.2 (Cq, C4), 129.0 (CH, C7), 128.7 (CH, C6), 127.7 (CH, C5), 127.3 (CH, C11), 126.0 (CH, C12), 121.9 (CH, C2). HR-EI-MS (70 eV): 561.06 $[M]^+$, 526.09 $[M–Cl]^+$.

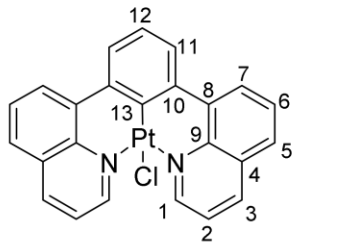

[Pt(PhPyQ)Cl] (3): HPhPyQ (50 mg, 0.18 mmol, 1.2 eq.) and K_2PtCl_4 (62.3 mg, 0.15 mmol, 1 eq.) were added to a microwave vial along with 10 mL of glacial HOAc. The mixture was heated to 160 °C at 250 W for 120 min. After cooling to room temperature, the formed yellow precipitate was filtered off. The filter residue was washed with demineralized water, MeOH and *c*-hexane. The remaining material was re-dissolved in CH_2Cl_2 and the solvent evaporated to yield orange powder (49.8 mg, 97.0 μmol, 66%). ^{1}H NMR ($CDCl_3$, 500 MHz): δ

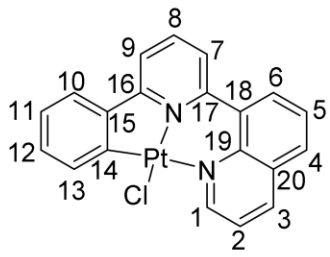

[ppm] = 10.38 (dd, ^3J = 5.1 Hz , ^4J = 1.7 Hz, 1H, H1), 8.51 (dd, ^3J = 8.2 Hz, ^4J = 1.6 Hz, 1H, H3), 8.36 (dd, ^3J = 7.5 Hz , ^4J = 1.3 Hz, 1H, H6), 8.18 (ddd, $J_{Pt\text{-}H}$ = 32.3 Hz, ^3J = 7.7 Hz, ^4J = 1.2 Hz, 0.4 Hz, 1H, H13), 8.08 (dd, ^3J = 8.0 Hz , ^4J = 1.2 Hz, 1H, H4), 7.99 (t, ^3J = 8.0 Hz, 1H, H8), 7.76–7.66 (m, 4H, H2, H6, H7, H9), 7.51 (dd, ^3J = 7.7 Hz , ^4J = 1.4 Hz, 1H, H10), 7.18–7.15 (m, 1H, H11). ^{13}C NMR ($CDCl_3$, 125 MHz): δ [ppm] = 168.2 (Cq, C16), 154.9 (CH, C1), 151.9 (Cq, C17), 144.5 (Cq, C15), 140.8 (Cq, C14), 140.4 (Cq, C19), 139.7 (CH, C3), 137.9 (CH, C8), 135.8 (CH, C13), 134.9 (CH, C6), 133.5 (Cq, C18), 132.4 (CH, C4), 129.8 (CH, C12), 129.5 (Cq, C20), 127.1 (CH, C7), 124.1 (CH, C11), 123.3 (CH, C10), 122.8 (CH, C9), 122.4 (CH, C2), 117.4 (CH, C5). ^{195}Pt NMR ($CDCl_3$, 54 MHz): δ [ppm] = −3357.6. HR-ESI-MS (70 eV): 533.03 [M+Na$^+$], 475.07 [M–Cl]$^+$. HR-EI-MS (70 eV): 511.04 [M$^{\cdot+}$], 475.07 [M−Cl$^+$].

1.5 Syntheses of the Palladium Complexes – General Procedure:
The ligand (1.2 eq.) and the K_2PdCl_4 (1 eq.) were mixed with glacial acetic acid in a round bottom flask and heated under reflux. Upon completion (indicated by the lack of any visible platinate leftover) the mixture was cooled to room temperature. The precipitate was filtered off using a glass frit and washed with demineralized water and diethyl ether. The complex was re-dissolved in CH_2Cl_2 and the solvent removed to yield the target complex.

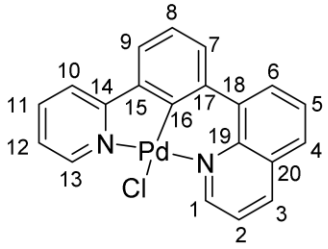

[Pd(PyPhQ)Cl] (4): PyHPhQ (60 mg, 0.21 mmol, 1.4 eq.) and K_2PdCl_4 (48.9 mg, 0.15 mmol, 1 eq.) were heated under reflux in glacial acetic acid for 19 h. The complex was isolated as yellow powder (56.2 mg, 133 mmol, 92%). ^{1}H NMR ($CDCl_3$, 500 MHz): δ [ppm] = 10.59 (dd, ^3J = 5.3 Hz, ^4J = 1.6 Hz, 1H, H1), 9.70 (d, ^3J = 4.8 Hz, 1H, H13), 8.43 (dd, ^3J = 8.1 Hz, ^4J = 1.6 Hz, 1H, H3), 8.40 (d, ^3J = 6.6 Hz, 1H, H4), 7.92–7.86 (m, 2H, H6, H11, H11), 7.80–7.75 (m, 2H, H7, H10), 7.74 (t, ^3J = 7.7 Hz, 1H, H5), 7.58 (dd, ^3J = 7.5 Hz, ^4J = 1.0 Hz, 1H, H9), 7.55 (dd, ^3J = 8.1 Hz, 5.4 Hz, 1H, H2), 7.35 (t, ^3J = 7.7 Hz, 1H, H8), 7.25 (ddd, ^3J = 7.3 Hz, 5.8 Hz, ^4J = 1.4 Hz, 1H, H12). ^{13}C NMR ($CDCl_3$, 125 MHz): δ [ppm] = 164.7 (Cq, C14), 158.7 (CH, C1), 153.7 (Cq, C16), 153.0 (CH, C13), 146.0 (Cq, C15), 140.3 (CH, C3), 139.4 (Cq, C19), 138.7 (CH, C11), 137.6 (Cq, C18), 132.6 (Cq, C17), 130.1 (CH, C4), 130.0 (Cq, C20), 129.0 (CH, C6), 127.6 (CH, C7), 127.2 (CH, C5), 125.8 (CH, C8), 123.3 (CH, C9), 122.5 (CH, C12), 120.9 (CH, C2), 118.4 (CH, C10). HR-ESI-MS (70 eV): 443.97 [M+Na]$^+$, 386.01 [M–Cl]$^+$.

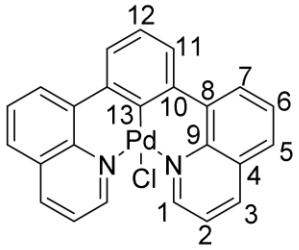

Synthesis of [Pd(QPhQ)Cl] (5): QHPhQ (60 mg, 0.18 mmol, 1.2 eq.) and K_2PdCl_4 (48.9 mg, 0.15 mmol, 1 eq.) were heated under reflux in glacial HOAc for 72 h. The complex was isolated as pale-yellow powder (34.4 mg, 73.0 mmol, 49%). ^{1}H NMR (DMSO-d_6, 500 MHz): δ [ppm] = 9.37 (dd, ^3J = 5.1 Hz, ^4J = 1.5 Hz, 2H, H1), 8.75 (dd, ^3J = 8.2 Hz, ^4J = 1.5 Hz, 2H, H3), 8.49 (dd, ^3J = 7.4 Hz, ^4J = 1.2 Hz, 2H, H7), 8.16 (dd, ^3J = 8.2 Hz, ^4J = 1.2 Hz, 2H, H5), 7.93–7.86 (m, 2H, H6), 7.65 (dd, ^3J = 8.2 Hz, 5.2 Hz, 2H, H2), 7.63 (d, ^3J = 7.7 Hz, 2H, H11), 7.38 (t, ^3J = 7.6 Hz, 1H, H12). ^{13}C NMR (DMSO-d_6, 125 MHz): δ [ppm] = 158.0 (CH, C1), 140.9 (Cq, C9), 140.5 (CH, C3), 140.4 (Cq, C8), 134.2 (Cq, C10), 129.7 (CH, C7), 129.0 (Cq, C4), 128.4 (CH, C5), 128.3 (CH, C6), 128.0 (CH, C11), 126.9 (CH, C12), 121.4 (CH, C2). HR-EI-MS (70 eV): 473.99 [M]$^+$, 437.03 [M–Cl]$^+$.

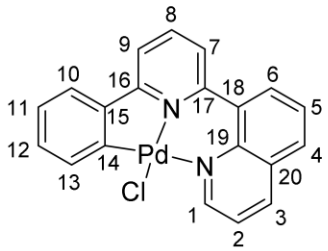

[Pd(PhPyQ)Cl] (6): HPhPyQ (50 mg, 0.18 mmol, 1.2 eq.) and K_2PtCl_4 (48.9 mg, 0.15 mmol, 1 eq.) were added to a microwave vial along with 10 mL of glacial HOAc. The mixture was heated to 160 °C at 250 W for 120 min. After cooling to room temperature, the formed pale-yellow precipitate was filtered off. The filter was washed with demineralized water, MeOH and *c*-hexane. The remaining powder was re-dissolved in CH_2Cl_2 and the solvent evaporated off to yield a pale-yellow powder (30 mg, 70 μmol, 47%). ^{1}H NMR ($CDCl_3$, 500 MHz): δ [ppm] = 10.2 (dd, ^3J = 5.0 Hz, ^4J = 1.7 Hz, 1H, H1), 8.40 (dd, ^3J = 8.2 Hz, ^4J = 1.7 Hz, 1H, H3), 8.32 (dd, ^3J = 7.5 Hz, ^4J = 1.2 Hz, 1H, H6), 8.14–8.10

(m, 1H, H13), 8.00 (dd, ^3J = 8.0 Hz, ^4J = 1.2 Hz, 1H, H4), 7.91 (t, ^3J = 8.0 Hz, 1H, H8), 7.71–7.61 (m, 3H, H2, H7, H9), 7.47–7.43 (m, 1H, H10), 7.16 (quin., ^3J = 5.8 Hz, ^4J = 2.0 Hz, 2H, H11, H12). ^{13}C NMR ($CDCl_3$, 125 MHz): δ [ppm] = 166.3 (Cq, C16), 155.9 (CH, C1), 153.9 (Cq, C17), 153.7 (Cq, C14), 145.5 (Cq, C15), 141.3 (Cq, C19), 139.6 (CH, C3), 138.8 (CH, C8), 137.5 (CH, C13), 135.2 (CH, C6), 132.9 (Cq, C18), 132.0 (CH, C4), 129.5 (CH, C12), 129.3 (Cq, C20), 126.9 (CH, C7), 124.7 (CH, C11), 123.5 (CH, C10), 123.4 (CH, C9), 121.9 (CH, C2), 117.4 (CH, C5). HR-ESI-MS (70 eV): 443.97 $[M+Na]^+$, 387.01 $[M–Cl]^+$. HR-EI-MS (70 eV): 421.98 $[M]^+$, 387.01 $[M–Cl]^+$.

1.6 Syntheses of the Nickel Complexes

Synthesis of [Ni(PyPhQ)Br] (7): PyHPhQ (100 mg, 0.35 mmol, 1 eq.), $NiBr_2$ (100 mg, 0.46 mmol, 1.3 eq.), K_2CO_3 (48.9 mg, 0.35 mmol, 1 eq.) and KOAc (34.7 mg, 0.35 mmol, 1 eq.) were added to an inert three-necked flask under argon. The mixture was suspended in freshly distilled *p*-xylene and fitted with a *Dean-Stark* apparatus filled with dried molecular sieves. The mixture was heated under reflux for 72 h. After cooling to ambient *T*, the dark orange solution was filtered over a glass frit and washed with *p*-xylene. The filtrate was evaporated off giving an orange solid, which was washed with *n*-pentane. Upon drying, a red powder was obtained (75.7 mg, 0.18 mmol, 51%). ^{1}H NMR ($CDCl_3$, 500 MHz): δ [ppm] = 10.09 (s, 1H, H1), 9.41 (s, 1H, H13), 8.36 (d, ^3J = 6.9 Hz, 1H, H4), 8.26 (d, ^3J = 7.6 Hz, 1H, H3), 7.77 (d, ^3J = 7.1 Hz, 2H, H11, H6), 7.73–7.64 (m, 2H, H5, H7), 7.57 (d, ^3J = 6.9 Hz, 1H, H10), 7.39–7.30 (m, 2H, H9, H2), 7.28 (s,1H, H8), 7.12–7.06 (m, 1H, H12). ^{13}C NMR ($CDCl_3$, 125 MHz): δ [ppm] = 162.7 (Cq, C14), 158.2 (CH, C1), 154.4 (CH, C13), 146.9 (Cq, C15), 146.7 (Cq, C16), 140.3 (Cq, C19), 139.0 (CH, C3), 138.3 (CH, C11), 135.2 (Cq, C18), 134.4 (Cq, C17), 129.2 (Cq, C20), 128.1 (CH, C6), 127.3 (CH, C5), 127.0 (CH, C4), 126.0 (CH, C8), 125.2 (CH, C7), 122.3 (CH, C9), 122.0 (CH, C12), 119.4 (CH, C2), 117.5 (CH, C10). HR-ESI-MS (70 eV): 418.97 $[M+H]^+$, 339.04 $[M–Br]^+$.

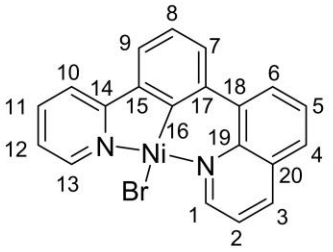

Synthesis of [Ni(QPhQ)Cl] (8): In a *Schlenk* flask, QClPhQ (100 mg, 0.27 mmol, 1.2 eq.) was mixed with freshly prepared $[Ni(COD)_2]$ (62.7 mg, 0.23 mmol, 1 eq.) in 20 mL THF. The solution quickly changed from a pale yellow to orange. The mixture was stirred at ambient temperature for 19 h before 20 mL of *n*-pentane were added, leading to an orange precipitate. The excess solvent was decanted. The crude product was washed with 3 × 20 mL *n*-pentane and dried under vacuum to yield a light orange powder (41.8 mg, 0.1 mmol, 43%). ^{1}H NMR ($CDCl_3$, 500 MHz): δ [ppm] = 9.34 (s, 2H, H1), 8.40–8.29 (m, 2H, H5), 8.21 (d, ^3J = 3.9 Hz, 2H, H3), 7.85–7.70 (m, 4H, H6, H7), 7.40 (d, ^3J = 4.2 Hz, 2H, H11), 7.26–7.18 (m, 3H, H2, H12). ^{13}C NMR ($CDCl_3$, 125 MHz): δ [ppm] = 158.5 (CH, C1), 142.0 (Cq, C9), 139.1 (Cq, C8), 138.3 (CH, C3), 136.6 (Cq, C13), 128.2 (Cq, C4), 127.6 (CH, C6), 127.0 (CH, C7), 126.5 (CH, C5), 125.7 (CH, C12), 125.5 (CH, C11), 119.4 (CH, C2). HR-ESI-MS (70 eV): 363.15 $[M–Ni–Cl+MeOH]^+$.

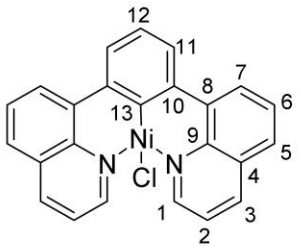

Synthesis of [Ni(PhPyQ)Br] (9): HPhPyQ (127 mg, 0.45 mmol, 1 eq.), $NiBr_2$ (129 mg, 0.59 mmol, 1.3 eq.), K_2CO_3 (62.2 mg, 0.45 mmol, 1 eq.) and KOAc (44.2 mg, 0.45 mmol, 1 eq.) were added to an inert three-necked flask under argon. The mixture was picked up in freshly distilled *p*-xylene and fitted with a *Dean-Stark* apparatus filled with dried molecular sieves. The mixture was heated under reflux for 72 h. Upon cooling to ambient temperature, the red solution was filtered over a glass frit and washed with *p*-xylene. The filter residue was dried and the product obtained as a dark red powder (51.5 mg, 0.11 mmol, 24%). The very high sensitivity against hydrolysis circumvented any characterization of this complex.

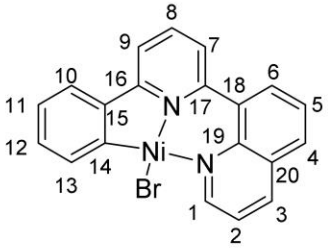

2. Supporting Figures

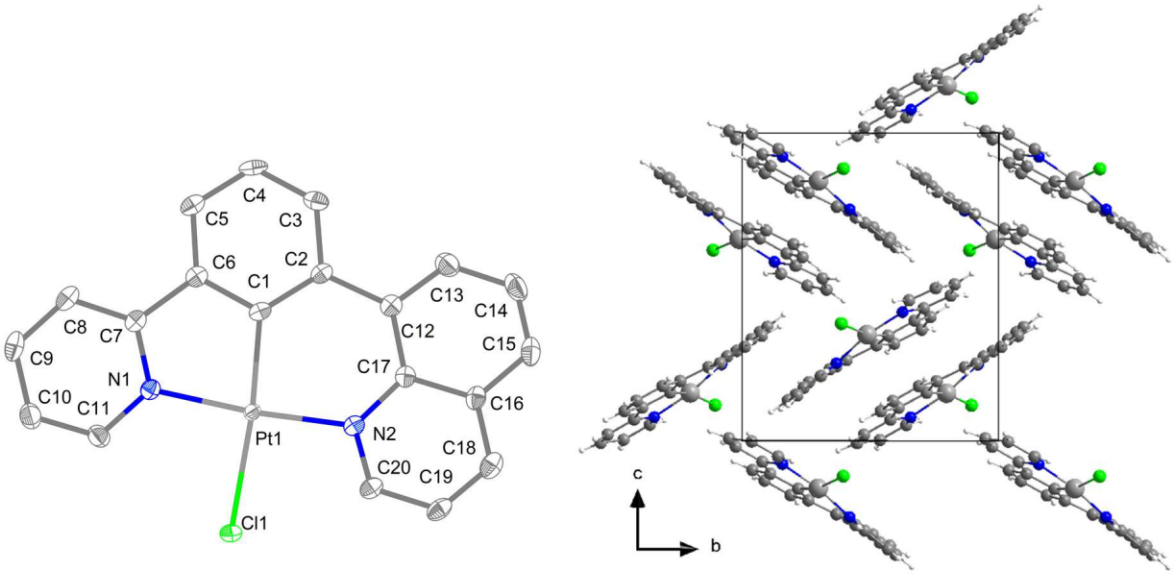

Figure S1. Molecular structure of [Pt(PyPhQ)Cl] (**1**) from single crystal X-ray diffraction (ORTEP plot with displacement ellipsoids at 50% probability)(left) and view on the crystal structure (right) along the crystallographic *a*-axis.

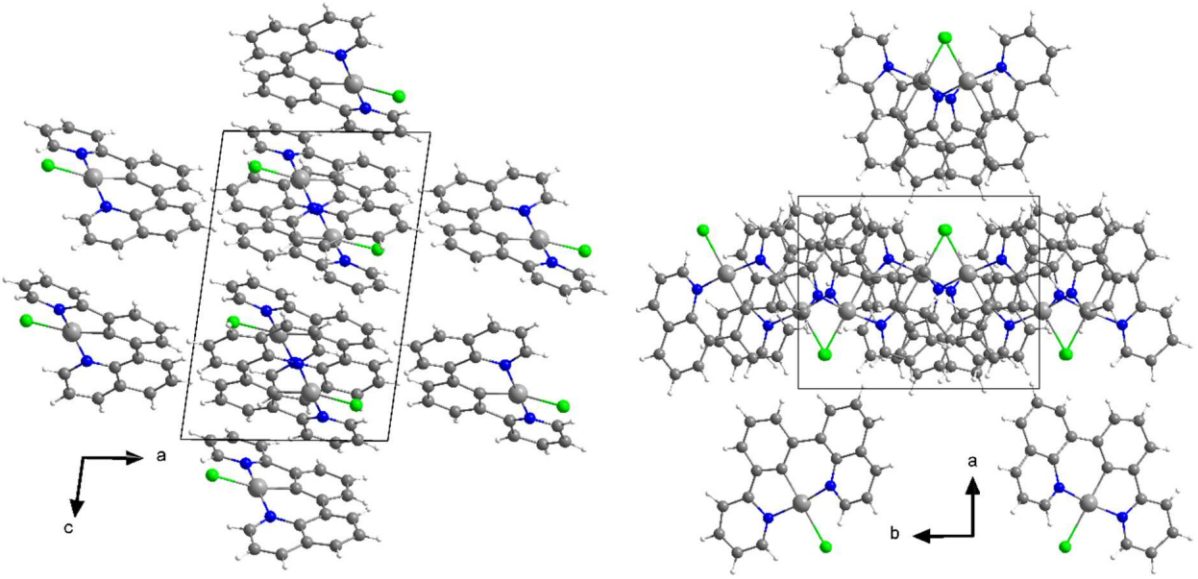

Figure S2. Views on the crystal structure of [Pt(PyPhQ)Cl] (**1**) along the crystallographic *b*-axis (left) and *c*-axis (right).

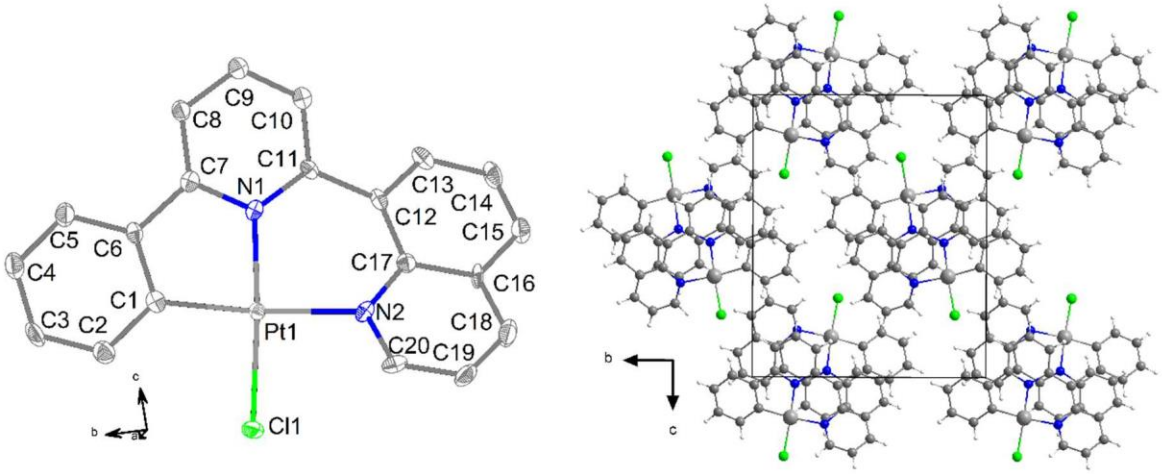

Figure S3. Molecular structure of [Pt(PhPyQ)Cl] (**3**) from single crystal X-ray diffraction (ORTEP plot with displacement ellipsoids at 50% probability) (left) and view of the crystal structure (right) along the crystallographic *a*-axis.

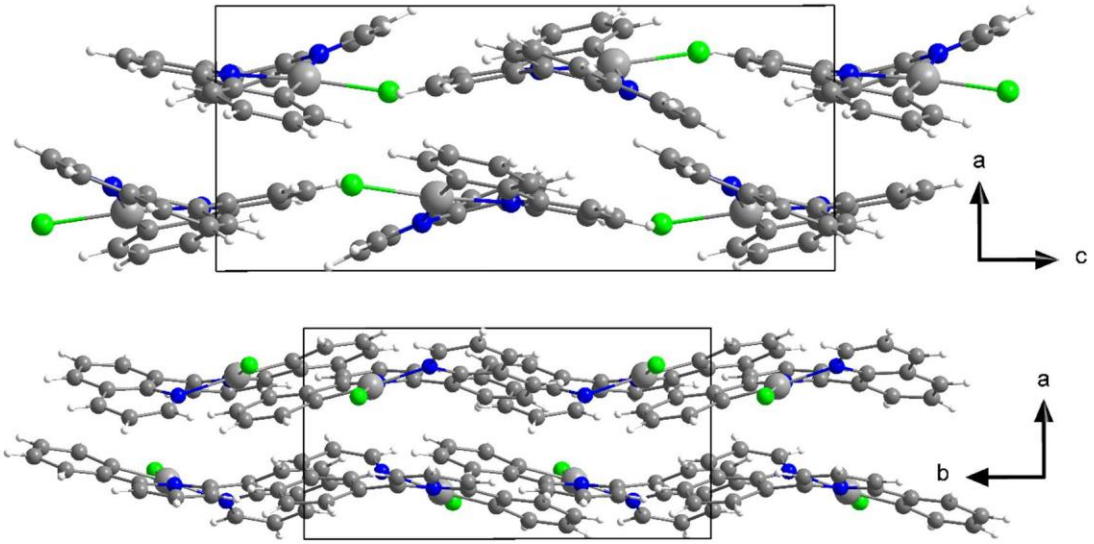

Figure S4. Views on the crystal structure of [Pt(PhPyQ)Cl] (**3**) along the crystallographic *b*-axis (top) and *c*-axis (bottom).

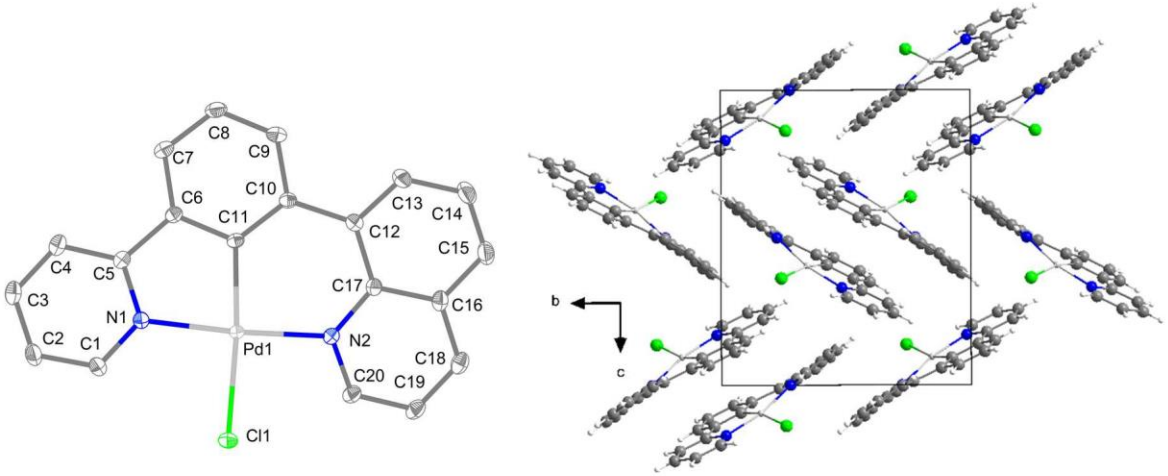

Figure S5. Molecular structure of [Pd(PyPhQ)Cl] (**4**) from single crystal X-ray diffraction (ORTEP plot with displacement ellipsoids at 50% probability) (left) and view of the crystal structure (right) along the crystallographic *a*-axis.

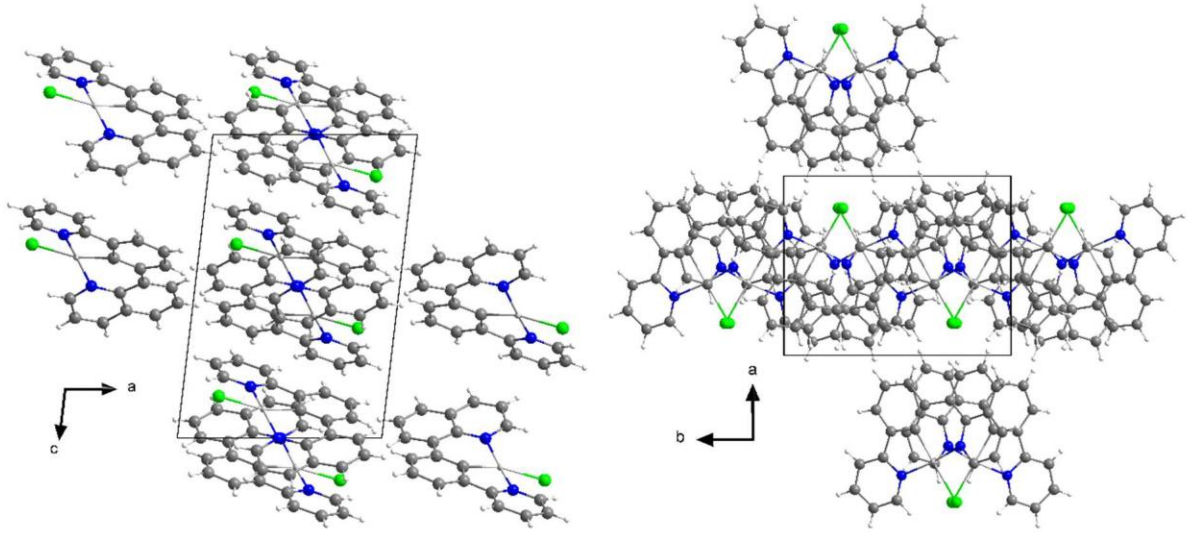

Figure S6. Views on the crystal structure of [Pd(PyPhQ)Cl] (**4**) along the crystallographic *b*-axis (left) and *c*-axis (right).

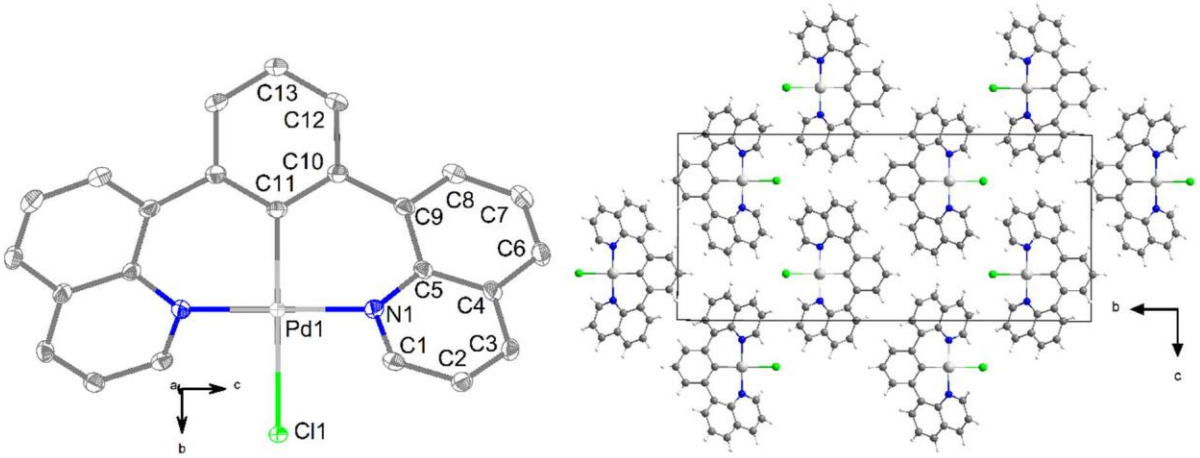

Figure S7. Molecular structure of [Pd(QPhQ)Cl] (**5**) from single crystal X-ray diffraction (ORTEP plot with displacement ellipsoids at 50% probability) (left) and view of the crystal structure (right) along the crystallographic *a*-axis.

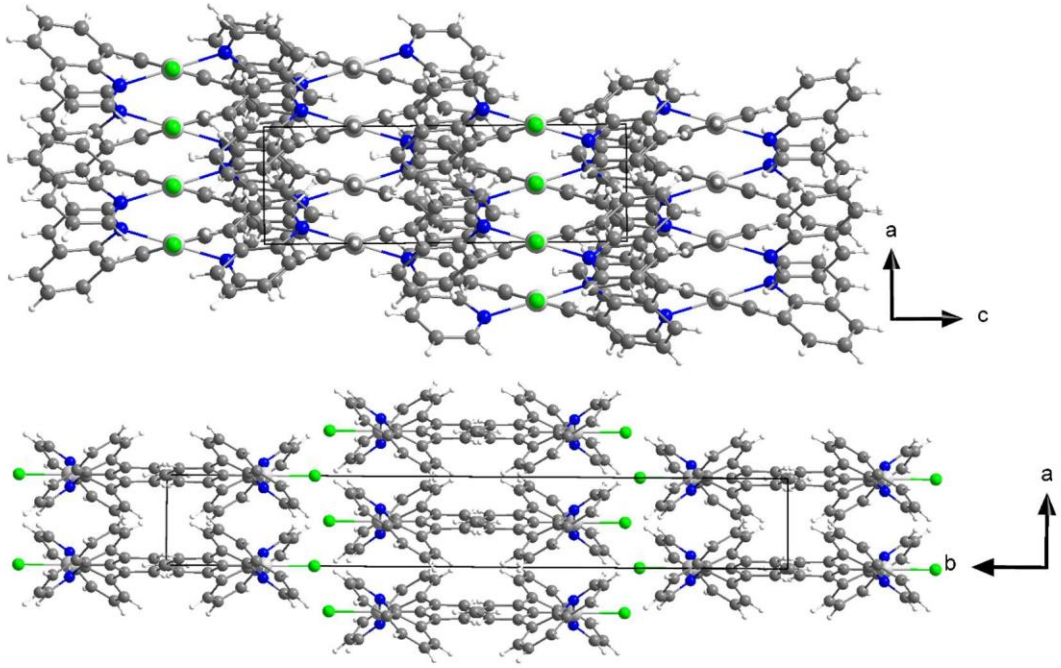

Figure S8. Views on the crystal structure of [Pt(QPyQ)Cl] (**5**) along the crystallographic *b*-axis (top) and *c*-axis (bottom).

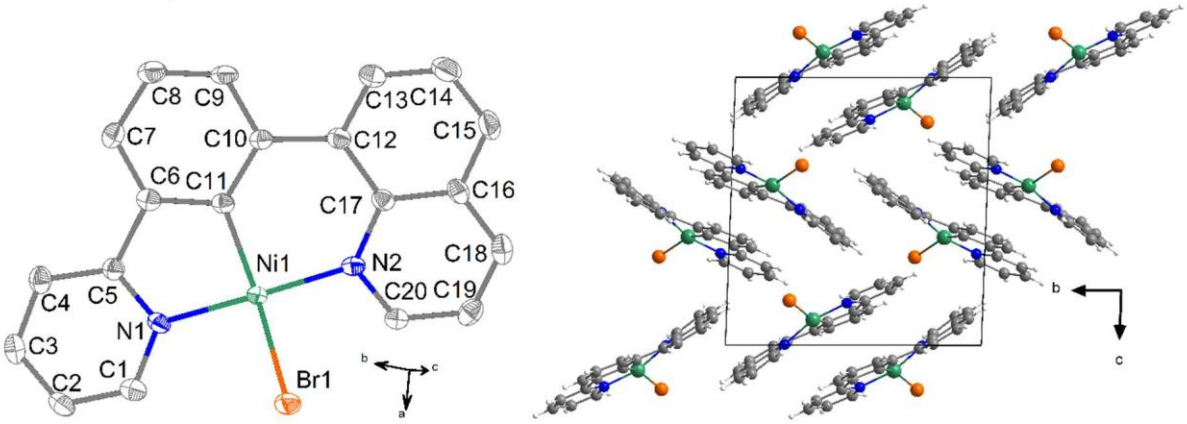

Figure S9. Molecular structure of [Ni(PyPhQ)Br] (**7**) from single crystal X-ray diffraction (ORTEP plot with displacement ellipsoids at 50% probability) (left) and view of the crystal structure (right) along the crystallographic *a*-axis.

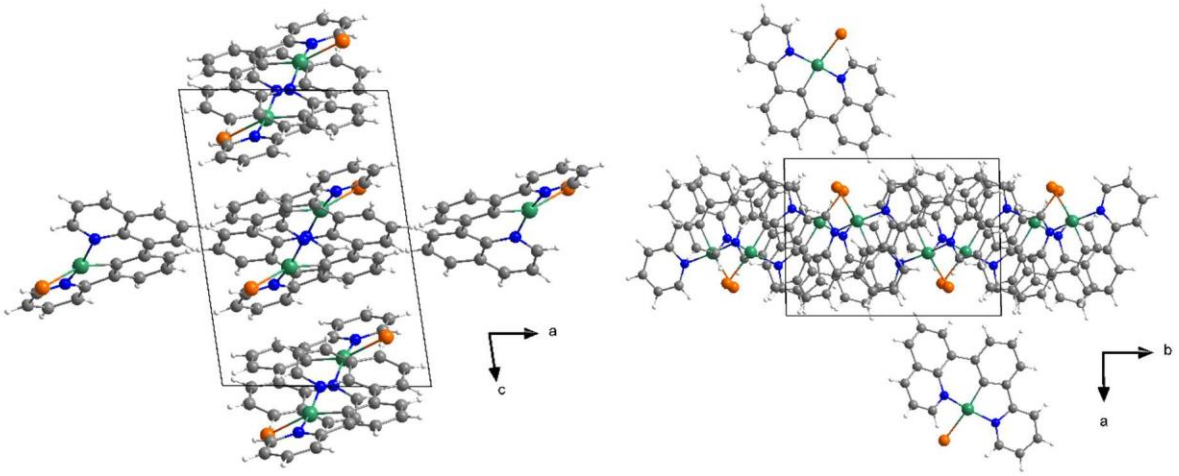

Figure S10. Views on the crystal structure of [Ni(PyPhQ)Br] (**7**) along the crystallographic *b*-axis (left) and *c*-axis (right).

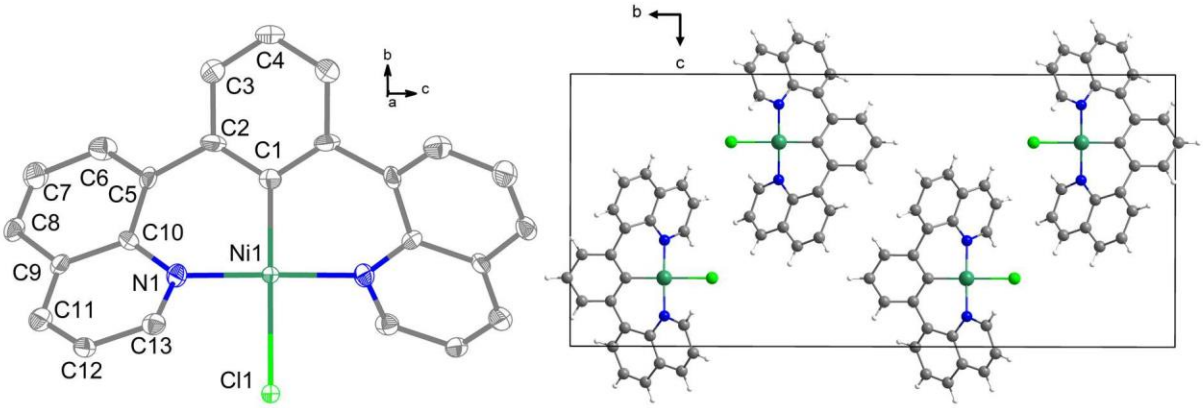

Figure S11. Molecular structure of [Ni(QPhQ)Br] (**8**) from single crystal X-ray diffraction (ORTEP plot with displacement ellipsoids at 50% probability) (left) and view of the crystal structure (right) along the crystallographic *a*-axis.

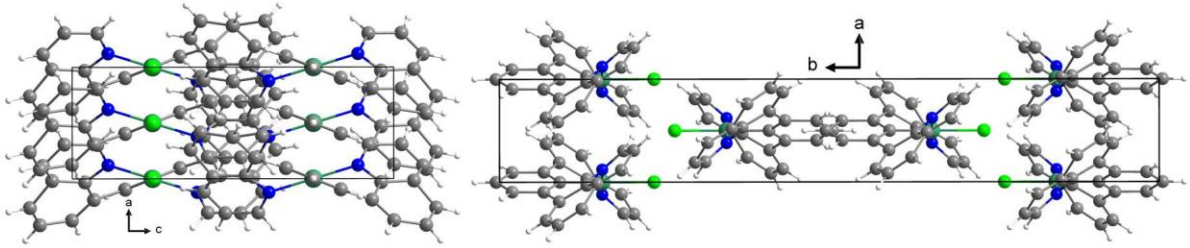

Figure S12. Views on the crystal structure of [Ni(QPhQ)Br] (**8**) along the crystallographic *b*-axis (left) and *c*-axis (right).

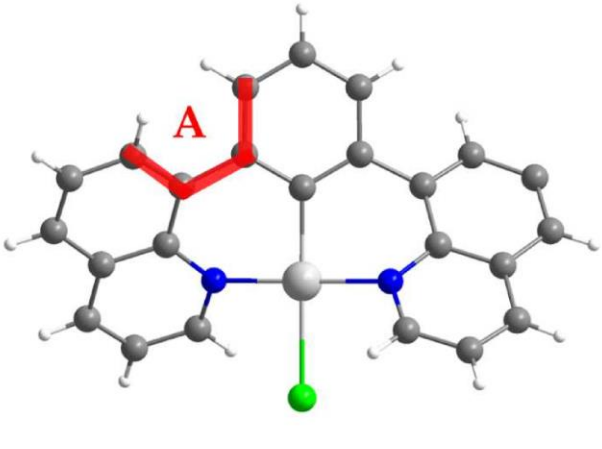

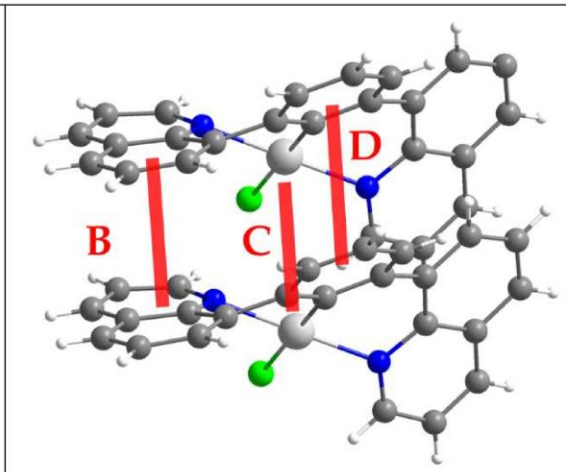

	[Pt(QPhQ)Cl] (2)	[Pd(QPhQ)Cl] (5)	[Ni(QPhQ)Cl] (8)
Interplanar torsion angles (°)			
A (phenyl-quinoline)	33.3(5)	33.9(6)	36.9 (5)
Centroid distances (Å)			
B (quinoline-quinoline)	3.4381(2)	3.4570(1)	3.4415(3)
C (metal-metal)	4.2626(3)	4.3395(2)	4.5440(6)
D (phenyl-phenyl)	4.2626(3)	4.3395(2)	4.5440(6)

Figure S13. Selected ring torsion angles (left, A), centroid distances (right, B: quinoline-quinoline, C: metal-metal, D: phenyl-phenyl) for complexes [M(QPhQ)X].

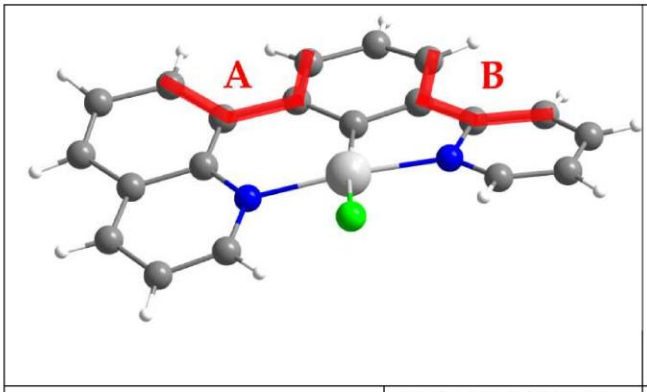

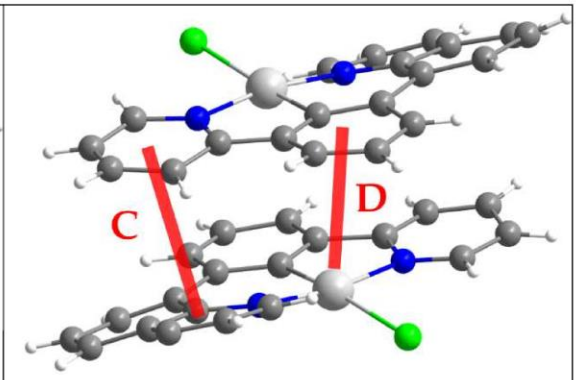

	[Pt(PyPhQ)Cl] (1)	[Pd(PyPhQ)Cl] (4)	[Ni(PyPhQ)Br] (7)
Interplanar torsion angles (°)			
A (phenyl-quinoline)	12.9(3)	14.3(4)	17.6(2)
B (phenyl-pyridine)	5.2(2)	4.9(6)	4.4(2)
Centroid distances (Å)			
C (pyridine-quinoline)	3.8851(2)	3.9288(1)	3.7638(6)
D (phenyl-metal)	3.6729(3)	3.6797(3)	4.2394(2)

Figure S14. Selected ring torsion angles (left, A and B), centroid distances (right, C: phenyl-quinoline, D: phenyl-metal) for complexes [M(PyPhQ)X].

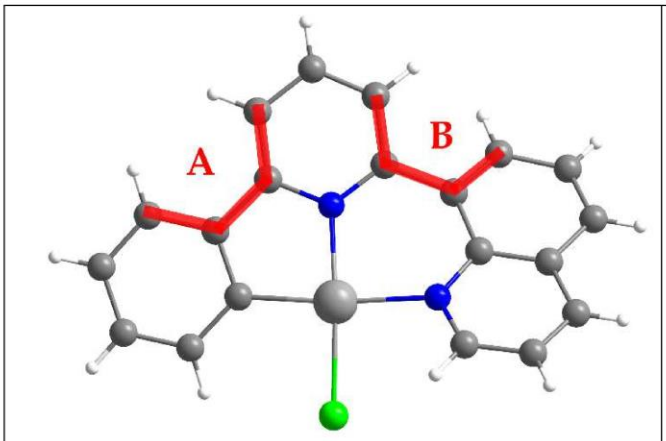

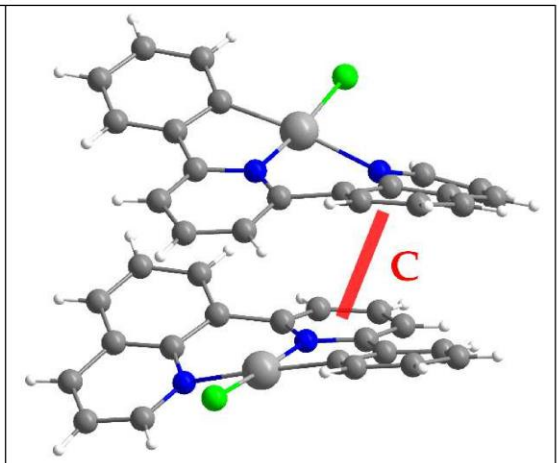

	[Pt(PhPyQ)Cl] (3)	[Pt(PhPyQ)Cl] (3) Calc.[a]	[Ni(PhPyQ)Br] (9) Calc.[a]
Interplanar torsion angles (°)			
A (pyridine-phenyl)	10.8(2)	8.3	16.9
B (pyridine-quinoline)	28.9(2)	34.6	31.8
Centroid distances (Å)			
C (pyridine-quinoline)	3.8178(1)	-	-

Figure S15. Selected ring torsion angles (left, A and B), centroid distances (right, C: pyridine-quinoline) for complexes [M(PhPyQ)X].[a] DFT calculations on B3LYP/def2-TZVP/CPCM(THF) level of theory.

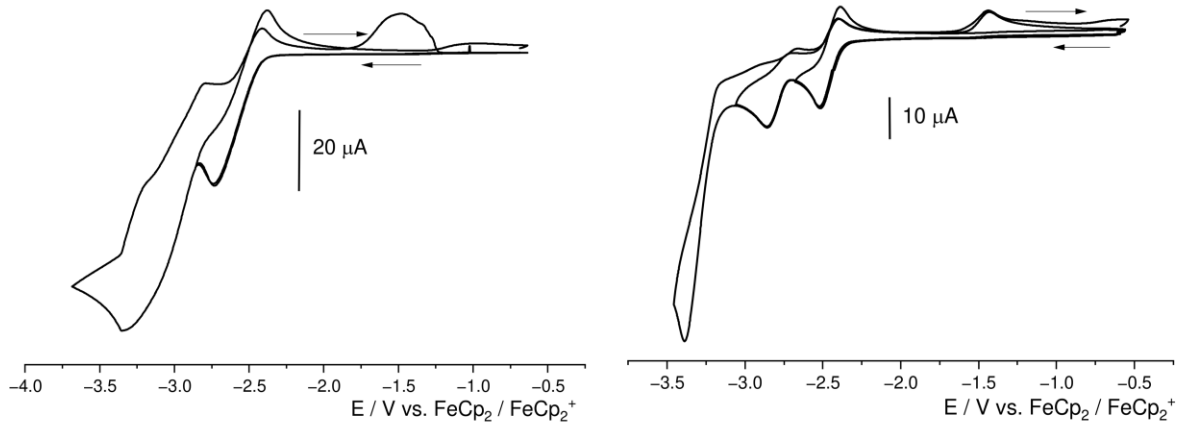

Figure S16. Cyclic voltammograms of PyHPhQ (left) and HPhPyQ (right), in 0.1 M *n*-Bu_4NPF_6 solution in THF at room temperature at a scan rate of 100 mV/s.

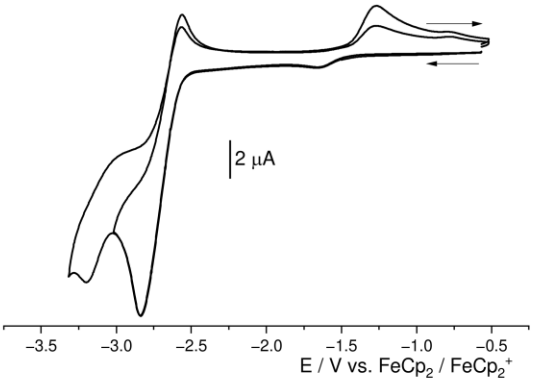

Figure S17. Cyclic voltammograms of QHPhQ in 0.1 M *n*-Bu_4NPF_6 solution in THF at room temperature at a scan rate of 100 mV/s.

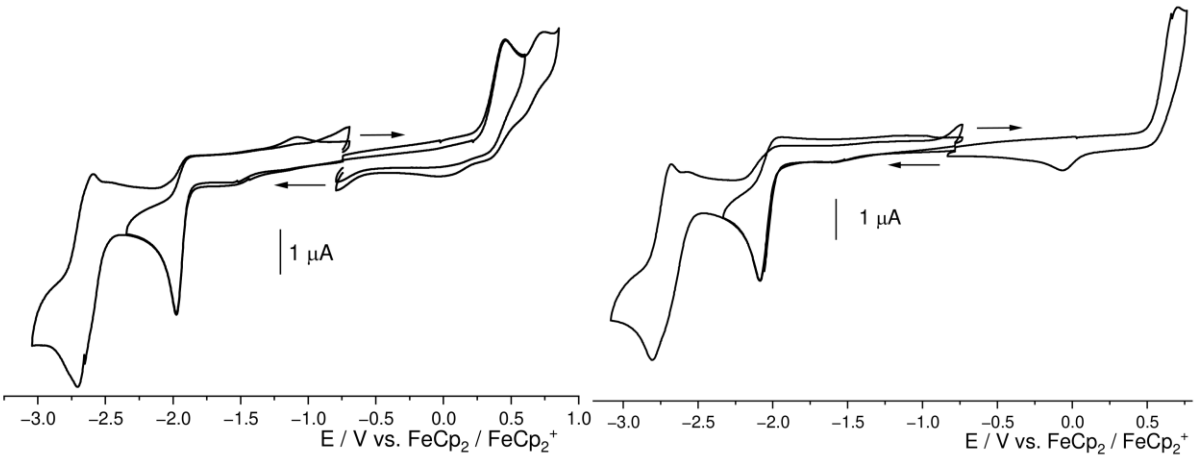

Figure S18. Cyclic voltammograms of [Pt(PyPhQ)Cl] (**1**) (left) and [Pd(PyPhQ)Cl] (**4**) (right), in 0.1 M *n*-Bu_4NPF_6 solution in THF at room temperature at a scan rate of 100 mV/s.

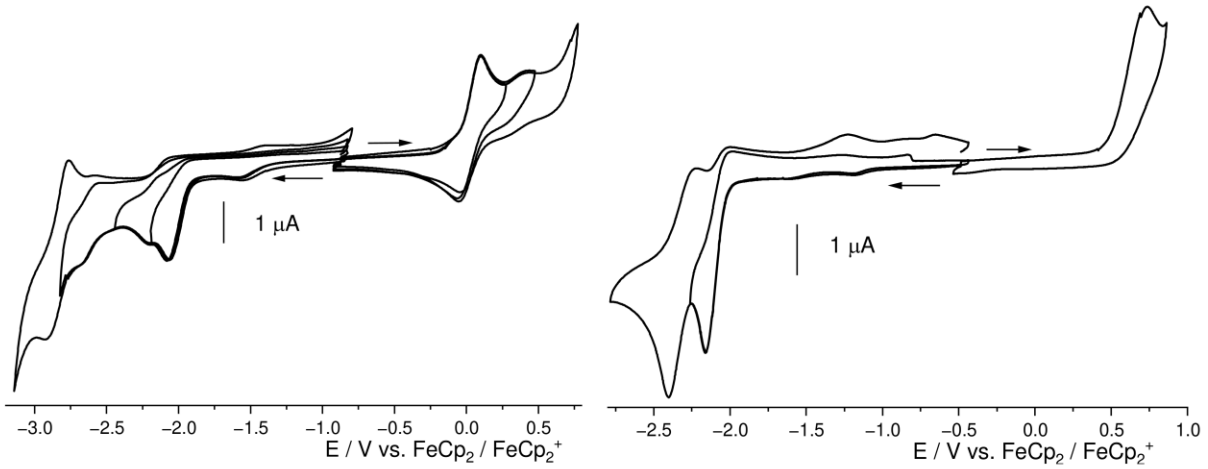

Figure S19. Cyclic voltammograms of [Ni(PyPhQ)Br] (**7**) (left) and [Pt(QPhQ)Cl] (**2**) (right), in 0.1 M *n*-Bu_4NPF_6 solution in THF at room temperature at a scan rate of 100 mV/s.

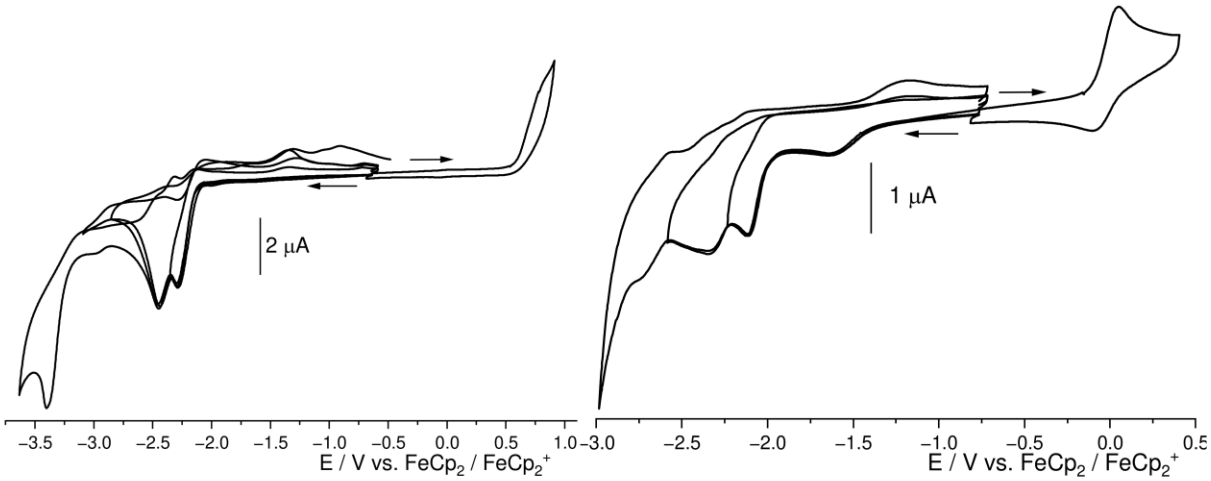

Figure S20. Cyclic voltammograms of [Pd(QPhQ)Cl] (**5**) (left) and [Ni(QPhQ)Cl] (**8**) (right) in 0.1 M *n*-Bu_4NPF_6 solution in THF at room temperature at a scan rate of 100 mV/s.

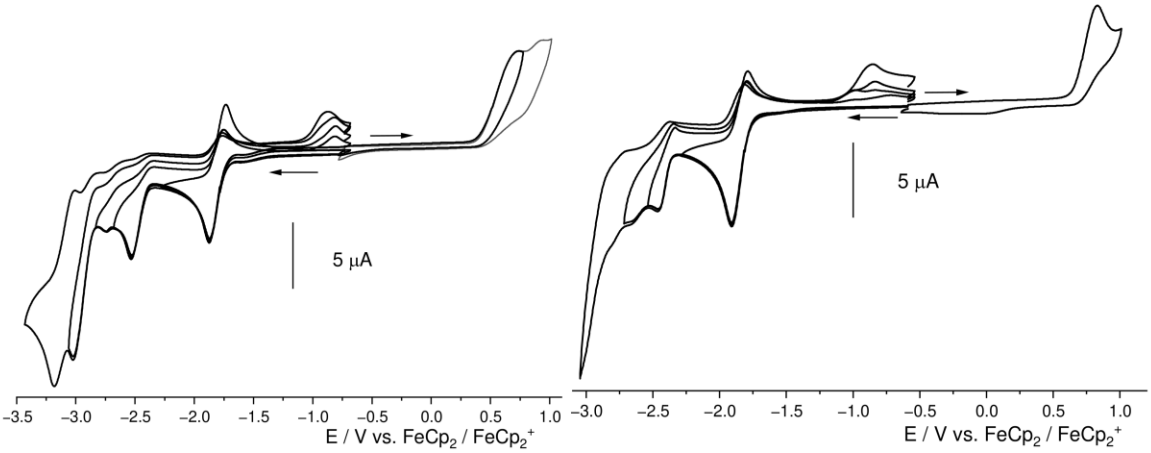

Figure S21. Cyclic voltammograms of [Pt(PhPyQ)Cl] (**3**) and [Pd(PhPyQ)Cl] (**6**) (right) (left) and, in 0.1 M *n*Bu_4NPF_6 solution in THF at room temperature at a scan rate of 100 mV/s.

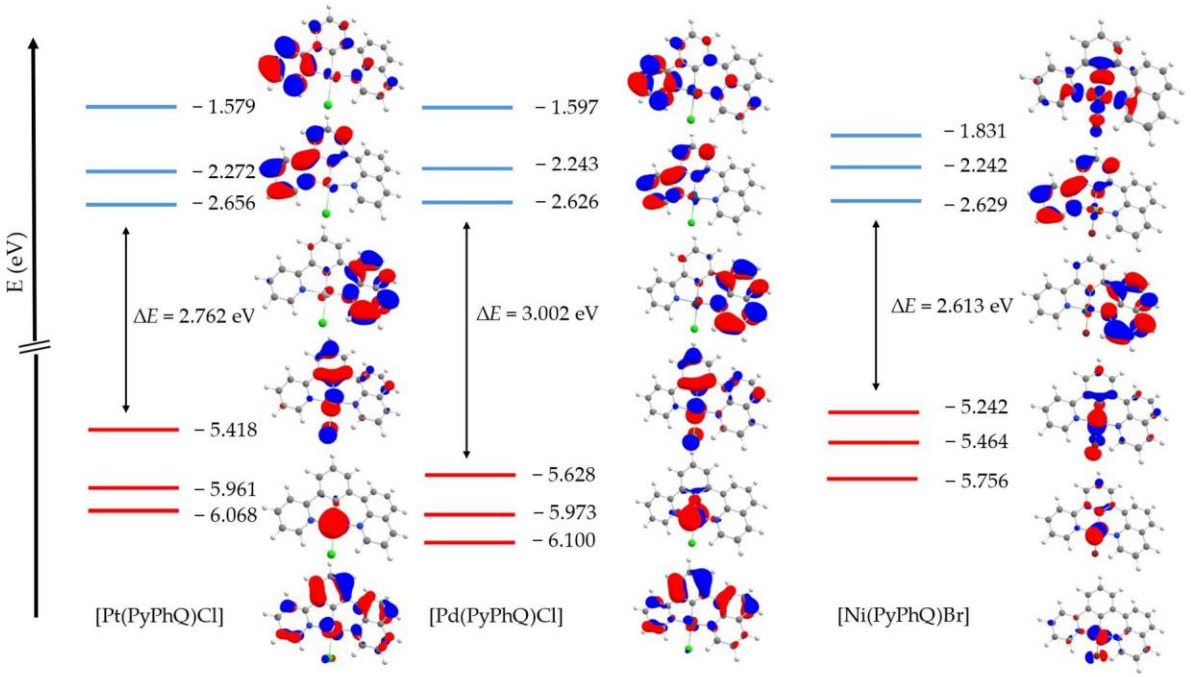

Figure S22. DFT-calculated composition and energies of selected molecular orbitals of [M(PyPhQ)X] type complexes **1**, **4** and **7**. Highest occupied molecular orbital = HOMO (red); lowest unoccupied molecular orbital = LUMO (blue) (Isovalue 0.04, TPSSh/def2-TZVP/CPCM(THF) level of theory.

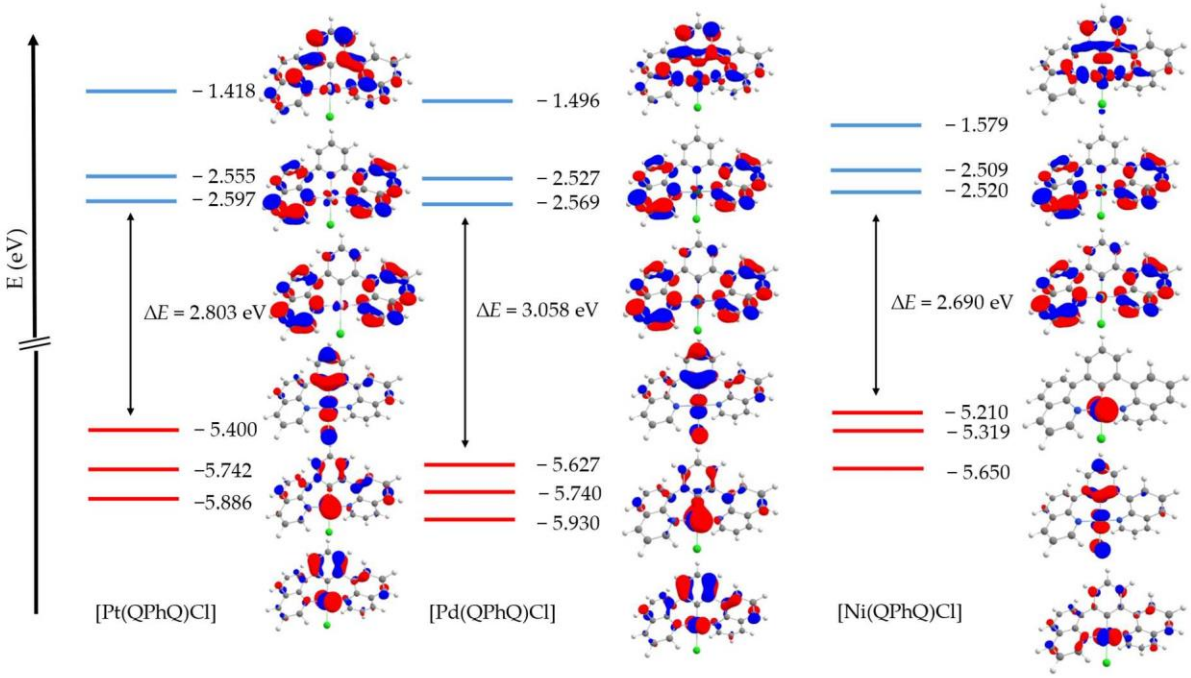

Figure S23. DFT-calculated composition and energies of selected molecular orbitals of [M(QPhQ)X] type complexes **2**, **5** and **8**. Highest occupied molecular orbital = HOMO (red); lowest unoccupied molecular orbital = LUMO (blue) (Isovalue 0.04, TPSSh /def2-TZVP/CPCM(THF) level of theory.

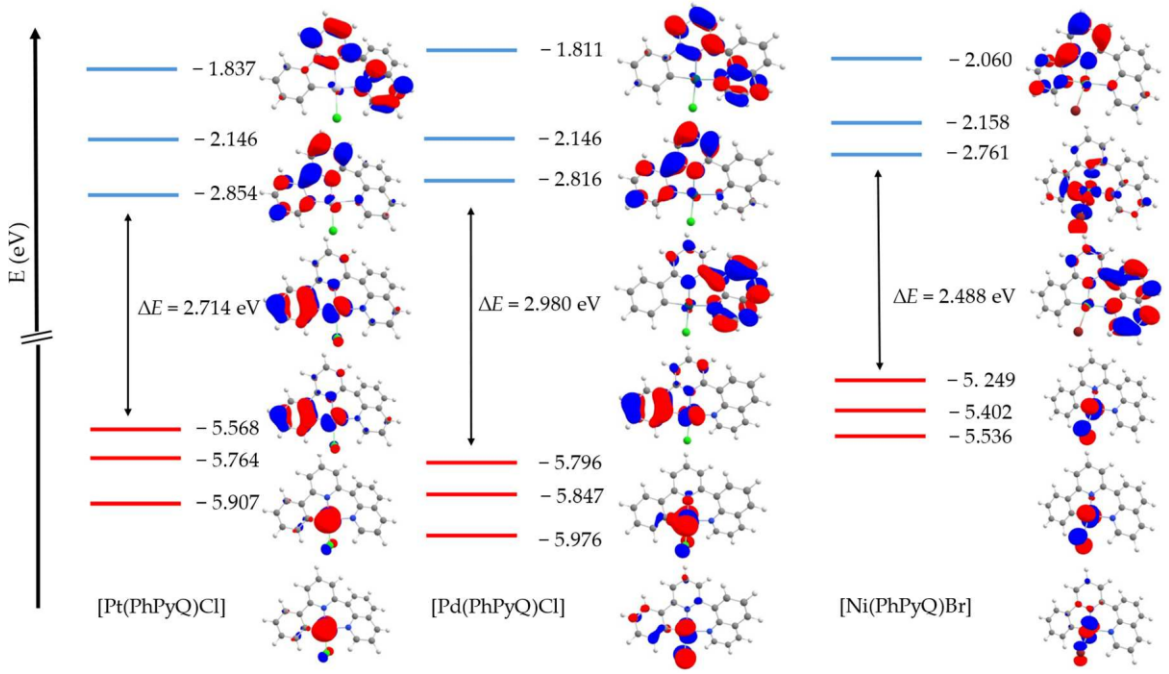

Figure S24. DFT-calculated composition and energies of selected molecular orbitals of [M(PhPyQ)X] type complexes **3**, **6** and **9**. Highest occupied molecular orbital = HOMO (red); lowest unoccupied molecular orbital = LUMO (blue) (Isovalue 0.04, TPSSh /def2-TZVP/CPCM(THF) level of theory.

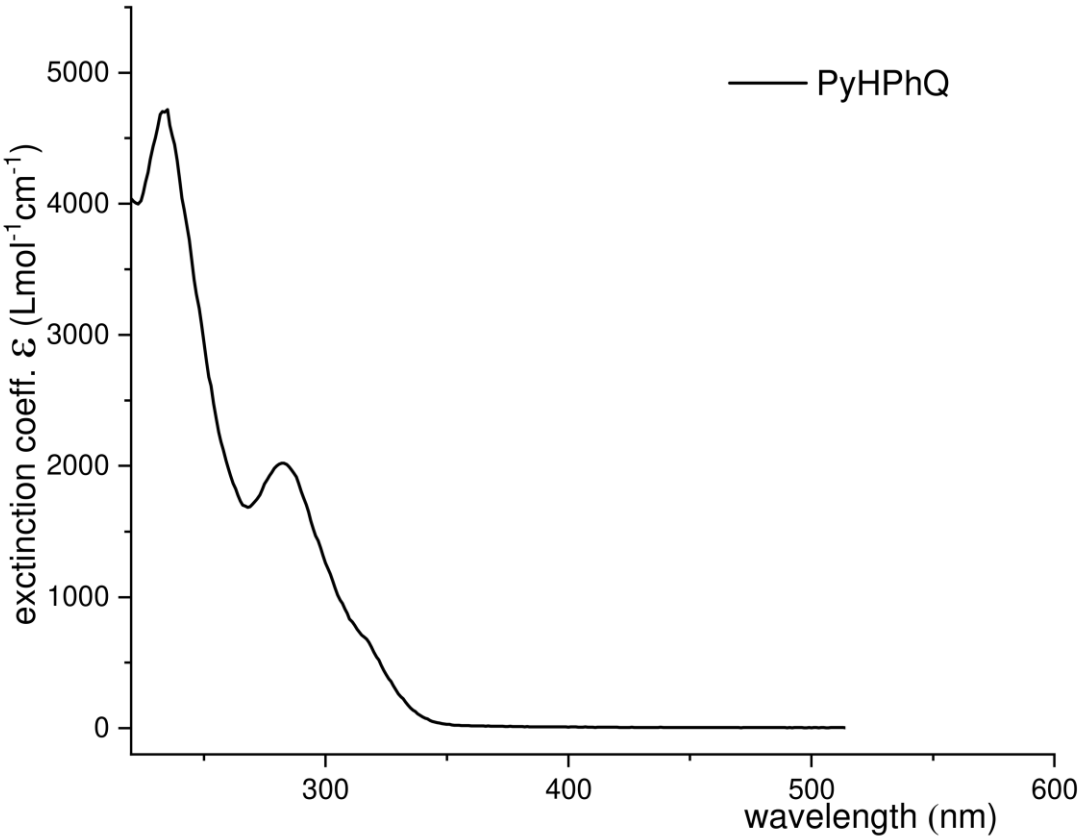

Figure S25. UV-vis absorption spectrum of PyHPhQ in THF at room temperature.

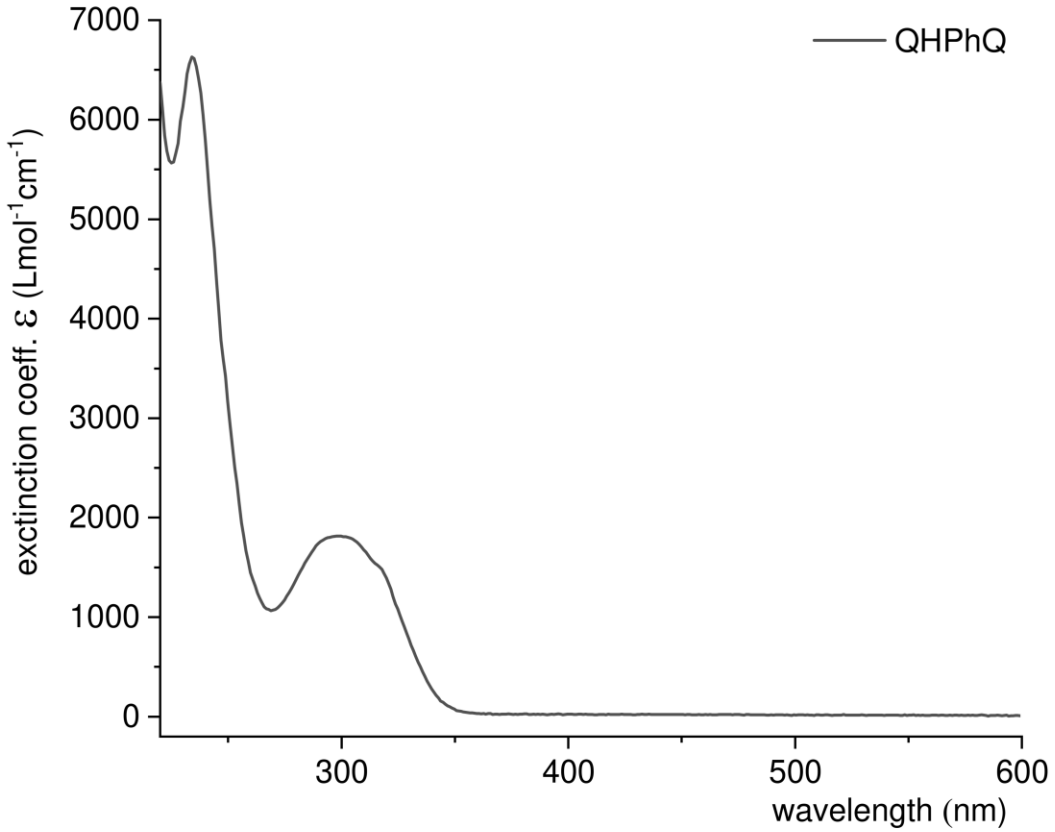

Figure S26. UV-vis absorption spectrum of QHPhQ in THF at room temperature.

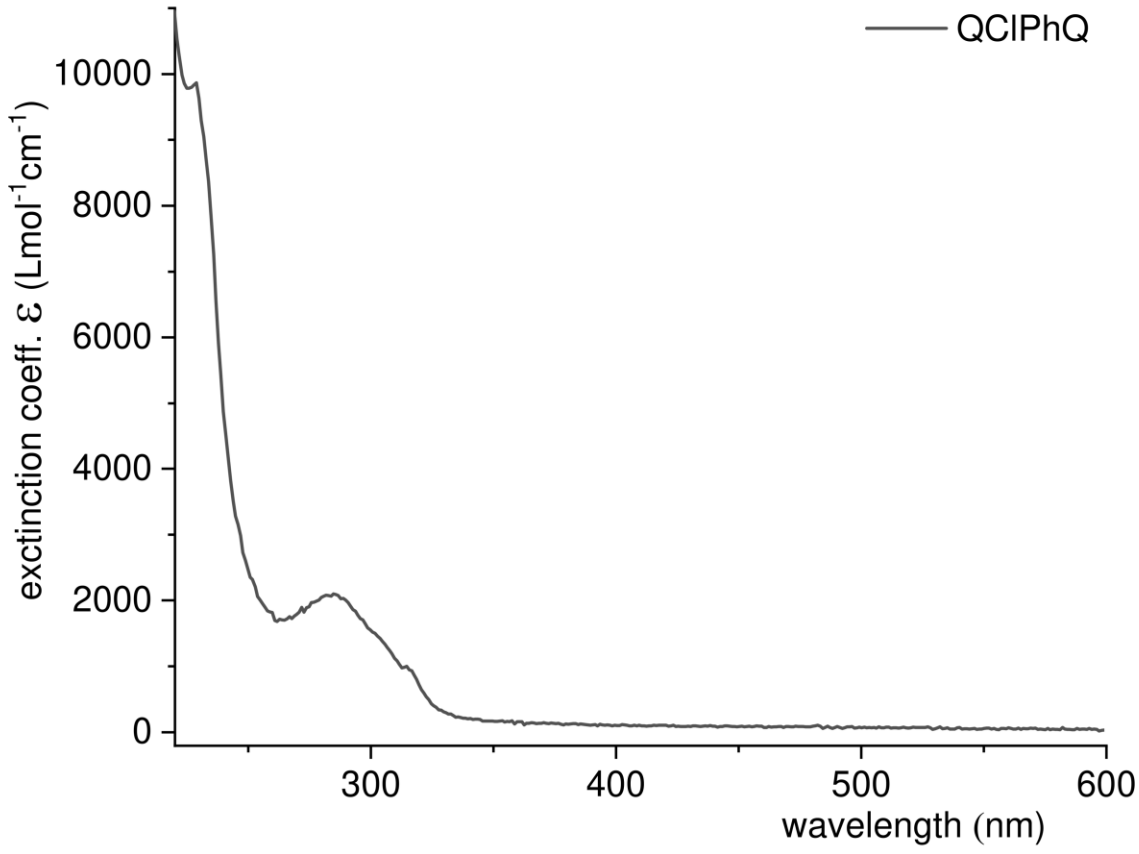

Figure S27. UV-vis absorption spectrum of QClPhQ in THF at room temperature.

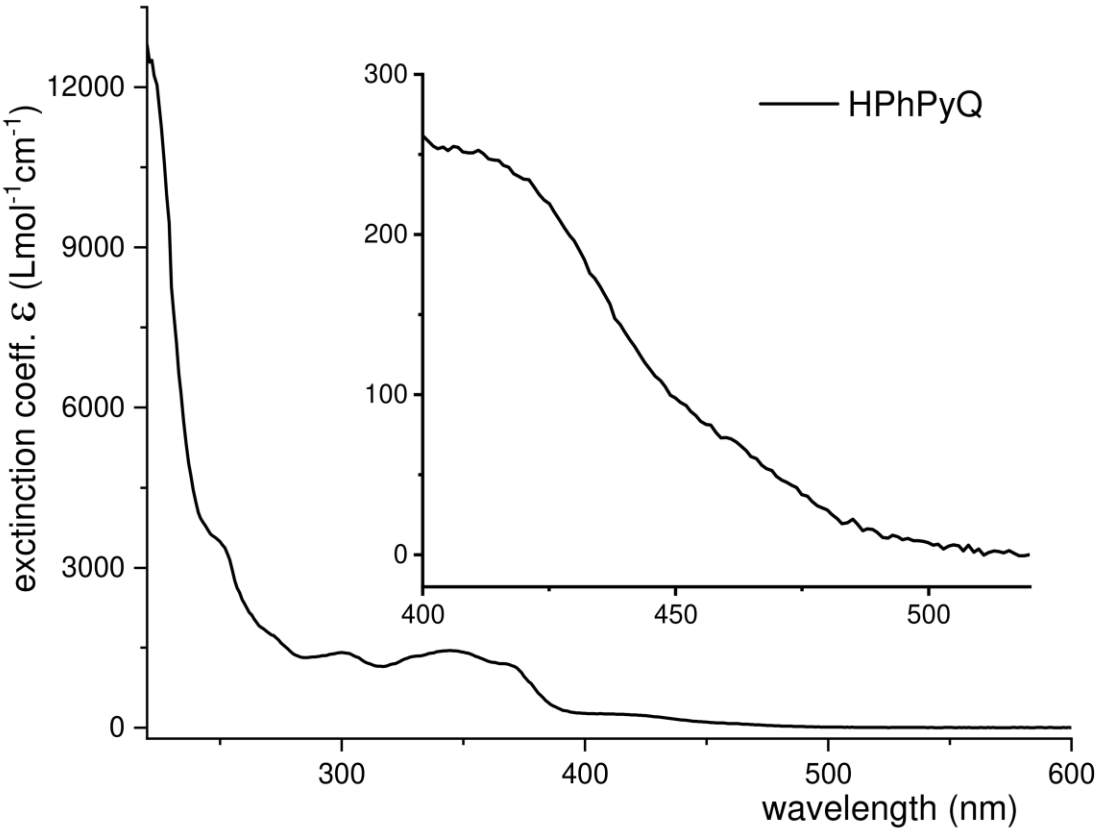

Figure S28. UV-vis absorption spectrum of HPhPyQ in THF at room temperature.

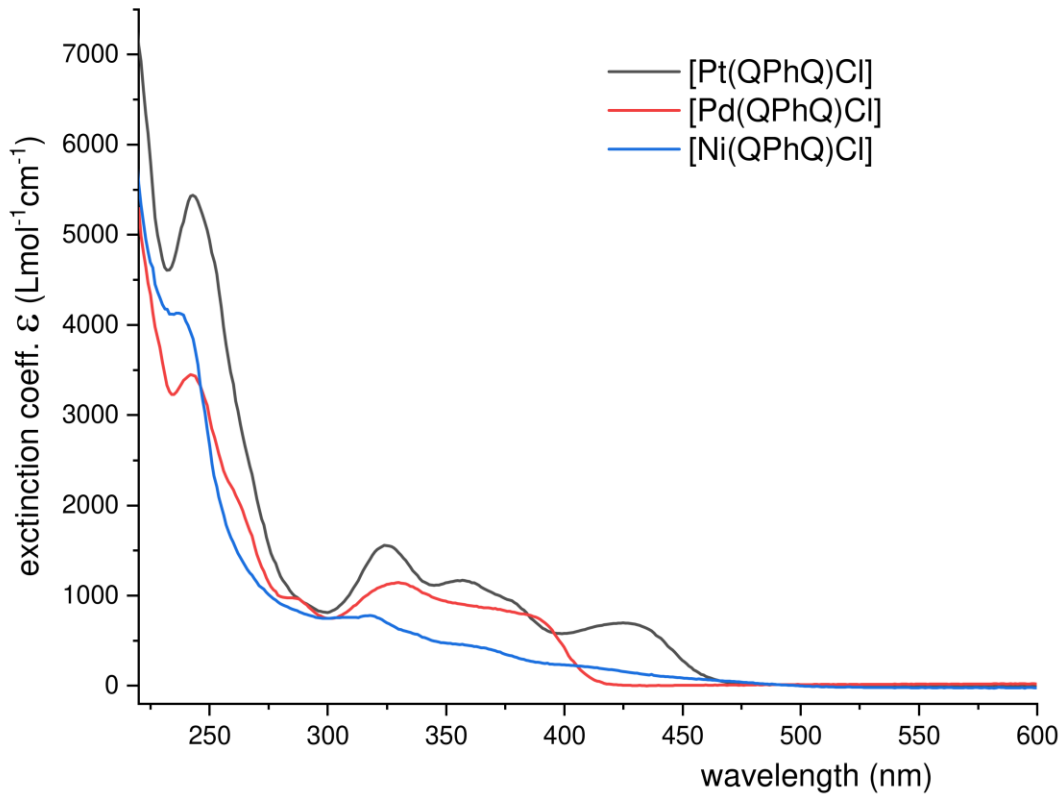

Figure S29. UV-vis absorption spectra of [Pt(QPhQ)Cl] (**2**) (black), [Pd(QPhQ)Cl] (**5**) (red), and [Ni(QPhQ)Cl] (**8**) (blue), and in THF at room temperature.

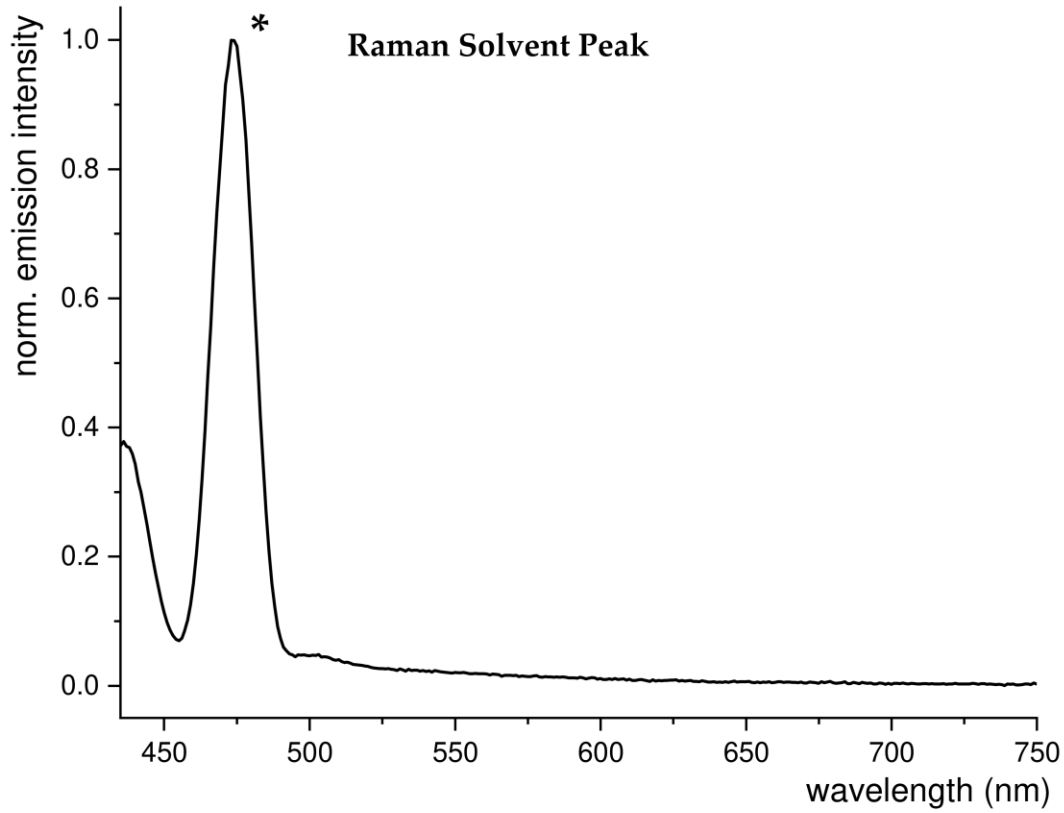

Figure S30. Photoluminescence spectrum of freshly distilled THF at 293 K, λ_{exc} = 416 nm. The Raman peak stemming from the THF solvent is marked with an *.

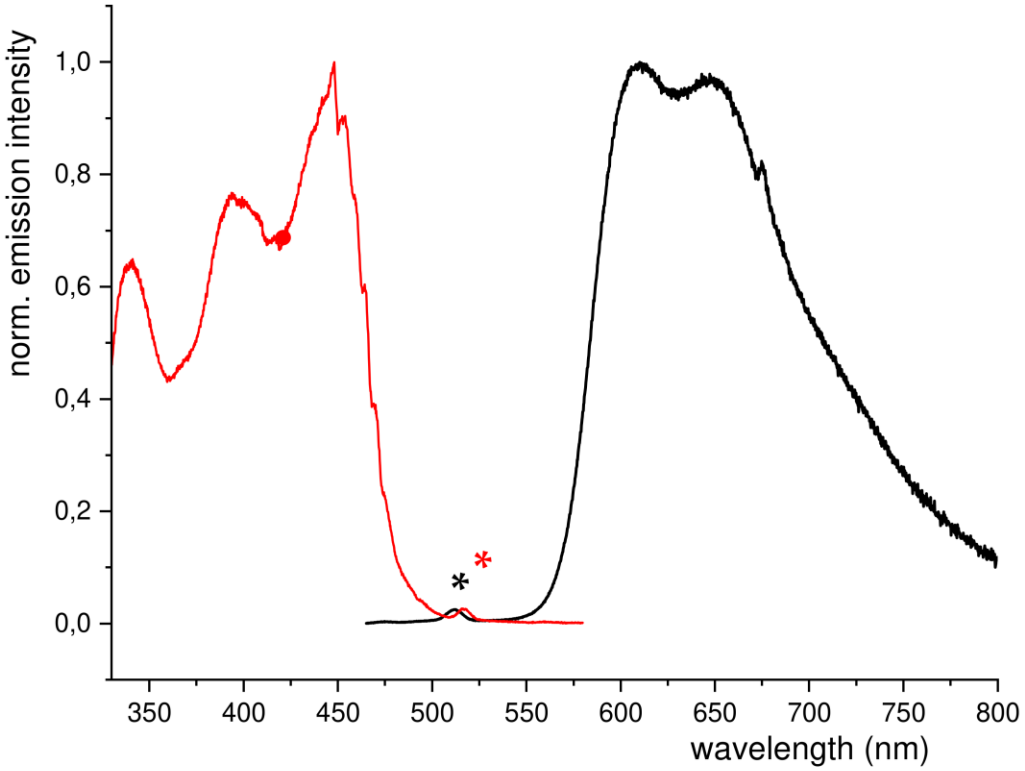

Figure S31. Photoluminescence excitation (left, red line; λ_{exc} = 610 nm) and emission (right, black line; λ_{exc} = 445 nm) spectra of [Pt(PyPhQ)Cl] (**1**) at 293 K in THF solution. A Raman peak stemming from the THF solvent is marked with an *.

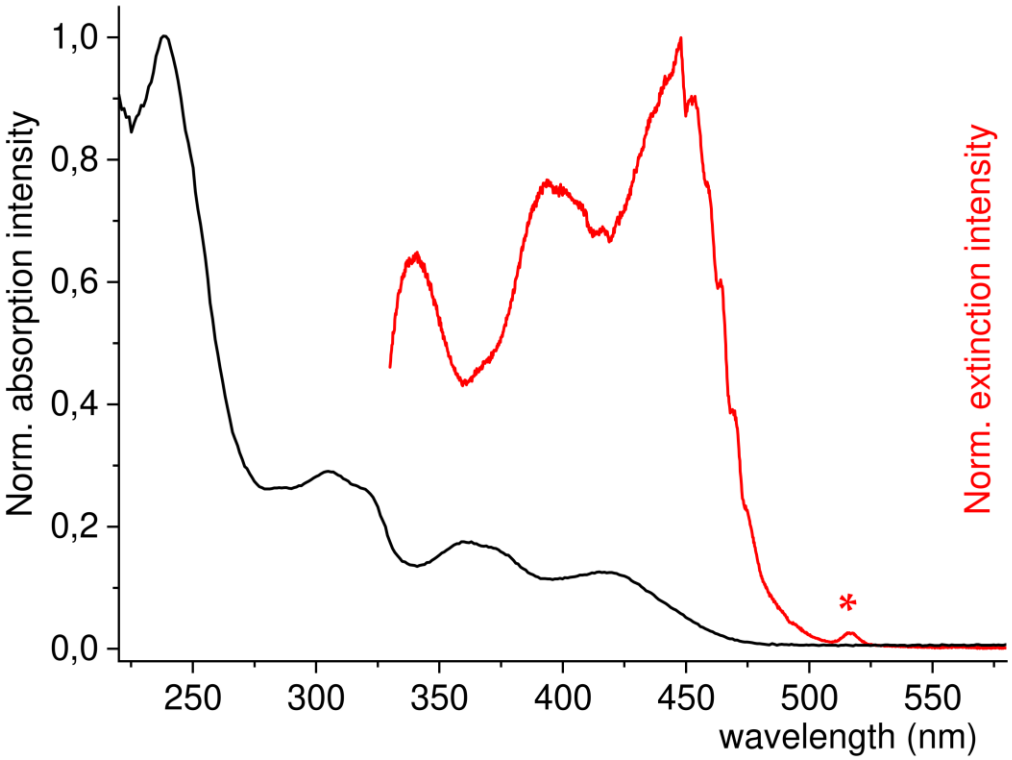

Figure S32. Photoluminescence excitation (red line; λ_{exc} = 610 nm) and absorption (black line) spectra of [Pt(PyPhQ)Cl] (**1**) at 293 K in THF solution. A Raman peak stemming from the THF solvent is marked with an *.

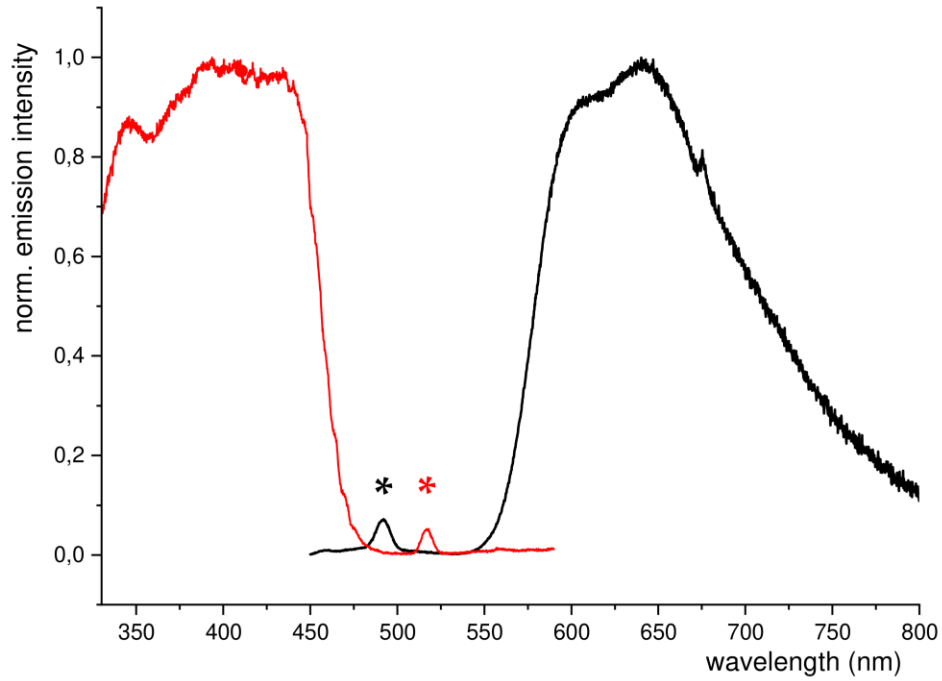

Figure S33. Photoluminescence excitation (left, red line; λ_{em} = 610 nm) and emission (right, black line; λ_{exc} = 430 nm) spectra of [Pt(QPhQ)Cl] (**2**) at 293 K in THF solution. Raman peaks stemming from the THF solvent are marked with an *.

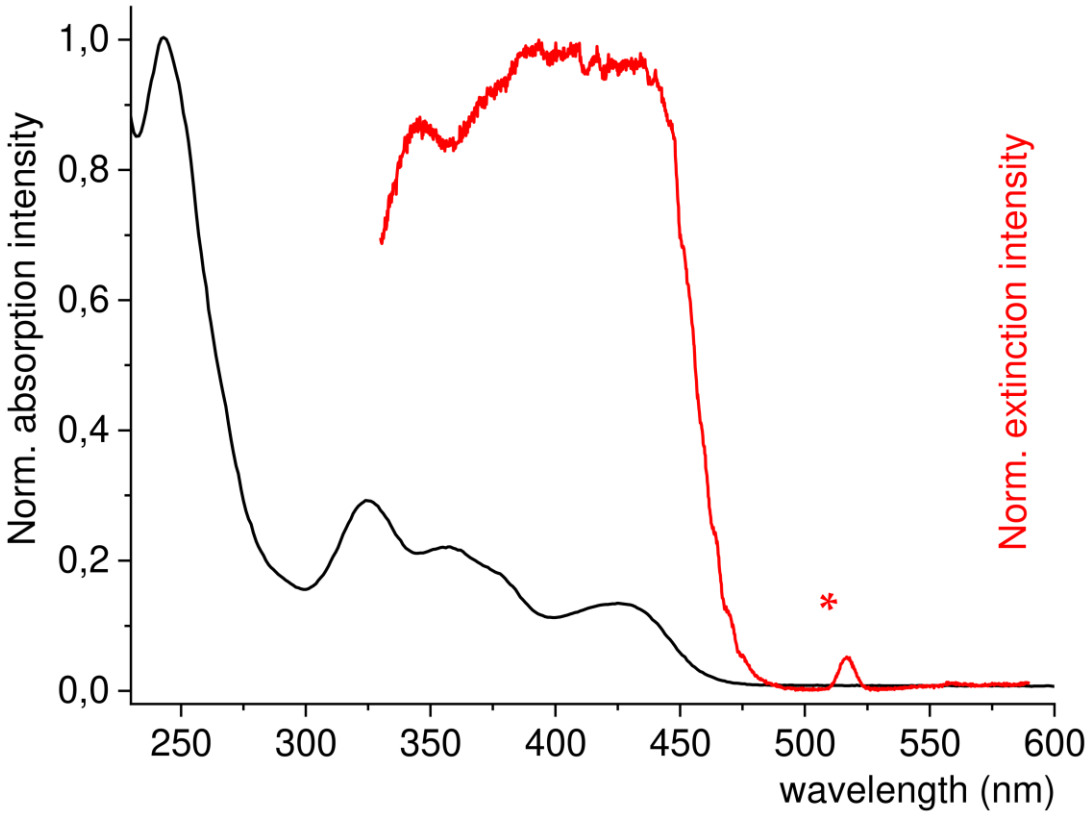

Figure S34. Photoluminescence excitation (red line; λ_{em} = 610 nm) and absorption (black line) spectra of [Pt(QPhQ)Cl] (**2**) at 293 K in THF solution. A Raman peak stemming from the THF solvent is marked with an *.

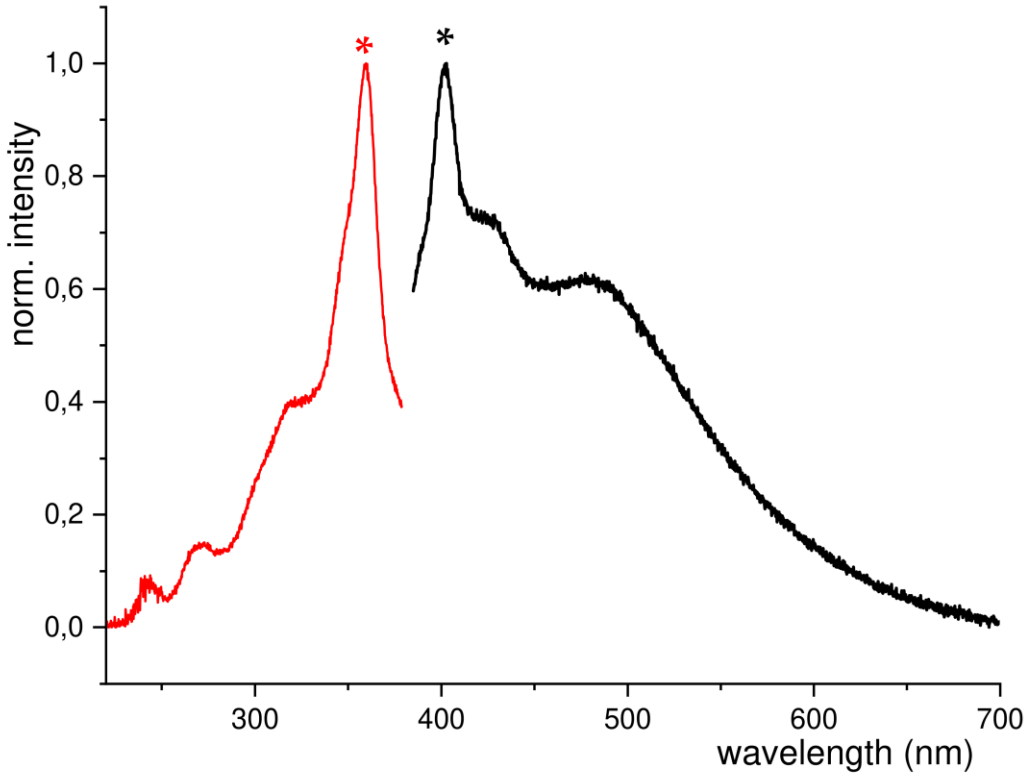

Figure S35. Photoluminescence excitation (left; red line λ_{em} = 402 nm) and emission (right, black line; λ_{exc} = 360 nm) spectra of [Ni(PyPhQ)Br] (**7**) at 293 K in THF solution. Raman peaks stemming from the THF solvent are marked with an *.

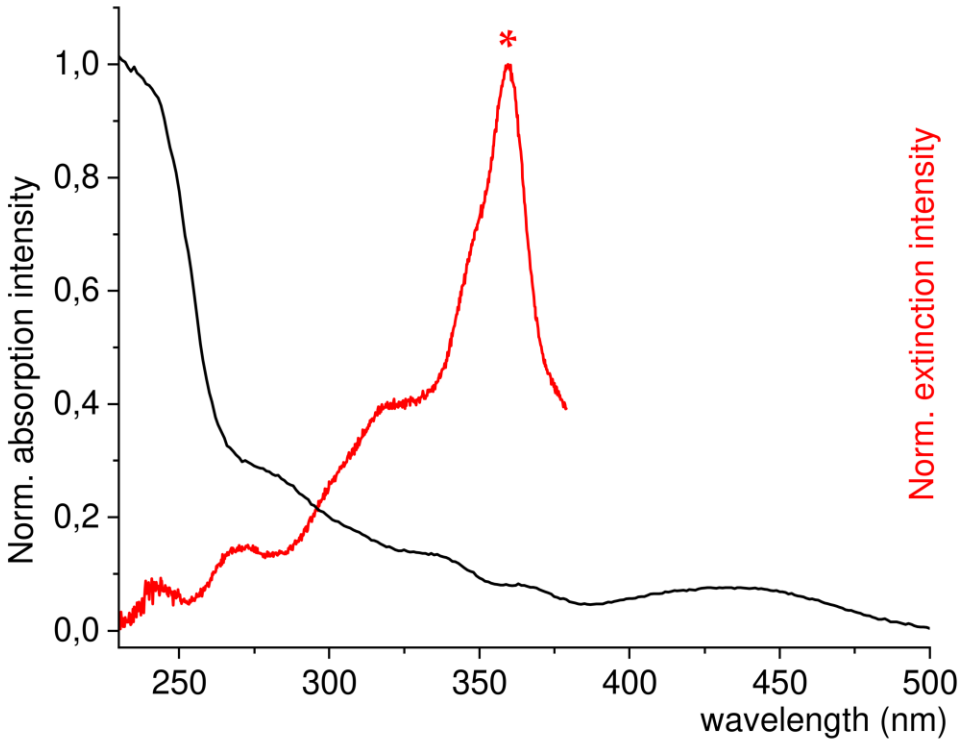

Figure S36. Photoluminescence excitation (red line; λ_{em} = 402 nm) and absorption (black line) spectra of [Ni(PyPhQ)Br] (**7**) at 293 K in THF solution. A Raman peak stemming from the THF solvent is marked with an *.

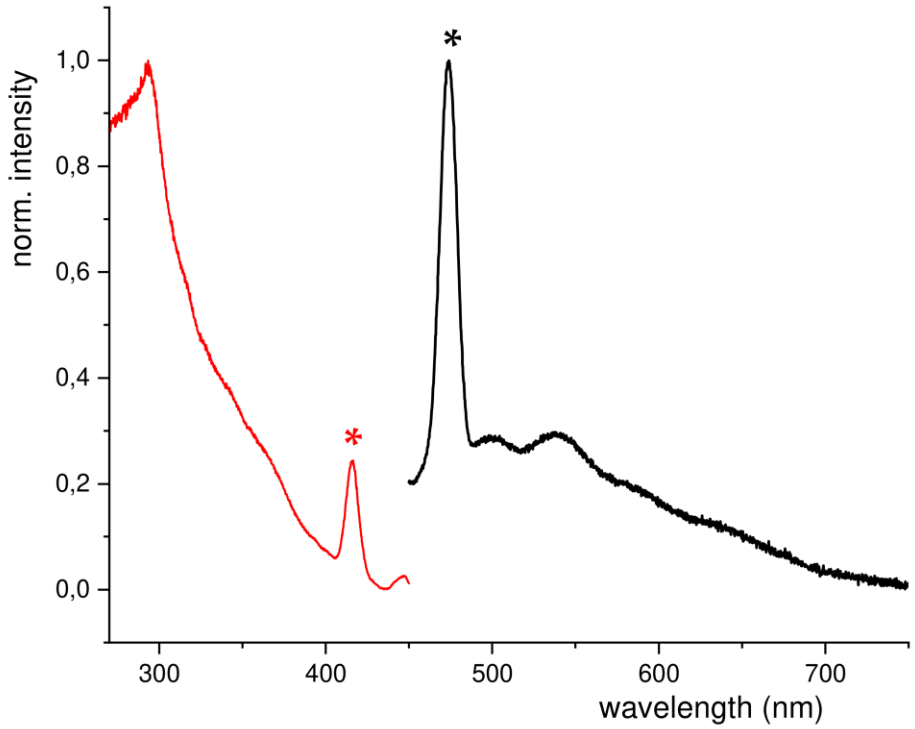

Figure S37. Photoluminescence excitation (left, red line; λ_{em} = 474 nm) and emission (right, black line; λ_{exc} = 416 nm) spectra of [Ni(QPhQ)Cl] (**8**) at 293 K in THF solution. Raman peaks stemming from the THF solvent are marked with an *.

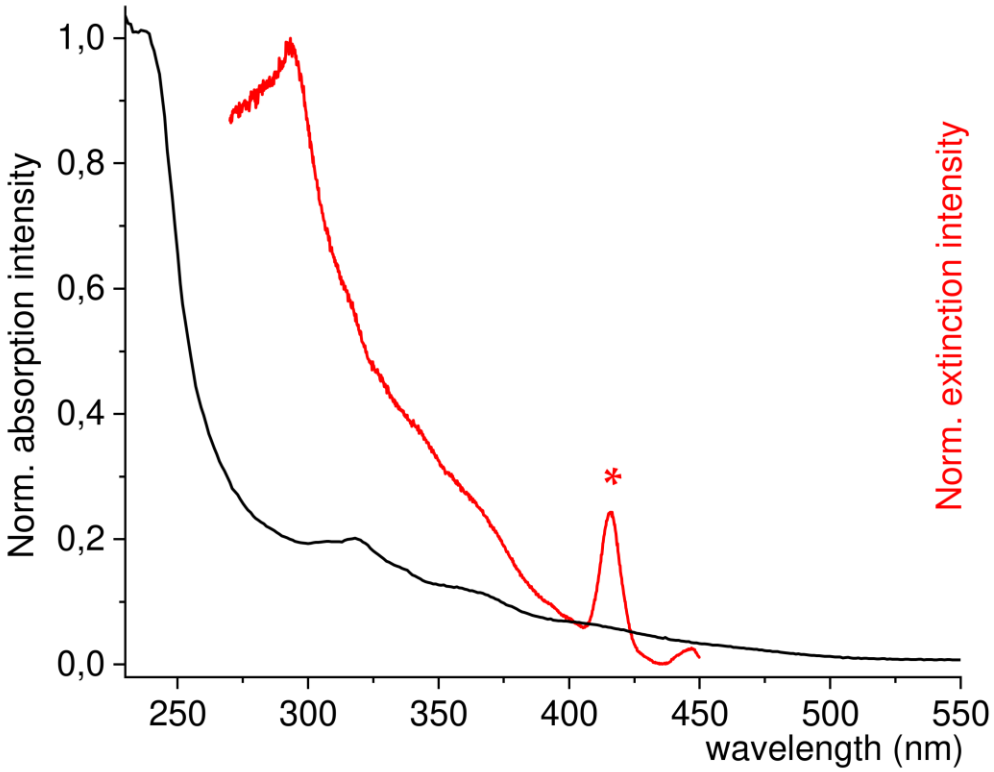

Figure S38. Photoluminescence excitation (red line; λ_{em} = 474 nm) and absorption (black; λ_{exc} = 416 nm) spectra of [Ni(QPhQ)Cl] (**8**) at 293 K in THF solution. A Raman peak stemming from the THF solvent is marked with an *.

3. Supporting Tables

Table S1. Crystal data and structure refinement for the complexes **1**, **4** and **7**.[a]

	[Pt(PyPhQ)Cl] (**1**)	[Pd(PyPhQ)Cl] (**4**)	[Ni(PyPhQ)Br] (**7**)
CCDC	2382070	2382071	2382072
Empirical formula	$C_{20}H_{13}ClN_2Pt$	$C_{20}H_{13}ClN_2Pd$	$C_{20}H_{13}BrN_2Ni$
Formula weight (g mol^{-1})	511.86	423.17	419.94
Temperature (K) / wavelength (Å)	100.00 / 0.71073	100.00 / 0.71073	100.00 / 0.71073
Crystal System	monoclinic	monoclinic	triclinic
Space group	*P* 2$_1$/c	*P* 2$_1$/c	*P* $\bar{1}$
Unit cell dimensions			
a (Å)	9.4072(6)	9.3747(4)	9.3479(4)
b (Å)	11.6931(7)	11.8008(6)	12.6540(7)
c (Å)	14.1504(8)	14.0288(7)	13.4024(7)
α (°)	90	90	87.881(2)
β (°)	97.513(2)	96.711(2)	81.397(2)
γ (°)	90	90	89.028(2)
Volume (Å^3) / Z	1543.2(2) / 4	1541.3(1) / 4	1566.3(1) / 4
δ_{calc} (Mg/m^3) / μ(mm^{-1})	2.203 / 9.268	1.824 / 1.379	1.782 / 3.793
F (000)	968.0	840.0	840.0
Crystal size (mm^3)	0.4 × 0.24 × 0.04	0.47 x 0.43 x 0.24	0.1 x 0.1 x 0.05
2θ range for data collection (°)	4.534 to 50.692	4.524 to 68.732	4.376 to 50.698
Index ranges	–11 ≤ h ≤ 11	–14 ≤ h ≤ 14	–11 ≤ h ≤ 11
	–14 ≤ k ≤ 14	–18 ≤ k ≤ 18	–15 ≤ k ≤ 15
	–17 ≤ l ≤ 17	–22 ≤ l ≤ 22	–16 ≤ l ≤ 16
Reflections collected / Independent	61059 / 2812	69675 / 6353	58639 / 5657
R_{int}	0.0560	0.0392	0.0820
Completeness to θ / angle (°)	0.998 / 25.24	0.959 / 25.24	0.987 / 25.35
Absorption correction	Multi-Scan	Multi-Scan	Multi-Scan
Data / restraints / parameters	2812 / 0 / 217	6353 / 0 / 217	5657 / 0 / 433
GOOF on F^2	1.156	1.163	1.136
Final *R* indices [I>2σ(I)][a]	R_1 = 0.0204, wR_2 = 0.0549	R_1 = 0.0215, wR_2 = 0.0516	R_1 = 0.0524, wR_2 = 0.1313
R indices (all data)	R_1 = 0.0206, wR_2 = 0.0550	R_1 = 0.0222, wR_2 = 0.0520	R_1 = 0.0623, wR_2 = 0.01361
Largest diff. peak / hole (e·Å^{-3})	1.50 / –1.34	0.97 / –0.63	1.82 / –0.63

[a] From single crystal X-ray diffraction. $R_1 = \Sigma||F_o| - |F_c||/\Sigma|F_o|$; $wR_2 = \left[\Sigma\left[w\left(F_o^2 - F_c^2\right)^2\right]/\Sigma\left[w\left(F_o^2\right)^2\right]\right]^{1/2}$

Table S2. Crystal data and structure refinement for the complexes **2**, **5** and **8**.[a]

	[Pt(QPhQ)Cl] (**2**)	[Pd(QPhQ)Cl] (**5**)	[Ni(QPhQ)Cl] (**8**)
CCDC	2382074	2382082	2382081
Empirical formula	$C_{24}H_{15}ClN_2Pt$	$C_{24}H_{15}ClN_2Pd$	$C_{24}H_{15}ClN_2Ni$
Formula weight (g mol^{-1})	561.92	473.23	425.54
Temperature (K) / wavelength (Å)	104.00 / 0.71073	102.00 / 0.71073	100.00 / 0.71073
Crystal System	orthorhombic	orthorhombic	orthorhombic
Space group	*C* mc2$_1$	*C* mc2$_1$	*C* mc2$_1$
Unit cell dimensions			
a (Å)	4.2626(3)	4.3395(2)	4.5440(6)
b (Å)	30.001(3)	29.8261(1)	29.179(2)

c (Å)	13.4349(1)	13.4094(7)	13.1196(2)
α (°) = β (°) = γ (°)	90	90	90
Volume (Å^3) / Z	1718(2) / 4	1735.58(2) / 4	1739.5(4) / 4
δ_{calc} (Mg/m^3) / μ(mm^{-1})	2.172 / 8.336	1.811 / 1.236	1.625 / 1.281
F (000)	1072.0	944.0	872.0
Crystal size (mm^3)	0.17 × 0.16 × 0.06	0.09 × 0.08 × 0.01	0.17 x 0.03 x 0.01
2θ range for data collection (°)	4.070 to 51.356	4.084 to 51.358	4.176 to 50.698
Index ranges	–5 ≤ h ≤ 5	–4 ≤ h ≤ 5	–5 ≤ h ≤ 5
	–36 ≤ k ≤ 36	–36 ≤ k ≤ 36	–33 ≤ k ≤ 34
	–16 ≤ l ≤ 16	–16 ≤ l ≤ 15	–15 ≤ l ≤ 15
Reflections collected / Independent	15540 / 1860	10964 / 1862	6506 / 1742
R_{int}	0.0447	0.0339	0.0513
Completeness to θ / angle (°)	0.990 / 25.68	0.992 / 30.43	0.846 / 25.24
Absorption correction	Multi-Scan	Multi-Scan	Multi-Scan
Data / restraints / parameters	1860/181/236	1862 / 181 / 236	1742 / 199 / 236
GOOF on F^2	1.109	1.109	1.089
Final *R* indices [I>2σ(I)] [b]	R_1 = 0.0135, wR_2 = 0.0321	R_1 = 0.0195, wR_2 = 0.0431	R_1 = 0.0624, wR_2 = 0.1688
R indices (all data)	R_1 = 0.0138, wR_2 = 0.0322	R_1 = 0.0232, wR_2 = 0.0443	R_1 = 0.0717, wR_2 = 0.1751
Largest diff. peak / hole (e·Å^{-3})	0.31 / –0.46	0.31 / –0.34	1.39 / –0.97

[a] From single crystal X-ray diffraction. [b] $R_1 = \Sigma||F_o| - |F_c||/\Sigma|F_o||$; $wR_2 = \left[\Sigma\left[w\left(F_o^2 - F_c^2\right)^2\right]/\Sigma\left[w\left(F_o^2\right)^2\right]\right]^{1/2}$

Table S3. Crystal data and structure refinement for complex **3**.[a]

	[Pt(PhPyQ)Cl] (**3**)	[Pd(PhPyQ)Cl] (**6**)
CCDC	2382073	Not crystallized
Empirical formula / Formula weight (g mol^{-1})	$C_{20}H_{13}ClN_2Pt$ / 511.86	
Temperature (K) / wavelength (Å)	100.00 / 0.71073	
Crystal System / Space group	Orthorhombic / $P\,2_12_12_1$	
Unit cell dimensions		
a (Å) / b (Å) / c (Å)	7.0071(2) / 13.5496(4) / 16.3653(6)	
α (°) / β (°) / γ (°)	90 / 90 / 90	
Volume (Å^3) / Z	1553.78(9) / 4	
δ_{calc} (Mg/m^3) / μ(mm^{-1})	2.188 / 9.205	
F (000)	968.0	
Crystal size (mm^3)	0.07 × 0.04 × 0.02	
2θ range for data collection (°)	3.902 to 66.36	
Index ranges	–10 ≤ h ≤ 10; –15 ≤ k ≤ 20; –24 ≤ l ≤ 25	
Reflections collected / Independent / R_{int}	38161 / 5916 / 0.0491	
Completeness to θ / angle (°)	0.995 / 25.24	
Absorption correction	Multi-Scan	
Data / restraints / parameters	5916 / 0 / 217	
GOOF on F^2	1.132	
Final *R* indices [I>2σ(I)] [b]	R_1 = 0.0352, wR_2 = 0.0801	
R indices (all data)	R_1 = 0.0379, wR_2 = 0.0812	
Largest diff. peak / hole (e·Å^{-3})	3.47 / – 3.39	

[a] From single crystal X-ray diffraction. [b] $R_1 = \Sigma||F_o| - |F_c||/\Sigma|F_o||$; $wR_2 = \left[\Sigma\left[w\left(F_o^2 - F_c^2\right)^2\right]/\Sigma\left[w\left(F_o^2\right)^2\right]\right]^{1/2}$

Table S4. Selected experimental bond lengths (Å) and angles (°) for the complexes **1** to **8**.[a]

	[Pt(PyPhQ)Cl] (**1**)	[Pt(QPhQ)Cl] (**2**)	[Pt(PhPyQ)Cl] (**3**)	[Pd(PyPhQ)Cl] (**4**)	[Pd(QPhQ)Cl] (**5**)	[Ni(PyPhQ)Br] (**7**)	[Ni(QPhQ)Cl] (**8**)
Distances (Å)							
M–C	1.957(4)	1.958(5)	1.986(7)	1.948(1)	1.962(4)	1.849(6)	1.857(1)
M–N1	2.024(3)	1.990(3)	1.984(5)	2.039(1)	1.985(2)	1.931(5)	1.910(3)
M–N2	2.029(3)	2.050(3)	2.116(6)	2.045(1)	2.092(2)	1.910(5)	1.930(3)
M–X	2.428(9)	2.431(1)	2.303(2)	2.438(3)	2.446(1)	2.433(9)	2.308(3)
Angles (°)							
C–M–N1	82.0(1)	93.8(1)	82.30(2)	82.47(4)	90.63(6)	84.7(2)	90.2(1)
C–M–N2	93.1(1)	88.0(1)	173.6(3)	91.77(4)	89.00(1)	92.2(2)	89.9(1)
N1–M–X	91.9(9)	87.7(6)	174.6(2)	91.93(3)	90.27(6)	93.50(2)	91.3(8)
N2–M–X	94.3(9)	90.5(6)	91.52(2)	95.50(3)	90.20(6)	94.69(2)	88.6(8)
N1–M–N2	170.6(1)	177.9(1)	92.7(2)	169.2(4)	179.0(7)	165.5(2)	178.0(2)
C–M–X	168.1(1)	178.4(9)	93.7(2)	167.0(3)	179.2(1)	157.5(2)	178.4(1)
Σ angles around M	361.3	356.3	360.2	361.7	358.2	365.1	356.4

[a] From single crystal X-ray diffraction.

Table S5. Experimental and DFT-calculated selected bond lengths (Å) and angles (°) for **3**, **6** and **9**.[a]

	[Pt(PhPyQ)Cl] (**3**) exp.	[Pt(PhPyQ)Cl] (**3**) calc.	[Pd(PhPyQ)Cl] (**6**) calc.	[Ni(PhPyQ)Br] (**9**) calc.
Distances (Å)				
M–C	1.986(7)	1.996	1.986	1.897
M–N1	1.984(5)	2.015	2.029	1.939
M–N2	2.116(6)	2.169	2.181	2.068
M–X	2.303(2)	2.351	2.349	2.387
Angles (°)				
C–M–N1	82.30(2)	81.90	82.18	84.33
C–M–N2	173.6(3)	172.6	171.7	167.8
N1–M–X	174.6(2)	176.0	175.9	152.8
N2–M–X	91.52(2)	92.28	93.53	97.06
N1–M–N2	92.7(2)	91.6	90.6	93.2
C–M–X	93.7(2)	94.1	93.7	90.4
Σ angles around M	360.2	359.9	360.0	365.0

[a] From single crystal X-ray diffraction.

Table S6. Experimental and DFT-calculated selected bond lengths (Å) and angles (°) for **1**, **4** and **7**.[a]

	[Pt(PyPhQ)Cl] (**1**) exp.	Calc.	[Pd(PyPhQ)Cl] (**4**) exp.	Calc.	[Ni(PyPhQ)Br] (**7**) exp.	Calc.
Distances (Å(						
M–C	1.957(4)	1.961	1.948(1)	1.955	1.849(6)	1.873
M–N1	2.024(3)	2.052	2.039(1)	2.062	1.931(5)	1.968
M–N2	2.029(3)	2.066	2.045(1)	2.073	1.910(5)	1.950
M–X	2.428(9)	2.498	2.438(3)	2.484	2.433(9)	2.547
Angles (°)						
C–M–N1	82.0(1)	81.4	82.47(4)	81.57	84.7(2)	83.9
C–M–N2	93.1(1)	92.2	91.77(4)	91.16	92.2(2)	91.8
N1–M–X	91.9(9)	92.3	91.93(3)	93.06	93.50(2)	95.4
N2–M–X	94.3(9)	94.1	95.50(3)	94.55	94.69(2)	93.3
N1–M–N2	170.6(1)	173.0	169.2(4)	170.6	165.5(2)	165.1

C–M–X	168.1(1)	173.7	167.0(3)	173.5	157.5(2)	160.8
Σ angles around M	361.3	360.0	361.7	360.3	365.1	364.4

[a] From single crystal X-ray diffraction.

Table S7. Experimental and DFT-calculated selected bond lengths (Å) and angles (°) for **2**, **5** and **8**.[a]

	[Pt(QPhQ)Cl] (**2**) Exp.	Calc.	[Pd(QPhQ)Cl] (**5**) Exp.	Calc.	[Ni(QPhQ)Cl] (**8**) Exp.	Calc.
Distances (Å)						
M–C	1.958(5)	1.975	1.962(4)	1.963	1.857(1)	1.877
M–N1	1.990(3)	2.054	1.985(2)	2.064	1.910(3)	1.959
M–N2	2.050(3)	2.054	2.092(2)	2.064	1.930(3)	1.959
M–X	2.431(1)	2.492	2.446(1)	2.487	2.308(3)	2.383
Angles (°)						
C–M–N1	93.8(1)	90.2	90.63(6)	89.4	90.2(1)	89.9
C–M–N2	88.0(1)	90.2	89.00(1)	89.4	89.9(1)	89.9
N1–M–X	87.7(6)	89.8	90.27(6)	90.7	91.3(8)	90.1
N2–M–X	90.5(6)	89.8	90.20(6)	90.7	88.6(8)	90.1
N1–M–N2	177.9(1)	179.7	179.0(7)	178.7	178.0(2)	179.9
C–M–X	178.4(9)	180.0	179.2(1)	180.0	178.4(1)	180.0
Σ angles around M	356.3	360.0	358.2	360.0	356.4	360.0

[a] From single crystal X-ray diffraction.

Table S8. Redox potentials of the protoligands.[a]

	red1	red2	red3
PyHPhQ	–2.56 $E_{1/2}$	–3.36 E_{pc}	-
QHPhQ	–2.71 $E_{1/2}$	–3.20 E_{pc}	-
HPhPyQ	–2.46 $E_{1/2}$	–2.86 E_{pc}	–3.39 E_{pc}
QClPhQ	–2.66 E_{pc}	–3.21 E_{pc}	-

[a] Electrochemical potentials in V with an accuracy of ±0.003 V, vs ferrocene/ferrocenium; $E_{1/2}$ for reversible redox waves, E_{pc} for irreversible reduction waves, measured in 0.1 M *n*-Bu_4NPF_6/THF at 298 K, scan rate 100 mV/s; plots in Figures S16 and S17.

Table S9. Selected redox potentials of the Pt, Pd, and Ni complexes.[a]

N^C^N	X	M (**No.**)	$E_{1/2}$ ox1	$E_{1/2}$ red1	$E_{1/2}$ red2	ΔE red2–red1	ΔE ox1–red1	reference
PyPhQ	Cl	Pt **(1)**	0.46 irr	–1.92	–2.65	0.73	2.38	This work
	Cl	Pd **(4)**	0.70 irr	–2.03	–2.75	0.72	2.73	This work
	Br	Ni **(7)**	0.04	–2.07 irr	–2.21 irr	0.14	2.11	This work
QPhQ	Cl	Pt **(2)**	0.73 irr	–2.08	–2.32	0.24	2.81	This work
	Cl	Pd **(5)**	0.83 irr	–2.21	–2.44 irr	0.23	3.04	This work
	Cl	Ni **(8)**	–0.04	–2.12 irr	–2.34 irr	0.22	2.08	This work
dpb	Cl	Pt	0.41 irr.	–2.17 irr	–2.60 irr	0.43	2.58	Ref. 1
Me_2dpb	Cl	Pd	0.74 irr.	–2.34 irr	–2.75 irr	0.41	3.08	Ref. 2
dpb	Cl	Ni	0.06	–2.33 irr	–2.57 irr	0.24	2.39	Ref. 3
C^N^N								
PhPyQ	Cl	Pt **(3)**	0.73 irr	–1.81	–2.53 irr	0.72	2.54	This work
	Cl	Pd **(6)**	0.83 irr	–1.85	–2.46 irr	0.61	2.68	This work
	Br	Ni **(9)**						This work
Phbpy	Cl	Pt	0.45 irr	–1.78	–2.48	0.70	2.23	Ref. 2,4

	Cl	Pd	0.80 [b]	–1.92	–2.60	0.68	2.72	Ref. 4
	Br	Ni	0.08	–1.90	–2.52	0.62	1.98	Ref. 5

[a] Plots in Figures S18 to S21. Electrochemical potentials in V with an accuracy of ±0.003 V, vs ferrocene/ferrocenium; $E_{1/2}$ for reversible redox waves, E_{pc} for irreversible reduction waves and E_{pa} for irreversible oxidation waves; measured in 0.1 M *n*-Bu_4NPF_6/THF at 298 K, scan rate 100 mV/s. [b] Measured in MeCN.

Table S10. UV-vis absorption maxima of the protoligands.[a]

HC^N^N	λ_1 (ε)	λ_2 (ε)	λ_3 (ε)	λ_4 (ε)	λ_5 (ε)	λ_6 (ε)
PyHPhQ	234 (4.72)	282 (2.02)	-	317sh (0.68)	-	-
QHPhQ	-	273 (3.65)	-	-	325 (1.21)	340sh (0.74)
HPhPyQ	250sh (3.49)	271 (1.77)	300 (1.43)		345 (1.45)	370 (1.16)
QClPhQ	228 (9.86)	284 (1.99)	-	316 (0.88)	-	-

[a] Measured in THF (298 K), sh = shoulder, wavelength λ in nm, extinction coefficients ε in 10^4 $M^{-1}cm^{-1}$.

Table S11. Selected UV-vis absorption data of the complexes **1** to **8** and related derivatives.[a]

			Long-wavelength maxima						reference
N^C^N	X	No.	λ_1 (ε)	λ_2 (ε)	λ_3 (ε)	λ_4 (ε)	λ_5 (ε)	λ_6 (ε)	
PyPhQ	Cl	Pt **(1)**	238 (5.47)	304 (1.55)	321 sh(1.41)	359 (0.92)	373 (0.86)	418 (0.66)	This work
	Cl	Pd **(4)**	241sh (4.56)	284 (2.23)	312 (1.45)	330 (1.27)	381 (0.90)		This work
	Cl	Ni **(7)**	243sh (4.80)	281sh (1.48)		336 (0.77)	365 (0.52)	436 (0.49)	This work
QPhQ	Cl	Pt **(2)**	242 (5.44)		324 (1.56)	357 (1.18)	378sh (0.92)	426 (0.70)	This work
	Cl	Pd **(5)**	242 (3.45)	286 (0.96)	329 (1.14)		388 (0.76)		This work
	Cl	Ni **(8)**	237 (4.13)	307 (0.76)	318 (0.78)	358sh (0.45)	403sh (0.23)	474sh (0.04)	This work
dpb	Cl	Pt	255 (2.50)	289 (2.10)	332 (0.63)	379 (0.86)	402 (0.70)	485 (0.10)	Ref. 1
Me_2dpb	Cl	Pd	239 (2.70)	275 (2.30)	283 (2.20)	327 (0.83)	360 (0.74)	375 (1.20)	Ref. 2
dpb	Cl	Ni	236 (3.55)	279 (2.68)		332 (5.73)	412 (6.31)	437 (6.68)	Ref. 3
C^N^N									
PhPyQ	Cl	Pt **(3)**	240 (2.03)	330 (1.33)	344 (2.00)	367 (1.66)	412sh (0.36)	460sh (0.12)	This work
	Cl	Pd **(6)**	243sh (2.01)	330 (1.33)			378sh (0.24)	398sh (0.12)	This work
Phbpy	Cl	Pt	278	302	330	363	410	430	Ref. 5
	Cl	Pd	266 (2.00)	278 (2.10)	311 (1.20)	325 (1.30)	342 (0.80)	402 (0.10)	Ref. 4
	Cl	Ni	281		321	354	391	506	Ref. 5

[a] Measured in THF (298 K), sh = shoulder, wavelength λ in nm, extinction coefficients ε in 10^4 $M^{-1}cm^{-1}$.

References

(1) Williams, J. A. G.; Beeby, A.; Davies, E. S.; Weinstein, J. A.; Wilson, C. An Alternative Route to Highly Luminescent Platinum(II) Complexes: Cyclometalation with N^C^N-Coordinating Dipyridylbenzene Ligands. *Inorg. Chem.* **2003**, *42*, 8609–8611. https://doi.org/10.1021/ic035083+

(2) Kletsch, L.; Jordan, R.; Köcher, A. S.; Buss, S.; Strassert, C. A.; Klein, A. Photoluminescence of Ni(II), Pd(II), and Pt(II) Complexes [M(Me_2dpb)Cl] Obtained from C–H Activation of 1,5-Di(2-pyridyl)-2,4-dimethylbenzene (Me_2dpbH). *Molecules* **2021**, *26*, 5051. https://doi.org/10.3390/molecules26165051

(3) Kletsch, L.; Hörner, G.; Klein, A. Cyclometalated Ni(II) complexes [Ni(N^C^N)X] of the tridentate 2,6-di(2-pyridyl)-phen-ide ligand. *Organometallics* **2020**, *39*, 2820−2829. https://doi.org/10.1021/acs.organomet.0c00355

(4) Von der Stück, R.; Schmitz, S.; Klein, A. C–X vs. C–H activation for the synthesis of the cyclometalated complexes [Pd(YPhbpy)X] (HPhbpy = 6-phenyl-2,2′-bipyridine; X/Y = (pseudo)halides). *Inorg. Chem. Res.* **2021**, 5, 173–192. https://doi.org/10.22036/icr.2021.278938.1101

(5) Vogt, N.; Sandleben, A.; Kletsch, L.; Schäfer, S.; Chin, M. T.; Vicic, D. A.; Hörner, G.; Klein, A. On the Role of the X Coligands in Cyclometalated [Ni(Phbpy)X] Complexes (HPhbpy = 6-phenyl-2,2′-bipyridine). *Organometallics* **2021**, *40*, 1776−1785. https://doi.org/10.1021/acs.organomet.1c00237

3.2 Alternative C–H Activation Methods

Various reactions conditions for cyclometalation reactions by direct C–H activation have been reported for N^C^N and C^N^N type systems.[17, 19, 20, 25, 81] Generally, these reactions all need higher energies than, for example, oxidative addition, where the redox chemistry of the substrates provides the activation energy.[3] An established method for CH-activation is the use of microwave irradiation to introduce a lot of energy in a short amount of time.[96, 97] To adapt this method to ring-expanded systems, reaction conditions were screened for using a previously reported model ligand system (Py*t*BuHPhPy) (see Scheme 10, table 1).[13]

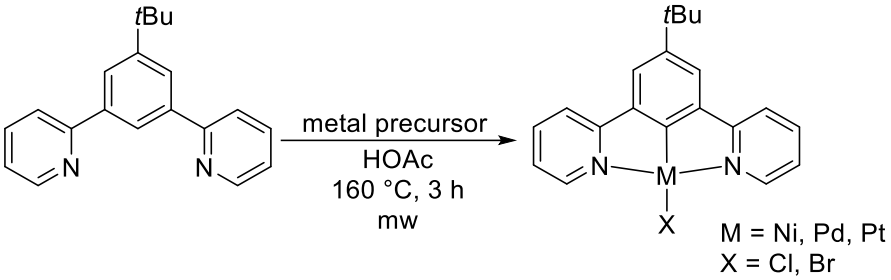

Scheme 10 Reaction screening for microwave cyclometalation reactions using [M(Py*t*BuHPhPy]X] (M, Pt, Pd, Ni; X= Cl, Br) as model compounds.

Table 1 Results of microwave cyclometalation screening reactions with complexes of [M(Py*t*BuHPhPy]X] (M, Pt, Pd, Ni; X= Cl, Br) as model compounds.

Ligand	**Metal precursor**	**Conditions**	**Yield**
Py*t*BuHPhPy (1.20 eq.)	$K_2[PtCl_4]$ (1.00 eq.)	HOAc, 300 W, 160 °C, 3 h	99%
	$K_2[PdCl_4]$ (1.00 eq.)	HOAc, 300 W, 160 °C, 3 h	88%
	$NiBr_2$	KOAc, K_2CO_3, p-xylene, 250 W, 160 °C, 3 h	65% [a, b]

[a] Previously reported.[13] [b] „pseudo-inert" conditions: solvent distilled and degassed, substrates pre-dried prior to use, microwave tube flushed with argon and kept sealed prior to irradiation.

The C–H activation was successful for platinum and palladium using similar conditions to thermal activation methods, giving excellent yield and high purity at drastically lower reaction times. Nickel C–H activation was also achieved by adapting thermal C–H activation protocols and using microwave irradiation as energy source.[26] However, special care had to be taken, because of the instability of nickel complexes and their susceptibility towards hydrolysis and solvolysis. Pseudo-inert conditions were applied: The solvent was distilled and degassed and substrates pre-dried prior to use. Since the microwave tubes cannot be fully sealed under argon atmosphere, they were flushed and sealed under argon prior to irradiation. This method yielded the desired complex in acceptable yields. If these conditions were not applied, hydrolysis occurred and $[Ni(H_2O)_6]^{2+}$-species were isolated instead.

These reaction conditions were then applied to the synthesis of [Pt(PyPhQ)Cl] and successfully yielded the desired compound in excellent yield (92%) while drastically cutting the reaction time needed from 96 h for thermal activation to 3 h for microwave reactions (see table 2).

Stemming from this success, different methods of C–H activations by applying high energy were tested for. The results are summarized in table 2.

Table 2 Overview of different C–H activation methods towards the synthesis of [Pt(PyPhQ)Cl] as model compound.

Substrates	**Method**	**Conditions**	**Outcome**
$K_2[PtCl_4]$ (1.0 eq.) PyHPhQ (1.4 eq.)	Reflux	HOAc, 160 °C, 96 h	95% yield
	Microwave	HOAc, 160 °C, 300 W, 3 h	92% yield
	Ampule	HOAc, Ramping to 150 °C, 72 h	Complex traces isolated as single crystals [a]
	Photoactivation[54]	Bu_4NCl, Na_2CO_3, acetone, 405 nm r.t., 18 h	Complex formation, impure, not isolated [b]
	Ball mill	HOAc, 15 Hz, 30 min	decomposition

[a] detected by SC-XRD, [b] detected by ^1H NMR spectroscopy.

All methods described, except for the ball mill synthesis, yielded the complex to some extent. However, of all "higher energy methods", only the microwave synthesis proved easily applicable and reliable and was therefore regularly used for complex synthesis. This proved especially valuable when synthesizing larger batches of complex repeatedly, for example for coligand exchange reactions (see chapter 3.6).

3.3 Further Complexes with N^C^N and C^N^N Type Ring-Expanded Ligand Systems

Based on the findings of chapter 3.1, more complexes with the N^C^N and C^N^N type ligand systems were synthesized.[49] These complexes were based on both quinoline and carbazole units being part of the ligand backbone, because of its interesting properties as a chromophore.[24, 95, 98, 99]Alternatively, derivatives of the QPyHPh system were synthesized by exchanging the phenyl ring for different chromophore systems. The synthesis of the complexes is depicted in Scheme 16, Figure 12 and table 4. Generally, the ring systems were built up step by step, by using appropriate cross coupling protocols, mostly *Suzuki*.[90] Special care had to be taken not to use the 2-pyridinyl boronic acid, because of its instability in solution. This problem has been previously reported and termed the "2-Pyridinyl Problem".[92]

Protoligand systems of the type quinoline-pyridine-fluorene (QPyHFluor) and quinoline-pyridine-spirobifluorene (QPyHSpiro) were synthesized by two subsequent *Suzuki* type cross coupling reactions (see Scheme 11). The two protoligands were obtained in excellent yields (see table 3).

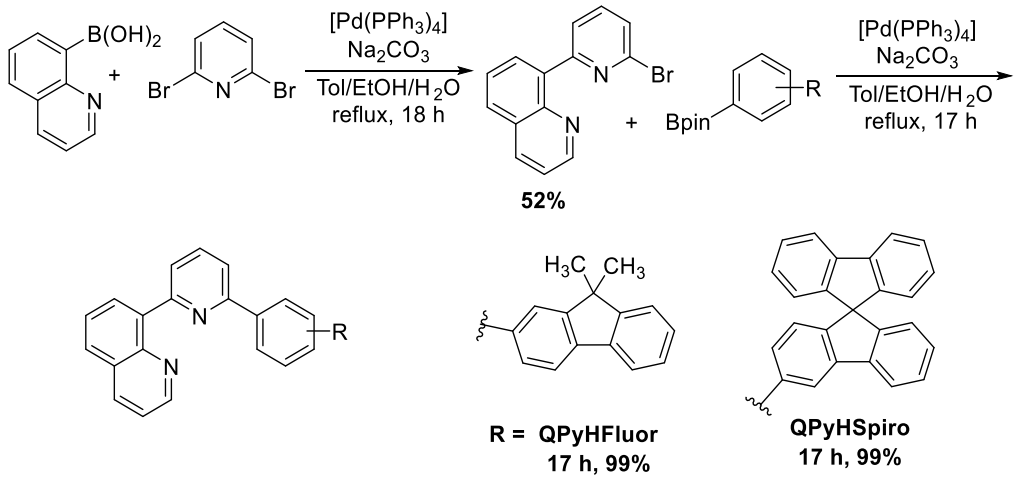

Scheme 11 Synthetic route towards protoligands QPyHFluor and QPyHSpiro, derived from a QPyHPh system.

The protoligand QPyHPh(N(Ph)2) was synthesized in a three-step synthesis starting from 2,6-dibromopyridine (see Scheme 12). After introducing a quinoline moiety via *Suzuki* cross coupling, the resulting QPyBr was transformed into its boronic acid pinacol ester. Finally, the obtained pinacol ester was cross coupled to 4-bromotriphenylamine to yield the desired protoligand in three steps in an overall yield of 13%.

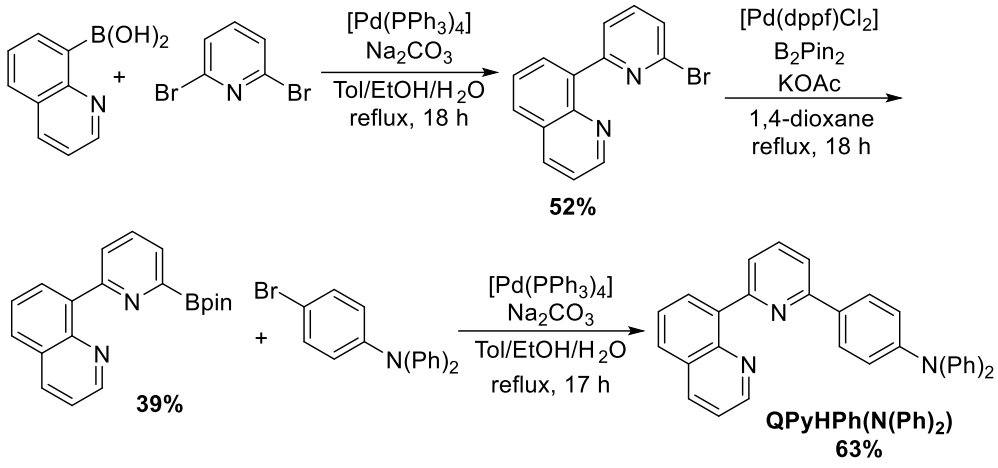

Scheme 12 Synthetic route towards the protoligand QPyHPh(N(Ph)2).

The protoligand PyHCarbQ was synthesized in a two-step synthesis, starting with a nucleophilic substitution reaction of 2-fluoropyridine and 2-bromocarbazole (see Scheme 13). The obtained PyHCarbBr building block was then reacted with 8-quinolinyl boronic acid under *Suzuki* conditions to yield the protoligand in an overall yield of 90% (see table 3).

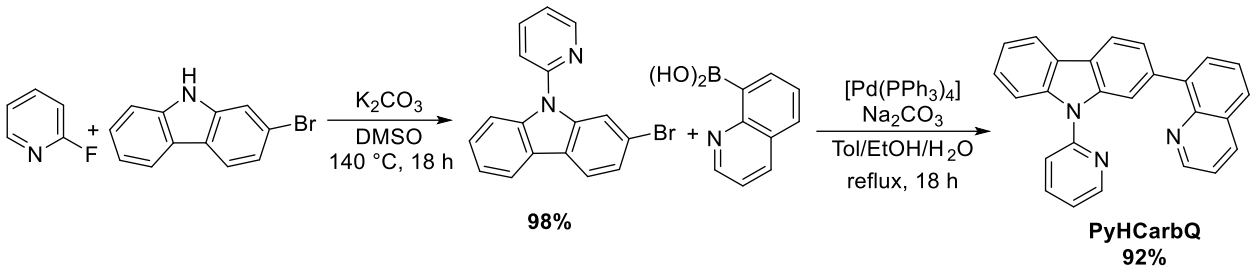

Scheme 13 Synthetic route towards protoligand PyHCarbQ.

The protoligand QPyHCarb was synthesized in two steps starting from 2-bromo-5-fluoro-pyridine and nucleophilic substitution with carbazole. The resulting CarbPyBr was then coupled to 8-quinolinyl boronic acid under *Suzuki* conditions to yield the protoligand in an overall yield of 79% (see Scheme 14).

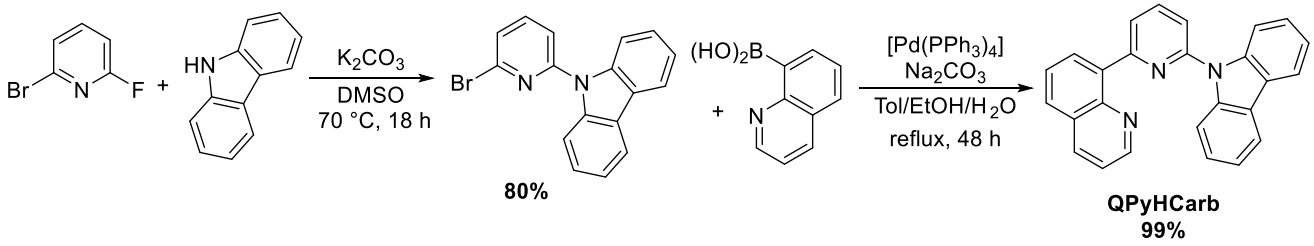

Scheme 14 Synthetic route towards protoligand QPyHCarb.

The protoligand PyPyHCarb was synthesized in a four-step synthesis. 2,2′-bipyridine was converted to 6-bromo-2,2′-bipyridine over three steps following a reported procedure and then coupled to carbazole, mediated by coper catalysis.[100] The desired protoligand was obtained in an overall yield of 14%. (see Scheme 15).

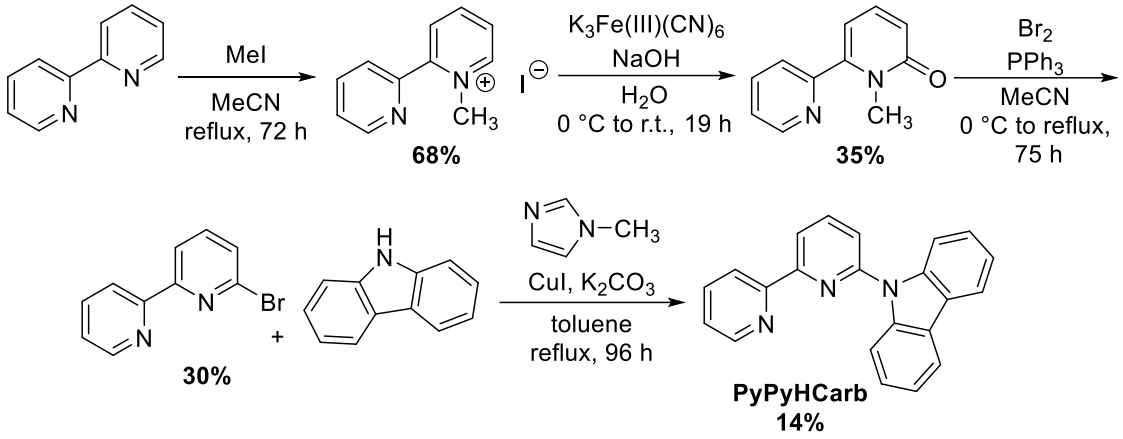

Scheme 15 Synthetic route towards protoligand PyPyHCarb.[100]

Table 3 Reaction conditions for ligand synthesis reactions of N^C^N and C^N^N type protoligand.

Substrates	**Conditions**	**Protoligand (Yield)**
QPyBr + fluorene boronic acid	[Pd(PPh$_3$)$_4$], Na$_2$CO$_3$, toluene/EtOH/H$_2$O, reflux, 17 h	QPyHFluor 51% in two steps
QPyBr + spiroboronic acid	[Pd(PPh$_3$)$_4$], Na$_2$CO$_3$, toluene/EtOH/H$_2$O, reflux, 17 h	QPyHSpiro 51% in two steps
PyHCarbBr + 8-quinoline-boronic acid	[Pd(PPh$_3$)$_4$], Na$_2$CO$_3$, toluene/EtOH/H$_2$O, reflux, 18 h	PyHCarbQ 90% in two steps
QPy-boronic acid pinacol ester + 4-bromotriphenylamine	[Pd(PPh$_3$)$_4$], Na$_2$CO$_3$, toluene/EtOH/H$_2$O, reflux, 17 h	QPyHPhN(Ph)$_2$ 13% in three steps
CarbPyBr + 8-quinoline-boronic acid	[Pd(PPh$_3$)$_4$], Na$_2$CO$_3$, toluene/EtOH/H$_2$O, reflux, 48 h	QPyHCarb 79% in two steps
5- [BrPyPy + carbazole	*N*-methylpyrazole, CuI, K$_2$CO$_3$, toluene, reflux, 96 h	PyPyHCarb 1% in four steps

Complexation reactions were carried out for all protoligands using direct C–H activation conditions, refluxing in acetic acid (see Scheme 16 and table 4). The Pt(II) and Pd(II) complexes were obtained in moderate to good yields. The only exception was the complexation of the QPyHPhN(Ph)$_2$ ligand, which did not yield the desired complexes. Instead, NMR spectroscopy indicated decomposition of the protoligand, implying the triphenylamine moiety is not stable under the acidic C–H activation conditions.

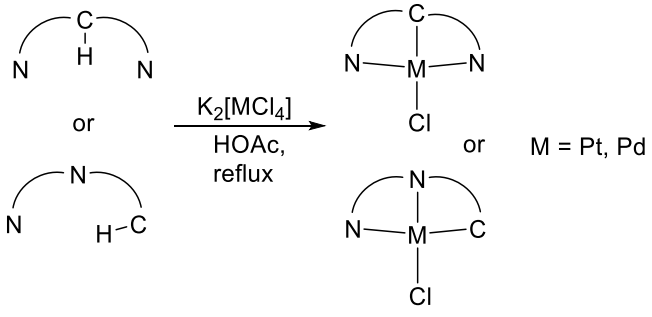

Scheme 16 General reaction Scheme for complexation of N^C^N and C^N^N type protoligands via direct C–H activation.

Complexation of nickel via base-assisted C–H activation was also attempted for several of the protoligands (see table 4). The protoligands were reacted with $NiBr_2$ and equimolar amounts of KOAc and K_2CO_3 in refluxing *p*-xylene. No conversion was observed under these reaction conditions.[26, 49] Instead, the protoligand was reisolated.

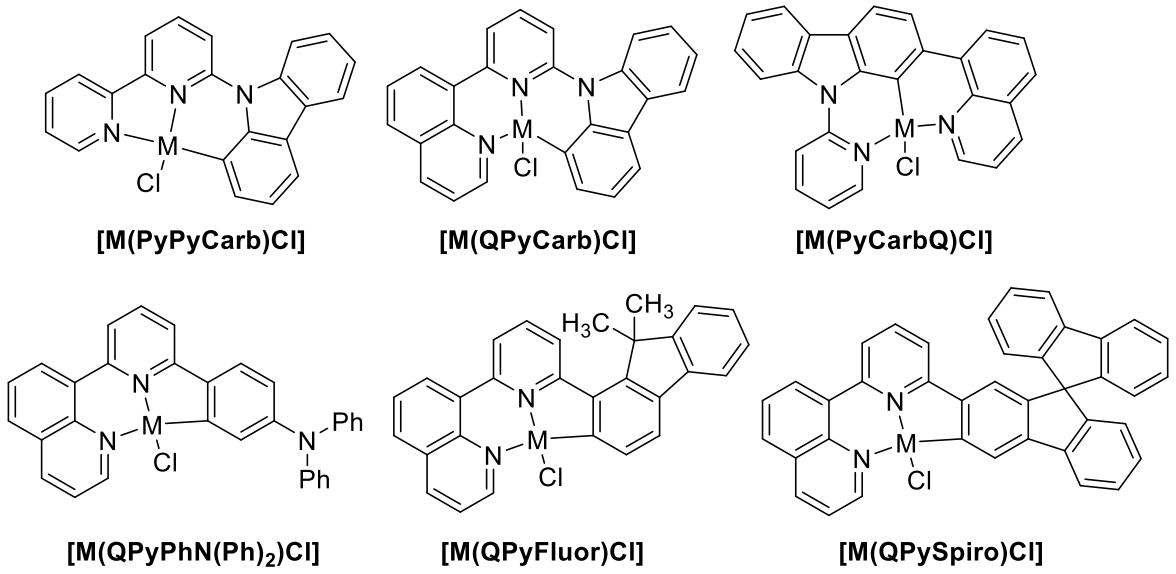

Figure 12 Overview of Ring-expanded complex systems with N^C^N and C^N^N type ligands.

Table 4 Reaction conditions of complexation reactions of N^C^N and C^N^N type complexes.

Protoligand	Metal precursor	Conditions	Habitus (Yield)
PyPyHCarb	$K_2[PtCl_4]$	HOAc, reflux, 72 h	Dark-orange powder (54%)
	$K_2[PdCl_4]$	HOAc, reflux, 72 h	Yellow powder (72%)
QPyHCarb	$K_2[PtCl_4]$	HOAc, reflux, 72 h	Orange powder (22%)
	$K_2[PdCl_4]$	MeCN/H_2O, 18 h	Yellow powder (22%)
PyHCarbQ	$K_2[PtCl_4]$	HOAc, reflux, 18 h	Orange powder (59%)
	$K_2[PdCl_4]$	HOAc, reflux, 42 h	Yellow powder (39%)
	$NiBr_2$	*p*-xylene, KOAc/K_2CO_3, reflux, 72 h	No conversion
QPyHPhN(Ph)$_2$	$K_2[PtCl_4]$	HOAc, reflux, 18 h	decomposition
QPyHFluor	$K_2[PtCl_4]$	HOAc, reflux, 21 h	Orange powder (91%)
	$K_2[PdCl_4]$	HOAc, reflux, 21 h	Yellow powder (34%)
	$NiBr_2$	*p*-xylene, KOAc/K_2CO_3, reflux, 72 h	No conversion
PyHSpiro	$K_2[PtCl_4]$	HOAc, reflux, 23 h	Orange powder (99%)
	$K_2[PdCl_4]$	HOAc, reflux, 21 h	Yellow powder (51%)

The UV/Vis-absorption spectra of the complexes with N^C^N and C^N^N ligands in

tetrahydrofuran (THF) are shown in figures 13 and 14, absorption maxima and corresponding extinction coefficients are listed in table 6.

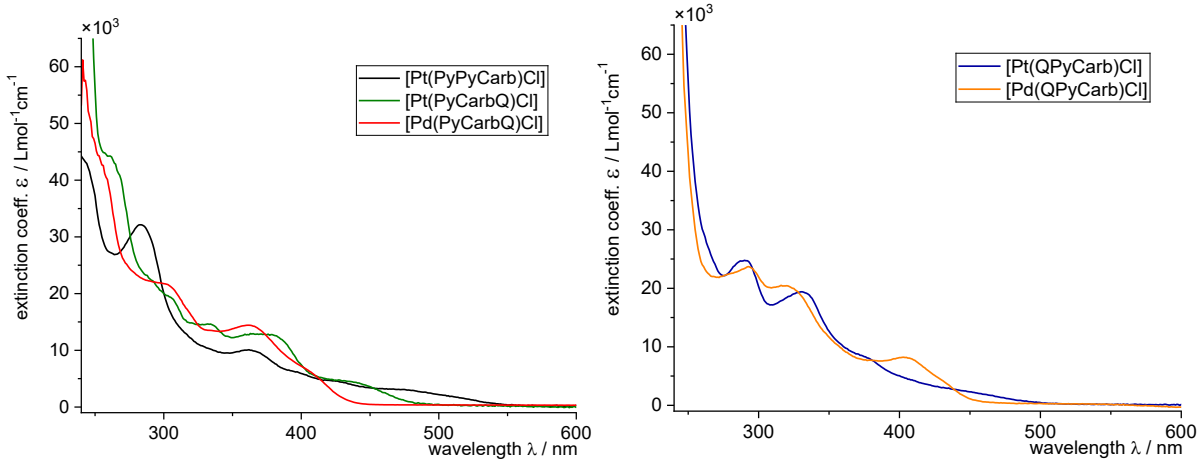

Figure 13 UV/Vis-absorption spectra of N^C^N and C^N^N type complexes. Measured in THF at room temperature.

All complexes feature several distinct absorption maxima between 240 nm and 350 nm, indicating more pronounced transitions of π-π* and n-π* nature when compared to the N^C^N and C^N^N complexes previously reported (see chapter 3.1).[49] This increase in absorptions can be attributed to the generally bigger chromophores and the introduction of carbazole into the ligand backbone, making more n- and π- states accessible.

The complexes [M(PyCarbQ)Cl] both feature absorption bands at 380 nm (Pt; 12.7 ε) and 362 nm (Pd; 14.6 ε), which are not present in the free protoligands (see table 5, extinction coefficient $\varepsilon = \frac{10^3 * L}{mol * cm}$ derived from the *Lambert-Beer* law). These maxima could therefore be attributed to LMCT absorptions or alternatively LL'CT absorptions with metal participation, not possible prior to complexation. The complexes also feature long wavelength absorption maxima with low extinction coefficients (Pt: 442 nm, 4.25 ε; Pd: 408 nm, 6.23 ε), indicating MLCT absorptions. These absorptions are significantly shifted bathochromically when compared to other N^C^N complexes like for example [M(PyPhQ)Cl] (Pt: 418 nm, 6.60 ε; Pd: 381 nm, 9.00 ε). This also results in smaller HOMO-LUMO gap energies for the [M(PyCarbQ)Cl] complexes. Assuming a metal-centred HOMO at similar energy levels, this would mean a large LUMO, lower in energy is present. It is therefore likely it extends across both quinoline and carbazole rings within in the ligand backbone. This can be further validated by suitable DFT calculations or by comparison to systems [M(PyCarbPy)Cl], where the quinoline is replaced by another pyridine moiety. The highest wavelength absorptions of complexes of [M(QPyCarb)Cl] type are found at similar wavelength (Pt: 449 nm, 2.48 ε; Pd: 404 nm, 9.05 ε), implying these transitions are similar in nature, most likely taking place partially within the carbazole subunit. The complex [Pt(PyPyCarb)Cl] is an exception here, having a red-shifted, low intensity, absorption maximum at 480 nm (3.03 ε). This is typically the case when comparing C^N^N to N^C^N systems with otherwise similar ligand backbones (see chapter 3.1).[49] However, even when accounting for this trend, this shift of, for example 50 nm when

compared to [Pt(PhPyPy)Cl] is still significant and implies a strong contribution of the carbazole to the LUMO, typically strongly centred on the bipyridine moiety.[26, 81]

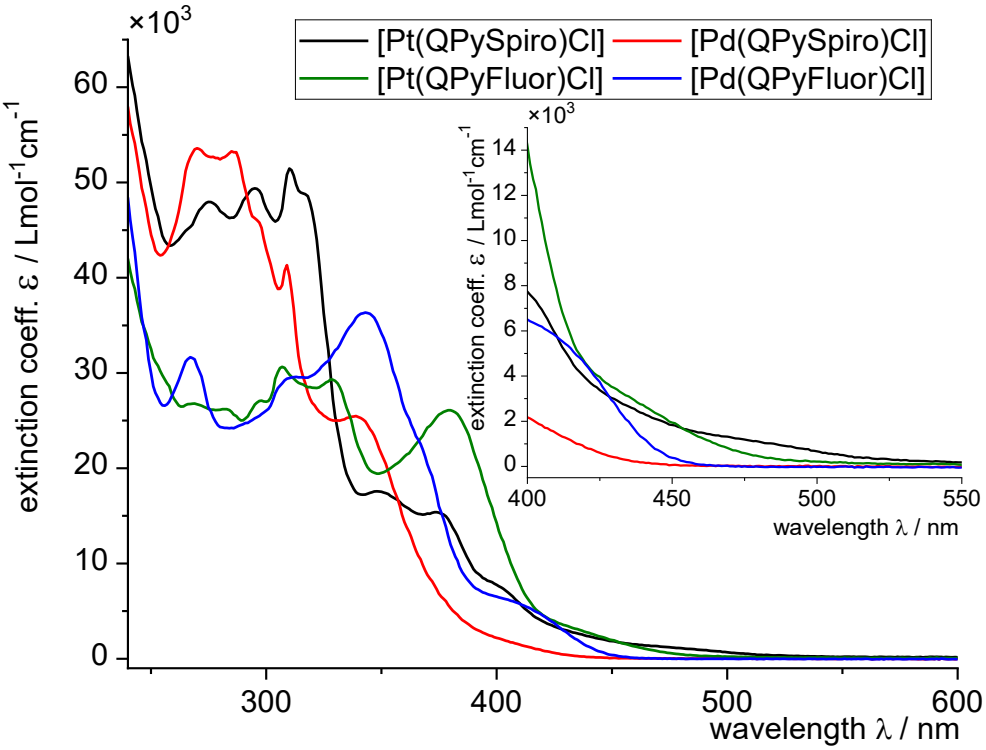

Figure 14 UV/Vis-absorption spectra of C^N^N type complexes, measured in THF at room temperature.

All complexes derived from the complex [M(PhPyQ)Cl], UV/Vis-absoprtion spectra detailed in Figure 14 and table 6, show very pronounced and detailed absorption bands within the range of 240 nm to 350 nm. These bands can be attributed to transitions of π-π* and n-π* nature, with strong contributions of the dimethylfluorene or spirofluorene chromophores.[101, 102] The complexes [M(QPyFluor)Cl] feature pronounced absorption bands at 379 nm (26.2 ε) for the platinum compound and 343 nm (36.5 ε) for the palladium compound. These are not present for the protoligand (see table 5) and imply strong interactions of the metal and the fluorene subunit. This is further supported by the fact the spirofluorene-bearing complexes do not show these absorptions, meaning they are not centred on the QPy-subunit. All complexes except [Pd(QPySpiro)Cl] show long range absorption bands at >400 nm, although their intensity is very low compared to the other absorption bands. Generally the palladium complexes have a strong blueshift of around 35 nm compared to their platinum counterparts, as was already observed for the previously reported ring-expanded N^C^N and C^N^N systems.[49]

Table 5 Optical properties of protoligands of N^C^N and C^N^N type. [a]

Substance	**λ_1 (ε)**	**λ_2 (ε)**	**λ_3 (ε)**	**λ_4 (ε)**	**λ_5 (ε)**	**$\Delta E_{opt.}$**
PyPyHCarb	243 (84.7)	279 (14.1)	-	-	335 (10.0)	3.53
PyHCarbQ	-	-	-	300 (16.3)	334 (10.9)	3.37
QPyHCarb	241 (91.4)	289 (53.6)	-	320 (20.0)	335 (16.8)	3.50
QPyHPhN(Ph)$_2$	232 (14.0)	289 (7.71)	306 (8.13)	318 (7.95)	-	3.49

QPyHFluor	-	290 (32.5)	-	319 (46.4)	334 (36.3)	3.49
QPyHSpiro [b]	250 (7.85)	296 (3.24)	309 (3.24)	322 (2.27)	-	3.53

[a] Wavelengths in nm, extinction coefficients in $\frac{10^3 * L}{mol * cm}$, $\mathbf{\Delta E_{opt.}}$ in eV. [b] extinction coefficients in $\frac{10^8 * L}{mol * cm}$.

Table 6 Optical properties of complexes of N^C^N and C^N^N type. [a]

Substance	**λ1 (ε)**	**λ2 (ε)**	**λ3 (ε)**	**λ4 (ε)**	**λ5 (ε)**	**λ6 (ε)**	**ΔEopt.**
[Pt(PyPyCarb)Cl]	283 (32.2)	-	-	362 (10.2)	426 (4.67)	480 (3.03)	2.15
[Pt(PyCarbQ)Cl]	262 (44.1)	306 (19.2)	334 (14.6)	380 (12.7)	442 (4.25)	-	2.47
[Pd(PyCarbQ)Cl]	257 (41.8)	304 (21.6)	-	362 (14.6)	408 (6.23)	-	2.82
[Pt(QPyCarb)Cl]	290 (24.8)	-	331 (19.5)	378 (8.15)	449 (2.48)	-	2.40
[Pd(QPyCarb)Cl]	292 (24.5)	-	321 (21.3)	-	404 (9.05)	-	2.68
[Pt(QPySpiro)Cl]	275 (48.0)	295 (49.5)	310 (51.5)	348 (17.7)	374 (15.5)	481 (1.21)	2.25
[Pd(QPySpiro)Cl]	270 (53.5)	285 (53.4)	308 (41.3)	339 (25.5)	-	-	3.19
[Pt(QPyFluor)Cl	268 (26.8)	282 (26.3)	297 (27.2)	306 (30.7)	328 (29.4)	379 (26.2)	2.94
[Pd(QPyFluor)Cl	267 (31.7)	309 (29.7)	-	-	343 (36.5)	414 (5.53)	2.74

[a] Wavelengths in nm, extinction coefficients in $\frac{10^3 * L}{mol * cm}$, $\mathbf{\Delta E_{opt.}}$ in eV.

The electrochemical properties of all N^C^N and C^N^N type complexes were investigated by carrying out cyclic voltammetry in THF solution with 0.1 M NBu_4PF_6. The electrochemical data of all protoligands and complexes is summarized in tables 7 and 8.

All protoligands feature a reversible first reduction at ranges between –2.25 V and –2.60 V, and a second irreversible reduction at between –2.74 V and –3.10 V. The only exception is PyPyHCarb, where both reductions are reversible, a typical behaviour of the 2,2'-bipyridine subunit.[103] Only two of the protoligands feature oxidations withing the measurement window, QPyHCarb (Ox 1: 0.90 V, Ox 2 1.25 V) and $QPyHPhN(Ph)_2$ (Ox 1: 0.54 V). The latter is particularly interesting because of its reversibility, indicating the oxidation most likely takes place in the triphenylamine-subunit.[104]

Table 7 Electrochemical properties of protoligands of N^C^N and C^N^N type. a

Substance	**Red 3**	**Red 2**	**Red 1**	**Ox 1**	**$\Delta E_{elec.}$**
PyPyHCarb	-	–3.10 $E_{1/2}$	–2.60 $E_{1/2}$		-
QPyHCarb [b]	-	–2.81	–2.25 $E_{1/2}$	0.90	3.15
$QPyHPhN(Ph)_2$	-	–3.15	–2.59 $E_{1/2}$	0.54 $E_{1/2}$	3.13
QPyHFluor	–3.01	–2.74	–2.30 $E_{1/2}$	-	-
QPyHSpiro	-	–3.00	–2.56 $E_{1/2}$	-	-

[a] Potentials, $\Delta E_{elec.}$ in V (Ox 1 – Red 1). Peak potentials given for irreversible processes or specified as reversible processes with half-wave potentials $E_{1/2}$. Measured in THF with 0.1 M NBu_4PF_6, referenced to $FeCp_2/FeCp_2^+$. [b] Ox 2: 1.25 V.

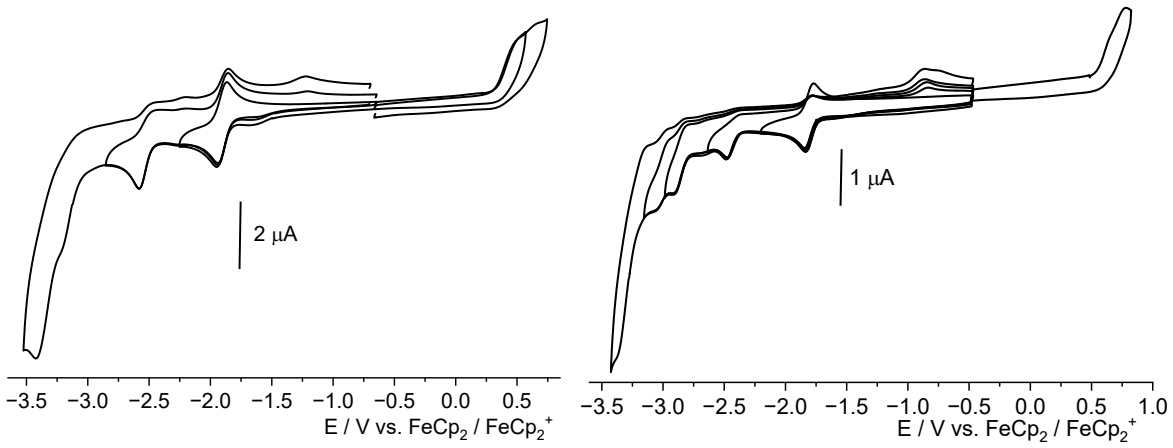

Figure 15 Cyclic voltammograms of [Pt(PyPyCarb)Cl] (left) and [Pt(QPySpiro)Cl] (right), measured in THF with 0.1 M NBu_4PF_6, referenced to $FeCp_2/FeCp_2^+$.

The reductions of all complexes are markedly shifted towards more positive potentials for all complexes as opposed to their protoligands (see table 7). Notably, most of the complexes retain the reversible character of this first reduction, implying the reduction takes places in the ligand backbone and does not involve the coligand. All reduction potentials lie in very similar ranges for all complexes, implying the LUMOs all lying mostly on the shared QPy-subunit (except for [M(PyPyCarb)Cl] and [M(PyCarbQ)Cl] complexes). This also means that the dimethylfluorene and spirofluorene subunits have very little contribution to electrochemical processes, making the compounds behave very similar to the complexes [M(PhPyQ)Cl] overall (see chapter 3.1).[49]

The lowest oxidation potential of all complexes is found for [Pt(PyPyCarb)Cl] at 0.51 V, also resulting in the smallest electrochemical HOMO-LUMO gap of 2.42 V. Assuming a mostly metal-centred HOMO, this underlines the strong σ-donor character of the cyclometalated carbazole subunit, donating electron density to the metal centre and raising its HOMO levels. Interestingly, the opposite is true for [Pt(QPyCarb)Cl, where the oxidation takes place at a higher potential of 0.76 V. This implies the coordination geometry of the ligand also directly affects the electrochemical properties. Quinoline can therefore compete more strongly with the trans-situated carbazole-carbanion and thus destabilize the metal-centred HOMO. The Pd(II) oxidations are shifted to slightly higher potentials compared to Pt(II), due to their electron-poorer nature.

Table 8 Electrochemical properties of protoligands of N^C^N and C^N^N type. [a]

Substance	Red 4	Red 3	Red 2	Red 1	Ox 1	$\Delta E_{elec.}$
[Pt(PyPyCarb)Cl] [b]	-	–3.42	–2.51 $E_{1/2}$	–1.91 $E_{1/2}$	0.51	2.42
[Pt(PyCarbQ)Cl]	-	-	–2.85	–2.02	0.56	2.58
[Pd(PyCarbQ)Cl]	-	–2.94	–2.79	–2.11	-	-
[Pt(QPyCarb)Cl]	-	–3.34	–2.50	–1.88 $E_{1/2}$	0.76	2.64
[Pd(QPyCarb)Cl]	-	–2.81	–2.49	–1.98	0.92	2.90
[Pt(QPySpiro)Cl] [c]	–3.06	–2.91	–2.48	–1.81 $E_{1/2}$	0.78	2.59
[Pd(QPySpiro)Cl] [d]	–2.97	–2.85	–2.53	–1.92 $E_{1/2}$	0.81	2.73

[Pt(QPyFluor)Cl	–2.98	–2.71	–2.49	–1.89 $E_{1/2}$	-	-
[Pd(QPyFluor)Cl [e]	–3.32	–2.82	–2.49	–1.80 $E_{1/2}$	0.63	2.43

[a] Potentials, $\Delta E_{elec.}$ in V (Ox 1 – Red 1). Peak potentials given for irreversible processes or specified as reversible processes with half-wave potentials $E_{1/2}$. Measured in THF with 0.1 M NBu_4PF_6, referenced to $FeCp_2/FeCp_2^+$. [b] Ox 2: 0.67 V. [c] Red 5: –3.37 V. [d] Red 5: –3.10 V. [e] Ox 2: 0.81 V.

Single crystals suitable for SC-XRD were obtained for several of the N^C^N and C^N^N type complexes. Crystals of [M(QPyFluor)Cl] and [M(QPySpiro)Cl] were obtained by isothermal evaporation of saturated solutions in dichloromethane (CH_2Cl_2) or CD_2Cl_2. Crystals of [Pd(QPyCarb)Cl] and [Pd(PyCarbQ)Cl] were obtained by overlaying saturated solution in CH_2Cl_2 with diethyl ether. The obtained structures are detailed in figures 16-25, crystal solution data are detailed in appendix (tables 38 and 39) and relevant bond lengths and angles are detailed in table 9. Torsion angles and stacking distances are summarized in Figure 26.

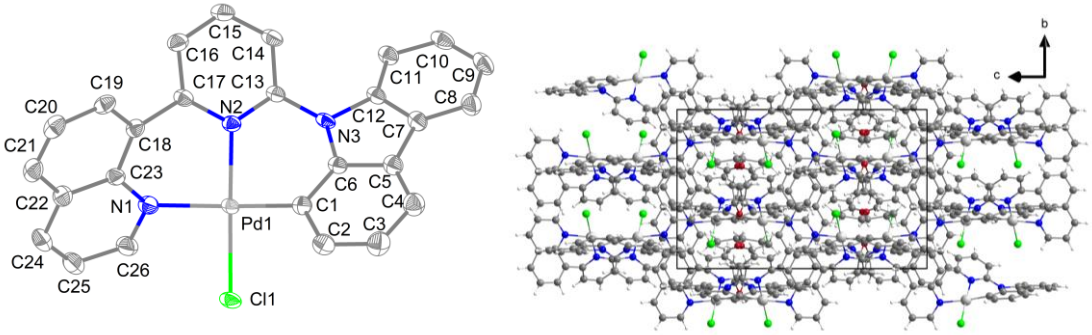

Figure 16 Asymmetric unit of [Pd(QPyCarb)Cl] from single crystal X-ray diffraction (displacement ellipsoids at 50% probability) (left), co-crystalized THF and hydrogens omitted for clarity, and view on the crystal structure (right) along the crystallographic *a*-axis.

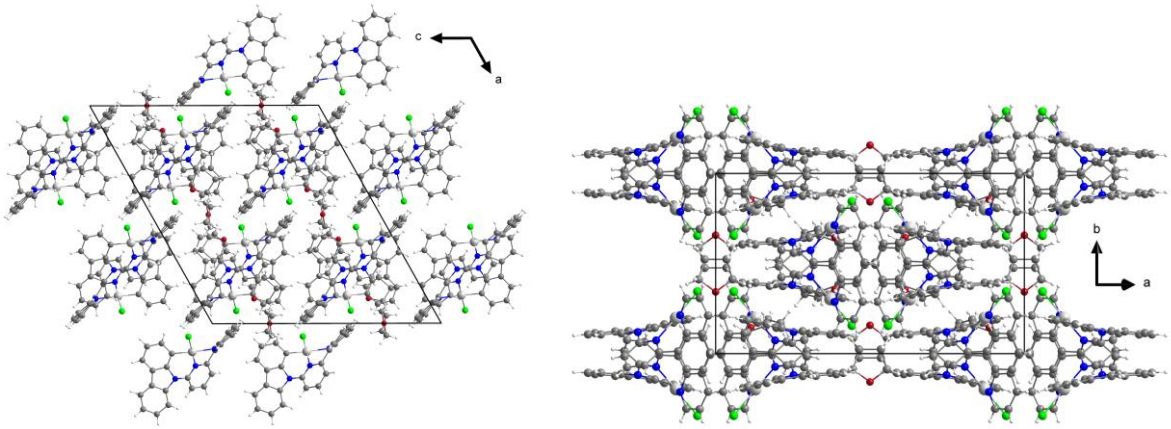

Figure 17 View on the crystal structure of [Pd(QPyCarb)Cl] along the crystallographic *b*-axis (left) and *c*-axis (right).

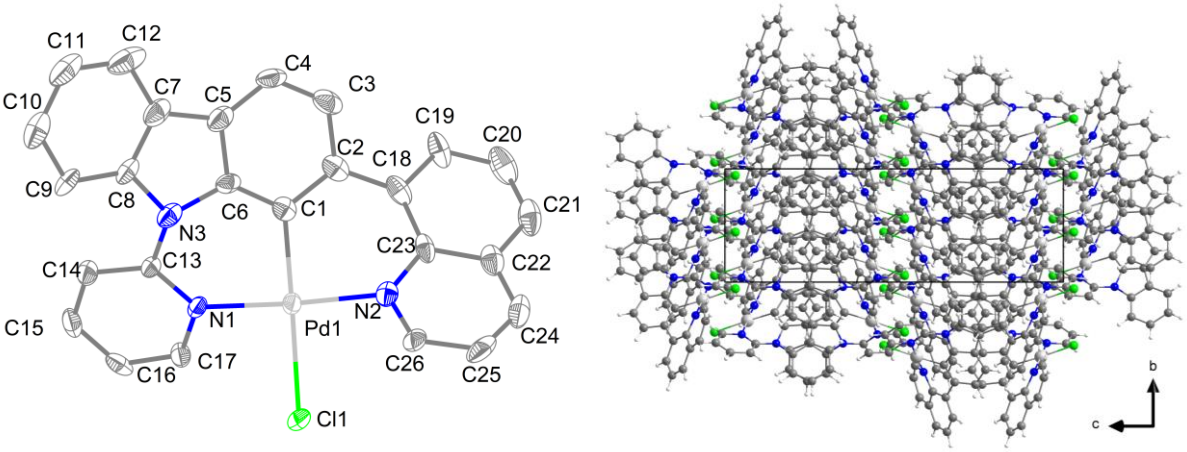

Figure 18 Asymmetric unit of [Pd(PyCarbQ)Cl] from single crystal X-ray diffraction (displacement ellipsoids at 50% probability, hydrogens omitted for clarity) (left) and view on the crystal structure (right) along the crystallographic *a*-axis.

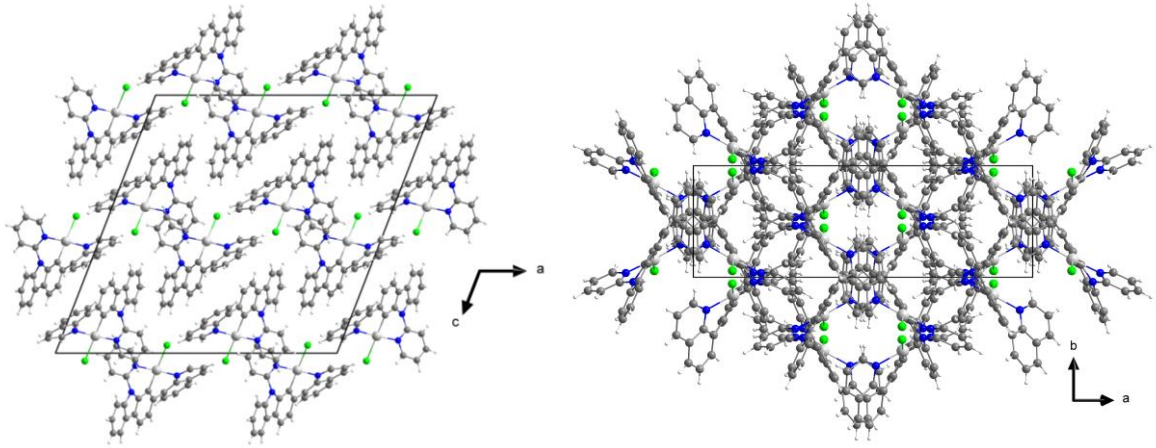

Figure 19 View on the crystal structure of [Pd(PyCarbQ)Cl] along the crystallographic *b*-axis (left) and *c*-axis (right).

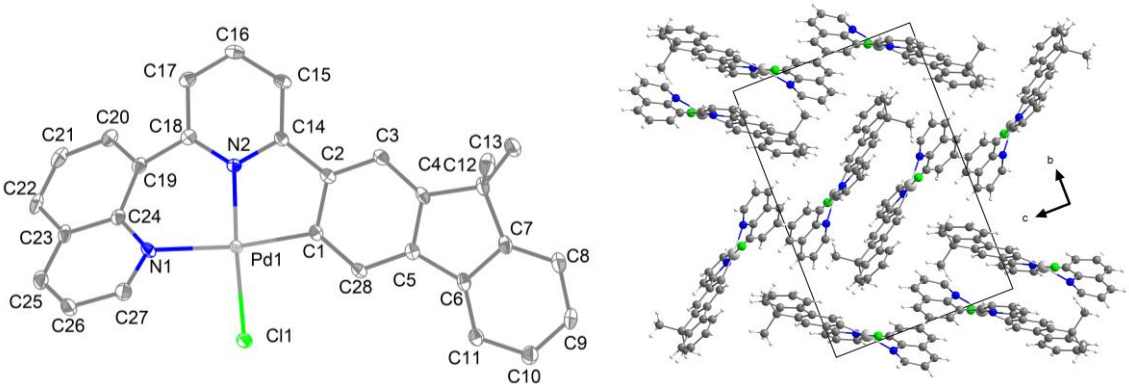

Figure 20 Asymmetric unit of [Pd(QPyFluor)Cl] from single crystal X-ray diffraction (displacement ellipsoids at 50% probability, hydrogens omitted for clarity) (left) and view on the crystal structure (right) along the crystallographic *a*-axis.

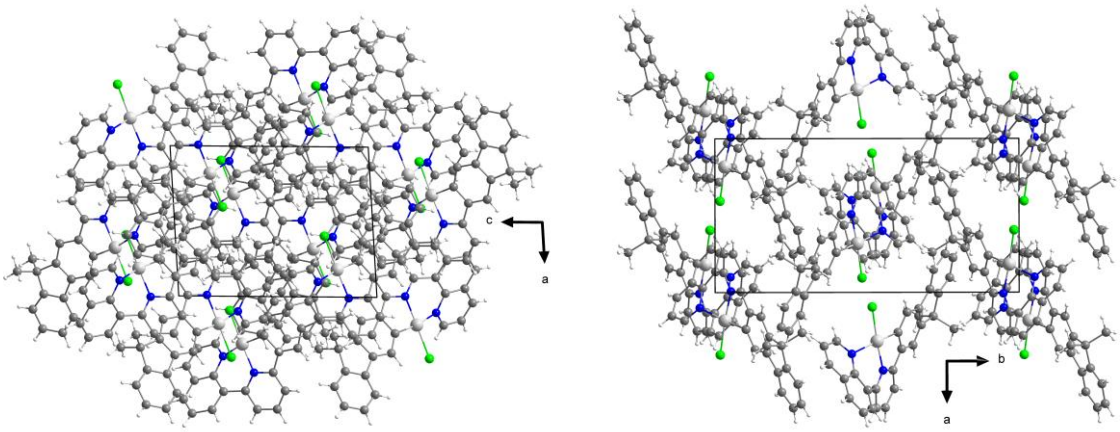

Figure 21 View on the crystal structure of [Pd(QPyFluor)Cl] along the crystallographic *b*-axis (left) and *c*-axis (right).

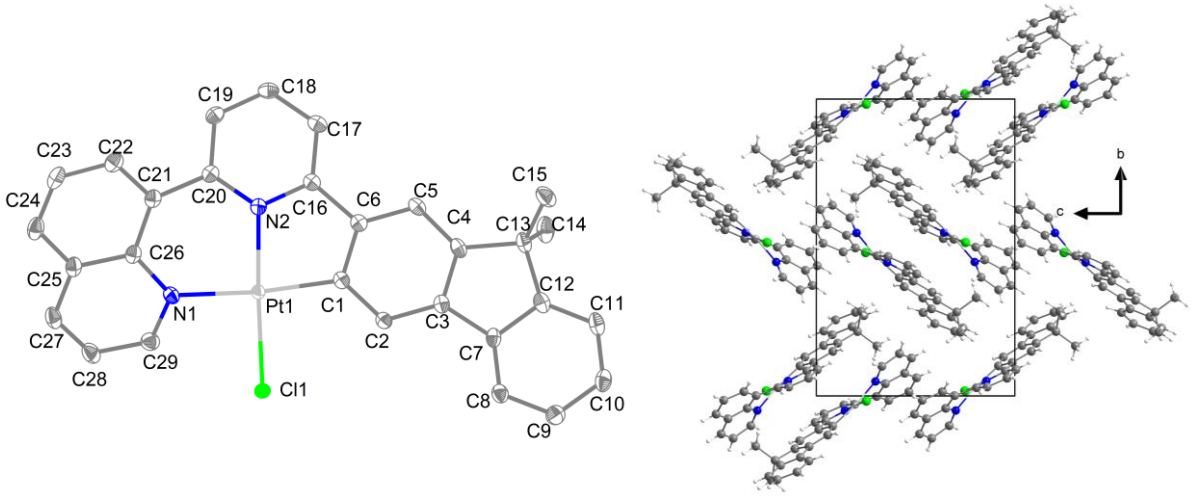

Figure 22 Asymmetric unit of [Pt(QPyFluor)Cl] from single crystal X-ray diffraction (displacement ellipsoids at 50% probability, hydrogens omitted for clarity) (left) and view on the crystal structure (right) along the crystallographic *a*-axis.

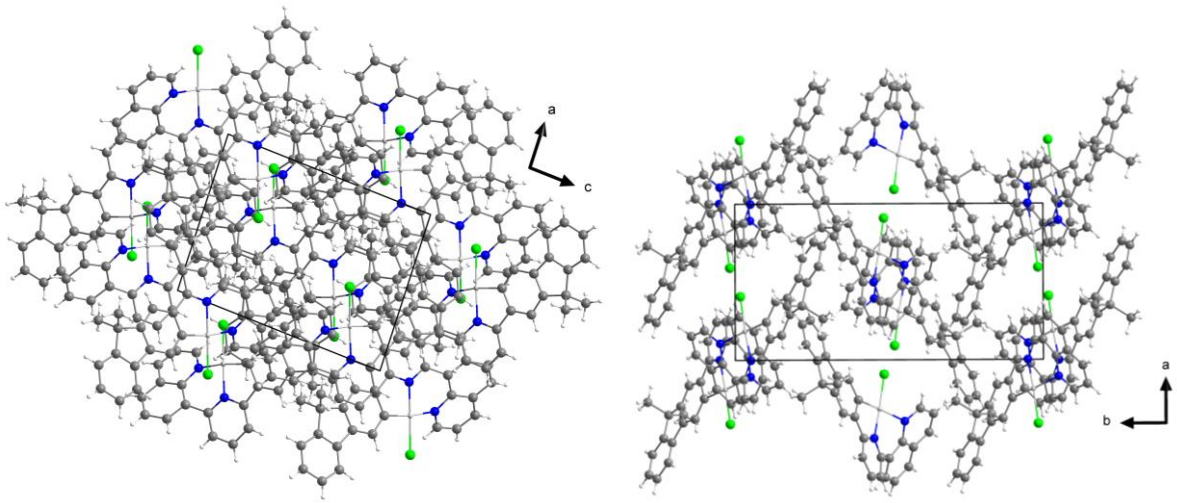

Figure 23 View on the crystal structure of [Pt(QPyFluor)Cl] along the crystallographic *b*-axis (left) and *c*-axis (right).

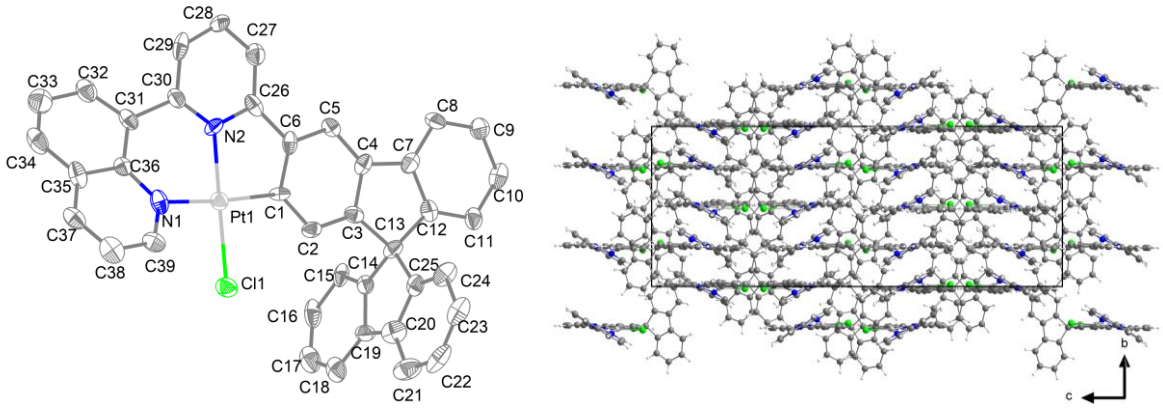

Figure 24 Asymmetric unit of [Pt(QPySpiro)Cl] from single crystal X-ray diffraction (displacement ellipsoids at 50% probability, hydrogens omitted for clarity) (left) and view on the crystal structure (right) along the crystallographic *a*-axis.

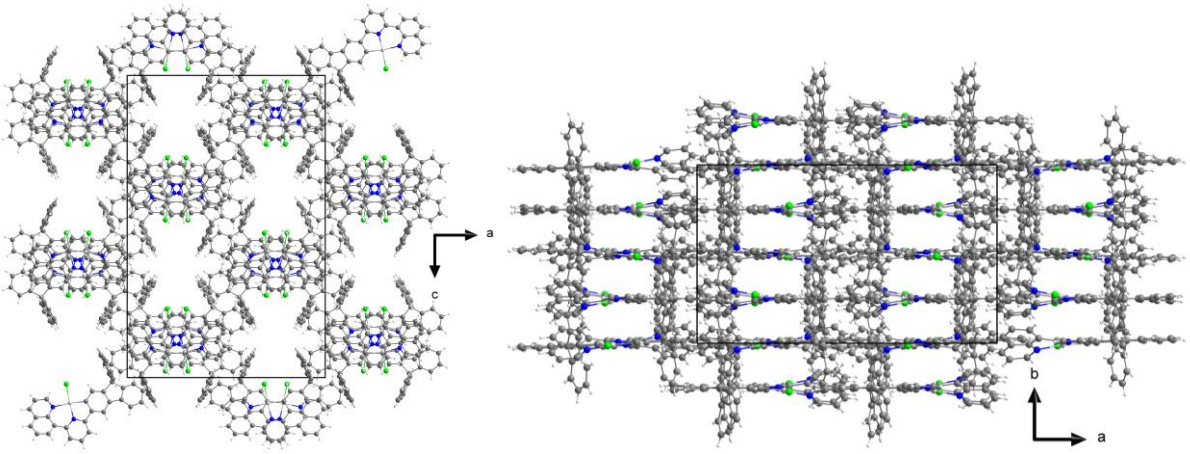

Figure 25 View on the crystal structure of [Pt(QPySpiro)Cl] along the crystallographic *b*-axis (left) and *c*-axis (right).

The carbazole-bearing complexes [Pd(QPyCarb)Cl] and [Pd(PyCarbQ)Cl] both feature two six-membered cyclometalated rings, similar to the previously reported compound [Pt(QPyQ)Cl].[18, 49] To accommodate the metal ion in an energy-minimizing way, the aromatic rings rotate around their connecting bond. This results in pronounced torsion of the ligand backbone and at the same time gives nearly perfectly square planar angles surrounding the metal centre. For [Pd(QPyCarb)Cl], the angles of the metal to the cyclometalated aromatic ring (in this case part of the carbazole subunit) must be perfectly aligned to allow for activation and therefore adhere to the bond angle of 120° (sp^2-hybrid) dictated by hybridization theory.[36] This results in pronounced torsion of the C-N bond between the carbazole and pyridine subunit, resulting in an interplanar angle of 39.65(1)° (see Figure 26, tab. 9). The angle between the central pyridine ring and the quinoline ring is even bigger, at 48.73(1)°. Both of these angles surpass the torsion reported for the related compound [Pd(QPhQ)Cl] (Interplanar angle Q-Ph: 33.9(6)°).[49] The same is true for the complex [Pd(PyCarbQ)Cl], where the carbazole subunit is part of the rigid central ring system. Here, the torsion of the bound pyridine (39.04(2)°) and

quinoline (39.74(2)°) rings is equally pronounced. For both complexes, the angles around the metal centre are close to 90° for all four donors (see table 9).
These pronounced distortions result in the loss of coplanarity of the different aromatic units of the ligand backbone. This means orbital overlap is harder to achieve, which could affect a ligand-centred LUMO, potentially decoupling the different aromatic rings in that regard. This would result in higher LUMO energies. However, when comparing, for example [Pt(QPhQ)Cl] and [Pt(PyCarbQ)Cl] as two N^C^N compounds with similar coordination, they do not differ much in their absorption or electrochemical properties (see chapter 3.1).[49] On the contrary, the highest absorption maximum and the first reduction of the [Pt(PyCarbQ)Cl] are slightly shifted towards lower energies (Red 1: –2.02 V, λ_{max}: 442 nm, [Pt(QPhQ)Cl] Red 1: –2.08 V, λ_{max}: 426 nm). This means the strong distortion present in the structure of [Py(PyCarbQ)Cl] does not affect the photo- and electrochemical properties much when compared to other N^C^N compounds. The larger π-system introduced by the carbazole is offset by the distortion of its structure, resulting in diminishing π-overlap with the other aromatic rings.
The complexes [Pt(QPySpiro)Cl], [Pt(QPyFluor)Cl] and [Pd(QPyFluor)Cl] are related to the previously reported complexes [M(QPyPh)Cl].[49] As such, they show very similar bond lengths and angles surrounding the metal (see table 9). As opposed to the structures previously discussed, here one six-membered and one five-membered cyclometalated ring is present in the structure. Accordingly, the angles around the metal are slightly distorted away from the perfect square planar 90° to 82.17(7)°- 83.7(4)° for the angle N_2–M–C (see table 9). This is also due to the M–C bond generally being shorter than its opposing M–N_1 bond (e.g. [Pt(QPySpiro)Cl] M–C: 1.974(1) Å, M–N_1: 2.108(1) Å). The central pyridine ring and the phenyl-derived subunit are nearly coplanar, having a small interplanar angle of 2.815(4)° for [Pt(QPySpiro)Cl]. The quinoline-pyridine interplanar angle of 27.50(4)° is much higher but still much less pronounced than was the case for the previously discussed carbazole-bearing complexes.
The complexes feature head to tail stacking, with two quinoline moieties showing π-stacking with distances of, for example, 3.606(2) Å for [Pt(QPySpiro)Cl] (see Figure 26). The stacking complex pairs are inverted, having the bulky dimethylfluorene- or spirobifluorene units facing away from each other. This results in voids within the crystal packing being apparent, which are not present in the carbazole-bearing complexes or the parent compound [M(QPyPh)Cl]. No stacking of the dimethylfluorene or spirobifluorene subunits is discernible (see Figure 22-26).

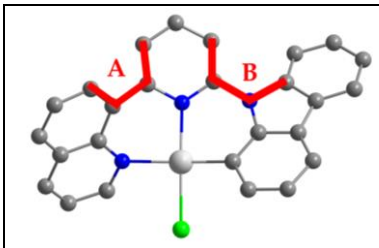	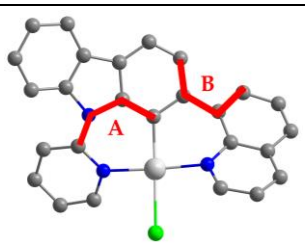	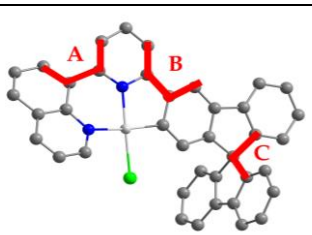	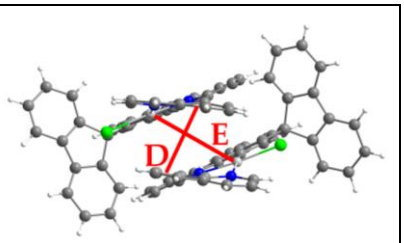
[Pd(QPyCarb)Cl]	**[Pd(PyCarbQ)Cl]**	**[Pt(QPySpiro)Cl]**	
Interplanar torsion angles (°)			
A	48.73(1)	39.04(2)	27.50(4)
B	39.65(1)	39.74(2)	2.815(4)
C	-	-	87.51(5)
Shortest distances (Å)			
D (Q-Q)	**-**	**-**	3.606(2)
E (M-M)	**-**	**-**	4.834(8)

Figure 26 Selected ring torsion angles (A,B,C) and distances (D, E) for complexes of Pd and Pt.

Table 9 Selected bond lengths (Å) and angles (°) for the Pt and Pd complexes. [a]

Distances (Å)	[Pd(QPyFluor)Cl]	[Pt(QPyFluor)Cl]	[Pt(QPySpiro)Cl]	[Pd(QPyCarb)Cl]	[Pd(PyCarbQ(Cl)]
M–C	1.977(2)	1.989(2)	1.974(1)	1.967(4)	1.987(7)
M–N_1	2.138(2)	2.116(2)	2.108(1)	2.155(3)	2.062(5)
M–N_2	1.999(2)	1.983(2)	2.009(9)	2.031(3)	2.057(6)
M–Cl	2.304(6)	2.302(5)	2.317(3)	2.313(9)	2.434(2)
Angles (°)					
N_1–M– N_2	91.12(8)	91.94(7)	92.4(4)	90.0(1)	175.9(2)
N_1–M–Cl	92.36(6)	91.07(5)	92.0(3)	90.26(9)	91.69(2)
N_2–M–Cl	176.4(6)	176.9(5)	174.0(3)	177.7(8)	91.79(2)
N_1–M–C	170.2(9)	171.1(7)	172.4(4)	175.0 (1)	87.90(2)
N_2–M–C	82.25(9)	82.17(7)	83.7(4)	88.73(1)	88.70(3)
C–M–Cl	94.43(7)	94.94(6)	92.4(3)	91.1(1)	177.5(2)
Σ angles	360.1	360.1	360.5	360.1	360.1

[a] From single crystal X-ray diffraction.

The complexes discussed vary greatly in their optical and electrochemical properties, with strong contributions of their respective ligand frameworks to their overall behaviour. This is especially due to the rigid structures of the carbazole- and fluorene-derived subunits and their optical properties. These units result in very strong distortions of the ligand backbone without affecting the optical or electrochemical properties much when compared to similar ring-expanded complex systems. Having the flexibility of the ligand backbone as integral part of ligand design without big impact on optical properties could help avoid non-radiative decay by distortion and help stabilize excited states.[43] This could be further investigated by carrying out luminescence spectroscopy and pairing it up with TD-DFT calculations on the excited states.

The exhibited properties can be further tuned by exchange of the coligand, with the methods detailed in chapter 3.6.

3.4 Complexes with Sulphur- and Oxygen-Donor Ring-Expanded Ligands

Ring-expansion of the ligand scaffold also opens the possibility of donor atoms other than nitrogen while retaining an easily synthesizable ligand system. For example, ligands with sulphur-bearing rings like thiophenes have already been explored for platinum complexes.[105] While complexes with tridentate ligands containing sulphur donors were previously reported, no direct N^C^S type coordination was explored yet.[8, 106]

Protoligands with sulphur and oxygen donor atoms were synthesized by introducing their corresponding heteroaromats (thianthrene (Thian), dibenzothiophene (DBT), dibenzofuran (DBF)) and replacing the quinoline moiety of already explored ligand systems (see Scheme 17 and table 10).

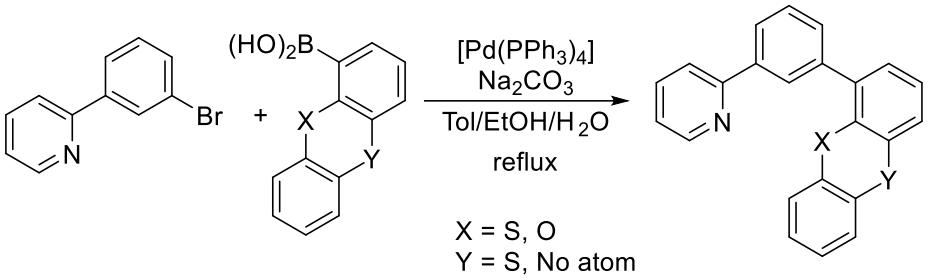

Scheme 17 Exemplary synthesis procedure of ligands bearing heteroaromatic ring systems, following general *Suzuki* protocol.

This method led to a variety of N^C^S or N^C^O type ligand systems. Similarly, reactions of 2,5-dibromobenzene with two sulphur-containing building blocks gave the symmetric S^C^S protoligands. These ligands where then subjected to complexation reaction conditions following the general procedures employed for their parent ligand systems of N^C^N or C^N^N type (see Scheme 18).

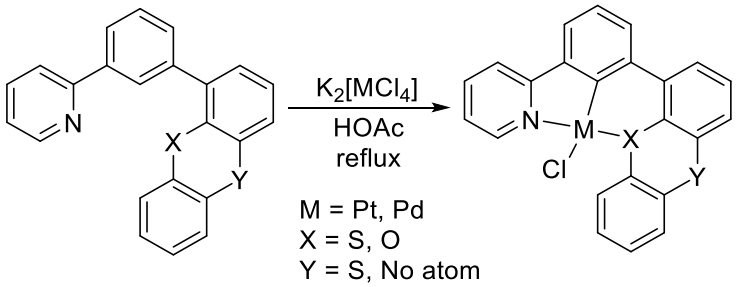

Scheme 18 General procedure of complexation reactions for N^C^S type systems, applicable to all heteroaromatic ligand systems (see table 10).

The resulting complexes are summarized in figure 27 with the reaction conditions detailed in table 10.

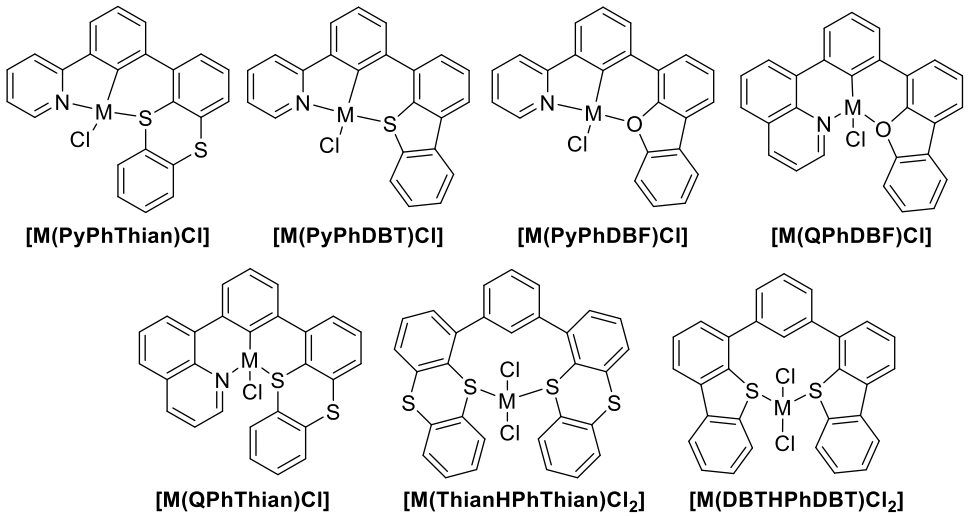

Figure 27 Overview of obtained Complexes of N^C^S, S^S or N^C^O type.

Table 10 Reaction conditions of complexation reactions of all N^C^S, S^S or N^C^O type complexes.

Protoligand	Metal precursor	Conditions	Habitus (Yield)
PyHPhThian	$K_2[PtCl_4]$	HOAc, reflux, 21 h	Yellow Powder (62%)
	$K_2[PdCl_4]$	HOAc, reflux, 16 h	Yellow Powder (45%)
	$NiBr_2$	KOAc, K_2CO_3, *p*-xyl., 22 h	No conversion
QHPhThian	$K_2[PtCl_4]$	HOAc, reflux, 16 h	Dark orange powder (14%)
	$K_2[PdCl_4]$	HOAc, reflux, 72 h	Light green powder (77%)
PyHPhDBT	$K_2[PtCl_4]$	HOAc, reflux, 16 h	Yellow Powder (63%)
	$K_2[PdCl_4]$	HOAc, reflux, 18 h	Yellow Powder (43%)
PyHPhDBF	$K_2[PtCl_4]$	HOAc, reflux, 44 h	Yellow Powder (27%)
	$K_2[PdCl_4]$	HOAc, reflux, 22 h	Yellow Powder (38%)
	$NiBr_2$	KOAc, K_2CO_3, *p*-xyl., MW (300 W), 5 h	No conversion
QHPhDBF	$K_2[PtCl_4]$	HOAc, reflux, 3 h	Orange Powder (48%)
	$K_2[PdCl_4]$	HOAc, reflux, 19 h	Green Powder (56%)
ThianHPhThian	$K_2[PtCl_4]$	HOAc, reflux, 2 h	Dark brown powder (59%)
DBTHPhDBT	$K_2[PtCl_4]$	HOAc, reflux, 22 h	Grey powder (57%)

The complexes were obtained in moderate to good yields in all cases, their formation and purity was confirmed by NMR and HR-Mass spectrometry. Generally, the reactivity of N^C^S and N^C^O type ligands mirror their parent N^C^N ligands (see chapter 3.1).[49] The C–H activation reaction times vary between 3h – 72 h, with an average of 25 h, implying the introduction of sulphur or oxygen to the ligand systems has no notable impact on C–H activation reactivity.

The only exception to this is the cyclometalation of nickel(II), which does not yield the desired products under typical base assisted C–H activation conditions.[13, 26, 49] Instead, the protoligand was reisolated, with no conversion taking place (see table 10).

The complexes of S^S type are a notable exception here. While conversion of the metal precursors was observed, NMR spectroscopy indicates no C–H activation took place. Instead, the ^{1}H NMR of [Pt(ThianHPhThian)Cl$_2$] shows the to-be-activated proton still being present. Additionally, the ^{195}Pt signal is also significantly shifted from, for example –3969.1 ppm for [Pt(PyHPhThian)Cl] (DMSO-d$_6$, 129 MHz) to –3440.1 ppm (DMSO-d$_6$, 129 MHz). This shift to higher ppm values also speaks for a non-cyclometalated coordination of the metal centre, being complexated by the lone pairs of the two inner sulphur atoms of each thianthrene ring. HR-ESI-Mass spectrometry (70 eV) experiments contradict this finding, showing a signal at 698.98 m/z, which would be the mass of the cyclometalated [Pt(ThianPhThian)Cl]$^{\cdot+}$, however a radical cation is only rarely encountered in ESI-mass experiments.[107] This corresponds to the cyclometalated product, however it is likely that cyclometalation was induced during the mass experiment as this has previously been reported for experiments at 70 eV.[108]

Similar observations were made for [Pt(DBTHPhDBT)Cl$_2$], however the resolution of NMR spectra did not allow for a clear assignment of signals. Interestingly, mass spectrometry does not show cyclometalation nor the loss of coligands. Instead, either the radical cation or cyclometalated product that underwent protonation [[Pt(DBTHPhDBT)Cl$_2$]+H]$^+$ was detected (706.99 m/z).

It is therefore likely, that in both cases, the S^S bound complexes were obtained. In the case of N^C^N type complexes, precoordination forms strong M–N bonds. These direct the metal into the tridentate binding pocket and bring it closer to the C–H-bond of the central phenyl ring.[26, 93]This strongly favours subsequent C–H-activation. For the S^S ligand systems, precoordination through elongated M–S bond results in a larger distance of the metal to the C–H-bond, potentially further increased by the unique bent structure of the thianthrene moieties (see Figure 40). This precoordination then inhibits subsequent C–H-activation under the detailed conditions (see table 10). The exact coordination of these S^S type complexes would need to be elucidated by SC-XRD, but no crystals of S^S complexes could be obtained.

The optical properties of N^C^S, N^C^O and S^S type complexes and their protoligands were investigated by UV/Vis-absorption spectroscopy carried out in THF solutions at room temperature. The results of these measurements are summarized in Figure 28 and 29, as well as tables 11-13.

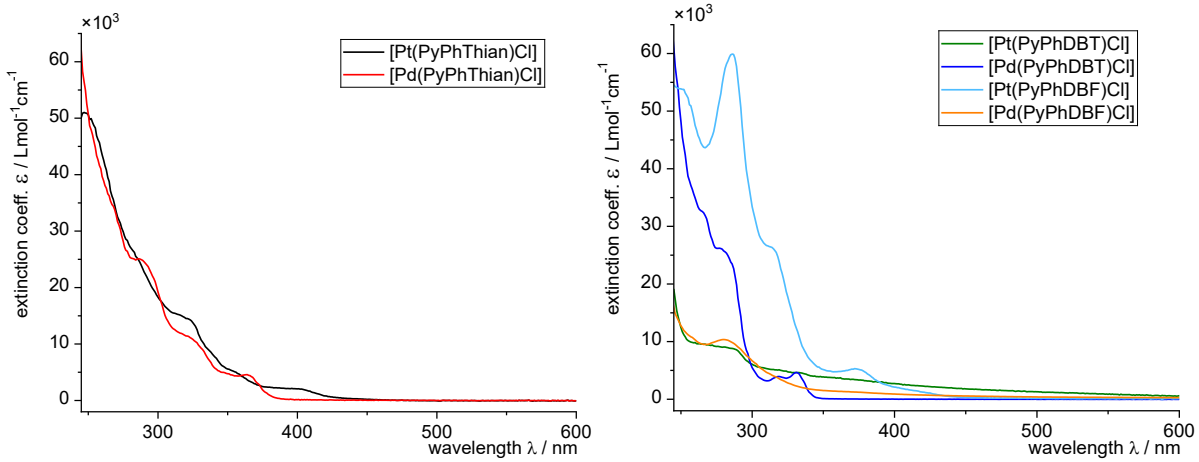

Figure 28 UV/Vis-absorption spectra of N^C^S and N^C^O type complexes derived from the pyridine-phenyl-heteroaromat type protoligands. Measured in THF at room temperature.

When comparing the absorption spectra of [Pt(PyPhThian)Cl] and [Pd(PyPhThian)Cl], the complexes share similar absorption maxima wavelengths and extinction coefficients for absorptions between 240 nm - 350 nm, which therefore can be attributed to ligand centred π-π* and n-π* transitions (see table 13). These absorption maxima are very similar to those exhibited by the N^C^N complex [Pt(PyPhQ)Cl], meaning there is little to no effect by the exchange of quinoline with thianthrene on the absorptions. This means the transitions mainly take place in the pyridine-phenyl part of the ligand backbone, implying the LUMO is mainly situated on this part of the molecule. While this is further backed by the fact the same holds true for [Pt(PyPhQ)Cl], further validation would require in depth DFT-calculations, as were carried out for the N^C^N compounds.[49] The long wavelength absorptions are shifted to higher energies when comparing [Pt(PyPhThian)Cl] to the N^C^N counterpart [Pt(PyPhQ)Cl] by 17 nm, resulting in a difference in optical HOMO-LUMO transitions of 0.21 eV.[49] The thianthrene sulphur atoms seem to stabilize the HOMO, lowering its energy and leading to higher $\Delta E_{opt.}$ (Assuming a mostly metal-centred HOMO being excited into a LUMO located on the pyridine-phenyl subunit of the ligand backbone, see table 13).

[Pd(PyPhThian)Cl] has its highest wavelength maximum (364 nm, 4.74 ε) significantly shifted by 37 nm (2535 cm^{-1}) compared to its platinum counterpart. This blueshift of palladium complexes vs. platinum complexes is typical for these types of compounds and also reported for the parent N^C^N compounds.[49]

Table 11 Comparison of N^C^N and N^C^S complexes based on the PyHPhQ and PyHPhThian protoligands. [a]

Substance	**λ_1 (ε)**	**λ_2 (ε)**	**λ_3 (ε)**	**λ_4 (ε)**	**λ_5 (ε)**	**λ_6 (ε)**	**$\Delta E_{opt.}$**
[Pt(PyPhThian)Cl]	-	285 (25.0)	322 (14.4)	354 (5.21)	-	401 (2.09)	2.76
[Pd(PyPhThian)Cl]	-	286 (25.2)	323 (11.1)	364 (4.74)	-	-	3.18
[Pt(PyPhQ)Cl][49]	238 (54.7)	304 (15.5)	321 (14.1)	359 (9.20)	373 (8.60)	418 (6.60)	2.97

[a] Wavelengths in nm, extinction coefficients in $\frac{10^3 * L}{mol * cm}$, $\Delta E_{opt.}$ in eV.

[Pt(PyPhDBF)Cl] shows very strong extinction, especially for the absorption maxima at 285 nm (59.9 ε) and 314 nm (26.4 ε), which is drastically higher than all other complexes in that wavelength region (see Figure 28, table 13). Absorptions at this range can be attributed to π-

π* transitions within the ligand backbone, the protoligand also features absorption maxima at the same wavelengths (281 nm, 32.5 ε; 312 nm, 9.10 ε). However, the lack of wavelength shift and much stronger extinction of the complex indicates impurities of protoligand might be present within the complex sample. While these impurities might have been introduced during workup of the complex synthesis, no traces of protoligand were found in NMR spectroscopy. However, UV/Vis-absorption spectroscopy generally is much more sensitive than NMR spectroscopy, so impurities from the synthesis cannot be ruled out. It is also possible that the complex partially decomposed during the preparation of UV/Vis samples, especially during sonification, releasing protoligand. Since the extinction coefficient is concentration-dependent, impurities by a lighter molecular weight protoligand in the same absorption range as the complex have a significant impact on the measurement. Two more absorption maxima at 373 nm (5.33 ε) and 406 nm (1.80 ε) are distinct to the complex, implying metal participation in the transitions. The longest wavelength absorption can be attributed to a transition between HOMO and LUMO level and only differs slightly from, for example, [Pt(PyPhThian)Cl] (401 nm, 2.09 ε). Assuming a metal-centred HOMO, this means the excitation most likely takes place into the pyridine-phenyl unit as the main location of the LUMO, explaining the small energetic difference between the two complexes.

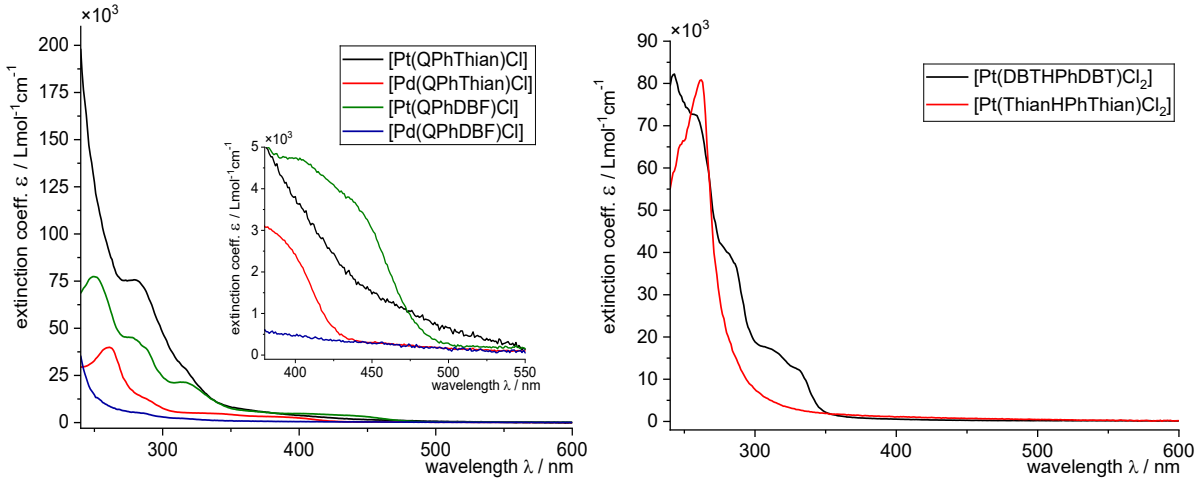

Figure 29 UV/Vis-absorption spectra of N^C^S and N^C^O type complexes (left) and of S^S type complexes (right). Measured in THF at room temperature.

Complexes featuring a quinoline ring instead of a pyridine ring (Figure 29) exhibited poor solubility generally, requiring prolonged sonification followed by filtration to obtain solutions suitable for UV/Vis-absorption spectroscopy. The resolution of the resulting spectra is still noticeably poorer, showing much less pronounced absorption bands overall up to only a faint "absorption ramp" in the case of [Pd(QPhDBF)Cl], indicating the presence of particles in solution. The lack of distinct long wavelength absorption bands >350 nm might indicate a similar effect as was described for [Pt(PyPhDBF)Cl], with protoligand being present in the analysed species, possibly due to decomposition during sonification. Similar poor resolution can also be seen [Pd(PyPhDBF)Cl] and especially [Pt(PyPhDBT)Cl] showing a pronounced ramping due to particles being present in solution.

S^S type complexes lack any absorption band above 350 nm, due to their lack of cyclometalation, which are typically associated with the MLCT absorptions in these complexes (see Figure 29). While [Pt(DBTHPhDBT)Cl_2] shows several distinct absorption bands between 240 nm and 350 nm, [Pt(ThianHPhTHian)Cl_2] only shows one absorption maximum at 261 nm (80.8 ε) and a slight ramp reaching down to 350 nm. This coincided with the data obtained from its protoligand ThianHPhThian (281 nm, 25.7 ε). This could either mean the complex is not stable in THF solution on the timescale of the UV/Vis experiment or the absorptions of both protoligand and complex mostly take place in the Phenyl-thianthrene units and do not change much upon complexation. Since the thianthrene subunits are bent by 98.84(1)° (see Figure 40) the π systems are separated and smaller, shifting the absorptions further into the ultraviolet region of the spectrum as opposed to [Pt(DBTHPhDBT)Cl_2], where no geometric distortion interferes with the π systems across the entire dibenzothiophene subunits (see Figure 40).

Table 12 Optical properties of protoligands of N^C^S, S^S or N^C^O type. [a]

Substance	**λ_1 (ε)**	**λ_2 (ε)**	**λ_3 (ε)**	**λ_4 (ε)**	**λ_5 (ε)**	**$\Delta E_{opt.}$**
PyHPhThian	-	262 (59.8)	281 (25.7)	-	-	3.99
QHPhThian	-	261 (45.6)	302 (12.9)	-	-	3.53
PyHPhDBT	-	266 (32.5)	280 (25.9)	318 (3.97)	331 (4.79)	3.55
PyHPhDBF	244 (54.5)	252 (51.7)	268 (34.0)	281 (32.5)	312 (9.10)	3.79
ThianHPhThian	-	262 (95.2)	-	-	-	4.10
DBTHPhDBT	-	266 (48.1)	282 (32.3)	319 (10.9)	332 (12.8)	3.56
QHPhDBF	244 (34.1)	-	288 (15.7)	300 (12.0)	313 (8.83)	3.67

[a] Wavelengths in nm, extinction coefficients in $\frac{10^3 * L}{mol * cm}$, $\Delta E_{opt.}$ in eV.

Table 13 Optical properties of complexes of N^C^S, S^S or N^C^O type. [a]

Substance	**λ_1 (ε)**	**λ_2 (ε)**	**λ_3 (ε)**	**λ_4 (ε)**	**λ_5 (ε)**	**$\Delta E_{opt.}$**
[Pt(PyPhThian)Cl]	-	285 (25.0)	322 (14.4)	354 (5.21)	401 (2.09)	2.76
[Pd(PyPhThian)Cl]	-	286 (25.2)	323 (11.1)	364 (4.74)	-	3.18
[Pt(QPhThian)Cl]	-	281 (76.1)	318 (28.5)	-	-	3.51
[Pd(QPhThian)Cl]	261 (39.9)	289 (12.8)	337 (5.06)	384 (3.61)	-	2.65
[Pt(PyPhDBT)Cl]	-	287 (8.80)	321 (5.01)	-	-	2.18
[Pd(PyPhDBT)Cl]	265 (32.6)	280 (26.0)	318 (4.06)	-	431 (4.79)	3.60
[Pt(PyPhDBF)Cl]	-	285 (59.9)	314 (26.4)	373 (5.33)	406 (1.80)	2.96
[Pd(PyPhDBF)Cl]	-	280 (10.4)	-	-	-	3.61
[Pt(QPhDBF)Cl]	250 (77.7)	279 (44.9)	317 (21.1)	-	442 (3.82)	2.48
[Pd(QPhDBF)Cl]	-	285 (5.42)	-	-	-	3.75
[Pt(ThianHPhThian)Cl_2]	261 (80.8)	-	-	-	-	4.37
[Pt(DBTHPhDBT)Cl_2]	258 (72.8)	282 (39.4)	311 (17.3)	331 (12.3)	-	3.75

[a] Wavelengths in nm, extinction coefficients in $\frac{10^3 * L}{mol * cm}$, $\Delta E_{opt.}$ in eV.

Cyclic voltammetry was carried out for all N^C^S, S^S or N^C^O type ligands and complexes. The electrochemical data is summarized in tables 14 and 15.

Table 14 Electrochemical properties of ligands of N^C^S, S^S or N^C^O type. [a]

Substance	Red 4	Red 3	Red 2	Red 1	Ox 1	$\Delta E_{elec.}$
PyHPhThian	-	-	–3.21	–2.84 $E_{1/2}$	0.93	3.77
QHPhThian	–3.21	–3.05	–3.00	–2.56 $E_{1/2}$	0.92	3.48
PyHPhDBT	-	-	–3.16	–2.97	-	-
PyHPhDBF	-	-	–3.38	–3.20	-	-
ThianHPhThian	-	-	–3.31	–3.10	0.89	3.99
DBTHPhDBT	-	-	–3.16	–2.97	-	-
QHPhDBF	–3.40	–3.22	–2.93	–2.60 $E_{1/2}$	-	-

[a] Potentials, $\Delta E_{elec.}$ in V (Ox 1 – Red 1). Peak potentials given for irreversible processes or specified as reversible processes with half-wave potentials $E_{1/2}$. Measured in THF with 0.1 M NBu_4PF_6, referenced to $FeCp_2/FeCp_2^+$.

Table 15 Electrochemical properties of complexes of N^C^S, S^S or N^C^O type. [a]

Substance	Red 3	Red 2	Red 1	Ox 1	Ox 2	$\Delta E_{elec.}$
[Pt(PyPhThian)Cl] [b]	–2.73	–2.54	–2.15	0.91	1.11	3.06
[Pd(PyPhThian)Cl]	–2.70	–2.20	–2.04	0.98	1.13	3.02
[Pt(PyPhDBT)Cl]	–2.78	–2.62	–2.23	0.83	-	3.06
[Pd(PyPhDBT)Cl]	-	–3.16	–2.98	-	-	-
[Pt(ThianHPhThian)Cl_2] [c]	-	–2.84	–1.32	0.06	0.38	1.38
[Pt(DBTHPhDBT)Cl_2]	–3.00	–2.86	–1.96	1.01	-	2.97

[a] Potentials, $\Delta E_{elec.}$ in V (Red 1 – Ox 1). Peak potentials given for irreversible processes or specified as reversible processes with half-wave potentials $E_{1/2}$. Measured in THF with 0.1 M NBu_4PF_6, referenced to $FeCp_2/FeCp_2^+$. [b] Ox 3: 1.52 V. [c] Ox 3: 0.91 V, Ox 4: 1.32 V.

The complexes generally feature additional reductions when compared to the corresponding ligands (see table 14 and 15), which can be attributed to the introduction of a coligand and its subsequent cleavage during reduction. Additionally, all potentials are cathodically shifted.

The complexes [Pt(PyPhThian)Cl] and [Pt(PyPhDBT)Cl] (see Figure 30) feature three irreversible reductions each, with [Pt(PyPhThian)Cl] being shifted to slightly more positive potentials (0.05 V to 0.08 V). This similar behaviour implies these reductions mainly involve the pyridine-phenyl subunit and the coligand. Significant differences can be observed when applying positive potentials. [Pt(PyPhDBT)Cl] only features one irreversible oxidation at 0.83 V. [Pt(PyPhThian)Cl] features three irreversible oxidations, starting from 0.91 V, 1.11 V and 1.52 V. The oxidation of the protoligand PyHPhThian is observed at 0.93 V, implying this first oxidation to be sulphur centred (see table 15). The second oxidation can then be attributed to the coordinating sulphur atom, shifting it's potential by an additional 0.2 V. This means the final oxidation at 1.52 V is attributed to the metal centred oxidation Pt(II)/Pt(III) . Additional evidence of this is provided by the potentials of [Pd(PyPhThian)Cl] being very similar to the platinum compound, although slightly shifted positively (see table 15). However, their two observed oxidations match the ones for the platinum compound almost exactly, which a third oxidation not being observed within the measuring window of the solvent. This further supports the oxidation taking place within the thianthrene subunit as the common

denominator. These sulphur oxidations is in line with thianthrene being reported as a well-known radical former and its use for radical catalysis.[109] [110] Electrochemical HOMO-LUMO gaps ($\Delta E_{elec.}$) listed in table 15 are therefore not indicative of a metal centred HOMO as is the case for all parent N^C^N compounds (see chapter 3.1). This is most likely an electrochemical exception for the sulphur bearing complexes, as the UV/Vis-absorption spectra do not differ significantly from the expected behaviour.

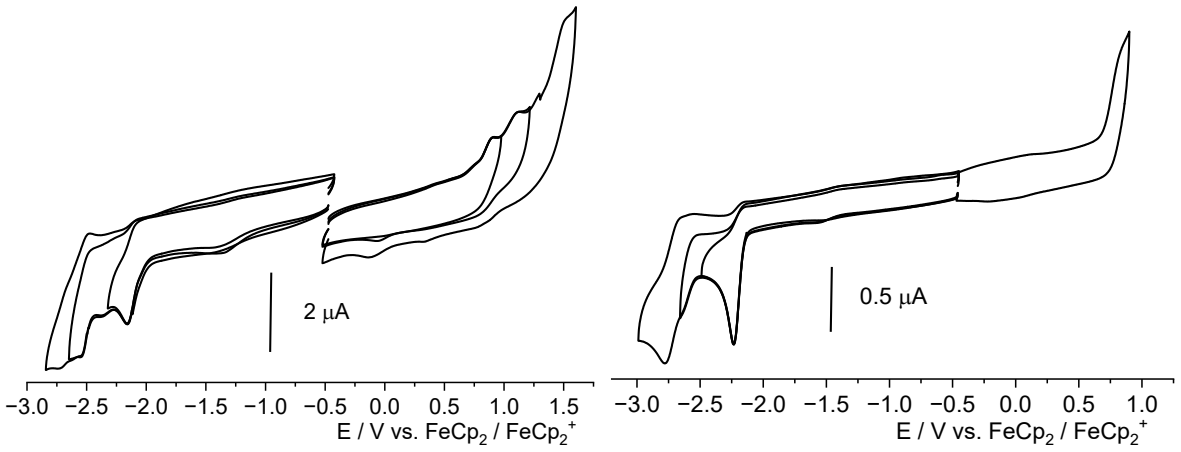

Figure 30 Cyclic voltammograms of [Pt(PyPhThian)Cl] (left) and [Pt(PyPhDBT)Cl] (right), measured in THF with 0.1 M NBu_4PF_6, referenced to $FeCp_2/FeCp_2^+$.

Electrochemical data of the S^S-type [Pt(ThianHPhThian)Cl_2] complex differs from the other, cyclometalated, N^C^S and N^C^O type compounds. The 1st reduction lies shifted to significantly more positive potentials compared to the N^C^S complexes (e.g. 1st Red.: –1.32 V [Pt(ThianHPhThian)Cl_2], –2.15 V [Pt(PyHPhThian)Cl],) (see table 15). The 1st oxidation of [Pt(ThianHPhThian)Cl_2] can be observed at 0.06 V, meaning it is shifted by –0.85 V compared to [Pt(PyHPhThian)Cl] (Ox 1: 0.91 V), with a total of four oxidations being observed in total. This differs strongly from the single oxidation of the protoligand (ThianHPhThian) at 0.89 V, which is more akin to the behaviour exhibited by PyHPhThian (Ox 1: 0.93 V). These early oxidations most likely take place at the sulphur atoms, leading to formation of thianthrenyl (radical) cationic species. These very early oxidations imply very electron-rich, low lying electrochemical HOMO levels. This means the thianthrene subunits are rather poor donors when compared to for example quinoline moieties (compare chapter 3.1). This implies poor backbonding of the platinum centre to the thianthrene units, which would result in longer bond lengths compared to, for example, [Pt(PyPhThian)Cl]. Unfortunately, no SC-XRD data was obtained for [Pt(ThianHPhThian)Cl_2] to verify this. Crystal structures for [Pt(PyPhThian)Cl] are listed below, crystal solution data is summarized in the appendix, table 40).

[Pt(DBTHPhDBT)Cl_2] does not show the same effects, instead behaving very similar to its cyclometalated N^C^S counterpart [Pt(PyPhDBT)Cl], except for slight shifts in potentials (see table 15).

Complexes of the type [M(QPhThian)Cl], [M(PyPhDBF)Cl] and [M(QPhDBF)Cl] showed extremely poor resolution in CV experiments. This was the case for both THF- and CH_2Cl_2-solutions, increasing the amount of substance (up to 5 mg for 10 mL of THF solution) did not change the result. This is most likely attributed to the poor solubility of these compounds, as indication of this were already visible in both NMR spectroscopy as well as UV/Vis-absorption spectroscopy. Additionally, the coordination of DBF-bearing ligands might be weak, resulting in exchange reactions with coordinating solvents like THF. ^{1}H NMR spectra of these complexes measured in deuterated dimethyl sulfoxide (DMSO-d_6) showed pronounced signal broadening, which could be attributed to the same effect (see Figure 31).

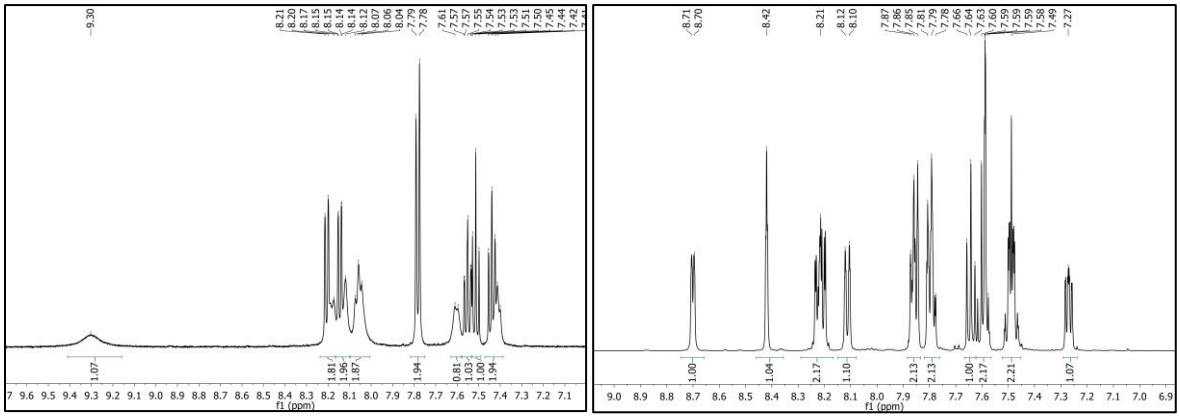

Figure 31 ^{1}H NMR spectra of [Pd(PyPhDBF)Cl] (left) and [Pd(PyPhDBT)Cl] (right). Signal broadening is visible for the α-pyridine proton signal (9.3 ppm) as well as the DBF-protons of the ligand backbone for [Pd(PyPhDBF)Cl] (DMSO-d_6, 500 MHz). This effect is not visible for [Pd(PyPhDBT)Cl], instead all signals are well resolved.

This weak coordination of the DBF-moiety should result in elongated M–O bonds, compared to the M–S bond of [M(PyPhDBT)Cl] and especially M–N bonds in [M(PyPhQ)Cl]. SC-XRD of these complexes could confirm this, however no suitable crystals could be obtained.

DFT calculations were carried out to investigate the frontier molecular orbitals of the complexes [M(PyPhThian)Cl] and [M(PyPhDBT)Cl] and their energies in detail. The results are summarized in the figures 32 and 33.

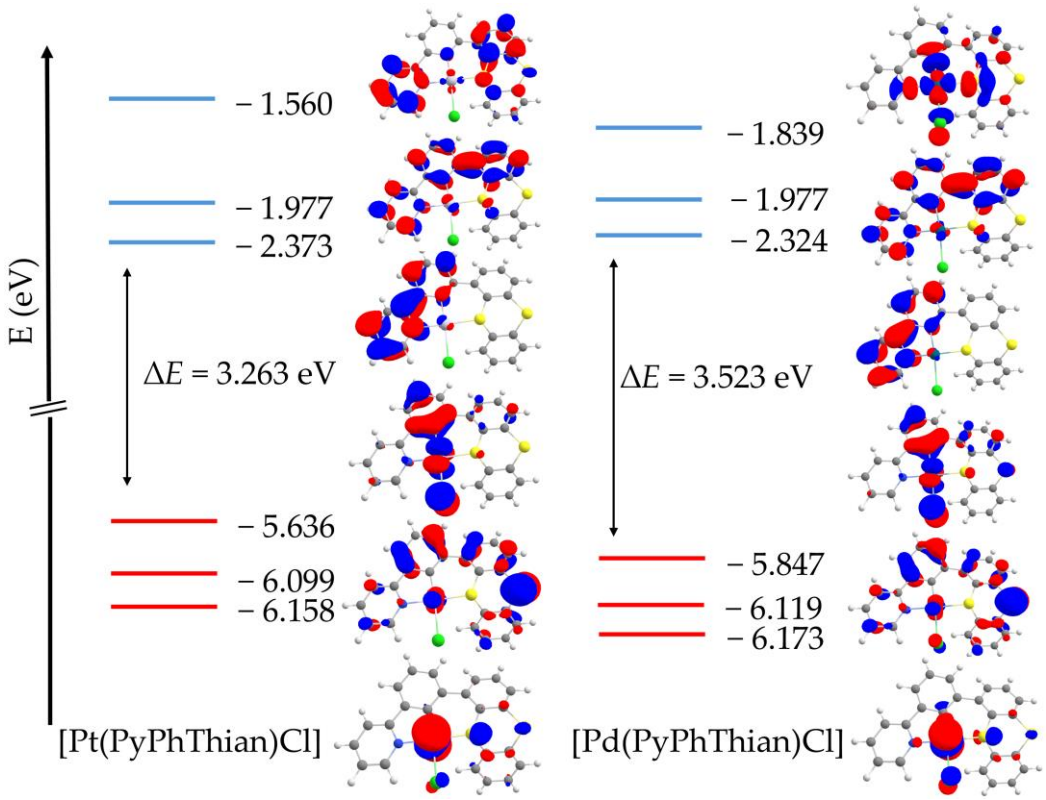

Figure 32 DFT-calculated composition and energies of selected molecular orbitals of [M(PyPhThian)Cl] type complexes. Highest occupied molecular orbital = HOMO (red bars); lowest unoccupied molecular orbital = LUMO (blue bars) (Isovalue 0.03, TPSSh/def2-TZVP/CPCM(THF)) level of theory.

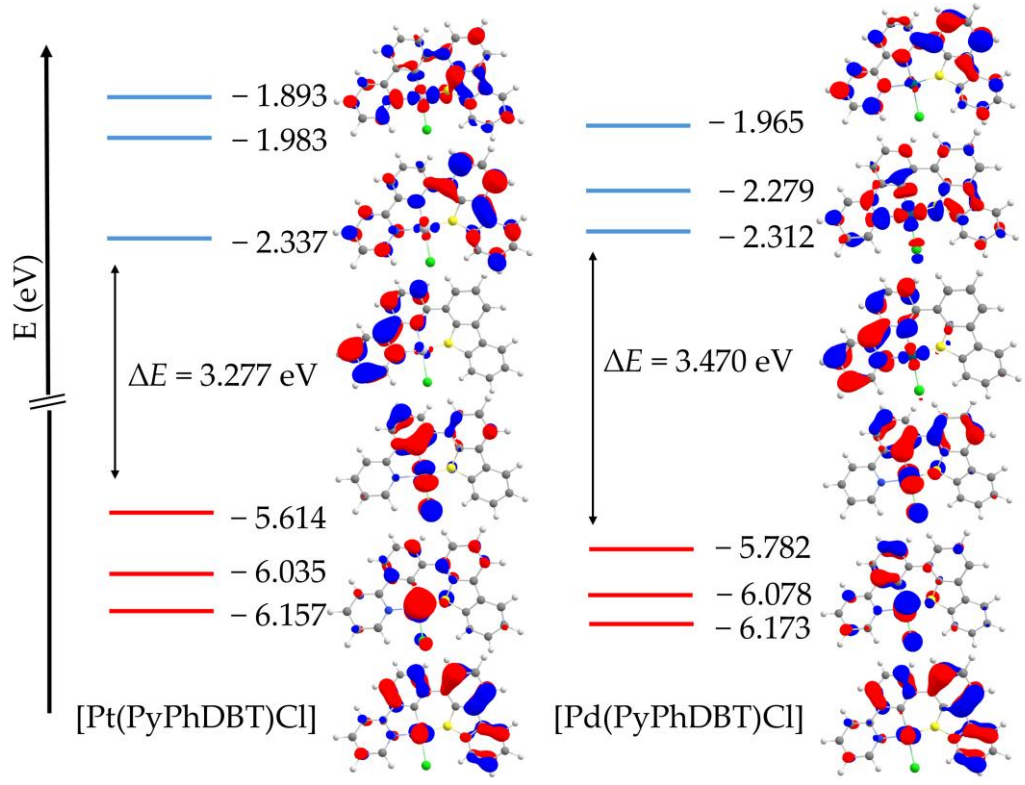

Figure 33 DFT-calculated composition and energies of selected molecular orbitals of [M(PyPhThian)Cl] type complexes. Highest occupied molecular orbital = HOMO (red bars); lowest unoccupied molecular orbital = LUMO (blue bars) (Isovalue 0.03, TPSSh/def2-TZVP/CPCM(THF)) level of theory.

For all complexes, the HOMO is located mainly on the metal and coligand, with contributions of the central phenyl ring. All complexes also feature small contributions of the sulphur-bearing aromat to the HOMO. Additionally, for [M(PyPhThian)Cl] complexes, the HOMO−1 is strongly located on the thianthrene, specifically the exterior sulphur atom. This means the second oxidation encountered for both compounds during cyclic voltammetry is indeed sulphur-centred. While parts of the HOMO−1 and HOMO−2 are localized on the thianthrene subunit, only the phenyl ring closest to the central phenyl-moiety sees any participation in the HOMO. This is most likely due to the strong bend of the thianthrene subunit prohibiting any interactions of the second phenyl ring. The LUMO of all four compounds is situated almost entirely on the pyridine-phenyl-subunit, affirming the main HOMO-LUMO transition to be of MLCT-character. The HOMO-LUMO gaps calculated are somewhat higher than experimental values found either in CV or UV/Vis-absorption spectroscopy, but the trends exhibited hold true. Specifically, the palladium compounds feature larger HOMO-LUMO gaps, resulting in bathochromic shift in their absorption spectra. The lower HOMO energies result in oxidations taking place at higher potentials. The same observations were made when applying similar models to N^C^N type compounds (see chapter 3.1).[49]

Overall, the DFT-calculations validate the observations made in previous measurements, featuring a metal-centred HOMO and strong contributions of the sulphur-donors to both optical and electrochemical behaviour.

Crystals suitable for single crystal x-ray diffraction were obtained for [Pt(PyPhThian)Cl], [Pd(PyPhThian)Cl] and [Pt(PyPhDBT)Cl]. They were grown by isothermal evaporation of saturated CH_2Cl_2 solutions or overlaying of saturated CH_2Cl_2 solutions with diethyl ether.

The molecular and crystal structures are depicted in Figure 34 - 39, relevant distances and angles are listed in Figure 40, 41 and tables 16, 17. Further data regarding the crystal data refinement can be found in table 40 (appendix).

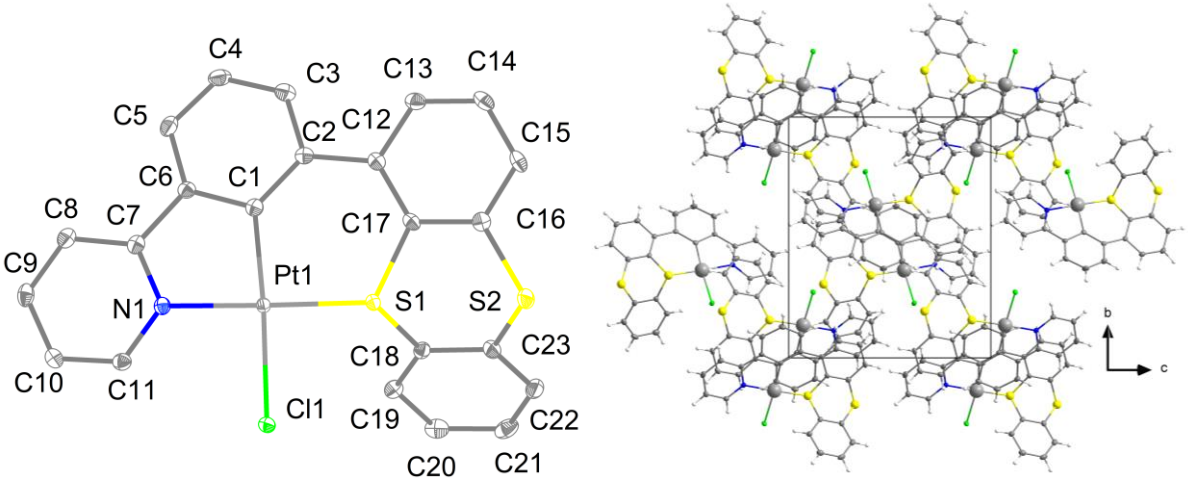

Figure 34 Asymmetric unit of [Pt(PyPhThian)Cl] from single crystal X-ray diffraction (displacement ellipsoids at 50% probability, hydrogens omitted for clarity) (left), and view on the crystal structure (right) along the crystallographic *a*-axis.

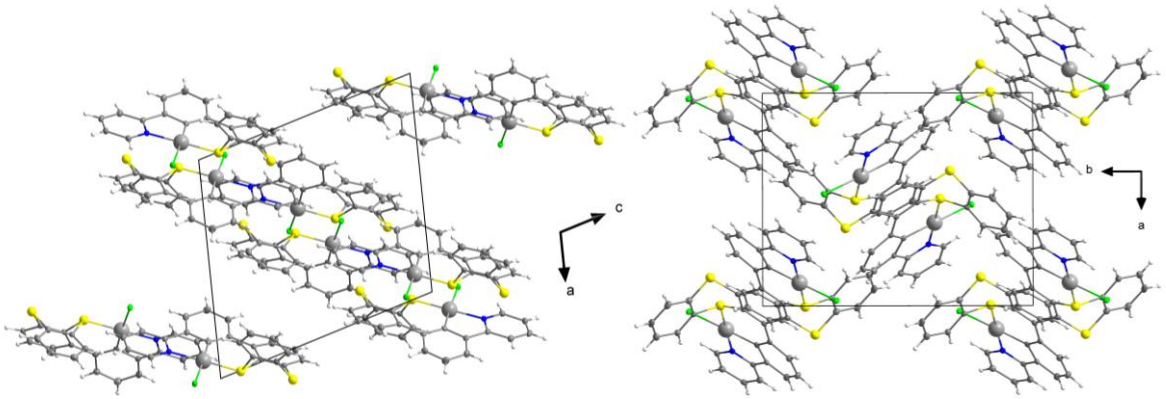

Figure 35 View on the crystal structure of [Pt(PyPhThian)Cl] along the crystallographic *b*-axis (left) and *c*-axis (right).

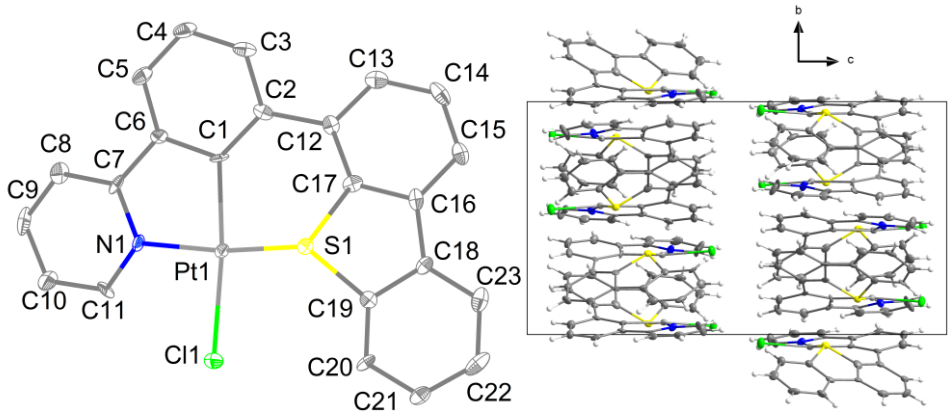

Figure 36 Asymmetric unit of [Pt(PhPyDBT)Cl] from single crystal X-ray diffraction (displacement ellipsoids at 50% probability, hydrogens omitted for clarity) (left) and view of the crystal structure (right) along the crystallographic *a*-axis.

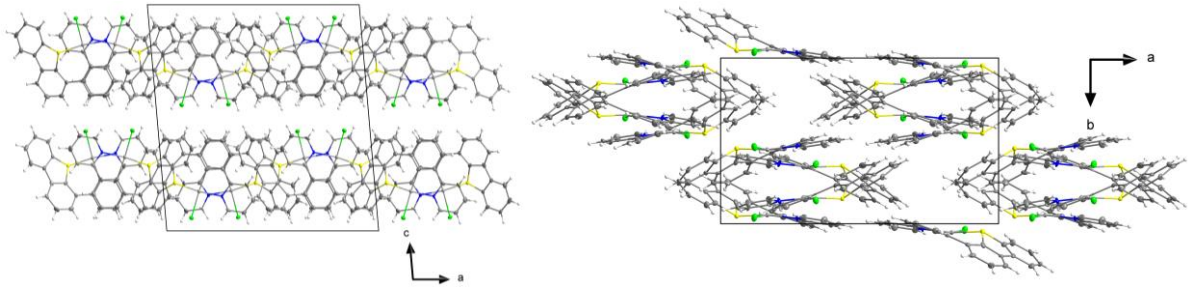

Figure 37 View on the crystal structure of [Pt(PhPyDBT)Cl] along the crystallographic *b*-axis (left) and *c*-axis (right).

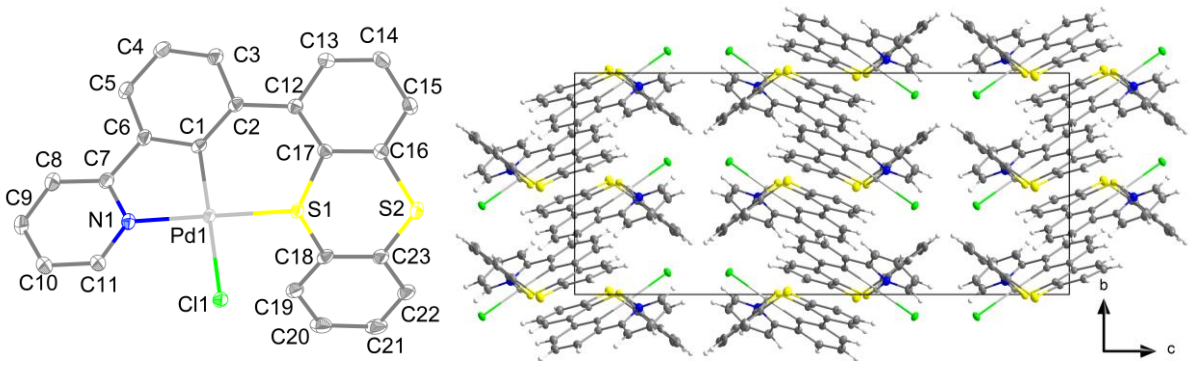

Figure 38 Asymmetric unit of [Pd(PyPhThian)Cl] from single crystal X-ray diffraction (displacement ellipsoids at 50% probability, hydrogens omitted for clarity) (left) and view of the crystal structure (right) along the crystallographic a-axis.

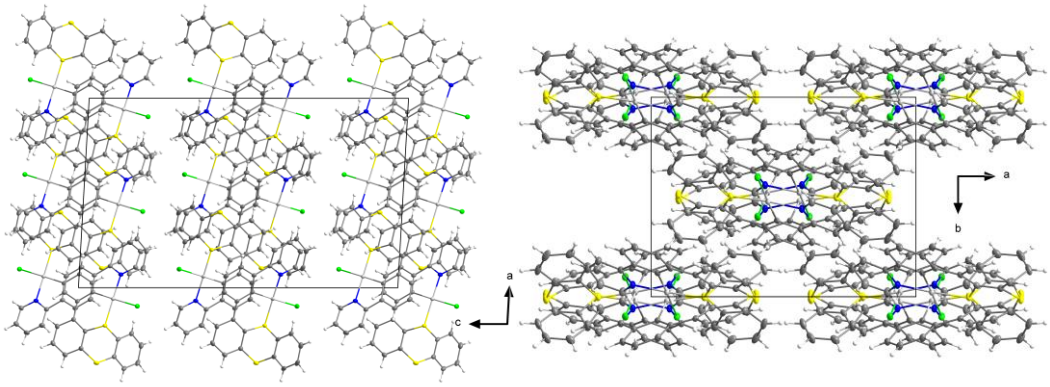

Figure 39 View on the crystal structure of [Pd(PyPhThian)Cl] along the crystallographic *b*-axis (left) and *c*-axis (right).

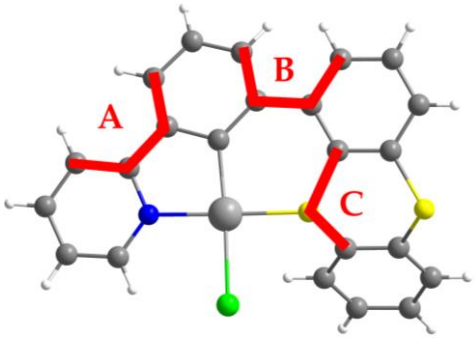

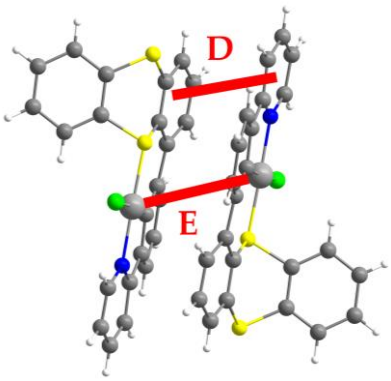

	[Pt(PyPhThian)Cl]	**[Pd(PyPhThian)Cl]**
Interplanar torsion angles (°)		
A (pyridine-phenyl)	5.30(4)	8.20(3)
B (phenyl-thianthrene)	14.56(3)	4.055(3)
C (thianthrene bend)	98.84(1)	98.65(9)
Shortest distances (Å)		
D (phenyl-pyridine)	3.6850(1)	3.9659(1)
E (metal-metal)	4.8574(4)	5.7346(7)

Figure 40 Selected ring torsion angles (left, A,B,C) and distances (right, D, E) for complexes [M(PyPhThian)Cl].

The complexes [M(PyPhThian)Cl] feature a pronounced bend in the thianthrene subunit, caused by the geometry of the two sulphur atoms (see Figure 40). This bend is featured for both platinum and palladium complexes (Figure 40, Pt: 98.84(1)°, Pd: 98.65(9)°) and does not seem affected by the change of central metal ion. The same is true for the bond lengths of the metal to the adjacent donor atoms, all of them being very similar from platinum to palladium. When compared to the N^C^N compound [Pt(PyPhQ)Cl], the bond lengths between M–C, M–N and M–Cl do not differ much (see table 16).[49]

Table 16 Comparison of bond lengths of [Pt(PyPhQ)Cl] vs. [Pt(PyPhThian)Cl].[49]

Bond length (Å)	M–C	M–N_1	M–N_2 or M–S	M–Cl
[Pt(PyPhQ)Cl]	1.957(4)	2.024(3)	2.029(3)	2.428(9)
[Pt(PyPhThian)Cl]	1.988(2)	2.034(2)	2.213(6)	2.418(5)

A notable exception is the distance M–S (2.213(6) Å), as opposed to M–N (2.029(3) Å) (see chapter 3.1; table 16).[49]

Interestingly, the two [M(PyPhThian)Cl] complexes differ more in the angles of the ligand backbone. While the palladium complex has a higher interplanar angle between the pyridine and phenyl ring (see Figure 40, Pt: 5.30(4)°, Pd: 8.20(3)°), the opposite is true for the angle between phenyl and thianthrene units. Here, the platinum complex shows a much higher angle of 14.56(3)° as opposed to the palladium complexes 4.055(3)°. These differences result in the two complexes crystalizing in two different space groups, $P2_1/n$ for the platinum compound, $C2/c$ for the palladium compound.

Both complexes feature head-to-tail stacking typical for these complexes with the shortest centroid distance being 3.685(1) Å for [Pt(PyPhThian)Cl] and 3.966(1) Å [Pd(PyPhThian)Cl], which would put them in the range of typical π-stacking.[111] This stacking does not proliferate throughout the entire structure, because of the pronounced bend in the thianthrene subunit breaking up these interactions. Instead, two molecular units are paired together in a head-to-tail fashion throughout the crystal structure. The metal-to-metal distances are rather long at 4.857(4) Å for [Pt(PyPhThian)Cl] and 5.735(7) Å for [Pd(PyPhThian)Cl].

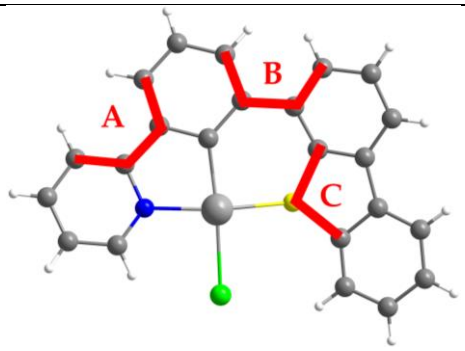

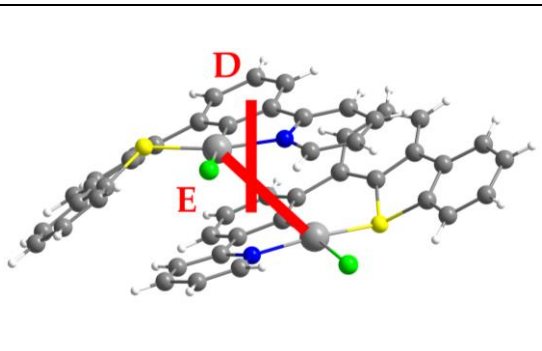

[Pt(PyPhDBT)Cl]	
Interplanar torsion angles (°)	
A (pyridine-phenyl)	6.243(1)
B (phenyl-dibenzothiophene)	23.50(1)

C (dibenzothiophene bend)	92.7(4)
Shortest distances (Å)	
D (phenyl-phenyl)	3.679(2)
E (metal-metal)	4.199(5)

Figure 41 Selected ring torsion angles (left, A,B,C) and distances (right, D, E) for complexes [M(PyPhDBT)Cl].

[Pt(PyPhDBT)Cl] differs from its thianthrene counterparts by not featuring the same pronounced bend in the DBT subunit (see Figure 41 and table 17). However, because of the sulphur lone-pair coordination the DBT ring is still significantly twisted out of plane to accommodate the metal central atom. As such, the interplanar angle between phenyl and DBT rings rises to 23.50(1)° as opposed to the [Pt(PyPhThian)Cl] angle of 14.56(3)°. This also affects the position of the metal centre within the binding pocket. While the bond lengths of M–S and M–N remain very similar to the ones found for the [Pt(PyPhThian)Cl] complex, the M–C distance is elongated by 0.23 Å, while the distance between metal and coligand are shortened by almost the same amount, 0.24 Å. In the case of [Pt(PyPhThian)Cl, the angles around the platinum atom are close to 180° (N-M-S: 178.5(6)°, C–M–Cl: 176.5(7)°). Because of the angled coordination of the sulphur donor in [Pt(PyPhDBT)Cl], this is not the case here. The angle is lowered to 169.3(2)°, also affecting the C–M–Cl angle and distorting it to 173.9(2)°.

Table 17 Selected bond lengths (Å) and angles (°) for the Pt and Pd complexes. [a]

Distances (Å)	[Pt(PyPhThian)Cl]	[Pd(PyPhThian)Cl]	[Pt(PhPyDBT)Cl]
M–C	1.988(2)	1.990(2)	2.011(8)
M–N	2.034(2)	2.042(2)	2.045(6)
M–S	2.213(6)	2.211(5)	2.209(2)
M–Cl	2.418(5)	2.408(5)	2.394(2)
Angles (°)			
N–M–S	178.5(6)	176.8(5)	169.3(2)
C–M–Cl	176.5(7)	177.7(5)	173.9(2)
N–M–Cl	94.01(6)	95.82(5)	93.60(2)
N–M–C	82.53(9)	83.60(7)	82.30(3)
S–M–Cl	86.86(2)	85.32(2)	92.72(7)
S–M–C	96.59(7)	95.37(6)	90.70(2)
Σ angles around M	360.0	360.1	359.3

[a] From single crystal X-ray diffraction.

Replacing nitrogen-bearing donor units of N^C^N complex motifs with sulphur-donors works well synthetically and results in the desired complexes. They feature interesting structural changes due to the sulphur coordination. Their redox chemistry could lead to applications in (redox-) catalysis or radical based catalysis.[109, 110] The same cannot be said for S^S type complexes, which only feature M–S precoordination and do not undergo cyclometalation. Complexes with oxygen-donor ligand systems feature weak coordination with measurements implying exchange of the oxygen donors with solvent molecules occurs.

3.5 Complexes with Ring-Expanded C^N^N Type Ligands and their Oxygen Reactivity

Investigating previous ring-expanded complex systems of N^C^N and C^N^N type saw the introduction of one or two six-membered chelate rings (see chapter 3.1).[49] However, these six membered chelate rings were limited to nitrogen-bearing aromatic rings. Therefore, new systems were envisaged, featuring six-membered chelate rings with carbon donors of C^N^N type. The first of these systems was chosen analogous to the pyridine-quinoline motif, bearing a naphthalene ring in place of the phenyl ring. The protoligand was synthesized by a *Negishi* type coupling of 6-bromo-2,2′-bipyridine (synthesis detailed in chapter 3.3, Scheme 15) and 1-bromonaphthalene (see Scheme 19).

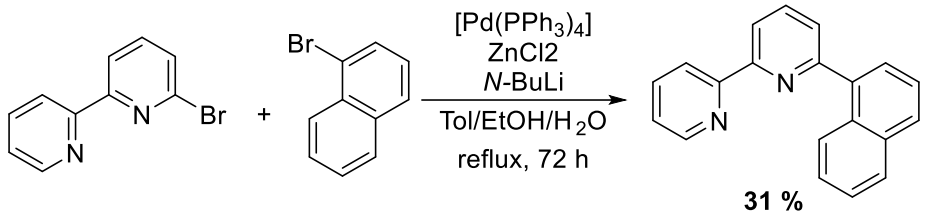

Scheme 19 Synthesis of PyPyHNaph under *Negishi* conditions.

The protoligand was then reacted with the corresponding $K_2[MCl_4]$ salts to yield the desired cyclometalated complexes (see Scheme 20). The detailed reaction conditions are specified in table 18.

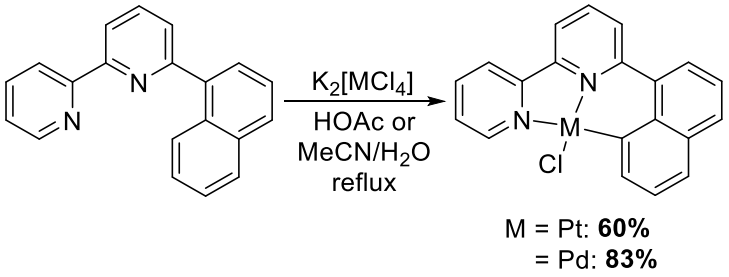

Scheme 20 Complexation of PyPyHNaph with Pt and Pd under C–H activation reaction conditions.

Table 18 Detailed reaction conditions for C–H activation reactions of PyPyHNaph.

Protoligand	Metal precursor	Conditions	Habitus (Yield)
PyPyHNaph	$K_2[PtCl_4]$	HOAc, reflux, MW (300 W), 30 min	Red-orange powder (60%)
	$K_2[PdCl_4]$	MeCN/H_2O, reflux, 72 h	Yellow powder (83%)

NMR Spectroscopy of the obtained complexes showed a mixture of two products formed (see Figure 42). Two constitutional isomers were identified, caused by the rotation of the naphthalene ring around its bond to the bipyridine subunit of the protoligand prior to C–H activation (see Scheme 21).

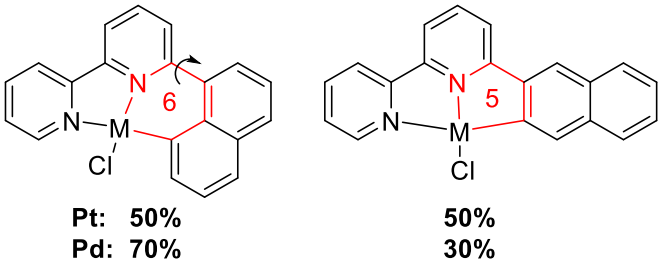

Scheme 21 Rotation of the naphthalene prior to C–H activation causes two isomers to form for complexes of type [M(PyPyNaph)Cl], six- and five membered cyclometalated rings marked in red, ratio of isomers determined via 1H NMR.

The exact ratio of the two isomers was determined to be exactly 50:50 for [Pt(PyPyNaph)Cl] and 70:30 for [Pd(PyPyNaph)Cl, favouring the six-membered cyclometalated ring (see Figure 42 and Scheme 21).

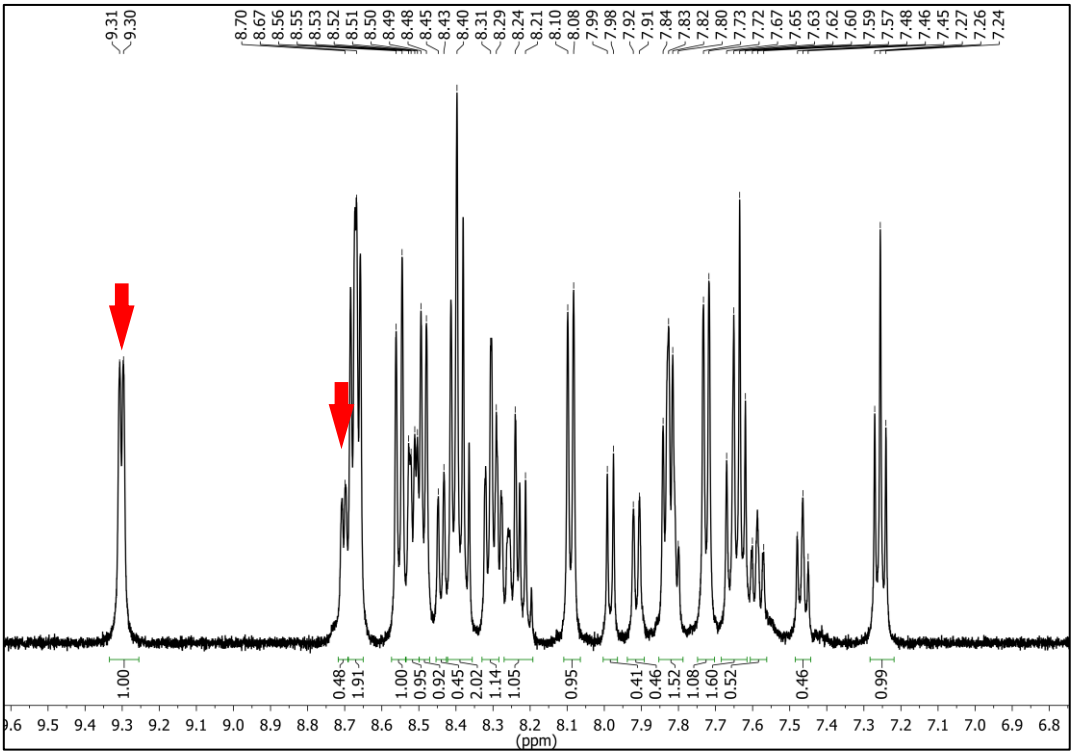

Figure 42 ^{1}H NMR spectrum of [Pd(PyPyNaph)Cl] (500 MHz, DMSO-d_6) showing two constitutional isomers. The two signals with highest chemical shift marked in red. These signals correspond to the protons in alpha position to the cyclometalated carbon of different isomers.

These results imply a slight bias towards six-membered cyclometalated rings when complexating palladium, while platinum does not seem to favour one of the isomers over the other. When compared to other C^N^N systems, platinum usually has a higher reaction rate (see chapter 3.3, table 4), which would mean both isomers are thermodynamically very close in energies. For palladium, generally having slower reaction rates, the six-membered could be slightly kinetically favoured.

Since different methods of complexation were applied, this ratio is somewhat misleading. To better compare the results, the complexation of both metals would need to be carried out under the same exact reaction conditions. Additionally, differences in the workup, for example caused by solubility, could further skew the results. Generally, the ratio of the two isomers does not differ much and no significant bias can be identified.

Because of the mixtures obtained for complexes of [M(PyPyNaph)Cl] no proper investigation into the optical and electrochemical properties of the desired six-membered cyclometalated species were carried out. The gathered data of the compound mixtures is listed in table 19.

Table 19 Optical and electrochemical data of complexes of [M(PyPyNaph)Cl] type. [a, b]

Substance	**λ_1 (ε)**	**λ_2 (ε)**	**λ_3 (ε)**	**λ_4 (ε)**	**λ_5 (ε)**	**$\Delta E_{opt.}$**
[Pt(PyPyNaph)Cl]	270 (31.4)	333 (7.40)	360 (5.31)	395 (4.68)	436 (2.68)	2.42
[Pd(PyPyNaph)Cl]	241 (80.6)	273 (67.6)	336 (29.8)	422 (11.3)	-	2.54
Substance	**Red 4**	**Red 3**	**Red 2**	**Red 1**	**Ox 1**	**$\Delta E_{elec.}$**
[Pt(PyPyNaph)Cl][c]	–2.53 $E_{1/2}$	–1.87 $E_{1/2}$	–1.60	–1.30	0.73	2.03
[Pd(PyPyNaph)Cl]	–3.00	–2.77	–2.51	–1.89 $E_{1/2}$	0.79	2.68

[a] Wavelengths in nm, extinction coefficients in $\frac{10^3 * L}{mol * cm}$, $\Delta E_{opt.}$ in eV. [b] Potentials, $\Delta E_{elec.}$ in V (Red 1 – Ox 1). Peak potentials given for irreversible processes or specified as reversible processes with half-wave potentials $E_{1/2}$. Measured in THF with 0.1 M NBu_4PF_6, referenced to $FeCp_2/FeCp_2^+$. [c] Red 5: –2.87 V, Red 6: –3.21 V.

Thus, the ligand was altered to block the unwanted activation position. This methodology was already reported to avoid, for example, the formation of tetrameric structures upon complexation of $K_2[PdCl_4]$ with PyHPhPy in acetic acid, by introducing additional methyl groups.[1, 2] However, because of the poor accessibility of functionalized methyl-naphthalene derivatives, instead an anthracene moiety was chosen to block the unwanted cyclometalation positions and guarantee a six-membered C^N^N cyclometalated product.

The protoligand was synthesized by reacting 6-bromo-2,2′-bipyridine and 9-anthraceneboronic acid under *Suzuki* conditions (see Scheme 22).

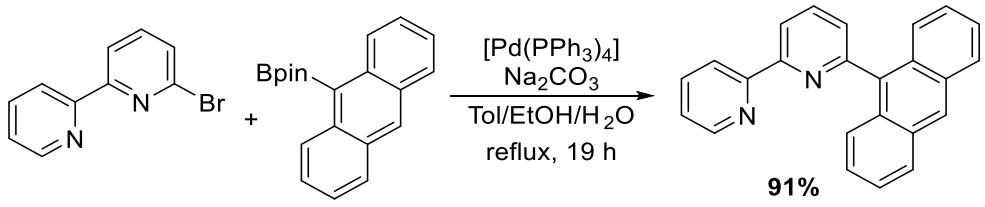

Scheme 22 Reaction conditions for the synthesis of PyPyHAnth.

The protoligand was reacted with $K_2[MCl_4]$ in a mixture of MeCN and distilled water (see Scheme 23, table 20).[81]

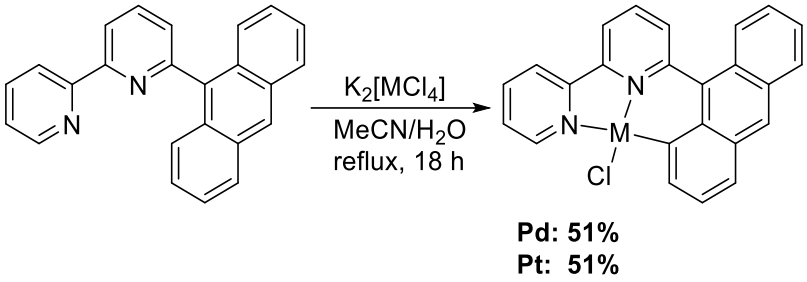

Scheme 23 Synthesis of [M(PyPyAnth)Cl] via C–H activation.[81]

Table 20 Detailed reaction conditions for synthesis of complexes [M(PyPyAnth)Cl].

Protoligand	Metal precursor	Conditions	Habitus (Yield)
PyPyHAnth	$K_2[PtCl_4]$	MeCN/H_2O, reflux, 18 h	Red powder (51%)
	$K_2[PdCl_4]$	MeCN/H_2O, reflux, 18 h	Orange powder (51%)

The desired complexes were obtained in both cases, and their formation was irrefutably confirmed by NMR spectroscopy and mass spectrometry (see experimental part). Their optical and electrochemical properties were fully characterized (see Figure 45, 46 and table 22, 23).

Problems were encountered when the synthesis of [Pd(PyPyAnth)Cl] was repeated. Instead of the desired compound, a mixture of products was obtained, as detected by ^{1}H NMR spectroscopy. Different reaction conditions were tested to obtain the desired cyclometalated compound (see table 21). However, in most cases, only mixtures of the cyclometalated compound as well as the precoordinated species was obtained, in different ratios (see Scheme 25). While platinum and nickel were also complexated, the detailed investigation was carried out with palladium as central metal (see table 21).

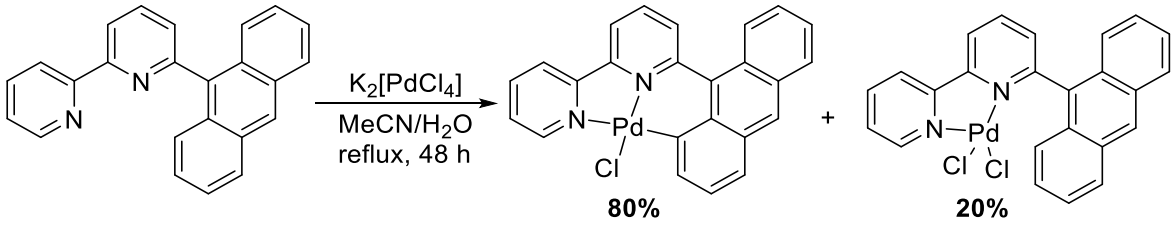

Scheme 24 Reaction of PyPyHAnth with $K_2[PdCl_4]$, yielding a mixture of cyclometalated and precoordinated complex.

Table 21 Reaction conditions for synthesis of complexes [M(PyPyAnth)Cl] with all outcomes detailed.

Protoligand	Metal	Conditions	Outcome (yield)
PyPyHAnth	$K_2[PtCl_4]$	MeCN/H_2O, reflux, 18 h	Cyclometalated compound 51%.
	$K_2[PdCl_4]$	MeCN/H_2O, reflux, 18 h	Cyclometalated compound 51%.
	$K_2[PdCl_4]$	MeCN/H_2O, reflux, 48 h	Mixture of cyclometalated (80%) and precoordinated compound (20%).

	$K_2[PdCl_4]$	KOAc, K_2CO_3, *p*-xylene, reflux, 72 h	Precoordinated compound 17%.
	$K_2[PdCl_4]$	HOAc, reflux 72 h	Precoordinated compound 81%.
	$NiBr_2$	KOAc, K_2CO_3, *p*-xylene, reflux, 72 h	Cyclometalated compound 85%.

Some of the conditions lead to the isolation of the precoordinated species as sole product. For example, heating the mixture of protoligand and metal precursor in glacial acetic acid yielded the precoordinated species in good yields with some unreacted protoligand and metal precursor leftover. However, after isolation, this precoordinated product did not react d to full conversion to the cyclometalated compound, as had previously been reported for similar species.[93] Instead, the same mixture of products was obtained as was the case for the originally successful synthesis (see Scheme 25). Interestingly, the C–H activation conditions for nickel did yield the desired cyclometalated compound.

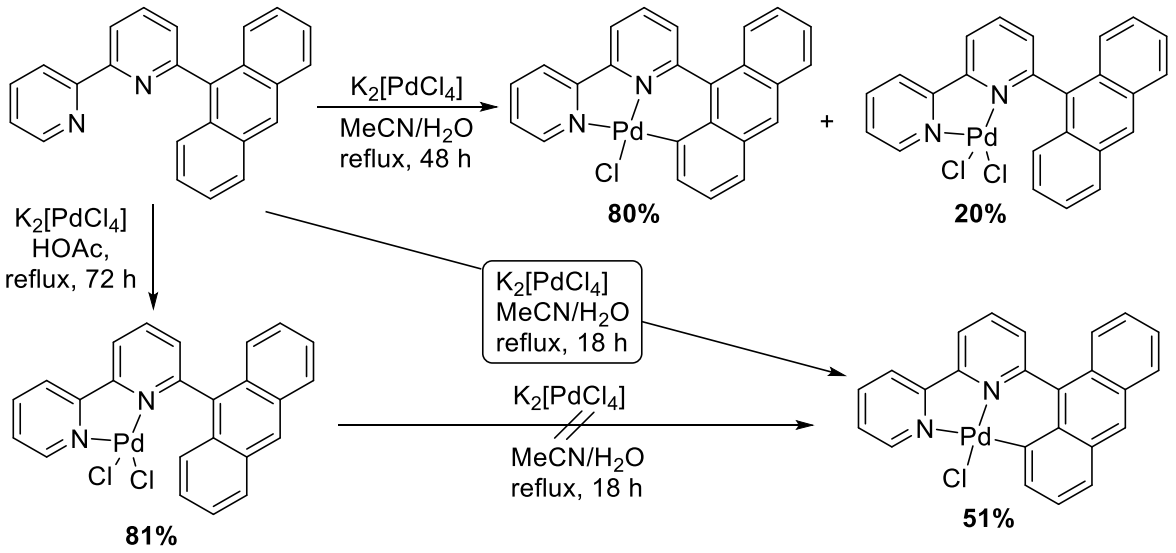

Scheme 25 Different reactions conditions and their diverging results in the synthesis of [Pd(PyPyAnth)Cl].

The cause for this diverging behaviour was not identified. Some additional, unknown mechanism must cause the inhibition of the activation of the precoordinated species towards the cyclometalated one. For example, formation of dimers by stacking of the anthracene moieties could affect reaction outcomes. Additionally, differences in solubility could cause some of the products to be washed out during reaction workup. However, no indications of this were found either in NMR spectroscopy, mass spectrometry nor optical and electrochemical investigations.

All syntheses discussed were carried out under strict inert conditions under strict exclusion of oxygen. When investigating NMR-solutions of the cyclometalated compound [Pd(PyPyAnth)Cl] in CD_2Cl_2, that had been exposed to both oxygen and ambient light, discolouration of the originally deep orange solution to colourless was observed (see Figure 45).

This observation was reproduced qualitatively by exposing a solution of the compound in chloroform ($CHCl_3$) without exclusion of oxygen to strong light from a LED lamp (see Figure 43). Rapid discolouration of the solution within 40 seconds was observed.

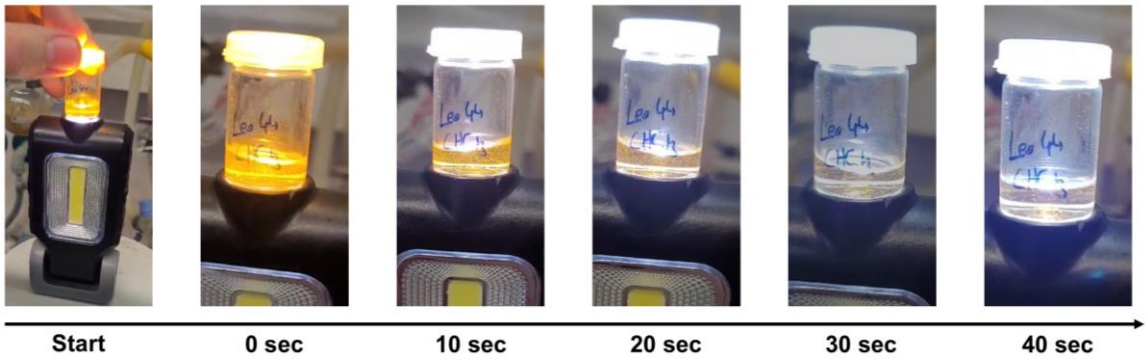

Figure 43 Exposing a solution of [Pd(PyPyAnth)Cl] in $CHCl_3$, in the presence of air oxygen, to LED light causes rapid discolouration of the solution within 40 seconds.

To elucidate the structure of the newly formed species after discolouration, the solution was overlayed with diethyl ether to grow crystals suitable for SC-XRD. The obtained crystals, picked and measured under exclusion of oxygen as far as possible, revealed an endoperoxide species had formed (see Figure 44). Details of the crystal structures are listed and discussed in Figure 47 - 51 and tables 24, 41 (appendix).

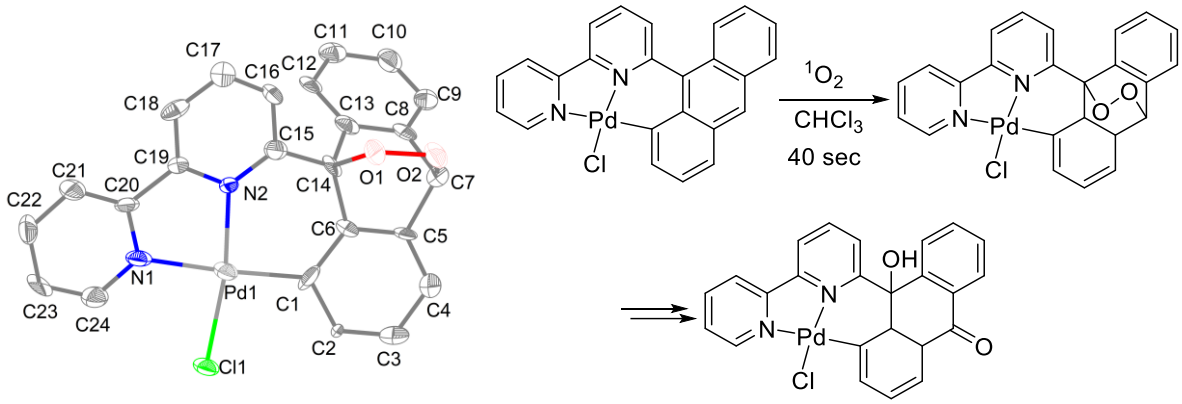

Figure 44 Asymmetric unit of [Pd(PyPyAnthO_2)Cl] single crystal X-ray diffraction (displacement ellipsoids at 50% probability, hydrogens omitted for clarity) (left) and likely reaction mechanism (right).

This endoperoxide moiety means a triplet-singlet oxygen conversion takes place, since only singlet oxygen is able to undergo addition to suitable aromatic systems like anthracene.[112] The energy barrier of the conversion $^3O_2$ to $^1O_2$ of 94.1 kJ/mol has to be overcome for the reaction to proceed, and it's spin-forbidden nature has to be overcome, necessitating a sensitizer.[112, 113] While anthracene has been reported as triplet sensitizer itself, no reaction with singlet oxygen was observed for the protoligand, meaning after complexation the palladium complex acts as sensitizer. Anthracene peroxides have been reported to be stable at room temperature, requiring heating to decompose and release singlet oxygen.[112, 114] This is not the case for the newly formed complex species [Pd(PyPyAnthO_2)Cl], instead a rapid decomposition to an

oxanthrone-moiety was confirmed by NMR spectroscopy of the obtained crystals (see Figure 44). The formation of this oxanthrone in itself is atypical, since decomposition of anthracene endorperoxides are usually either reversible, releasing $^1O_2$ and yielding the anthracene back, or decomposing completely via radical pathways.[112] While oxanthrones have been reported, they rarely constitute the main product of the decomposition.[115] Surprisingly, the bond Pd–C is not affected in its stability and the cyclometalation is retained for all three species. This could mean the straining of the anthracene unit because of its bond to the metal facilitates the decomposition towards the oxanthrone species, undergoing the reported mechanisms and inhibiting the backreaction, the release of singlet oxygen.

Further proof of this was gathered by carrying out the same illumination of a [Pd(PyPyAnth)Cl] solution in $CDCl_3$ with an excess of anthracene added (see Scheme 26). $CDCl_3$ was chosen because of the long $^1O_2$ lifetimes in solution (7.0 ms), dodecane was added as internal standard for GC-MS analysis upon workup.[116]

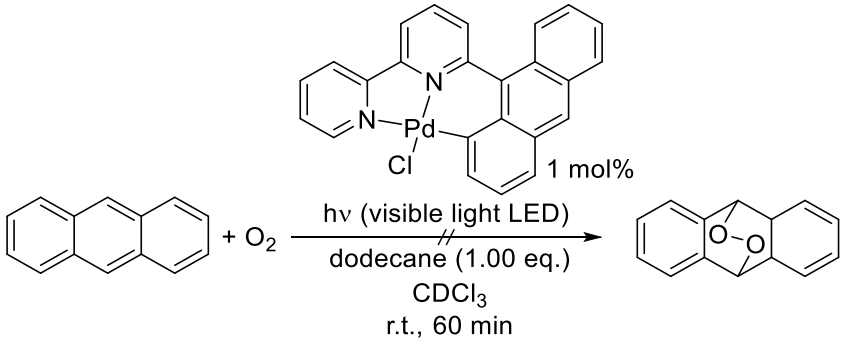

Scheme 26 Attempted synthesis of anthracene endoperoxide using [Pd(PyPyAnth)Cl] as sensitizer.

The analysis of the resulting mixture showed only pure anthracene being present, without any traces of the endoperoxide being formed. However, the pale orange solution had fully discoloured, indicating full consumption of the added [Pd(PyPyAnth)Cl] sensitizer. This means the generated $^1O_2$ was fully converted intramolecularly to form [Pd(PyPyAnthO_2)Cl]. [Pd(PyPyAnth)Cl] can therefore not be used as sensitizer nor as $^1O_2$-releasing molecule under these reaction conditions.

Unfortunately, the few crystals measured via NMR spectroscopy could not be reisolated and therefore detailed UV/Vis-absorption spectroscopy and cyclic voltammetry of the oxygen-bearing species was not carried out. The optical and electrochemical properties of the other discussed species were however investigated and are discussed in Figure 45, 46 and tables 22, 23.

Since all syntheses were carried out under strict exclusion of oxygen, the affinity of [Pd(PyPyAnth)Cl] towards it cannot be the cause for the strange behaviour encountered during syntheses, discussed earlier. An in-depth screening of reaction conditions both aerobic and anaerobic could give further insights into the reaction mechanisms in order to selectively yield the desired cyclometalated species and then properly investigate its reactions with oxygen.

The optical properties of all complexes with the protoligand PyPyHAnth were investigated by UV/Vis-absorption spectroscopy. The results are summarized in Figure 45 and table 22.

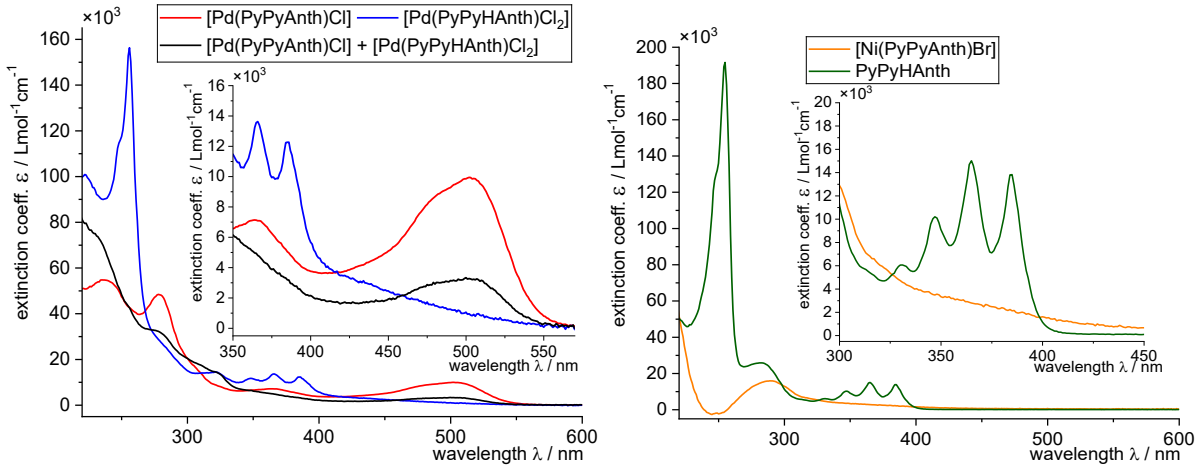

Figure 45 UV/Vis-absorption spectra of complexes derived from the PyPyHAnth protoligand. Measured in THF at room temperature.

Table 22 Optical properties of complexes of [M(PyPyAnth)X] type, its derivatives and its protoligand. [a]

Substance	**λ_1 (ε)**	**λ_2 (ε)**	**λ_3 (ε)**	**λ_4 (ε)**	**λ_5 (ε)**	**$\Delta E_{opt.}$**
[Pd(PyPyAnth)Cl]	237 (55.2)	278 (48.7)	365 (7.58)	502 (10.4)	-	2.21
[Pd(PyPyHAnth)Cl$_2$]	255 (157)	321 (16.0)	347 (13.2)	365 (15.2)	385 (13.8)	2.96
[Pd(PyPyAnth)Cl] + [Pd(PyPyHAnth)Cl$_2$]	233 (73.0)	279 (32.5)	323 (14.4)	501 (3.75)	-	2.13
[Ni(PyPyAnth)Br]	289 (16.4)	-	-	-	-	3.64
PyPyHAnth	254 (191)	282 (26.3)	346 (10.6)	365 (15.4)	385 (14.3)	3.09

[a] Wavelengths in nm, extinction coefficients in $\frac{10^3 * L}{mol * cm}$, $\Delta E_{opt.}$ in eV.

The most striking feature are pronounced and intense absorption bands at around 255 nm found for [Pd(PyPyHAnth)Cl$_2$] and the protoligand PyPyHAnth, as well as structured, less intense bands between 300 and 400 nm (see Figure 45). These structured bands can be attributed to the anthracene moiety, π-π* transitions with different vibronic contributions take place and can also be observed in free anthracene.[117] The lack of any shift of the absorption bands observed for [Pd(PyPyHAnth)Cl$_2$] compared to the protoligand shows very little, if any, metal contribution to the absorptions take place. This is in stark difference to the absorption spectrum of the cyclometalated complex [Pd(PyPyAnth)Cl]. Here, the characteristic bands attributed to anthracene can no longer be observed. Instead, a pronounced and intense absorption band at 502 nm (10.4 ε) can be attributed to an MLCT absorption, giving the compound its strong orange colour. This absorption is also significantly shifted when compared to other previously discussed palladium complexes of C^N^N type. This implies a significant donor contribution of the anthracene moiety, making it more of a MLL'CT, with a HOMO lying on the metal an anthracene moiety and an excitation to the mostly bipyridine centred LUMO (similar to complexes of [M(PyPyPh)X]).[81] However, exact HOMO and LUMO constitutions are to be confirmed by detailed TD-DFT calculations.

This absorption can be directly linked to the role of [Pd(PyPyAnth)Cl] as sensitizer and its reaction with oxygen, since the cyclometalated species is the only one to exhibit this reactivity. The absorption maxima at 502 nm (19920 cm^{-1}) and its corresponding electronic transition lies at energies high enough to allow the conversion of $^3O_2$ to $^1O_2$ (ΔE = 94.1 kJ/mol). This conversion could also be a result of a non-radiative decay of an anthracene-centred excitation with metal contribution, explaining the lack of the characteristic absorption bands encountered for PyPyHAnth and [Pd(PyPyHAnth)Cl_2]. The proximity of the anthracene moiety to the metal centre caused by cyclometalation could also play a role in the reactivity of [Pd(PyPyAnth)Cl] towards [Pd(PyPyAnthO_2)Cl] as opposed to the precoordinated species, where the anthracene can rotate around the connecting bond to bipyridine. As expected, the mixture of the cyclometalated and pre-coordinated species result is a superposition of the two separate spectra previously discussed.

The absorption spectrum of [Ni(PyPyAnth)Br] shows only one strong absorption band (289 nm, 16.4 ε) and a pronounced dip to almost zero extinction. This implies the complex decomposed during or prior to the measurement since neither long-wavelength absorptions nor the characteristic absorptions of anthracene can be observed. This is not surprising, since similar C^N^N complexes like [Ni(PhPyQ)Br] already showed strong susceptibility to solvolysis (see chapter 3.1).[49] Additionally, similar problems were encountered during NMR spectroscopy. While the sample was stable long enough for measurement of a ^1H NMR spectrum (500 MHz, CD_2Cl_2), ^{13}C-measurements could not be carried out with satisfactory signal-to-noise ratios. Instead, decomposition of the compound into undefinable fragments along with line broadening cause by nickel particles was observed.

The electrochemical properties of complexes derived from the PyPyHAnth protoligand were investigated by carrying out cyclic voltammetry. The results are summarised in Figure 46 and table 23.

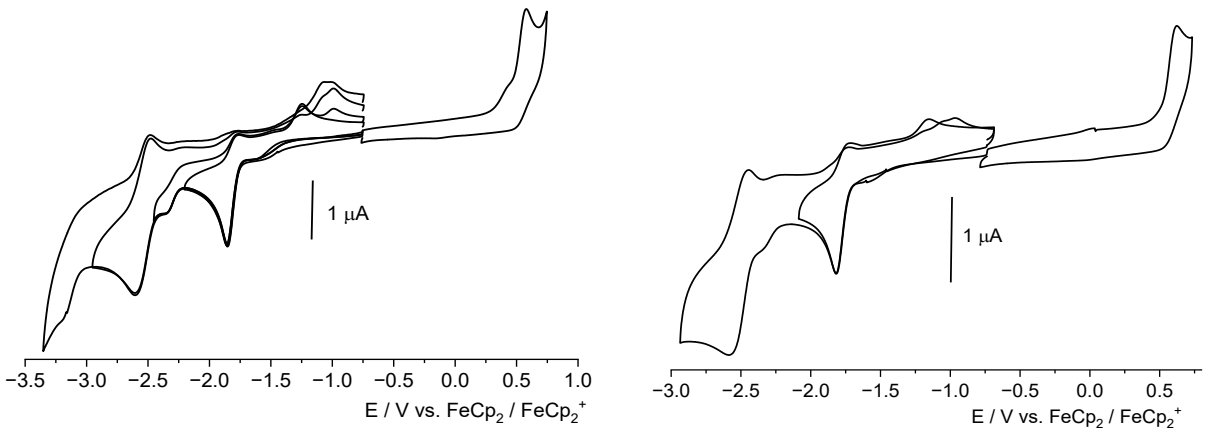

Figure 46 Cyclic voltammogram of [Pd(PyPyHAnth)Cl_2] (left) and [Pd(PyPyAnth)Cl] (right), measured in THF with 0.1 M NBu_4PF_6, referenced to $FeCp_2/FeCp_2^+$.

Table 23 Electrochemical properties of complexes of [M(PyPyAnth)X] type, its derivatives and its protoligand. [a]

Substance	Red 4	Red 3	Red 2	Red 1	Ox 1	$\Delta E_{elec.}$
[Pd(PyPyAnth)Cl]	-	-	–2.59	–1.82	0.62	2.44
[Pd(PyPyHAnth)Cl_2]	-	–2.77	–2.47	–1.27	0.56	1.83
[Pd(PyPyAnth)Cl] + [Pd(PyPyHAnth)Cl_2]	–3.20	–2.54 $E_{1/2}$	–2.34	–1.85	0.58	2.43
[Ni(PyPyAnth)Br] [b]	–2.73	–2.57	–2.43	–1.64 $E_{1/2}$	0.21	1.85
PyPyHAnth	-	-	–3.51	–3.17	-	-

[a] Potentials, $\Delta E_{elec.}$ in V (Red 1 – Ox 1). Peak potentials given for irreversible processes or specified as reversible processes with half-wave potentials $E_{1/2}$. Measured in THF with 0.1 M NBu_4PF_6, referenced to $FeCp_2/FeCp_2^+$. [b] Ox 2: 0.51 V.

The free protoligand features the most negatively shifted reductions, starting at –3.17 V. Complexation shifts the reduction potentials towards more positive potentials significantly. Notably, the first reduction of the cyclometalated species [Pd(PyPyAnth)Cl] (Red 1: –1.82 V) is shifted significantly by 0.55 V compared to the precoordinated species [Pd(PyPyHAnth)Cl_2] (Red 1: –1.27 V). This means the LUMO is not situated on the same part of the molecule. It is likely irreversible reductions involve cleavage of the chloride coligands in an EC mechanism.[118] Further reductions would then take place in the bipyridine subunit of the ligand backbone. All oxidations of palladium complexes take place at very similar potentials, between 0.58-0.62 V. This implies a strongly metal-centred HOMO, that is not strongly affected by the ligand backbone and the cyclometalation compared to the non-cyclometalated species. This is contradictory to the observations made during absorption spectroscopy, where the cyclometalation had a big impact on the absorption of the complexes and implied a stronger contribution of the anthracene subunit. The mixture of complexes shows reductions of both individual species being present, as expected. However, the character of the cyclometalated species dominates, due to the ratio of this complex being higher (see table 21). The nickel complex [Ni(PyPyAnth)Br] has its reduction slightly shifted towards more positive potentials compared to the palladium species, in line with the lower expected ligand field splitting of nickel vs. palladium. Interestingly the nickel complex exhibits more reductions overall and the first reduction is noticeably reversible. This implies the overall constitution of the LUMO levels are different. Potentially the LUMO contributions of the bipyridine subunit are higher, allowing for reversible reductions similar to [Ni(PhPyPy)Br] systems.[119] The oxidation of the nickel complex is shifted to lower potential by 0.41 V compared to its palladium counterpart, which can also be attributed to the smaller ligand field splitting. The cyclic voltammetry of [Ni(PyPyAnth)Br] showed no signs of decomposition within solution, as was the case during UV/vis-absorption spectroscopy or NMR Spectroscopy. This implies solvolysis was drastically slowed down by the inert conditions within the electrochemical cell. This could mean that the decomposition is sped up by the presence of oxygen, since dry THF was used for both CV and UV/Vis-absorption measurements equally and water should not be present in either. Carrying out UV/Vis-absorption or NMR studies on [Ni(PyPyAnth)Br] or generally complexes of type

[M(PyPyAnth)X] in degassed solvents and preparing the samples in a glove box should prolong their lifetime in solution and help gather more useful data.

Crystals suitable for single crystals XRD were obtained for [Pd(PyPyHAnth)Cl_2] and [Pd(PyPyAnthO_2)Cl] by overlaying saturated solutions in CD_2Cl_2 with diethyl ether. The crystal structures are pictured in Figure 47 - 50, crystallographic data is detailed in table 41 (appendix) and selected bond lengths and angles are listed in Figure 41 and table 24.

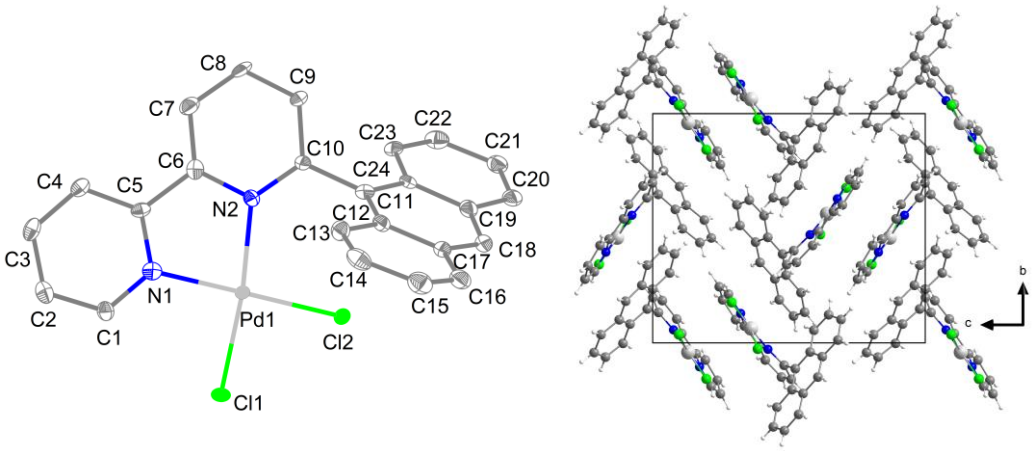

Figure 47 Asymmetric unit of [Pd(PyPyHAnth)Cl_2] single crystal X-ray diffraction (displacement ellipsoids at 50% probability, hydrogens omitted for clarity) (left) and view of the crystal structure (right) along the crystallographic *a*-axis.

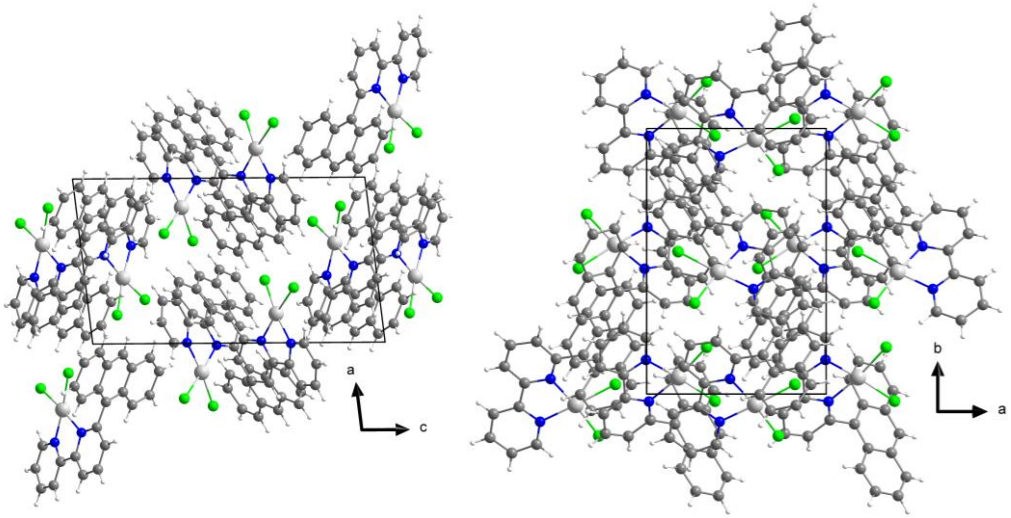

Figure 48 View on the crystal structure of [Pd(PyPyHAnth)Cl_2] along the crystallographic *b*-axis (left) and *c*-axis (right).

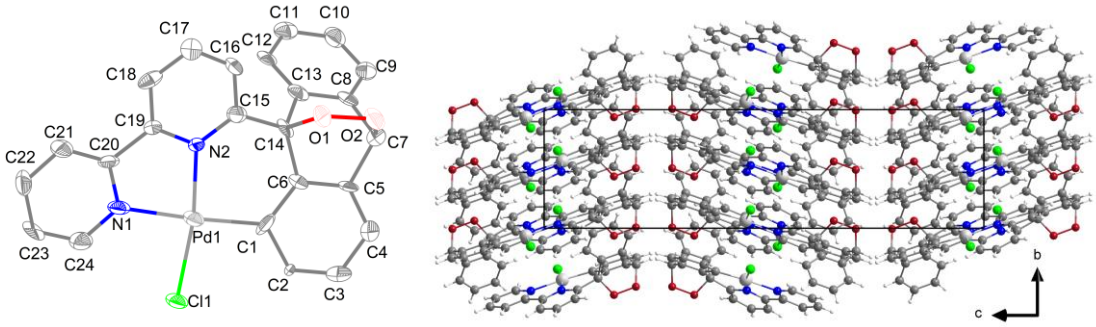

Figure 49 Asymmetric unit of [Pd(PyPyAnthO$_2$)Cl] single crystal X-ray diffraction (displacement ellipsoids at 50% probability, hydrogens omitted for clarity) (left) and view of the crystal structure (right) along the crystallographic *a*-axis.

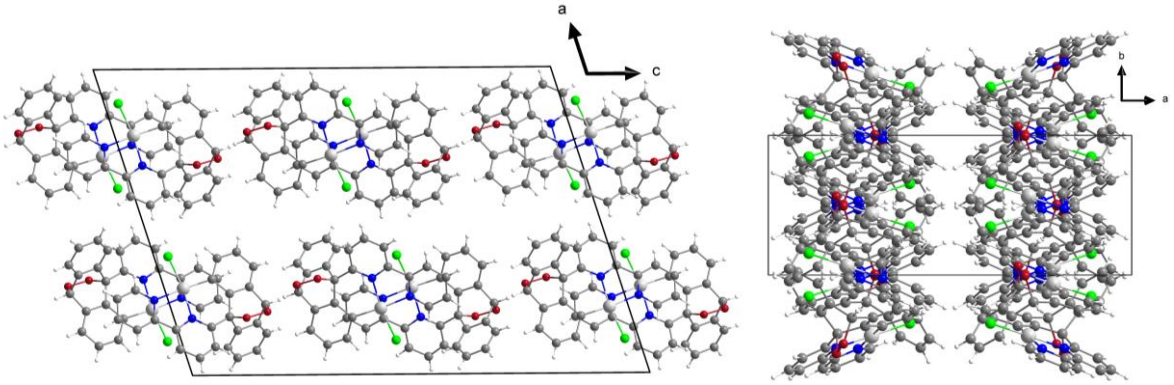

Figure 50 View on the crystal structure of [Pd(PyPyAnthO$_2$)Cl] along the crystallographic *b*-axis (left) and *c*-axis (right).

As already discerned in NMR spectroscopy and mass spectrometry the complex [Pd(PyPyHAnth)Cl$_2$] is not cyclometalated, instead the palladium is bound to the bipyridine-subunit and retains to chloride ions as coligands. The anthracene moiety is turned away of the bipyridine plane by 69.84(2)°, thus minimizing interactions with the chloride coligand (Figure 47). While the bond lengths of Pd-N$_1$ and Pd-N$_2$ do not differ much between the two complexes, the bond lengths of Pd to the chlorides do change. For [Pd(PyPyHAnth)Cl$_2$] they are shorter at 2.295(1) Å (M–Cl$_1$), 2.289(1) Å (M–Cl$_2$), compared to [Pd(PyPyAnthO$_2$)Cl] at 2.351(3) Å
(M–Cl). This elongation of the Pd–Cl bond length of the cyclometalated complex is a result of the strong carbanionic donor increasing electron density at the metal, thus weakening the Pd–Cl σ-bond. In both complexes, the angles between the two nitrogen donors and the metal, N$_1$–M–N$_2$ are distorted away from the ideal square planar 90° to 80.8(2)° and 79.2(3)° respectively (see table 24), due to the fixed structure of the bipyridine-subunit. For [Pd(PyPyHAnth)Cl$_2$] the remaining angles (e.g. N$_1$–M–Cl$_1$) around the metal are much less distorted, closer to 90°.

The endoperoxide bond O$_1$–O$_2$ is at a typical length of 1.479, similar to reported data for other anthracene endoperoxides and does not seem affected by the coordination of Palladium.[120]

The reaction with oxygen also means the anthracene moiety is no longer fully sp^2-hybridized, therefore the endoperoxide-bearing ring system is bent at an angle of 56.96°.

This happens while retaining the cyclometalation. The angle around the metal (C_1–M–N_2) is slightly higher than 90° at 96.2(3)° and much bigger than the angles calculated for [Pd(PhPyQ)Cl)] (82.18°), (see chapter 3.1) due to this distortion of the anthracene peroxide.[49] However, the Pd–C_1 bond itself seems unaffected, with the bond length of 1.989(2) Å being essentially the same as the one calculated for [Pd(QPyPh)Cl] at 1.986 Å.

Both complexes show typical head-to-tail stacking with two complex moieties forming pairs within the asymmetric unit. The anthracene units of [Pd(PyPyHAnth)Cl_2] break up further stacking and no significant packing trends can be observed. The opposite is true for [Pd(PyPyAnthO_2)Cl], where the stacking leads to layers being visible, especially along the crystallographic A-axis. The metal-to-metal distances are within the upper range of typical Pd-Pd interactions at 3.655(2) Å.[121]

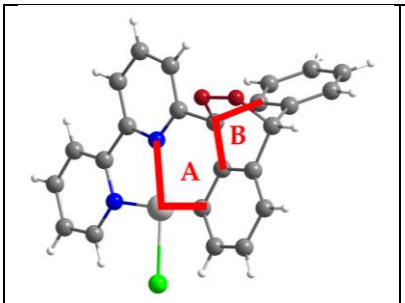

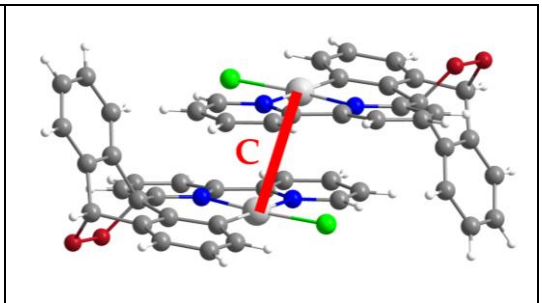

[Pd(PyPyAnthO_2)Cl]	
Angles (°)	
A	96.2(3)
B	56.96(3)
Shortest distances (Å)	
C	3.655(2)

Figure 51 Selected ring torsion angles and distances for complexes [Pd(PyPyAnthO_2)Cl].

Table 24 Selected bond lengths (Å) and angles (°) for the complexes [Pd(PyPyHAnth)Cl_2] and [Pd(PyPyAnthO_2)Cl].[a]

Distances (Å)	[Pd(PyPyHAnth)Cl_2]	Distances (Å)	[Pd(PyPyAnthO_2)Cl]
M–N_1	2.030(5)	M–C_1	1.989(9)
M–N_2	2.085(5)	M–N_1	2.113(7)
M–Cl_1	2.2948(1)	M–N_2	2.090(6)
M–Cl_2	2.289(1)	M–Cl	2.351(3)
		O_1–O_2	1.479(7)
		C_{14}–O_1	1.513(8)
		C_7–O_2	1.473(8)
Angles (°)		Angles (°)	
N_1–M–N_2	80.8(2)	N_1–M–N_2	79.2(3)
N_1–M–Cl_1	92.91(2)	C_1–M–N_1	174.7(3)
N_1–M–Cl_2	174.99(2)	C_1–M–N_2	96.2(3)
N_2–M–Cl_1	173.67(1)	C_1–M–Cl	92.7(2)
N_2–M–Cl_2	100.20(1)	N_1–M–Cl	91.92(2)

Cl_1–M–Cl_2	86.08(5)	N_2–M–Cl	171.0(2)
Σ angles around M	360.0	Σ angles around M	360.0

[a] From single crystal X-ray diffraction.

The introduction of anthracene-moieties into the ligand backbone resulted in high reactivity of the resulting complexes [M(PyPyAnth)Cl] with oxygen. Triplett-singlet interconversion led to intramolecular addition, yielding the endoperoxide species [M(PyPyAnthO_2)Cl]. To further investigate these compounds, the synthesis needs to be optimized to selectively yield the cyclometalated product instead of mixture with precoordinated species. The exact dynamics of the oxygen reactions as well as the very strong absorptions of the complexes should be studied in detail by (time-resolved) luminescence spectroscopy backed up by TD-DFT calculations.

3.6 Coligand Exchange Reactions

To further derivatize existing systems and change their optical and electrochemical properties, coligand exchange reactions were carried out on fully characterized ring-expanded cyclometalated complexes. The complexes of type [M(PyPhQ)X] were chosen as model compounds for coligand exchange reactions. For Pt(II) complexes, a well-established reaction is the introduction of phenylacetylene as coligand under *Sonogashira*-type conditions (see Scheme 27). Base-assisted nucleophilic substitution is also commonly applied to introduce various new coligands (e.g. carbazole).[9]

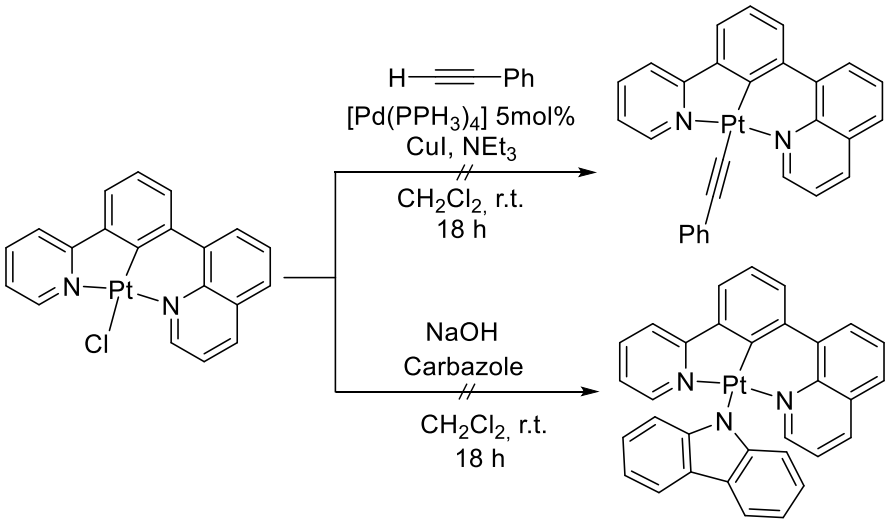

Scheme 27 Attempted coligand exchange reaction towards [Pt(PyPhQ)C_2Ph] and [Pt(PyPhQ)($NC_{12}H_8$)] under reported conditions.[9, 24, 25]

However, under these conditions, not the desired product is obtained, instead the chloride-bearing substrate is reisolated. The same problem was encountered when carrying out coligand exchange reactions with alkali metal salts with varying anions. These methods had been previously employed successfully for similar complexes, using the precipitation of alkali metal chlorides in CH_2Cl_2 as driving force.[24, 25]

Adding silver nitrate to increase the driving force of the reaction by precipitation of AgCl also did not yield the desired product (see Scheme 28).[122] However, upon stirring the chlorido-complex with silver nitrate a colour change of the solution from orange to lighter yellow was observed. The chlorido-complex was therefore reacted with a slight excess of silver nitrate and the newly formed complex species was isolated (see Scheme 28).

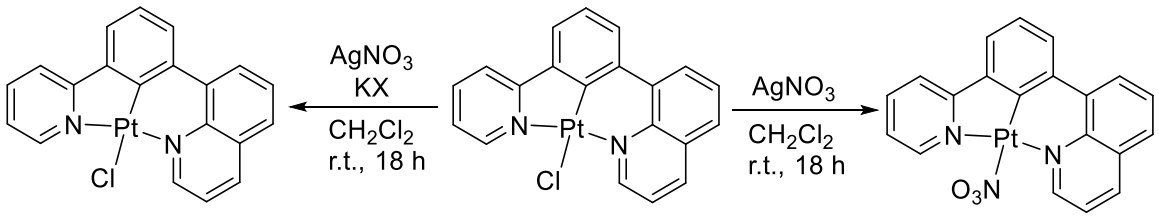

Scheme 28 Reactions of [Pt(PyPhQ)Cl] with silver nitrate as additive (left) and as main reagent (right) towards coligand exchange.[122]

The newly obtained complex was identified as [Pt(PyPhQ)NO_3] by SC-XRD, supported by NMR and mass spectrometry. The ^{1}H NMR spectrum shows a strong shift of the two proton signals in alpha-position to the coordinating nitrogen atoms of the quinoline and pyridine moieties (see Figure 52). These proton signals typically exhibit a direct coupling to the NMR-active ^{195}Pt-core and produce platinum satellite signals.[123] They are therefore most strongly affected by changes to the coordination of the metal.

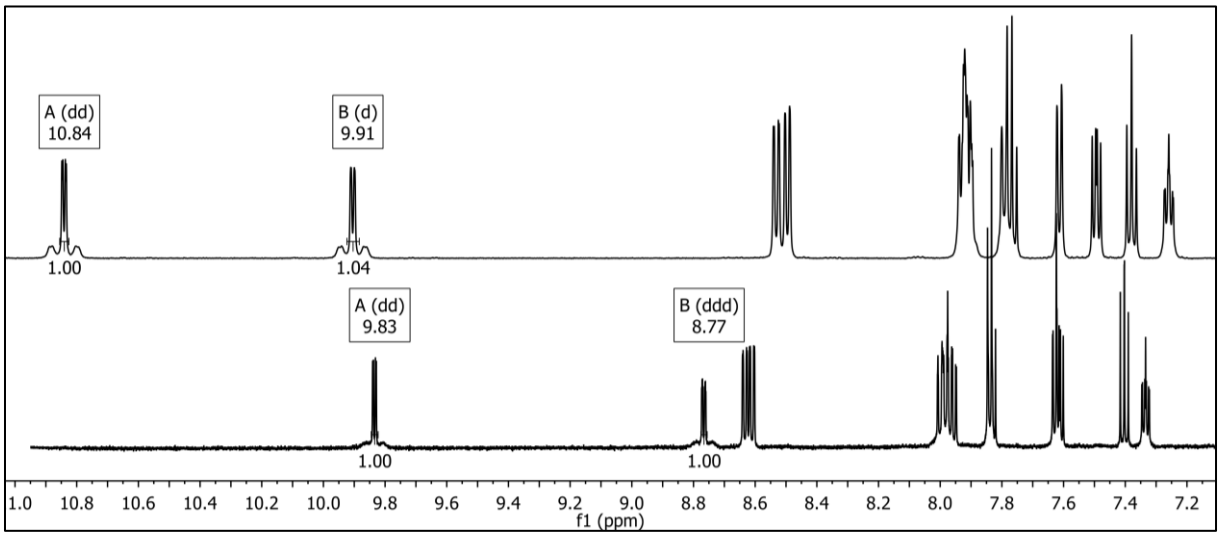

Figure 52 ^{1}H NMR spectra of [Pt(PyPhQ)Cl] (top) and [Pt(PyPhQ)NO_3] (bottom) (CD_2Cl_2, 500 MHz). Alpha-pyridine and -quinoline signals are marked as multiplets and integrated.

The strong upfield shift of almost 1 ppm seen in [Pt(PyPhQ)NO_3] as opposed to [Pt(PyPhQ)Cl] implies the nitrate coligand is much less electron-withdrawing than chloride. This is somewhat counterintuitive, as chloride is typically not thought of as a strong ligand featuring strong backbonding.[35] During more time-intensive ^{13}C NMR measurements, an initially pure sample of [Pt(PyPhQ)NO_3] started exhibiting traces of [Pt(PyPhQ)Cl]. Since the sample was otherwise pure, a reaction of the nitrato-complex to the chloride-complex must have taken place with chloride ions stemming from decomposition of the solvent CD_2Cl_2.[124] This was verified by reacting a pure sample of [Pt(PyPhQ)NO_3] with an excess of NaCl in a 50:50 mixture of DMSO-d_6 and D_2O (see Scheme 29). After less than 5min, full conversion had taken place, with no trace of the nitrato-species being detectable via NMR spectroscopy.

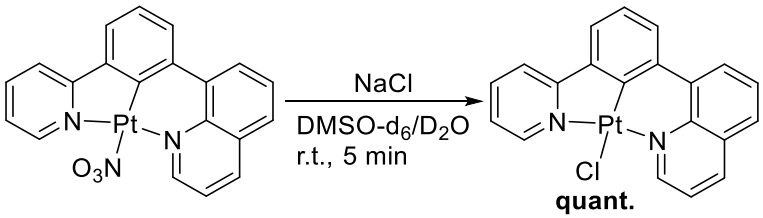

Scheme 29 Reaction of [Pt(PyPhQ)NO_3] with chloride ions yield [Pt(PyPhQ)Cl] quantitatively.

This very high affinity towards chloride ions also explains why previously mentioned attempts at coligand exchange reactions failed. If any chloride is present within the reaction, the reaction back to [Pt(PyPhQ)Cl] outcompetes all other species being formed. This behaviour

seems to be unique to [Pt(PyPhQ)Cl] systems and has not been reported for other N^C^N Platinum systems. The same reactivity is also encountered for the complexes [Pd(PyPhQ)NO_3] and [Ni(PyPhQ)NO_3] respectively and extends to both chloride and bromide coligands.

The rapid conversion of [Pt(PyPhQ)NO_3] back to the chloride-bearing complex also made it interesting for coligand exchange reactions with other anions. Indeed, if [Pt(PyPhQ)NO_3] is reacted with any source of suitable anions, a coligand exchange is observed under very mild conditions (see Scheme 30). This is not the case if $AgNO_3$ is added as an additive or if a notable source of halogen-ions is present, both resulting in the formation of [Pt(PyPhQ)X] as the main product.

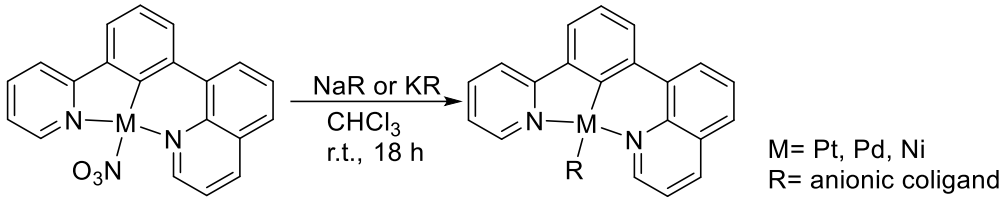

Scheme 30 General reaction Scheme for coligand exchange reactions starting from [M(PyPhQ)NO_3].

While CH_2Cl_2 can be used for these reactions, it can be a source of chloride ions, especially for solvent that has been exposed to moisture and light. However, halogen-free solvents that still dissolve the complexes [M(PyPhQ)NO_3] well enough, like THF and DMSO, also increase the solubility of AgX (X= Cl for Pt, Pd, X= Br for Ni). Since the precipitation of AgX is the main driving force, increasing its solubility not only inhibits conversion towards the desired product but also promotes the reaction back to [M(PyPhQ)X] (X= Cl for Pt, Pd, X= Br for Ni). The best results were achieved using $CHCl_3$, retaining good solubility of the complexes, while still precipitating AgX. While using HPLC-grade $CHCl_3$, much less impurities with chloride were observed when compared to HPLC-grade CH_2Cl_2. With this methodology in hand, various coligand exchange reactions were achieved. The obtained complexes are summarized in Figure 53 and the conditions detailed in table 25.

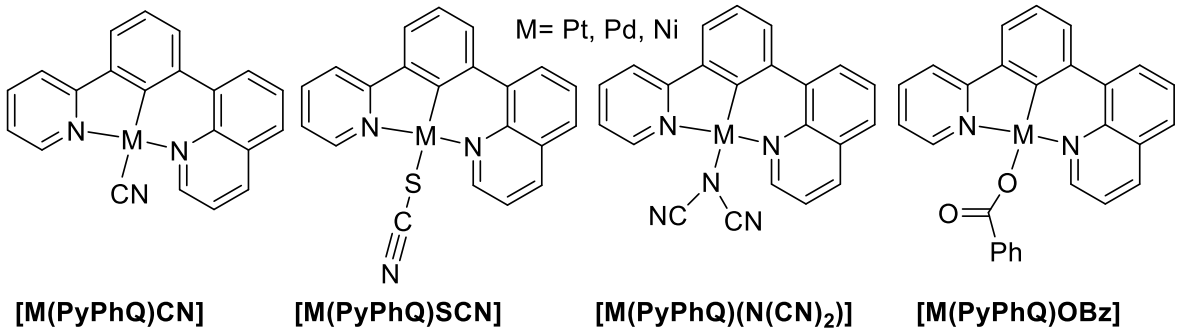

Figure 53 Overview of all complexes obtained from coligand exchange reactions starting from [M(PyPhQ)NO_3] (compare table 25).

Table 25 Reaction conditions for coligand exchange reactions of complexes [M(PyPhQ)NO_3] and [M(PyPhQ)X] type.

Starting complex	Reagent	Conditions	Yield
[Pt(PyPhQ)Cl]	$AgNO_3$	CH_2Cl_2, r.t., 18 h	[Pt(PyPhQ)NO_3], 86%
[Pd(PyPhQ)Cl]		CH_2Cl_2, r.t., 18 h	[Pd(PyPhQ)NO_3], 76%
[Ni(PyPhQ)Br]		$CHCl_3$, r.t., 24 h	[Ni(PyPhQ)NO_3], 57%
[Pt(PyPhQ)NO_3]	KOBz	$CHCl_3$, r.t., 18 h	[Pt(PyPhQ)OBz], 74%
	KCN	$CHCl_3$, r.t., 18 h	[Pt(PyPhQ)CN], 71%
	NaSCN	$CHCl_3$, r.t., 18 h	[Pt(PyPhQ)SCN], 65%
	Na($N(CN)_2$)	$CHCl_3$, r.t., 18 h	[Pt(PyPhQ)($N(CN)_2$)], 91%
[Pd(PyPhQ)NO_3]	KOBz	THF, r.t., 18 h	[Pd(PyPhQ)OBz], 45%
	KCN	$CHCl_3$, r.t., 18 h	[Pd(PyPhQ)CN], 39%
	NaSCN	$CHCl_3$, r.t., 18 h	[Pd(PyPhQ)SCN], 55%
	Na($N(CN)_2$)	$CHCl_3$, r.t., 18 h	[Pd(PyPhQ)($N(CN)_2$)], 62%
[Ni(PyPhQ)NO_3]	KCN	$CHCl_3$, r.t., 18 h	[Ni(PyPhQ)CN], 78%
	NaSCN	$CHCl_3$, r.t., 18 h	[Ni(PyPhQ)SCN], 47%
	Na($N(CN)_2$)	$CHCl_3$, r.t., 20 h	[Pd(PyPhQ)($N(CN)_2$)], 16%

Generally, all exchange reactions were successful except for some cases with [Ni(PyPhQ)NO_3]. Since nickel complexes are generally more prone to decomposition and hydrolysis, exchange reactions that took longer for Pt(II) and Pd(II) usually lead to decomposition of the Ni(II) complexes, with undefinable products. Using an excess (1.20 eq.) of $AgNO_3$ when preparing the complexes [M(PyPhQ)NO_3] ensures clean conversion and eliminates potentially present chloride impurities from the solvent or other sources. Special care must be taken during further coligand exchange reactions not to introduce any chloride impurities, be it via the reagent or solvent during workup and washing. While CH_2Cl_2 and $CHCl_3$ can be used, they must ideally be fresh and dry. A separation of mixtures [M(PyPhQ)Cl] and [M(PyPhQ)NO_3] via, for example, column chromatography was not possible, instead further promoting the decomposition of the nitrato-species.

This is especially problematic when the coligands require prior preparation. For example, deprotonating carbazole with *n*-BuLi and reacting it with [Pt(PyPhQ)NO_3] yielded [Pt(PyPhQ)Cl] quantitively, because of LiCl impurities from the *n*-BuLi synthesis (compare Scheme 29).[125]

A different method for preparation of coligands, especially acetylene-derivatives, was therefore applied, guaranteeing a chloride free synthesis (see Schemes 31, 32).[126] Acetylene gas was introduced into an electride solution (Na/ dry NH_3) at – 77 °C until the mixture turned colourless. The mixture was then heated to room temperature to obtain sodium hydrogen acetylide (NaC_2H). This salt was then mixed with various acetylenes or nitrogen-bearing aromats in liquid ammonia to obtain different sodium acetylide salts as well as sodium salts of the nitrogen aromats (see Scheme 31).

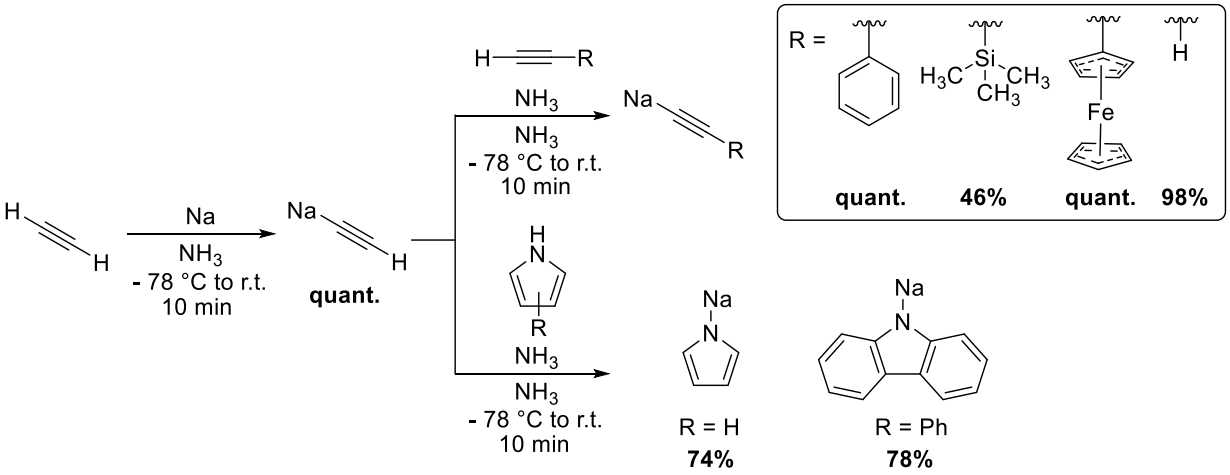

Scheme 31 Synthetic route towards halogen-free salts to be used in coligand exchange reactions.

These sodium salts with various anions were reacted with [M(PyPhQ)NO_3] under very mild conditions (THF, r.t.), like the coligand exchange reaction conditions already applied for previously mentioned anions (see Scheme 32).

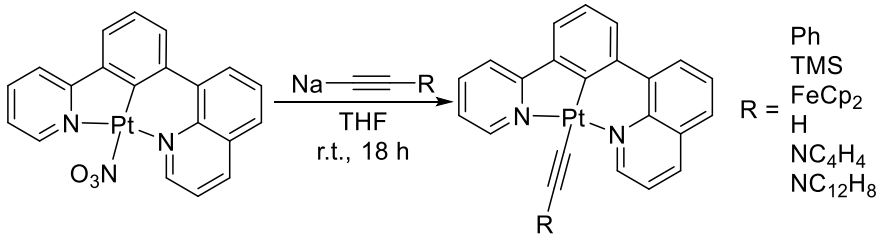

Scheme 32 General reaction Scheme for coligand exchange reactions with coligand salts from the hydrogen acetylene based synthetic approach.

An overview of all newly synthesized complexes with differing coligands is provided in Figure 54, detailed reaction conditions and yields are summarized in table 26.

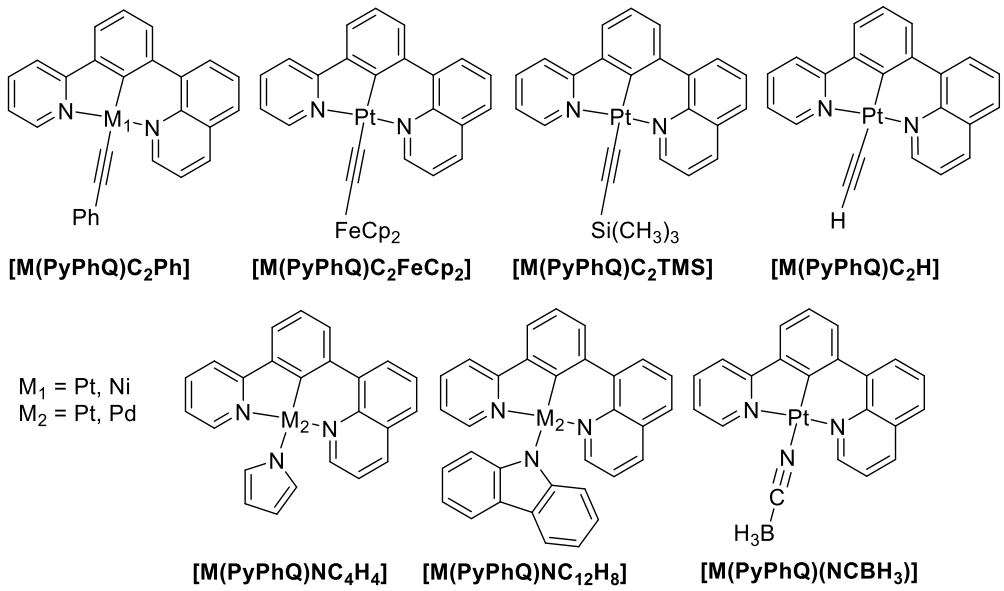

Figure 54 Overview of all complexes obtained from coligand exchange reactions using the hydrogen acetylene based synthetic approach (compare table 26).

Table 26 Reaction conditions for coligand exchange reactions of complexes [M(PyPhQ)R] with salts from the hydrogen acetylene based synthetic approach.

Starting complex	Reagent	Conditions	Yield
[Pt(PyPhQ)NO_3]	NaC_2Ph	THF, r.t., 18 h	[Pt(PyPhQ)C_2Ph], 28%
	NaC_2H	THF, r.t., 18 h	[Pt(PyPhQ)C_2H], unclear [a]
	NaC_2FeCp_2	THF, r.t., 24 h	[Pt(PyPhQ)C_2FeCp_2], 70%
	NaC_2TMS	THF, r.t., 3 h	[Pt(PyPhQ)C_2TMS], 47%
	$Na(NC_4H_4)$	THF, r.t., 18 h	[Pt(PyPhQ)NC_4H_4], 97%
	$Na(NC_{12}H_8)$	THF, r.t., 18 h	[Pt(PyPhQ)$(NC_{12}H_8)$], 34%
	$Na(NCBH_3)$	THF, r.t., 24 h	[Pt(PyPhQ) $(NCBH_3)$], 56%
[Pd(PyPhQ)NO_3]	$Na(NC_4H_4)$	THF, r.t., 18 h	[Pd(PyPhQ)NC_4H_4], 99%
	$Na(NC_{12}H_8)$	THF, r.t., 18 h	[Pd(PyPhQ)$(NC_{12}H_8)$], 36%
[Ni(PyPhQ)NO_3]	NaC_2Ph	THF, r.t., 10 min	[Ni(PyPhQ)C_2Ph], 11%

[a] NMR spectroscopy and cyclic voltammetry indicates formation of the desired [Pt(PyPhQ)C_2H], while UV/Vis-absorption spectroscopy indicates formation of [Pt(PyPhQ)Cl], probably from decomposition of [Pt(PyPhQ)C_2H] during measurements.

Generally, all reactions with acetylide salts yielded the desired product in moderate to good yields. Importantly, no signs of any side products like the chloride complexes were detected in any of the reactions. Additionally, the synthetic approach proved to work equally well for anions that are susceptible to moisture and air and require deprotonation with strong bases. While the synthesis of carbazole complexes had previously been reported, the method detailed here was also applied to the much more sensitive pyrrole complexes, which were obtained in excellent yields.[24, 95]

The reaction of [Ni(PyPhQ)NO_3] with NaC_2Ph showed a strong discolouration of the initially vibrantly orange solution in THF after 10 min. This could indicate the formation of nickel particles due to unwanted reductive elimination of the forming [Ni(PyPhQ)C_2Ph]. To avoid potential further decomposition, the reaction was stopped by addition of diethyl ether and precipitation of the product. NMR spectroscopy indicated complex formation (see Figure 55).

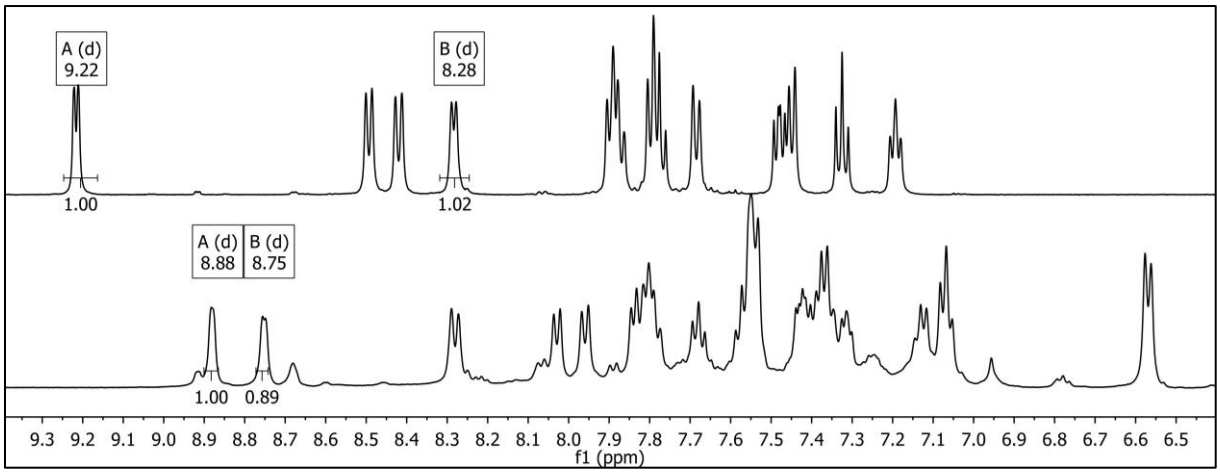

Figure 55 ^1H NMR Spectra of [Ni(PyPhQ)NO_3] (top) and [Ni(PyPhQ)C_2Ph] (bottom) (CD_2Cl_2, 500 MHz). The alpha-quinoline and -pyridine signals are integrated and marked.

Although some impurities are present in the baseline, the integration of all signals sums up to the desired total of 18 protons. New signals can be observed within the aromatic region (7.0 ppm to 7.5 ppm) which can be attributed to the phenylacetylene moiety. The proton signals in alpha position to the nitrogen atoms of the pyridine and quinoline moieties shift notably. Interestingly, they do not shift in the same direction, but instead the quinoline signal shifts towards higher fields (9.22 ppm for -NO_3 to 8.88 ppm for -C_2Ph), and the pyridine signal moves further downfield (8.28 ppm for -NO_3 to 8.75 ppm for -C_2Ph). This behaviour is not mirrored by the other proton signals, which instead exhibit a general upfield shift. Overall, this speaks for phenylacetylene having a strong σ-donor character and introducing higher electron density into both the metal and in turn the ligand backbone.

The resolution of the spectrum of [Ni(PyPhQ)NO_3] diminished while trying to measure ^{13}C spectra, exhibiting more and more line broadening. This implies the decomposition of the formed complex takes place in solution, be it in the THF reaction solution or the CD_2Cl_2 NMR solution, again speaking for a reductive elimination and the formation of paramagnetic particles of Ni(0).

An attempt to replace the nitrato coligand with hydride was made by reacting [Pt(PyPhQ)NO_3] with sodium cyanoborohydride under the previously discussed conditions (see table 26). Interestingly, the mild hydride donor did not react in the intended way and the hydrido-complex was not obtained. Instead, SC-XRD analysis revealed the anion coordinated with its cyano-moiety, while retaining all three hydrides bound to the boron atom. Similar coordination has been previously reported for iron, vanadium and nickel complexes.[127-129] Interestingly, the compound was not overly sensitive to air nor moisture, meaning the coordination to platinum may help stabilize the cyanoborohydride coligand. The same is true for all acetylene-based coligands, with exception of [Pt(PyPhQ)C_2H].

All complexes obtained from coligand exchange reactions were subjected to UV/Vis-absorption measurements to investigate their optical properties. An overview of the spectra is given in Figure 56 and 57, detailed data is listed in table 27.

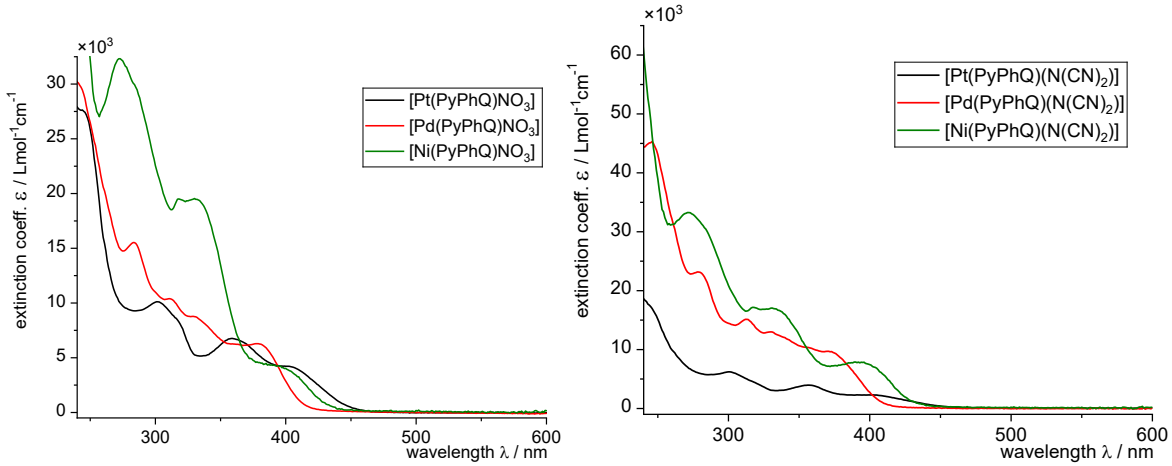

Figure 56 UV/Vis-absorption spectra of [M(PyPhQ)NO_3] (left) and [M(PyPhQ)$(N(CN)_2)$] (right), measured in THF at room temperature.

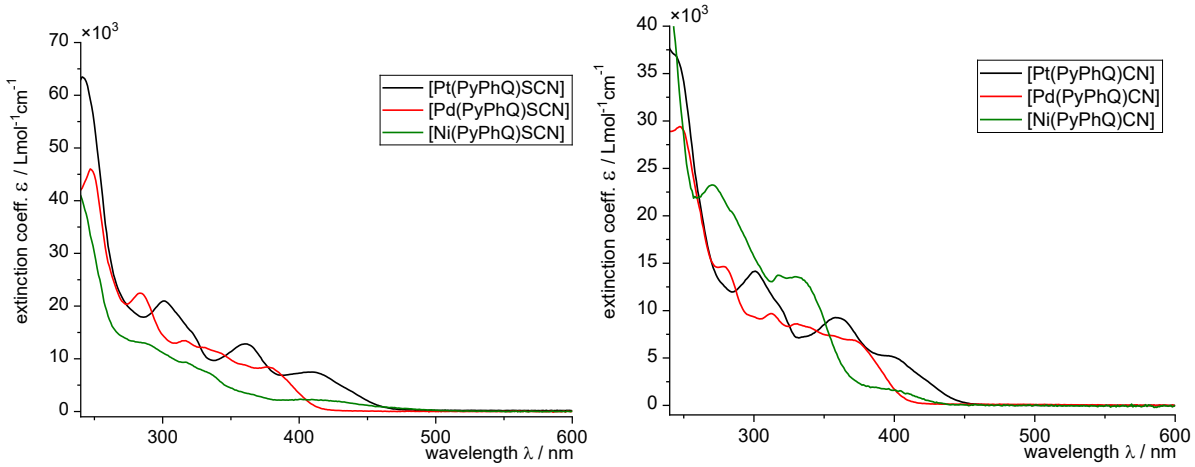

Figure 57 UV/Vis-absorption spectra of [M(PyPhQ)SCN] (left) and [M(PyPhQ)CN] (right), measured in THF at room temperature.

As is the case for the parent complexes [M(PyPhQ)X] (X(Pt, Pd) = Cl, X(Ni) = Br) all complexes feature pronounced absorption bands between 240 nm and 350 nm, which are also present for the protoligands and can be attributed to π-π* and n-π* transitions within the ligand backbone. A pronounced absorption band at around 365 nm can be observed for most complexes (see table 27), regardless of their coligand. This implies little contribution of the coligand and the metal, pointing to LL'CT/ILCT transitions, either between the pyridine or phenyl rings and the quinoline-centred LUMO (see Figure 58).

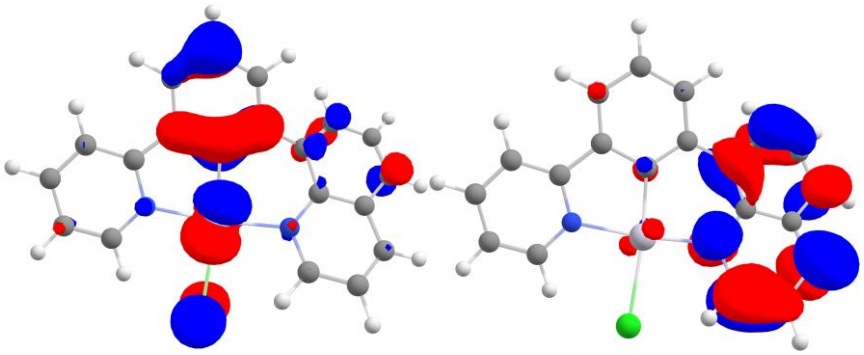

Figure 58 DFT-calculated frontier molecular orbital surfaces of the HOMO (left) and LUMO (right) of [Pt(PyPhQ)Cl] (TPSSh hybrid functional, def2-TZVP base set, Isovalue of 0.03).[49]

The longest wavelength absorption band can generally be attributed to the lowest energy transition (HOMO-LUMO). Since the HOMO of [M(PyPhQ)X] complexes is heavily centred on the metal, central phenyl ring and chloride coligand, the exchange of said coligand should have a big impact on the HOMO energy levels (see Figure 58). When comparing this longest wavelength absorption band of all coligand-exchanged [M(PyPhQ)R] complexes to their parent compound [M(PyPhQ)Cl] they all feature a markable blue-shift of between 15 nm (1100 cm^{-1}) for [Pt(PyPhQ)R] up to 40 nm (2000 cm^{-1}) for complexes of [Ni(PyPhQ)R]. Interestingly, when comparing the different coligands to each other, the impact of their different structures on the absorption band wavelength seems to be minimal. This implies the HOMO is still mainly centred on the metal and phenyl unit, with very little contribution of the coligand. As was the case for its synthetical behaviour, the chloride-coligand seems to hold a special place here. The red-shift it causes means significant backbonding reduces the electron density of the metal centre. This is further backed up by the strong downfield-shifts encountered in NMR spectroscopy (see Figure 55).

Although the differences are small, cyanide causes the strongest blue-shift of all coligands, due to its strong electron-withdrawing character and its ability for strong backbonding.[130]

Generally, the MLCT-bands of [Pd(PyPhQ)R] type complexes are the most blue-shifted of the three metals, which is in line with the same trend observed for the parent complexes [M(PyPhQ)Cl] and other similar compounds (MLCT-absorption band wavelength: Pd > Pt > Ni).[2, 20, 26, 49, 67] However, the differences in MLCT-absorption wavelength of platinum and nickel complexes are minimal, which is surprising.

Table 27 Optical properties of complexes of complexes resulting from coligand exchange reaction of [M(PyPhQ)R] type. [a]

Substance	**λ_1 (ε)**	**λ_2 (ε)**	**λ_3 (ε)**	**λ_4 (ε)**	**λ_5 (ε)**	**λ_6(ε)**	**$\Delta E_{opt.}$**
[Pt(PyPhQ)Cl][49]	238 (5.47)	304 (1.55)	321 (1.41)	359 (0.92)	373 (0.86)	418 (0.66)	2.97
[Pd(PyPhQ)Cl][49]	241(4.56)	284 (2.23)	312 (1.45)	330 (1.27)	381 (0.90)	-	3.25
[Ni(PyPhQ)Br][49]	243 (4.80)	281 (1.48)	-	336 (0.77)	365 (0.52)	436 (0.49)	2.84
[Pt(PyPhQ)NO_3]	245 (27.6)	-	301 (10.2)	-	358 (6.81)	404 (4.24)	2.73
[Pd(PyPhQ)NO_3]	-	283 (16.0)	311 (10.8)	330 (9.20)	362 (6.66)	378 (6.73)	2.96

[Ni(PyPhQ)NO_3]	-	272 (32.4)	317 (19.6)	331 (19.5)	-	397 (4.18)	2.81
[Pt(PyPhQ)SCN]	241 (63.5)	301 (21.1)	-	-	361 (12.9)	409 (7.59)	2.64
[Pd(PyPhQ)SCN]	247 (46.1)	283 (22.5)	316 (13.5)	331 (12.2)	359 (8.91)	377 (8.51)	2.98
[Ni(PyPhQ)SCN]	-	287 (13.0)	317 (9.36)	334 (7.29)	366 (3.26)	409 (2.32)	2.44
[Pt(PyPhQ)CN]	244 (37.0)	-	301 (14.2)	-	358 (9.33)	398 (5.25)	2.73
[Pd(PyPhQ)CN]	247 (29.4)	279 (14.7)	312 (9.74)	331 (8.65)	356 (7.42)	372 (6.90)	2.99
[Ni(PyPhQ)CN]	-	270 (23.3)	317 (13.8)	331 (13.6)	-	398 (1.75)	2.73
[Pt(PyPhQ)($N(CN)_2$)]	237 (18.9)	-	300 (6.22)	-	356 (3.98)	403 (2.31)	2.66
[Pd(PyPhQ)($N(CN)_2$)]	246 (45.4)	278 (23.2)	313 (15.2)	330 (13.0)	356 (10.4)	372 (9.75)	2.99
[Ni(PyPhQ)($N(CN)_2$)]	271 (33.3)	-	317 (17.3)	331 (17.1)	-	394 (7.95)	2.85
[Pt(PyPhQ)OBz]	248 (36.7)	282 (19.1)	312 (14.2)	330 (11.9)	363 (9.36)	380 (9.74)	2.99
[Pd(PyPhQ)OBz]	-	305 (11.0)	319 (9.91)	361 (6.56)	376 (6.26)	417 (4.74)	2.63

[a] Wavelengths in nm, extinction coefficients in $\frac{10^3 * L}{mol * cm}$, $\mathbf{\Delta E_{opt.}}$ in eV.

The electrochemical properties of complexes resulting from coligand exchange reactions were investigated by cyclic voltammetry in THF solution (0.1 M NBu_4PF_6, referenced to $FeCp_2/FeCp_2^+$). The detailed data is summarized in Figure 59 and table 28.

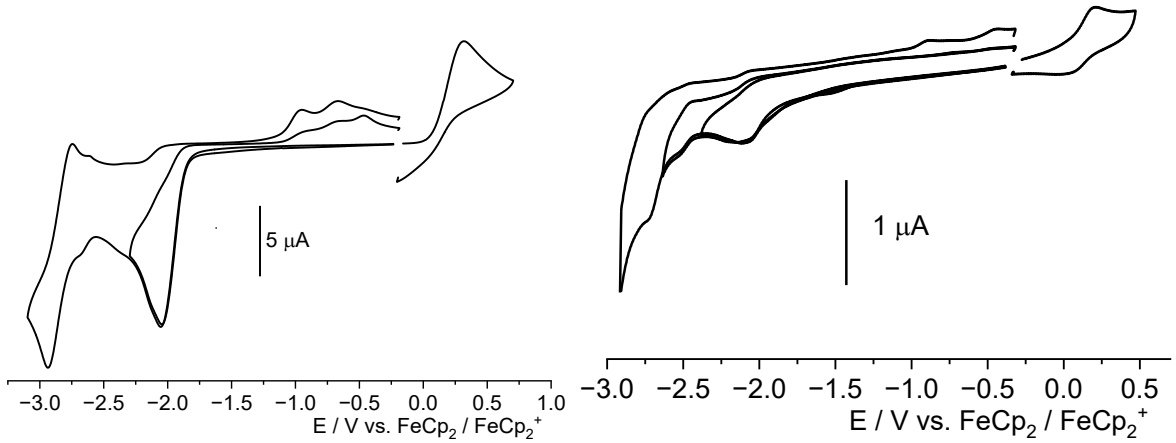

Figure 59 Cyclic voltammogram of [Ni(PyPhQ)NO_3] (left) and [Ni(PyPhQ)CN] (right), measured in THF with 0.1 M NBu_4PF_6, referenced to $FeCp_2/FeCp_2^+$.

All complexes obtained from coligand exchange reactions feature first reductions that are markedly shifted to lower potentials when compared to [M(PyPhQ)NO_3]. Typically, this reduction takes place in the electrochemical LUMO. DFT-calculations on the [M(PyPhQ)X] compounds have shown it to be mainly located on the quinoline ring of the ligand backbone (see Figure 58).[49] If the LUMO is still mainly situated on the quinoline subunit, it should not be strongly affected by the change in coligand. The opposite is the case, with the 1st reduction shifting up to a maximum 0.38 V ([Pt(PyPhQ)OBz] compared to the nitrato-complex). This suggests the coligands other than chloride have a stronger impact on the molecular orbital composition, potentially shifting the LUMO partially onto different parts of the molecule, like the central phenyl ring. Their strong donor character raises the overall electron density of the molecule, around the metal but also affecting the LUMO levels and shifting their reduction potentials.

A similar observation can be made when comparing the 1st oxidation of the coligand-exchanged complexes. Here, the oxidations shift to generally lower potentials when compared to the [M(PyPhQ)NO_3] complex. However, when compared to [M(PyPhQ)X] compounds, their behaviour diverges. Coligands with the ability to act as acceptor units, like cyanides or dicyanamides, shift the oxidation to more positive values. This means backbonding is occurring, reducing the electron density around the metal and increasing oxidation potentials. For coligands like thiocyanate or benzoate, the opposite is true. Here their donor character increases electron density around the metal, shifting oxidation potentials to lower voltages. For thiocyanate, this lack of electron-withdrawing back-bonding speaks for coordination of the sulphur atom as opposed to the nitrogen. Structure elucidation by SC-XRD would be needed to clarify the exact coordination type.

Table 28 Electrochemical properties of complexes resulting from coligand exchange reaction of [M(PyPhQ)X] type. [a]

Substance	Red 4	Red 3	Red 2	Red 1	Ox 1	$\Delta E_{elec.}$
[Pt(PyPhQ)Cl][49]	-	-	–2.65	–1.92	0.46	2.38
[Pd(PyPhQ)Cl][49]	-	-	–2.75	–2.03	0.70	2.73
[Ni(PyPhQ)Br][49]	-	-	–2.21	–2.07	0.04	2.11
[Pt(PyPhQ)NO_3]	-	–2.49	–2.00	–1.61	0.63	2.24
[Pd(PyPhQ)NO_3] [b]	–2.86	–2.75	–2.19	–1.70	0.67	2.37
[Ni(PyPhQ)NO_3]	-	-	–2.85 $E_{1/2}$	–2.05	0.32	2.37
[Pt(PyPhQ)SCN]	-	-	–2.59 $E_{1/2}$	–1.94	0.29	2.18
[Pd(PyPhQ)SCN]	–2.79	–2.65	–2.14	–2.02	0.62	2.64
[Ni(PyPhQ)SCN]	-	-	–2.75	–2.36	0.22	2.58
[Pt(PyPhQ)CN]	-	-	–2.63 $E_{1/2}$	–1.96	0.67	2.63
[Pd(PyPhQ)CN]	-	-	–2.74	–2.05	0.71	1.88
[Ni(PyPhQ)CN]	-	–2.73	–2.52	–2.16	0.21	2.37
[Pt(PyPhQ)($N(CN)_2$)]	–2.80	–2.60	–2.08	–1.90	0.58	2.48
[Pd(PyPhQ)($N(CN)_2$)]	-	–2.73 $E_{1/2}$	–2.60	–1.96	0.73	2.69
[Pt(PyPhQ)OBz]	-	-	–2.73	–1.99	0.32	2.31
[Pd(PyPhQ)OBz]	-	-	–2.72 $E_{1/2}$	–2.04	0.73	2.77

[a] Potentials, $\Delta E_{elec.}$ in V (Red 1 – Ox 1). Peak potentials given for irreversible processes or specified as reversible processes with half-wave potentials $E_{1/2}$. Measured in THF with 0.1 M NBu_4PF_6, referenced to $FeCp_2/FeCp_2^+$. [b] Red 5: –3.07 V.

Complexes resulting from coligand exchange reactions using the hydrogen acetylene based synthetic approach were investigated by UV/Vis-absorption spectroscopy. The resulting spectra are displayed in Figure 60, the detailed spectroscopic data is summarized in table 29.

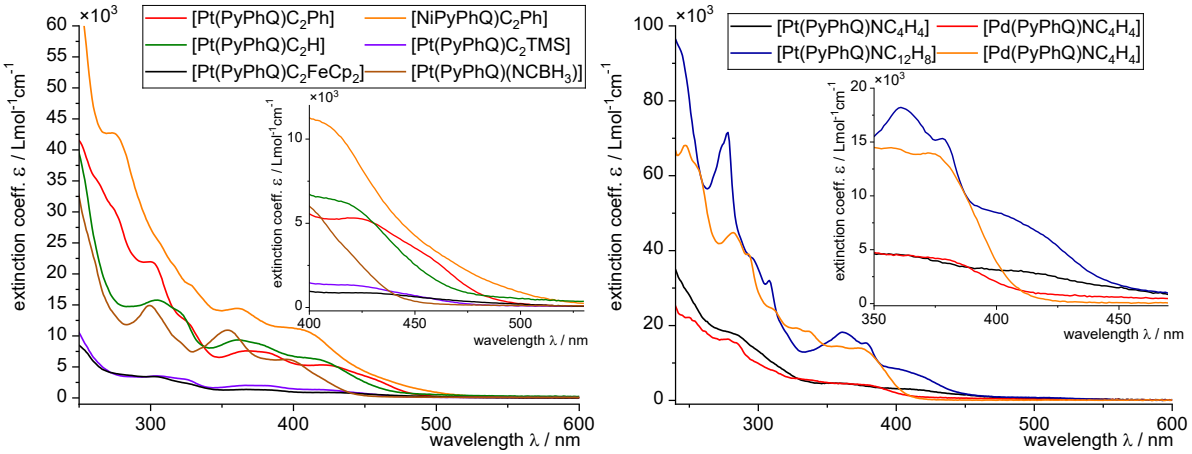

Figure 60 UV/Vis-absorption spectra of [M(PyPhQ)C2R] (left) and [M(PyPhQ)(NCxHy)] (right), measured in THF at room temperature.

The same ligand-based absorptions attributed to the PyPhQ-backbone previously discussed for other coligand exchange reactions are also present. Again, because of the orbital compositions, the longest wavelength absorption bands are of biggest interest when comparing these new types of coligands.

Generally, complexes with acetylide-coligands reverse the trend exhibited by the pseudo-halogenido-coligands previously discussed. They all exhibit red-shifted MLCT absorption bands, compared to the [M(PyPhQ)NO3] complex they are derived from. The most notable case is [Pt(PyPhQ)C2Ph], which shifts its longest wavelength absorption band to 456 nm compared to the nitrato complex (404 nm, ΔE = 2800 cm^{-1}). This means the strong σ-donor character of the acetylenes effectively increases the electron density of the metal, while having a stronger participation on the HOMO levels overall, lowering its energies throughout. More electron-rich groups bound to the acetylene enhance this effect (-Ph, -FeCp2), while more electron-poor or -withdrawing groups have the opposite effect (-H, -TMS). This means a stronger interaction of acetylene-type coligands with the metal ion is present, than was the case for the pseudohalgenido-coligands previously discussed (-CN, -SCN, -N(CN)2), even though they also have the potential for π-backbonding.

The two complexes [Pt(PyPhQ)C2FeCp2] and [Pt(PyPhQ)C2TMS] have strikingly lower absorption intensity overall, with extinction coefficient values far lower than their acetylene-coligand counterparts. This means their respective functional groups (-FeCp2, -TMS) break up the conjugation of the molecule found, for example, for phenylacetylene.

In contrast, [Ni(PyPhQ)C2Ph] shows very strong absorption intensities, akin to the other [Ni(PyPhQ)R] complexes with similarly strong absorptions (see table 27). Compared to the platinum species [Pt(PyPhQ)C2Ph], its longest wavelength absorption is significantly blue-shifted (from Pt: 456 nm to Ni: 408 nm, ΔE = 2580 cm^{-1}). This difference means the phenylacetylene is a weaker donor for nickel as opposed to platinum and less interactions between the metal and the phenylacetylene take place. This means the HOMO remains mostly located on the nickel atom and central phenyl ring and less on the acetylene coligand. The spectra of [Ni(PyPhQ)C2Ph] do however show that a complex species distinct of either the

chloride- or nitrato-bearing species is present. No signs of decomposition were observed on the time scale of the experiment (carried out in distilled, dried THF). While the NMR spectra of the complex remain somewhat ambiguous, the UV/Vis-absorption spectrum provides further evidence in favour of the successful synthesis of the desired species.

Notably, the absorptions bands of [Pt(PyPhQ)C_2H] match the ones previously reported for the parent compound [Pt(PyPhQ)Cl] exactly.[49] While the purity of the obtained compound was verified by NMR spectroscopy and mass spectrometry, it is very likely the compound decomposed in the THF-solution the UV/Vis-absorption spectra were measured in. The strong affinity of [M(PyPhQ)X] complexes towards chlorides previously discussed then lead to the formation of [Pt(PyPhQ)Cl] in situ.

The complexes bearing nitrogen donor coligands [M(PyPhQ)NC_4H_4] and [M(PyPhQ)($NC_{12}H_8$)] also show a slight red-shift of their MLCT-absorption bands. It is however much less pronounced than for the acetylide-complexes previously discussed and resembles the absorptions present for other nitrogen donors like -($N(CN)_2$) or even -NO_3. This speaks for a σ-donating character, without major HOMO contributions on the coligand itself, although DFT-calculations would be needed to verify this. Complexes with the carbazole coligand show more structures and intense absorption bands between 300 nm and 400 nm, which could be indicative of LL'CT or even LMCT transitions with strong contributions of the carbazole moiety. The pyrrole-bearing complexes lack these absorption bands and generally show much weaker extinction overall.

Table 29 Optical properties of complexes of complexes of [M(PyPhQ)C2R]- and [M(PyPhQ)NCxHy]-type. [a]

Substance	**λ_1 (ε)**	**λ_2 (ε)**	**λ_3 (ε)**	**λ_4 (ε)**	**λ_5 (ε)**	**λ_6(ε)**	**$\Delta E_{opt.}$**
[Pt(PyPhQ)Cl][49]	238 (5.47)	304 (1.55)	321 (1.41)	359 (0.92)	373 (0.86)	418 (0.66)	2.97
[Pt(PyPhQ)NO_3]	245 (27.6)	-	301 (10.2)	358 (6.81)	-	404 (4.24)	2.73
[Pt(PyPhQ)C_2Ph]	247 (41.8)	301 (22.0)	326 (12.1)	370 (7.62)	425 (5.38)	456 (3.16)	2.50
[Ni(PyPhQ)C_2Ph]	231 (20.4)	276 (8.66)	-	361(2.90)	-	408 (2.41)	2.60
[Pt(PyPhQ)C_2H]	-	304 (15.8)	321 (13.9)	361 (9.43)	-	416 (6.35)	2.60
[Pt(PyPhQ)C_2FeCp_2]	250 (8.32)	304 (3.45)	-	375 (1.39)	-	430 (0.89)	2.31
[Pt(PyPhQ)C_2TMS]	-	304 (3.56)	325 (3.02)	373 (2.04)	-	421 (1.35)	2.47
[Pt(PyPhQ)($NCBH_3$)]	-	299 (15.0)	-	353 (11.0)	-	396 (6.28)	2.78
[Pt(PyPhQ)(NC_4H_4)]	-	281 (17.9)	-	360 (4.62)	-	410 (3.05)	2.57
[Pd(PyPhQ)(NC_4H_4)]	249 (22.2)	278 (16.4)	335 (5.56)	-	-	379 (4.18)	2.92
[Pt(PyPhQ)($NC_{12}H_8$)]	277 (71.5)	307 (32.1)	361 (18.4)	378 (15.5)	-	411 (7.59)	2.69
[Pd(PyPhQ)($NC_{12}H_8$)]	281 (44.8)	309 (24.6)	327 (19.4)	336 (18.5)	357 (14.6)	373 (14.1)	3.00

[a] Wavelengths in nm, extinction coefficients in $\frac{10^3 * L}{mol * cm}$, $\Delta E_{opt.}$ in eV.

The complexes obtained from the hydrogen acetylene based synthetic approach were investigated by cyclic voltammetry. The detailed data is summarized in Figure 61 and table 30.

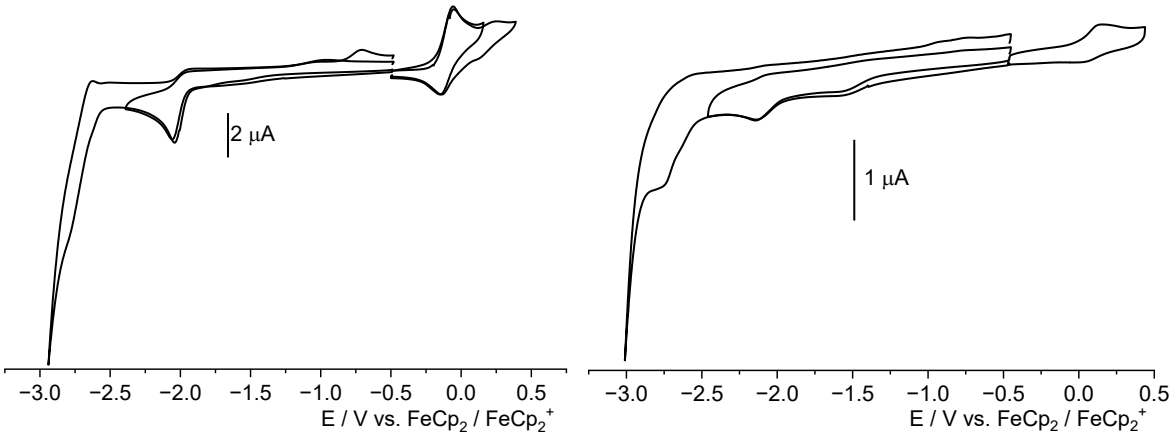

Figure 61 Cyclic voltammogram of [Pt(PyPhQ)C_2FeCp_2] (left) and [Ni(PyPhQ)C_2Ph] (right), measured in THF with 0.1 M NBu_4PF_6, referenced to $FeCp_2/FeCp_2^+$.

All complexes have their reduction onset potentials significantly shifted to more negative values when compared to the [M(PyPhQ)NO_3] complexes they're derived from. (e.g. [Pt(PyPhQ)NO_3] Red1: –1.61 V, [Pt(PyPhQ)C_2Ph] Red 1: –2.02 V). This is most pronounced for complexes bearing nitrogen containing aromatic coligands (pyrrole, carbazole). As already apparent in UV/Vis-absorption spectroscopy, they act as strong donors, increasing the electron density of the overall complex, shifting the LUMO levels situated mostly on the ligand backbone (see Figure 58). In addition to this, their oxidation potentials shift towards lower voltages, again speaking for their strong σ-donor character.

Aromatic, electron rich acetylenes like -C_2Ph and -C_2FeCp_2 act as strong σ-donors, increasing electron density at the metal centre. Since the metal has large HOMO-contributions, this results in a lowering of oxidation potentials. Interestingly, for both complexes [Pt(PyPhQ)C_2Ph] and [Pt(PyPhQ)C_2FeCp_2] a second oxidation is observed. For [Pt(PyPhQ)C_2Ph] the first oxidation most likely takes place on the metal centre, involving a reaction of the Pt^{2+}/Pt^{3+} redox pair. This oxidation might promote a subsequent reaction involving the coligand. For example, a reductive elimination and cleavage of the phenylacetylene would reduce the platinum back to Pt^{2+}, which would then undergo oxidation again.

For [Pt(PyPhQ)$FeCp_2$], the first oxidation is fully reversible and drastically shifted to negative voltages (Ox 1: -–0.10 V). This highly suggests, the oxidation of the ancillary ferrocene unit is observed, followed by the platinum oxidation at higher voltages (Ox 2: 0.26 V). This means both metal centres of the molecule are independent in their electrochemical behaviour. Formally, this also places the electrochemical HOMO of the molecule on the ferrocene unit, explaining the lowest $\Delta E_{elec.}$ value of the complexes. Based on the observations of UV/Vis-absorption spectroscopy for this complex, the HOMO-LUMO transition is closer to what would be expected for these types of compounds, implying here the main transitions stem from excitations from metal-centred orbitals into the ligand backbone. While this then formally wouldn't be the HOMO of the molecule, it is essentially the same process observed for the other complexes.

The complex [Pt(PyPhQ)C_2H] seems to be stable in THF solution under cyclic voltammetry conditions. No signs of impurities or formation of [Pt(PyPhQ)Cl] were observed, in contrast to UV/Vis-absorption spectroscopy measurements.

The same is true for [Ni(PyPhQ)C_2Ph], also being stable under CV conditions. The oxidation of the nickel centre is strongly shifted to lower potentials when compared to [Pt(PyPhQ)C_2Ph], as is the case for all complexes of the type.

A very strong shift of oxidation potentials is exhibited by [Pt(PyPhQ)($NCBH_3$)] (Ox 1: 1.18 V). This implies a very strong π-backbonding takes place between the platinum centre and the cyano-moiety of the coligand. This also increases the electron density of the coligand and help stabilize the hydride-bearing boron atom, which helps explain the formation of this complex species instead of the originally intended hydride complex. This should result in elongated bond lengths both for the cyano-subunit and the boron-hydride bond (see Figure 72, 73, table 32).

Table 30 Electrochemical properties of complexes of [M(PyPhQ)C_2R- and [M(PyPhQ)NC_xH_y]-type. [a]

Substance	**Red 2**	**Red 1**	**Ox 1**	**Ox 2**	**$\Delta E_{elec.}$**
[Pt(PyPhQ)Cl][49]	–2.65	–1.92	0.46	-	2.38
[Pt(PyPhQ)NO_3]	–2.00	–1.61	0.63	-	2.24
[Pt(PyPhQ)C_2Ph]	–2.69 $E_{1/2}$	–2.02	0.35	0.65	2.37
[Ni(PyPhQ)C_2Ph]	–2.75	–2.13	0.15	-	2.28
[Pt(PyPhQ)C_2H]	–2.76	–2.01	0.40	-	2.41
[Pt(PyPhQ)C_2FeCp_2]	–2.78	–2.05	–0.10 $E_{1/2}$	0.26	1.95
[Pt(PyPhQ)C_2TMS]	–2.72 $E_{1/2}$	–2.03	0.69	-	2.72
[Pt(PyPhQ)($NCBH_3$)]	–2.54 $E_{1/2}$	–1.91	1.18	-	3.09
[Pt(PyPhQ)(NC_4H_4)]	–2.75 $E_{1/2}$	–2.15	0.40	1.23	2.55
[Pd(PyPhQ)(NC_4H_4]	–2.89	–2.23	0.27	0.96	2.50
[Pt(PyPhQ)($NC_{12}H_8$)]	–2.83	–2.22	0.09	-	2.31
[Pd(PyPhQ)($NC_{12}H_8$)]	–2.91	–2.17	0.71	-	2.88

[a] Potentials, $\Delta E_{elec.}$ in V (Red 1 – Ox 1). Peak potentials given for irreversible processes or specified as reversible processes with half-wave potentials $E_{1/2}$. Measured in THF with 0.1 M NBu_4PF_6, referenced to $FeCp_2/FeCp_2^+$.

Crystals of complexes from coligand exchange reactions were obtained by isothermal evaporation of NMR-solutions in CD_2Cl_2, overlaying of saturated complex solutions in CH_2Cl_2 with diethyl ether or isothermal heating of complex solutions in glass ampules. Molecular and crystal structures are visualized in Figure 62 - 77, bond lengths and angles are detailed in tables 31, 32. Crystal solution data is specified in tables 42 - 44 (appendix).

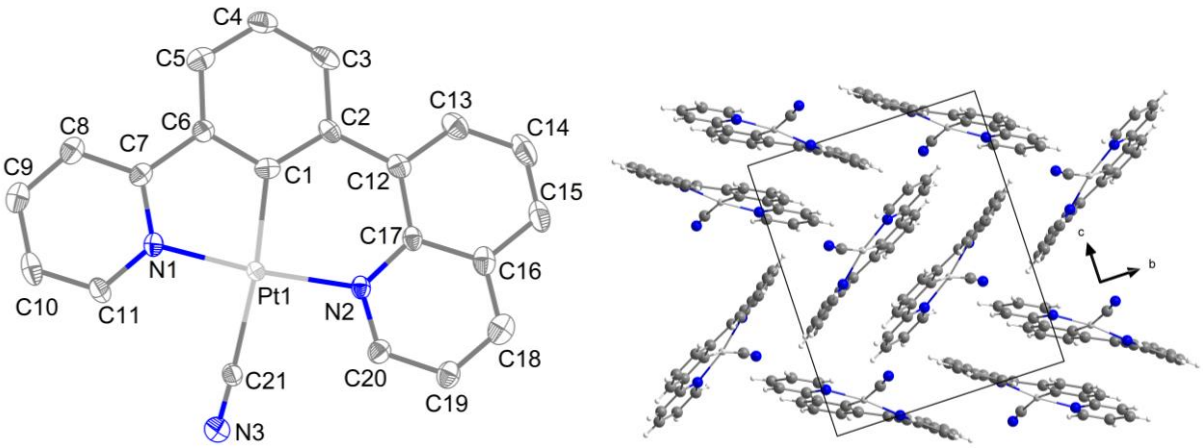

Figure 62 Asymmetric unit of [Pt(PyPhQ)CN] single crystal X-ray diffraction (displacement ellipsoids at 50% probability, hydrogens omitted for clarity) (left) and view of the crystal structure (right) along the crystallographic *a*-axis.

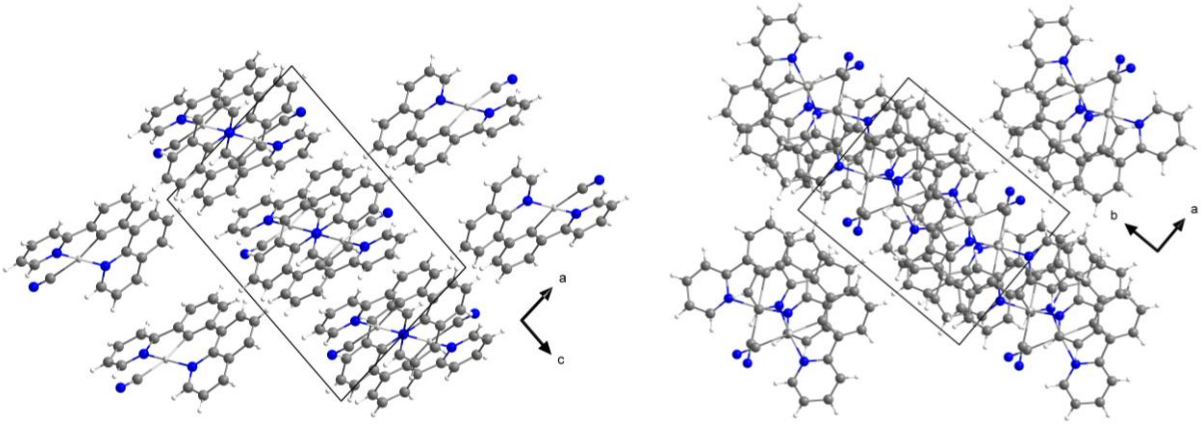

Figure 63 View on the crystal structure of [Pt(PyPhQ)CN] along the crystallographic *b*-axis (left) and *c*-axis (right).

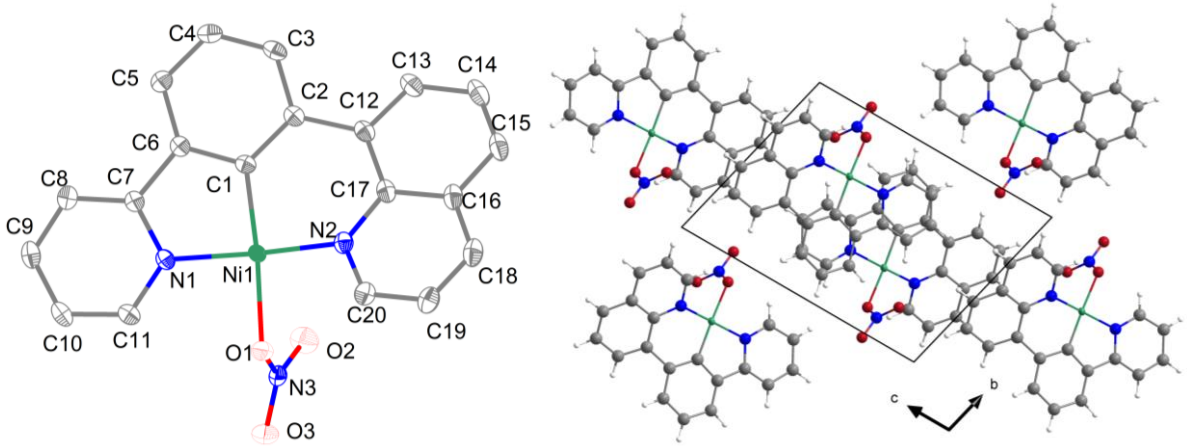

Figure 64 Asymmetric unit of [Ni(PyPhQ)NO_3] single crystal X-ray diffraction (displacement ellipsoids at 50% probability, hydrogens omitted for clarity) (left) and view of the crystal structure (right) along the crystallographic *a*-axis.

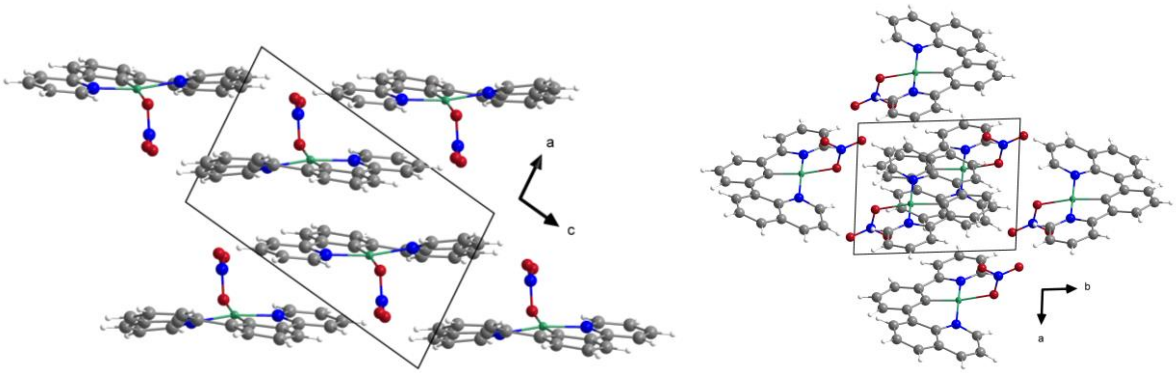

Figure 65 View on the crystal structure of [Ni(PyPhQ)NO3] along the crystallographic *b*-axis (left) and *c*-axis (right).

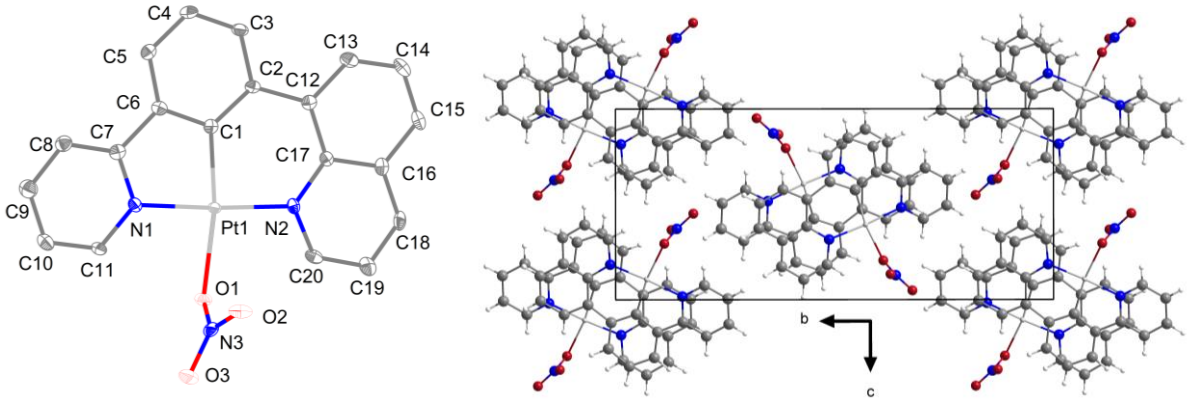

Figure 66 Asymmetric unit of [Pt(PyPhQ)NO3] single crystal X-ray diffraction (displacement ellipsoids at 50% probability, hydrogens omitted for clarity) (left) and view of the crystal structure (right) along the crystallographic *a*-axis.

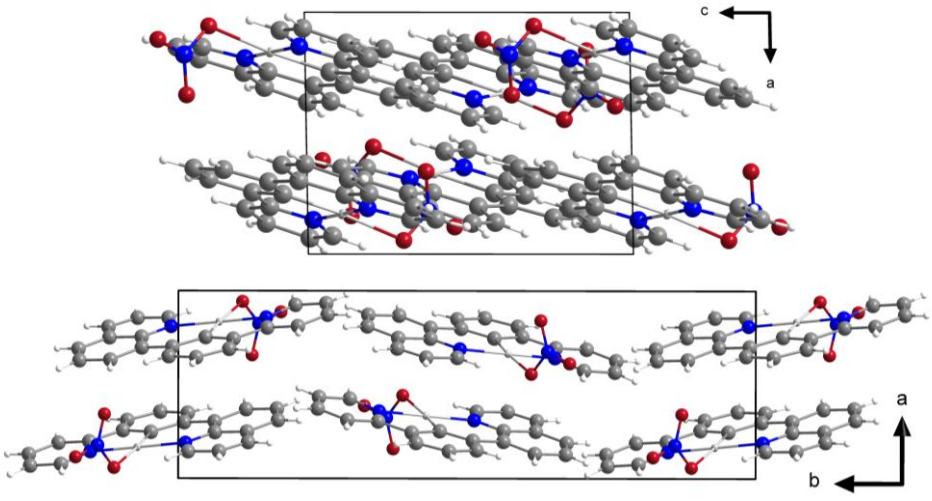

Figure 67 View on the crystal structure of [Ni(PyPhQ)NO3] along the crystallographic *b*-axis (top) and *c*-axis (bottom).

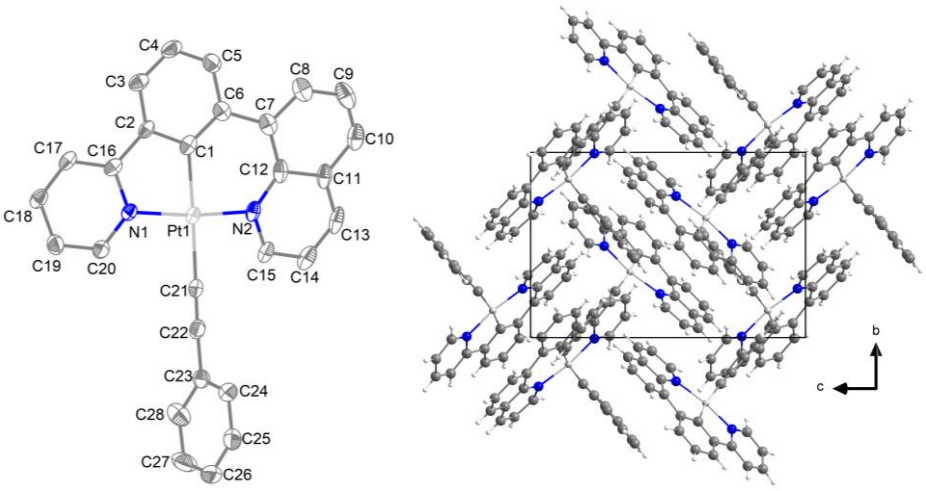

Figure 68 Asymmetric unit of [Pt(PyPhQ)C2Ph] single crystal X-ray diffraction (displacement ellipsoids at 50% probability, hydrogens omitted for clarity) (left) and view of the crystal structure (right) along the crystallographic *a*-axis.

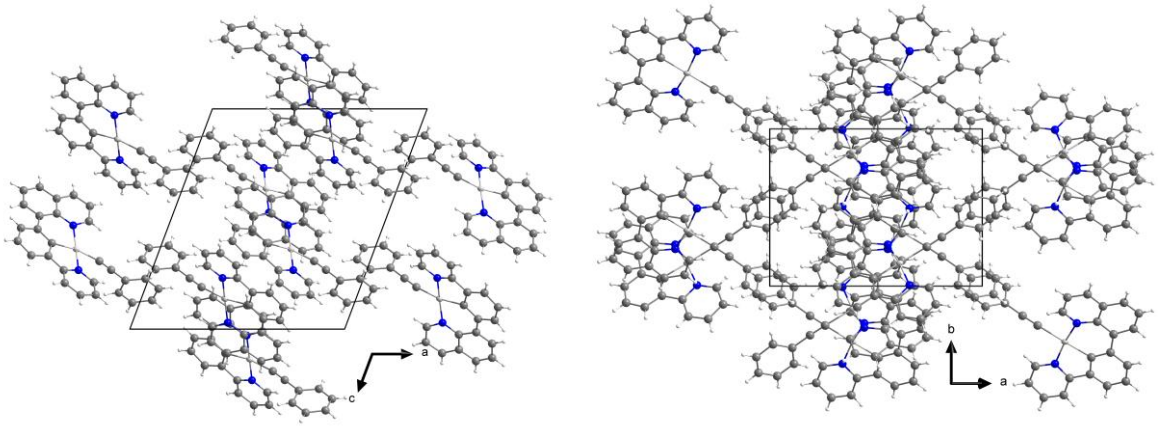

Figure 69 View on the crystal structure of [Pt(PyPhQ)C2Ph] along the crystallographic *b*-axis (left) and *c*-axis (right).

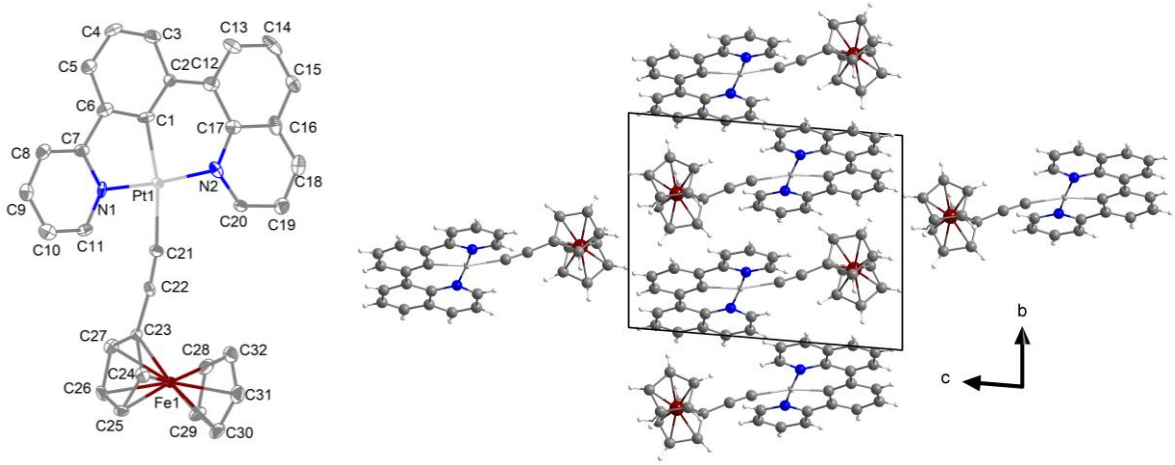

Figure 70 Asymmetric unit of [Pt(PyPhQ)C2FeCp2] single crystal X-ray diffraction (displacement ellipsoids at 50% probability, hydrogens omitted for clarity) (left) and view of the crystal structure (right) along the crystallographic *a*-axis.

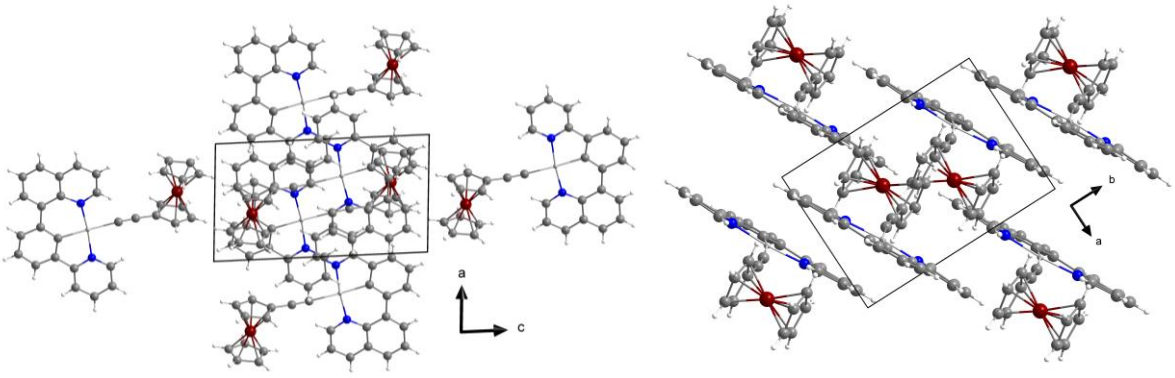

Figure 71 View on the crystal structure of [Pt(PyPhQ)C_2FeCp$_2$] along the crystallographic *b*-axis (left) and *c*-axis (right).

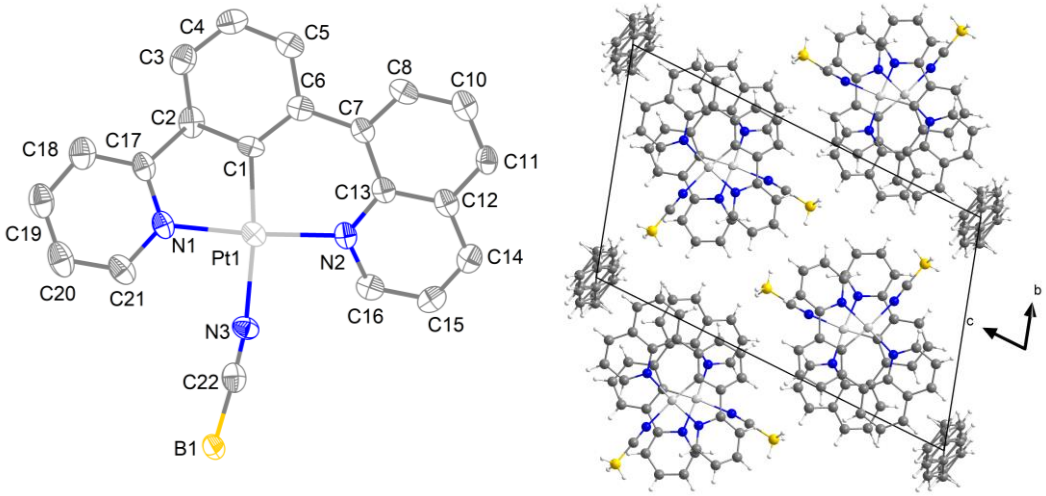

Figure 72 Molecular structure of [Pt(PyPhQ)(NCBH$_3$)] single crystal X-ray diffraction (displacement ellipsoids at 50% probability, hydrogens omitted for clarity) (left) and view of the crystal structure (right) along the crystallographic *a*-axis with a toluene molecule as co-crystallite.

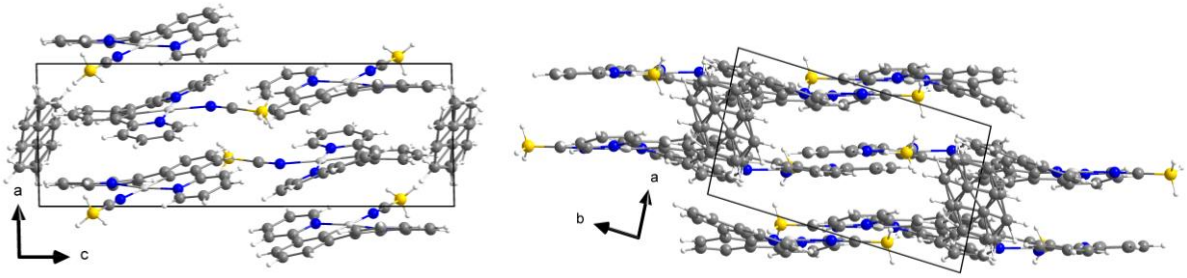

Figure 73 View on the crystal structure of [Pt(PyPhQ)(NCBH$_3$)] along the crystallographic *b*-axis (left) and *c*-axis (right) with a toluene molecule as co-crystallite.

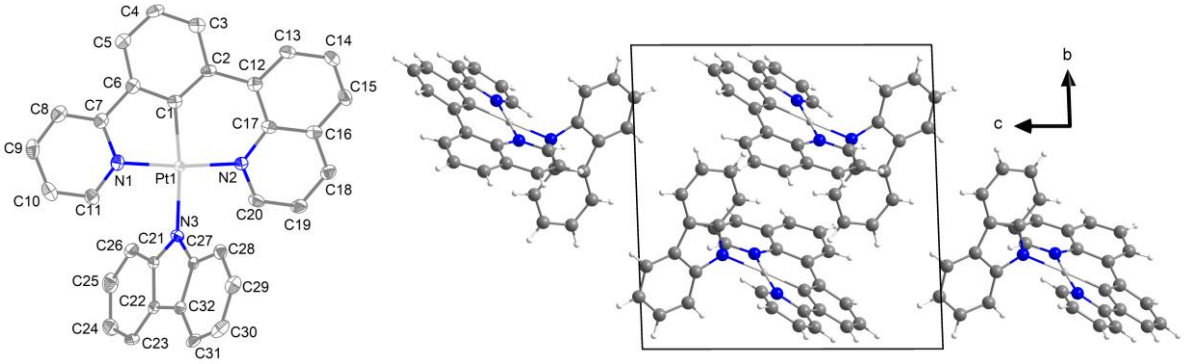

Figure 74 Asymmetric unit of [Pt(PyPhQ)(NC$_{12}$H$_8$)] single crystal X-ray diffraction (displacement ellipsoids at 50% probability, hydrogens omitted for clarity) (left) and view of the crystal structure (right) along the crystallographic *a*-axis.

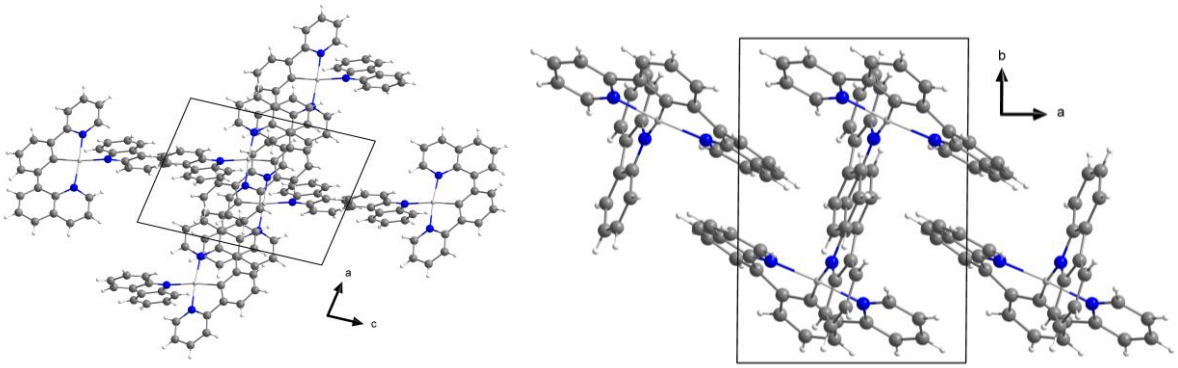

Figure 75 View on the crystal structure of [Pt(PyPhQ)(NCBH$_3$)] along the crystallographic *b*-axis (left) and *c*-axis (right).

All complexes crystalized feature the characteristic head-to-tail stacking pattern already present for the parent compounds [M(PyPhQ)X].[49] For the nitrato-complexes [Pt(PyPhQ)NO$_3$] and [Ni(PyPhQ)NO$_3$], this is accompanied by π-stacking, with stacking distances well within the range of typical π-interactions (e.g. 3.6687(1) Å, see Figure 77).[111] Two complexes are paired together mirroring each other around an inversion centre, forming enantiomeric pairs of the axially prochiral complex moieties. The bond lengths and angles around the metal centres of the nitrato-complexes [M(PyPhQ)NO$_3$] remain very similar to their parent compounds [M(PyPhQ)X], with one exception. They differ greatly in the distances between the metal and the coligand. For example, the bond length is shortened by 0.232 Å for [Pt(PyPhQ]NO$_3$] (Pt–NO$_3$: 2.196(4) Å, Pt–Cl: 2.428(9) Å). This stronger bonding exhibited by the nitrato-coligand is surprising when considering its reactivity. The strong affinity to chloride and the efficient exchange of nitrate with basically any anion would have suggested a weak, elongated bonding between metal and nitrate. A major difference between the [M(PyPhQ)NO$_3$] and [M(PyPhQ)X] complexes is the distortion of the ligand backbone. While this distortion was striking and characteristic for the halogenido-complexes, the nitrato-complexes have an almost planar ligand backbone ([Pt(PyPhQ)Cl] biggest interplanar angle: 12.9(3)°, [Pt(PyPhQ)NO$_3$]: 4.204(2)°). While the nitrato-coligand reaches out of the formed complex plane, it is not involved in any bridging or interactions with other complex molecules, as was, for example, reported for similar acetato-bearing complexes.[1]

The complex [Pt(PyPhQ)C_2FeCp_2] also features this lack of torsion of the ligand backbone (see Figure 70, 71). Here, the ferrocene coligand takes up a big space within the asymmetric unit, dictating the spacing of the complexes. No significant metal-metal interaction can be deduced from their large relative distances.

While the head-to-tail stacking motif remains throughout, complexes with bulkier coligands exhibits less stacking, with much bigger distances in between the complex moieties. This is especially the case for the complexes [Pt(PyPhQ)C_2FeCp_2] and [Pt(PyPhQ)($NC_{12}H_8$)]. For the latter, the carbazole complex is dramatically twisted by 77.217(7)° relative to the ligand backbone. While it is close in distance to the ligand backbone of the next complex moiety (3.5251(5) Å), this strong torsion makes any π-stacking impossible (see Figure 76). This also means π-backbonding from the metal and ligand to ligand charge transfers are much less likely. Observations made in UV/Vis-absorption spectroscopy showed additional absorptions being visible upon introduction of the carbazole coligand. With the information of the crystal structure in hand, these absorptions can then be attributed to LMCT transitions instead of LL'CT transitions. However, the crystal structure does not necessarily reflect the complex geometry in solution, meaning the exact constitution of these absorptions would need to be further investigated, for example by TD-DFT-calculations.

The complex [Pt(PyPhQ)CN] exhibits the shortest metal-coligand bond length of all crystalized complexes (Pt–CN: 2.057(5) Å, see table 31). This further indicates a strong π-backbonding of the metal to the antibonding orbitals of the coligand. This is in line with similar reported complexes and also backed up by the observations made in UV/Vis-absorption spectroscopy as well as cyclic voltammetry.[130]

The complex [Pt(PyPhQ)($NCBH_3$)] features a coordination of the anion via the nitrogen atom and co-crystallized toluene. The M–N bond length is one of the longest of all complexes crystalized (Pt–$NCBH_3$: 2.101(6) Å, see tables 31, 32). The N–C bond length match the reported distances for the same anion coordinated to vanadium exactly (N–C: 1.134(9) Å).[128] π-backbonding of the platinum metal into antibonding orbitals of the cyano-moiety results in an increase of the bond length of C–N, even when compared to the cyanido-complex ([Pt(PyPhQ)($NCBH_3$) C–N: 1.134(9) Å, [Pt(PyPhQ)CN] C–N: 1.128(6) Å; see tables 31, 32), where similar strong backbonding occurs.[130] This should increase the electron density around the boron atom as well and result in an elongation of the boron-hydride bonds. However, since the hydrogen atoms in the crystal structure are not determined by crystallographic measurement but added later via suitable models (H-FIX), the obtained data cannot be sensibly interpreted in that regard. The backbonding exhibited explains the relative stability of the anion in solution and as a coligand in general.

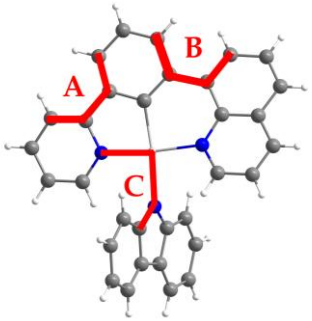	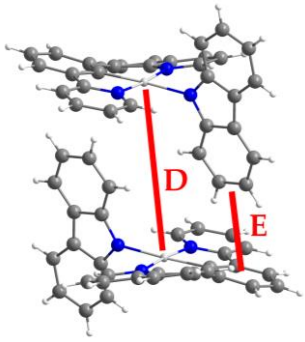
[Pt(PyPhQ)(NC$_{12}$H$_8$)]	
Interplanar torsion angles (°)	
A (pyridine-phenyl)	5.328(1)
B (phenyl-quinoline)	20.599(9)
C (carbazole-pyridine)	77.217(7)
Shortest distances (Å)	
D (metal-metal)	7.1153(5)
E (carbazole-phenyl)	3.5251(5)

Figure 76 Selected ring torsion angles (A,B, C) and distances (D, E) for the complex [Pt(PyPhQ)(NC$_{12}$H$_8$)].

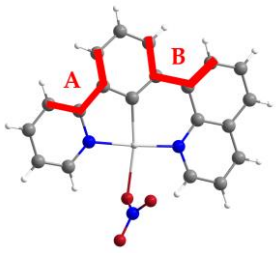	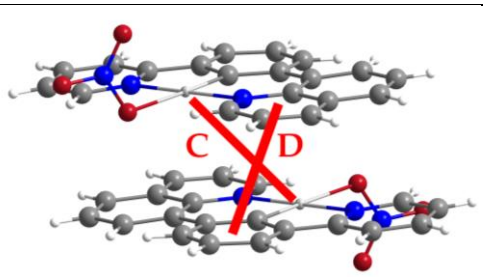
[Pt(PyPhQ)NO$_3$]	
Interplanar torsion angles (°)	
A (pyridine-phenyl)	4.204(2)
B (phenyl-quinoline)	3.757(2)
Shortest distances (Å)	
C (metal-metal)	4.4551(3)
D (quinoline-phenyl)	3.6687(1)

Figure 77 Selected ring torsion angles (A,B) and distances (C, D) for the complex [Pt(PyPhQ)NO$_3$].

Table 31 Selected bond lengths (Å) and angles (°) for complexes of type [M(PyPhQ)X] with various coligands .[a]

Distances (Å)	[Pt(PyPhQ)CN]	[Ni(PyPhQ)NO$_3$]	[Pt(PyPhQ)NO$_3$]	[Pt(PyPhQ)(NC$_{12}$H$_8$)]
M–C	1.982(4)	1.856(2)	1.950(6)	1.967(3)
M–N$_1$	2.022(4)	1.915(1)	2.019(5)	2.024(3)
M–N$_2$	2.040(4)	1.908(1)	2.013(5)	2.036(3)
M–Coligand	2.057(5)	1.995(1)	2.196(4)	2.109(2)
C–N (cyanide)	1.128(6)	-	-	-
Angles (°)				
N$_1$–M–N$_2$	171.0(1)	169.8(5)	176.7(2)	174.3(1)

C–M–Col.	169.1(2)	170.9(6)	170.4(2)	173.2(1)
N_1–M–Col.	92.02(2)	89.06(5)	87.70(2)	91.54(1)
N_2–M– Col.	94.55(2)	93.74(5)	95.45(2)	93.88(1)
N_1–M–C	81.88(2)	84.94(6)	82.90(2)	81.64(1)
N_2–M–C	92.55(2)	93.35(6)	93.90(2)	92.95(1)
Σ angles around M	361.0	361.1	360.0	360.0

[a] From single crystal X-ray diffraction.

Table 32 Selected bond lengths (Å) and angles (°) for complexes of type [M(PyPhQ)X] with various coligands .[a]

Distances (Å)	[Pt(PyPhQ)C_2Ph]	[Pt(PyPhQ)C_2FeCp_2]	[Pt(PyPhQ)$CNBH_3$]
M–C	1.991(4)	1.998(1)	1.962(7)
M–N_1	2.017(4)	2.022(9)	2.017(6)
M–N_2	2.042(4)	2.031(9)	2.039(5)
M–Coligand	2.069(5)	2.070(1)	2.101(6)
C–N ($CNBH_3$)	-	-	1.134(9)
C–B			1.598(1)
B–H	-	-	0.9800
Angles (°)			
N_1–M–N_2	171.3(2)	172.2(4)	173.8(2)
C–M–Col.	169.2(2)	168.8(5)	173.6(3)
N_1–M–Col.	91.72(2)	91.60(4)	91.20(2)
N_2–M– Col.	94.87(2)	94.80(4)	93.80(2)
N_1–M–C	81.97(2)	81.80(4)	83.0(3)
N_2–M–C	92.33(2)	92.50(5)	92.2(3)
Σ angles around M	360.9	360.7	360.2

[a] From single crystal X-ray diffraction.

Coligand exchange is a very useful tool to change specific complex properties in terms of late stage-functionalization. The nitrato-exchange approach is an easy, reliable and efficient method to introduce various pseudo-halogenido type coligands. The optical and electronic properties can be changed depending on the choice of anion introduced. The method can also be extended to previously hard-to-handle coligands like various acetylenes and nitrogen-bearing aromatic systems. These later coligands vary the optical and electrochemical properties as well as the complex crystal structures greatly. They are therefore very interesting for fine-tuning of properties of existing complexes with applications in mind. In catalysis, specific HOMO-LUMO gaps would allow for targeted reactivity. The stabilization of the excited states by strong donors with strong backbonding is beneficial for quantum yields and lifetimes in luminescence applications.

With a desired application in mind, coligand-exchange reactions can be useful in matching and enhancing effects of ring-expanded ligand design previously discussed.

4 Summary

The first ring-expanded ligand systems were generated through exchange of one or two of the pyridine moieties of the prototypical N^C^N type ligand dipyridylbenzene (PyPhPy) with 8-quinolinyl, yielding the symmetric ligand QPhQ and the asymmetric ligand PyPhQ (Figure 78, left and centre). Replacing the peripheral pyridine-moiety of the C^N^N ligand 6-phenyl-2,2′-bipyridine (PhPyPy) with 8-quinolinyl yielded the ligand PhPyQ (Figure 78, right).

Based on these protoligands, complexes of Pt(II), Pd(II) and Ni(II) with halido coligands were synthesized and the results summarized in chapter 3.1. This chapter was published in Organometallics (2025, 44, 7, 847–857, https://doi.org/10.1021/acs.organomet.4c00500).[49]

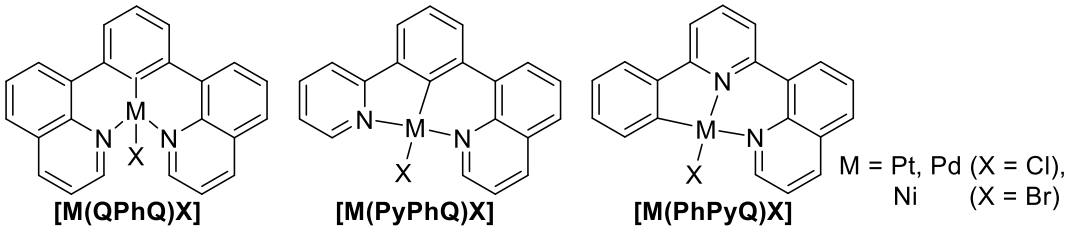

Figure 78 Overview of complexes with ring-expanded ligand systems, featuring the 8-quinolinyl building block.[49]

Ligand systems were built up through *Suzuki*-type cross-coupling reactions using suitable, commercially available building blocks. The complexes were obtained via CH-activation, adapting previously reported methods.[1, 26] The only notable exception was [Ni(QPhQ)Cl], which was synthesized via an oxidative addition route. The complex [Ni(PhPyQ)Br] was obtained but no characterisation was possible due to its inherent instability in solution. The complex rapidly decomposes upon solvation, yielding the protoligand HPhPyQ, pointing to hydrolysis and solvolysis.

Single crystal X-ray diffraction data on these complexes showed their structures to feature pronounced twisting of the ligand backbone around the bonds connecting the aromatic rings. This led to nearly perfectly square planar geometries for [M(QPhQ)X] complexes (N–Pt–N: 177.9(1)° for [Pt(QPhQ)Cl]) at the cost of high interplanar angles of the quinoline-moieties (Q/Q angle: 66.7(8)°). The asymmetric complexes [M(PyPhQ)X] and [M(PhPyQ)X] lie in between [M(QPhQ)X] and the five-membered complexes [M(PyPhPy)X] with bond angles around 170° and lessened interplanar angles of a maximum of 37.9(2)° ([Pt(PhPyQ)Cl].

The increase in ligand field splitting increases from the more square planar coordination and the bigger π-system of quinoline as opposed to pyridine. This is opposed by this loss of coplanarity of the aromatic ligand backbone.

The optical and electrochemical properties of all complexes were studied and DFT calculations were carried out to elucidate orbital compositions (see Figure 79).

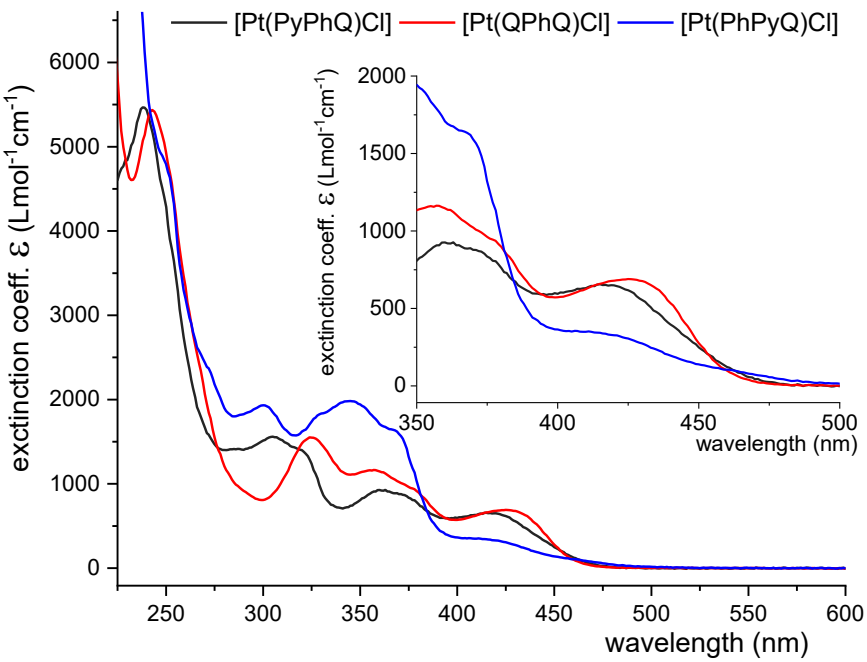

Figure 79 Top: UV/Vis-absorption spectra of [Pt(PyPhQ)Cl] (black), [Pt(QPhQ)Cl] (red) and [Pt(PhPyQ)Cl] (blue) in THF at room temperature.

The symmetric complexes [M(QPhQ)Cl] absorptions undergo a red-shift and show an earlier reduction onset when compared to their five-membered metallacycle derivatives, due to the better donor qualities of the quinoline. The opposite is true for asymmetric complexes [M(PyPhQ)X] and [M(PhPyQ)X]. Here the loss of coplanarity, and conjugation, offsets the strong donor-character of the quinoline and the more square-planar geometry induced by the six-membered chelation. This results in a blueshift of absorptions and negatively shifted reductions.

DFT-calculations confirmed a mostly metal centred HOMO with strong contributions of the coligand and the phenyl ring, while the LUMO is mainly located on the quinoline moiety (see Figure 58). This confirms the long-wavelength absorptions to be of MLCT ^{3}[d(M)–π^*] character. The oxidation potential onsets concur with the trend of energies of the long-wavelength absorption maxima (MLCT Pt < Ni < Pd) and electrochemical HOMO-LUMO energies also matches the one of these long-wavelength absorption maxima.

Luminescence spectroscopy confirmed observations previously made on [Pt(QPhQ)Cl].[18] The asymmetric complex [Pt(PyPhQ)Cl] also showed promising luminescence with emission peaks around 610 nm (see Figure 80) in aerated THF solutions at room temperature. Interestingly, weak luminescence was also observed for [Ni(PyPhQ)Br] under the same conditions. This nickel luminescence should be better detectable by low temperature measurements in degassed solvent or glassy frozen matrices.

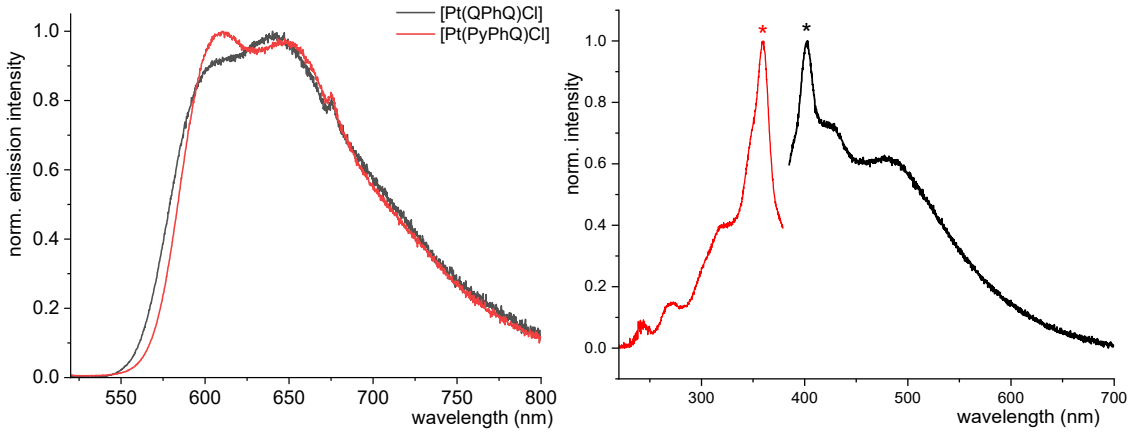

Figure 80 Left: Photoluminescence spectrum of [Pt(QPhQ)Cl] (black), λ_{exc} = 430 nm and [Pt(PyPhQ)Cl] (red), λ_{exc} = 445 nm at 293 K in a THF solution. Right: Photoluminescence excitation (left; red line λ_{em} = 402 nm) and emission (right, black line; λ_{exc} = 360 nm) spectra of [Ni(PyPhQ)Br] at 293 K in a THF solution. Raman peaks stemming from the THF solvent are marked with an *.[49]

To facilitate the synthesis of cyclometalated complexes, microwave reaction conditions were adapted to be applied to the desired ring-expanded complexes (Scheme 33 and table 33).[96, 97]

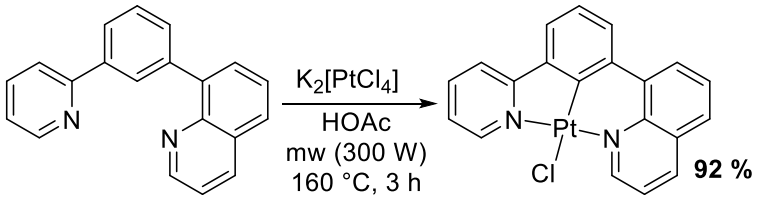

Scheme 33 Synthesis of [Pt(PyPhQ)Cl] using microwave irradiation.

Using the microwave, reaction times were dramatically reduced, making the complexes much more easily accessible. CH-activations have a considerable activation energy that needs to be overcome. Several more methods of introducing these high energies were tested for, including syntheses in glass ampules, ball mill reactions and recently published photoactivation methods (see table).[54] Except for the microwave synthesis, none of these methods yielded the desired results in acceptable yields.

Table 33 Overview of different C–H activation methods towards the synthesis of [Pt(PyPhQ)Cl] as model compound.

Substrates	Method	Conditions	Outcome
$K_2[PtCl_4]$ (1.0 eq.) PyHPhQ (1.4 eq.)	Reflux	HOAc, 160 °C, 96 h	95 % yield
	Microwave	HOAc, 160 °C, 300 W, 3 h	92 % yield
	Ampule	HOAc, Ramping to 150 °C, 72 h	Traces of complex isolated as single crystals [a]
	Photoactivation[54]	Bu_4NCl, Na_2CO_3, acetone, 405 nm r.t., 18 h	Complex formation, impure, not isolated [b]
	Ball mill	HOAc, 15 Hz, 30 min	Decomposition

[a] detected by SC-XRD, [b] detected by ^{1}H NMR-spectroscopy.

Based on the complexes obtained from introduction of the 8-quinolinyl moiety, more ring-expanded N^C^N and C^N^N type complexes were synthesized.[49] These complexes introduce sterically demanding chromophore units mostly based on either carbazole or fluorene, making use of the new ligand design possibilities afforded by the ring-expansion (see Figure 81).

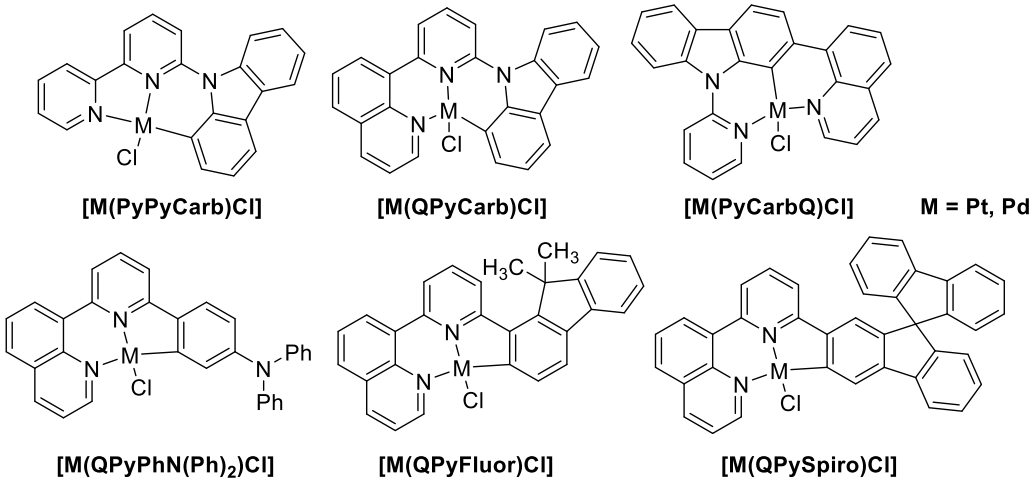

Figure 81 Overview of synthesized complexes with ring-expanded N^C^N or C^N^N ligands.

The ligands were synthesized by subsequent *Suzuki*-couplings or similar reactions. Complexation took place under the previously applied conditions. Detailed conditions are summarized in table 34. Notably, complexation of nickel was not successful, mirroring issues encountered previously for [Ni(PhPyQ)Br].[49]

Table 34 Reaction conditions of CH-activations towards N^C^N and C^N^N type complexes.

Protoligand	Metal precursor	Conditions	Habitus (Yield)
PyPyHCarb	$K_2[PtCl_4]$	HOAc, reflux, 72 h	Dark-orange powder (54%)
	$K_2[PdCl_4]$	HOAc, reflux, 72 h	Yellow powder (72%)
QPyHCarb	$K_2[PtCl_4]$	HOAc, reflux, 72 h	Orange powder (22%)
	$K_2[PdCl_4]$	MeCN/H_2O, 18 h	Yellow powder (22%)
PyHCarbQ	$K_2[PtCl_4]$	HOAc, reflux, 18 h	Orange powder (59%)
	$K_2[PdCl_4]$	HOAc, reflux, 42 h	Yellow powder (39%)
	$NiBr_2$	*p*-xylene, KOAc/K_2CO_3, reflux, 72 h	No conversion
QPyHPhN(Ph)$_2$	$K_2[PtCl_4]$	HOAc, reflux, 18 h	Decomposition
QPyHFluor	$K_2[PtCl_4]$	HOAc, reflux, 21 h	Orange powder (91%)
	$K_2[PdCl_4]$	HOAc, reflux, 21 h	Yellow powder (34%)
	$NiBr_2$	*p*-xylene, KOAc/K_2CO_3, reflux, 72 h	No conversion
PyHSpiro	$K_2[PtCl_4]$	HOAc, reflux, 23 h	Orange powder (99%)
	$K_2[PdCl_4]$	HOAc, reflux, 21 h	Yellow powder (51%)

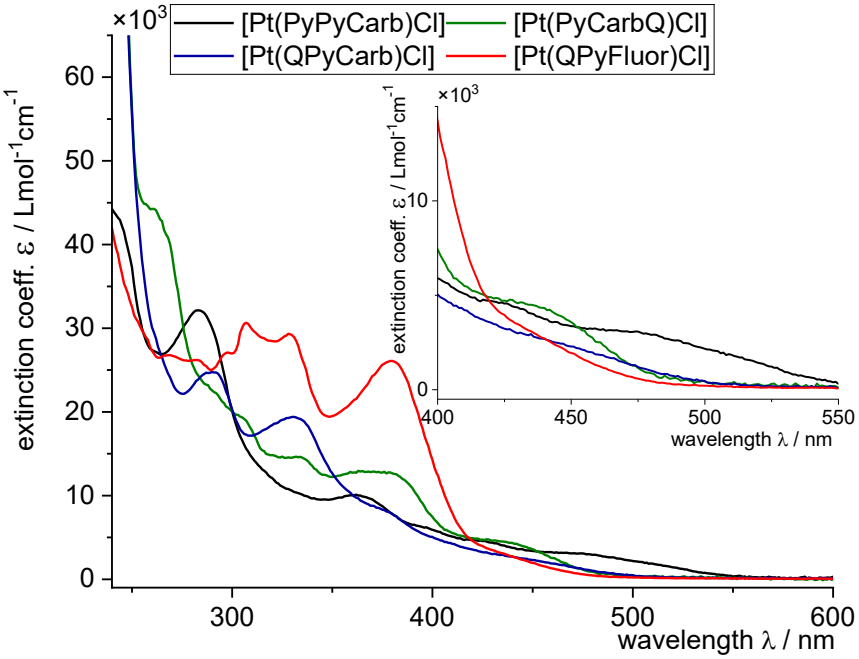

Figure 82 UV/Vis-absorption spectra of complexes with ring-expanded N^C^N and C^N^N type ligands containing carbazole- or fluorene-derived chromophores. Measured in THF at room temperature.

The absorption spectra show strong absorptions between 240-350 nm, that can be attributed to π-π* and n-π* transitions, with distinct LMCT/LL'CT absorption bands not present in the protoligands (e.g. [M(PyCarbQ)Cl], indicating significant contributions of the carbazole moiety to the LUMO. Complexes with fluorene-derived ligands show pronounced blue-shifts with broad absorption maxima at 343 nm ([Pd(QPyFluor)Cl] and 379 nm ([Pt(QPyFluor)Cl] compared to the [M(PyPhQ)Cl] complexes they're derived from, suggesting strong metal-fluorene interactions, affecting the MLCT transitions.

The reduction potentials of the complexes suggest the fluorene units have little to no effect on the electrochemistry of the complexes, with the potentials being very similar to other N^C^N complexes with the Py-Q unit (see Figure 83; compare chapter 3.1).[49]

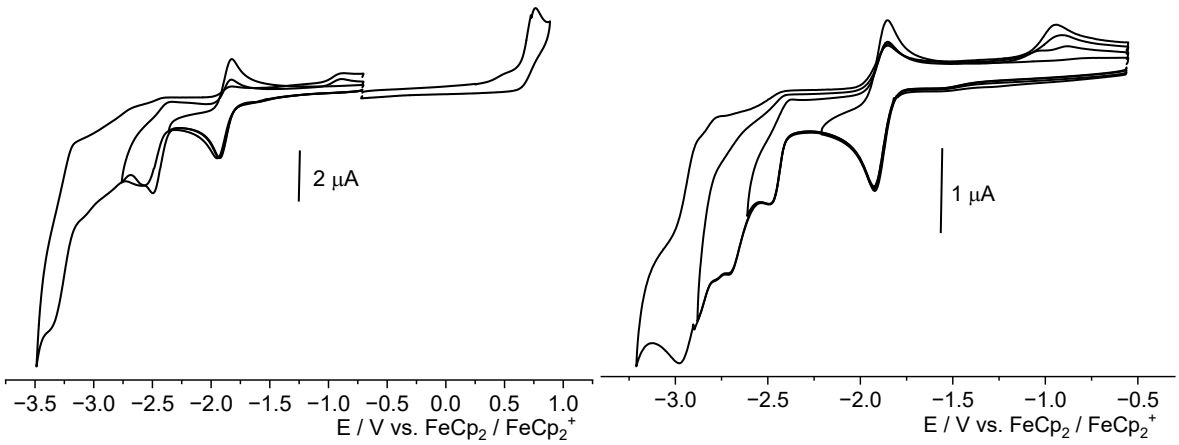

Figure 83 Cyclic voltammograms of [Pt(QPyCarb)Cl] (left) and [Pt(QPyFluor)Cl] (right), measured in THF with 0.1 M NBu_4PF_6, referenced to $FeCp_2/FeCp_2^+$.

Cyclometalation at the carbazole moiety in [Pt(PyPyCarb)Cl] shifts its oxidation to the lowest potential observed (0.51 V), with the smallest HOMO-LUMO gap (2.42 V), making it a strong σ-donor. When the cyclometalated carbazole is in *trans* position to a quinoline unit (e.g. [Pt(QPyCarb)Cl], higher oxidation potentials (0.76 V) are observed, indicating competition and marking quinoline as a stronger donor than pyridine.

Structural analysis revealed significant distortion of carbazole-containing ligand backbones, with interplanar angles up to 48.73° for [Pd(QPyCarb)Cl], while retaining close to perfectly square planar coordination geometries (see Figure 84). These strong distortions break up the conjugation significantly, implying more localized LUMO levels on the chromophore units, helping to explain observation made in UV/Vis-absorption spectroscopy.

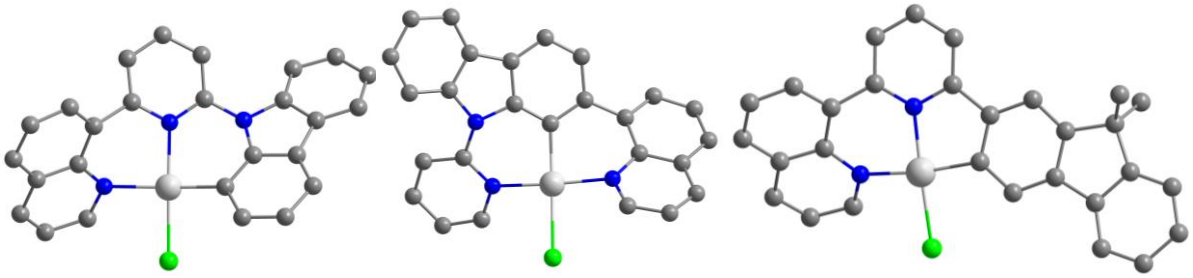

Figure 84 Molecular structures of [Pd(QPyCarb)Cl] (left), [Pd(PyCarbQ)Cl] (middle) and [Pt(QPyFluor)Cl] from single crystal X-ray diffraction (hydrogens omitted for clarity).

All complexes feature head-to-tail stacking (3.6 Å, closest Q-Q contact) with the bulky fluorene-derivative containing units being on opposing ends of the packing pairs. This leads to voids withing the crystal packing, not observed for the carbazole-based systems.

Ring-expanded nitrogen donors were exchanged for sulphur or oxygen containing moieties. The same reaction conditions previously used successfully yielded the desired protoligands. Complexation was successful under the conditions detailed in table 35, yielding the desired complexes (see Figure 85).

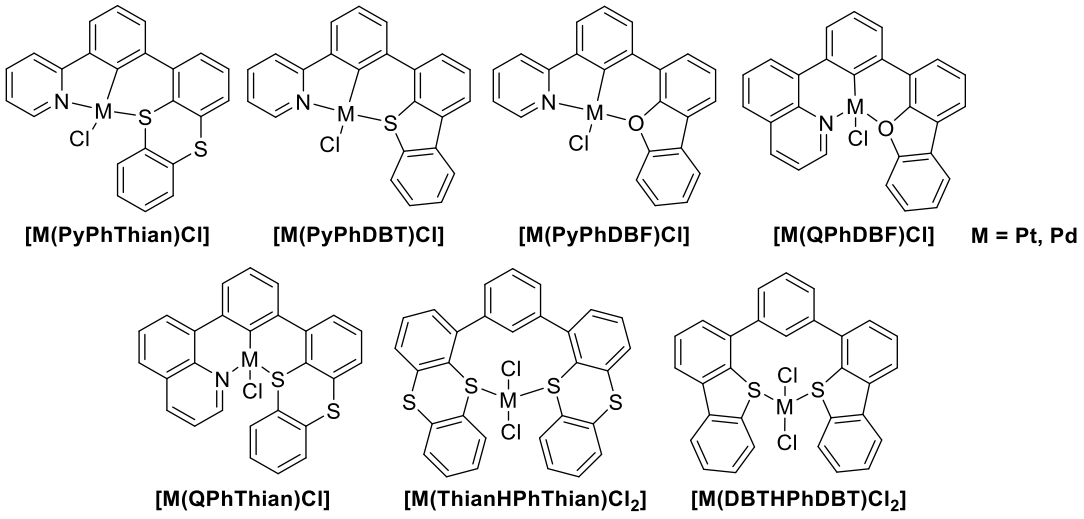

Figure 85 Overview of obtained Complexes of N^C^S, S^S or N^C^O type.

The only exception to this were the S^S type complexes [M(ThianHPhThian)Cl_2] and [M(DBTHPhDBT)Cl_2], that did not undergo cyclometalation. Instead, a precoordinated type of complex was isolated.

Table 35 Reaction conditions of complexation reactions of all N^C^S, S^S or N^C^O type complexes.

Protoligand	Metal precursor	Conditions	Habitus (Yield)
PyHPhThian	$K_2[PtCl_4]$	HOAc, reflux, 21 h	Yellow Powder (62%)
	$K_2[PdCl_4]$	HOAc, reflux, 16 h	Yellow Powder (45%)
	$NiBr_2$	KOAc, K_2CO_3, *p*-xyl., 2 h	No conversion
QHPhThian	$K_2[PtCl_4]$	HOAc, reflux, 16h	Dark orange powder (14%)
	$K_2[PdCl_4]$	HOAc, reflux, 72h	Light green powder (77%)
PyHPhDBT	$K_2[PtCl_4]$	HOAc, reflux, 16h	Yellow Powder (63%)
	$K_2[PdCl_4]$	HOAc, reflux, 18h	Yellow Powder (43%)
PyHPhDBF	$K_2[PtCl_4]$	HOAc, reflux, 44h	Yellow Powder (27%)
	$K_2[PdCl_4]$	HOAc, reflux, 22h	Yellow Powder (38%)
	$NiBr_2$	KOAc, K_2CO_3, *p*-xyl., mw (300 W), 5h	No conversion
QHPhDBF	$K_2[PtCl_4]$	HOAc, reflux, 3h	Orange Powder (48%)
	$K_2[PdCl_4]$	HOAc, reflux, 19h	Green Powder (56%)
ThianHPhThian	$K_2[PtCl_4]$	HOAc, reflux, 2h	Dark brown powder (59%)
DBTHPhDBT	$K_2[PtCl_4]$	HOAc, reflux, 22h	Grey powder (57%)

NMR studies of the dibenzofuran containing complexes showed poor signal-to-noise ratio, suggesting poor coordination of the oxygen donors and potential exchange with coordinating solvent molecules (e.g. THF, DMSO).

UV/Vis-absorption spectroscopy revealed a strong red shift of the MLCT-bands for the sulphur containing [M(PyPhThian)Cl] complexes, leading to smaller HOMO-LUMO gaps when compared to their [M(PyPhQ)Cl] counterparts (see Figure 86).

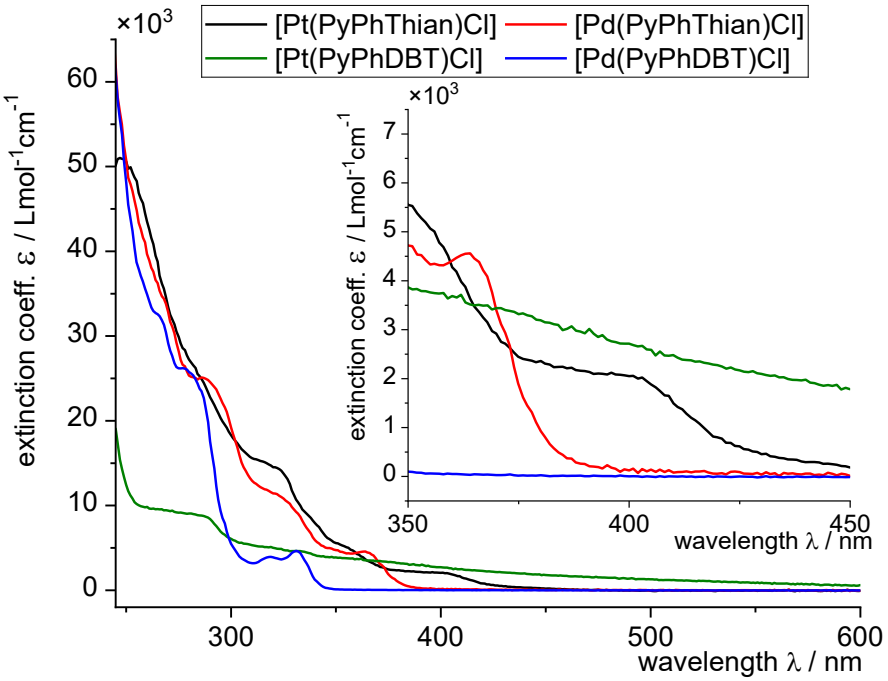

Figure 86 UV/Vis-absorption spectra of N^C^S type complexes, measured in THF at room temperature.

This marks the thianthrene units as stronger donors compared to quinoline. The lack of long wavelength MLCT-absorption bands for the S^S type complexes further suggest the lack of cyclometalation. The poor solubility of DBT- or DBF- containing complexes, especially with QHPhDBT or QHPhDBF ligands lead to pronounced absorption ramping. Similar problems were encountered for these complexes when carrying out cyclovoltammetry. The thianthrene bearing complexes exhibited reductions like their N^C^N counterparts, with their LUMO situated on the same pyridine-phenyl subunit (see Figure 87). Additional oxidations at the non-coordinating sulphur atom can take place, as confirmed by DFT-calculations.

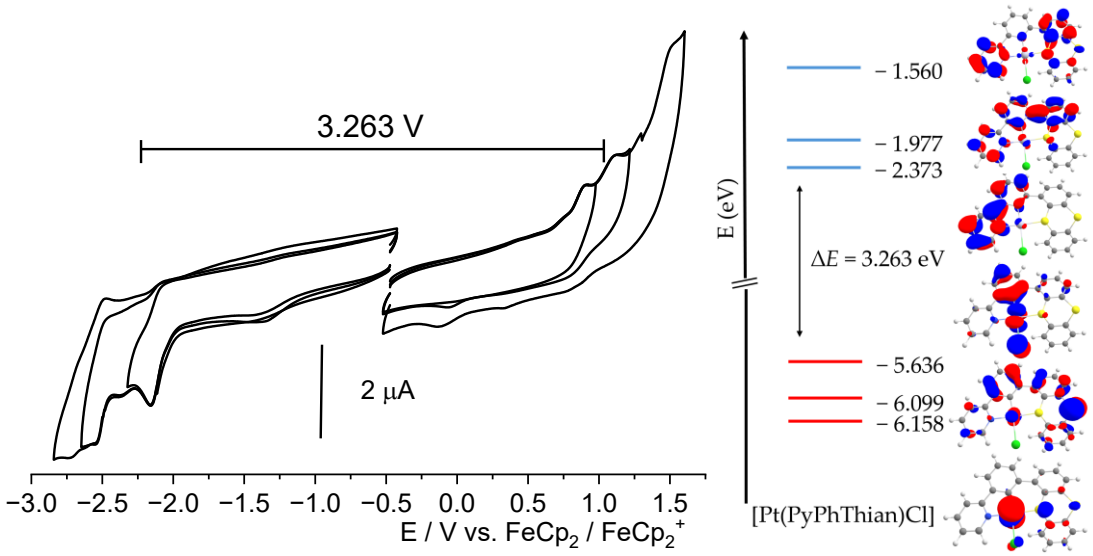

Figure 87 Left: Cyclic voltammograms of [Pt(PyPhThian)Cl] (left), measured in THF with 0.1 M NBu_4PF_6, referenced to $FeCp_2/FeCp_2^+$. Right: DFT-calculated composition and energies of selected molecular orbitals of [Pt(PyPhThian)Cl]. HOMO levels (red bars); LUMO levels (blue bars) (Isovalue 0.03, TPSSh/def2-TZVP/CPCM(THF)) level of theory.

The structures of [M(PyPhThian)Cl] reveal a strong bend of the thianthrene unit within the ligand backbone (Pt: 98.84(1)°, Pd: 98.65(9)°) and significantly longer M–S bond lengths (Pt: 2.213(6) Å, Pd: 2.211(5) Å) compared to the M–N bond lengths (Pt: 2.034(2) Å, Pd: 2.042(2) Å) (see Figure 88). The ligand backbone of [M(PyPhThian)Cl] feature less distortion (max. interplanar angle: 14.56(3)°), while these angles increase for [Pt(PyPhDBT)Cl] (max. interplanar angle: 23.50(1)°).

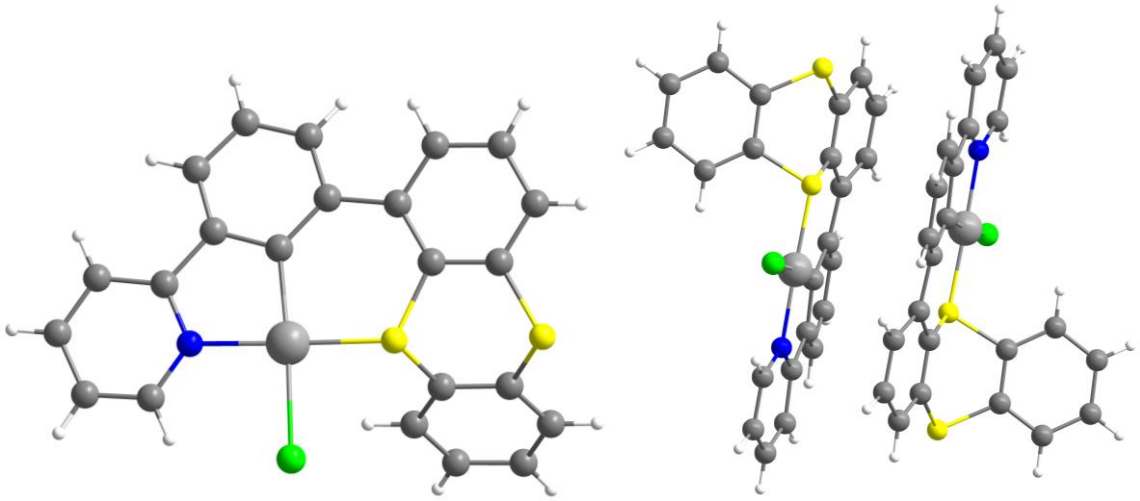

Figure 88 Molecular structures (left) and stacking of complex [Pt(PyPhThian)Cl] (right), from single crystal X-ray diffraction.

Attempts to synthesize complexes of [M(PyPyNaph)Cl] type resulted in either activation at different positions of the ligand or partial roll-over cyclometalation, giving isomer mixtures. To circumvent this, the [M(PyPyAnth)Cl] system was synthesized instead, where the two potential activation sites are chemically equivalent. While initial synthesis of the [Pd(PyPyAnth)Cl] complex was successful, subsequent reactions yielded product mixtures of the cyclometalated and precoordinated product (see Scheme 34).

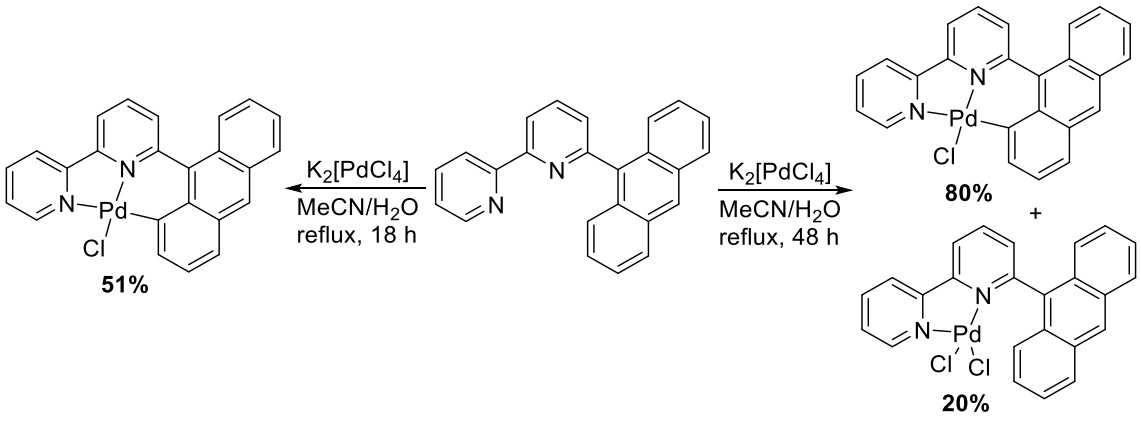

Scheme 34 Different reactions conditions and their diverging results in the synthesis of [Pd(PyPyAnth)Cl].

The obtained sample of cyclometalated complex [Pd(PyPyAnth)Cl] showed a very strong orange colour, which is reflected in a distinct, very broad absorption band with a maximum at around 502 nm (see Figure 89). The cyclic voltammetry shows reversible reduction

behaviour typical for the bipyridine unit and a palladium oxidation potential (Ox 1: 0.62 V) significantly lower than its related compound [Pd(PhPyPy)Cl] (Ox 1: 0.80 V). This implies the anthracene moiety to be a stronger σ-donor compared to phenyl, raising HOMO levels and facilitating metal-centred oxidation.[81]

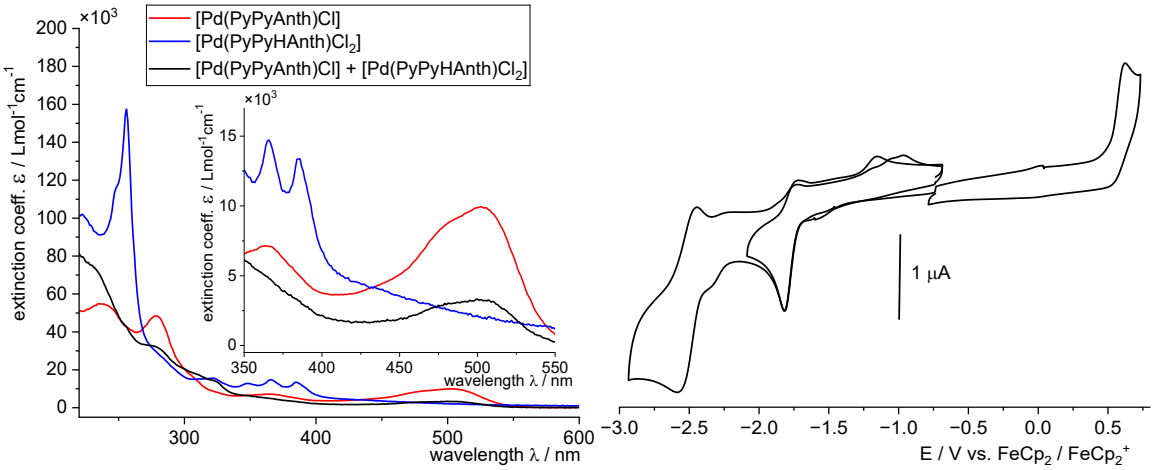

Figure 89 Left: UV/Vis-absorption spectra of complexes derived from the PyPyHAnth protoligand. Measured in THF at room temperature. Right: Cyclic voltammogram of [Pd(PyPyAnth)Cl] (right), measured in THF with 0.1 M NBu_4PF_6, referenced to $FeCp_2/FeCp_2^+$.

Irradiation of [Pd(PyPyAnth)Cl] samples in $CDCl_3$ with visible range white LED light caused a discoloration of the sample. Structural analysis of the resulting species revealed a reaction with oxygen. Triplet-singlet interconversion followed by intramolecular addition took place, leading to an endoperoxide species (see Scheme 35). Subsequent hydrolysis yields an open oxanthrone-containing species.

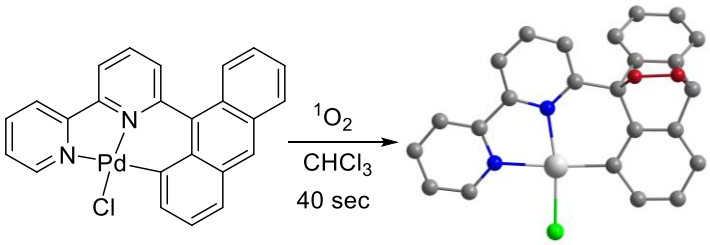

Scheme 35 Reaction yielding [Pd(PyPyAnthO_2)Cl] with molecular structure (right) from single crystal X-ray diffraction (hydrogen atoms omitted for clarity).

In future, the synthesis of the pure cyclometalated complex needs to be refined further, to then be able to study the reactivity of [Pd(PyPyAnth)Cl] with oxygen in more detail.

Coligand exchange reactions were carried out by reacting [M(PyPhQ)Cl] with silver nitrate, yielding [M(PyPhQ)NO_3] (see Scheme 36). The nitrato coligand was then systematically exchanged under mild conditions, by addition of coligand salts in solution at room temperature.

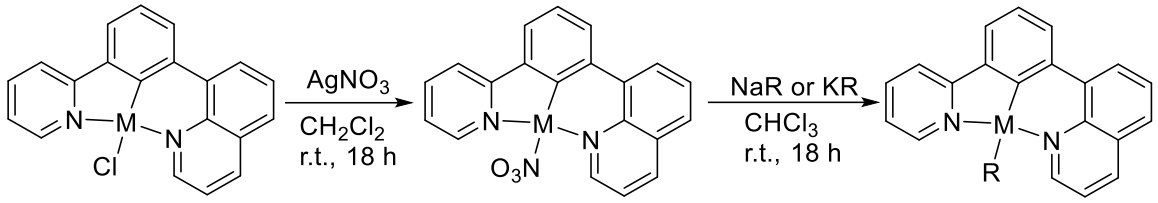

Scheme 36 General reaction Scheme for coligand exchange reactions starting from [M(PyPhQ)NO_3].

Using this approach a variety of new coligands were introduced in good yields (see Figure 90, table 36). During these reactions, care had to be taken to avoid excess free halogenide ions is solution, which would otherwise react to form [M(PyPhQ)X].

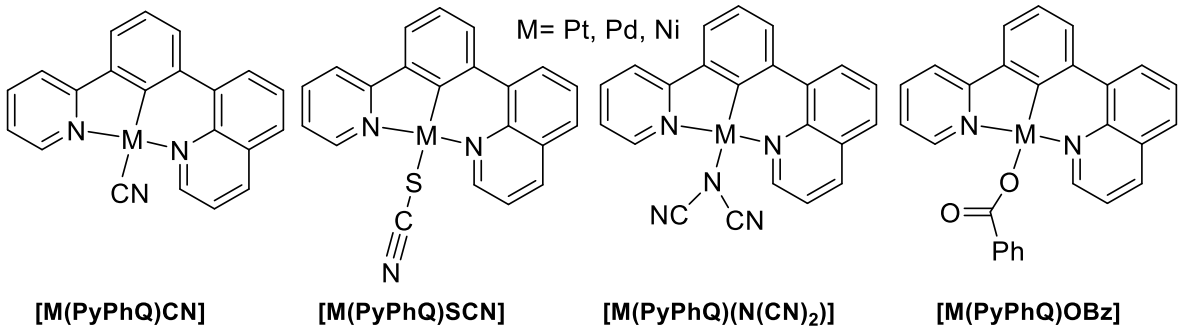

Figure 90 Overview of all complexes obtained from coligand exchange reactions starting from [M(PyPhQ)NO_3] (compare table 36).

Table 36 Reaction conditions for coligand exchange reactions of complexes [M(PyPhQ)NO_3] and [M(PyPhQ)X] type.

Starting complex	Reagent	Conditions	Yield
[Pt(PyPhQ)Cl]	$AgNO_3$	CH_2Cl_2, r.t., 18 h	[Pt(PyPhQ)NO_3], 86%
[Pd(PyPhQ)Cl]		CH_2Cl_2, r.t., 18 h	[Pd(PyPhQ)NO_3], 76%
[Ni(PyPhQ)Br]		$CHCl_3$, r.t., 24 h	[Ni(PyPhQ)NO_3], 57%
[Pt(PyPhQ)NO_3]	KOBz	$CHCl_3$, r.t., 18 h	[Pt(PyPhQ)OBz], 74%
	KCN	$CHCl_3$, r.t., 18 h	[Pt(PyPhQ)CN], 71%
	NaSCN	$CHCl_3$, r.t., 18 h	[Pt(PyPhQ)SCN], 65%
	$Na(N(CN)_2)$	$CHCl_3$, r.t., 18 h	[Pt(PyPhQ)$(N(CN)_2)$], 91%
[Pd(PyPhQ)NO_3]	KOBz	THF, r.t., 18 h	[Pd(PyPhQ)OBz], 45%
	KCN	$CHCl_3$, r.t., 18 h	[Pd(PyPhQ)CN], 39%
	NaSCN	$CHCl_3$, r.t., 18 h	[Pd(PyPhQ)SCN], 55%
	$Na(N(CN)_2)$	$CHCl_3$, r.t., 18 h	[Pd(PyPhQ)$(N(CN)_2)$], 62%
[Ni(PyPhQ)NO_3]	KCN	$CHCl_3$, r.t., 18 h	[Ni(PyPhQ)CN], 78%
	NaSCN	$CHCl_3$, r.t., 18 h	[Ni(PyPhQ)SCN], 47%
	$Na(N(CN)_2)$	$CHCl_3$, r.t., 20 h	[Pd(PyPhQ)$(N(CN)_2)$], 16%

The same methodology was then applied to more sensitive acetylene- or pyrrole-derived anions, prepared from a halogen-free, ammonia-based synthesis. The reactivity remained similar, yielding the desired compounds (see Figure 91 and table 37).

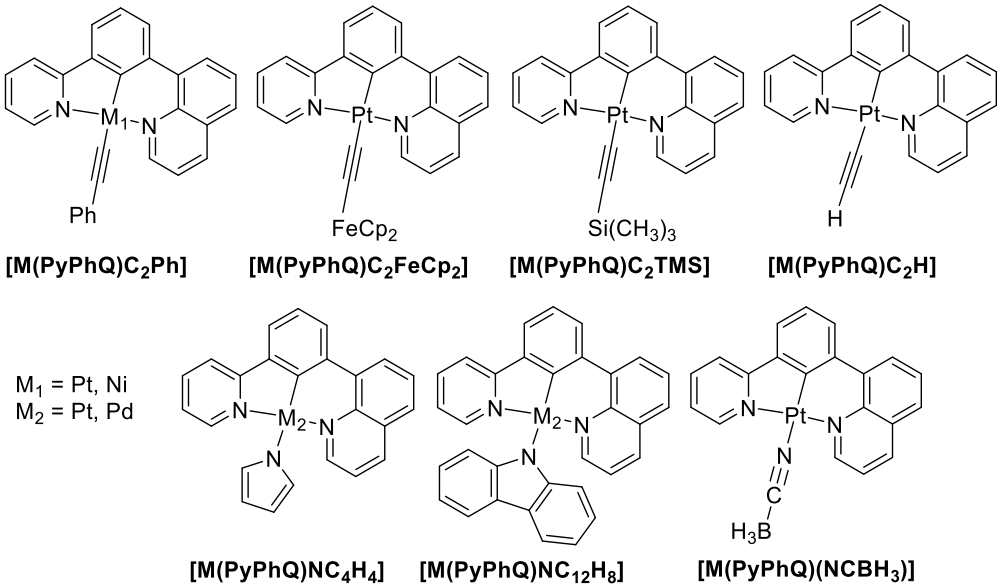

Figure 91 Overview of all complexes obtained from coligand exchange reactions using the ammonia-based synthetic approach (compare table 37).

Table 37 Reaction conditions for coligand exchange reactions of complexes [M(PyPhQ)R] with salts from the ammonia-based synthetic approach.

Starting complex	Reagent	Conditions	Yield
[Pt(PyPhQ)NO3]	NaC_2Ph	THF, r.t., 18 h	[Pt(PyPhQ)C_2Ph], 28%
	NaC_2FeCp_2	THF, r.t., 24 h	[Pt(PyPhQ)C_2FeCp_2], 70%
	NaC_2TMS	THF, r.t., 3 h	[Pt(PyPhQ)C_2TMS], 47%
	$Na(NC_4H_4)$	THF, r.t., 18 h	[Pt(PyPhQ)(NC_4H_4)], 97%
	$Na(NC_{12}H_8)$	THF, r.t., 18 h	[Pt(PyPhQ)$(NC_{12}H_8)$], 34%
	$Na(NCBH_3)$	THF, r.t., 24 h	[Pt(PyPhQ)$(NCBH_3)$], 56%
[Pd(PyPhQ)NO3]	$Na(NC_4H_4)$	THF, r.t., 18 h	[Pd(PyPhQ)(NC_4H_4)], 99%
	$Na(NC_{12}H_8)$	THF, r.t., 18 h	[Pd(PyPhQ)$(NC_{12}H_8)$], 36%
[Ni(PyPhQ)NO3]	NaC_2Ph	THF, r.t., 10 min	[Ni(PyPhQ)C_2Ph], 11%

Exchange of the chloride for electron-withdrawing coligands like thiocyanate or cyanides results in blue-shifts of the MLCT-absorption bands, suggesting reduced energies of the metal-centred HOMO (see Figure 92). The opposite is true for acetylide-containing coligands, were the strong σ-donor character causes red-shift of the MLCT-absorption bands. Nitrogen-containing coligands feature intense and structured absorptions, indicating LL'CT or LMCT character.

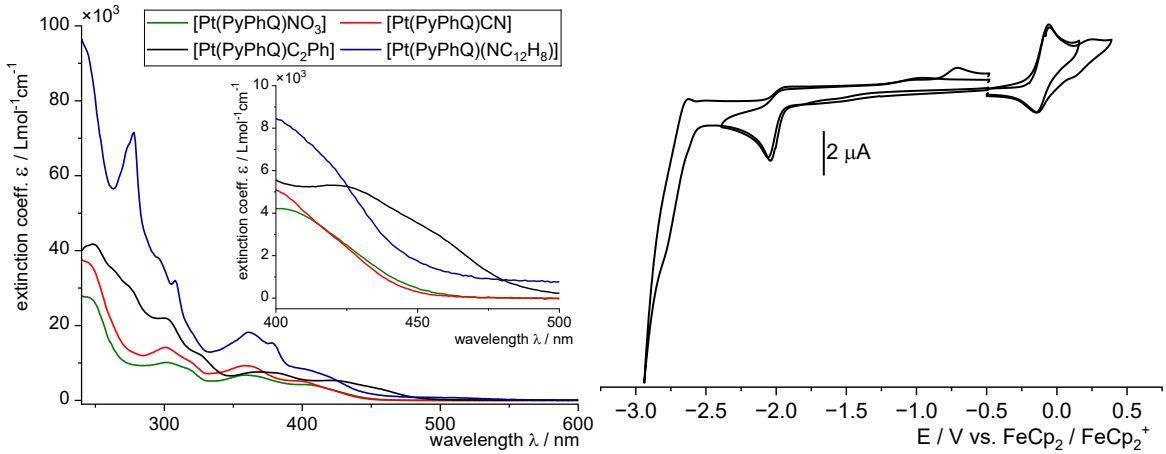

Figure 92 Left: UV/Vis-absorption spectra of [M(PyPhQ)X] with various coligands, measured in THF at room temperature. Right: Cyclic voltammogram of [Pt(PyPhQ)C$_2$FeCp$_2$], measured in THF with 0.1 M NBu$_4$PF$_6$, referenced to FeCp$_2$/FeCp$_2^+$.

The redox chemistry is characterized by a general negative shift of reduction potentials of all coligand-exchanged complexes compared to [M(PyPhQ)NO$_3$]. This implies a direct contribution of the coligands to the electrochemical processes, for example the coligand cleavage in an EC mechanism. Metal centred oxidation potentials decrease with electron-donating coligands (e.g. OBz$^-$, C$_2$Ph$^-$), while electron-withdrawing coligands (CN$^-$, N(CN)$_2^-$) have the opposite effect. [Pt(PyPhQ)C$_2$FeCp$_2$] exhibits a unique reversible oxidation, indicating independent electrochemistry of the ferrocene coligand and the platinum centre.

Crystal structure data of coligand-exchanged complexes consistently show head-to-tail stacking of complex pairs. Structures of [M(PyPhQ)NO$_3$] show much less pronounced distortion of the ligand backbone (max angle: 4.204(2)°) than their counterparts [M(PyPhQ)Cl] (see Figure 93). Strong distortion is found for [Pt(PyPhQ)C$_{12}$H$_8$], with the carbazole having an 77.217(7)° interplanar angle to the ligand backbone. This speaks for an LMCT rather than LL'CT character of its distinct absorptions.

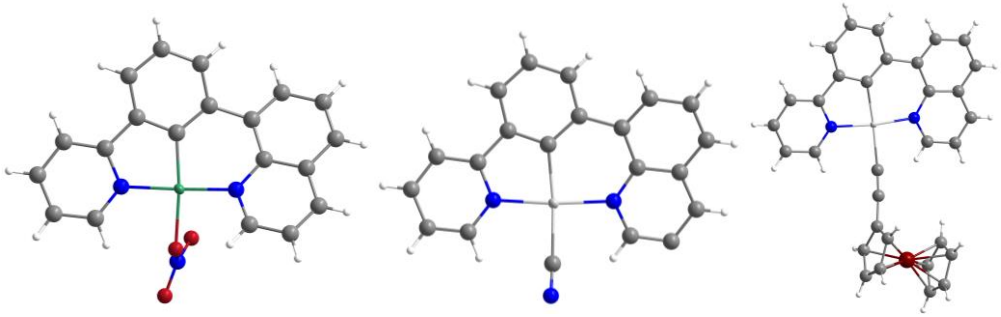

Figure 93 Molecular structures of [Ni(PyPhQ)NO$_3$] (left), [Pt(PyPhQ)CN] (middle) and [Pt(PyPhQ)C$_2$FeCp$_2$] (right) from single crystal X-ray diffraction.

[Pt(PyPhQ)CN] features the shortest metal-coligand distance of 2.057(5) Å, shortened by M–π* backbonding, also explaining the strong shifts visible in both absorption spectra and cyclic voltammetry. Similar backbonding effects can also be seen for [Pt(PyPhQ)(NCBH$_3$)].

Overall, coligand exchange reactions are a potent method to significantly influence the properties of a complex. Strong shift in both absorptions and electrochemical potentials make this a suitable method to fine-tune a specific system towards a desired application. Combining the varying ring-expanded ligand systems of previous chapters with specific coligand exchanges could help expand the potential application of these complexes greatly.

5 Conclusions and Outlook

Square planar Pt(II), Pd(II) and Ni(II) complexes [M(L)X] with ring-expanded, tridentate, cyclometalated (N^C^N or C^N^N type) ligands were synthesized through direct C–H-activation methods. The ring-expansion has a notable impact on coordination geometry of the resulting complexes. The six-membered metallacycles enlarge the bite angles of the donor moieties to the metal ions, bringing the complex geometry closer to perfectly square planar. For asymmetric 5^6-membered complexes (e.g. [M(PyPhQ)Cl), Py = pyridyl, Ph = phenyl, Q = 8-quinolinyl)) angles of ~170° were found, ~180° for symmetric 6^6-membered complexes (e.g. [M(QPhQ)Cl]). The increase in ligand field splitting is offset by the loss of coplanarity and conjugation in the ligand backbone. This results in very different UV/Vis-absorption spectra and electrochemistry when compared to their derivatives with the established N^C^N or C^N^N ligands, producing only five-membered metalacyclic binding. The specific effects induced by the ring-expansion depends strongly on the ligand, making predictions of the resulting complex properties difficult.

Introducing sulphur or oxygen donor atoms into the ligands resulted in smaller HOMO-LUMO gaps due to increased donor strength, but at the cost of loss of solubility and weak coordination in the case of oxygen-donor complexes.

Coligand exchange reactions were carried out in a systematic way using the [M(PyPhQ)NO_3] complexes as intermediates. Electron-donating σ-donors, like acetylide-derived coligands, increase metal-centred HOMO energies, causing red-shifts of absorptions and smaller oxidation potentials. The opposite is true for coligands like cyanides, showing pronounced blue-shifts and larger oxidation potentials, indicating even larger ligand field splitting and larger HOMO-LUMO gaps.

The complexes with ring-expanded 6^6-membered ligands seem to be most suitable towards potential luminescence application, maximizing the ligand field splitting achieved by the unique geometry of the six-membered metallacycles. The strong distortion from coplanarity of the ligand backbones might cause undesired non-radiative decay. To compensate for this, the ligands should feature strong donors to maximize on ligand field splitting. This could be either achieved through incorporation of strong donor functions into the tridentate ligands or by introduction of strong donor coligand (e.g. phenylacetylene, pyrrole) into existing 6^6-membered complexes. The complexes with 5^6-membered ligands have the potential to strike the balance between the increase in ligand field splitting afforded by the six-membered metallacycle and the retention of coplanarity between the aromatic rings forming the five-membered metallacycle. This can be further exploited by rigidifying the five-membered metallacycle, for example by synthesizing phenanthroline-like systems.

The synthetic methods for Ni(II) need to be revised, since many of the ligands did not undergo CH-activation under the applied conditions. Nickel complexes would benefit the most from

the increase in ligand field strength caused by the ring-expansion and remains an interesting target.

Finally, pushing the coligand exchange method towards even stronger donors (e.g. pentafluorophenylacetylene) could increase ligand field splitting even further and improve on the exhibited luminescent properties.

6 Experimental Section

6.1 Materials and Syntheses

Chemicals and Materials. All commercially available chemicals were purchased from *ACROS*, *ABCR*, *Alfa Aesar*, *BLD Pharm*, *Sigma Aldrich* or *TCI* and used without further purification. Dry tetrahydrofuran (THF) was distilled over a Na/K alloy (3:7) and dry *p*-xylene was distilled over sodium metal prior to use. All other solvents were provided by *Fischer chemical* in HPLC or LCMS grade and used without further purification or drying, if not specified otherwise. Oxygen and moisture sensitive reactions were carried out using Schleck-technique under argon gas by *Linde* (99.998%).

Microwave Reactions. Reactions using microwave irradiation were carried out on a *CEM* Discover 2.0 microwave (*CEM*, Kamp-Lintfort, Germany) in pyrex reaction tubes (35 mL) with non-crimped teflon-coated pop-on lids. A pressurised seal was provided by an automated lid with a safety pressure limit of 20.7 bar. Upon completion, reactions were cooled using an external nitrogen gas stream until 50 °C were reached, upon which pressure was release and the reaction vessel unsealed. Detailed reaction conditions and irradiation energies (W) are specified in the experimental procedures.

NMR Spectroscopy. ^{1}H, ^{13}C and ^{195}Pt NMR spectra were measured on a *Bruker* Avance II 300 MHz (^{1}H: 300 MHz, ^{13}C: 75 MHz) with a double resonance (BBFO) 5 mm observe probe head with z-gradient coil, a *Bruker* Avance Neo 400 MHz (^{1}H: 400 MHz, ^{13}C: 101 MHz) with 2 frequency channels and iProbe BBFO 5 mm probe head, a *Bruker* Avance III 500 MHz (^{1}H: 500 MHz, ^{13}C: 126 MHz) and *Bruker* Avance II 600 MHz spectrometer (^{1}H: 600 MHz, ^{13}C: 151 MHz, ^{195}Pt: 129 MHz) with a triple resonance (TBI) 5 mm inverse probe head with z-gradient coil using a triple resonance (*Bruker*, Rheinhausen, Germany). Spectra were referenced to tetramethylsilane as internal standard (δ = 0.00 ppm). 2D experiments (^{1}H ^{1}H COSY, ^{1}H ^{13}C HSQC, ^{1}H ^{13}C HMBC, ^{1}H ^{195}Pt HMBC) were carried out for signal assignments using a standard *Bruker* pulse sequence. The multiplicity of signals is given as follows: singlet “s”, doublet “d”, triplet “t”, quartet “q”, quintet “quint” and multiplet “m” for proton signals, “CH” and “Cq” for carbon signals. Combinations of multiplicities are given as combinations of these descriptors (e.g. ”dd”: doublet-doublet). If signals have equivalent chemical shifts, their double

naming will be marked accordingly (e.g.H1, H1’). Data was interpreted and visualized using MestReNova v12.0.0.[131]

Mass Spectroscopy. High resolution electrospray ionization (HR-ESI) spectra were collected using a *Thermo Scientific* LTQ OrbitrapXL mass spectrometer with a FTMS Analyzer and an ionization energy of 70 eV. Simulations were performed using ISOPRO 3.0. High resolution electron ionization (HR-EI) spectra were collected using a *Thermo Scientific* Exactive GC Orbitrap analyser mass spectrometer or a *Finnigan* MAT 95 spectrometer with an ionization energy of 70 eV (*Thermo Fisher Scientific GmbH*, Dreieich, Germany; *Finnigan Instrument Corporation*, Bremen, Germany). Complexes were dissolved in DMSO/MeOH mixtures prior to injection and measured using direct inlet methods. Simulations were performed using

ISOPRO 3.0. Gas chromatography with electron impact ionization was performed on an *Agilent Hewlett Packard 6890* system with a HP 5973 detector. The column used was a *Macherey-Nagel* Optima 5 MS Accent capillary column (30 m x 0.25 mm), using hydrogen as carrier gas. Electron impact ionization at 70 eV was used. The heating program used was method 50300M (50 °C for 2 min, heat ramp 25 °C /min up to 300 °C, 300 °C for 5 min, 320 °C for 5 min).
Elemental Analysis. Elemental analyses were carried out on a *HEKAtech* CHNS EuroEA 3000 analyser (*HEKAtech*, Wegberg, Germany).
Single Crystal X-Ray diffractometry and crystal structure determination. Singe crystal X-Ray diffraction was carried out on a *Bruker* D8 Venture with a *Bruker* Photon 100 CMOS detector at 100 K using Mo-Kα radiation (λ = 0.71073 Å). Crystal data was collected and multi-scan absorption correction applied using APEX3 v2015.5-2[132] with SAINT[133] and SADABS.[134] The structures were solved in OLEX2 v1.5[135] by intrinsic phasing methods using SHELXT (*Sheldrick* 2015)[136] and structural refinement was carried out with SHELXL 2015[137] with full-matrix least-squares methods on $F_0^2 \geq 2\sigma(F_0^2)$. Non-hydrogen atoms were refined with anisotropic displacement parameters without any constraints. The hydrogen atoms were added by suitable riding models. Illustrations of crystal structures were made in Diamond v4.2.[138] The data of structural solutions and refinements of published crystals is available at the Cambridge Crystallographic Data Centre (CCDC) via https://summary.ccdc.cam.ac.uk/.
UV/Vis-absorption spectroscopy. UV/Vis-absorption spectra were measured on a *Varian Cary* 60 spectrophotometer (Varian Medical Systems, Darmstadt, Germany) at ambient temperature in quartz glass cuvettes (optical pathlength = 1cm). All spectra were baseline corrected.
Luminescence Spectroscopy. Luminescence measurements were carried out on a FLS1000 Photoluminescence spectrometer (*Edinburgh Instruments Ltd*, Livingston, United Kingdom) containing a 450 W xenon arc lamp with a *Czerny-Turner* monochromator and a PMT900 detector. Data was evaluated using OriginPro version 2025.[139]
Cyclic Voltammetry. Cyclovoltammetric measurements were carried in a 0.1 M nBu$_4$NPF$_6$ solution in degassed THF at a scan rate of 100 mV/s. A three-electrode setup was used, with a glassy carbon working electrode, platinum counter electrode and Ag/AgCl pseudo-reference. Currents were applied by an *Autolab* PGSTAT30 or µStat400 potentiostat by *Metrohm* (*Metrohm*, Filderstadt, Germany) were used. The potentials were referenced to ferrocene/ferrocenium as an internal standard. Data was evaluated using OriginPro version 2025.[139]
Quantum chemical calculations using density functional theory (DFT). DFT calculations were carried out using the Gaussian 16 suite of programs.[140] The def2-TZVP base set[141] was used for all atoms with the effective core potentials (def2-ECPs) for Pt and Pd (ecp-46, ecp-28).[142] The S_0 geometries were optimised using the TPSSh hybrid functional.[143] *Grimmes* D3 dispersion correction[144] and the conductor-like polarizable continuum model (CPCM) for THF was used as a solvent model.[145, 146] Visualization of the orbital isosurfaces was carried out in Chemcraft by extracting the data from single point calculations with an isovalue of 0.03.

6.2 Experimental Procedures

6.2.1 Synthesis of Protoligand Precursors

Synthesis of *N*-methyl-2,2'-bipyridinium iodide

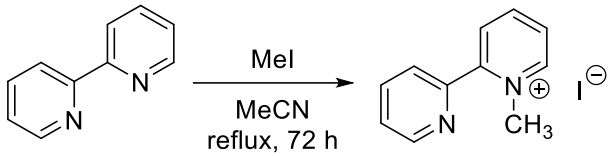

2,2'-Biypyridine (10.0 g, 64.0 mmol, 1.00 eq.) and MeI (27.3 g, 12.0 mL, 192 mmol, 3.00 eq.) were dissolved in MeCN and heated to reflux for 72 h. The bright yellow precipitate was filtrated off and washed with MeCN, giving a bright yellow filtrate. The filtrate was mixed with diethyl ether, leading to a pale-yellow solid precipitating out. The precipitate was filtered off, washed with diethyl ether and dried to yield the desired product (13.0 g, 43.6 mmol, 68%).

Habitus Yellow powder (13.0 g, 43.6 mmol, 68%).

^{1}H NMR (300 MHz, $CDCl_3$) δ [ppm]: 9.63 (d, *J* = 6.1 Hz, 1H), 8.80 (ddd, *J* = 4.9, 1.8, 1.0 Hz, 1H), 8.72 (td, *J* = 7.9, 1.4 Hz, 1H), 8.27 (ddd, *J* = 7.9, 6.2, 1.6 Hz, 1H), 8.14 (dd, *J* = 7.8, 1.5, 1.0 Hz, 2H), 8.06 (td, *J* = 7.8, 1.8 Hz, 1H), 7.59 (ddd, *J* = 7.8, 4.8, 1.2 Hz, 1H), 4.54 (s, 3H).

The compounds analytical data matches previously reported data.[100]

Synthesis of *N*-methyl-6-(2-pyridinyl)-pyrid-2-one

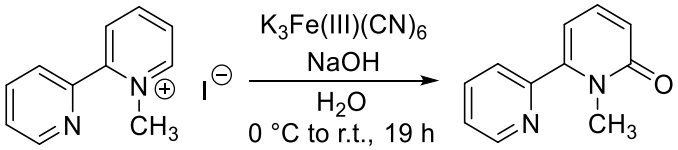

$K_3Fe(CN)_6$ (16.5 g, 50.0 mmol, 2.50 eq.) was dissolved in 65 mL of H_2O and cooled to 0 °C. Solutions of NaOH (16.6 g, 415 mmol, 20.6 eq., in 75 mL of H_2O) and *N*-methyl-2,2'-bipyridinium iodide (6.00 g, 20.1 mmol, 1.00 eq., in 60 mL of H_2O) in two separate addition funnels were added over 1 h. The reaction mixture was stirred for further 1 h at 0 °C, during which the initially yellow solution slowly turned dark brown. The mixture was then left to heat to r.t. and stirred for a total of 19 h. After addition of 300 mL of brine the mixture was extracted with CH_2Cl_2 and the organic phase dried over $MgSO_4$. The obtained crude brown oil was purified by filtering through a silica plug (SiO_2, EtOAc/MeOH 4:1). The product was obtained as a brown solid (1.35 g, 7.25 mmol, 36%).

Habitus Brown powder (1.35 g, 7.25 mmol, 36%).

^{1}H NMR (300 MHz, $CDCl_3$) δ [ppm]: 8.74 (ddd, *J* = 4.8, 1.8, 0.9 Hz, 1H), 7.85 (td, *J* = 7.7, 1.8 Hz, 1H), 7.50 - 7.34 (m, 3H), 6.67 (dd, *J* = 9.2, 1.4 Hz, 1H), 6.22 (dd, *J* = 6.8, 1.4 Hz, 1H), 3.47 (s, 3H).

The compounds analytical data matches previously reported data.[100]

Synthesis of 6-bromo-2,2′-bipyridine

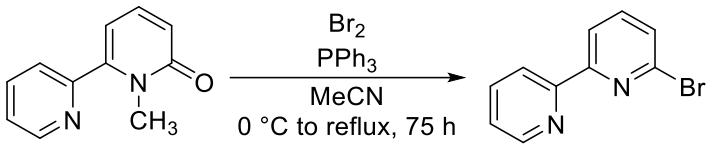

PPh_3 (21.7 g, 82.8 mmol, 1.40 eq.) was dissolved in 100 mL of MeCN and cooled to 0 °C. Bromine (12.5 g, 3.95 mL, 78.1 mmol, 1.33 eq.) was added over 30 min. The solution was stirred for a further 180 min at 0 °C. *N*-Methyl-6-(2-pyridinyl)-pyrid-2-one (11.0 g, 59.1 mmol, 1.00 eq.) dissolved in 20 mL of MeCN was added over 30 min. The mixture was heated to reflux for 72 h, cooled to r.t. and the reaction terminated by addition of 300 mL of sat. $NaHCO_3$ solution. The mixture was extracted with CH_2Cl_2 and the organic phases evaporated off to yield a brown solid (4.11 g, 17.5 mmol, 30%).

Habitus Brown powder (4.11 g, 17.5 mmol, 30%).

^{1}H NMR (300 MHz, $CDCl_3$) δ [ppm]: 8.68 (ddd, *J* = 4.9, 1.8, 0.9 Hz, 1H), 8.41 (t, *J* = 8.0 Hz, 2H), 7.83 (td, *J* = 7.7, 1.8 Hz, 1H), 7.68 (t, *J* = 7.8 Hz, 1H), 7.51 (dd, *J* = 7.8, 0.9 Hz, 1H), 7.34 (ddd, *J* = 7.5, 4.8, 1.2 Hz, 1H).

The compounds analytical data matches previously reported data.[100]

General Procedure "Suzuki" (A)

Under inert conditions, an aryl-boronic acid or its pinacol ester (1.00 eq.) was reacted with a bromo-aryl (1.00 eq.) with 10.0 eq. of Na_2CO_3 in a degassed solvent mixture of toluene, ethanol and water (1:1:1 volume, adjusted to give a 2M base concentration in the aqueous part). After addition of $[Pd(PPh_3)_4]$ (2-5 mol%) the mixture was heated to reflux. After cooling, the organic solvents were evaporated off and the mixture extracted with CH_2Cl_2. The crude product was purified by column chromatography to yield the desired product.

Synthesis of 1-(2-pyridinyl)-3-bromobenzene

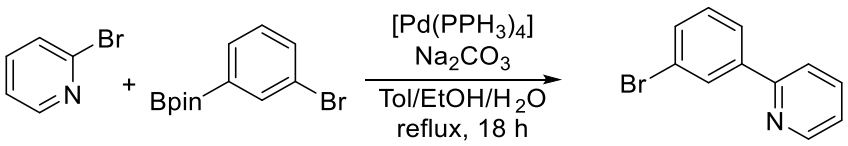

1-Bromo-5-phenylboronic acid pinacol ester (5.00 g, 17.7 mmol, 1.00 eq.) and 2-bromopyridine (2.80 g, 1.72 mL, 17.7 mmol, 1.00 eq.) were reacted with $[Pd(PPh_3)_4]$ (1.03 g, 0.89 mmol, 5 mol%) according to general procedure A. After column chromatography (SiO_2, CHex/EtOAc 40:1, r_f = 0.17) the product was obtained as a colourless oil (2.07 g, 8.84 mmol, 50%).

Habitus Colourless oil (2.07 g, 8.84 mmol, 50%).

^{1}H NMR (300 MHz, $CDCl_3$) δ [ppm]: 8.72 (d, *J* = 4.8 Hz, 1H), 8.20 (t, *J* = 1.9 Hz, 1H), 7.93 (dt, *J* = 7.9, 1.3 Hz, 1H), 7.84 - 7.69 (m, 2H), 7.56 (ddd, *J* = 8.0, 2.1, 1.1 Hz, 1H), 7.37 (t, *J* = 7.9 Hz, 1H), 7.31 - 7.25 (m, 1H).

GC-MS 235 $[M]^{+\cdot}$.

The compounds analytical data matches previously reported data.[68]

Synthesis of 2-phenyl-6-bromopyridine

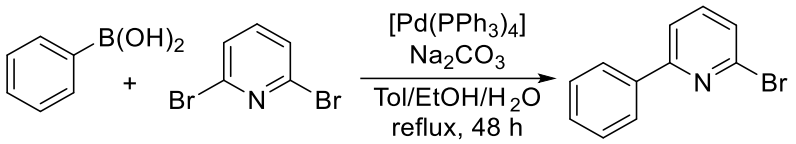

1-Phenylboronic acid pinacol ester (3.08 g, 25.3 mmol, 1.00 eq.) and 1,3-dibromopyridine (6.00 g, 25.3 mmol, 1.00 eq.) were reacted with $[Pd(PPh_3)_4]$ (1.27 g, 1.10 mmol, 5 mol%) according to general procedures A, heating to reflux for 48 After column chromatography (SiO_2, CHex/EtOAc 50:1, r_f = 0.19) the product was obtained as a colourless oil (2.80 g, 11.9 mmol, 47%).

Habitus Colourless oil (2.80 g, 11.9 mmol, 47%).

^{1}H NMR (300 MHz, $CDCl_3$) δ [ppm]: 8.21 - 8.15 (m, 1H), 8.05–7.97 (m, 1H), 7.75 - 7.68 (m, 2H), 7.55 - 7.40 (m, 4H).

GC-MS 235 $[M]^{+\cdot}$.

The compounds analytical data matches previously reported data.[147]

Synthesis of 1-bromo-3-(8-quinolinyl)-benzene

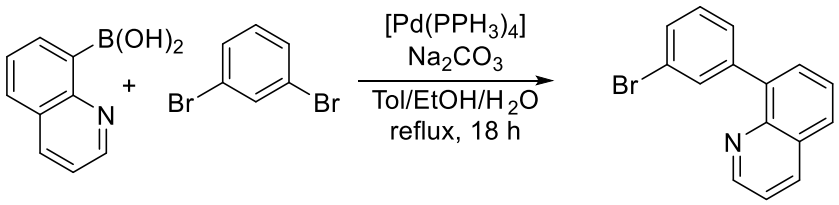

8-Quinolinylboronic acid (5.00 g, 28.9 mmol, 1.00 eq.) and 1,3-dibromobezene (6.82 g, 28.9 mmol, 1.00 eq.) were reacted with $[Pd(PPh_3)_4]$ (1.67 g, 1.45 mmol, 5 mol%) following general procedure A for 18 h. After column chromatography (SiO_2, CHex/EtOAc 10:1, r_f = 0.31) the product was obtained as a colourless oil (4.98 g, 17.5 mmol, 61%).

Habitus Colourless oil (4.98 g, 17.5 mmol, 61%).

^{1}H NMR (300 MHz, CD_2Cl_2) δ [ppm]: 8.90 (dd, *J* = 4.1, 1.8 Hz, 1H), 8.23 (dd, *J* = 8.3, 1.8 Hz, 1H), 7.87 (dd, *J* = 8.2, 1.5 Hz, 1H), 7.84 (t, *J* = 1.8 Hz, 1H), 7.71 (dd, *J* = 7.2, 1.5 Hz, 1H), 7.64 - 7.58 (m, 2H), 7.54 (ddd, *J* = 8.0, 2.1, 1.1 Hz, 1H), 7.44 (dd, *J* = 8.3, 4.1 Hz, 1H), 7.36 (t, *J* = 7.8 Hz, 1H).

Synthesis of 2-bromo-6-(8-quinolinyl)-pyridine

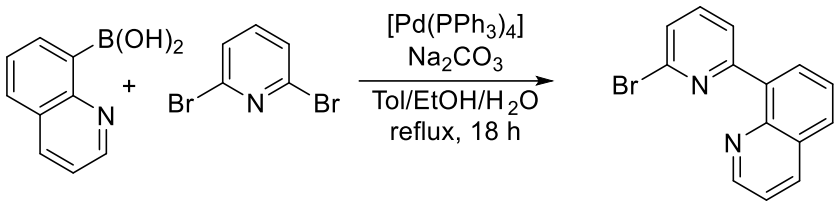

8-Quinolinylboronic acid (4.00 g, 23.1 mmol, 1.00 eq.) and 2,6-dibromopyridine (5.47 g, 23.1 mmol, 1.00 eq.) were reacted with [Pd(PPh$_3$)$_4$] (534 mg, 0.46 mmol, 2 mol%) following general procedure A for 18 h. After column chromatography (SiO_2, CHex/EtOAc 10:1, r_f = 0.25) the product was obtained as a colourless oil (3.45 g, 12.1 mmol, 52%).

Habitus **C**olourless oil (3.45 g, 12.1 mmol, 52%).

^{1}H NMR (300 MHz, $CDCl_3$) δ [ppm]: 8.95 (dd, *J* = 4.1, 1.8 Hz, 1H), 8.25 - 8.18 (m, 3H), 7.90 (dd, *J* = 8.1, 1.5 Hz, 1H), 7.67 (t, *J* = 7.7 Hz, 2H), 7.49 (dd, *J* = 7.9, 0.9 Hz, 1H), 7.44 (dd, *J* = 8.3, 4.2 Hz, 1H).

The compounds analytical data matches previously reported data.[148]

Synthesis of 6-(8-quinolinyl)-pyridine-2-boronic acid pinacol ester

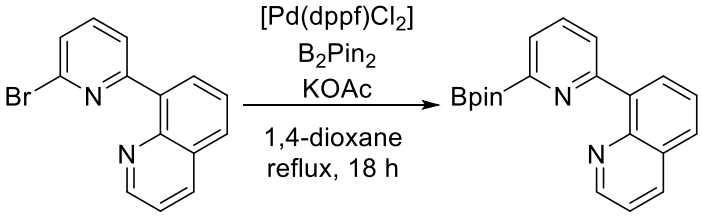

Under inert conditions, 2-bromo-6-(8-quinolinyl)-pyridine (1.48 g, 5.19 mmol, 1.00 eq.) were mixed with B_2Pin_2 (2.53 g, 9.97 mmol, 1.92 eq.), KOAc (2.44 g, 24.9 mmol, 4.79 eq.) and [Pd(dppf)Cl_2] (0.13 g, 0.18 mmol, 3.6 mol%) in 25 mL of degassed 1,4-dioxane. The mixture was heated to reflux for 18 h and cooled back down to room temperature. The solvent was evaporated off, the crude mixture picked up in CH_2Cl_2 and filtered over a silica plug with MeOH as eluent. After solvent evaporation, the product was obtained as dark brown oil (646 mg, 1.95 mmol, 39%).

Habitus Dark brown oil (646 mg, 1.95 mmol, 39%).

^{1}H NMR (300 MHz, $CDCl_3$) δ [ppm]: 8.94 (dd, *J* = 4.2, 1.8 Hz, 1H), 8.19 (dd, *J* = 8.3, 1.8 Hz, 1H), 8.07 (s,1H), 7.92 - 7.79 (m, 2H), 7.75 (dd, *J* = 7.2, 1.5 Hz, 1H), 7.58 (dd, *J* = 8.1, 7.1 Hz, 1H), 7.50 (t, *J* = 7.50 Hz, 1H), 7.40 (dd, *J* = 8.3, 4.2 Hz, 1H), 1.37 (s, 12H).

Synthesis of 2-(*N*-carbazolyl)-6-bromopyridine

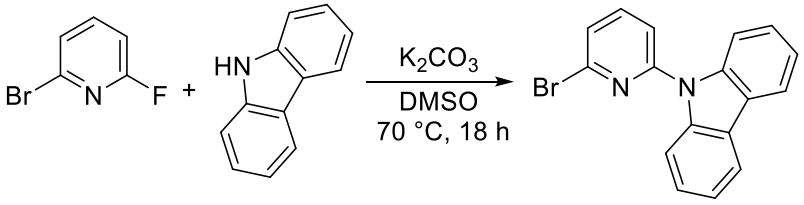

2-Bromo-6-fluoro-pyridine (2.00 g, 11.4 mmol, 1.00 eq.), carbazole (3.81 g, 22.8 mmol, 2.00 eq.) and K_2CO_3 (3.15 g, 22.8 mmol, 2.00 eq.) were dissolved in 40 mL of DMSO. The mixture was heated to 70 °C for 18 h and cooled to r.t. before the crude product was precipitated out of solution by addition of water. The mixture was extracted with CH_2Cl_2 and the solvent evaporated to give a yellow-orange oil. The crude product was picked up in a mixture of CHex/EtOAc 10:1 and filtered off over a silica plug to yield a yellow filtrate. Evaporation of the solvent gave a yellow powder (2.94 g, 9.09 mmol, 80%).

Habitus Yellow powder (2.94 g, 9.09 mmol, 80%).

^{1}H NMR (300 MHz, $CDCl_3$) δ [ppm]: 8.26 (d, *J* = 7.7 Hz, 2H), 8.05 (t, *J* = 7.8 Hz, 1H), 7.86 (dd, *J* = 8.1, 4.9 Hz, 3H), 7.72 (d, *J* = 7.8 Hz, 1H), 7.50 (ddd, *J* = 8.3, 7.1, 1.3 Hz, 2H), 7.40 - 7.35 (m, 2H).

The compounds analytical data matches previously reported data.[149]

Synthesis of 2-bromo-9-(pyridine-2-yl)-carbazole

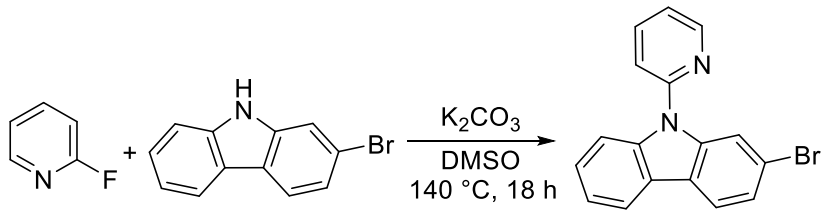

2-Fluoropyridine (1.58 g, 1.40 mL, 16.3 mmol, 2.00 eq.), 2-bromocarbazole (2.00 g, 8.13 mmol, 1.00 eq.) and K_2CO_3 (3.37 g, 24.4 mmol, 3.00 eq.) were added to 20 mL of DMSO and heated to 140 °C for 18 h. After cooling to r.t. a colourless precipitate formed upon addition of water to the reaction mixture. The precipitate was filtered off and recrystalized twice from hot cyclohexane to yield a colourless powder (2.57 g, 7.95 mmol, 98%).

Habitus Colourless powder (2.57 g, 7.95 mmol, 98%).

^{1}H NMR (300 MHz, $CDCl_3$) δ [ppm]: 8.76 (dd, *J* = 4.9, 2.0 Hz, 1H), 8.11 (d, *J* = 7.8 Hz, 1H), 8.04 (d, *J* = 1.7 Hz, 1H), 7.97 (td, *J* = 7.8, 1.8 Hz, 2H), 7.80 (d, *J* = 8.2 Hz, 1H), 7.64 (d, *J* = 8.0 Hz, 1H), 7.47 (ddd, *J* = 8.1, 7.7, 1.5 Hz, 2H), 7.41 – 7.31 (m, 2H).

The compounds analytical data matches previously reported data.[150]

Synthesis of 2,7-dibromo-9-(2-pyrimidyl)-carbazole

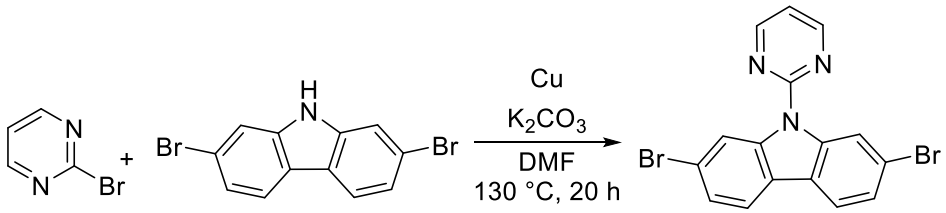

2,7-Dibromocarbazole (2.00 g, 6.15 mmol, 1.00 eq.) and 2-bromopyrimidine (1.47 g, 9.23 mmol, 1.50 eq.) were mixed with copper powder (196 mg, 3.08 mmol, 0.50 eq.) and K_2CO_3 (1.70 g, 12.3 mmol, 2.00 eq.) in DMF. The mixture was heated to 130 °C for 20 h and cooled to r.t., leading to a colourless precipitate. After addition of water, the reaction mixture was extracted with CH_2Cl_2/EtOAc and the solvent evaporated. The obtained light brown solid was recrystalized from hot cyclohexane to yield the desired product as colourless powder (2.13 g, 5.28 mmol, 86%).

Habitus Colourless powder (2.13 g, 5.28 mmol, 86%).

^{1}H NMR ($CDCl_3$) δ [ppm]: 9.06 (d, *J* = 4.9 Hz, 2H), 9.04 (d, *J* = 1.8 Hz, 2H), 8.24 (d, *J* = 8.2 Hz, 2H), 7.60 (dd, *J* = 8.2, 1.8 Hz, 2H), 7.49 (t, *J* = 4.8 Hz, 1H).

The compounds analytical data matches previously reported data.[151]

6.2.2 Synthesis of Protoligands

Synthesis of pyridine-phenyl-quinoline (PyHPhQ)

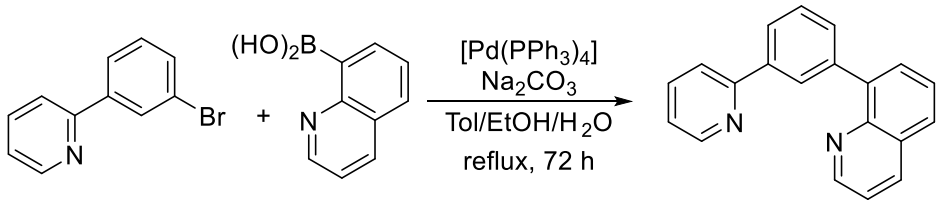

1-(2-Pyridinyl)-3-bromobenzene (1.00 g, 4.27 mmol, 1.00 eq.) and quinoline-8-boronic acid (739 mg, 4.27 mmol, 1.00 eq.) were reacted with $[Pd(PPh_3)_4]$ (243 mg, 0.21 mmol, 5 mol%) following general procedure A for 72 h. The obtained crude oil was purified by column chromatography (SiO_2, CHex/EtOAc 2:1, r_f = 0.26). The product was obtained as light-yellow oil (1.14 g, 4.04 mmol, 95%).

Habitus Light-yellow oil (1.14 g, 4.04 mmol, 95%).

^{1}H NMR ($CDCl_3$, 500 MHz) δ [ppm]: 8.93 (d, *J* = 4.8 Hz, 1H, H1), 8.68 (d, *J* = 4.8 Hz, 1H, H13), 8.31 (s, 1H, H16), 8.14 (d, *J* = 8.3 Hz, 1H, H3), 8.05 (d, *J* = 7.8 Hz, 1H, H9), 7.81 - 7.73 (m, 4H, H4, H6, H7, H10), 7.67 (t, *J* = 7.5 Hz, 1H, H11), 7.58 (dt, *J* = 15.1 Hz, 7.7 Hz, 2H, H5, H8), 7.35 (dd, *J* = 8.3 Hz, 4.2 Hz, 1H, H2), 7.16 (dd, *J* = 7.5 Hz, 4.8 Hz, 1H, H12).

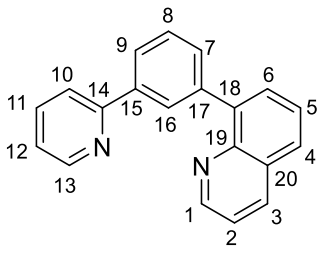

^{13}C NMR ($CDCl_3$, 126 MHz) δ [ppm]: 157.6 (Cq, C14), 150.3 (CH, C1), 149.6 (CH, C13), 146.1 (Cq, C19), 140.7 (Cq, C18), 140.1 (Cq, C15), 139.2 (Cq, C17), 136.7 (CH, C10), 136.3 (CH, C3), 131.4 (CH, C7), 130.4 (CH, C6), 129.2 (CH, C16), 128.7 (Cq, C20), 128.4 (CH, C11), 127.7 (CH, C4), 126.3 (CH, C5) 126.0 (CH, C9), 122.0 (CH, C12), 121.0 (CH, C2), 120.7 (CH, C8).

HR-EI-MS (70 eV): 282.11 $[M]^{\cdot+}$.

Synthesis of quinoline-phenyl-quinoline (QHPhQ)

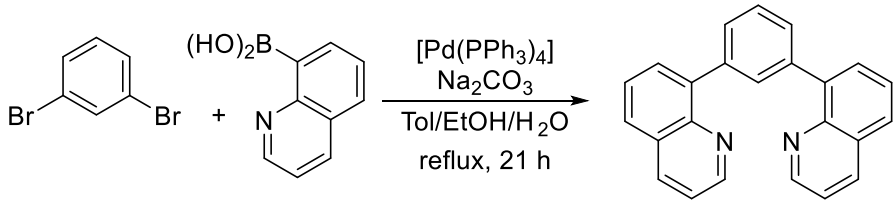

Quinoline-8-boronic acid (1.50 g, 8.67 mmol, 2.00 eq.) and 1,3-dibromobenzene (1.02 g, 4.34 mmol, 1.00 eq.) were reacted with $[Pd(PPh_3)_4]$ (69.7 mg, 0.06 mmol, 1.40 mol%) for 20 h following general procedure A. The obtained crude oil was purified by column chromatography (SiO_2, CHex/EtOAc 2:1, r_f = 0.21). The product was obtained as light-yellow solid (1.21 g, 3.64 mmol, 84%).

Habitus Light-yellow solid (1.21 g, 3.64 mmol, 84%).

^{1}H NMR (CD_2Cl_2, 500 MHz) δ [ppm]: 8.91 (dd, *J* = 4.1, 1.8 Hz, 2H, H1, H1'), 8.22 (dd, *J* = 8.3, 1.7 Hz, 2H, H3, H3'), 7.92 (t, *J* = 1.5 Hz, 1H, H13), 7.84 (ddd, *J* = 10.6, 7.7, 1.3 Hz, 4H, H5, H5', H7, H7'), 7.72 (dd, *J* = 7.7, 1.7 Hz, 2H, H11, H11'), 7.64 - 7.60 (m, 2H, H6, H6'), 7.58 (t, *J* = 7.6 Hz, 1H, H12), 7.42 (dd, *J* = 8.3, 4.1 Hz, 2H, H2, H2').

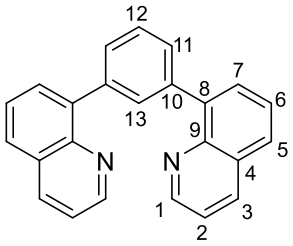

^{13}C NMR (CD_2Cl_2, 126 MHz) δ [ppm]: 150.7 (CH, C1, C1'), 146.8 (Cq, C9, C9'), 141.5 (Cq, C8, C8'), 139.9 (Cq, C10, C10'), 136.7 (CH, C3, C3'), 133.4 (CH, C13), 130.7 (CH, C5, C5'), 130.3 (CH, C11, C11'), 129.3 (Cq, C4, C4'), 128.1 (CH, C7, C7'), 127.6 (CH, C12), 126.8 (CH, C6, C6'), 121.6 (CH, C2, C2').

GC-MS 332 $[M]^{\cdot+}$.

Synthesis of quinoline-chlorophenyl-quinoline (QClPhQ)

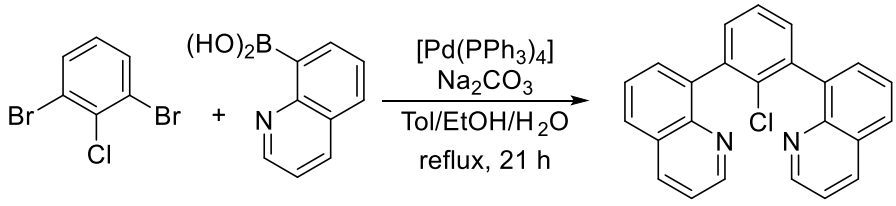

Quinoline-8-boronic acid (1.36 g, 7.84 mmol, 2.20 eq.) and 1,3-dibromo-2-chlorobenzene (962 mg, 3.56 mmol, 1.00 eq.) were reacted with $[Pd(PPh_3)_4]$ (452 mg, 0.39 mmol, 11 mol%) for 21 h following general procedure A. The obtained crude oil was purified by filtering over a

silica plug using MeOH as eluent followed by recrystallization from hot CHex. The product was obtained as light-yellow solid (302 mg, 0.82 mmol, 23%).

Habitus Light-yellow solid (302 mg, 0.82 mmol, 23%).

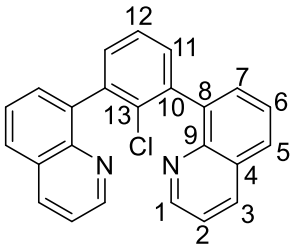

^{1}H NMR ($CDCl_3$, 500 MHz) δ [ppm]: 8.95 (s, 2H, H1, H1'), 8.20 (d, *J* = 7.1 Hz, 2H, H3, H3'), 7.90 - 7.83 (m, 4H, H5, H5' H7, H7'), 7.72 (d, *J* = 6.7 Hz, 1H, H12), 7.64 - 7.60 (m, 2H, H6, H6'), 7.52 - 7.47 (m, 2H, H11, H11'), 7.40 (dd, *J* = 7.9 Hz, 4.0 Hz, 2H, H2, H2').

^{13}C NMR ($CDCl_3$, 126 MHz) δ [ppm]: 150.4 (CH, C1, C1'), 146.5 (Cq, C9, C9'), 139.4 (Cq, C8, C8'), 139.3 (Cq, C13), 139.2 (Cq, C10, C10'), 136.2 (CH, C3, C3'), 131.5 (CH, C11, C11'), 131.3 (CH, C7, C7'), 130.5 (CH, C12), 128.4 (Cq, C4, C4'), 128.0 (Cq, C5, C5'), 126.0 (CH, C6, C6'), 121.0 (CH, C2, C2').

HR-ESI-MS (70 eV): 367.10 $[M+H]^+$, 389.08 $[M+Na]^+$.

Synthesis of phenyl-pyridine-quinoline (HPhPyQ)

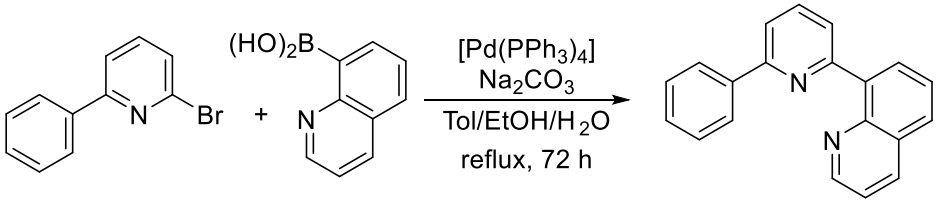

2-Phenyl-6-bromopyridine (2.20 g, 9.40 mmol, 1.00 eq.) and quinolinyl-8-boronic acid (1.63 g, 9.40 mmol, 1.00 eq.) were reacted with $[Pd(PPh_3)_4]$ (543 mg, 0.47 mmol, 5 mol%) for 72 h following general procedure A. The obtained brown crude oil was purified by column chromatography (SiO_2, CHex/EtOAc 20:1). The product was obtained as a yellow solid (1.81 g, 6.41 mmol, 68%).

Habitus Yellow solid (1.81 g, 6.41 mmol, 68%).

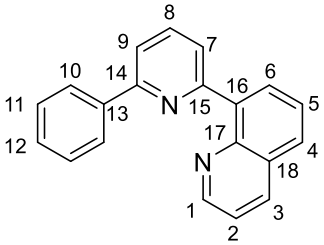

^{1}H NMR ($CDCl_3$, 300 MHz) δ [ppm] : 8.98 (dd, *J* = 4.1, 1.8 Hz, 1H, H1), 8.34 (dd, *J* = 7.2, 1.4 Hz, 1H, H6), 8.22 (dd, *J* = 8.3, 1.7 Hz, 1H, H3), 8.12 (d, *J* = 7.4 Hz, 3H, H9, H10, H10'), 7.88 (t, *J* = 7.9 Hz, 1H, H8), 7.75 (d, *J* = 7.4 Hz, 1H, H7), 7.72 - 7.67 (m, 2H, H4, H5), 7.48 (t, *J* = 7.5 Hz, 2H, H11, H11'), 7.44 - 7.38 (m, 2H, H2, H12).

^{13}C NMR ($CDCl_3$, 75 MHz) δ [ppm]: 157.2 (Cq, C14), 156.6 (Cq, C15), 150.3 (CH, C1), 146.0 (Cq, C17), 139.9 (Cq, C13), 139.1 (Cq, C16), 136.5 (CH, C3), 136.2 (CH, C8), 131.6 (CH, C6), 128.8 (CH, C4), 128.73 (CH, C12), 128.7 (Cq, C18), 128.6 (CH, C11, C11'), 127.1 (CH, C10, C10'), 126.6 (CH, C5), 125.6 (CH, C9), 121.0 (CH, C2), 119.0 (CH, C7).

HR-EI-MS (70 eV): 282.11 $[M]^{\cdot+}$.

Synthesis of pyridine-pyridine-carbazole (PyPyHCarb)

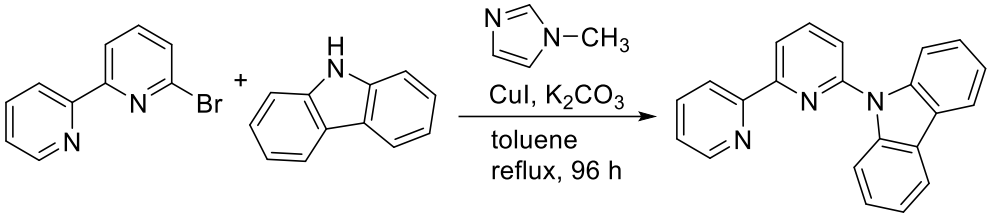

Under inert conditions, 6-bromo-2,2′-bipyridine (1.00 g, 4.25 mmol, 1.00 eq.), carbazole (1.10 g, 6.58 mmol, 1.55 eq.) and CuI (0.08 g, 0.42 mmol, 10 mol%) were added to a flask. *N*-methylimidazole (0.20 g, 2.43 mmol, 0.57 eq.) and 20 mL of dry toluene were added and the mixture heated to reflux for 96 h. After cooling, the crude mixture was filtered over a celite plug and purified by column chromatography (SiO_2, CHex/EtOAc, r_f = 0.24). The product was obtained as a yellow solid (0.41 g, 1.28 mmol, 30%).

Habitus Yellow solid (0.41 g, 1.28 mmol, 30%).

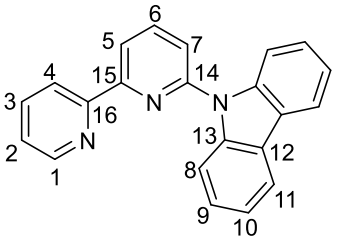

^{1}H NMR (CD_2Cl_2, 500 MHz) δ [ppm]: 8.72 (dd, *J* = 4.9, 0.9 Hz, 1H, H1), 8.48 (dd, *J* = 7.9, 1.0 Hz, 2H, H4, H5), 8.16 (d, *J* = 7.8 Hz, 2H, H8, H8′), 8.09 (t, *J* = 7.8 Hz, 1H, H6), 7.94 (d, *J* = 8.3 Hz, 2H, H11, H11′), 7.85 (td, *J* = 7.7, 1.8 Hz, 1H, H3), 7.68 (dd, *J* = 7.9, 0.9 Hz, 1H, H7), 7.47 (ddd, *J* = 8.4, 7.2, 1.3 Hz, 2H, H10, H10′), 7.39 - 7.29 (m, 3H, H2, H9, H9′).**^{13}C NMR** (CD_2Cl_2, 126 MHz) δ [ppm]: 156.7 (Cq, C14), 156.0 (Cq, C16), 151.6 (Cq, C15), 149.9 (CH, C1), 140.1 (CH, C6), 137.6 (CH, C3), 126.8 (CH, C10, C10′), 124.8 (Cq, C12, C12′, C13, C13′), 124.7 (CH, C2), 121.6 (CH, C4), 121.5 (CH, C9, C9′), 120.7 (CH, C8, C8′), 119.4 (CH, C7), 118.8 (CH, C5), 111.9 (CH, C11, C11′).

Synthesis of quinoline-pyridine-carbazole (QPyHCarb)

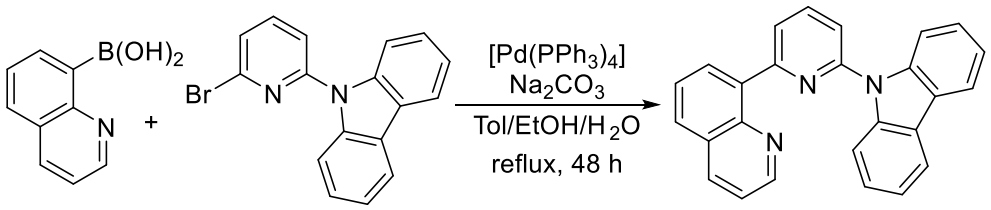

2-(*N*-carbazolyl)-6-bromopyridine (1.00 g, 3.09 mmol, 1.00 eq.) and quinoline-8-boronic acid (1.07 g, 6.18 mmol, 2.00 eq.) were reacted with [$Pd(PPh_3)_4$] (173 mg, 0.15 mmol, 5 mol%) following general procedure A for 48 h. After column chromatography (SiO_2, CHex/EtOAc 4:1, r_f = 0.65) a yellow solid was obtained (1.14 g, 3.06 mmol, 99%).

Habitus Yellow solid (1.14 g, 3.06 mmol, 99%).

^{1}H NMR (CD_2Cl_2, 500 MHz) δ [ppm]: 9.02 (dd, *J* = 4.1, 1.8 Hz, 1H, H1), 8.36 - 8.25 (m, 2H, H3, H6), 8.22 (d, *J* = 7.8 Hz, 1H, H7), 8.14 (d, *J* = 7.8 Hz, 2H, H10, H10'), 8.07 (t, *J* = 7.9 Hz, 1H, H8), 8.00 (d, *J* = 8.2Hz, 2H, H13, H13'), 7.95 (dd, *J* = 8.2, 1.3 Hz, 1H, H4), 7.72 – 7.68 (m, 1H, H5), 7.66 (d, *J* = 7.9 Hz, 1H, H9), 7.50 (dd, *J* = 8.2, 4.1 Hz, 1H, H2), 7.48 - 7.43 (m, 2H, H12, H12'), 7.32 (t, *J* = 7.1 Hz, 2H, H11, H11').

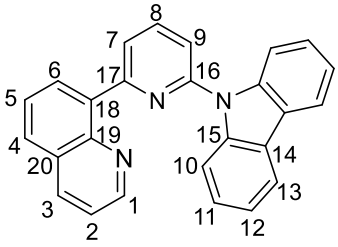

^{13}C NMR (CD_2Cl_2, 126 MHz) δ [ppm]: 157.8 (Cq, C16), 151.7 (Cq, C17), 150.9 (CH, C1), 146.5 (Cq, C19), 140.3 (Cq, C14, C14'), 138.6 (Cq, C18), 138.6 (CH, C8), 137.0 (CH, C3), 131.7 (CH, C6), 129.7 (CH, C4), 129.3 (Cq, C20), 127.0 (CH, C5), 126.7 (CH, C12, C12'), 125.2 (CH, C7), 124.6 (Cq, C15, C15'), 121.8 (CH, C2), 121.3 (CH, C11, C11'), 120.6 (CH, C10, C10'), 117.9 (CH, C9), 112.0 (CH, C13, C13').

HR-ESI-MS (70 eV): 372.15 $[M+H]^+$, 394.13 $[M+Na]^+$.

Synthesis of pyridine-carbazole-quinoline (PyHCarbQ)

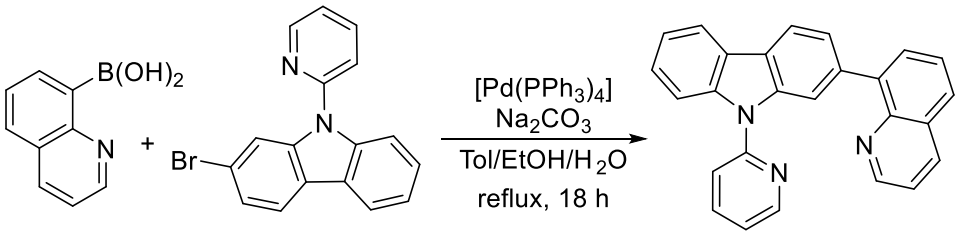

2-Bromo-9-(pyridine-2-yl)-carbazole (2.00 g, 6.19 mmol, 1.00 eq.) and quinoline-8-boronic acid (1.07 g, 6.18 mmol, 1.00 eq.) were reacted with $[Pd(PPh_3)_4]$ (358 mg, 0.31 mmol, 5 mol%) following general procedure A for 17 h. After column chromatography (SiO_2, CHex/EtOAc, gradient 10:1 to 4:1), the product was obtained as a colourless solid (2.12 g, 5.70 mmol, 92%).

Habitus Colourless solid (2.12 g, 5.70 mmol, 92%).

^{1}H NMR (CD_2Cl_2, 500 MHz) δ [ppm]: 8.89 (dd, *J* = 4.1, 1.9 Hz, 1H, H17), 8.66 (dd, *J* = 4.8, 1.2 Hz, 1H, H1), 8.23 - 8.16 (m, 3H, H8, H9, H15), 8.11 (d, *J* = 0.8 Hz, 1H, H11), 7.90 (d, *J* = 8.4 Hz, 1H, H3), 7.89 - 7.83 (m, 2H, H12, H14), 7.80 (dd, *J* = 7.2, 1.4 Hz, 1H, H6), 7.70 (d, *J* = 8.1 Hz, 1H, H5), 7.61 - 7.58 (m, 2H, H7, H13), 7.49 - 7.43 (m, 1H, H4), 7.41 (dd, *J* = 8.3, 4.1 Hz, 1H, H16), 7.34 (t, *J* = 7.1 Hz, 1H, H10), 7.25 (ddd, *J* = 7.4, 4.9, 0.9 Hz, 1H, H2).

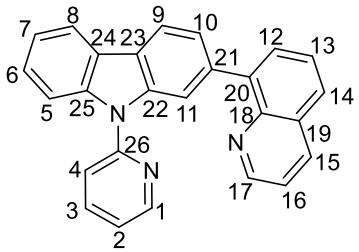

^{13}C NMR (CD_2Cl_2, 126 MHz) δ [ppm]: 152.3 (Cq, C26), 150.7 (CH, C17), 150.1 (CH, C1), 146.9 (Cq, C18), 142.0 (Cq, C20), 140.7 (Cq, C21), 140.0 (Cq, C25), 139.0 (CH, C12), 138.6 (Cq, C22), 136.7 (CH, C15), 131.0 (CH, C6), 129.3 (Cq, C19), 128.1

(CH, C14), 126.8 (CH, C13), 126.7 (CH, C4), 124.7 (Cq, C24), 124.6 (CH, C7), 123.8 (Cq, C23), 121.8 (CH, C2), 121.6 (CH, C16), 121.5 (CH, C10), 120.7 (CH, C9), 119.7 (CH, C8), 119.6 (CH, C5), 114.0 (CH, C11), 112.0 (CH, C3).

HR-ESI-MS (70 eV): 372.14 $[M+H]^+$, 394.13 $[M+Na]^+$.

Synthesis of 2,7-di(quinolin-8-yl)-9-(pyrimidin-2-yl)-carbazole (BisQHCarbPym)

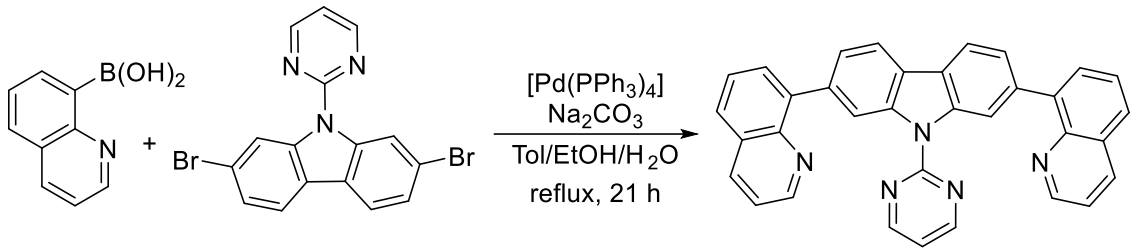

2,7-Dibromo-9-(2-pyrimidyl)-carbazole (1.00 g, 2.48 mmol, 1.00 eq.) and 8-quinolinyl boronic acid (1.07 g, 6.18 mmol, 2.50 eq.) were reacted with $[Pd(PPh_3)_4]$ (57.3 mg, 49.6 µmol, 2 mol%) following general procedure A for 21 h. After column chromatography (SiO_2, CHex/EtOAc 2:1, r_f = 0.13) the product was obtained as a light-yellow solid (300 mg, 0.60 mmol, 24%).

Habitus light-yellow solid (300 mg, 0.60 mmol, 24%).

^{1}H NMR (500 MHz, CD_2Cl_2) δ [ppm]: 9.15 (s, 2H, H9, H9'), 8.93 (dd, *J* = 4.0, 1.7 Hz, 2H, H1, H1'), 8.75 (d, *J* = 4.7 Hz, 2H, H10, H10'), 8.28 (dd, *J* = 8.2, 1.7 Hz, 2H, H3, H3'), 8.23 (d, *J* = 7.9 Hz, 2H, H8, H8'), 7.91 (dd, *J* = 7.6, 1.7 Hz, 4H, H4, H4', H6, H6'), 7.72 (dd, *J* = 7.9, 1.4 Hz, 2H, H7, H7'), 7.68 (t, *J* = 7.6 Hz, 2H, H5, H5'), 7.46 (dd, *J* = 8.3, 4.0 Hz, 2H, H2, H2'), 7.07 (t, *J* = 4.7 Hz, 1H, H11).

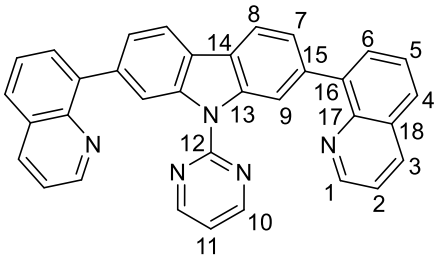

^{13}C NMR (126 MHz, CD_2Cl_2) δ [ppm]: 159.8 (Cq, C12), 158.5 (CH, C10, C10'), 150.7 (CH, C1, C1'), 147.0 (Cq, C17, C17'), 142.4 (Cq, C16, C16'), 140.1 (Cq, C13, C13') 139.1 (Cq, C15, C15'), 136.7 (CH, C3, C3'), 131.2 (CH, C6, C6'), 129.3 (CH, C18, C18'), 128.1 (Cq, C4, C4'), 126.8 (CH, C5, C5'), 126.1 (CH, C7, C7'), 125.2 (Cq, C14, C14'), 121.6 (CH, C2, C2'), 119.1 (CH, C8, C8'), 118.9 (CH, C9, C9'), 116.7 (CH, C11).

GC-MS (70 eV): 499 $[M]^+$.

Synthesis of quinoline-pyridine-4-(*N,N*-diphenyl)-amino-phenyl (QPyHPh(N(Ph)$_2$))

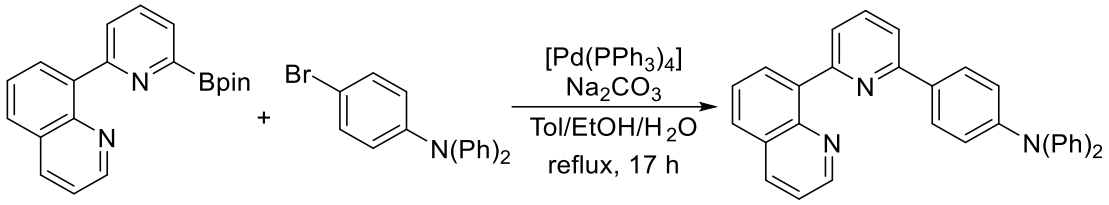

6-(8-Quinolinyl)-pyridine-2-boronic acid pinacol ester (646 mg, 1.94 mmol, 1.00 eq.) and 1-bromo-4-(*N*,*N*-diphenyl)-amino-benzene (631 mg, 1.94 mmol, 1.00 eq.) were reacted with [Pd(PPh$_3$)$_4$] (45.0 mg, 38.9 µmol, 2 mol%) following general procedure A for 17 h. After column chromatography (SiO$_2$, CHex/EtOAc 4:1, r_f = 0.18), the product was obtained as a colourless solid (550 mg, 1.20 mmol, 63%).

Habitus Colourless solid (550 mg, 1.20 mmol, 63%).

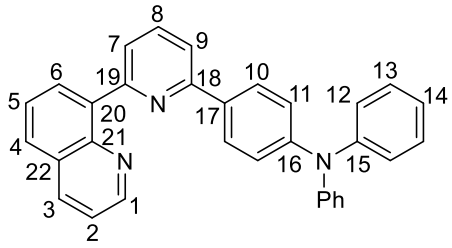

^{1}H NMR (CD$_2$Cl$_2$, 500 MHz) δ [ppm]: 8.90 (dd, *J* = 4.1, 1.9 Hz, 1H, H1), 8.21 (dd, *J* = 8.3, 1.9 Hz, 1H, H3), 7.87 (t, *J* = 1.7 Hz, 1H, H7), 7.85 (dd, *J* = 8.2, 1.4 Hz, 1H, H4), 7.77 (dd, *J* = 7.1, 1.4 Hz, 1H, H6), 7.63 - 7.58 (m, 3H, H5, H9, H12), 7.58 - 7.53 (m, 2H, H10, H10'), 7.51 (t, *J* = 7.6 Hz, 1H, H8), 7.41 (dd, *J* = 8.3, 4.1 Hz, 1H, H2), 7.25 (dd, *J* = 8.4, 7.4 Hz, 4H, H13, H13', H13'', H13'''), 7.11 (m, 6H, H11, H11', H12, H12', H12'', H12'''), 7.02 (t, *J* = 7.3 Hz, 2H, H14, H14'). **^{13}C NMR** (CD$_2$Cl$_2$, 126 MHz) δ [ppm]: δ 150.9 (CH, C1), 148.3 (Cq, C15, C15'), 147.8 (Cq, C16), 146.7 (Cq, C21), 141.4 (Cq, C20), 140.9 (Cq, C19), 140.7 (Cq, C18), 136.7 (CH, C3), 135.7 (Cq, C17), 130.7 (CH, C6), 129.9 (CH, C5), 129.8 (CH, , C13, C13', C13'', C13'''), 129.7 (CH, C7) , 129.3 (Cq, C22), 128.8 (CH, C8), 128.4 (CH, C4), 128.3 (CH, C10, C10'), 126.0 (CH, C9), 125.0 (CH, C12, C12', C12'', C12'''), 124.4 (CH, C11, C11'), 123.5 (CH, C14, C14'), 121.7 (CH, C2).

HR-ESI-MS (70 eV): 449.20 $[M]^{+\cdot}$.

Synthesis of dimethylfluoren-pyridine-quinoline (HFluorPyQ)

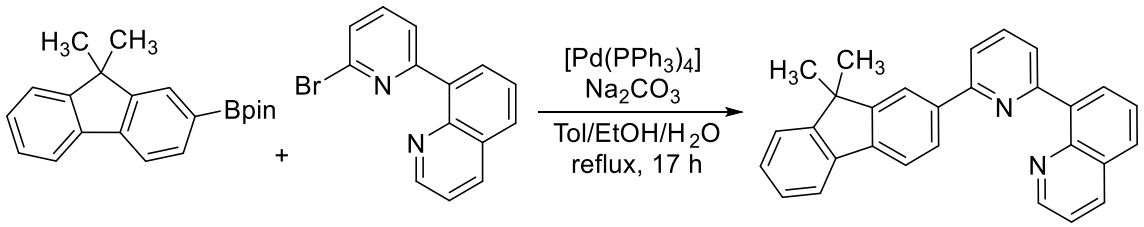

9,9-Dimethyl-fluorene-1-boronic acid pinacol ester (0.79 g, 2.46 mmol, 1.00 eq.) and 2-bromo-6-(8-quinolinyl)-pyridine (0.70 g, 2.46 mmol, 1.00 eq.) were reacted following general procedure A with [Pd(PPh$_3$)$_4$] (49.0 mg, 42.4 µmol, 2 mol%). After column chromatography (SiO$_2$, CHex/EtOAc 10:1, r_f = 0.20) the product was obtained as colourless powder (972 mg, 2.44 mmol, 99%).

Habitus Colourless powder (972 mg, 2.44 mmol, 99%).

^{1}H NMR (500 MHz, CD_2Cl_2) δ [ppm]: 8.96 (dd, *J* = 4.0, 1.8 Hz, 1H, H1), 8.32 (dd, *J* = 7.2, 1.5 Hz, 1H, H6), 8.29 (dd, *J* = 8.2, 1.7 Hz, 1H, H3), 8.23 - 8.19 (m, 1H, H16), 8.13 (dd, *J* = 7.9, 1.5 Hz, 1H, H10), 8.09 (dd, *J* = 7.6, 1.0 Hz, 1H, H11), 7.96 (dd, *J* = 8.1, 1.4 Hz, 1H, H4), 7.90 (t, *J* = 7.7 Hz, 1H, H8), 7.86 - 7.83 (m, 2H, H7, H9), 7.79 (dd, *J* = 6.1, 1.8 Hz, 1H, H12), 7.76 - 7.71 (m, 1H, H5), 7.49 - 7.45 (m, 2H, H2, H15), 7.40 - 7.31 (m, 2H, H13, H14), 1.55 (s, 6H, H17, H17′).

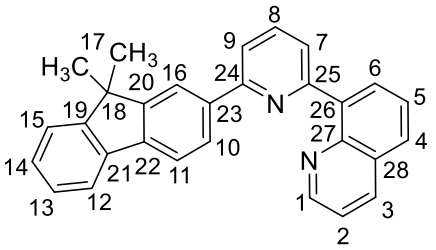

^{13}C NMR (126 MHz, CD_2Cl_2) δ [ppm]: 157.6 (Cq, C24), 157.3 (Cq, C25), 154.9 (Cq, C19), 154.7 (Cq, C20), 150.8 (CH, C1), 146.6 (Cq, C27), 140.4 (Cq, C22), 139.7 (Cq, C26), 139.5 (Cq, C23), 139.3 (Cq, C21), 136.9 (CH, C3), 136.4 (CH, C8), 131.8 (CH, C6), 129.3 (CH, C4), 129.2 (Cq, C28), 128.0 (CH, C13), 127.6 (CH, C14), 127.0 (CH, C5), 126.7 (CH, C10), 126.1 (CH, C11), 123.2 (CH, C15), 121.8 (CH, C16), 121.7 (CH, C2), 120.8 (CH, C12), 120.6 (CH, C7), 119.3 (CH, C9), 47.5 (Cq, C18), 27.5 (CH, C17, C17′).

GC-MS (70 eV): 398.2 $[M]^{\cdot+}$.

Synthesis of spirobifluorene-pyridine-quinoline (HSpiroPyQ)

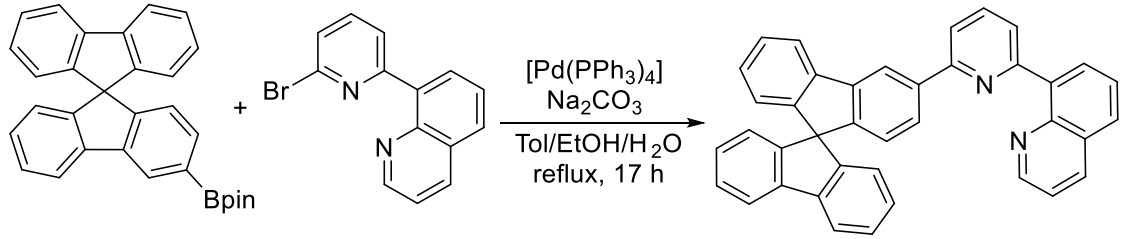

9,9′-Spirobifluorene-2-boronic acid pinacol ester (500 mg, 1.13 mmol, 1.00 eq.) and 2-bromo-6-(8-quinolinyl)-pyridine (332 mg, 1.16 mmol, 1.00 eq.) were reacted with $[Pd(PPh_3)_4]$ (26.0 mg, 22.5 µmol, 2 mol%) according to general procedure A for 17 h. After column chromatography (SiO_2, CHex/EtOAc 10:1, r_f = 0.22) the product was obtained as a colourless powder (590 mg, 1.13 mmol, 99%).

Habitus Colourless powder (590 mg, 1.13 mmol, 99%).

^{1}H NMR (500 MHz, $CDCl_3$) δ [ppm]: 8.95 (dd, *J* = 4.1, 1.8 Hz, 1H, H1), 8.63 (d, *J* = 1.7 Hz, 1H, H10), 8.32 (dd, *J* = 7.2, 1.5 Hz, 1H, H6), 8.28 (dd, *J* = 8.3, 1.8 Hz, 1H, H3), 8.12 (dd, *J* = 7.7, 1.1 Hz, 1H, H7), 8.00 (d, *J* = 7.7 Hz, 1H, H12), 7.95 (dd, *J* = 8.1, 1.5 Hz, 1H, H4), 7.90 (dd, *J* = 8.2, 6.8 Hz, 3H, H9, H20, H20′), 7.85 (ddd, *J* = 9.0, 7.9, 1.4 Hz, 2H, H8, H11), 7.73 (dd, *J* = 8.1, 7.2 Hz, 1H, H5), 7.47 (dd, *J* = 8.3, 4.1 Hz, 1H, H2), 7.40 (tdd, *J* = 7.6, 4.5, 1.1 Hz, 3H, H13,

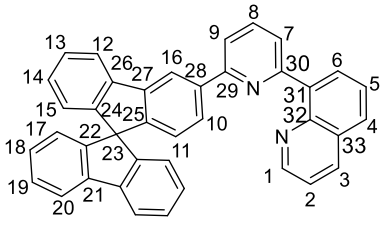

H19, H19'), 7.13 (tt, *J* = 7.4, 1.6 Hz, 3H, H14, H18, H18'), 6.80 (d, *J* = 8.0 Hz, 1H, H16), 6.74 (d, *J* = 7.6 Hz, 2H, H17, H17'), 6.70 (d, *J* = 7.6 Hz, 1H, H15).

^{13}C NMR (126 MHz, $CDCl_3$) δ [ppm]: 157.4 (Cq, C29, C30), 150.8 (CH, C1), 150.0 (Cq, C27), 149.7 (Cq, C26), 149.2 (Cq, C21, C21'), 146.5 (Cq, C32), 143.0 (Cq, C25), 142.4 (Cq, C22, C22'), 142.2 (Cq, C24), 140.4 (Cq, C28), 139.6 (Cq, C31), 137.0 (CH, C3), 136.5 (CH, C9), 131.8 (CH, C6), 129.4 (CH, C4), 129.2 (Cq, C33), 128.5 (CH, C13), 128.4 (CH, C19, C19', C18, C18', C14), 127.4 (CH, C11), 127.0 (CH, C5), 126.3 (CH, C7), 124.4 (CH, C17, C17', C16), 124.3 (CH, C15), 121.7 (CH, C2), 121.0 (CH, C12), 120.7 (CH, C20, C20'), 119.5 (CH, C8), 119.4 (CH, C10).

GC-MS (70 eV): 520.19 $[M]^{+\cdot}$.

Synthesis of pyridine-pyridine-naphthalene (PyPyHNaph)

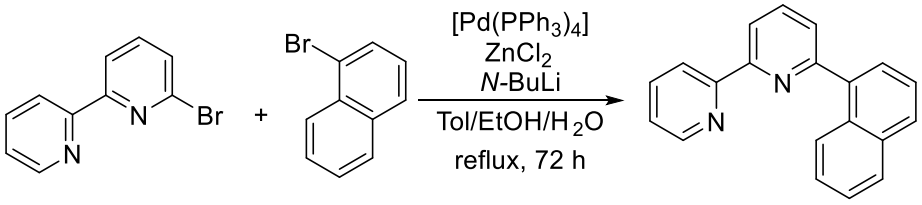

Under inert conditions, *N*-BuLi (2.50 M, 2.72 mL, 6.80 mmol, 1.60 eq.) was dissolved in 50 mL of THF at – 78 °C. 1-Bromonapthalene (1.32 g, 6.38 mmol, 1.50 eq.) was added dropwise over 30 min and the mixture then stirred for further 2 h at – 78 °C, resulting in a yellow solution. To this, a suspension of dried $ZnCl_2$ (1.16 g, 8.53 mmol, 2.00 eq.) in 25 mL of THF was added over 10 min, turning the mixture to light-yellow colour. The mixture was stirred 30 min and left to heat up to room temperature. A solution of 6-bromo-2,2'-bipyridine (1.00 g, 4.25 mmol, 1.00 eq.) in 25 mL of THF was added alongside the catalyst $[Pd(PPh_3)_4]$ (246 mg, 0.21 mmol, 5 mol%). The mixture was heated to reflux for 17 h, during which the mixture turned cloudy. The reaction was quenched by addition of sat. NH_4Cl-solution and extracted with CH_2Cl_2. The obtained crude product was purified *via* column chromatography (SiO_2, CHex/EtOAc, 5:1, r_f = 0.2) to yield the desired product as a yellow powder (320 mg, 1.13 mmol, 27%).

Habitus Yellow powder (320 mg, 1.13 mmol, 27%).

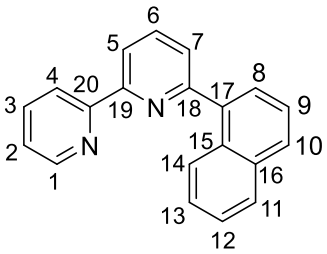

^{1}H NMR ($CDCl_3$, 500 MHz) δ [ppm]: 8.71 (d, *J* = 4.0 Hz, 1H, H1), 8.54 - 8.44 (m, 2H, H2, H5), 8.25 (d, *J* = 9.1 Hz, 1H, H14), 8.01 - 7.89 (m, 3H, H6, H10, H12), 7.77 (td, *J* = 7.7, 1.8 Hz, 1H, H3), 7.70 (dd, *J* = 7.0, 1.2 Hz, 1H, H8), 7.60 (dd, *J* = 7.5, 4.1 Hz, 2H, H7, H9), 7.50 (ddt, *J* = 9.8, 6.7, 3.4 Hz, 2H, H11, H13), 7.31 (dd, *J* = 6.2, 4.8 Hz, 1H, H4).**^{13}C NMR** ($CDCl_3$, 126 MHz) δ [ppm]: 158.7 (Cq, C18), 156.4 (Cq, C20), 155.9 (Cq, C19), 149.2 (CH, C1), 138.8 (Cq, C17), 137.5 (CH, C6), 137.1 (CH, C3), 134.2 (Cq, C15), 131.4 (Cq, C16), 129.1 (CH, C10), 128.5 (CH, C12), 127.8 (CH, C8), 126.5 (CH, C11), 126.0 (CH, C13, C14), 125.5 (CH, C9), 125.2 (CH, C7), 123.9 (CH, C4), 121.6 (CH, C2), 119.3 (CH, C5).

Synthesis of pyridine-pyridine-anthracene (PyPyHAnth)

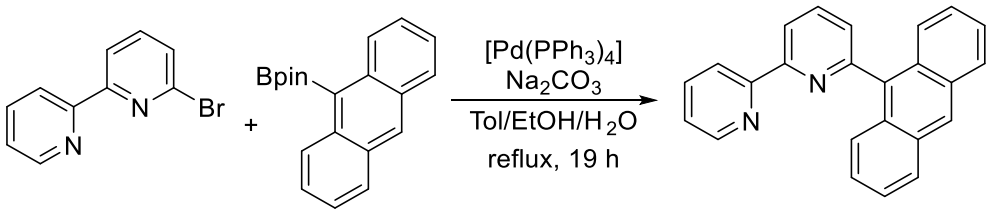

6-Bromo-2,2′-bipyridine (1.50 g, 6.38 mmol, 1.00 eq.) and 9-anthracene boronic acid pinacol ester (1.94 g, 6.38 mmol, 1.00 eq.) were reacted with [Pd(PPh$_3$)$_4$] (368 mg, 319 µmol, 5 mol%) following general procedure A for 19 h. After column chromatography (SiO$_2$, CHex/EtOAc 5:1, r_f = 0.45) the product was obtained as a pale-yellow powder (1.94 g, 5.83 mmol, 91%).

Habitus Pale-yellow powder (1.94 g, 5.83 mmol, 91%).

^{1}H NMR (CD_2Cl_2, 500 MHz) δ [ppm]: 8.78 (s, 1H, H1), 8.76 (d, *J* = 4.1 Hz, 1H, H8), 8.59 (d, *J* = 7.2 Hz, 1H, H5), 8.26 – 8.17 (m, 4H, H4, H6, H9, H9′), 7.84 (td, *J* = 7.8, 1.7 Hz, 1H, H3), 7.66 (d, *J* = 7.5 Hz, 1H, H7), 7.56 (t, *J* = 7.9 Hz, 4H, H10, H10′, H11, H11′), 7.45 (dd, *J* = 8.9, 6.4 Hz, 3H, H2, H12, H12′).

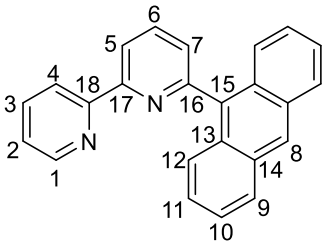

^{13}C NMR (CD_2Cl_2, 126 MHz) δ [ppm]: 156.7 (Cq, C17), 155.6 (Cq, C18), 155.2 (Cq, C16), 149.4 (CH, C1), 138.0 (CH, C4), 137.4 (CH, C3), 135.0 (Cq, C15), 130.9 (Cq, C13, C13′), 129.4 (Cq, C14, C14′), 128.5 (CH, C9, C9′), 127.3 (CH, C8), 126.9 (CH, C7), 126.3 (CH, C12, C12′), 125.6 (CH, C11, C11′), 125.4 (CH, C10, C10′), 124.4 (CH, C2), 120.7 (CH, C6), 119.4 (CH, C5).

GC-MS (70 eV): 332.1 $[M]^{\cdot+}$.

HR-EI-MS (70 eV): 332.12 $[M]^{\cdot+}$, 281.10 $[M–C_4H_4]^{\cdot+}$.

Synthesis of phenanthroline-anthracene (PhenHAnth)

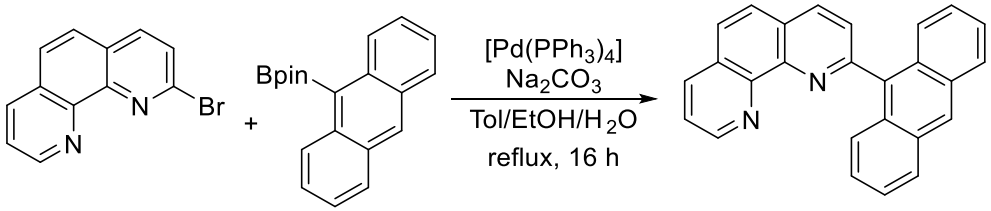

2-Bromo-1,10-phenantroline (500 mg, 1.93 mmol, 1.00 eq.) and 9-anthracene boronic acid pinacol ester (587 mg, 1.93 mmol, 1.00 eq.) were reacted with [Pd(PPh$_3$)$_4$] (116 mg, 100 µmol, 5 mol%) following general procedure A for 16 h. After column chromatography (SiO$_2$, CHex/EtOAc 9:1, r_f = 0.20) the product was obtained as a pale-yellow powder (254 mg, 0.71 mmol, 37%).

Habitus Pale-yellow powder (254 mg, 0.71 mmol, 37%).

^{1}H NMR (CD_2Cl_2, 500 MHz) δ [ppm]: 9.07 (s, 1H, H1), 8.63 (s, 1H, H8), 8.50 (d, *J* = 8.1 Hz, 1H, H6), 8.33 (dd, *J* = 8.1, 1.8 Hz, 1H, H3), 8.13 (d, *J* = 8.5 Hz, 2H, H12, H12′), 8.00 (d, *J* = 8.8 Hz, 1H, H5), 7.94 (d, *J* = 8.8 Hz, 1H, H4), 7.85 (d, *J* = 8.1 Hz, 1H, H7), 7.64 (dd, *J* = 8.1, 4.2 Hz, 1H, H2), 7.56 (d, *J* = 8.8 Hz, 2H, H9, H9′), 7.51 - 7.46 (m, 2H, H11, H11′), 7.36 - 7.32 (m, 2H, H10, H10′).

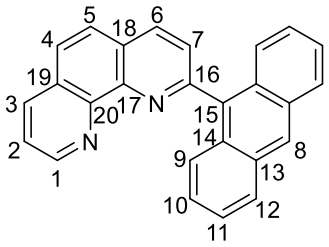

^{13}C NMR (CD_2Cl_2, 126 MHz) δ [ppm]: 159.0 (Cq, C16), 150.9 (CH, C1), 147.1 (Cq, C20), 147.0 (Cq, C17), 136.8 (CH, C6), 136.5 (CH, C3), 136.3 (Cq, C15), 132.0 (Cq, C13, C13′), 130.8 (Cq, C14, C14′), 129.6 (Cq, C19), 129.0 (CH, C12, C12′), 128.2 (Cq, C18), 128.1 (CH, C8), 127.5 (CH, C4), 127.0 (CH, C5), 126.8 (CH, C7), 126.6 (CH, C9, C9′), 126.4 (CH, C10, C10′), 125.7 (CH, C11, C11′), 123.6 (CH, C2).

Synthesis of quinoline-pyridine-anthracene (QPyHAnth)

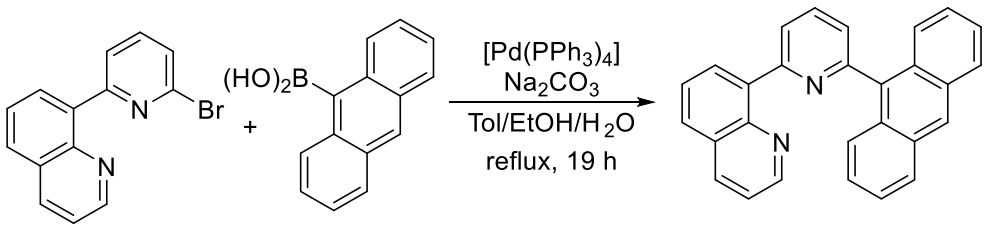

2-Bromo-6-(8-quinolinyl)-pyridine (1.00 g, 3.51 mmol, 1.00 eq.) and anthracene-9-boronic acid (779 mg, 3.51 mmol, 1.00 eq.) were reacted with $[Pd(PPh_3)_4]$ (208 mg, 180 µmol, 5 mol%) following general procedure A for 19 h. After column chromatography (SiO_2, CHex/EtOAc 1:1, r_f = 0.26) the product was obtained as a pale-yellow powder (1.02 g, 2.66 mmol, 76%).

Habitus Pale-yellow powder (1.02 g, 2.66 mmol, 76%).

^{1}H NMR (CD_2Cl_2, 400 MHz) δ [ppm]: 9.02 (dd, *J* = 4.1, 1.9 Hz, 1H, H1), 8.57 (s, 1H, H10), 8.41 (dd, *J* = 8.0, 0.9 Hz, 1H, H7), 8.29 - 8.18 (m, 2H, H3, H6), 8.08 (d, *J* = 8.5 Hz, 2H, H14, H14′), 8.04 (t, *J* = 7.8 Hz, 1H, H8), 7.88 (dd, *J* = 8.1, 1.4 Hz, 1H, H4), 7.79 (d, *J* = 8.0 Hz, 2H, H11, H11′), 7.62 - 7.57 (m, 1H, H5), 7.52 (dd, *J* = 7.6, 0.9 Hz, 1H, H9), 7.50 - 7.46 (m, 3H, H2, H13, H13′), 7.42 - 7.37 (m, 2H, H12, H12′).

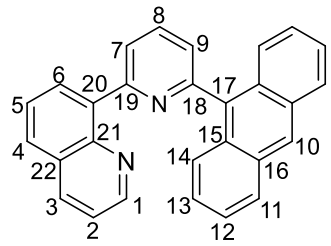

^{13}C NMR (CD_2Cl_2, 101 MHz) δ [ppm]: 158.1 (Cq, C18), 157.6 (Cq, C19), 150.8 (CH, C1), 146.5 (Cq, C21), 139.1 (Cq, C20), 137.0 (CH, C3), 136.4 (Cq, C17), 136.0 (CH, C8), 132.0 (CH, C6), 132.0 (Cq, C16, C16′), 130.7 (Cq, C15, C15′), 129.4 (CH, C4), 129.3 (Cq, C22), 128.9 (CH, C14, C14′), 127.8 (CH, C10), 127.0 (CH, C5), 126.9 (CH, C11, C11′), 126.4 (CH, C7), 126.3 (CH, C12, C12′), 125.7 (CH, C13, C13′), 125.7 (CH, C9), 121.7 (CH, C2).

HR-ESI-MS (70 eV): 405.14 $[M+Na]^+$, 383.15 $[M+H]^+$.

Synthesis of dibenzothiophene-phenyl-dibenzothiophene (DBTHPhDBT)

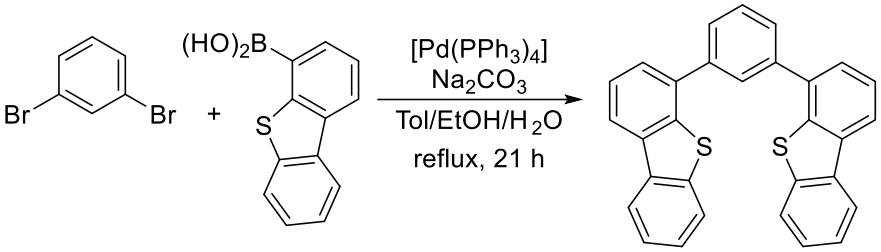

Dibenzothiophen-4-boronic acid (2.00 g, 8.77 mmol, 2.00 eq.) and 1,3-dibromobenzene (1.03 g, 4.38 mmol, 1.00 eq.) were reacted with $[Pd(PPh_3)_4]$ (104 mg, 90 µmol, 2 mol%) according to general procedures A for 21 h. After column chromatography (CHex/EtOAc 50:1, r_f= 0.34) the product was obtained as a colourless solid (0.69 g, 1.56 mmol, 36%).

Habitus Colourless solid (0.69 g, 1.56 mmol, 36%).

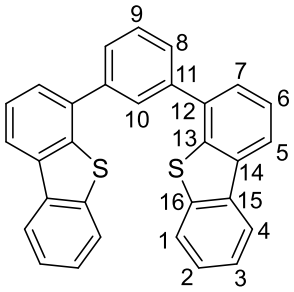

^{1}H NMR (CD_2Cl_2, 500 MHz) δ [ppm]: 8.25 – 8.18 (m, 4H, H1, H1', H6, H6'), 8.13 (t, *J* = 1.8 Hz, 1H, H10), 7.92 - 7.80 (m, 4H, H4, H4', H8, H8'), 7.70 (t, *J* = 7.7 Hz, 1H, H9), 7.66 - 7.57 (m, 4H, H5, H5', H7, H7'), 7.54 - 7.45 (m, 4H, H2, H2', H3, H3').

^{13}C NMR (CD_2Cl_2, 126 MHz) δ [ppm]: 141.8 (Cq, C11, C11'), 140.0 (Cq, C16, C16'), 139.0 (Cq, C13, C13'), 137.2 (Cq, C12, C12'), 136.9 (Cq, C14, C14'), 136.3 (Cq, C15, C15'), 130.0 (CH, C9), 128.7 (CH, C10), 128.4 (CH, C8, C8'), 127.7 (CH, C5, C5'), 127.5 (CH, C3, C3'), 125.9 (CH, C7, C7'), 125.1 (CH, C2, C2'), 123.2 (CH, C4, C4'), 122.4 (CH, C1, C1'), 121.3 (CH, C6, C6').

GC-MS (70 eV): 442 $[M]^+$.

Synthesis of pyridine-phenyl-thianthrene (PyHPhThian)

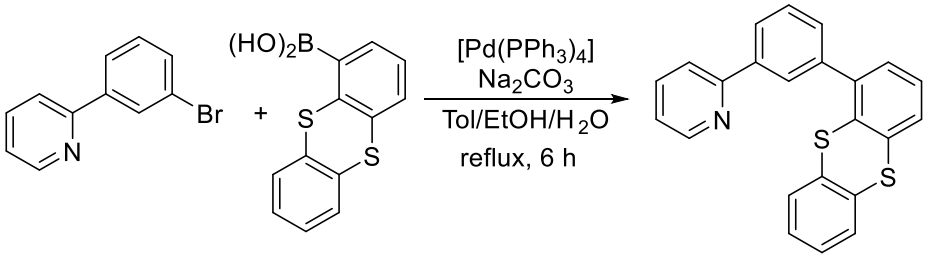

1-(2-Pyridinyl)-3-bromobenzene (1.00 g, 4.27 mmol, 1.00 eq.), and thianthrenyl-1-boronic acid (1.11 g, 4.27 mmol, 1.00 eq.) were reacted with $[Pd(PPh_3)_4]$ (243 mg, 210 µmol, 5 mol%) following general procedure A for 6 h. The obtained crude oil was purified by column chromatography (SiO_2, CHex/EtOAc 10:1, r_f= 0.36). The product was obtained as a colourless solid (1.36 g, 3.68 mmol, 86%).

Habitus Colourless solid (1.36 g, 3.68 mmol, 86%).

^{1}H NMR (CD_2Cl_2, 500 MHz) δ [ppm]: 8.68 (d, *J* = 4.2 Hz, 1H, H1), 8.11 (d, *J* = 7.9 Hz, 1H, H5), 8.06 (s, 1H, H8), 7.82 (d, *J* = 8.0 Hz, 1H, H4), 7.77 (td, *J* = 7.7, 1.7 Hz, 1H, H3), 7.59 (t, *J* = 7.7 Hz, 1H, H6), 7.55 (dd, *J* = 7.1, 2.0 Hz, 1H, H10), 7.50 (dd, *J* = 7.7, 1.1 Hz, 1H, H13), 7.46 (d, *J* = 7.6 Hz, 1H, H7), 7.37 - 7.29 (m, 3H, H9, H11, H14), 7.28 - 7.22 (m, 2H, H2, H12), 7.18 (td, *J* = 7.5, 1.3 Hz, 1H, H15).

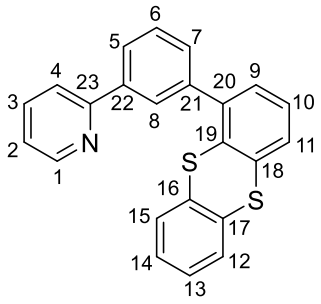

^{13}C NMR (CD_2Cl_2, 126 MHz): δ [ppm] = 157.3 (Cq, C23), 150.3 (CH, C1), 142.9 (Cq, C20), 141.2 (Cq, C22), 139.9 (Cq, C21), 137.4 (CH, C3), 136.8 (Cq, C16), 136.4 (Cq, C17), 135.9 (Cq, C19), 135.5 (Cq, C18), 130.5 (CH, C7), 129.9 (CH, C11), 129.4 (CH, C14), 129.1 (CH, C6), 129.0 (CH, C13), 128.9 (CH, C10) 128.5 (CH, C8), 128.4 (CH, C12), 128.2 (CH, C15), 127.8 (CH, C9), 126.8 (CH, C5), 122.9 (CH, C2), 121.0 (CH, C4).

HR-EI-MS (70 eV): 369.06 $[M]^{\cdot+}$.

Synthesis of pyridine-phenyl-dibenzofuran (PyHPhDBF)

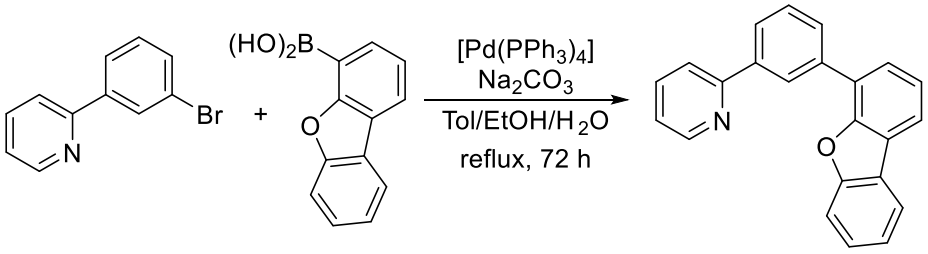

1-(2-Pyridinyl)-3-bromobenzene (1.00 g, 4.27 mmol, 1.00 eq.) and dibenzofurane-1-boronic acid (905 mg, 4.27 mmol, 1.00 eq.) were reacted with $[Pd(PPH_3)_4]$ (247mg, 214 μmol, 5 mol%) according to general procedure for 72 h. After column chromatography (SiO_2, CHex/EtOAc, 10:1, r_f = 0.28) the product was obtained as a colourless solid (1.33 g, 4.14 mmol, 97%).

Habitus Colourless solid (1.33 g, 4.14 mmol, 97%).

^{1}H NMR (CD_2Cl_2, 500 MHz) δ [ppm]: 8.71 (d, *J* = 4.1 Hz, 1H, H1), 8.53 (t, *J* = 1.5 Hz, 1H, H8), 8.09 (d, *J* = 7.8 Hz, 1H, H5), 8.03 (d, *J* = 7.2 Hz, 1H, H15), 8.01 - 7.97 (m, 2H, H7, H11), 7.87 (d, *J* = 7.9 Hz, 1H, H4), 7.80 (td, *J* = 7.7, 1.8 Hz, 1H, H3), 7.70 (dd, *J* = 7.6, 1.1 Hz, 1H, H9), 7.64 (dd, *J* = 16.3, 8.4 Hz, 2H, H2, H6), 7.52 - 7.44 (m, 2H, H10, H13), 7.39 (t, *J* = 7.1 Hz, 1H, H14), 7.27 (ddd, *J* = 7.3, 4.9, 1.1 Hz, 1H, H2).

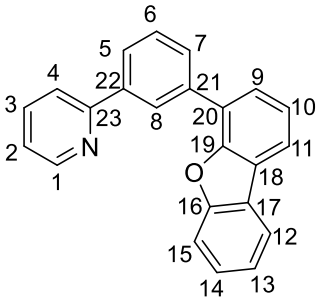

^{13}C NMR (CD_2Cl_2, 126 MHz) δ [ppm]: 157.6 (Cq, C23), 156.8 (Cq, C16), 154.0 (Cq, C19), 150.3 (CH, C1), 140.4 (Cq, C22), 137.5 (Cq, C21), 137.4 (CH, C3), 130.0 (CH, C7), 129.6 (CH, C6), 127.9 (CH, C13), 127.8 (CH C8), 127.6 (CH, C9), 126.9 (CH, C5), 126.3 (Cq, C17), 125.5 (Cq, C18), 124.7 (Cq, C20), 123.9 (CH, C10), 123.4 (CH,

C14), 122.9 (CH, C2), 121.3 (Cq, C15), 121.1 (Cq, C4), 120.5 (CH, C11), 112.3 (CH, C12).

HR-EI-MS (70 eV): 321.11 $[M]^{\cdot+}$.

Synthesis of thianthrene-phenyl-thianthrene (ThianHPhThian)

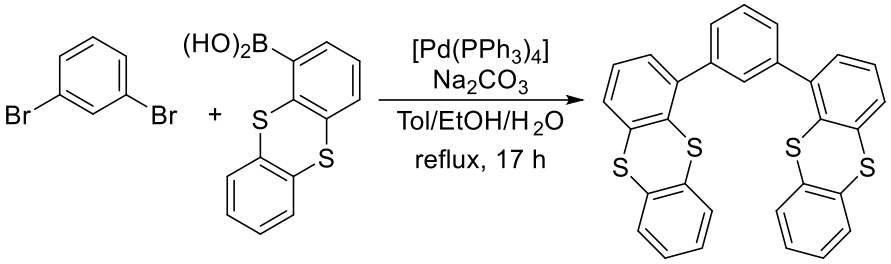

1,3-Dibromobenzene (907 mg, 3.84 mmol, 1.00 eq.) and thianthrene-1-boronic acid (2.00 g, 7.69 mmol, 2.00 eq.) were reacted with $[Pd(PPh_3)_4]$ (221 mg, 191 µmol, 5 mol%) following general procedure A for 17 h. After column chromatography (SiO_2, CHex/EtOAc 5:1, r_f = 0.72) the product was obtained as a colourless powder (1.68 g, 3.31 mmol, 86%).

Habitus Colourless powder (1.68 g, 3.31 mmol, 86%).

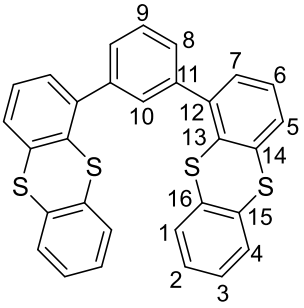

^{1}H NMR (CD_2Cl_2, 500 MHz) δ [ppm]: 7.63 - 7.58 (m, 1H, H9), 7.54 (dd, *J* = 7.6, 1.4 Hz, 2H, H5, H5′), 7.52 - 7.46 (m, 5H, H1, H1′, H8, H8′, H10), 7.43 (dd, *J* = 7.6, 1.1 Hz, 2H, H4, H4′), 7.37 (dd, *J* = 7.6, 1.5 Hz, 2H, H7, H7′), 7.32 (t, *J* = 7.6 Hz, 2H, H6, H6′), 7.25 (td, *J* = 7.5, 1.4 Hz, 2H, H2, H2′), 7.20 (td, *J* = 7.6, 1.4 Hz, 2H, H3, H3′).

^{13}C NMR (CD_2Cl_2, 126 MHz) δ [ppm]: 142.6 (Cq, C13, C13′), 140.7 (Cq, C11, C11′), 136.9 (Cq, C16, C16′), 136.3 (Cq, C12, C12′), 136.1 (Cq, C15, C15′), 135.5 (Cq, C14, C14′), 131.0 (CH, C10), 130.0 (CH, C7, C7′), 129.5 (CH, C4, C4′), 129.4 (CH, C8, C8′), 129.0 (CH, C1, C1′), 128.9 (CH, C5, C5′), 128.6 (CH, C9), 128.5 (CH, C2, C2′), 128.2 (CH, C3, C3′), 127.8 (CH, C6, C6′).

HR-EI-MS (70 eV): 506.03 $[M]^{\cdot+}$.

Synthesis of quinoline-phenyl-dibenzofuran (QHPhDBF)

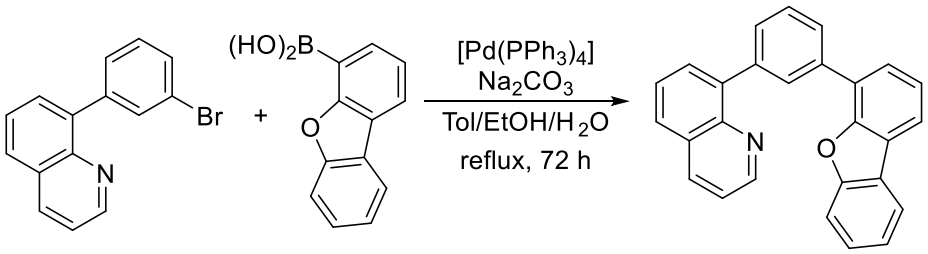

1-Bromo-3-(8-quinolinyl)-benzene (1.00 g, 3.52 mmol, 1.00 eq.) and dibenzofurane-1-boronic acid (746 mg, 3.52 mmol, 1.00 eq.) were reacted with $[Pd(PPh_3)_4]$ (106 mg, 91.7 µmol, 3 mol%) following general procedure A for 72 h. After column chromatography (SiO_2, CHex/EtOAc 15:1, r_f = 0.15) the product was obtained as a colourless powder (850 mg, 2.29 mmol, 65%).

Habitus Colourless powder (850 mg, 2.29 mmol, 65%).

^{1}H NMR (CD_2Cl_2, 500 MHz) δ [ppm]: 8.94 (dd, *J* = 4.0, 1.8 Hz, 1H, H1), 8.26 (dd, *J* = 8.3, 1.8 Hz, 1H, H3), 8.19 (t, *J* = 1.6 Hz, 1H, H10), 8.03 (d, *J* = 7.6 Hz, 1H, H17), 7.97 (ddd, *J* = 9.2, 6.8, 1.2 Hz, 2H, H4, H13), 7.89 (dd, *J* = 8.2, 1.4 Hz, 1H, H7), 7.86 (dd, *J* = 7.1, 1.4 Hz, 1H, H6), 7,75 (dt, *J* = 7.8, 1.4 Hz, 1H, H9), 7.70 (dd, *J* = 7.6, 1.2 Hz, 1H, H11), 7.68 - 7.64 (m, 2H, H5, H8), 7.60 (d, *J* = 8.2 Hz, 1H, H14), 7.51 - 7.43 (m, 3H, H2, H12, H15), 7.38 (td, *J* = 7.6, 0.9 Hz, 1H, H16).

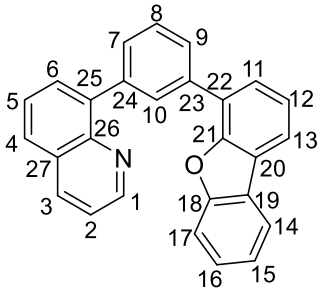

^{13}C NMR (CD_2Cl_2, 126 MHz) δ [ppm]: 156.8 (Cq, C18), 154.0 (Cq, C21), 150.8 (CH, C1), 146.7 (Cq, C26), 141.3 (Cq, C25), 140.8 (Cq, C24), 136.7 (CH, C3), 136.5 (Cq, C23), 131.7 (CH, C10), 130.9 (CH, C9), 130.8 (CH, C6), 129.3 (Cq, C27), 128.6 (CH, C8), 128.4 (CH, C7), 128.3 (CH, C4), 127.8 (CH, C15), 127.6 (CH, C11), 126.9 (CH, C5), 126.5 (Cq, C19), 125.4 (Cq, C20), 124.7 (Cq, C22), 123.8 (CH, C12), 123.4 (CH, C16), 121.7 (CH, C2), 121.3 (CH, C17), 120.3 (CH, C13), 112.3 (CH, C14).

HR-EI-MS (70 eV): 371.12 $[M]^{\cdot+}$.

Synthesis of quinoline-phenyl-thianthrene (QHPhThian)

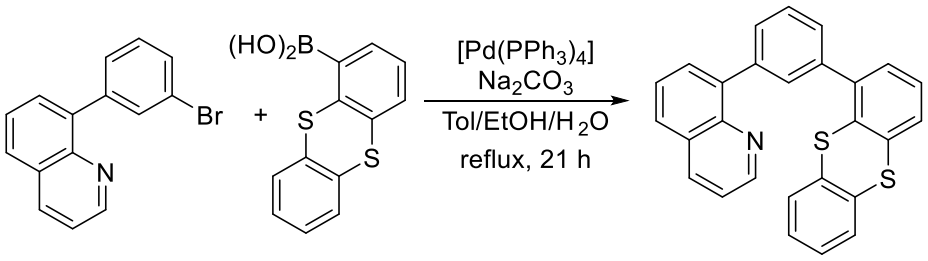

1-Bromo-3-(8-quinolinyl)-benzene (1.50g, 5.28 mmol, 1.00 eq.), and thianthrene-1-boronic acid (1.37 g, 5.28 mmol, 1.00 eq.) were reacted with [Pd(PPh$_3$)$_4$] (264 mg, 228 µmol, 5 mol%) for 21 h according to general procedure A. After column chromatography (SiO_2, CHex/EtOAc 10:1, r_f = 0.20) the product was obtained as a colourless solid (1.77 g, 4.20 mmol, 80%).

Habitus Colourless solid (1.77 g, 4.20 mmol, 80%).

^{1}H NMR (CD_2Cl_2, 500 MHz) δ [ppm]: 8.94 (dd, *J* = 4.1, 1.7 Hz, 1H, H1), 8.25 (dd, *J* = 8.2, 1.7 Hz, 1H, H3), 7.88 (d, *J* = 8.1 Hz, 1H, H4), 7.84 (dd, *J* = 7.1, 1.3 Hz, 1H, H6), 7.80 (d, *J* = 7.8 Hz, 1H, H13), 7.73 (s, 1H, H10), 7.67 - 7.63 (m, 1H, H5), 7.60 (t, *J* = 7.7 Hz, 1H, H12), 7.54 (dd, *J* = 7.8, 1.4 Hz, 1H, H7), 7.50 (dd, *J* = 7.6, 1.1 Hz, 1H, H14), 7.49 – 7.43 (m, 3H, H2, H11, H17), 7.39 (d, *J* = 7.5 Hz, 1H, H9), 7.32 (t, *J* = 7.6 Hz, 1H, H8), 7.26 (td, *J* = 7.6, 1.4 Hz, 1H, H15), 7.20 (td, *J* = 7.6, 1.4 Hz, 1H, H16).

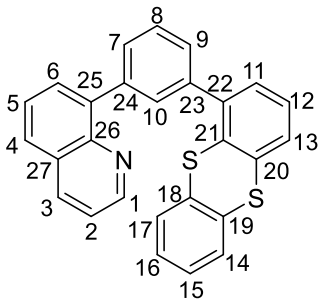

^{13}C NMR (CD_2Cl_2, 126 MHz) δ [ppm]: 150.8 (CH, C1), 146.6 (Cq, C26), 143.1 (Cq, C24), 140.9 (Cq, C19), 140.3 (Cq, C18), 140.2 (Cq, C22), 136.9 (Cq, C21), 136.8 (CH, C3), 136.5 (Cq, C20), 135.8 (Cq, C23), 135.6 (Cq, C25), 132.2 (CH, C10), 131.1 (CH, C13), 130.8 (CH, C6), 130.1 (CH, C9), 129.4 (CH, C17), 129.3 (Cq, C27), 129.2 (CH, C14), 128.8 (CH, C7), 128.8 (CH, 11), 128.4 (CH,C4), 128.4 (CH, C15) 128.2 (CH, C12), 128.1 (CH, C16), 127.7 (CH, C8), 126.9 (CH, C5), 121.7 (CH, C2).

HR-EI-MS (70 eV): 419.09 $[M]^{\cdot+}$.

Synthesis of pyridine-phenyl-dibenzothiophene (PyHPhDBT)

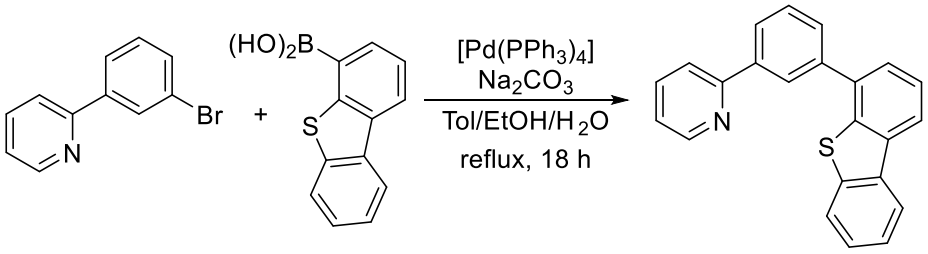

1-(2-Pyridinyl)-3-bromobenzene (1.00 g, 4.27 mmol, 1.00 eq.) and dibenzothiophene-1-boronic acid (0.97 g, 4.27 mmol, 1.00 eq.) were reacted with [Pd(PPh$_3$)$_4$] (99.0 mg, 85.7 µmol, 2 mol%) following

general procedure A for 18 h. The obtained crude oil was purified by column chromatography (SiO_2, CHex/EtOAc 10:1, r_f = 0.23). The product was obtained as a colourless solid (1.31 g, 3.88 mmol, 91%).

Habitus Colourless solid (1.31 g, 3.88 mmol, 91%).

^{1}H NMR (CD_2Cl_2, 500 MHz) δ [ppm]: 8.70 (d, *J* = 4.2 Hz, 1H, H1), 8.42 (t, *J* = 1.6 Hz, 1H, H8), 8.25 - 8.18 (m, 2H, H5, H13), 8.11 (dt, *J* = 7.8, 1.5 Hz, 1H, H11), 7.89 - 7.83 (m, 2H, H4, H9), 7.82 - 7.77 (m, 2H, H3, H7), 7.64 (t, *J* = 7.7 Hz, 1H, H6), 7.62 - 7.56 (m, 2H, H12, H14), 7.52 - 7.44 (m, 2H, H10, H15), 7.27 (ddd, *J* = 7.3, 4.8 ,1.1 Hz, 1H, H2).

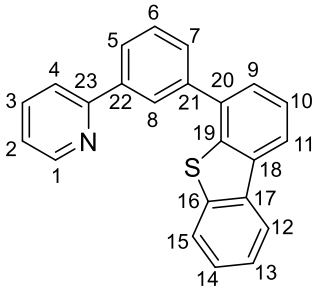

^{13}C NMR (CD_2Cl_2, 126 MHz) δ [ppm]: 156.8 (Cq, C23), 149.8 (CH, C1), 141.0 (Cq, C21), 140.0 (Cq, C22), 139.5 (Cq, C19), 138.5 (Cq, C16), 136.8 (CH, Cq, C3, C20), 136.3 (Cq, C17), 135.8 (Cq, C18), 129.3 (CH, C6) , 128.7 (CH, C7), 127.0 (CH, C14), 126.9 (CH, C10), 126.8 (CH, C8), 126.5 (CH, C5), 125.3 (CH, C12), 124.5 (CH, C15), 122.6 (CH, C9), 122.4 (CH, C2), 121.8 (CH, C11), 120.7 (CH, C13), 120.5 (CH, C4).

HR-EI-MS (70 eV): 337.09 $[M]^{\cdot+}$.

6.2.3 Synthesis of Complexes

General Procedure B

The ligand and $[K_2(MCl_4)]$ were mixed in glacial HOAc (30 mL) in a round bottom flask. The mixture was heated to reflux and after cooling to room temperature, the mixture was filtered off over a glass frit and washed with diethyl ether and distilled water. The filter residue was redissolved in $CHCl_3$ or CH_2Cl_2 and the solvent evaporated off to yield the product.

General Procedure C

The ligand and $[K_2(MCl_4)]$ were mixed in 5 mL of glacial HOAc in a microwave tube. The mixture was heated to 160 °C at 300 W irradiation energy. After cooling to room temperature, the mixture was filtered off over a glass frit and washed with diethyl ether and distilled water. The filter residue was redissolved in $CHCl_3$ or CH_2Cl_2 and the solvent evaporated off to yield the product.

General Procedure D

Under inert conditions, the ligand (1.00 eq.) and $NiBr_2$ (1.00 eq.) were mixed with pre-dried KOAc (1.00 eq.) and K_2CO_3(1.00 eq.). Freshly distilled *p*-xylene was added (150 mL) and a *Dean-Stark* water trap filled with freshly activated molecular sieves (heated in a *Schlenk* flask at 300 °C overnight). The mixture was heated for 72 h at reflux temperatures. After cooling to room temperature, the mixture was filtered off over a glass frit. The residue was washed with *p*-xylene or *n*-pentane if the complex was partially soluble in *p*-xylene, indicated by a colour

change of the solution. The filter residue was dissolved in either THF or CH_2Cl_2 and the solvent evaporated off to yield the complex.

Synthesis of [Pt(Py*t*BuPhPy)Cl]

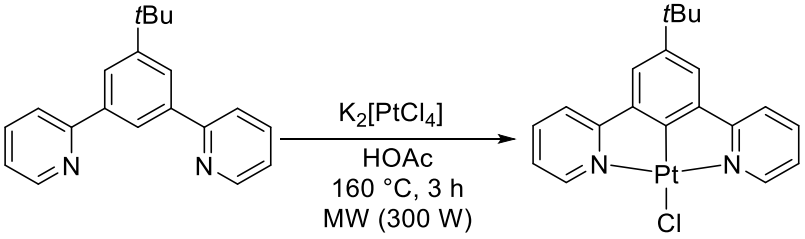

Py*t*BuHPhPy (83.6 mg, 0.29 mmol, 1.20 eq.) and $K_2[PtCl_4]$ (100 mg, 0.24 mmol, 1.00 eq.) were reacted according to general procedure C for 3 h. The product was obtained as an orange powder (124 mg, 0.24 mmol, 99%).

Habitus Orange powder (124 mg, 0.24 mmol, 99%).

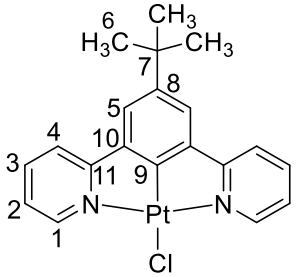

^{1}H NMR (CD_2Cl_2, 500 MHz) δ [ppm]: 9.25 (dd, $J^{Pt\text{-}H}$ = 41.2 Hz, J = 4.3 Hz, 2H, H1, H1′), 7.97 (t, J = 7.0 Hz, 2H, H3, H3′), 7.76 (d, J = 7.8 Hz, 2H, H4, H4′), 7.58 (s, 2H, H5, H5′), 7.30 (t, J = 6.5 Hz, 2H, H2, H2′), 1.43 (s, 9H, H6, H6′, H6′′).

^{13}C NMR (CD_2Cl_2, 126 MHz) δ [ppm]: 168.2 (Cq, C11, C11′), 159.2 (Cq, C10, C10′) , 152.6 (CH, C1, C1′), 147.0 (Cq, C8), 141.1 (Cq, C9), 139.7 (CH, C3, C3′), 123.8 (CH, C2, C2′), 122.1 (CH, C5, C5′), 119.8 (CH, C4, C4′), 35.8 (Cq, C7), 31.8 (CH, C6, C6′, C6′′).

^{195}Pt NMR (CD_2Cl_2, 107 MHz) δ [ppm]: −3664.3.

HR-ESI-MS (70 eV): 999.21 $[2xM–Cl]^+$, 482.12 $[M–Cl]^+$, 289.17 $[L+H]^+$.

Synthesis of [Pd(Py*t*BuPhPy)Cl]

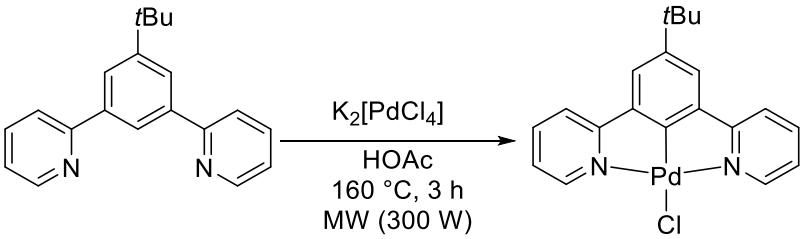

Py*t*BuHPhPy (83.6 mg, 0.29 mmol, 1.20 eq.) and $K_2[PdCl_4]$ (78.3 mg, 0.24 mmol, 1.00 eq.) were reacted according to general procedure C for 3 h. The product was obtained as a colourless powder (91.2 mg, 0.21 mmol, 88%).

Habitus Colourless powder (91.2 mg, 0.21 mmol, 88%).

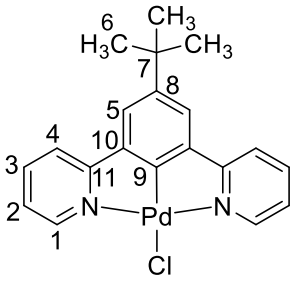

^{1}H NMR (CD_2Cl_2, 500 MHz) δ [ppm]: 9.02 (ddd, *J* = 5.6, 1.7, 0.8 Hz, 2H, H1, H1′), 7.92 (ddd, *J* = 8.0, 7.6, 1.7 Hz, 2H, H3, H3′), 7.74 (ddd, *J* = 8.0, 1.4, 0.8 Hz, 2H, H4, H4′), 7.52 (s, 2H, H5, H5′), 7.28 (ddd, *J* = 7.6, 5.5, 1.4 Hz, 2H, H2, H2′), 1.41 (s, 9H, H6, H6′, H6′′).

^{13}C NMR (CD_2Cl_2, 126 MHz) δ [ppm]: 170.2 (Cq, C11, C11′), 165.9 (Cq, C10, C10′), 153.1 (CH, C1, C1′), 148.6 (Cq, C8), 143.4 (Cq, C9), 139.7 (CH, C3, C3′), 123.8 (CH, C2, C2′), 121.9 (CH, C5, C5′), 119.4 (CH, C4, C4′), 35.6 (Cq, C7) 31.8 (CH, C6, C6′, C6′′).

HR-ESI-MS (70 eV): 823.09 $[2xM–Cl]^+$, 393.06 $[M–Cl]^+$, 289.17 $[L+H]^+$.

Synthesis of [Ni(Py*t*BuPhPy)Br]

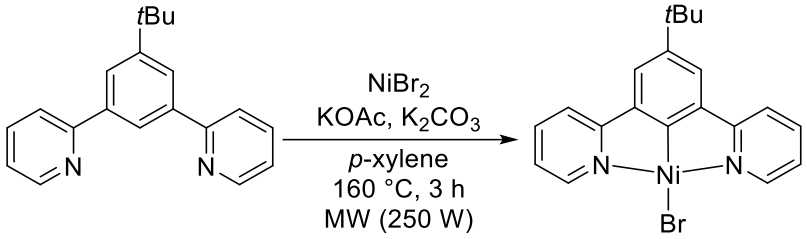

Py*t*BuHPhPy (173 mg, 0.60 mmol, 1.00 eq.) and $NiBr_2$ (200 mg, 0.91 mmol, 1.52 eq.) were reacted with KOAc (59.0 mg, 0.60 mmol, 1.00 eq.) and K_2CO_3 (83.0 mg, 0.60 mmol, 1.00 eq.) in distilled *p*-xylene. The solids were pre-dried prior to use and the solvent degassed with argon. The filled microwave tube was flushed with argon and sealed. The tube was then irradiated and heated to 160 °C for 3 h at 250 W. The resulting solids were filtered off over a glass frit and washed with *p*-xylene. The filter residue was dissolved in distilled THF and the solvent evaporated off. The resulting solid was redissolved in little THF and precipitated by addition of *n*-pentane. After filtration and drying the product was obtained as an orange powder (165 mg, 0.39 mmol, 65%).

Habitus Orange powder (165 mg, 0.39 mmol, 65%).

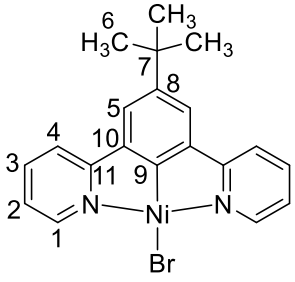

^{1}H NMR ($CDCl_3$, 300 MHz) δ [ppm]: 9.30 (d, *J* = 5.9 Hz, 2H, H1, H1′), 7.77 (td, *J* = 7.7, 1.6 Hz, 2H, H3, H3′), 7.53 (d, *J* = 7.8 Hz, 2H, H4, H4′), 7.30 (d, *J* = 20.7 Hz, 2H, H5, H5′), 7.07 (ddd, *J* = 7.4, 5.7, 1.4 Hz, 2H, H2, H2′), 1.39 (s, 9H, H6)

The compounds analytical data matches previously reported data.[13]

Synthesis of [Pt(PhPyQ)Cl]

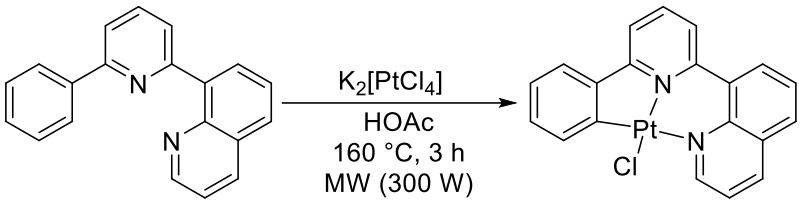

HPhPyQ (50.0 mg, 0.18 mmol, 1.20 eq.) and $K_2[PtCl_4]$ (62.3 mg, 0.15 mmol, 1.00 eq.) were reacted according to general procedure C for 3 h. The product was obtained as an orange powder (49.8 mg, 97.0 µmol, 66%).

Habitus Orange powder (49.8 mg, 97.0 µmol, 66%).

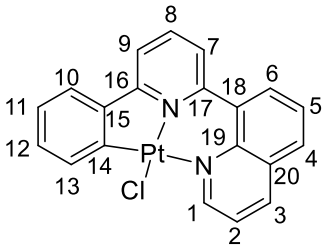

^{1}H NMR ($CDCl_3$, 500 MHz) δ [ppm]: 10.38 (dd, *J* = 5.1, 1.7 Hz, 1H, H1), 8.51 (dd, *J* = 8.2, 1.6 Hz, 1H, H3), 8.36 (dd, *J* = 7.5, 1.3 Hz, 1H, H6), 8.18 (ddd, $J^{Pt\text{-}H}$ = 32.3 Hz, *J* = 7.7, 1.2 Hz, 0.4 Hz, 1H, H13), 8.08 (dd, *J* = 8.0, 1.2 Hz, 1H, H4), 7.99 (t, *J* = 8.0 Hz, 1H, H8), 7.76 - 7.66 (m, 4H, H2, H5, H7, H9), 7.51 (dd, *J* = 7.7, 1.4 Hz, 1H, H10), 7.18–7.15 (m, 2H, H11, H12).

^{13}C NMR ($CDCl_3$, 126 MHz) δ [ppm]: 168.2 (Cq, C16), 154.9 (CH, C1), 151.9 (Cq, C17), 144.5 (Cq, C15), 140.8 (Cq, C14), 140.4 (Cq, C19), 139.7 (CH, C3), 137.9 (CH, C8), 135.8 (CH, C13), 134.9 (CH, C6), 133.5 (Cq, C18), 132.4 (CH, C4), 129.8 (CH, C12), 129.5 (Cq, C20), 127.1 (CH, C7), 124.1 (CH, C11), 123.3 (CH, C10), 122.8 (CH, C9), 122.4 (CH, C2), 117.4 (CH, C5).

^{195}Pt NMR ($CDCl_3$, 107 MHz): δ [ppm] = −3357.6.

HR-ESI-MS (70 eV): 533.03 $[M+Na]^+$, 475.07 $[M–Cl]^+$.

HR-EI-MS (70 eV): 511.04 $[M]^{\cdot+}$, 475.07 $[M−Cl]^+$.

Synthesis of [Pd(PhPyQ)Cl]

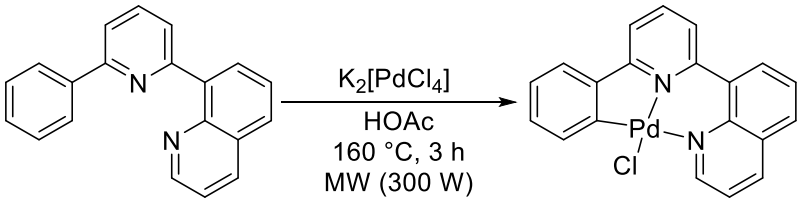

HPhPyQ (50.0 mg, 0.18 mmol, 1.20 eq.) and $K_2[PdCl_4]$ (48.9 mg, 0.15 mmol, 1.00 eq.) were reacted according to general procedure C for 3 h. The product was obtained as a pale-yellow powder (30.0 mg, 70.9 µmol, 47%).

Habitus Pale-yellow powder (30 mg, 70 μmol, 47%).

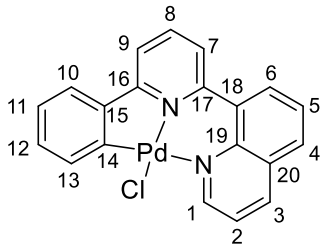

^{1}H NMR ($CDCl_3$, 500 MHz) δ [ppm]: 10.2 (dd, *J* = 5.0, 1.7 Hz, 1H, H1), 8.40 (dd, *J* = 8.2, 1.7 Hz, 1H, H3), 8.32 (dd, *J* = 7.5, 1.2 Hz, 1H, H6), 8.14 - 8.10 (m, 1H, H13), 8.00 (dd, *J* = 8.0, 1.2 Hz, 1H, H4), 7.91 (t, *J* = 8.0 Hz, 1H, H8), 7.71 - 7.61 (m, 4H, H2, H5, H7, H9), 7.47 - 7.43 (m, 1H, H10), 7.16 (quin., *J* = 5.8, 2.0 Hz, 2H, H11, H12).

^{13}C NMR ($CDCl_3$, 126 MHz) δ [ppm]: 166.3 (Cq, C16), 155.9 (CH, C1), 153.9 (Cq, C17), 153.7 (Cq, C14), 145.5 (Cq, C15), 141.3 (Cq, C19), 139.6 (CH, C3), 138.8 (CH, C8), 137.5 (CH, C13), 135.2 (CH, C6), 132.9 (Cq, C18), 132.0 (CH, C4), 129.5 (CH, C12), 129.3 (Cq, C20), 126.9 (CH, C7), 124.7 (CH, C11), 123.5 (CH, C10), 123.4 (CH, C9), 121.9 (CH, C2), 117.4 (CH, C5).

HR-ESI-MS (70 eV): 443.97 $[M+Na]^+$, 387.01 $[M–Cl]^+$.

HR-EI-MS (70 eV): 421.98 $[M]^+$, 387.01 $[M–Cl]^+$.

Synthesis of [Ni(PhPyQ)Br]

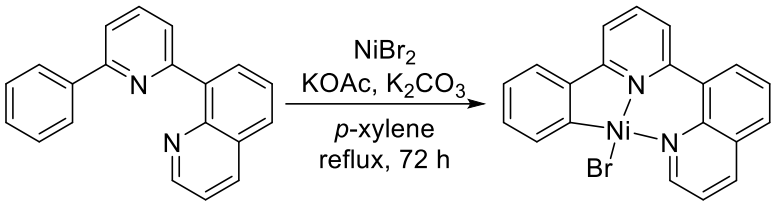

HPhPyQ (127 mg, 0.45 mmol, 1.00 eq.), $NiBr_2$ (129 mg, 0.59 mmol, 1.30 eq.), K_2CO_3 (62.2 mg, 0.45 mmol, 1.00 eq.) and KOAc (44.2 mg, 0.45 mmol, 1.00 eq.) were reacted according to general procedure D for 72 h. The product was obtained as a dark red powder (51.5 mg, 0.11 mmol, 24%).

Habitus Dark red powder (51.5 mg, 0.11 mmol, 24%).

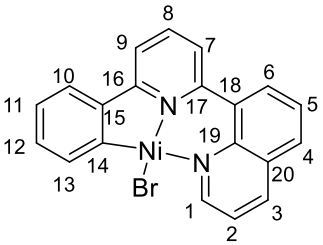

HR-ESI-MS (70 eV): 283.12 $[L+H]^+$.

EA Calc.: N: 6.67%, C: 57.20%, H: 3.12%. Found: N: 4.85%, C: 46.36%, H: 3.78%.

Synthesis of [Pt(PyPhQ)Cl]

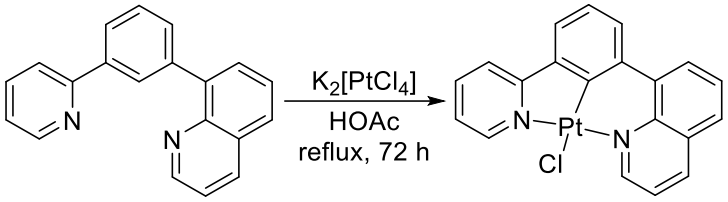

PyHPhQ (800 mg, 2.82 mmol, 1.00 eq.) and $K_2[PtCl_4]$ (1.17 g, 2.82 mmol, 1.00 eq.) were reacted following general procedure B for 72 h. The complex was isolated as orange powder (1.38 g, 2.69 mmol, 95%).

Habitus Orange powder (1.38 g, 2.69 mmol, 95%).

^{1}H NMR ($CDCl_3$, 600 MHz): δ [ppm] = 10.88 (dd, $J^{Pt\text{-}H}$ = 39.7 Hz, J = 5.5, 1.7 Hz, 1H, H1), 9.98 (ddd, $J^{Pt\text{-}H}$ = 37.7 Hz, J = 5.9, 1.5, 0.6 Hz, 1H, H13), 8.50 (dd, J = 8.1, 1.6 Hz, 1H, H3), 8.47 (dd, J = 7.6, 1.2 Hz, 1H, H4), 7.92–7.88 (m, 3H, H5, H7, H11), 7.80 - 7.74 (m, 2H, H6, H10), 7.59 (dd, J = 7.5, 0.9 Hz, 1H, H9), 7.50 (dd, J = 8.0, 5.5 Hz, 1H, H2), 7.38 (t, J = 7.7 Hz, 1H, H8), 7.26 (ddd, J = 7.4, 5.9, 1.5 Hz, 1H, H12).

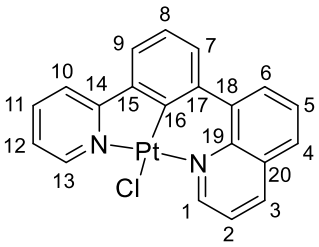

^{13}C NMR ($CDCl_3$, 151 MHz) δ [ppm]: 166.2 (Cq, C14), 158.8 (CH, C1), 152.4 (CH, C13), 144.8 (Cq, C16), 141.3 (Cq, C18), 140.6 (CH, C3), 139.2 (Cq, C19), 138.8 (CH, C5), 137.4 (Cq, C15), 131.4 (Cq, C17), 130.5 (CH, C4), 130.3 (Cq, C20), 129.2 (CH, C11), 127.4 (CH, C7), 127.1 (CH, C10), 124.5 (CH, C8), 123.2 (CH, C9), 122.3 (CH, C12), 121.2 (CH, C2), 118.4 (CH, C6).

^{195}Pt NMR ($CDCl_3$, 129MHz): δ [ppm] = −3656.5.

HR-ESI-MS (70 eV): 475.07 $[M–Cl]^+$.

Synthesis of [Pd(PyPhQ)Cl]

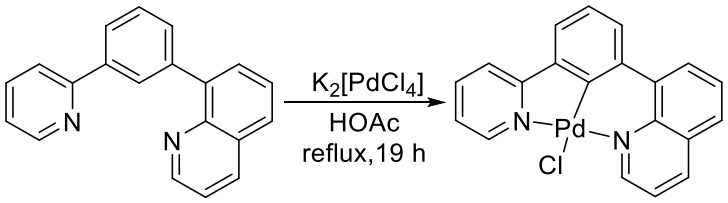

PyHPhQ (60.0 mg, 0.21 mmol, 1.40 eq.) and $K_2[PdCl_4]$ (48.9 mg, 0.15 mmol, 1.00 eq.) were reacted following general procedure B for 19 h. The complex was isolated as yellow powder (56.2 mg, 133 μmol, 89%).

Habitus Yellow powder (56.2 mg, 133 μmol, 89%).

^{1}H NMR ($CDCl_3$, 500 MHz): δ [ppm] = 10.59 (dd, *J* = 5.3, 1.6 Hz, 1H, H1), 9.70 (d, *J* = 4.8 Hz, 1H, H13), 8.43 (dd, *J* = 8.1, 1.6 Hz, 1H, H3) 8.40 (d, *J* = 6.6 Hz, 1H, H4), 7.92 - 7.86 (m, 2H, H6, H11), 7.80 - 7.75 (m, 2H, H7, H10), 7.74 (t, *J* = 7.7 Hz, 1H, H5), 7.58 (dd, *J* = 7.5, 1.0 Hz, 1H, H9), 7.55 (dd, *J* = 8.1, 5.4 Hz, 1H, H2), 7.35 (t, *J* = 7.7 Hz, 1H, H8), 7.25 (ddd, *J* = 7.3, 5.8, 1.4 Hz, 1H, H12).

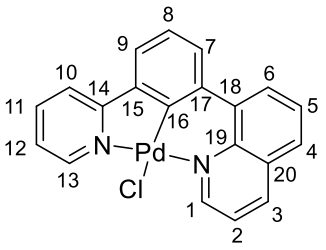

^{13}C NMR ($CDCl_3$, 126 MHz): δ [ppm] = 164.7 (Cq, C14), 158.7 (CH, C1), 153.7 (Cq, C16), 153.0 (CH, C13), 146.0 (Cq, C15), 140.3 (CH, C3), 139.4 (Cq, C19), 138.7 (CH, C11), 137.6 (Cq, C18), 132.6 (Cq, C17), 130.1 (CH, C4), 130.0 (Cq, C20), 129.0 (CH, C6), 127.6 (CH, C7), 127.2 (CH, C5), 125.8 (CH, C8), 123.3 (CH, C9), 122.5 (CH, C12), 120.9 (CH, C2), 118.4 (CH, C10).

HR-ESI-MS (70 eV): 443.97 $[M+Na]^+$, 386.01 $[M–Cl]^+$.

Synthesis of [Ni(PyPhQ)Br]

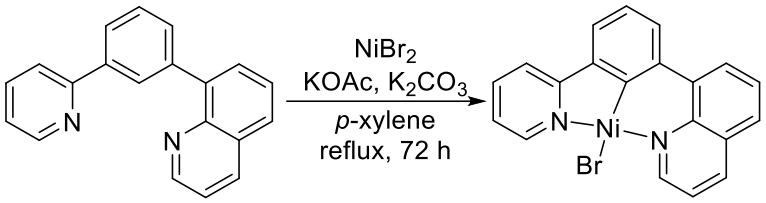

PyHPhQ (100 mg, 0.35 mmol, 1.00 eq.), $NiBr_2$ (100 mg, 0.46 mmol, 1.30 eq.), K_2CO_3 (48.9 mg, 0.35 mmol, 1.00 eq.) and KOAc (34.7 mg, 0.35 mmol, 1.00 eq.) were reacted following general procedure D for 72 h. The complex was obtained as a red powder (75.7 mg, 0.18 mmol, 51%).

Habitus Red powder (75.7 mg, 0.18 mmol, 51%).

^{1}H NMR ($CDCl_3$, 500 MHz) δ [ppm]: 10.09 (s, 1H, H1), 9.41 (s, 1H, H13), 8.36 (d, *J* = 6.9 Hz, 1H, H4), 8.26 (d, *J* = 7.6 Hz, 1H, H3), 7.77 (d, *J* = 7.1 Hz, 2H, H11, H6), 7.73 - 7.64 (m, 2H, H5, H7), 7.57 (d, *J* = 6.9 Hz, 1H, H10), 7.39 - 7.30 (m, 2H, H9, H2), 7.28 (s,1H, H8), 7.12 - 7.06 (m, 1H, H12).

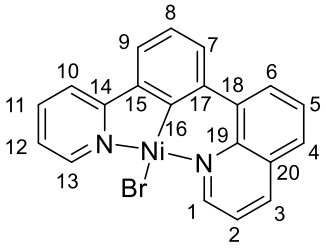

^{13}C NMR ($CDCl_3$, 126 MHz) δ [ppm]: 162.7 (Cq, C14), 158.2 (CH, C1), 154.4 (CH, C13), 146.9 (Cq, C15), 146.7 (Cq, C16), 140.3 (Cq, C19), 139.0 (CH, C3), 138.3 (CH, C11), 135.2 (Cq, C18), 134.4 (Cq, C17), 129.2 (Cq, C20), 128.1 (CH, C6), 127.3 (CH, C5), 127.0 (CH, C4), 126.0 (CH, C8), 125.2 (CH, C7), 122.3 (CH, C9), 122.0 (CH, C12), 119.4 (CH, C2), 117.5 (CH, C10).

HR-ESI-MS (70 eV): 418.97 $[M+H]^+$, 339.04 $[M–Br]^+$.

Synthesis of [Pt(QPhQ)Cl]

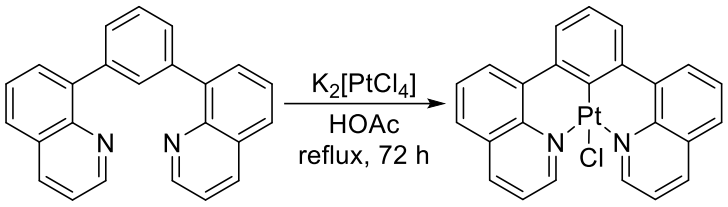

QHPhQ (60.0 mg, 0.18 mmol, 1.20 eq.) and $K_2[PtCl_4]$ (62.3 mg, 0.15 mmol, 1.00 eq.) were reacted following general procedure B for 72 h. The complex was isolated as orange powder (66.1 mg, 0.12 mmol, 80%).

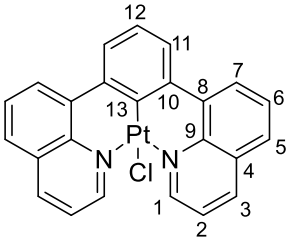

Habitus Orange powder (66.1 mg, 0.12 mmol, 80%).

^{1}H NMR (DMSO-d_6, 500 MHz): δ [ppm] = 9.54 (dd, *J* = 5.3, 1.4 Hz, 2H, H1, H1′), 8.78 (dd, *J* = 8.2, 1.3 Hz, 2H, H3, H3′), 8.48 (d, *J* = 6.6 Hz, 2H, H7, H7′), 8.14 (d, *J* = 7.6 Hz, 2H, H5, H5′), 7.85 (t, *J* = 7.7 Hz, 2H, H6, H6′), 7.63–7.55 (m, 4H, H2, H2′, H11, H11′), 7.32 (t, *J* = 7.7 Hz, 1H, H12).

^{13}C NMR (DMSO-d_6, 126 MHz): δ [ppm] = 157.6 (CH, C1, C1′), 141.7 (Cq, C9, C9′), 140.5 (Cq, C8, C8′), 140.1 (CH, C3, C3′), 134.6 (Cq, C10, C10′), 129.2 (Cq, C4, C4′), 129.0 (CH, C7, C7′), 128.7 (CH, C6, C6′), 127.7 (CH, C5, C5′), 127.3 (CH, C11, C11′), 126.0 (CH, C12), 121.9 (CH, C2, C2′).

HR-EI-MS (70 eV): 561.06 $[M]^+$, 526.09 $[M–Cl]^+$.

Synthesis of [Pd(QPhQ)Cl]

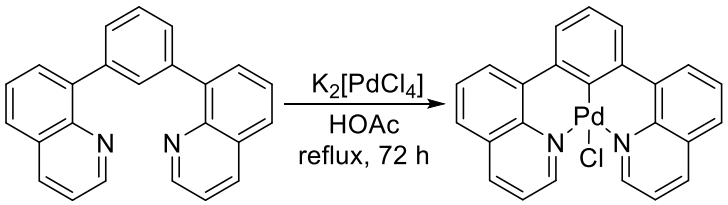

QHPhQ (60.0 mg, 0.18 mmol, 1.20 eq.) and $K_2[PdCl_4]$ (48.9 mg, 0.15 mmol, 1.00 eq.) were reacted following general procedure B for 72 h. The complex was isolated as pale-yellow powder (34.4 mg, 73.0 μmol, 49%).

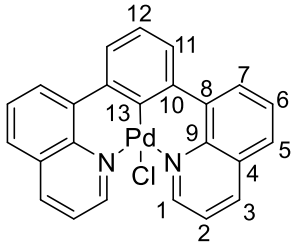

Habitus Pale-yellow powder (34.4 mg, 73.0 μmol, 49%).

^{1}H NMR (DMSO-d_6, 500 MHz) δ [ppm]: 9.37 (dd, *J* = 5.1, 1.5 Hz, 2H, H1, H1′), 8.75 (dd, *J* = 8.2, 1.5 Hz, 2H, H3, H3′), 8.49 (dd, *J* = 7.4, 1.2 Hz, 2H, H7, H7′), 8.16 (dd, *J* = 8.2, 1.2 Hz, 2H, H5, H5′), 7.93 - 7.86 (m, 2H, H6, H6′), 7.65 (dd, *J* = 8.2, 5.2 Hz, 2H, H2, H2′), 7.63 (d, *J* = 7.7 Hz, 2H, H11, H11′), 7.38 (t, *J* = 7.6 Hz, 1H, H12).

^{13}C NMR (DMSO-d_6, 126 MHz) δ [ppm]: 158.0 (CH, C1, C1′), 140.9 (Cq, C9, C9′), 140.5 (CH, C3, C3′), 140.4 (Cq, C8, C8′), 134.2 (Cq, C10, C10′), 129.7 (CH, C7, C7′), 129.0 (Cq, C4, C4′), 128.4 (CH, C5, C5′), 128.3 (CH, C6, C6′), 128.0 (CH, C11, C11′), 126.9 (CH, C12), 121.4 (CH, C2, C2′).

HR-EI-MS (70 eV): 473.99 $[M]^+$, 437.03 $[M–Cl]^+$.

Synthesis of [Ni(QPhQ)Cl]

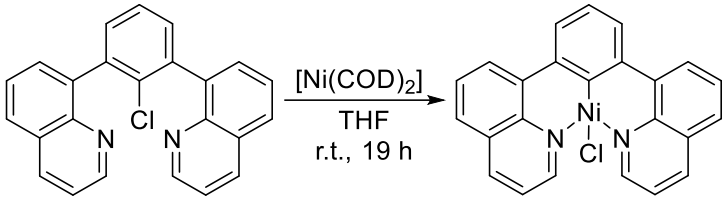

In a *Schlenk* flask, QClPhQ (100 mg, 0.27 mmol, 1.20 eq.) was mixed with freshly prepared $[Ni(COD)_2]$ (62.7 mg, 0.23 mmol, 1.00 eq.) in 20 mL THF. The solution quickly changed from pale yellow to orange. The mixture was stirred at ambient temperature for 19 h before 20 mL of *n*-pentane were added, leading to an orange precipitate. The excess solvent was decanted. The crude product was washed with 3 × 20 mL *n*-pentane and dried under vacuum to yield a light orange powder (41.8 mg, 98.1 μmol, 43%).

Habitus Light orange powder (41.8 mg, 98.1 μmol, 43%).

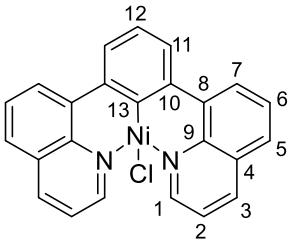

^{1}H NMR ($CDCl_3$, 500 MHz): δ [ppm] = 9.34 (s, 2H, H1), 8.40–8.29 (m, 2H, H5, H5′), 8.21 (d, *J* = 3.9 Hz, 2H, H3, H3′), 7.85 - 7.70 (m, 4H, H6, H6′, H7, H7′), 7.40 (d, *J* = 4.2 Hz, 2H, H11, H11′), 7.26 - 7.18 (m, 3H, H2, H2′, H12).

^{13}C NMR ($CDCl_3$, 126 MHz): δ [ppm] = 158.5 (CH, C1, C1′), 142.0 (Cq, C9, C9′), 139.1 (Cq, C8, C8′), 138.3 (CH, C3, C3′), 136.6 (Cq, C13), 128.2 (Cq, C4, C4′), 127.6 (CH, C6, C6′), 127.0 (CH, C7, C7′), 126.5 (CH, C5, C5′), 125.7 (CH, C12), 125.5 (CH, C11, C11′), 119.4 (CH, C2, C2′).

HR-ESI-MS (70 eV): 363.15 $[M–Ni–Cl+MeOH]^+$.

Synthesis of [Pt(PyPyCarb)Cl]

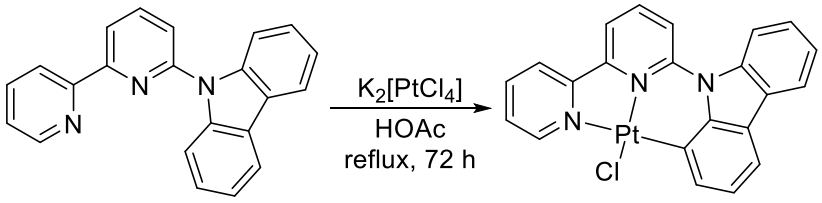

PyPyHCarb (100 mg, 0.31 mmol, 1.00 eq.) and $K_2[PtCl_4]$ (130 mg, 0.31 mmol, 1.00 eq.) were reacted following general procedure B for 72 h. The product was obtained as a dark-orange powder (90 mg, 0.17 mmol, 54%).

Habitus Dark-orange powder (90 mg, 0.17 mmol, 54%).

^{1}H NMR (CD_2Cl_2, 500 MHz) δ [ppm]: 9.74 (dd, *J* = 5.4, 1.5 Hz, 1H), 8.46 (dd, *J* = 7.6, 1.2 Hz, 1H), 8.39 - 8.30 (m, 1H), 8.23 - 8.11 (m, 4H), 7.96 (dd, *J* = 7.5, 1.7 Hz, 1H), 7.89 - 7.84 (m, 1H), 7.81 (dd, *J* = 7.4, 1.2 Hz, 1H), 7.67 (ddd, *J* = 7.1, 5.5, 1.5 Hz, 1H), 7.52 - 7.39 (m, 2H), 7.30 (t, *J* = 7.5 Hz, 1H).

HR-ESI-MS (70 eV): 573.04 $[M+Na]^+$, 514.08 $[M–X]^+$.

Synthesis of [Pd(PyPyCarb)Cl]

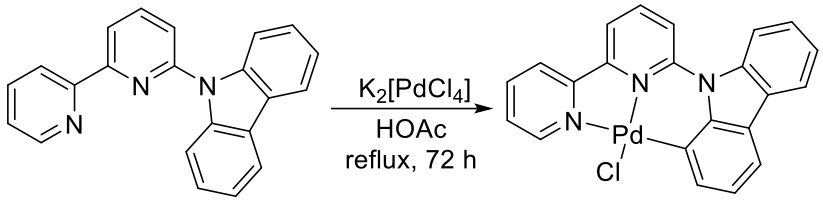

PyPyHCarb (50.0 mg, 0.16 mmol, 1.20 eq.) and $K_2[PdCl_4]$ (42.4 mg, 0.13 mmol, 1.00 eq.) were reacted following general procedure B for 72 h. The product was obtained as a yellow powder (43.4 mg, 93.9 μmol, 72%).

Habitus Yellow powder (43.4 mg, 93.9 μmol, 72%).

^{1}H NMR (CD_2Cl_2, 500 MHz) δ [ppm]: 9.47 (dd, *J* = 5.3, 1.2 Hz, 1H, H1), 8.39 (dd, *J* = 7.7, 1.0 Hz, 1H, H14), 8.34 (d, *J* = 8.4 Hz, 1H, H5), 8.17 (d, *J* = 8.1 Hz, 1H, H4), 8.14 - 8.04 (m, 3H, H3, H6, H9), 7.97 (d, *J* = 8.7 Hz, 1H, H11), 7.92 (m, 1H, H8), 7.82 (dd, *J* = 7.3, 1.0 Hz, 1H, H12), 7.64 - 7.60 (m, 1H, H2), 7.47 (ddd, *J* = 8.3, 7.8, 1.3 Hz, 1H, H10), 7.41 (ddd, *J* = 8.1, 7.6, 0.8 Hz, 1H, H7), 7.20 (t, *J* = 7.5 Hz, 1H, H13).

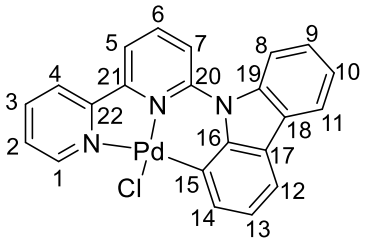

^{13}C NMR (CD_2Cl_2, 126 MHz) δ [ppm]: 156.0 (Cq, C22), 154.6 (Cq, C21), 148.0 (Cq, C20), 147.9 (CH, C1), 138.6 (CH, C3), 138.6 (CH, C9), 137.7 (Cq, C16), 137.1 (CH, C14), 129.6 (Cq, C19), 126.2 (Cq, C18), 125.7 (CH, C2), 125.5 (CH, C10), 123.3 (CH, C7), 122.0 (Cq, C17), 121.8 (CH, C13), 121.6 (CH, C4), 120.4 (CH, C6), 116.7 (CH, C5), 116.1 (CH, C8), 116.0 (CH, C12), 114.3 (CH, C11).

HR-ESI-MS (70 eV): 460.99 $[M]^+$.

Synthesis of [Pd(QPyCarb)Cl]

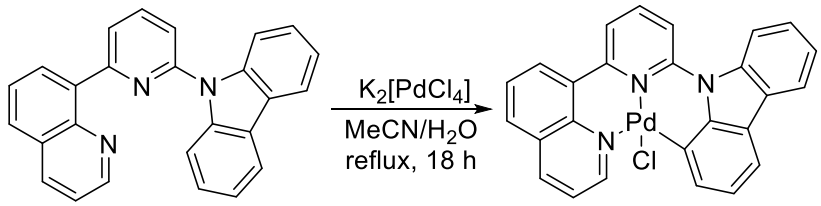

QPyHCarb (120 mg, 0.32 mmol, 1.40 eq.) and $K_2[PdCl_4]$ (75.1 mg, 0.23 mmol, 1.00 eq.) were dissolved in a mixture of MeCN and distilled water (1:1 volume) and heated to reflux for 18 h.

After cooling to room temperature, the precipitate was filtered off over a glass frit and washed with diethyl ether and distilled water. The product was obtained as a yellow powder (25.5 mg, 49.8 μmol, 22%).

Habitus Yellow powder (25.5 mg, 49.8 μmol, 22%).

^{1}H NMR (CH_2Cl_2, 600 MHz) δ [ppm]: 9.29 (dd, *J* = 4.9, 1.3 Hz, 1H, H1), 8.50 (dd, *J* = 8.3, 1.6 Hz, 1H, H3), 8.26 (d, *J* = 8.3 Hz, 1H, H7), 8.20 - 8.14 (m, 2H, H4, H6), 8.10 (d, *J* = 7.8 Hz, 1H, H10), 8.01 (d, *J* = 8.4 Hz, 1H, H13), 7.99 – 7.92 (m, 1H, H8), 7.83 - 7.79 (m, 1H, H5), 7.67 (d, *J* = 6.5 Hz, 1H, H16), 7.63 (dd, *J* = 8.4, 4.7 Hz, 1H, H2), 7.57 - 7.53 (m, 1H, H12), 7.51 (d, *J* = 7.6 Hz, 1H, H14), 7.46 - 7.41 (m, 1H, H11), 7.34 (d, *J* = 7.1 Hz, 1H, H9), 7.11 (t, *J* = 7.4 Hz, 1H, H15).

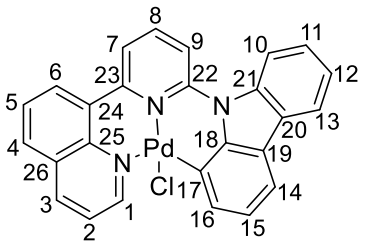

^{13}C NMR (CH_2Cl_2, 151 MHz) δ [ppm]: 156.4 (Cq, C24), 154.5 (Cq, C23), 148.4 (Cq, C22), 144.0 (Cq, C25), 139.3 (Cq, C21), 139.3 (CH, C8), 139.1 (Cq, C18), 138.8 (CH, C3), 136.3 (CH, C14), 135.6 (Cq, C26), 133.2 (CH, C6), 131.1 (CH, C4), 130.3 (Cq, C20), 127.1 (CH, C5), 125.5 (CH, C12), 123.5 (CH, C11), 122.8 (CH, C15), 122.4 (CH, C9), 121.7 (CH, C2), 121.2 (Cq, C19), 120.8 (CH, C10), 116.3 (CH, C13), 115.4 (CH, C16), 113.0 (CH, C7).

HR-EI-MS (70 eV): 511.00 $[M]^{+\cdot}$.

Synthesis of [Pt(QPyCarb)Cl]

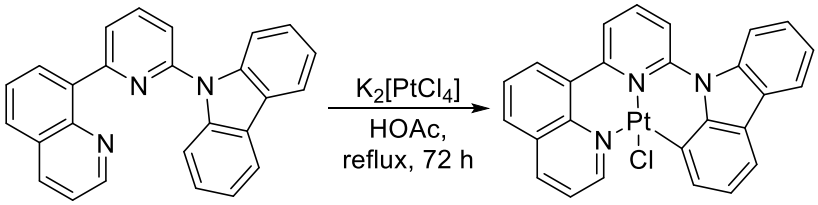

QPyHCarb (120 mg, 0.32 mmol, 1.40 eq.) and $K_2[PtCl_4]$ (95.5 mg, 0.23 mmol, 1.00 eq.) were reacted following general procedure B for 72 h. The product was obtained as an orange powder (29.7 mg, 49.4 μmol, 22%).

Habitus Orange powder (29.7 mg, 49.4 μmol, 22%).

^{1}H NMR (CH_2Cl_2, 600 MHz) δ [ppm]: 9.39 (dd, *J* = 4.9, 1.6 Hz, 1H, H1), 8.53 (dd, *J* = 8.3, 1.6 Hz, 1H, H3), 8.25 (dd, *J* = 7.3, 1.2 Hz, 1H, H6), 8.18 (ddd, *J* = 8.2, 4.7, 1.2 Hz, 2H, H4, H7), 8.09 (ddd, *J* = 7.7, 1.3, 0.6 Hz, 1H, H10), 7.98 - 7.92 (m, 2H, H8, H13), 7.79 (dd, *J* = 8.2, 7.4 Hz, 1H, H5), 7.64 - 7.59 (m,

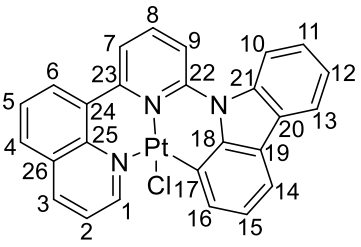

2H, H2, H16), 7.54 (dd, *J* = 7.4, 1.1 Hz, 1H, H14), 7.54 - 7.48 (m, 1H, H12), 7.43 (td, *J* = 7.7, 0.9 Hz, 1H, H11), 7.38 - 7.33 (m, 1H, H9), 7.14 (t, *J* = 7.4 Hz, 1H, H15).

^{13}C NMR (CH_2Cl_2, 151 MHz) δ [ppm]: 154.5 (CH, C1), 153.8 (Cq, C23), 149.2 (Cq, C22), 144.4 (Cq, C25), 138.4 (CH, C8), 138.0 (CH, C3), 136.1 (Cq, C26), 135.3 (CH, C14), 132.2 (Cq, C24), 131.7 (CH, C6), 130.3 (Cq, C21), 130.2 (CH, C4), 128.1 (Cq, C18), 127.4 (CH, C5), 125.1 (CH, C12), 123.5 (Cq, C20), 123.2 (CH, C11), 122.7 (CH, C15), 122.5 (CH, C2), 122.2 (CH, C9), 120.8 (CH, C10), 120.5 (Cq, C19), 115.9 (CH, C13), 114.4 (CH, C16), 113.5 (CH, C7), 109.8 (Cq, C17).

^{195}Pt NMR (CH_2Cl_2, 129 MHz) δ [ppm]: –3233.0.

HR-ESI-MS (70 eV): 622.06 $[M+Na]^+$, 600.07 $[M+H]^+$, 564.10 $[M–X]^+$.

Synthesis of [Pt(QPyFluor)Cl]

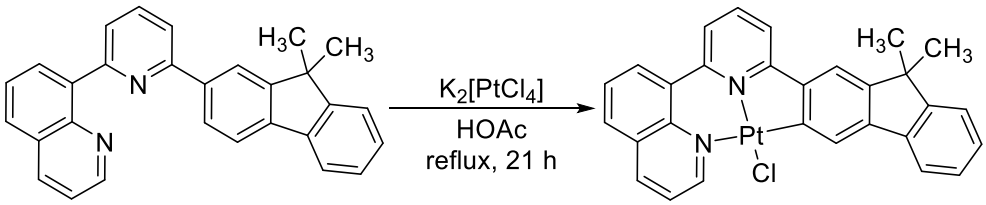

HFluorPyQ (100 mg, 0.25 mmol, 1.20 eq.) and $K_2[PtCl_4]$ (87.2 mg, 0.21 mmol, 1.00 eq.) were reacted following general procedure B for 21 h. The product was obtained as an orange powder (120 mg, 0.19 mmol, 91%).

Habitus Orange powder (120 mg, 0.19 mmol, 91%).

^{1}H NMR (DMSO-d_6, 600 MHz) δ [ppm]: 10.18 (dd, *J* = 5.1, 1.7 Hz, 1H, H1), 8.93 (dd, *J* = 8.2, 1.7 Hz, 1H, H3), 8.63 (d, *J* = 6.4 Hz, 1H, H7), 8.42 (d, *J* = 6.8 Hz, 1H, H5), 8.29 (s, 1H, H26), 8.28 - 8.23 (m, 2H, H11, H12), 8.03 (dd, *J* = 7.1, 2.1 Hz, 1H, H13), 7.99 (s, 1H, H16), 7.96 - 7.90 (m, 2H, H6, H2), 7.75 (dd, *J* = 6.1, 1.9 Hz, 1H, H23), 7.56 (dd, *J* = 6.0, 2.0 Hz, 1H, H21), 7.38 - 7.31 (m, 2H, H20, H22), 1.54 (s, 6H, H28, H28').

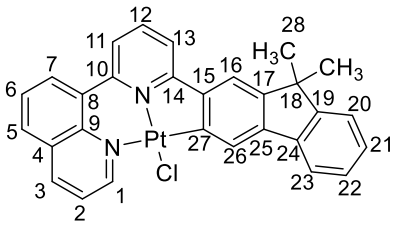

^{13}C NMR (DMSO-d_6, 151 MHz) δ [ppm]: 166.6 (Cq, C14), 154.5 (Cq, C1), 154.2 (Cq, C19), 151.0 (Cq, C10), 149.3 (Cq, C17), 143.8 (Cq, C15), 140.9 (CH, C3), 139.8 (Cq, C27), 139.2 (Cq, C9), 139.0 (Cq, C25), 139.0 (CH, C12), 138.7 (Cq, C24), 136.0 (CH, C7), 133.2 (CH, C5), 132.0 (Cq, C8), 129.2 (CH, C4), 127.7 (CH, C6), 127.3 (CH, C20, C22), 126.0 (CH, C26), 123.7 (CH, C13), 122.8 (CH, C21), 122.5 (CH, C2), 120.1 (CH, C23), 118.5 (CH, C16), 118.1 (CH, C11), 46.0 (Cq, C18), 27.1 (CH, C28).

^{195}Pt NMR (DMSO-d_6, 129 MHz) δ [ppm]: −3351.0.

HR-ESI-MS (70 eV)**:** 529.59 $[M–X]^+$, 615.57 $[M+Na]^+$.

Synthesis of [Pd(QPyFluor)Cl]

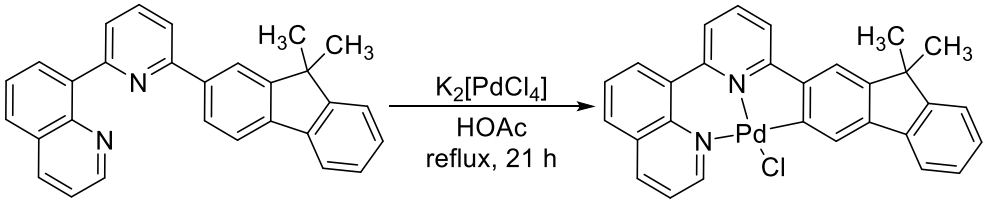

HFluorPyQ (100 mg, 0.25 mmol, 1.00 eq.) and $K_2[PdCl_4]$ (81.9 mg, 0.25 mmol, 1.00 eq.) were reacted following general procedure B for 21 h. The product was obtained as a yellow powder (38.3 mg, 71.1 µmol, 34%).

Habitus Yellow powder (38.3 mg, 71.1 µmol, 34%).

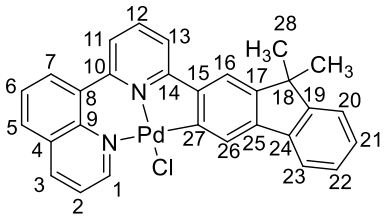

^{1}H NMR (DMSO-d_6, 600 MHz) δ [ppm]: 9.97 (dd, *J* = 5.0, 1.7 Hz, 1H, H1), 8.87 (dd, *J* = 8.2, 1.6 Hz, 1H, H3), 8.56 (d, *J* = 6.6 Hz, 1H, H7), 8.41 (d, *J* = 7.1 Hz, 1H, H5), 8.32 (d, *J* = 7.4 Hz, 1H, H11), 8.29 - 8.23 (m, 2H, H12, H26), 8.03 (s, 1H, H16), 8.00 (d, *J* = 7.3 Hz, 1H, H13), 7.94 (t, *J* = 7.8 Hz, 1H, H6), 7.90 (dd, *J* = 8.1, 5.0 Hz, 1H, H2), 7.75 - 7.69 (m, 1H, H23), 7.59 - 7.54 (m, 1H, H21), 7.34 (qd, *J* = 7.6, 3.7 Hz, 2H, H20, H22), 1.51 (s, 6H, H28).

^{13}C NMR (DMSO-d_6, 151 MHz) δ [ppm]: 165.3 (Cq, C14), 155.6 (Cq, C1), 154.1 (Cq, C19), 153.2 (Cq, C10), 150.1 (Cq, C27), 150.0 (Cq, C17), 144.4 (Cq, C15), 141.1 (CH, C3), 140.2 (CH, C12), 140.3 (CH, C9), 138.7 (Cq, C25), 138.5 (Cq, C24), 136.3 (CH, C7), 132.9 (CH, C5), 131.8 (Cq, C8), 129.2 (Cq, C4), 128.0 (CH, C26), 127.7 (CH, C6), 127.5 (CH, C20, C22), 124.4 (CH, C13), 123.0 (CH, C21), 122.1 (CH, C2), 120.2 (CH, C23), 118.8 (CH, C16), 118.5 (CH, C11), 46.1 (CH, C18), 27.1 (CH, C28).

HR-ESI-MS (70 eV)**:** 1043.12 $[2xM–X]^+$, 560.03 $[M+Na]^+$, 502.07 $[M–X]^+$.

Synthesis of [Pt(QPySpiro)Cl]

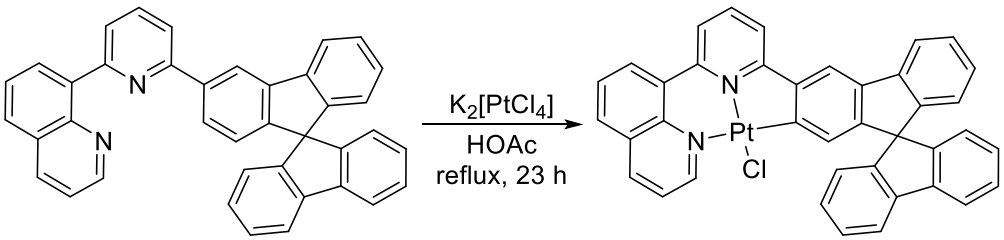

QPyHSpiro (80.0 mg, 0.15 mmol, 1.20 eq.) and $K_2[PtCl_4]$ (53.2 mg, 0.13 mmol, 1.00 eq.) were reacted following general procedure B for 23 h. The product was obtained as an orange powder (97.5 mg, 0.13 mmol, 99%).

Habitus Orange powder (97.5 mg, 0.13 mmol, 99%).

^{1}H NMR (CD_2Cl_2, 500 MHz) δ [ppm]: 10.13 (dd, *J* = 5.2, 1.7 Hz, 1H, H1), 8.49 (d, *J* = 6.6 Hz, 1H, H3), 8.36 (dd, J = 7.6, 1.2 Hz, 1H, H7), 8.07 - 8.05 (m, 1H, H5), 8.03 (m, 1H, H12), 7.95 - 7.91 (m, 3H, H13, H32, H32'), 7.72 (dd, *J* = 7.1, 0.8 Hz, 2H, H11, H22), 7.69 (t, *J* = 7.8 Hz, 1H, H6), 7.60 (dd, *J* = 8.1, 5.3 Hz, 1H, H2), 7.43 (td, *J* = 7.6, 1.1 Hz, 2H, H31, H31'), 7.40 (td, *J* = 7.4, 1.2 Hz, 1H, H23), 7.33 (d, *J* = 3.0 Hz, 1H, H17), 7.24 (t, *J* = 7.5 Hz, 1H, H20), 7.16 (td, *J* = 7.5, 1.1 Hz, 2H, H30, H30'), 7.11 (td, *J* = 7.5, 1.1 Hz, 1H, H24), 6.80 (d, *J* = 7.5 Hz, 2H, H29, H29'), 6.65 (d, *J* = 7.4 Hz, 1H, H25).

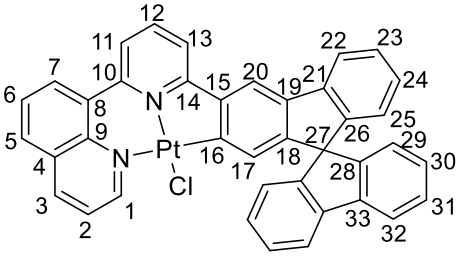

^{13}C NMR (CD_2Cl_2, 126 MHz) δ [ppm]: 167.8 (Cq, C14), 155.1 (CH, C1), 152.3 (Cq, C10), 150.4 (Cq, C15), 149.6 (Cq, C28, C28'), 149.2 (Cq, C19), 144.8 (Cq, C21), 142.7 (Cq, C18), 142.4 (Cq, C26), 142.2 (Cq, C33, C33'), 140.6 (Cq, C9), 140.4 (CH, C3), 138.4 (Cq, C16), 135.6 (CH, C7), 133.5 (Cq, C8), 132.9 (CH, C5), 130.8 (CH, C17), 129.9 (Cq, C4), 128.6 (CH, C20), 128.3 (CH, C30, C30'), 128.2 (CH, C31, C31'), 128.1 (CH, C23), 127.6 (CH, C24), 127.5 (CH, C6), 124.3 (CH, C29, C29'), 124.1 (CH, C25), 123.7 (CH, C11), 122.7 (CH, C2), 120.7 (CH, C32, C32'), 119.8 (CH, C22), 118.0 (CH, C13), 115.4 (CH, C12), 68.2 (Cq, C27).

HR-ESI-MS (70 eV): 714.15 $[M–X]^+$.

Synthesis of [Pd(QPySpiro)Cl]

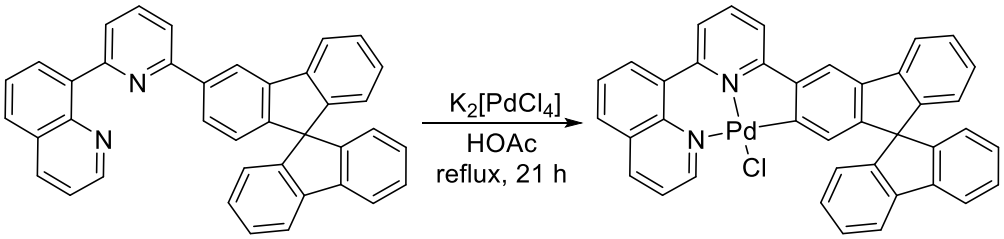

QPyHSpiro (80.0 mg, 0.15 mmol, 1.10 eq.) and $K_2[PdCl_4]$ (47.1 mg, 0.14 mmol, 1.00 eq.) were reacted following general procedure B for 21 h. The product was obtained as a yellow powder (43.9mg, 66.4 μmol, 46%).

Habitus Yellow powder (43.9mg, 66.4 μmol, 46%).

^{1}H NMR (CD_2Cl_2, 500 MHz) δ [ppm]: 9.94 (dd, *J* = 5.0, 1.8 Hz, 1H, H1), 8.42 (dd, *J* = 8.2, 1.7 Hz, 1H, H3), 8.30 (dd, *J* = 7.6, 1.2 Hz, 1H, H7), 8.04 (d, *J* = 5.8 Hz, 1H, H5), 8.01 (d, *J* = 7.9 Hz, 1H, H12), 7.97 (dd, *J* = 8.0, 1.1 Hz, 1H, H13), 7.92 (dd, *J* = 7.6, 5.1 Hz, 3H, H22, H32, H32'), 7.73 - 7.66 (m, 2H, H6, H11), 7.59 (dd, *J* = 8.2, 5.0 Hz, 1H, H2), 7.41 (qd, *J* = 7.8, 1.0 Hz, 3H, H23, H31, H31'), 7.36 (d, *J* = 4.5 Hz, 1H, H20), 7.31

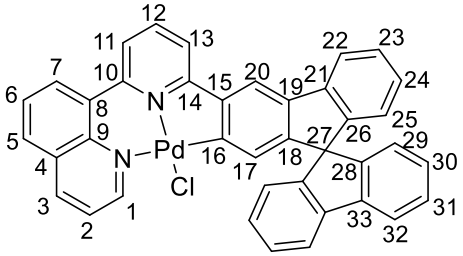

(s, 1H, H17), 7.16 (td, *J* = 7.5, 1.0 Hz, 2H, H30, H30'), 7.11 (td, *J* = 7.5, 1.0 Hz, 1H, H24), 6.78 (d, *J* = 7.6 Hz, 2H, H29, H29'), 6.65 (d, *J* = 7.5 Hz, 1H, H25).

^{13}C NMR (CD_2Cl_2, 126 MHz) δ [ppm]: 165.8 (Cq, C14), 155.8 (CH, C1), 154.8 (Cq, C18), 153.9 (Cq, C10), 149.4 (Cq, C28, C28'), 148.9 (Cq, C21), 145.0 (Cq, C19), 141.8 (Cq, C33, C33'), 141.6 (Cq, C26), 141.2 (Cq, C9), 139.9 (CH, C3), 139.2 (CH, C12), 138.6 (Cq, C15), 135.3 (CH, C7), 132.7 (Cq, C8), 132.3 (CH, C17), 132.2 (CH, C5), 129.4 (Cq, C4), 128.4 (Cq, C16), 127.8 (CH, C30, C30'), 127.8 (CH, C31, C31'), 127.7 (CH, C23), 127.4 (CH, C24), 126.9 (CH, C6), 123.8 (CH, C11), 123.7 (CH, C29, C29'), 123.7 (CH, C25), 121.7 (CH, C2), 120.3 (CH, C32, C32'), 119.5 (CH, C22), 117.6 (CH, C13), 114.9 (CH, C20), 66.0 (Cq, C27).

HR-ESI-MS (70 eV)**:** 625.09 $[M–X]^+$.

Synthesis of [Pt(PyCarbQ)Cl]

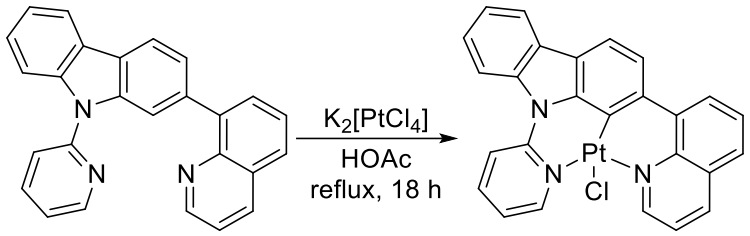

PyHCarbQ (100 mg, 0.27 mmol, 1.20 eq.) and $K_2[PtCl_4]$ (93.4 mg, 0.23 mmol, 1.00 eq.) were reacted following general procedure B for 18 h. The product was obtained as an orange powder (79.4 mg, 0.13 mmol, 59%).

Habitus Orange powder (79.4 mg, 0.13 mmol, 59%).

^{1}H NMR (CD_2Cl_2, 600 MHz) δ [ppm]: δ 10.22 (dd, *J* = 5.4, 1.5 Hz, 1H, H16), 9.73 (dd, *J* = 6.3, 1.8 Hz, 1H, H1), 8.48 (dd, *J* = 8.1, 1.6 Hz, 1H, H14), 8.28 (dd, *J* = 7.3, 1.3 Hz, 1H, H11), 8.10 (d, *J* = 7.7 Hz, 1H, H8), 8.05 (d, *J* = 7.8 Hz, 1H, H4), 7.98 (d, *J* = 8.2 Hz, 1H, H5), 7.89 (dd, *J* = 8.1, 1.2 Hz, 1H, H13), 7.85 (ddd, *J* = 8.8, 7.1, 1.8 Hz, 1H, H3), 7.82 (d, *J* = 8.0 Hz, 1H, H9), 7.78 - 7.72 (m, 1H, H12), 7.56 (ddd, *J* = 8.3, 7.4, 1.2 Hz, 1H, H6), 7.53 (d, *J* = 8.0 Hz, 1H, H10), 7.47 - 7.41 (m, 1H, H7), 7.40 (dd, *J* = 8.1, 5.4 Hz, 1H, H15), 6.97 (ddd, *J* = 7.4, 6.4, 1.4 Hz, 1H, H2).

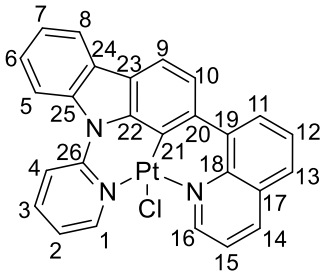

^{13}C NMR (CD_2Cl_2, 151 MHz) δ [ppm]: 159.0 (CH, C16), 156.8 (CH, C1), 149.6 (Cq, C26), 140.8 (Cq, C19), 140.8 (CH, C14), 140.1 (Cq, C25), 140.0 (CH, C3), 141.6 (Cq, C18), 141.5 (Cq, C22), 131.9 (Cq, C20), 130.3 (CH, C11), 130.2 (Cq, C17), 129.5 (Cq, C24), 128.4 (CH, C12), 128.0 (CH, C13), 126.9 (CH, C6), 124.2 (CH, C7), 124.0 (CH, C10), 122.1 (Cq, C23), 122.0 (CH, C8), 121.5 (CH, C15), 119.1 (CH, C2), 116.6 (CH, C5), 116.5 (CH, C9), 114.0 (CH, C4).

^{195}Pt NMR (CD_2Cl_2, 129 MHz) δ [ppm]: −3107.4.

HR-ESI-MS (70 eV): 565.10 $[M–X]^+$.

Synthesis of [Pd(PyCarbQ)Cl]

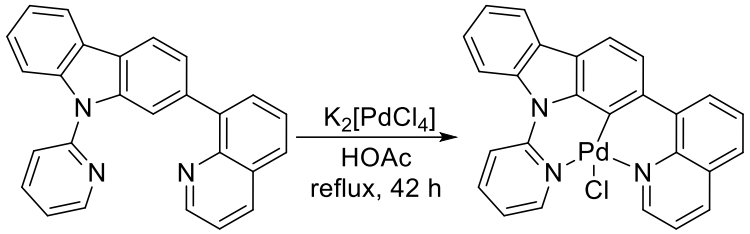

PyHCarbQ (100 mg, 0.27 mmol, 1.20 eq.) and $K_2[PdCl_4]$ (73.4 mg, 0.23 mmol, 1.00 eq.) were reacted following general procedure B for 42 h. The product was obtained as a yellow powder (44.7 mg, 87.3 μmol, 39%).

Habitus Yellow powder (44.7 mg, 87.3 μmol, 39%).

^{1}H NMR (CD_2Cl_2, 500 MHz) δ [ppm]: 10.09 (d, *J* = 4.2 Hz, 1H, H16), 9.54 (d, *J* = 5.4 Hz, 1H, H1), 8.45 (d, *J* = 7.9 Hz, 1H, H14), 8.26 (d, *J* = 7.1 Hz, 1H, H11), 8.11 (d, *J* = 7.7 Hz, 1H, H8), 8.05 (d, *J* = 8.7 Hz, 1H, H4), 8.01 (d, *J* = 8.2 Hz, 1H, H9), 7.92 (dd, *J* = 8.1, 1.1 Hz, 1H, H13), 7.87 (d, *J* = 7.9 Hz, 1H, H5), 7.85 - 7.80 (m, 1H, H3), 7.77 (t, *J* = 7.7 Hz, 1H, H12), 7.58 (t, *J* = 8.1 Hz, 1H, H6), 7.52 - 7.47 (m, 2H, H10, H15), 7.44 (t, *J* = 7.3 Hz, 1H, H7), 7.05 - 7.00 (m, 1H, H2).

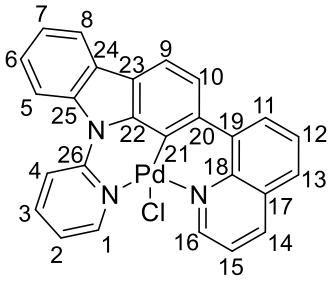

^{13}C NMR (CD_2Cl_2, 126 MHz) δ [ppm]: 158.7 (CH, C16), 155.5 (CH, C1), 148.9 (Cq, C26), 141.6 (Cq, C18), 141.5 (Cq, C22), 140.9 (Cq, C19), 140.5 (CH, C14), 140.0 (CH, C3), 139.9 (Cq, C25), 132.4 (Cq, C20), 130.3 (CH, C11), 129.8 (Cq, C17), 129.2 (Cq, C24), 128.0 (CH, C12), 127.9 (CH, C13), 126.8 (CH, C6), 123.9 (CH, C10), 123.8 (Cq, C23), 123.8 (CH, C7), 121.6 (CH, C8), 120.7 (CH, C15), 118.4 (CH, C2), 117.3 (CH, C5), 116.3 (CH, C9), 113.3 (CH, C4).

HR-EI-MS (70 eV): 476.04 $[M–X]^{\cdot+}$.

Synthesis of [Pt(PyPhThian)Cl]

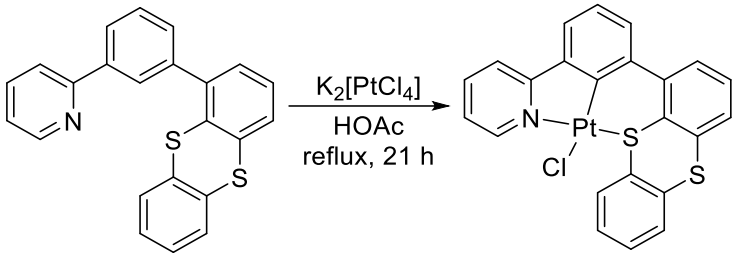

PyHPhThian (107 mg, 0.29 mmol, 1.20 eq.) and $K_2[PtCl_4]$ (100 mg, 0.24 mmol, 1.00 eq.) were reacted following general procedure B for 21 h. The complex was isolated as yellow powder (89.0 mg, 0.15 mmol, 62%).

Habitus Yellow powder (89.0 mg, 0.15 mmol, 62%).

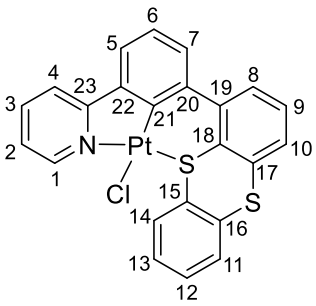

^{1}H NMR (DMSO-d_6, 600 MHz) δ [ppm]: 9.60 (d, $J^{Pt\text{-}H}$ = 35.1 Hz, J = 5.0 Hz, 1H, H1), 8.39 (d, J = 8.1 Hz, 1H, H8), 8.36-8.33 (m, 1H, H14), 8.31 (d, J = 8.0 Hz, 1H, H4), 8.25 (td, J = 7.8, 1.4 Hz, 1H, H3), 8.03 (d, J = 7.9 Hz, 1H, H7), 7.97 (d, J = 7.5 Hz, 1H, H5), 7.92 (d, J = 6.8 Hz, 1H, H10), 7.85 (dd, J = 7.2 , 1.7 Hz, 1H, H12), 7.70 - 7.67 (m, 1H, H2), 7.65 (t, J = 7.9 Hz, 1H, H9), 7.54 - 7.48 (m, 2H, H11, H13), 7.38 (t, J = 7.8 Hz, 1H, H6).

^{13}C NMR (DMSO-d_6, 151 MHz) δ [ppm]: 164.6 (Cq, C23), 148.1 (CH, C1), 146.4 (Cq, C22), 141.2 (CH, C3), 140.9 (CH, C19), 137.8 (Cq, C17), 137.7 (Cq, C21), 134.9 (Cq, C16), 134.2 (Cq, C15), 133.2 (CH, C14), 131.0 (Cq, C20), 130.7 (CH, C7), 130.0 (CH, C11), 129.9 (CH, C9), 129.2 (CH, C12), 128.9 (CH, C8), 128.5 (CH, C10), 128.4 (CH, C13), 125.6 (CH, C5), 125.5 (CH, C6), 123.5 (CH, C2), 120.1 (CH, C4), 116.4 (Cq, C18).

^{195}Pt NMR (DMSO-d_6, 129 MHz): δ [ppm] = –3969.1.

HR-ESI-MS (70 eV): 677.01 $[M+DMSO]^+$, 641.04 $[M-Cl+DMSO]^+$, 563.02 $[M-Cl]^+$.

Synthesis of [Pd(PyPhThian)Cl]

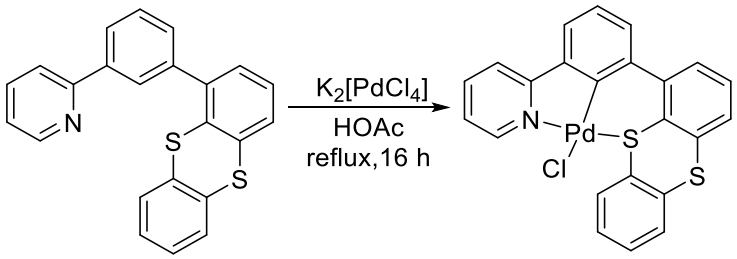

PyHPhThian (107 mg, 0.29 mmol, 1.20 eq.) and $K_2[PdCl_4]$ (78.3 mg, 0.24 mmol, 1.00 eq.) were reacted following general procedure B for 16 h. The complex was isolated as yellow powder (55.2 mg, 0.11 mmol, 45%).

Habitus Yellow powder (55.2 mg, 0.11 mmol, 45%).

^{1}H NMR (DMSO-d$_6$, 600 MHz) δ [ppm]: 9.37 (d, *J* = 4.7 Hz, 1H, H1), 8.45 (dd, *J* = 6.0, 3.2 Hz, 1H, H14), 8.34 (d, *J* = 8.1 Hz 1H, H8), 8.31 (d, *J* = 7.9 Hz, 1H, H4), 8.23 (td, *J* = 7.8, 1.7 Hz, 1H, H3), 8.03 (d, *J* = 6.7 Hz, 1H, H5), 7.99 (d, *J* = 7.6 Hz, 1H, H7), 7.94 (dd, *J* = 7.5, 1.0 Hz, 1H, H10), 7.87 (dd, *J* = 6.3, 2.7 Hz, 1H, H11), 7.68 - 7.61 (m, 2H, H2, H9), 7.54 - 7.49 (m, 2H, H12, H13), 7.43 (t, *J* = 7.8 Hz, 1H, H6).

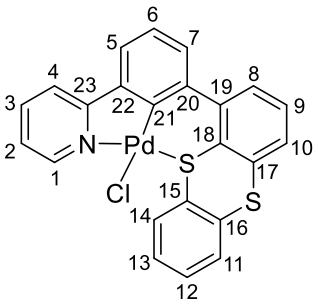

^{13}C NMR (DMSO-d$_6$, 151 MHz) δ [ppm]: 164.2 (Cq, C23), 150.6 (CH, C21), 149.5 (CH, C1), 147.9 (Cq, C22), 140.9 (CH, C3), 140.6 (Cq, C19), 138.1 (Cq, C17), 135.2 (Cq, C16), 134.0 (CH, C14), 133.6 (Cq, C15), 133.5 (Cq, C20), 131.1 (CH, C12), 130.1 (CH, C9), 129.9 (CH, C7), 129.3 (CH, C8), 129.1 (CH, C11), 128.9 (CH, C10), 128.7 (CH, C13), 126.7 (CH, C6), 126.1 (CH, C5), 123.7 (CH, C2), 120.3 (CH, C4), 118.0 (Cq, C18).

HR-ESI-MS (70 eV): 551.97 [M–Cl+DMSO]$^+$, 473.96 [M–Cl]$^+$.

Synthesis of [Pt(PyPhDBT)Cl]

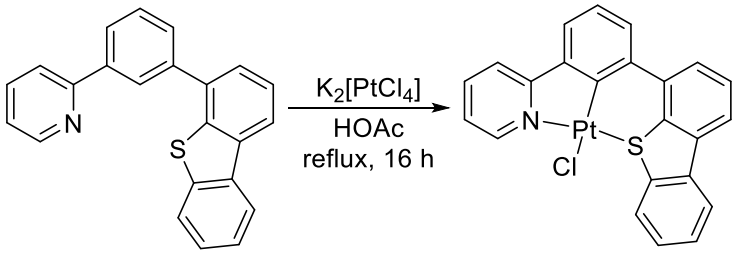

PyHPhDBT (100 mg, 0.30 mmol, 1.20 eq.) and K$_2$[PtCl$_4$] (103 mg, 0.25 mmol, 1.00 eq.) were reacted following general procedure B for 16 h. The complex was isolated as yellow powder (87.6 mg, 0.16 mmol, 63%).

Habitus Yellow powder (87.6 mg, 0.16 mmol, 63%).

^{1}H NMR (DMSO-d$_6$, 600 MHz) δ [ppm]: 9.33 (ddd, $J^{Pt\text{-}H}$ = 36.3 Hz, *J* = 5.9, 1.5, 0.6 Hz, 1H, H1), 8.50 (d, *J* = 7.8 Hz, 1H, H11), 8.47 (d, *J* = 7.9 Hz, 1H, H14), 8.34 (dd, *J* = 7.7, 0.8 Hz, 1H, H10), 8.27 - 8.23 (m, 1H, H4), 8.19 (ddd, *J* = 8.2 , 7.5, 1.6 Hz, 1H, H3) 8.07 (d, *J* = 7.3 Hz, 1H, H7), 7.93 (dd, *J* = 7.7, 1.0 Hz, 1H, H5), 7.89 (d, *J* = 7.4 Hz, 1H, H8), 7.80 - 7.74 (m, 2H, H9, H12), 7.67 (dt, *J* = 7.5, 1.0 Hz, 1H, H13), 7.58 (ddd, *J* = 7.3, 5.9, 1.5 Hz, 1H, H2), 7.42 (t, *J* = 7.6 Hz, 1H, H6).

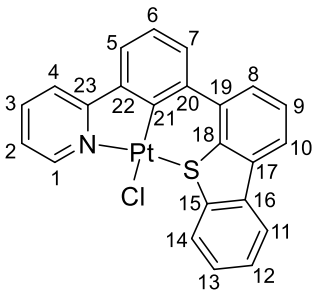

^{13}C NMR (DMSO-d$_6$, 151 MHz) δ [ppm]: 165.6 (Cq, C23), 147.9 (Cq, C21), 147.6 (CH, C1), 145.2 (Cq, C22), 140.9 (CH, C3), 139.2 (Cq, C19), 137.8 (Cq, C16), 135.4 (Cq, C17, C18), 134.8 (Cq, C20), 134.2 (Cq, C15), 129.8 (CH, C12), 129.5 (CH, C9), 129.3 (CH, C14), 128.2 (CH, C13), 127.8 (CH, C8), 127.4 (CH, C7), 126.0 (CH, C6), 124.8 (CH, C5), 123.5 (CH, C11), 123.4 (CH, C2), 121.1 (CH, C10), 120.4 (CH, C4).

^{195}Pt NMR (DMSO-d$_6$, 129 MHz) δ [ppm]: −3887.4.

HR-ESI-MS (70 eV): 563.08 $[M]^+$, 531.05 $[M–Cl]^+$.

Synthesis of [Pd(PyPhDBT)Cl]

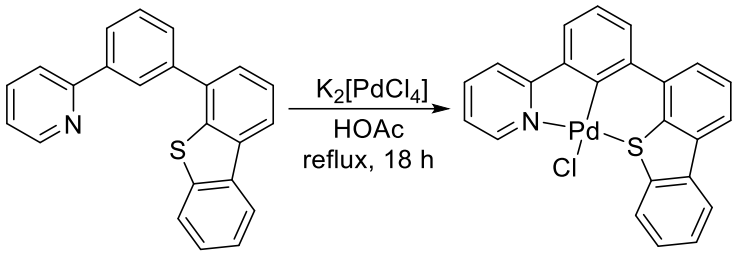

PyHPhDBT (100 mg, 0.30 mmol, 1.20 eq.) and $K_2[PdCl_4]$ (81.6 mg, 0.25 mmol, 1.00 eq.) were reacted following general procedure B for 18 h. The complex was isolated as yellow powder (51.9 mg, 0.11 mmol, 43%).

Habitus Yellow powder (51.9 mg, 0.11 mmol, 43%).

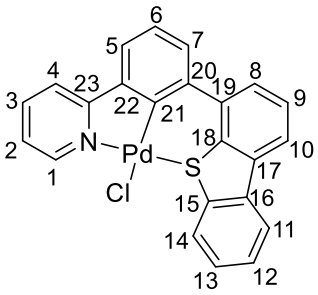

^{1}H NMR (CD_2Cl_2, 400 MHz) δ [ppm]: 8.69 (ddd, *J* = 4.8, 1.8, 1.0 Hz, 1H, H1), 8.22 - 8.16 (m, 2H, H10, H14), 8.10 (ddd, *J* = 7.9, 1.8, 1.1 Hz, 1H, H5), 7.89 - 7.81 (m, 3H, H3, H4, H12), 7.81 - 7.75 (m, 2H, H7, H11), 7.63 (t, *J* = 7.7 Hz, 1H, H6), 7.59 - 7.56 (m, 2H, H8, H9), 7.49 - 7.45 (m, 1H, H13), 7.25 (ddd, *J* = 7.3, 4.8, 1.2 Hz, 1H, H2).

^{13}C NMR (CD_2Cl_2, 101 MHz) δ [ppm]: 157.3 (Cq, C23), 150.2 (CH, C1), 141.5 (Cq, C22), 140.5 (Cq, C20), 140.0 (Cq, C19), 139.0 (Cq, C18), 137.4 (CH, C3), 137.4 (CH, C11), 137.3 (Cq, C15), 136.8 (Cq, C17), 136.3 (Cq, C16), 129.8 (CH, C6), 129.3 (CH, C7), 127.5 (CH, C8), 127.5 (CH, C13), 127.0 (CH, C5), 125.8 (CH, C9), 123.2 (CH, C12), 122.9 (CH, C2), 122.4 (CH, C14), 121.2 (CH, C10), 121.0 (CH, C4).

HR-ESI-MS (70 eV): 441.99 $[M–Cl]^+$.

Synthesis of [Pt(QPhThian)Cl]

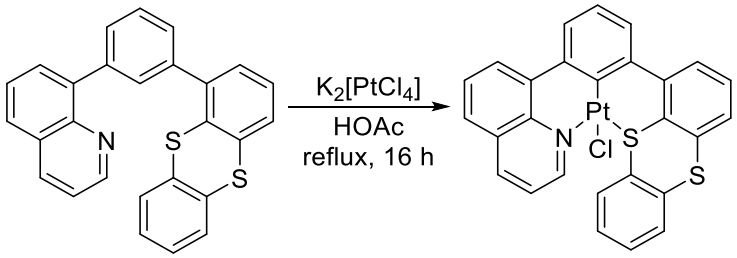

QHPhThian (122 mg, 0.29 mmol, 1.20 eq.) and $K_2[PtCl_4]$ (100 mg, 0.24 mmol, 1.00 eq.) were reacted following general procedure B for 16 h. The product was obtained as a dark orange powder (21.9 mg, 33.7 µmol, 14%).

Habitus Dark orange powder (21.9 mg, 33.7 µmol, 14%).

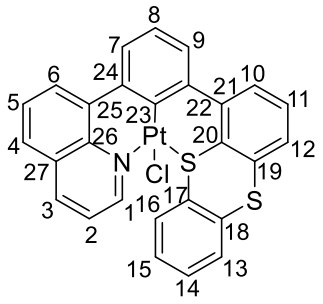

^{1}H NMR (CD_2Cl_2, 600 MHz) δ [ppm]: 9.50 (dd, *J* = 5.3, 1.5 Hz, 1H, H1), 8.49 (dd, *J* = 8.1, 1.4 Hz, 1H, H3), 8.43 (dd, *J* = 7.4, 1.1 Hz, 1H, H6), 7.94 (dd, *J* = 8.1, 1.0 Hz, 1H, H4), 7.79 - 7.76 (m, 1H, H5), 7.63 (m, 1H, H10), 7.58 (d, *J* = 7.3 Hz, 1H, H9), 7.50 - 7.45 (m, 2H, H2, H12), 7.43 - 7.40 (m, 1H, H16), 7.37 (t, *J* = 7.7 Hz, 1H, H8), 7.33 (d, *J* = 6.4 Hz, 2H, H7, H15), 7.30 (t, *J* = 7.7 Hz, 1H, H11), 7.26 (td, *J* = 7.6, 1.3 Hz, 1H, H14), 7.17 - 7.12 (m, 1H, H13).

^{13}C NMR (CD_2Cl_2, 151 MHz) δ [ppm]: 155.9 (CH, C1), 154.1 (Cq, C25), 146.1 (Cq, C20), 145.8 (Cq, C24), 142.0 (Cq, C26), 141.6 (Cq, C17), 140.4 (CH, C3), 138.6 (Cq, C19), 136.3 (Cq, C18), 131.9 (CH, C16), 131.0 (Cq, C22), 130.5 (CH, C14), 129.8 (CH, C8), 129.6 (CH, C6), 129.2 (CH, C2), 129.0 (CH, C9), 128.9 (CH, C10), 128.8 (CH, C5), 127.7 (CH, C4), 127.6 (CH, C15), 127.5 (CH, C13), 126.9 (CH, C11), 125.6 (CH, C7), 124.7 (Cq, C27), 121.9 (CH, C12), 118.3 (Cq, C21).

^{195}Pt NMR (CD_2Cl_2, 129 MHz) δ [ppm]: −3816.5.

HR-ESI-MS (70 eV): 669.99 $[M+Na]^+$, 649.02 $[M+H]^+$, 612.03 $[M–Cl]^+$.

Synthesis of [Pd(QPhThian)Cl]

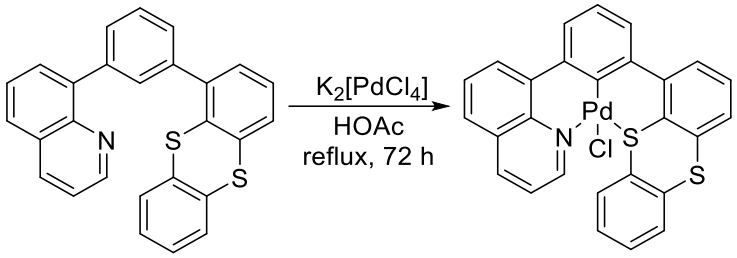

QHPhThian (122 mg, 0.29 mmol, 1.20 eq.) and $K_2[PdCl_4]$ (78.3 mg, 0.24 mmol, 1.00 eq.) were reacted following general procedure for 72 h. The product was obtained as a light green powder (104 mg, 0.19 mmol, 77%).

Habitus Light green powder (104 mg, 0.19 mmol, 77%).

^{1}H NMR (DMSO-d_6, 500 MHz) δ [ppm]: 9.47 (s, 1H), 9.15 (s, 1H), 8.74 (s, 1H), 8.44 (s, 1H), 8.10 (s, 1H), 7.83 (s, 2H), 7.70 (s, 1H), 7.59 (td, *J* = 7.4, 2.1 Hz, 2H), 7.48 (s, 1H), 7.41 - 7.37 (m, 2H), 7.34 (td, *J* = 7.6, 1.4 Hz, 1H), 7.25 (*td*, J = 7.6, 1.4 Hz, 1H), 6.98 (s, 1H).

HR-ESI-MS (70 eV)**:** 522.98 $[M–Cl]^+$.

Synthesis of [Pt(ThianHPhThian)Cl$_2$]

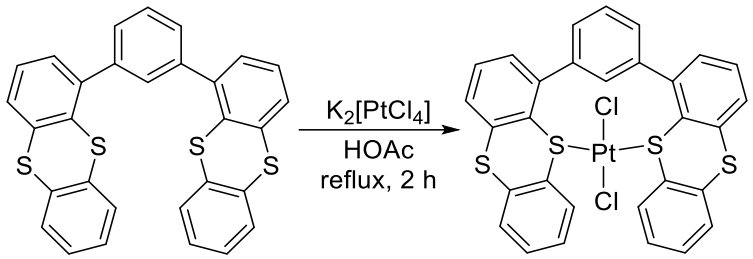

ThianHPhThian (146 mg, 0.29 mmol, 1.20 eq.) and $K_2[PtCl_4]$ (100 mg, 0.24 mmol, 1.00 eq.) were reacted following general procedure B for 2 h. The complex was obtained as a dark brown powder (110 mg, 0.14 mmol, 59%).

Habitus Dark brown powder (110 mg, 0.14 mmol, 59%).

^{1}H NMR (DMSO-d_6, 600 MHz) δ [ppm]: 7.67 (t, *J* = 7.6 Hz, 1H, H9), 7.64 (dd, *J* = 7.2, 2.0 Hz, 2H, H1, H1'), 7.60 (dd, *J* = 7.8, 1.2 Hz, 2H, H3, H3'), 7.53 (dd, *J* = 7.6, 1.8 Hz, 2H, H8, H8'), 7.50 (dd, *J* = 7.8, 1.3 Hz, 2H, H6, H6'), 7.46 - 7.45 (m, 2H, H7, H7'), 7.44 (s, 1H, H10), 7.42 (dd, *J* = 3.1, 1.6 Hz, 2H, H2, H2'), 7.35 (td, *J* = 7.5, 1.4 Hz, 2H, H4, H4'), 7.29 (td, *J* = 7.5, 1.4 Hz, 2H, H5, H5').

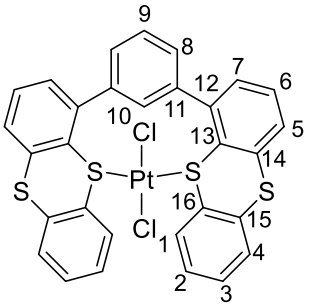

^{13}C NMR (DMSO-d_6, 151 MHz) δ [ppm]: 141.5 (Cq, C12, C12') 139.3 (Cq, C11, C11') 135.2 (Cq, C14, C14') 134.7 (Cq, C15, C15') 134.5 (Cq, C16, C16') 133.8 (Cq, C13, C13') 130.4 (CH, C2, C2') 130.2 (CH, C7, C7') 129.4 (CH, C8, C8') 129.4 (CH, C6, C6') 129.1 (CH, C1, C1') 129.1 (CH, C9) 129.1 (CH, C3, C3') 128.9 (CH, C4, C4') 128.7 (CH, C5, C5') 128.4 (CH, C10)

^{195}Pt NMR (DMSO-d_6, 129 MHz) δ [ppm]: −3440.1.

HR-ESI-MS (70 eV): 698.98 $[M–Cl–H]^+$.

Synthesis of [Pt(DBTHPhDBT)Cl$_2$]

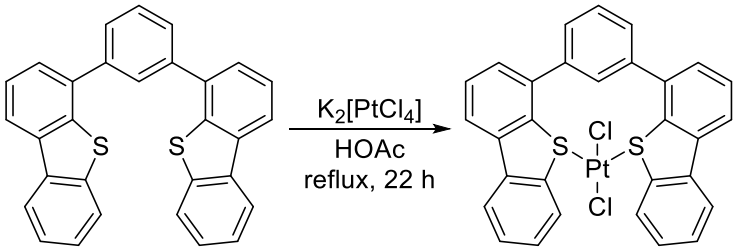

DBTHPhDBT (100 mg, 0.23 mmol, 1.20 eq.) and $K_2[PtCl_4]$ (78.1 mg, 0.19 mmol, 1.00 eq.) were reacted following general procedure B for 22 h. The product was obtained as a grey powder (90.0 mg, 0.13 mmol, 67%).

Habitus Grey powder (90.0 mg, 0.13 mmol, 67%).

^{1}H NMR ($CDCl_3$, 500 MHz) δ [ppm]: 8.20 (t, *J* = 5.8 Hz, 2H), 8.13 (d, *J* = 9.3 Hz, 2H), 7.97 (d, *J* = 7.7 Hz, 1H), 7.84 (dd, *J* = 8.2, 4.0 Hz, 4H), 7.74 (d, *J* = 7.4 Hz, 1H), 7.67 (t, *J* = 7.8 Hz, 1H), 7.64 - 7.59 (m, 3H), 7.47 (dd, *J* = 6.8, 3.2 Hz, 2H), 7.46 - 7.36 (m, 2H).

HR-ESI-MS (70 eV)**:** 762.00 $[M+MeOH+Na]^+$, 706.99 $[M]^{+\cdot}$.

Synthesis of [Pt(PyPhDBF)Cl]

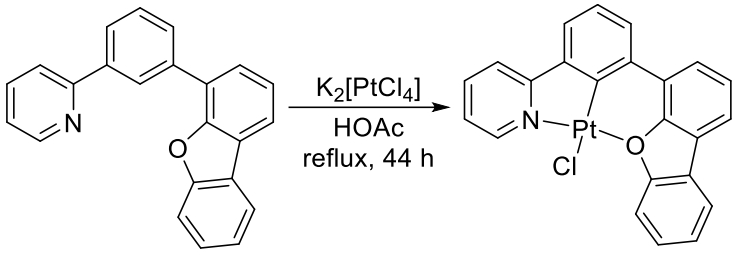

PyHPhDBF (93.2 mg, 0.29 mmol, 1.20 eq.) and $K_2[PtCl_4]$ (100 mg, 0.24 mmol, 1.00 eq.) were reacted following general procedure B for 44 h. The complex was isolated as yellow powder (35.6 mg, 64.6 µmol, 27%).

Habitus Yellow powder (35.6 mg, 64.6 µmol, 27%).

^{1}H NMR (DMSO-d_6, 600 MHz) δ [ppm]: 9.55 (d, *J* = 5.0 Hz, 1H, H1), 8.41 (d, *J* = 8.3 Hz, 1H, H5), 8.35 (d, *J* = 7.9 Hz, 1H, H4), 8.27 (d, *J* = 2.1 Hz, 1H, H8), 8.19 (t, *J* = 7.3 Hz, 2H, H3, H14), 8.17 - 8.14 (m, 1H, H10), 7.83 (dd, *J* = 7.6, 1.2 Hz, 1H, H11), 7.80 - 7.74 (m, 2H, H6, H7), 7.59 - 7.54 (m, 2H, H2, H12), 7.52 (t, *J* = 7.6 Hz, 1H, H9), 7.44 (t, *J* = 7.5 Hz, 1H, H13).

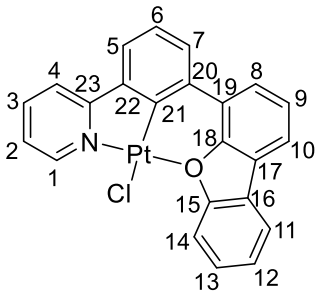

^{13}C NMR (DMSO-d_6, 151 MHz) δ [ppm]: 164.8 (Cq, C23), 155.4 (Cq, C22), 152.5 (Cq, C15), 149.3 (CH, C1), 145.1 (Cq, C18), 141.6 (CH, C3), 140.2 (Cq, C20), 133.8 (CH, C5), 132.3 (Cq, C16), 130.0 (CH, C7), 127.6 (CH, C12), 126.6 (CH, C11), 124.8 (Cq, C21), 124.3 (Cq, C17), 123.9 (CH, C8), 123.6 (CH, C9), 123.5 (Cq, C19), 123.1 (CH, C13), 123.0 (CH, C2), 121.1 (CH, C14), 120.0 (CH, C10), 119.9 (CH, C4), 111.9 (CH, C6).

^{195}Pt NMR (DMSO-d_6, 129 MHz) δ [ppm]: −3794.0.

HR-ESI-MS (70 eV)**:** 572.03 $[M+Na]^+$, 514.07 $[M-Cl]^+$.

Synthesis of [Pd(PyPhDBF)Cl]

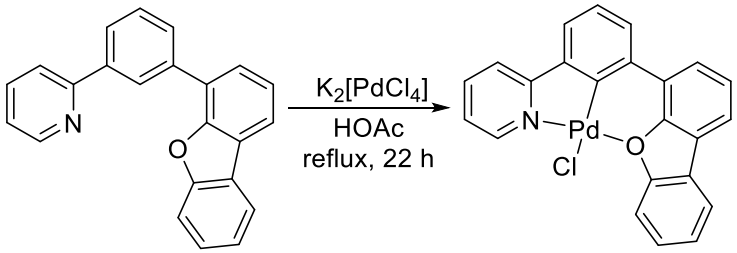

PyHPhDBF (93.2 mg, 0.29 mmol, 1.20 eq.) and $K_2[PdCl_4]$ (78.3 mg, 0.24 mmol, 1.00 eq.) were reacted following general procedure B for 22 h. The complex was isolated as a yellow powder (42.0 mg, 90.9 µmol, 38%).

Habitus Yellow powder (42.0 mg, 90.9 µmol, 38%).

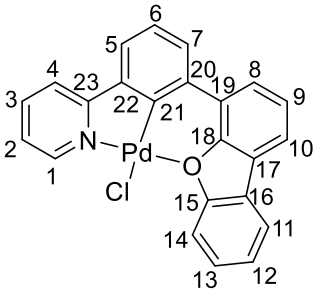

^{1}H NMR (DMSO-d_6, 500 MHz) δ [ppm]: 9.30 (s, 1H, H1), 8.20 (d, *J* = 7.3 Hz, 1H, H14), 8.19 - 8.16 (m, 1H, H4), 8.14 (d, *J* = 6.8 Hz, 1H, H10), 8.13 – 8.10 (m, 1H, H5) 8.08 - 8.02 (m, 2H, H3, H7), 7.78 (d, *J* = 8.1 Hz, 2H, H8, H11), 7.60 (d, *J* = 8.3 Hz, 1H, H2), 7.55 (t, *J* = 7.8 Hz, 1H, H12), 7.51 (t, *J* = 7.6 Hz, 1H, H9), 7.44 (t, *J* = 7.5 Hz, 1H, H13), 7.40 (d, *J* = 6.7 Hz, 1H, H6).

^{13}C NMR (DMSO-d_6, 151 MHz) δ [ppm]: 164.9 (Cq, C23), 155.9 (Cq, C15), 153.0 (Cq, C22), 150.3 (Cq, C20), 139.7 (CH, C3), 132.3 (Cq, C16),128.8 (CH, C2), 128.1 (CH, C12), 127.2 (CH, C8), 125.7 (Cq, C18), 124.8 (Cq, C19), 124.1 (CH, C9), 124.1 (CH, C7), 124.0 (Cq, C17), 123.6 (CH, C5), 123.2 (CH, C13), 123.1 (CH, C6), 121.6 (CH, C14), 120.4 (CH, C10), 119.7 (CH, C4), 112.4 (CH, C11).

HR-ESI-MS (70 eV)**:** 540.26 $[M+H+DMSO]^+$, 425.01 $[M–Cl]^+$.

Synthesis of [Pt(QPhDBF)Cl]

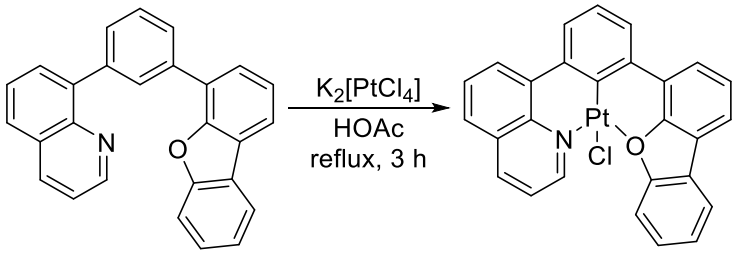

QHPhDBF (54.0 mg, 0.14 mmol, 1.20 eq.) and $K_2[PtCl_4]$ (50.0 mg, 0.11 mmol, 1.00 eq.) were reacted following general procedure B for 3 h. The complex was isolated as an orange powder (40.1 mg, 66.7 µmol, 55%).

Habitus Orange powder (40.1 mg, 66.7 µmol, 55%).

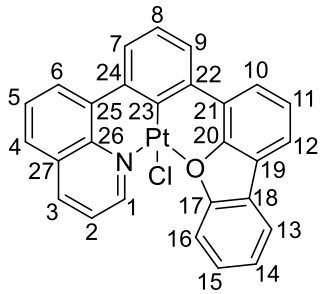

^{1}H NMR (DMSO-d_6, 500 MHz) δ [ppm]: 9.49 (dd, *J* = 5.3, 1.5 Hz, 1H, H1), 8.82 (dd, *J* = 8.3, 1.4 Hz, 1H, H3), 8.57 (dd, *J* = 7.4, 1.1 Hz, 1H, H6), 8.18 (ddd, *J* = 7.7, 1.3, 0.6 Hz, 1H, H16), 8.16 (dd, *J* = 8.2, 1.1 Hz, 1H, H4), 8.11 (dd, *J* = 7.7, 1.2 Hz, 1H, H7), 8.03 (d, *J* = 8.1 Hz, 1H, H10), 7.92 - 7.86 (m, 2H, H5, H12), 7.78 - 7.73 (m, 3H, H2, H9, H13), 7.60 (dd, *J* = 8.1, 2.0 Hz, 1H, H11), 7.53 (ddd, *J* = 8.4, 7.3, 1.3 Hz, 1H, H14), 7.48 (t, *J* = 7.6 Hz, 1H, H8), 7.42 (td, *J* = 7.6, 0.9 Hz, 1H, H15).

^{13}C NMR (DMSO-d_6, 151 MHz) δ [ppm]: 156.5 (CH, C1), 155.4 (Cq, C17), 152.5 (Cq, C25), 141.0 (CH, C3), 140.7 (Cq, C26), 140.0 (Cq, C27), 138.2 (CH, C10), 134.5 (Cq, C24), 1132.5 (Cq, C21), 131.1 (Cq, C20), 128.6 (CH, C12), 128.5 (Cq, C23), 128.4 (CH, C6), 127.5 (CH, C14), 127.3 (CH, C4), 126.9 (CH, C11), 126.6 (CH, C9), 126.3 (CH, C5), 125.2 (Cq, C22), 124.2 (Cq, C18), 123.5 (Cq, C19), 123.5 (CH, C8), 123.1 (CH, C15), 121.7 (CH, C2), 121.1 (CH, C16), 119.7 (CH, C7), 111.8 (CH, C13).

^{195}Pt NMR (DMSO-d_6, 129 MHz) δ [ppm]: –3683.3.

HR-ESI-MS (70 eV)**:** 622.04 $[M+Na]^+$, 564.09 $[M–Cl]^+$.

Synthesis of [Pt(QPhDBF)Cl]

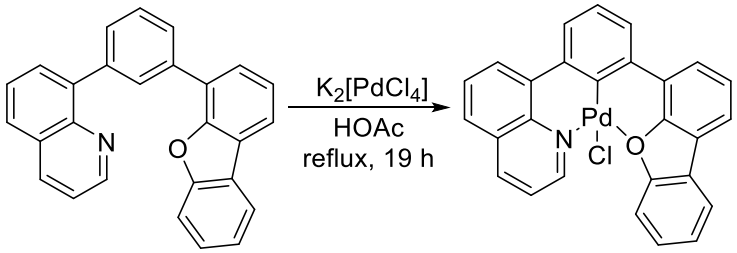

QHPhDBF (54.0 mg, 0.14 mmol, 1.20 eq.) and $K_2[PdCl_4]$ (39.0 mg, 0.12 mmol, 1.00 eq.) were reacted following general procedure B for 19 h. The complex was isolated as a green powder (40.0 mg, 78.1 μmol, 65%).

Habitus Green powder (40.0 mg, 78.1 μmol, 65%).

^{1}H NMR (MeOH-d_4, 500 MHz) δ [ppm]: 8.91 (d, *J* = 5.5 Hz, 1H), 8.17 (s, 1H), 8.11 – 8.02 (m, 4H), 7.95 (s, 1H), 7.82 (d, *J* = 8.4 Hz, 1H), 7.75 (d, *J* = 7.6 Hz, 1H), 7.70 (t, *J* = 7.0 Hz, 3H), 7.60 (d, *J* = 8.3 Hz, 1H), 7.48 (t, *J* = 7.0 Hz, 2H), 7.39 (t, *J* = 7.5 Hz, 1H).

HR-ESI-MS (70 eV)**:** 532.99 $[M+Na]^+$, 475.03 $[M–Cl]^+$.

Synthesis of [Pt(PyPyNaph)Cl]

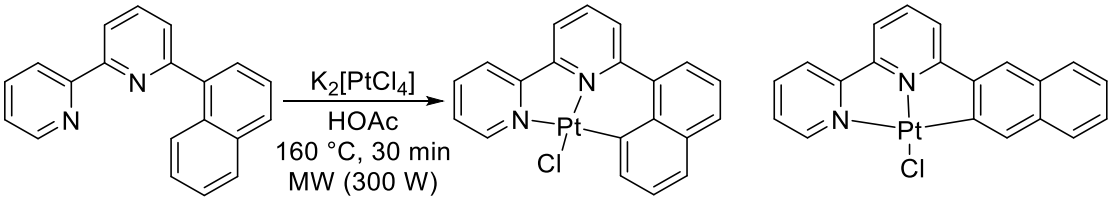

PyPyHNaph (60.0 mg, 0.21 mmol, 1.20 eq.) and $K_2[PtCl_4]$ (72.6 mg, 0.18 mmol, 1.00 eq.) were reacted following general procedure C for 30 min. The product mixture was obtained as a red-orange powder (36.2 mg, 70.7 μmol, 40%, both isomers).

Habitus Red-orange powder (36.2 mg, 70.7 μmol, 40%, 50:50 mixture of both isomers).

^{1}H NMR (DMSO-d_6, 500 MHz) δ [ppm]: 9.64 - 9.61 (m, 1H), 9.60 (dd, *J* = 5.6, 1.6 Hz, 1H), 9.22 - 9.15 (m, 1H), 9.04 (d, *J* = 8.3 Hz, 1H), 8.98 (dd, *J* = 7.9, 1.2 Hz, 1H), 8.95 (ddd, *J* = 7.2, 5.3, 1.0 Hz, 2H), 8.77 (d, *J* = 8.1 Hz, 1H), 8.76 - 8.71 (m, 3H), 8.68 (dd, *J* = 7.9, 1.3 Hz, 1H), 8.61 (dd, *J* = 8.4, 1.3 Hz, 1H), 8.59 - 8.55 (m, 2H), 8.53 - 8.51 (m, 3H), 8.50 - 8.46 (m, 2H), 8.43 - 8.40 (m, 2H), 8.33 (dd, *J* = 7.6, 1.2 Hz, 1H), 8.26 - 8.21 (m, 2H), 8.18 (d, *J* = 8.1 Hz, 1H), 8.16 - 8.12 (m, 3H), 8.10 (dd, *J* = 8.1, 1.2 Hz, 1H), 8.04 (s, 1H), 7.96 (ddd, *J* = 7.4, 5.2, 1.4 Hz, 2H), 7.90 (dd, *J* = 8.1, 1.5 Hz, 1H), 7.86 - 7.81 (m, 1H), 7.76 (t, *J* = 7.8 Hz, 2H), 7.74 - 7.72 (m, 1H), 7.68 (dd, *J* = 7.8, 1.5 Hz, 1H), 7.64 (t, *J* = 7.7 Hz, 1H), 7.47 (t, *J* = 7.7 Hz, 1H).

HR-EI-MS (70 eV): 555.99$[M–Cl+DMSO]^+$,511.04 $[M]^{+\cdot}$, 281.11 $[L]^{+\cdot}$.

Synthesis of [Pd(PyPyNaph)Cl]

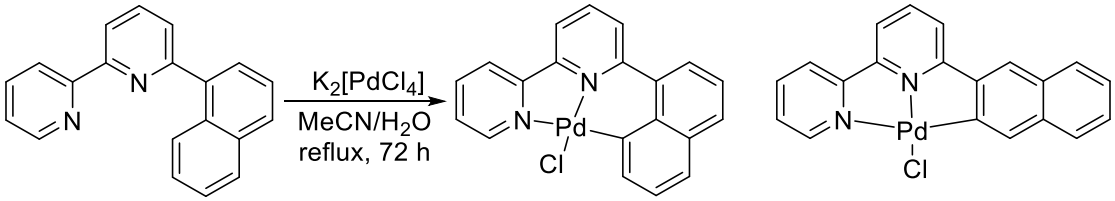

PyPyHNaph (60.0 mg, 0.21 mmol, 1.20 eq.) and $K_2[PtCl_4]$ (57.1 mg, 0.18 mmol, 1.00 eq.) heated to reflux in 15 mL of MeCN/H_2O (1:1). After cooling to room temperature, the mixture was filtered off over a glass frit and washed with distilled water and diethyl ether. The product mixture was obtained as a yellow powder (61.4 mg, 0.15 mmol, 83%, both isomers).

Habitus Yellow powder (61.4 mg, 0.15 mmol, 83%, both isomers).

^{1}H NMR (DMSO-d_6, 500 MHz) δ [ppm]: Mixture of isomers, ratio ca. 70:30.

Major isomer: 9.31 (d, *J* = 5.3 Hz, 1H), 8.68 (dd, *J* = 8.0, 5.3 Hz, 2H), 8.56 (d, *J* = 8.2 Hz, 1H), 8.50 (d, *J* = 7.4 Hz, 1H), 8.40 (q, *J* = 8.0 Hz, 2H), 8.32 (td, *J* = 7.8, 1.7 Hz, 1H), 8.10 (d, *J* = 7.9 Hz, 1H), 7.84 (dd, *J* = 7.8, 5.4 Hz, 1H), 7.74 (d, *J* = 7.7 Hz, 1H), 7.65 (dd, *J* = 8.5, 7.7 Hz, 1H), 7.27 (t, *J* = 7.6 Hz, 1H).

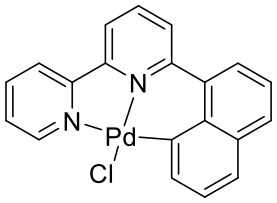

Minor isomer: 8.71 (d, *J* = 5.7 Hz, 1H), 8.54 - 8.50 (m, 2H), 8.45 (d, *J* = 7.9 Hz, 1H), 8.31 - 8.25 (m, 3H), 7.99 (d, *J* = 8.4 Hz, 1H), 7.92 (d, *J* = 8.1 Hz, 1H), 7.83 - 7.80 (m, 2H), 7.62 - 7.57 (m, 1H), 7.47 (t, *J* = 7.4 Hz, 1H).

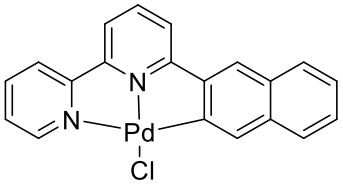

HR-ESI-MS (70 eV): 387.01 $[M–Cl]^+$.

HR-EI-MS (70 eV): 282.11 $[L]^+$, 421.98 $[M]^+$, 387.01 $[M–Cl]^+$.

Synthesis of [Pt(PyPyAnth)Cl]

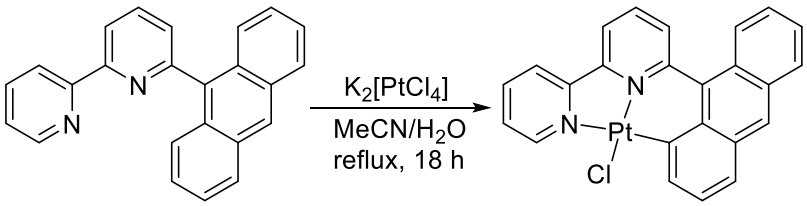

PyPyHAnth (120 mg, 0.36 mmol, 1.20 eq.) and $K_2[PtCl_4]$ (125 mg, 0.30 mmol, 1.00 eq.) were mixed in a mixture of MeCN and distilled water (10 mL each). The mixture was heated to reflux for 18 h and cooled to room temperature. The red precipitate was filtered off over a glass frit and washed with MeCN and distilled water. The solid was dissolved in CH_2Cl_2 and the solvent evaporated off to yield the product as a red powder (80.0 mg, 0.14 mmol, 48%).

Habitus Red powder (80.0 mg, 0.14 mmol, 48%).

^{1}H NMR ($CDCl_3$, 500 MHz) δ [ppm]: 9.55 (dd, *J* = 5.2, 1.6 Hz, 2H), 8.35 (ddd, *J* = 12.1, 7.7, 1.5 Hz, 4H), 7.87 (dd, *J* = 8.1, 1.4 Hz, 2H), 7.74 (dd, *J* = 8.2, 7.3 Hz, 2H), 7.56 (d, *J* = 7.6 Hz, 2H), 7.44 (dd, *J* = 8.2, 5.2 Hz, 2H), 7.35 (t, *J* = 7.6 Hz, 1H).

HR-EI-MS (70 eV)**:** 332.12 $[L]^+$.

HR-ESI-MS (70 eV)**:** 525.26 $[M–Cl]^+$, 333.14 $[L+H]^+$.

Synthesis of [Pd(PyPyAnth)Cl]

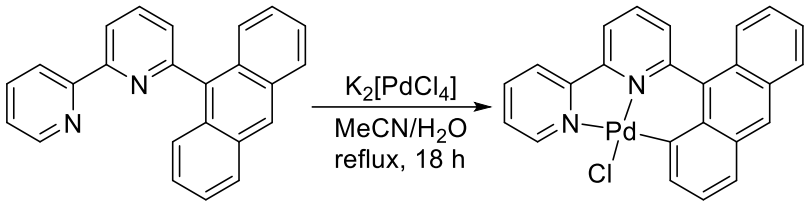

PyPyHAnth (120 mg, 0.36 mmol, 1.20 eq.) and $K_2[PdCl_4]$ (97.8 mg, 0.30 mmol, 1.00 eq.) were mixed in a mixture of MeCN and distilled water (10 mL each). The mixture was heated to reflux for 18 h and cooled to room temperature. The orange precipitate was filtered off over a glass frit and washed with MeCN and distilled water. The solid was dissolved in CH_2Cl_2 and the solvent evaporated off to yield the product as a vibrant orange powder (87.2 mg, 0.18 mmol, 61%).

Habitus Vibrant orange powder (87.2 mg, 0.18 mmol, 61%).

^{1}H NMR (DMSO-d_6, 300 MHz) δ [ppm]: 9.14 (d, *J* = 5.2 Hz, 1H), 8.70 (dd, *J* = 8.3, 7.7 Hz, 3H), 8.35 (t, *J* = 7.4 Hz, 1H), 8.23 (ddd, *J* = 13.3, 11.1, 7.5 Hz, 4H), 8.03 (d, *J* = 8.1 Hz, 1H), 7.86 (d, *J* = 7.5 Hz, 2H), 7.55 (dt, *J* = 5.2, 2.4 Hz, 2H), 7.25 (t, *J* = 7.6 Hz, 1H).

HR-EI-MS (70 eV)**:** 332.12 $[L]^+$.

HR-ESI-MS (70 eV): 805.14 $[M+L+H]^+$, 473.00 $[M+H]^+$, 333.14 $[L+H]^+$.

Synthesis of [Pd(PyPyAnth)Cl]

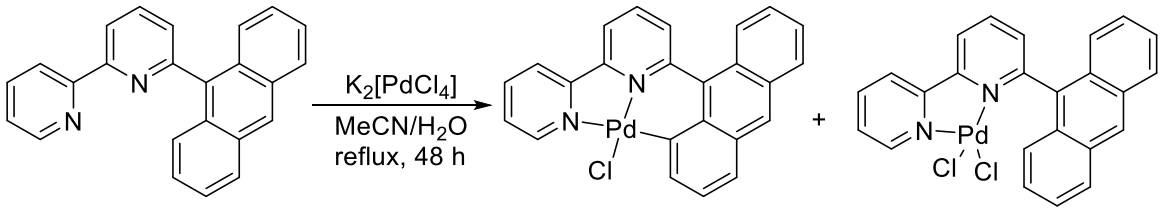

Under inert conditions, PyPyHAnth (61.0 mg, 0.18 mmol, 1.20 eq.) and $K_2[PdCl_4]$ (50.0 mg, 0.15 mmol, 1.00 eq.) were mixed in a degassed mixture of MeCN and distilled water (10 mL each). The mixture was heated to reflux for 48 h and cooled to room temperature. The orange precipitate was filtered off over a glass frit and washed with diethyl ether and distilled water. The solid was dissolved in CH_2Cl_2 and the solvent evaporated off to yield the products as an orange powder (31.0 mg, mixture of products, 4:1).

Habitus Orange powder (31.0 mg, mixture of products, 4:1).

^{1}H NMR (CD_2Cl_2, 500 MHz) δ [ppm]:

Major product (cyclometalated complex, 80%):

9.55 (d, *J* = 4.6 Hz, 1H), 8.35 (d, *J* = 7.7 Hz, 1H), 8.27 (t, *J* = 7.4 Hz, 2H), 8.19 (d, *J* = 7.7 Hz, 1H), 8.14 (d, *J* = 7.9 Hz, 1H), 8.10 (t, *J* = 7.0 Hz, 1H), 7.68 – 7.61 (m, 1H), 7.49 (d, *J* = 7.4 Hz, 1H), 7.30 (t, *J* = 7.5 Hz, 1H), 7.21 (d, *J* = 6.8 Hz, 1H), 7.15 (t, *J* = 7.6 Hz, 1H), 7.01 (t, *J* = 7.5 Hz, 1H), 6.58 (d, *J* = 7.4 Hz, 1H), 6.03 (s, 1H).

Minor product (precoordinated complex, 20%):

9.25 (d, *J* = 4.6 Hz, 1H), 8.54 (s, 1H), 8.38 – 8.34 (m, 1H), 8.30 – 8.25 (m, 1H), 8.23 – 8.18 (m 1H), 8.16 – 8.07 (m, 3H), 8.01 (t, *J* = 8.6Hz, 2H), 7.81 (d, *J* = 8.3 Hz, 1H), 7.68 – 7.61 (m, 1H), 7.54 – 7.44 (m, 3H), 7.29 – 7.24 (m, 1H).

HR-ESI-MS (70 eV): 493.99 $[M(cyclometalated)+Na]^+$, 436.03 $[M(cyclometalated)–Cl]^+$.

Synthesis of [Pd(PyPyHAnth)Cl$_2$]

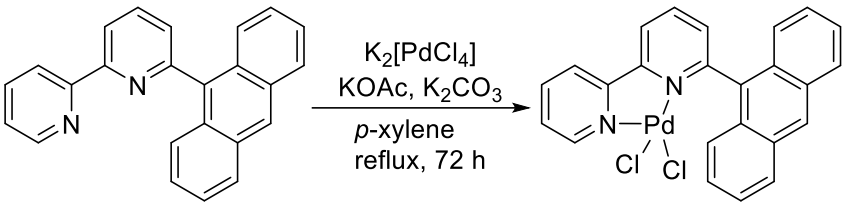

PyPyHAnth (61.0 mg, 0.18 mmol, 1.20 eq.) and $K_2[PdCl_4]$ (50.0 mg, 0.15 mmol, 1.00 eq.) were reacted following general procedure D for 72 h under strict exclusion of oxygen. The product was obtained as a brown powder (15.2 mg, 29.8 μmol, 19%).

Habitus Brown powder (15.2 mg, 29.8 μmol, 19%).

^{1}H NMR (CD_2Cl_2, 500 MHz) δ [ppm]: 8.71 (d, *J* = 4.0 Hz, 1H, H1), 8.61 (dd, *J* = 8.0, 0.9 Hz, 1H, H7), 8.59 (s, 1H, H12), 8.34 (d, *J* = 7.9 Hz, 1H, H4), 8.10 (d, *J* = 8.5 Hz, 2H, H11, H11'), 8.07 (t, *J* = 7.8 Hz, 1H, H6), 7.72 (td, *J* = 7.8, 1.8 Hz, 1H, H3), 7.67 (d, *J* = 9.6 Hz, 2H, H8, H8'), 7.53 (dd, *J* = 7.6, 0.9 Hz, 1H, H5), 7.51 - 7.46 (m, 2H, H10, H10'), 7.38 (ddd, *J* = 8.7, 6.5, 1.1 Hz, 2H, H9, H9'), 7.31 (ddd, *J* = 7.5, 4.9, 1.1 Hz, 1H, H2).

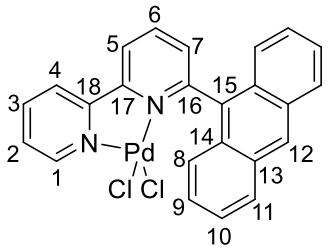

^{13}C NMR (CD_2Cl_2, 126 MHz) δ [ppm]: 157.9 (Cq, C17), 157.0 (Cq, C16), 156.7 (Cq, C18), 149.7 (CH, C1), 137.8 (CH, C6), 137.4 (CH, C3), 136.1 (Cq, C15), 132.0 (Cq, C13, C13'), 130.6 (Cq, C14, C14'), 129.0 (CH, C11, C11'), 128.0 (CH, C12), 127.4 (CH, C5), 126.7 (CH, C8, C8'), 126.4 (CH, C9, C9'), 125.8 (CH, C10, C10'), 124.4 (CH, C2), 121.7 (CH, C4), 120.1 (CH, C7).

HR-ESI-MS (70 eV): 473.00 $[M+H]^+$, 333.14 $[L+H]^+$.

Synthesis of [Pd(PyPyHAnth)Cl$_2$]

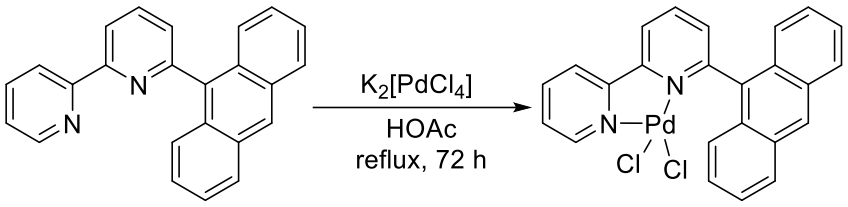

PyPyHAnth (306 mg, 0.92 mmol, 1.00 eq.) and $K_2[PdCl_4]$ (360 mg, 1.10 mmol, 1.20 eq.) were reacted following general procedure C for 72 h under strict exclusion of oxygen. The product was obtained as an orange powder (380 mg, 0.75 mmol, 81%).

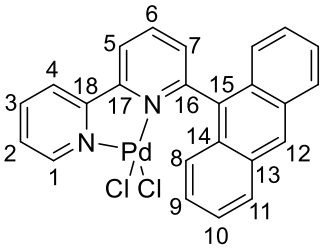

Habitus Orange powder (380 mg, 0.75 mmol, 81%).

^{1}H NMR (CD_2Cl_2, 500 MHz) δ [ppm]: 9.35 (dt, *J* = 5.7, 1.2 Hz, 1H), 8.66 (s, 1H), 8.30 - 8.22 (m, 2H), 8.18 (d, *J* = 3.8 Hz, 2H), 8.16 - 8.10 (m, 2H), 7.78 - 7.69 (m, 3H), 7.60 (dt, *J* = 5.7, 4.6 Hz, 1H), 7.57 – 7.51 (m, 4H).

HR-ESI-MS (70 eV): 805.14 $[M–Cl+L]^+$, 472.00 $[M–Cl]^+$, 439.03 [M(cyclometalated)–Cl]$^+$, 333.14 $[L+H]^+$.

Synthesis of [Ni(PyPyAnth)Br]

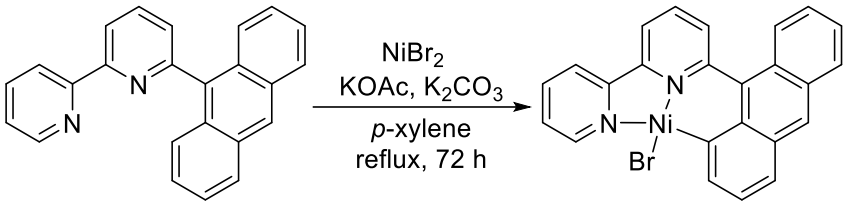

PyPyHAnth (150 mg, 0.45 mmol, 1.00 eq.) and $NiBr_2$ (100 mg, 0.45 mmol, 1.00 eq.) were reacted following general procedure D for 72 h under strict exclusion of oxygen. The product was obtained as a green powder (180 mg, 0.38 mmol, 85%).

Habitus Green powder (180 mg, 0.38 mmol, 85%).

^{1}H NMR (CD_2Cl_2, 500 MHz) δ [ppm]: 15.11 (s, br, 1H), 12.46 (s, br 1H), 9.79 (s, br, 2H), 9.40 (s, br, 2H), 8.86 (s, br, 2H), 7.40 (s, br, 2H), 7.25 (s, br, 2H), 6.41 (s, br, 2H).

HR-ESI-MS (70 eV): 390.07 $[M–Br]^+$, 333.14 $[L+H]^+$.

Synthesis of [Pd(PyPyO$_2$Anth)Cl]

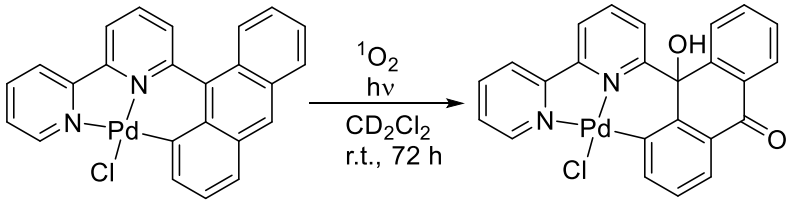

An NMR sample of [Pd(PyPyAnth)Cl] (ca. 5 mg) in CD_2Cl_2 was left in solution at room temperature for 72 h. Red crystals formed, which could be isolated by filtration and washing with small amounts of *n*-pentane. The product was obtained as red crystals (traces).

Habitus Red crystals (traces).

^{1}H NMR (CD_2Cl_2, 500 MHz) δ [ppm]: 9.57 (dd, *J* = 5.3, 0.9 Hz, 1H, H1), 8.36 (d, *J* = 7.9 Hz, 1H, H7), 8.31 - 8.24 (m, 2H, H6, H8), 8.20 (d, *J* = 8.1 Hz, 1H, H4), 8.16 (d, *J* = 7.9 Hz, 1H, H5), 8.13 (td, *J* = 7.9, 1.7 Hz, 1H, H3), 7.67 (ddd, *J* = 7.4, 5.4, 1.1 Hz, 1H, H2), 7.50 (d, *J* = 7.3 Hz, 1H, H11), 7.31 (td, *J* = 7.6, 1.0 Hz, 1H, H12), 7.21 (dd, *J* = 7.0, 0.9 Hz, 1H, H10), 7.16 (td, *J* = 7.6, 1.1 Hz, 1H, H13), 7.01 (dd, *J* = 8.1, 7.0 Hz, 1H, H9), 6.59 (d, *J* = 7.5 Hz, 1H, H14).

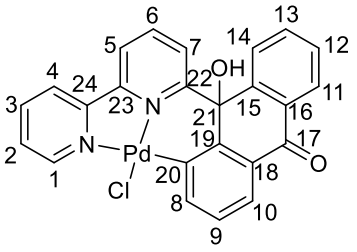

^{13}C NMR (CD_2Cl_2, 126 MHz) δ [ppm]: 167.1 (Cq, C24), 157.6 (Cq, C23), 151.6 (Cq, C22), 150.3 (CH, C1), 141.5 (Cq, C15), 139.7 (CH, C3), 139.6 (Cq, C16), 139.2 (CH, C6), 139.2 (CH, C8), 139.1 (Cq, C19), 134.8 (Cq, C18), 133.6 (Cq, C20), 130.8 (CH, C5), 128.1 (CH, C12), 127.3 (CH, C13), 126.7 (CH, C2), 126.1 (CH, C9), 124.2 (CH, C7), 123.3 (CH, C11), 123.1 (Cq, C21), 122.5 (CH, C14), 122.4 (Cq, C17), 122.1 (CH, C4), 121.1 (CH, C10).

Synthesis of anthracene endoperoxide

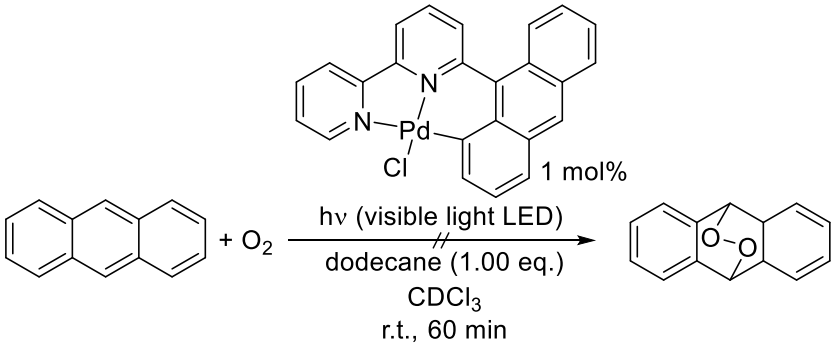

In a round small glass vial without exclusion of oxygen or light, anthracene (100 mg, 0.56 mmol, 1.00 eq.) was mixed with [Pd(PyPyAnth)Cl] (2.50 mg, 1mol%) and dodecane (95.6 mg, 0.13 mL, 0.56 mmol, 1.00 eq.) as internal standard in $CDCl_3$. The mixture was stirred at room temperature while irradiating with a visible light LED for 60 min, during which the originally orange solution turned colourless. The mixture was filtered off over a glass pipette plugged with cotton and packed with silica using EtOAc. The obtained solution was investigated via GC-MS-spectrometry. No traces of the endoperoxide could be found, instead anthracene was reisolated.

Synthesis of [Pt(QPyAnth)Cl]

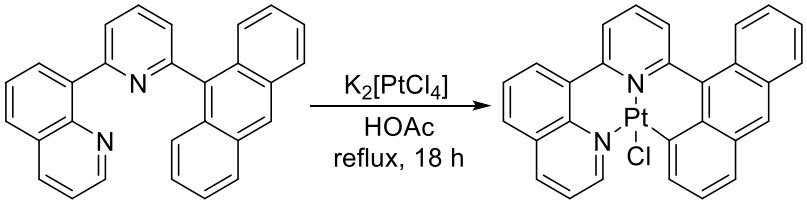

QPyHAnth (100 mg, 0.26 mmol, 1.4 eq.) and $K_2[PtCl_4]$ (77.2 mg, 0.19 mmol, 1.00 eq.) were reacted following general procedure B for 18 h. The product was obtained as an orange powder (62.1 mg, 0.10 mmol, 54%).

Habitus Orange powder (62.1 mg, 0.10 mmol, 54%).

^{1}H NMR (CD_2Cl_2, 500 MHz) δ [ppm]: 8.89 (dd, *J* = 5.2, 1.5 Hz, 1H), 8.79 (s, 1H), 8.71 (dd, *J* = 7.4, 1.3 Hz, 1H), 8.51 (dd, *J* = 8.2, 1.5 Hz, 1H), 8.29 (d, *J* = 8.5 Hz, 1H), 8.20 - 8.11 (m, 3H), 8.10 - 8.04 (m, 1H), 7.98 (dd, *J* = 8.1, 1.4 Hz, 1H), 7.89 (t, *J* = 7.8 Hz, 1H), 7.75 (dd, *J* = 7.6, 1.4 Hz, 1H), 7.65 - 7.54 (m, 2H), 7.49 (dd, *J* = 8.2, 5.2 Hz, 1H), 7.37 – 7.34 (m, 2H).

HR-ESI-MS (70 eV): 611.08 $[M+H]^+$, 575.10 $[M–X]^+$.

Synthesis of [Pd(QPyAnth)Cl]

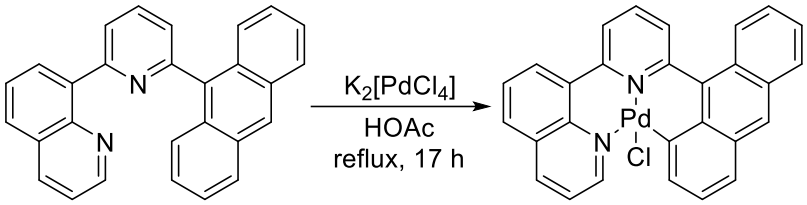

QPyHAnth (100 mg, 0.26 mmol, 1.4 eq.) and $K_2[PdCl_4]$ (60.7 mg, 0.19 mmol, 1.00 eq.) were reacted following general procedure B for 17 h. The product was obtained as an orange powder (68.9 mg, 0.13 mmol, 70%).

Habitus Orange powder (68.9 mg, 0.13 mmol, 70%).

^{1}H NMR (CD_2Cl_2, 500 MHz) δ [ppm]: 8.86 - 8.79 (m, 2H), 8.70 (d, *J* = 7.4 Hz, 1H), 8.52 (d, *J* = 8.4 Hz, 1H), 8.36 (d, *J* = 8.4 Hz, 1H), 8.18 (d, *J* = 7.1 Hz, 2H), 8.18 - 8.08 (m, 1H), 8.05 - 7.99 (m, 1H), 7.96 (t, *J* = 7.9 Hz, 1H), 7.82 (d, *J* = 7.6 Hz, 1H), 7.75 - 7.66 (m, 1H), 7.63 - 7.51 (m, 4H), 7.48 (dd, *J* = 8.9, 6.5 Hz, 1H).

HR-ESI-MS (70 eV): 522.02 $[M+H]^+$, 486.04 $[M–Cl]^+$.

6.2.4 Coligand Exchange Reactions

General Procedure E

[M(PyPhQ)X] (1.00 eq.) and the coligand salt (1.20 eq.) were stirred in distilled THF at room temperature. The mixtures solvent was evaporated off partially and diethyl ether was added until a precipitate formed. The precipitate was filtered off and washed with more diethyl ether. The precipitate was then redissolved with CH_2Cl_2 and the solvent evaporated off to yield the desired complex.

General Procedure F

The acetylide salt (1.20 eq.) was dissolved in dry THF under inert conditions. [M(PyPhQ)NO_3] (1.00 eq.) was added and the mixture was stirred at room temperature. THF was evaporated off under reduced pressure and diethyl ether was added to precipitate the desired product. The mixture was filtered over a glass frit and washed with more diethyl ether. The precipitated solid was redissolved in CH_2Cl_2 and the solvent evaporated off to yield the product as a powder.

Synthesis of [Pt(PyPhQ)NO$_3$]

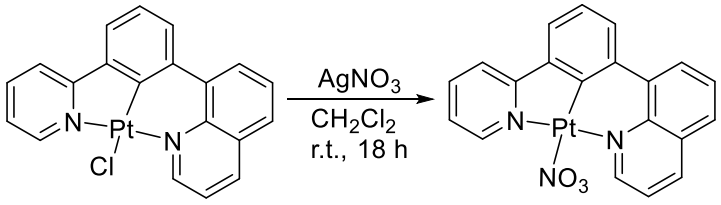

[Pt(PyPhQ)Cl] (300 mg, 0.59 mmol, 1.00 eq.) and $AgNO_3$ (100 mg, 0.59 mmol, 1.00 eq.) were stirred in HPLC grade CH_2Cl_2 for 18 h at room temperature, the solution changing colour from orange to yellow. The mixture was filtered over a glass frit and washed with CH_2Cl_2. The solvent was evaporated off to yield a yellow solid (273 mg, 0.51 mmol, 86%).

Habitus Yellow solid (273 mg, 0.51 mmol, 86%).

^{1}H NMR (CD_2Cl_2, 500 MHz) δ [ppm]: 9.87 (dd, $J^{Pt\text{-}H}$ = 33.7 Hz, J = 5.5, 1.6 Hz, 1H, H1), 8.81 (ddd, $J^{Pt\text{-}H}$ = 31.4 Hz, J = 5.8, 1.5, 0.8 Hz, 1H, H13), 8.67 (dd, J = 7.9, 1.1 Hz, 1H, H5), 8.65 (dd, J = 8.1, 1.6 Hz, 2H, H3, H6), 8.06 - 7.98 (m, 3H, H4, H7, H11), 7.87 (t, J = 7.8 Hz, 1H, H10), 7.68 – 7.64 (m, 2H, H2, H9), 7.44 (dd, J = 8.0, 7.5 Hz, 1H, H8), 7.37 (ddd, J = 7.3, 5.8, 1.4 Hz, 1H, H12).

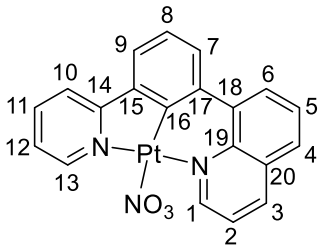

^{13}C NMR (CD_2Cl_2, 126 MHz) δ [ppm]: 165.2 (Cq, C14), 154.5 (CH, C1), 149.1 (CH, C13), 145.2 (Cq, C15), 141.4 (CH, C3), 139.5 (CH, C11), 138.1 (Cq, C19), 136.0 (Cq, C18), 133.3 (Cq, C16), 131.9 (Cq, C17), 130.5 (Cq, C20), 130.0 (CH, C5), 127.4 (CH, C7, C4), 127.1 (CH, C6), 125.0 (CH, C8), 123.6 (CH, C9), 123.0 (CH, C12), 121.3 (CH, C2), 119.0 (CH, C10).

HR-ESI-MS (70 eV): 476.07 $[M–X]^+$.

Synthesis of [Pd(PyPhQ)NO$_3$]

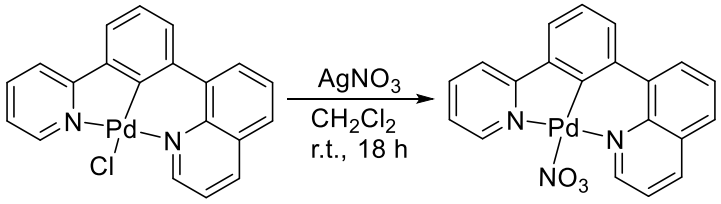

[Pd(PyPhQ)Cl] (180 mg, 0.42 mmol, 1.00 eq.) and $AgNO_3$ (86.9 mg, 0.51 mmol, 1.20 eq.) were stirred in HPLC grade CH_2Cl_2 for 18 h at room temperature. The mixture was filtered over a glass frit and washed with diethyl ether. The precipitate was redissolved in CH_2Cl_2. The solvent was evaporated off to yield a yellow solid (145 mg, 0.32 mmol, 76%).

Habitus Yellow solid (145 mg, 0.32 mmol, 76%).

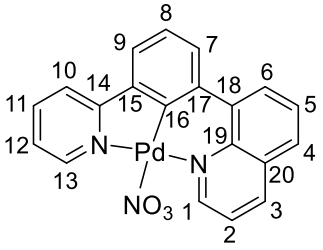

^{1}H NMR (CD_2Cl_2, 500 MHz,) δ [ppm]: 9.50 (d, *J* = 4.5 Hz, 1H, H1), 8.94 (d, *J* = 3.3 Hz, 1H, H3), 8.76 (s, 1H, H6), 8.64 (s, 1H, H13), 8.30 - 8.15 (m, 3H, H4, H10, H11), 8.07 (d, *J* = 7.5 Hz, 1H, H7), 7.97 - 7.88 (m, 3H, H2, H5, H9), 7.54 (s, 1H, H12), 7.46 (t, *J* = 7.6 Hz, 1H, H8).

^{13}C NMR (CD_2Cl_2, 126 MHz) δ [ppm]: 163.6 (Cq, C14), 154.9 (CH, C1), 149.9 (CH, C13), 149.2 (Cq, C16), 146.4 (Cq, C15), 142.5 (CH, C3), 141.1 (CH, C11), 137.9 (Cq, C19), 135.7 (Cq, C18), 132.3 (Cq, C17), 131.4 (CH, C6), 130.5 (CH, C4), 130.4 (Cq, C20), 128.5 (CH, C5), 128.3 (CH, C7), 127.1 (CH, C8), 125.3 (CH, C9), 124.4 (CH, C12), 122.3 (CH, C2), 120.5 (CH, C10).

HR-ESI-MS (70 eV): 387.01 $[M–X]^+$.

Synthesis of [Ni(PyPhQ)NO$_3$]

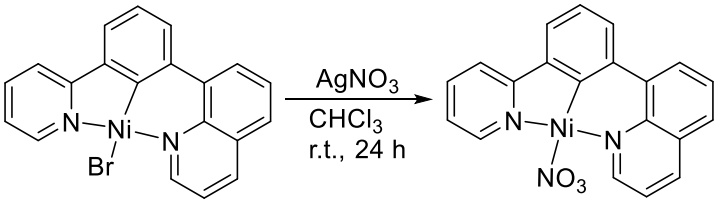

[Ni(PyPhQ)Br] (100 mg, 0.23 mmol, 1.00 eq.) and $AgNO_3$ (40.2 mg, 0.23 mmol, 1.00 eq.) were stirred in HPLC grade chloroform in an aluminium foil covered round bottom flask for 24 h until the colour changed from orange to yellow. The yellowish precipitate was dissolved in CH_2Cl_2, the solution filtered over a glass frit and further washed with CH_2Cl_2. The filtrate was evaporated under reduced pressure to yield a yellow powder (55.0 mg, 0.13 mmol, 57%).

Habitus Yellow powder (55.0 mg, 0.13 mmol, 57%).

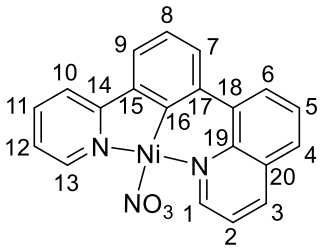

^{1}H NMR (CD_2Cl_2, 500 MHz) δ [ppm]: 9.20 (d, J = 4.9 Hz, 1H, H1), 8.47 (d, J = 7.1 Hz, 1H, H6), 8.40 (d, J = 6.2 Hz, 1H, H3), 8.32 - 8.23 (m, 1H, H13), 7.92 - 7.83 (m, 2H, H4, H11), 7.81 - 7.73 (m, 2H, H5, H7), 7.67 (d, J = 8.6 Hz, 1H, H10), 7.50 - 7.40 (m, 2H, H2, H9), 7.31 (t, J = 7.4 Hz, 1H, H8), 7.21 - 7.15 (m, 1H, H12).

^{13}C NMR (CD_2Cl_2, 126 MHz) δ [ppm]: 163.6 (Cq, C14), 150.1 (CH, C13), 154.5 (CH, C1), 147.2 (Cq, C15), 146.7 (Cq, C16), 140.7 (CH, C3), 139.7 (CH, C11), 136.1 (Cq, C17), 135.2 (Cq, C19), 134.9 (Cq, C18), 130.1 (Cq, C20), 129.2 (CH, C4), 128.6 (CH, C6), 128.2 (CH, C5), 126.7 (CH, C8), 126.0 (CH, C7), 123.3 (CH, C12), 122.7 (CH, C9), 121.3 (CH, C2), 118.5 (CH, C10).

HR-ESI-MS (70 eV): 339.04 $[M–X]^+$.

Synthesis of [Pt(PyPhQ)OBz]

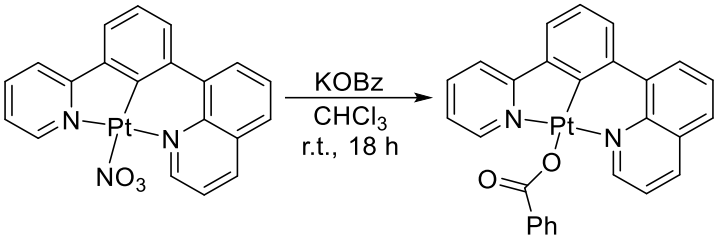

[Pt(PyPhQ)NO_3] (50.0 mg, 0.09 mmol, 1.00 eq.) and potassium benzoate (16.3 mg, 0.10 mmol, 1.10 eq.) were reacted following general procedure E in chloroform for 18 h. The product was obtained as a dark red powder (40.0 mg, 0.07 mmol, 74%).

Habitus Dark red powder (40.0 mg, 0.07 mmol, 74%).

^{1}H NMR (CD_2Cl_2, 600 MHz) δ [ppm]: 10.04 (d, $J^{Pt\text{-}H}$ = 37.6 Hz, J = 4.7 Hz, 1H, H13), 8.80 (d, $J^{Pt\text{-}H}$ = 37.6 Hz, J = 5.3 Hz, 1H, H1), 8.62 (d, J = 7.6 Hz, 1H, H8), 8.52 (d, J = 8.3 Hz, 1H, H11), 8.27 (d, J = 7.9 Hz, 2H, H21, H21'), 8.01 (d, J = 8.0 Hz, 1H, H5), 7.93 (d, J = 7.7 Hz, 1H, H10), 7.91 - 7.86 (m, 1H, H3), 7.80 (t, J = 8.3 Hz, 2H, H4, H9), 7.62 (d, J = 7.9 Hz, 1H, H7), 7.54 - 7.47 (m, 3H, H22, H22', H23), 7.46 - 7.43 (m, 1H, H12), 7.38 (t, J = 8.0 Hz, 1H, H6), 7.21 - 7.15 (m, 1H, H2).

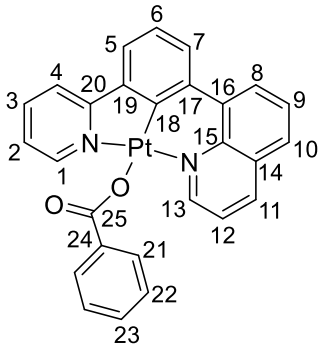

^{13}C NMR (CD_2Cl_2, 151 MHz) δ [ppm]: 172.2 (Cq, C25), 166.6 (Cq, C20), 156.0 (CH, C13), 150.3 (CH, C1), 146.0 (Cq, C19), 141.5 (CH, C11), 139.5 (CH, C3), 138.9 (Cq, C15, C24), 137.3 (Cq, C16), 132.4 (Cq, C17), 131.5 (CH, C8), 131.1 (Cq, C14), 131.1 (CH, C23), 130.3 (CH, C10, C21, C21'), 128.4 (CH, C22, C22'), 127.7 (CH, C9), 127.6 (CH, C5), 124.7 (CH, C6), 124.0 (CH, C7) , 123.0 (CH, C2), 121.6 (CH, C12), 119.2 (CH, C4).

^{195}Pt NMR (CD_2Cl_2, 129 MHz) δ [ppm]: –3206.2.

HR-ESI-MS **(**70 eV): 476.07 $[M–X]^+$.

Synthesis of [Pd(PyPhQ)OBz]

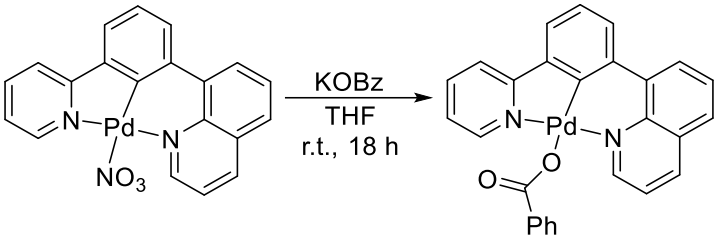

[Pd(PyPhQ)NO_3] (50.0 mg, 0.11 mmol, 1.00 eq.) and potassium benzoate (19.5 mg, 0.12 mmol, 1.10 eq.) were reacted following general procedure E for 18 h. The product was obtained as a yellow powder (28.3 mg, 0.05 mmol, 45%).

Habitus Yellow powder (28.3 mg, 0.05 mmol, 45%).

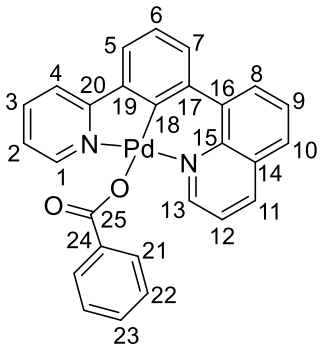

^{1}H NMR (CD_2Cl_2, 500 MHz) δ [ppm]: 9.75 (s, 1H, H13), 8.58 - 8.51 (m, 1H, H11), 8.48 (d, *J* = 9.0 Hz, 1H, H8), 8.42 (d, *J* = 7.0 Hz, 1H, H1), 8.21 (d, *J* = 6.6 Hz, 2H, H21, H21'), 7.96 - 7.82 (m, 3H, H3, H5, H10), 7.76 (t, *J* = 7.7 Hz, 2H, H4, H9), 7.58 (d, *J* = 7.5 Hz, 1H, H7), 7.47 (dq, *J* = 14.3, 7.1 Hz, 4H, H12, H22, H22', H23), 7.36 (t, *J* = 7.7 Hz, 1H, H6), 7.18 - 7.13 (m, 1H, H2).

^{13}C NMR (CD_2Cl_2, 126 MHz) δ [ppm]: 164.9 (Cq, C20), 153.0 (Cq, C16), 150.4 (Cq, C19), 146.7 (Cq, C17), 141.1 (CH, C1), 139.4 (CH, C3), 138.1 (Cq, C24), 137.5 (Cq, C14), 133.4 (Cq, C18), 130.9 (CH, C12), 130.8 (CH, C10, C11), 130.7 (Cq, C25), 130.5 (CH, C21, C21'), 129.7 (CH, C8), 128.3 (Cq, C15), 128.0 (CH, C9), 127.9 (CH, C22, C22'), 127.8 (CH, C5), 126.1 (CH, C6), 124.1 (CH, C7), 123.3 (CH, C2), 121.6 (CH, C23), 119.2 (CH, C4).

HR-ESI-MS (70 eV): 387.01 $[M–X]^+$.

Synthesis of [Pt(PyPhQ)CN]

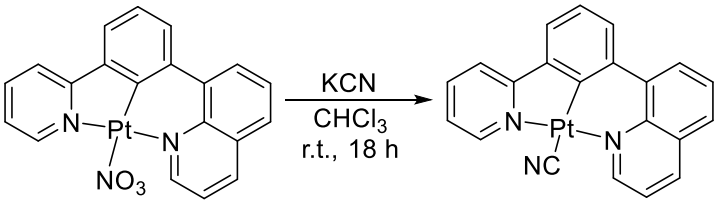

[Pt(PyPhQ)NO_3] (50.0 mg, 0.09 mmol, 1.00 eq.) and KCN (6.63 mg, 0.10 mmol, 1.10 eq.) were reacted following general procedure E in chloroform for 18 h. The product was obtained as an orange powder (34.5 mg, 0.07 mmol, 71%).

Habitus Orange powder (34.5 mg, 0.07 mmol, 71%).

^{1}H NMR (CD_2Cl_2, 600 MHz) δ [ppm]: 10.76 (dd, *J* = 5.5, 1.7 Hz, 1H, H13), 9.70 (ddd, *J* = 5.8, 1.5, 0.7 Hz, 1H, H1), 8.62 – 8.55 (m, 2H, H8, H11), 8.05 (dt, *J* = 7.9, 0.9 Hz, 1H, H5), 7.94 (ddd, *J* = 7.5, 2.1, 1.1 Hz, 2H, H3, H10), 7.83 – 7.81 (m, 1H, H4), 7.79 (t, *J* = 7.7 Hz, 1H, H9), 7.66 (dd, *J* = 7.6, 1.0 Hz, 1H, H7), 7.49 (dd, *J* = 8.1, 5.6 Hz, 1H, H12), 7.40 (dd, *J* = 8.0, 7.5 Hz, 1H, H6), 7.23 (ddd, *J* = 7.4, 5.9, 1.5 Hz, 1H, H2).

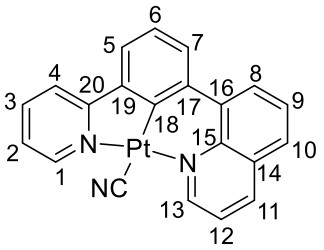

^{13}C NMR (CD_2Cl_2, 151 MHz) δ [ppm]: 167.3 (Cq, C20), 164.4 (CH, C13), 155.9 (Cq, C18), 154.9 (CH, C1), 146.9 (Cq, C19), 141.6 (CH, C11), 139.4 (Cq, C15), 138.9 (CH, C3), 138.7 (Cq, C16), 133.1 (Cq, C17), 131.3 (CH, C8), 130.7 (Cq, C14), 129.9 (CH, C10), 127.2 (CH, C9), 126.7 (CH, C5), 125.3 (CH, C6), 123.4 (CH, C2), 123.2 (CH, C7), 121.8 (CH, C12), 119.1 (CH, C4).

^{195}Pt NMR (CD_2Cl_2, 129 MHz) δ [ppm]: –3276.7.

HR-EI-MS **(**70 eV): 476.07 $[M–X]^+$.

Synthesis of [Pd(PyPhQ)CN]

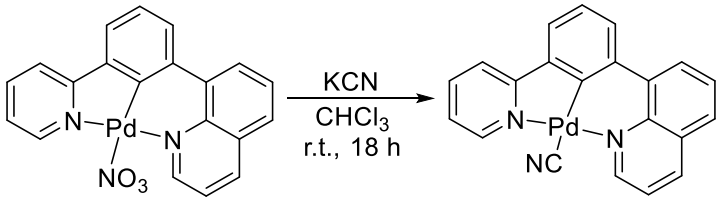

[Pd(PyPhQ)NO_3] (50.0 mg, 0.11 mmol, 1.00 eq.) and KCN (7.93 mg, 0.12 mmol, 1.10 eq.) were reacted following general procedure E in chloroform for 18 h. The product was obtained as a yellow powder (17.0 mg, 0.04 mmol, 39%).

Habitus Yellow powder (17.0 mg, 0.04 mmol, 39%).

^{1}H NMR (CD_2Cl_2, 600 MHz) δ [ppm]: 9.94 (s, 1H, H13), 8.99 (s, 1H, H1), 8.87 (d, *J* = 7.9 Hz, 1H, H11), 8.62 (d, *J* = 7.5 Hz, 1H, H8), 8.24 – 8.16 (m, 2H, H10, H4), 8.14 (d, *J* = 7.2 Hz, 1H, H3), 7.97 (d, *J* = 7.9 Hz, 1H, H5), 7.88 (t, *J* = 7.8 Hz, 2H, H7, H9), 7.81 (s, 1H, H12), 7.48 (s, 1H, H2), 7.40 (t, *J* = 7.7 Hz, 1H, H6).

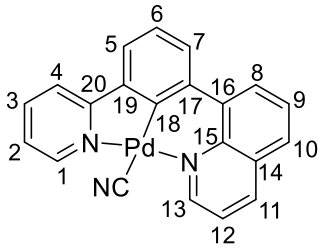

^{13}C NMR (CD_2Cl_2, 151 MHz) δ [ppm]: 165.0 (Cq, C20), 164.4 (CH, C13), 155.9 (Cq, C18), 154.9 (CH, C1), 147.1 (Cq, C19), 142.6 (CH, C11), 140.7 (CH, C3), 138.6 (Cq, C15), 136.8 (Cq, C17), 133.1 (Cq, C16), 131.5 (CH, C8), 130.6 (Cq, C14), 130.3 (CH, C10), 128.2 (CH, C9), 127.9 (CH, C5), 127.0 (CH, C6) 124.7 (CH, C7), 122.0 (CH, C12), 120.4 (CH, C4), 124.4 (CH, C2)

HR-ESI-MS **(**70 eV): 387.01 $[M–X]^+$.

HR-EI-MS (70 eV): 413.01 $[M]^+$.

Synthesis of [Ni(PyPhQ)CN]

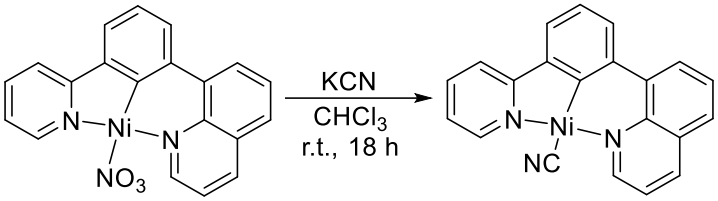

$[Ni(PyPhQ)NO_3]$ (50.0 mg, 0.13 mmol, 1.00 eq.) and KCN (9.58 mg, 0.15 mmol, 1.15 eq.) were reacted following general procedure E in chloroform for 18 h. The product was obtained as an orange powder (36.1 mg, 0.10 mmol, 78%).

Habitus Orange powder (36.1 mg, 0.10 mmol, 78%).

^{1}H NMR (CD_2Cl_2, 500 MHz) δ [ppm]: 9.24 (s, 1H), 8.49 (d, *J* = 7.4 Hz, 1H), 8.42 (d, *J* = 8.0 Hz, 1H), 8.30 (s, 1H), 7.88 (dd, *J* = 8.8, 8.0 Hz, 2H), 7.78 (q, *J* = 7.4 Hz, 2H), 7.68 (d, *J* = 7.9 Hz, 1H), 7.51 - 7.41 (m, 2H), 7.33 (dd, *J* = 9.1, 6.1 Hz, 1H), 7.19 (s, 1H).

HR-ESI-MS (70 eV): 339.04 $[M–X]^+$.

Synthesis of [Pt(PyPhQ)SCN]

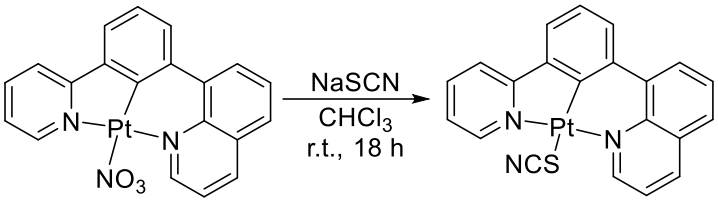

$[Pt(PyPhQ)NO_3]$ (50.0 mg, 0.09 mmol, 1.00 eq.) and NaSCN (9.00 mg, 0.11 mmol, 1.20 eq.) were reacted following general procedure E in chloroform for 18 h. The product was obtained as an orange powder (32.0 mg, 0.06 mmol, 65%).

Habitus Orange powder (32.0 mg, 0.06 mmol, 65%).

^{1}H NMR (CD_2Cl_2, 500 MHz) δ [ppm]: 9.99 (dd, *J* = 5.5, 1.6 Hz, 1H, H13), 8.90 (ddd, *J* = 5.8, 1.5, 0.7 Hz, 1H, H1), 8.49 (dd, *J* = 8.2, 1.4 Hz, 1H, H11), 8.40 (dd, *J* = 7.6, 0.9 Hz, 1H, H8), 7.89 (ddd, *J* = 8.1, 7.5, 1.5 Hz, 1H, H3), 7.85 (dd, *J* = 8.0, 1.2 Hz, 1H, H10), 7.80 (dt, *J* = 8.0, 0.9 Hz, 1H, H4), 7.74 - 7.68 (m, 2H, H5, H9), 7.52 - 7.45 (m, 2H, H7, H12), 7.28 - 7.22 (m, 2H, H2, H6).

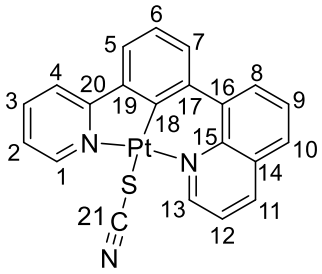

^{13}C NMR (CD_2Cl_2, 126 MHz) δ [ppm]: 178.1 (Cq, C21), 166.5 (Cq, C20), 158.8 (CH, C13), 151.4 (CH, C1), 146.3 (Cq, C19), 141.9 (CH, C11), 141.4 (Cq, C18), 139.7 (CH, C3), 139.0 (Cq, C15), 137.4 (Cq, C16), 132.5 (Cq, C17), 131.7 (CH, C8), 130.9 (Cq, C14),

130.3 (CH, C10), 127.7 (CH, C9), 127.5 (CH, C4), 125.3 (CH, C6), 124.0 (CH, C7), 123.5 (CH, C2), 121.9 (CH, C12), 119.4 (CH, C5).

^{195}Pt NMR (CD_2Cl_2, 107 MHz) δ [ppm]: −3301.5.

HR-ESI-MS **(**70 eV): 476.07 $[M–X]^+$.

Synthesis of [Pd(PyPhQ)SCN]

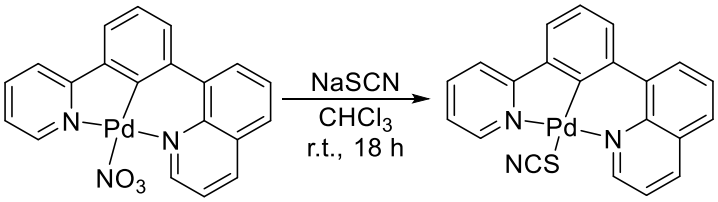

$[Pd(PyPhQ)NO_3]$ (50.0 mg, 0.11 mmol, 1.00 eq.) and NaSCN (10.8 mg, 0.13 mmol, 1.20 eq.) were reacted following general procedure E in chloroform for 18 h. The product was obtained as a yellow powder (27.7 mg, 0.06 mmol, 55%).

Habitus Yellow powder (27.7 mg, 0.06 mmol, 55%).

^{1}H NMR (CD_2Cl_2, 500 MHz) δ [ppm]: 9.86 (dd, *J* = 5.3, 1.5 Hz, 1H, H13), 8.87 (d, *J* = 5.1 Hz, 1H, H1), 8.51 (dd, *J* = 8.0, 1.5 Hz, 1H, H11), 8.46 - 8.40 (m, 1H, H8), 7.98 - 7.89 (m, 2H, H3, H10), 7.80 (t, *J* = 7.7 Hz, 2H, H7, H4), 7.76 (t, *J* = 7.7 Hz, 1H, H9), 7.63 (dd, *J* = 8.1, 5.3 Hz, 1H, H12), 7.61 - 7.56 (m, 1H, H5), 7.38 - 7.31 (m, 2H, H2, H6).

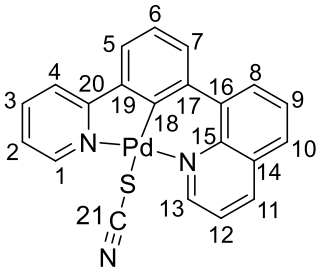

^{13}C NMR (CD_2Cl_2, 126 MHz) δ [ppm]: 171.7 (Cq, C21), 165.2 (Cq, C20), 158.2 (CH, C13), 153.4 (Cq, C18), 151.9 (CH, C1), 147.1 (Cq, C19), 141.7 (CH, C11), 139.8 (CH, C10), 139.6 (Cq, C15), 137.7 (Cq, C16), 133.6 (Cq, C17), 131.2 (CH, C8), 130.8 (Cq, C14), 129.9 (CH, C3), 128.1 (CH, C9), 128.0 (CH, C7), 126.6 (CH, C6), 124.2 (CH, C5), 123.8 (CH, C2), 121.9 (CH, C12), 119.5 (CH, C4).

HR-ESI-MS **(**70 eV): 387.01 $[M–X]^+$.

Synthesis of [Ni(PyPhQ)SCN]

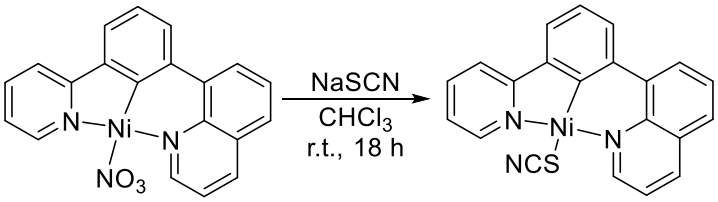

$[Ni(PyPhQ)NO_3]$ (49.2 mg, 0.12 mmol, 1.00 eq.) and NaSCN (12.7 mg, 0.16 mmol, 1.30 eq.) were reacted following general procedure E in chloroform for 18 h. The product was obtained as an orange powder (23.9 mg, 0.06 mmol, 47%).

Habitus Orange powder (23.9 mg, 0.06 mmol, 47%).

^{1}H NMR (CD_2Cl_2, 500 MHz) δ [ppm]: 9.24 (s, 1H), 8.49 (d, *J* = 7.5 Hz, 1H), 8.42 (d, *J* = 8.0 Hz, 1H), 8.30 (s, 1H), 7.88 (dd, *J* = 8.7, 7.8 Hz, 2H), 7.79 (t, *J* = 6.8 Hz, 1H), 7.68 (d, *J* = 7.9 Hz, 1H), 7.46 (dt, *J* = 22.7, 8.5 Hz, 3H), 7.33 (dd, *J* = 9.1, 6.1 Hz, 1H), 7.19 (s, 1H).

HR-ESI-MS **(**70 eV): 339.04 $[M–X]^+$.

Synthesis of [Pt(PyPhQ)C$_2$Ph]

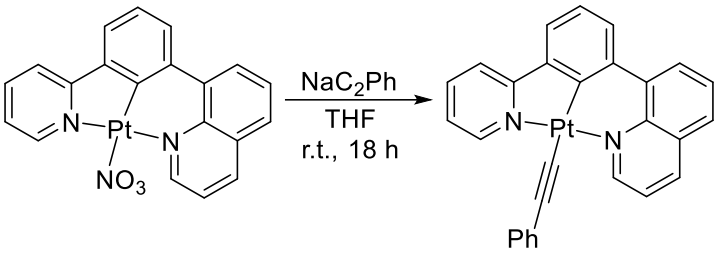

NaC_2Ph (13.7 mg, 0.11 mmol, 1.20 eq.) and [Pt(PyPhQ)NO_3] (50.0 mg, 0.09 mmol, 1.00 eq.) were reacted for 18 h following general procedure F, during which the solution changed colour from yellow to orange. The complex was obtained as an orange powder (15.0 mg, 0.02 mmol, 28%).

Habitus Orange powder (15.0 mg, 0.02 mmol, 28%).

^{1}H NMR (500 MHz, CD_2Cl_2) δ [ppm]: 11.27 (dd, J^{Pt-H} = 49.0 Hz, *J* = 5.6, 1.6 Hz, 1H, H1), 10.03 (dd, J^{Pt-H} = 44.8 Hz, *J* = 5.7 Hz, 1H, H13), 8.49 (d, *J* = 6.7 Hz, 1H, H6), 8.45 (dd, *J* = 8.1, 1.5 Hz, 1H, H3), 8.00 (d, *J* = 8.0 Hz, 1H, H9), 7.85 - 7.77 (m, 2H, H4, H11), 7.71 (d, *J* = 7.7 Hz, 1H, H12), 7.67 (t, *J* = 7.7 Hz, 1H, H5), 7.59 (d, *J* = 7.5 Hz, 1H, H7), 7.45 - 7.42 (m, 2H, H21, H21'), 7.35 (dd, *J* = 8.0, 5.6 Hz, 1H, H2), 7.29 (t, *J* = 7.7 Hz, 1H, H8), 7.22 (t, *J* = 7.6 Hz, 2H, H22, H22'), 7.16 - 7.07 (m, 2H, H23, H10).

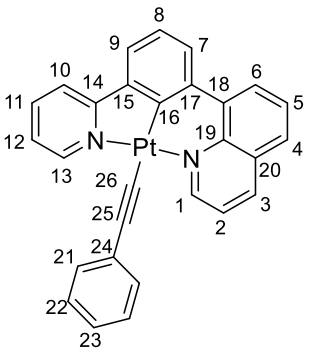

^{13}C NMR (CD_2Cl_2, 126 MHz) δ [ppm]: 168.9 (Cq, C14), 164.1 (CH, C1), 161.2 (Cq, C16), 154.7 (CH, C13), 146.4 (Cq, C15), 141.1 (CH, C3), 139.2 (Cq, C18), 139.1 (Cq, C20), 138.4 (CH, C11), 133.3 (Cq, C17), 131.1 (CH, C21, C21'), 130.8 (CH, C6), 130.7 (Cq, C19), 129.6 (CH, C4), 128.0 (CH, C22, C22'), 126.9 (CH, C5), 126.6 (CH, C9), 125.3 (CH, C23), 124.5 (CH, C8), 123.0 (CH, C7), 122.7 (CH, C10), 121.5 (CH, C2), 118.7 (CH, C12), 107.9 (Cq, C25).

HR-EI-MS **(**70 eV): 577.11 $[M]^{\cdot+}$, 476.07 $[M–X]^+$.

Synthesis of [Ni(PyPhQ)C$_2$Ph]

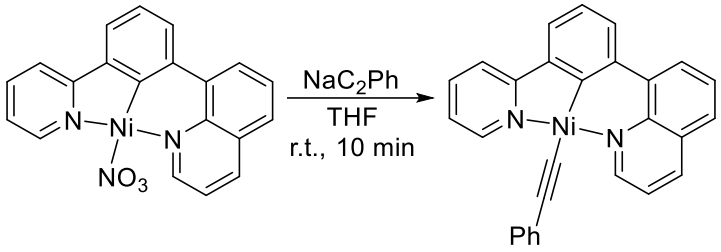

NaC_2Ph (15.3 mg, 0.12 mmol, 1.00 eq.) and [Ni(PyPhQ)NO_3] (50.0 mg, 0.12 mmol, 1.00 eq.) were reacted following general procedure F for 10 min while the solution changed colour from yellow to dark red. The complex was obtained as a red powder (6.30 mg, 0.01 mmol, 11%).

Habitus Red powder (6.30 mg, 0.01 mmol, 11%).

^{1}H NMR (500 MHz, CD_2Cl_2) δ [ppm]: 8.79 (d, *J* = 4.2 Hz, 1H), 8.67 (d, *J* = 4.8 Hz, 1H), 8.19 (d, *J* = 8.3 Hz, 1H), 7.95 (d, *J* = 7.9 Hz, 1H), 7.87 (d, *J* = 8.2 Hz, 1H), 7.72 (ddd, *J* = 16.8, 8.1, 7.5 Hz, 2H), 7.59 (t, *J* = 7.6 Hz, 1H), 7.51-7.43 (m, 2H), 7.37 - 7.18 (m, 4H), 7.09 - 6.94 (m, 2H), 6.49 (d, *J* = 7.3 Hz, 2H).

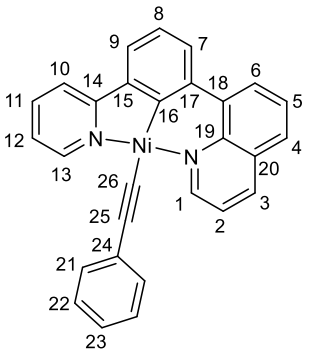

Synthesis of [Pt(PyPhQ)C$_2$Cp$_2$Fe]

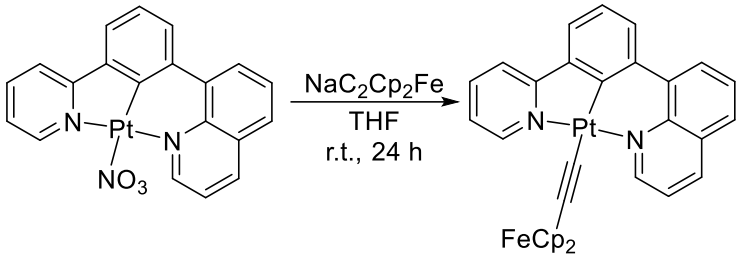

NaC_2Cp_2Fe (23.1 mg, 0.09 mmol, 1.20 eq.) and [Pt(PyPhQ)NO_3] (50.0 mg, 0.09 mmol, 1.00 eq.) were reacted for 18 h following general procedure F while the solution changed from yellow to orange. The complex was obtained as an orange powder (40.0 mg, 0.05 mmol, 70%).

Habitus Orange powder (40.0 mg, 0.05 mmol, 70%).

^{1}H NMR (500 MHz, CD_2Cl_2) δ [ppm]: 11.39 (d, $J^{Pt\text{-}H}$ = 53.3 Hz, *J* = 4.7 Hz, 1H, H1), 10.16 (d, $J^{Pt\text{-}H}$ = 51.4 Hz, *J* = 5.4 Hz, 1H, H13), 8.58 (d, *J* = 7.4 Hz, 1H, H4), 8.54 (d, *J* = 7.3 Hz, 1H, H2), 8.09 (d, *J* = 8.1 Hz, 1H, H9), 7.94 - 7.90 (m, 1H, H6), 7.92 - 7.86 (m, 1H, H10), 7.80 (d, *J* = 8.1 Hz, 1H, H12), 7.76 (t, *J* = 7.7 Hz, 1H, H5), 7.67 (d, *J* = 7.5 Hz, 1H, H7), 7.43 (dd, *J* = 8.0, 5.6 Hz, 1H, H3), 7.38 (t, *J* = 7.8 Hz, 1H, H8), 7.20 (t, *J* = 6.5 Hz, 1H, H11), 4.45 (t, *J* = 1.9 Hz, 2H, H21, H21'), 4.27 (s, 5H, H23'), 4.15 (t, *J* = 1.8 Hz, 2H, H22, H22').

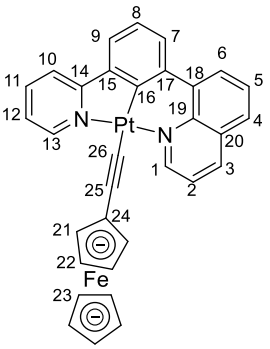

^{13}C NMR (126 MHz, CD_2Cl_2) δ [ppm]: 169.8 (Cq, C14), 164.4 (CH, C1), 161.4 (Cq, C16), 154.9 (CH, C13), 141.0 (CH, C2), 139.3 (Cq, C19), 139.0 (Cq, C18), 138.3 (CH, C10), 133.6 (Cq, C17), 133.3 (Cq, C20), 130.9 (CH, C4), 129.5 (CH, C6), 126.9 (CH, C5), 126.7 (CH, C9), 124.4 (CH, C8), 123.0 (CH, C7), 122.4 (CH, C11), 121.3 (CH,C3), 118.7 (CH, C12), 70.5 (CH, C21, C21'), 69.1 (CH, C23'), 67.1 (CH, C22, C22')

HR-EI-MS **(**70 eV): 476.07 $[M–X]^+$, 281.1 $[L]^+$, 210.0 $[Cp_2Fe]^+$.

Synthesis of [Pt(PyPhQ)C$_2$TMS]

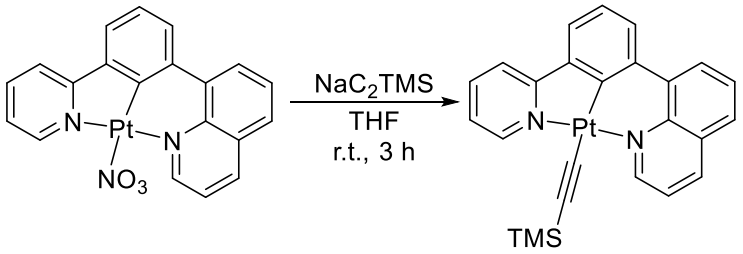

NaC_2TMS (13.3 mg, 0.11 mmol, 1.20 eq.) and [Pt(PyPhQ)NO_3] (50.0 mg, 0.09 mmol, 1.00 eq.) were reacted for 18 h following general procedure F while the solution changed colour from yellow to orange. The complex was obtained as an orange powder (25.0 mg, 0.04 mmol, 47%).

Habitus Orange powder (25.0 mg, 0.04 mmol, 47%).

^{1}H NMR (500 MHz, CD_2Cl_2) δ [ppm]: 11.35 (dd, J^{Pt-H} = 51.6 Hz, J = 5.5, 1.7 Hz, 1H, H1), 10.13 (t, J^{Pt-H} = 48.9 Hz, J = 6.5 Hz, 1H, H13), 8.54 (s, 1H, H4), 8.51 (m, 1H, H2), 8.05 (d, J = 7.9 Hz, 1H, H7), 7.89 (m, 1H, H11), 7.88 - 7.84 (m, 1H, H6), 7.77 (d, J = 7.9 Hz, 1H, H12), 7.73 (t, J = 7.8 Hz, 1H, H5), 7.64 (d, J = 7.5 Hz, 1H, H9), 7.42 - 7.37 (m, 1H, H3), 7.37 - 7.31 (m, 1H, H8), 7.19 - 7.11 (m, 1H, H10), 0.25 (s, 9H, H21')

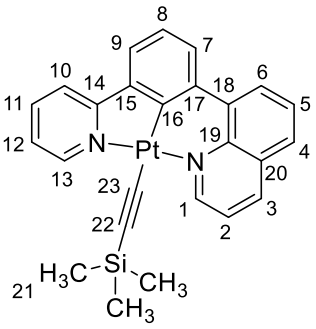

^{13}C NMR (126 MHz, CD_2Cl_2) δ [ppm]: 164.3 (CH, C1), 168.4 (Cq, C14), 161.6 (Cq, C16), 154.7 (CH, C13), 146.6 (Cq, C15), 141.0 (CH, C2), 139.4 (Cq, C19), 139.0 (Cq, C20), 138.9 (Cq, C18), 138.4 (CH, C11), 133.5 (Cq, C17), 130.9 (CH, C4), 129.5 (CH, C6), 126.9 (CH, C5), 126.6 (CH, C7), 124.5 (CH, C8), 122.9 (CH, C9), 122.5 (CH, C10), 121.3 (CH, C3), 118.6 (CH, C12), 111.3 (Cq, C22), 0.96 (CH, C21').

HR-EI-MS **(**70 eV): 573.12 $[M]^+$, 476.07 $[M–X]^+$.

Synthesis of [Pt(PyPhQ)NCBH$_3$]

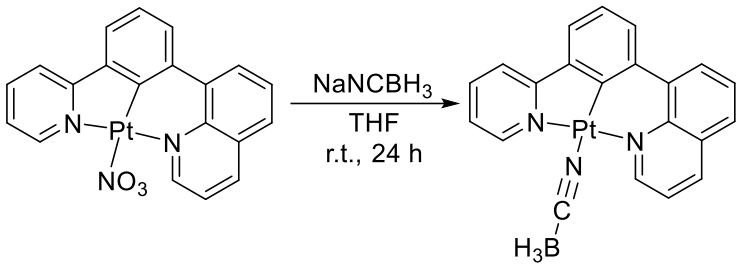

$NaNCBH_3$ (6.97 mg, 0.11 mmol, 1.20 eq.) and [Pt(PyPhQ)NO_3] (50.0 mg, 0.09 mmol, 1.00 eq.) were reacted for 24 h following general procedure F. The product was obtained as a yellow powder (25.0 mg, 0.05 mmol, 56%).

Habitus Yellow powder (25.0 mg, 0.05 mmol, 56%).

^{1}H NMR (500 MHz, CD_2Cl_2) δ [ppm]: 10.01 (dd, J^{Pt-H} = 42.0 Hz, J = 5.5 Hz, 1.3 Hz 1H), 9.01 (dd, J^{Pt-H} = 37.2 Hz, J = 5.8 Hz, 1.3 Hz, 1H), 8.60 (dd, J = 8.1, 1.2 Hz, 1H), 8.51 (d, J = 7.5 Hz, 1H), 8.00 - 7.89 (m, 3H), 7.84 - 7.77 (m, 2H), 7.71 – 7.68 (m, 1H), 7.60 (d, J = 7.6 Hz, 1H), 7.59 – 7.53 (m, 1H), 7.37 (t, J = 7.7 Hz, 1H), 7.32 (ddd, J = 7.4, 5.7, 1.5 Hz, 1H), 1.15 (s, 3H).

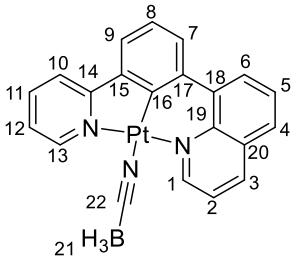

HR-EI-MS **(**70 eV): 502.08 $[M–BH_3]^+$.

Synthesis of [Pt(PyPhQ)(N(CN)$_2$)]

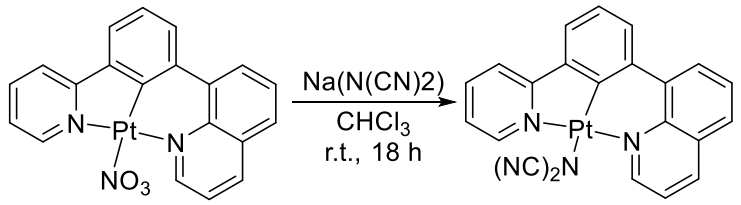

Na(N(CN)$_2$) (9.90 mg, 0.11 mmol, 1.20 eq.) and [Pt(PyPhQ)NO_3] (50.0 mg, 0.09 mmol, 1.00 eq.) were reacted following general procedure F for 18 h. The complex was obtained as an orange powder (46.0 mg, 0.09 mmol, 91%).

Habitus Orange powder (46.0 mg, 0.09 mmol, 91%).

^{1}H NMR (600 MHz, CD_2Cl_2) δ [ppm]: 9.85 (d, J = 4.2 Hz, 1H, H13), 8.80 (d, J = 5.9 Hz, 1H, H1), 8.56 (d, J = 7.1 Hz, 1H, H11), 8.47 (d, J = 7.5 Hz, 1H, H8), 7.98 - 7.91 (m, 2H, H3, H10), 7.88 (d, J = 7.8 Hz, 1H, H7), 7.82 - 7.75 (m, 2H, H4, H9), 7.58 (d, J = 7.4 Hz, 1H, H5), 7.52 (dd, J = 7.8, 5.8 Hz, 1H, H12), 7.35 (t, J = 7.7 Hz, 1H, H6), 7.29 (t, J = 6.1 Hz, 1H, H2).

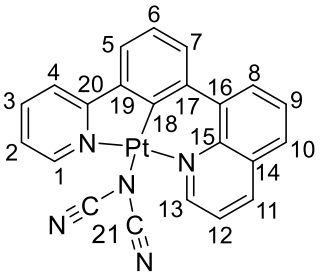

^{13}C NMR (151 MHz, CD_2Cl_2) δ [ppm]: 166.5 (Cq, C20), 158.2 (Cq, C13), 146.0 (Cq, C19), 142.3 (Cq, C11), 140.3 (Cq, C18), 140.3 (CH, C3), 139.1 (Cq, C15), 137.2 (Cq, C16), 132.4 (Cq, C17), 131.9 (CH, C8), 131.0 (Cq, C14), 130.5 (CH, C10), 128.2 (CH, C9), 127.8 (CH, C7), 125.8 (CH, C6), 124.3 (CH, C5), 123.7 (CH, C2), 122.0 (CH, C12), 119.7 (CH, C4), 115.2 (Cq, C21, C21').

HR-ESI-MS (70 eV): 476.07 $[M–X]^+$.

Synthesis of [Pd(PyPhQ)(N(CN)$_2$)]

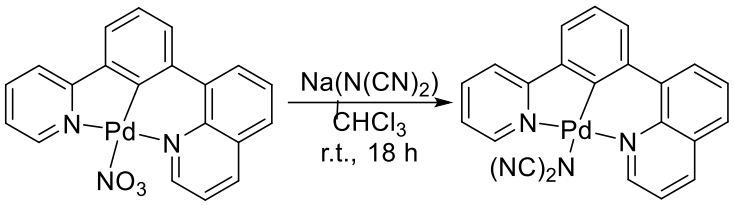

$Na(N(CN)_2)$ (11.8 mg, 0.13 mmol, 1.20 eq.) and $[Pd(PyPhQ)NO_3]$ (50.0 mg, 0.12 mmol, 1.00 eq.) were reacted following general procedure F for 18 h. The complex was obtained as a yellow powder (31.0 mg, 0.07 mmol, 62%).

Habitus Yellow powder (31.0 mg, 0.07 mmol, 62%).

^{1}H NMR (600 MHz, CD_2Cl_2) δ [ppm]: 9.62 (d, *J* = 4.7 Hz, 1H, H13), 8.65 (d, *J* = 5.3 Hz, 1H, H1), 8.52 (d, *J* = 7.0 Hz, 1H, H11), 8.41 (dd, *J* = 7.7, 0.9 Hz, 1H, H8), 7.98 - 7.91 (m, 2H, H3, H10), 7.82 - 7.74 (m, 3H, H4, H7, H9), 7.62 - 7.56 (m, 2H, H5, H12), 7.37 - 7.33 (m, 1H, H6), 7.31 (t, *J* = 6.2 Hz, 1H, H2).

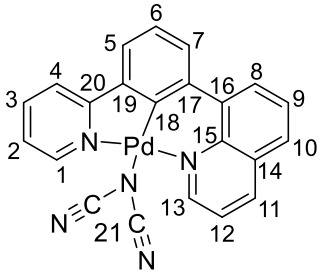

^{13}C NMR (151 MHz, CD_2Cl_2) δ [ppm]: 165.1 (Cq, C20), 157.5 (CH, C13), 152.7 (Cq, C18), 151.2 (CH, C1), 146.8 (Cq, C19), 141.8 (CH, C11), 140.1 (CH, C3), 139.5 (Cq, C15), 137.6 (Cq, C16), 133.4 (Cq, C17), 130.7 (Cq, C14), 129.8 (CH, C10), 128.1 (CH, C4), 126.9 (CH, C6), 124.2 (CH, C5), 123.8 (CH, C2), 121.9 (CH, C12), 119.6 (CH, C7).

HR-ESI-MS (70 eV): 387.01 $[M–X]^+$.

Synthesis of [Ni(PyPhQ)(N(CN)$_2$)]

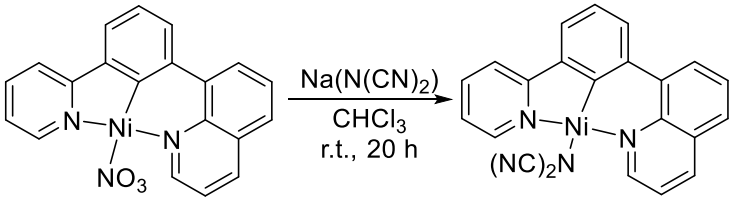

$Na(N(CN)_2)$ (14.6 mg, 0.16 mmol, 1.30 eq.) and $[Ni(PyPhQ)NO_3]$ (50.0 mg, 0.12 mmol, 1.00 eq.) were reacted following general procedure F for 20 h. The complex was obtained as an orange powder (8.08 mg, 0.02 mmol, 16%).

Habitus Orange powder (8.08 mg, 0.02 mmol, 16%).

^{1}H NMR (500 MHz, CD_2Cl_2) δ [ppm]: 9.43 (d, *J* = 4.4 Hz, 1H, H13), 8.44 (dd, *J* = 6.5, 6.0 Hz, 3H, H1, H8, H11), 7.89 (t, *J* = 7.4 Hz, 2H, H3, H10), 7.77 (t, *J* = 7.9 Hz, 2H, H7, H9), 7.68 (d, *J* = 8.1 Hz, 1H, H4), 7.55 - 7.48 (m, 1H, H12), 7.45 (d, *J* = 7.3 Hz, 1H, H5), 7.32 (t, *J* = 7.6 Hz, 1H, H6), 7.22 (t, *J* = 6.4 Hz, 1H, H2).

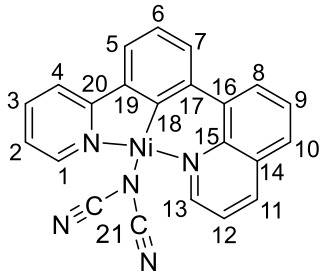

^{13}C NMR (126 MHz, CD_2Cl_2) δ [ppm]: 163.4 (Cq, C20), 156.3 (CH, C13), 153.0 (Cq, C18), 150.8 (CH, C1), 147.1 (Cq, C19), 140. 2 (CH, C11), 140.0 (Cq, C15), 139.1 (CH, C10), 135.1 (Cq, C16), 134.9 (Cq, C17), 129.5 (Cq, C14), 128.3 (CH, C3), 127.7 (CH, C8), 127.3 (CH, C9), 126.1 (CH, C6), 125.2 (CH, C7), 122.5 (CH, C2), 121.9 (CH, C5), 120.1 (CH, C12), 117.8 (CH, C4).

HR-ESI-MS **(**70 eV): 339.04 $[M–X]^+$.

Synthesis of [Pt(PyPhQ)($NC_{12}H_8$)]

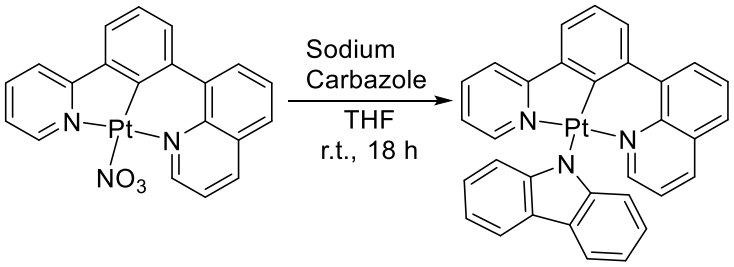

Sodium carbazole (17.6 mg, 0.09 mmol, 1.35 eq.) and [Pt(PyPhQ)NO_3] (37.1 mg, 0.07 mmol, 1.00 eq.) were reacted following general procedure F for 18 h. The complex was obtained as an orange powder (15.3 mg, 0.02 mmol, 34%).

Habitus Orange powder (15.3 mg, 0.02 mmol, 34%).

^{1}H NMR (600 MHz, CD_2Cl_2) δ [ppm]: 9.12 (dd, *J* = 5.6, 1.7 Hz, 1H, H13), 8.72 (dd, *J* = 7.8, 1.5 Hz, 1H, H1), 8.52 - 8.37 (m, 1H, H11), 8.24 (ddd, *J* = 7.8, 1.3, 0.7 Hz, 2H, H24, H24'), 8.17 (d, *J* = 8.0 Hz, 1H, H5), 8.03 - 7.93 (m, 1H, H10), 7.87 (t, *J* = 7.8 Hz, 1H, H3), 7.85 (d, *J* = 8.4 Hz, 1H, H4), 7.82 - 7.79 (m, 3H, H9, H21, H21'), 7.76 (dd, *J* = 7.7, 1.0 Hz, 1H, H7), 7.51 (dd, *J* = 8.1, 7.5 Hz, 1H, H6), 7.32 (ddd, *J* = 5.9, 1.6, 0.8 Hz, 1H, H2), 7.24 (ddd, *J* = 8.1, 6.9, 1.3 Hz, 2H, H22, H22'), 7.08 (ddd, *J* = 7.8, 6.9, 1.0 Hz, 2H, H23, H23'), 6.98 (dd, *J* = 8.0, 5.6 Hz, 1H, H12), 6.74 (ddd, *J* = 7.4, 5.9, 1.5 Hz, 1H, H8).

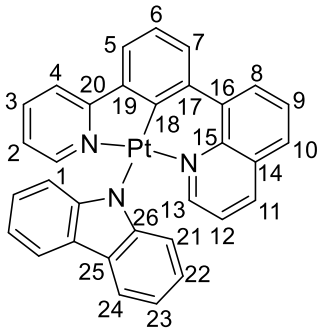

^{13}C NMR (151 MHz, CD_2Cl_2) δ [ppm]: 167.0 (Cq, C20), 158.2 (CH, C13), 149.2 (Cq, C26, C26'), 148.5 (Cq, C18), 146.1 (Cq, C19), 140.4 (CH, C11), 139.4 (Cq, C15), 139.2 (Cq, C16), 138.9 (CH, C9), 138.0 (CH, C2), 132.8 (Cq, C17), 131.0 (CH, C1), 127.2 (CH, C5), 126.8 (CH, C3), 125.5 (Cq, C25, C25'), 124.6 (CH, C6), 123.6 (CH, C22,

C22'), 123.3 (CH, C7), 122.4 (CH, C8), 121.0 (CH, C12), 119.5 (CH, C24, C24'), 118.5 (CH, C4), 115.7 (CH, C23, C23'), 114.2 (CH, C21, C21').

^{195}Pt NMR (CD_2Cl_2, 107 MHz) δ [ppm]: –3203.4.

HR-ESI-MS **(**70 eV): 476.07 $[M–X]^+$.

Synthesis of [Pd(PyPhQ)($NC_{12}H_8$)]

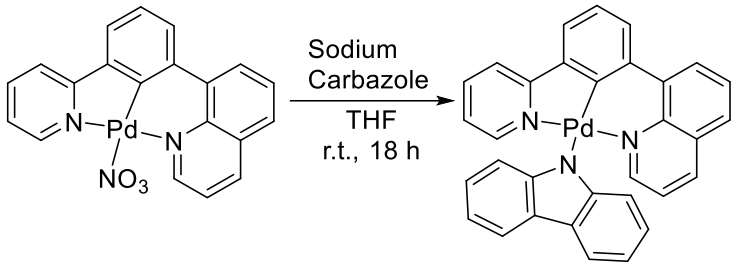

Sodium carbazole (21.0 mg, 0.11 mmol, 1.00 eq.) and [Pd(PyPhQ)NO_3] (50.0 mg, 0.11 mmol, 1.00 eq.) were reacted following general procedure F for 18 h. The complex was obtained as a yellow powder (22.5 mg, 0.04 mmol, 36%).

Habitus Yellow powder (22.5 mg, 0.04 mmol, 36%).

^{1}H NMR (600 MHz, CD_2Cl_2) δ [ppm]: 9.30 (s, 1H), 8.31 (s, 1H), 8.16 - 8.10 (s, 1H), 8.07 (ddt, *J* = 7.8, 1.4, 0.8 Hz, 2H), 7.79 - 7.56 (m, 4H), 7.48 (t, *J* = 0.9 Hz, 1H), 7.47 (t, *J* = 0.9 Hz, 2H), 7.43 (d, *J* = 1.2 Hz, 1H), 7.41 (t, *J* = 1.1 Hz, 2H), 7.40 (d, *J* = 1.2 Hz, 1H), 7.35 (s, 1H), 7.22 (ddd, *J* = 8.0, 7.1, 1.1 Hz, 2H), 7.20 - 7.17 (m, 1H), 7.02 (s, 1H).

HR-EI-MS **(**70 eV): 387.01 $[M–X]^+$.

Synthesis of [Pt(PyPhQ)(NC_4H_4)]

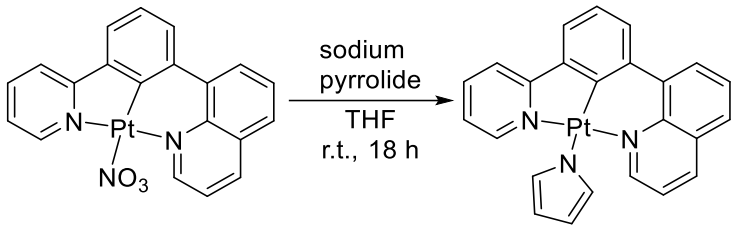

Sodium pyrrolide (21.7 mg, 0.21 mmol, 1.40 eq.) and [Pt(PyPhQ)NO_3] (78.6 mg, 0.15 mmol, 1.00 eq.) were reacted following general procedure F for 18 h. The product was obtained as a yellow-brown solid (77.2 mg, 0.14 mmol, 97%).

Habitus Yellow-brown solid (77.2 mg, 0.14 mmol, 97%).

^{1}H NMR (600 MHz, CD_2Cl_2) δ [ppm]: 9.07 (dd, *J* = 5.5, 1.8 Hz, 1H, H1), 8.60 (dd, *J* = 7.8, 1.2 Hz, 1H, H13), 8.47 (dd, *J* = 8.2, 1.5 Hz, 1H, H3), 8.04 (d, *J* = 8.0 Hz, 1H, H7), 7.92 (dd, *J* = 7.9, 1.2 Hz, 1H, H6), 7.83 (td, *J* = 7.7, 1.5 Hz, 1H, H10), 7.79 (d, *J* = 7.7 Hz, 1H, H11), 7.77 (m, 1H, H5), 7.66 - 7.62 (m, 1H, H9), 7.41 - 7.36 (m, 1H, H8), 7.33 - 7.29 (m, 1H, H12), 7.26 (dd, *J* = 8.0, 5.5 Hz, 1H, H2), 7.02 (ddd, *J* = 7.3, 5.8, 1.5 Hz, 1H, H4), 6.93 (t, *J* = 1.7 Hz, 2H, H21, H21'), 6.38 (t, *J* = 1.7 Hz, 2H, H22, H22').

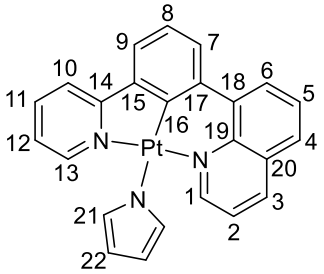

^{13}C NMR (151 MHz, CD_2Cl_2) δ [ppm]: 167.1 (Cq, C14), 158.3 (CH, C1), 151.7 (CH, C12), 148.0 (Cq, C16), 146.28 (Cq, C15), 140.9 (CH, C3), 139.1 (Cq, C19), 138.6 (CH, C10), 137.8 (Cq, C18), 133.0 (Cq, C17), 131.0 (CH, C13), 130.5 (Cq, C20), 129.7 (CH, C6), 127.1 (CH, C21, C21'), 126.9 (CH, C11), 126.8 (CH, C7), 124.3 (CH, C8), 123.1 (CH, C9), 122.6 (CH, C4), 121.2 (CH, C2), 118.4 (CH, C5), 108.1 (CH, C22, C22').

HR-ESI-MS **(**70 eV): 476.07 $[M–X]^+$.

Synthesis of [Pd(PyPhQ)(NC_4H_4)]

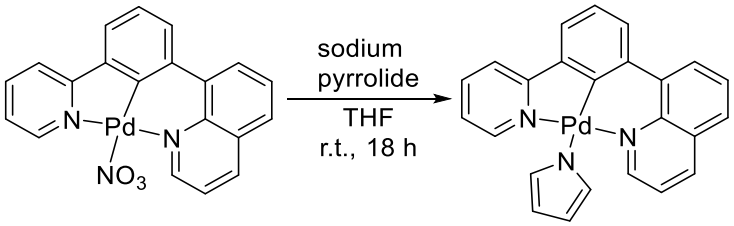

Sodium pyrrolide (20.5 mg, 0.20 mmol, 1.33 eq.) and [Pd(PyPhQ)NO_3] (65.6 mg, 0.15 mmol, 1.00 eq.) were reacted following general procedure F for 18h. The product was obtained as a yellow solid (65.3 mg, 0.14 mmol, 99%).

Habitus Yellow solid (65.3 mg, 0.14 mmol, 99%).

^{1}H NMR (400 MHz, CD_2Cl_2) δ [ppm] = 8.89 (dd, *J* = 5.3, 1.7 Hz, 1H, H1), 8.51 (d, *J* = 6.5 Hz, 1H, H13), 8.40 (dd, *J* = 8.1, 1.7 Hz, 1H, H3), 7.93 (d, *J* = 3.7 Hz, 1H, H6), 7.92 - 7.89 (m, 1H, H7), 7.84 - 7.78 (m, 1H, H10), 7.78 - 7.74 (m, 2H, H11, H5), 7.63 (d, *J* = 6.4 Hz, 1H, H9), 7.41 - 7.34 (m, 1H, H8), 7.31 (dd, *J* = 8.1, 5.3 Hz, 1H, H2), 7.07 (d, *J* = 4.9 Hz, 1H, H12), 7.04 - 6.99 (m, 1H, H4), 6.94 (t, *J* = 1.6 Hz, 2H, H21, H21'), 6.30 (t, *J* = 1.6 Hz, 2H, H22, H22').

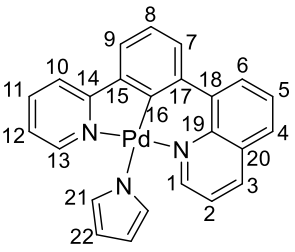

^{13}C NMR (101 MHz, CD_2Cl_2) δ [ppm]: 165.6 (Cq, C14), 158.4 (CH, C1), 157.8 (Cq, C16), 152.1 (CH, C12), 146.7 (Cq, C15), 140.6 (CH, C3), 139.7 (Cq, C19), 138.6 (CH, C10), 137.8 (Cq, C18), 134.0 (Cq, C17), 130.5 (CH, C13), 130.2 (Cq, C20), 129.2 (CH, C6), 127.1 (CH, C7), 127.1 (CH, C11), 126.9 (CH, C21, C21'), 125.6 (CH, C8),

123.1 (CH, C9), 122.7 (CH, C4), 121.1 (CH, C2), 118.4 (CH, C5), 107.6 (CH, C22, C22′).

HR-ESI-MS **(**70 eV): 387.01 $[M–X]^+$.

7 References

[1] D. J. Cárdenas, A. M. Echavarren, M. C. Ramírez de Arellano, *Organometallics* **1999**, *18*, 3337-3341.

[2] L. Kletsch, R. Jordan, A. S. Köcher, S. Buss, C. A. Strassert, A. Klein, *Molecules* **2021**, *26*.

[3] A. Klein, B. Rausch, A. Kaiser, N. Vogt, A. Krest, *J. Organomet. Chem.* **2014**, *774*, 86-93.

[4] H.-K. Yip, L.-K. Cheng, K.-K. Cheung, C.-M. Che, *J. Chem. Soc., Dalton Trans.* **1993**, 2933-2938.

[5] K. W. Jennette, J. T. Gill, J. A. Sadownick, S. J. Lippard, *J. Am. Chem. Soc.* **1976**, *98*, 6159-6168.

[6] M. Krause, D. Kourkoulos, D. González-Abradelo, K. Meerholz, C. A. Strassert, A. Klein, *Eur. J. Inorg. Chem.* **2017**, *2017*, 5215-5223.

[7] E. A. Wood, L. F. Gildea, D. S. Yufit, J. A. G. Williams, *Polyhedron* **2021**, *207*, 115401.

[8] E. C. Constable, R. P. G. Henney, D. A. Tocher, *J. Chem. Soc., Dalton Trans.* **1992**, 2467-2474.

[9] W. Lu, B.-X. Mi, M. C. W. Chan, Z. Hui, C.-M. Che, N. Zhu, S.-T. Lee, *J. Am. Chem. Soc.* **2004**, *126*, 4958-4971.

[10] S. Develay, O. Blackburn, A. L. Thompson, J. A. G. Williams, *Inorg. Chem.* **2008**, *47*, 11129-11142.

[11] R. von der Stück, M. Krause, D. Brünink, S. Buss, N. L. Doltsinis, C. A. Strassert, A. Klein, *Z. Anorg. Allg. Chem.* **2022**, *648*, e202100278.

[12] L. Kletsch, R. Jordan, J. Strippel, D. A. Vicic, A. Klein, *Inorganics* **2025**, *13*, 41.

[13] L. Kletsch, Dissertation, *University of Cologne, Cologne* **2024**.

[14] D. E. Herbert, *Can. J. Chem.* **2023**, *101*, 892-902.

[15] A. Haque, H. El Moll, K. M. Alenezi, M. S. Khan, W.-Y. Wong, *Materials* **2021**, *14*, 4236.

[16] E. C. Constable, R. P. G. Henney, T. A. Leese, D. A. Tocher, *J. Chem. Soc., Dalton Trans.* **1990**, 443-449.

[17] A. H. Mousa, K. Chakrabarti, G. Isapour, J. Bendix, O. F. Wendt, *Eur. J. Inorg. Chem.* **2020**, *2020*, 4270-4277.

[18] K. L. Garner, L. F. Parkes, J. D. Piper, J. A. G. Williams, *Inorg. Chem.* **2010**, *49*, 476-487.

[19] M. Albrecht, *Chem. Rev.* **2010**, *110*, 576-623.

[20] J. A. G. Williams, A. Beeby, E. S. Davies, J. A. Weinstein, C. Wilson, *Inorg. Chem.* **2003**, *42*, 8609-8611.

[21] Z. Wang, E. Turner, V. Mahoney, S. Madakuni, T. Groy, J. Li, *Inorg. Chem.* **2010**, *49*, 11276-11286.

[22] W. Sotoyama, T. Satoh, H. Sato, A. Matsuura, N. Sawatari, *J. Phys. Chem. A* **2005**, *109*, 9760-9766.

[23] A. F. Rausch, L. Murphy, J. A. G. Williams, H. Yersin, *Inorg. Chem.* **2009**, *48*, 11407-11414.

[24] Y.-S. Wong, M.-C. Tang, M. Ng, V. W.-W. Yam, *J. Am. Chem. Soc.* **2020**, *142*, 7638-7646.

[25] B. Soro, S. Stoccoro, G. Minghetti, A. Zucca, M. A. Cinellu, S. Gladiali, M. Manassero, M. Sansoni, *Organometallics* **2005**, *24*, 53-61.

[26] L. Kletsch, G. Hörner, A. Klein, *Organometallics* **2020**, *39*, 2820-2829.

[27] E. C. Constable, R. P. G. Henney, T. A. Leese, D. A. Tocher, *J. Chem. Soc., Chem. Commun.* **1990**, 513-515.

[28] R. Kumar, C. Nevado, *Angew. Chem. Int. Ed. Engl.* **2017**, *56*, 1994-2015.

[29] Y. Jiang, C. Gendy, R. Roesler, *Organometallics* **2018**, *37*, 1123-1132.

[30] J.-i. Ito, K. Sugino, S. Matsushima, H. Sakaguchi, H. Iwata, T. Ishihara, H. Nishiyama, *Organometallics* **2016**, *35*, 1885-1894.

[31] R. Castro-Rodrigo, M. A. Esteruelas, D. Gómez-Bautista, V. Lezáun, A. M. López, M. Oliván, E. Oñate, *Organometallics* **2019**, *38*, 3707-3718.

[32] P. Brulatti, R. J. Gildea, J. A. K. Howard, V. Fattori, M. Cocchi, J. A. G. Williams, *Inorg. Chem.* **2012**, *51*, 3813-3826.

[33] J. Pecak, W. Eder, G. Tomsu, B. Stöger, M. Pignitter, K. Kirchner, *Eur. J. Inorg. Chem.* **2021**, *2021*, 4280-4285.

[34] P. Zimmer, P. Müller, L. Burkhardt, R. Schepper, A. Neuba, J. Steube, F. Dietrich, U. Flörke, S. Mangold, M. Gerhards, M. Bauer, *Eur. J. Inorg. Chem.* **2017**, *2017*, 1504-1509.

[35] E. Riedel, C. Janiak, *Anorganische Chemie*, 9 ed., De Gruyter, Berlin, **2018**.

[36] L. Pauling, *The Nature of the chemical bond and the structure of molecules and crystals : an introduction to modern structural chemistry*, 2. , 7. pr. ed., Cornell Univ. Pr. [u.a.], Ithaca, N.Y. [u.a.], **1948**.

[37] P. S. Wagenknecht, P. C. Ford, *Coord. Chem. Rev.* **2011**, *255*, 591-616.

[38] G. S.-M. Tong, C.-M. Che, *Chem. - Eur. J.* **2009**, *15*, 7225-7237.

[39] A. M. Prokhorov, T. Hofbeck, R. Czerwieniec, A. F. Suleymanova, D. N. Kozhevnikov, H. Yersin, *J. Am. Chem. Soc.* **2014**, *136*, 9637-9642.

[40] A. F. Rausch, L. Murphy, J. A. G. Williams, H. Yersin, *Inorg. Chem.* **2012**, *51*, 312-319.

[41] T. Ogawa, O. S. Wenger, *Angew. Chem., Int. Ed.* **2023**, *62*, e202312851.

[42] A. Haque, L. Xu, R. A. Al-Balushi, M. K. Al-Suti, R. Ilmi, Z. Guo, M. S. Khan, W.-Y. Wong, P. R. Raithby, *Chem. Soc. Rev.* **2019**, *48*, 5547-5563.

[43] K. Li, G. S. Ming Tong, Q. Wan, G. Cheng, W.-Y. Tong, W.-H. Ang, W.-L. Kwong, C.-M. Che, *Chem. Sci.* **2016**, *7*, 1653-1673.

[44] J. Kalinowski, V. Fattori, M. Cocchi, J. A. G. Williams, *Coord. Chem. Rev.* **2011**, *255*, 2401-2425.

[45] I. O. Koshevoy, M. Krause, A. Klein, *Coord. Chem. Rev.* **2020**, *405*, 213094.

[46] R. Jordan, I. Maisuls, S. S. Nair, B. Dietzek-Ivanšić, C. A. Strassert, A. Klein, *Dalton Trans.* **2023**, *52*, 18220-18232.

[47] R. J. Ortiz, E. Garcia-Torres, P. L. Brothwood, J. A. G. Williams, D. E. Herbert, *Chem. - Eur. J.* **2025**, *31*, e202403766.

[48] S. Buss, L. Geerkens, R. Jordan, L. Kletsch, A. Hepp, J. Kösters, A. Klein, C. A. Strassert, *Organometallics* **2025**, *44*, 487-501.

[49] L. Payen, T. Lapić, M. Wickleder, A. Klein, *Organometallics* **2025**, *44*, 847-857.

[50] S. N. Natoli, L. M. Hight, M. Zeller, D. R. McMillin, *Inorg. Chem.* **2018**, *57*, 6521-6529.
[51] D. K. Crites, C. T. Cunningham, D. R. McMillin, *Inorg. Chim. Acta* **1998**, *273*, 346-353.
[52] D. Ravindranathan, D. A. K. Vezzu, L. Bartolotti, P. D. Boyle, S. Huo, *Inorg. Chem.* **2010**, *49*, 8922-8928.
[53] C. F. Harris, D. A. K. Vezzu, L. Bartolotti, P. D. Boyle, S. Huo, *Inorg. Chem.* **2013**, *52*, 11711-11722.
[54] D. Poveda, Á. Vivancos, D. Bautista, P. González-Herrero, *Inorg. Chem.* **2023**, *62*, 6207-6213.
[55] D. Song, Q. Wu, A. Hook, I. Kozin, S. Wang, *Organometallics* **2001**, *20*, 4683-4689.
[56] I. M. Wekesa, D. and Jaganyi, *J. Coord. Chem.* **2016**, *69*, 389-403.
[57] Z.-Q. Zhu, K. Klimes, S. Holloway, J. Li, *Adv. Mater.* **2017**, *29*, 1605002.
[58] G. Li, L. Ameri, T. Fleetham, Z.-Q. Zhu, J. Li, *Appl. Phys. Lett.* **2020**, *117*.
[59] M. Saini, T. E. Keyes, *Dalton Trans.* **2023**, *52*, 7787-7791.
[60] M. L. Bochman, K. Paeschke, V. A. Zakian, *Nat. Rev. Genet.* **2012**, *13*, 770-780.
[61] S. Aghazada, I. Zimmermann, Y. Ren, P. Wang, M. K. Nazeeruddin, *ChemistrySelect* **2018**, *3*, 1585-1592.
[62] C. Friebe, M. Jäger, U. S. Schubert, *RSC Advances* **2013**, *3*, 11686-11690.
[63] E. E. Luneva, D. O. Kozina, A. V. Mozzhukhina, V. V. Porsev, A. I. Solomatina, S. P. Tunik, *Inorganics* **2023**, *11*, 198.
[64] M. Hruzd, N. le Poul, M. Cordier, S. Kahlal, J.-Y. Saillard, S. Achelle, S. Gauthier, F. Robin-le Guen, *Dalton Trans.* **2022**, *51*, 5546-5560.
[65] D. Bi, Y. Feng, Q. Zhao, H. Wang, Y. Zhu, X. Bao, H. Fan, L. Yu, Q. Yang, D. Qiu, *RSC Advances* **2017**, *7*, 46980-46988.
[66] C. Lorenzo-Aparicio, S. Moreno-Blázquez, M. Oliván, M. A. Esteruelas, M. Gómez Gallego, P. García-Álvarez, J. A. Cabeza, M. A. Sierra, *Inorg. Chem.* **2023**, *62*, 8232-8248.
[67] M. Niazi, I. Maisuls, C. A. Strassert, A. Klein, *Organometallics* **2024**, *43*, 1547-1556.
[68] R. J. Salthouse, A. Sil, L. F. Gildea, D. S. Yufit, J. A. G. Williams, *Inorg. Chem.* **2023**, *62*, 12356-12371.
[69] V. V. Sivchik, E. V. Grachova, A. S. Melnikov, S. N. Smirnov, A. Y. Ivanov, P. Hirva, S. P. Tunik, I. O. Koshevoy, *Inorg. Chem.* **2016**, *55*, 3351-3363.
[70] J. Hu, J. H. K. Yip, *Organometallics* **2009**, *28*, 1093-1100.
[71] J. S. Fossey, C. J. Richards, *Organometallics* **2004**, *23*, 367-373.
[72] J. W. Slater, D. P. Lydon, N. W. Alcock, J. P. Rourke, *Organometallics* **2001**, *20*, 4418-4423.
[73] T. M. Kirse, I. Maisuls, L. Spierling, A. Hepp, J. Kösters, C. A. Strassert, *Adv. Sci.* **2024**, *11*, 2306801.
[74] I. G. Jung, S. U. Son, K. H. Park, K.-C. Chung, J. W. Lee, Y. K. Chung, *Organometallics* **2003**, *22*, 4715-4720.
[75] F. Neve, A. Crispini, C. Di Pietro, S. Campagna, *Organometallics* **2002**, *21*, 3511-3518.
[76] C. Fernández-Rivas, D. J. Cárdenas, B. Martín-Matute, Á. Monge, E. Gutiérrez-Puebla, A. M. Echavarren, *Organometallics* **2001**, *20*, 2998-3006.

[77] L. Payen, L. Kletsch, T. Lapić, M. Wickleder, A. Klein, *Inorganics* **2023**, *11*, 174.
[78] T. Nishikata, A. R. Abela, S. Huang, B. H. Lipshutz, *Beilstein J. Org. Chem* **2016**, *12*, 1040-1064.
[79] A. Gray, A. Tsybizova, J. Roithova, *Chem. Sci.* **2015**, *6*, 5544-5553.
[80] A. Maleckis, J. W. Kampf, M. S. Sanford, *J. Am. Chem. Soc.* **2013**, *135*, 6618-6625.
[81] R. von der Stück, S. Schmitz, A. Klein, *Inorg. Chem. Res.* **2021**, *5*, 173-192.
[82] C. Y. Chang, M. J. Sgro, W. E. Piers, W. Zhou, *Can. J. Chem.*, *0*, null.
[83] D. Himmelbauer, H. Schratzberger, M. G. Käfer, B. Stöger, L. F. Veiros, K. Kirchner, *Organometallics* **2021**, *40*, 3331-3340.
[84] D. Moreth, M. V. Cappellari, A. Müller, A. Oster, D. Schwab, N. L. Doltsinis, C. A. Strassert, U. Schatzschneider, *Inorg. Chem.* **2025**, *64*, 4223-4235.
[85] D. Moreth, G. Hörner, V. V. L. Müller, L. Geyer, U. Schatzschneider, *Inorg. Chem.* **2023**, *62*, 16000-16012.
[86] L. Kletsch, L. Payen, A. Fiorentino, B. Blom, D. Romano, G. Hörner, A. Klein, *Organometallics* **2023**, *42*, 2206-2215.
[87] N. Vogt, A. Sandleben, L. Kletsch, S. Schäfer, M. T. Chin, D. A. Vicic, G. Hörner, A. Klein, *Organometallics* **2021**, *40*, 1776-1785.
[88] R. Alrefai, G. Hörner, H. Schubert, A. Berkefeld, *Organometallics* **2021**, *40*, 1163-1177.
[89] Y. B. Kim, J. Won, J. Lee, J. Kim, B. Zhou, J.-W. Park, M.-H. Baik, S. Chang, *ACS Catal.* **2021**, *11*, 3067-3072.
[90] N. Miyaura, K. Yamada, A. Suzuki, *Tetrahedron Lett.* **1979**, *20*, 3437-3440.
[91] N. Miyaura, A. Suzuki, *Chem. Rev.* **1995**, *95*, 2457-2483.
[92] X. A. F. Cook, A. de Gombert, J. McKnight, L. R. E. Pantaine, M. C. Willis, *Angew. Chem., Int. Ed.* **2021**, *60*, 11068-11091.
[93] N. Vogt, V. Sivchik, A. Sandleben, G. Hörner, A. Klein, *Molecules* **2020**, *25*.
[94] R. G. Pearson, *J. Am. Chem. Soc.* **1963**, *85*, 3533-3539.
[95] A. K.-W. Chan, M. Ng, Y.-C. Wong, M.-Y. Chan, W.-T. Wong, V. W.-W. Yam, *J. Am. Chem. Soc.* **2017**, *139*, 10750-10761.
[96] P. C. Dhanush, P. V. Saranya, G. Anilkumar, *Tetrahedron* **2022**, *105*, 132614.
[97] O. H. Winkelmann, O. Navarro, *Adv. Synth. Catal.* **2010**, *352*, 212-214.
[98] Z.-L. Gong, K. Tang, Y.-W. Zhong, *Inorg. Chem.* **2021**, *60*, 6607-6615.
[99] S. Fuertes, L. Mardegan, I. Martínez, S. Ventura, I. Ara, D. Tordera, H. J. Bolink, V. Sicilia, *J. Mater. Chem. C* **2022**, *10*, 15491-15500.
[100] M. Böttger, B. Wiegmann, S. Schaumburg, P. G. Jones, W. Kowalsky, H.-H. Johannes, *Beilstein J. Org. Chem* **2012**, *8*, 1037-1047.
[101] X. Qiu, S. Ying, C. Wang, M. Hanif, Y. Xu, Y. Li, R. Zhao, D. Hu, D. Ma, Y. Ma, *J. Mater. Chem. C* **2019**, *7*, 592-600.
[102] S. Daskeviciute-Geguziene, M. A. Truong, K. Rakstys, M. Daskeviciene, R. Hashimoto, R. Murdey, T. Yamada, Y. Kanemitsu, V. Jankauskas, A. Wakamiya, V. Getautis, *ACS Appl. Mater. Interfaces* **2024**, *16*, 1206-1216.
[103] M. Krejčik, A. A. Viček, *J. Electroanal. Chem. Interfac. Electrochem.* **1991**, *313*, 243-257.

[104] K. M. Omer, S.-Y. Ku, J.-Z. Cheng, S.-H. Chou, K.-T. Wong, A. J. Bard, *J. Am. Chem. Soc.* **2011**, *133*, 5492-5499.

[105] F. Zhan, G.-L. Lin, T.-S. Zhang, K. Xu, Y.-F. Yang, G. Li, Y. She, *Inorg. Chem.* **2024**, *63*, 8822-8831.

[106] M. Krause, J. Friedel, S. Buss, D. Brünink, A. Berger, C. A. Strassert, N. L. Doltsinis, A. Klein, *Dalton Trans.* **2022**, *51*, 16181-16194.

[107] G. J. Van Berkel, S. A. McLuckey, G. L. Glish, *Anal. Chem.* **1992**, *64*, 1586-1593.

[108] B. Butschke, M. Schlangen, D. Schröder, H. Schwarz, *Chem. - Eur. J.* **2008**, *14*, 11050-11060.

[109] T. Michiyuki, L. Ackermann, *ChemElectroChem* **2025**, *n/a*, e202400711.

[110] D. E. Holst, D. J. Wang, M. J. Kim, I. A. Guzei, Z. K. Wickens, *Nature* **2021**, *596*, 74-79.

[111] C. Janiak, *J. Chem. Soc., Dalton Trans.* **2000**, 3885-3896.

[112] W. Fudickar, T. Linker, *J. Am. Chem. Soc.* **2012**, *134*, 15071-15082.

[113] O. Laporte, W. F. Meggers, *J. Opt. Soc. Am.* **1925**, *11*, 459-463.

[114] M. S. Oliveira, G. Chorociejus, J. P. F. Angeli, G. V. Verde, G. L. B. Aquino, G. E. Ronsein, M. C. B. de Oliveira, L. F. Barbosa, M. H. G. Medeiros, A. Greer, P. Di Mascio, *Photochem. Photobiol. Sci.* **2020**, *19*, 1590-1602.

[115] H. Fidder, A. Lauer, W. Freyer, B. Koeppe, K. Heyne, *J. Phys. Chem. A* **2009**, *113*, 6289-6296.

[116] J. Al-Nu'airat, I. Oluwoye, N. Zeinali, M. Altarawneh, B. Z. Dlugogorski, *Chem. Rec.* **2021**, *21*, 315-342.

[117] C. Schäfer, F. Herrmann, J. Mattay, *Beilstein J. Org. Chem* **2008**, *4*, 41.

[118] N. Elgrishi, K. J. Rountree, B. D. McCarthy, E. S. Rountree, T. T. Eisenhart, J. L. Dempsey, *J. Chem. Educ.* **2018**, *95*, 197-206.

[119] A. Sandleben, N. Vogt, G. Hörner, A. Klein, *Organometallics* **2018**, *37*, 3332-3341.

[120] A. Putta, A. G. Sykes, H. Sun, *J. Fluorine Chem.* **2020**, *235*, 109548.

[121] X.-Q. Zhou, M. Xiao, V. Ramu, J. Hilgendorf, X. Li, P. Papadopoulou, M. A. Siegler, A. Kros, W. Sun, S. Bonnet, *J. Am. Chem. Soc.* **2020**, *142*, 10383-10399.

[122] V. Sivchik, A. Kochetov, T. Eskelinen, K. S. Kisel, A. I. Solomatina, E. V. Grachova, S. P. Tunik, P. Hirva, I. O. Koshevoy, *Chem. - Eur. J.* **2021**, *27*, 1787-1794.

[123] B. M. Still, P. G. A. Kumar, J. R. Aldrich-Wright, W. S. Price, *Chem. Soc. Rev.* **2007**, *36*, 665-686.

[124] K. TANABE, *J. Res. Inst. Catal., Hokkaido Univ.* **1961**, *9*, 246-255.

[125] L. Brandsma, H. D. Verkruijsse, *Preparative Polar Organometallic Chemistry I*, Springer-Verlag, Berlin, **1987**.

[126] U. Ruschewitz, *Z. Anorg. Allg. Chem.* **2006**, *632*, 705-719.

[127] H. Dote, H. Yasuhara, S. Nakashima, *J. Radioanal. Nucl. Chem.* **2015**, *303*, 1589-1593.

[128] R. Hedelt, C. Schulzke, D. Rehder, *Inorg. Chem. Commun.* **2000**, *3*, 300-302.

[129] B. G. Segal, S. J. Lippard, *Inorg. Chem.* **1977**, *16*, 1623-1629.

[130] T. Eskelinen, S. Buss, S. K. Petrovskii, E. V. Grachova, M. Krause, L. Kletsch, A. Klein, C. A. Strassert, I. O. Koshevoy, P. Hirva, *Inorg. Chem.* **2021**, *60*, 8777-8789.

[131] MestReNova 12.0.0, Mestrelab Research S.L., Santiago de Compostela, Spain, **2017**.
[132] APEX3 - Software Suite for Crystallographic Progams, Bruker AXS Inc., Madison, WI, USA, **2015**.
[133] SAINT, Bruker AXS Inc., Madison, WI, USA 2016., **2016**.
[134] G. Sheldrick, University of Göttingen: Göttingen, Germany, **1997**.
[135] O. V. Dolomanov, L. J. Bourhis, R. J. Gildea, J. A. K. Howard, H. Puschmann, *J. Appl. Crystallogr.* **2009**, *42*, 339-341.
[136] G. Sheldrick, *Acta Crystallogr. Sect. A* **2015**, *71*, 3-8.
[137] G. Sheldrick, *Acta Crystallogr. Sect. C* **2015**, *71*, 3-8.
[138] Diamond v4.2 - Crystal and Molecular Structure Visualization, Crystal Impact, Germany, **2016**.
[139] Origin(Pro) Version 2025, Originlab Corporation, Northampton, MA, USA, **2025**.
[140] Gaussian 16, M. J. Frisch, G. W. Trucks, H. B. Schlegel, G. E. Scuseria, M. A. Robb, J. R. Cheeseman, G. Scalmani, V. Barone, G. A. Petersson, H. Nakatsuji, X. Li, M. Caricato, A. V. Marenich, J. Bloino, B. G. Janesko, R. Gomperts, B. Mennucci, H. P. Hratchian, J. V. Ortiz, A. F. Izmaylov, J. L. Sonnenberg, Williams, F. Ding, F. Lipparini, F. Egidi, J. Goings, B. Peng, A. Petrone, T. Henderson, D. Ranasinghe, V. G. Zakrzewski, J. Gao, N. Rega, G. Zheng, W. Liang, M. Hada, M. Ehara, K. Toyota, R. Fukuda, J. Hasegawa, M. Ishida, T. Nakajima, Y. Honda, O. Kitao, H. Nakai, T. Vreven, K. Throssell, J. A. Montgomery Jr., J. E. Peralta, F. Ogliaro, M. J. Bearpark, J. J. Heyd, E. N. Brothers, K. N. Kudin, V. N. Staroverov, T. A. Keith, R. Kobayashi, J. Normand, K. Raghavachari, A. P. Rendell, J. C. Burant, S. S. Iyengar, J. Tomasi, M. Cossi, J. M. Millam, M. Klene, C. Adamo, R. Cammi, J. W. Ochterski, R. L. Martin, K. Morokuma, O. Farkas, J. B. Foresman, D. J. Fox, Wallingford, CT, **2016**.
[141] F. Weigend, R. Ahlrichs, *Phys. Chem. Chem. Phys.* **2005**, *7*, 3297-3305.
[142] D. Andrae, U. Häußermann, M. Dolg, H. Stoll, H. Preuß, *Theor. Chim. Acta* **1990**, *77*, 123-141.
[143] V. N. Staroverov, G. E. Scuseria, J. Tao, J. P. Perdew, *J. Chem. Phys.* **2003**, *119*, 12129-12137.
[144] S. Grimme, S. Ehrlich, L. Goerigk, *J. Comput. Chem.* **2011**, *32*, 1456-1465.
[145] M. Cossi, N. Rega, G. Scalmani, V. Barone, *J. Comput. Chem.* **2003**, *24*, 669-681.
[146] V. Barone, M. Cossi, *J. Phys. Chem. A* **1998**, *102*, 1995-2001.
[147] O. Kuleshova, S. Asako, L. Ilies, *ACS Catal.* **2021**, *11*, 5968-5973.
[148] B. Laramée-Milette, G. S. Hanan, *Dalton Trans.* **2016**, *45*, 12507-12517.
[149] L. Wang, N. Liu, B. Dai, *RSC Advances* **2015**, *5*, 82097-82111.
[150] C. Brouillac, A. Serez, N. McIntosh, J. Rault-Berthelot, O. Jeannin, B. Heinrich, C. Quinton, O. De Sagazan, E. Jacques, J. Cornil, C. Poriel, *J. Mater. Chem. C* **2024**, *12*, 12598-12607.
[151] G. Li, X. Zhao, K. Fang, J. Li, Y. She, *J. Org. Chem.* **2017**, *82*, 8634-8644.

8 Appendix

8.1 UV/Vis Absorption Spectra

8.1.1 UV/Vis Absorption Spectra of Protoligands

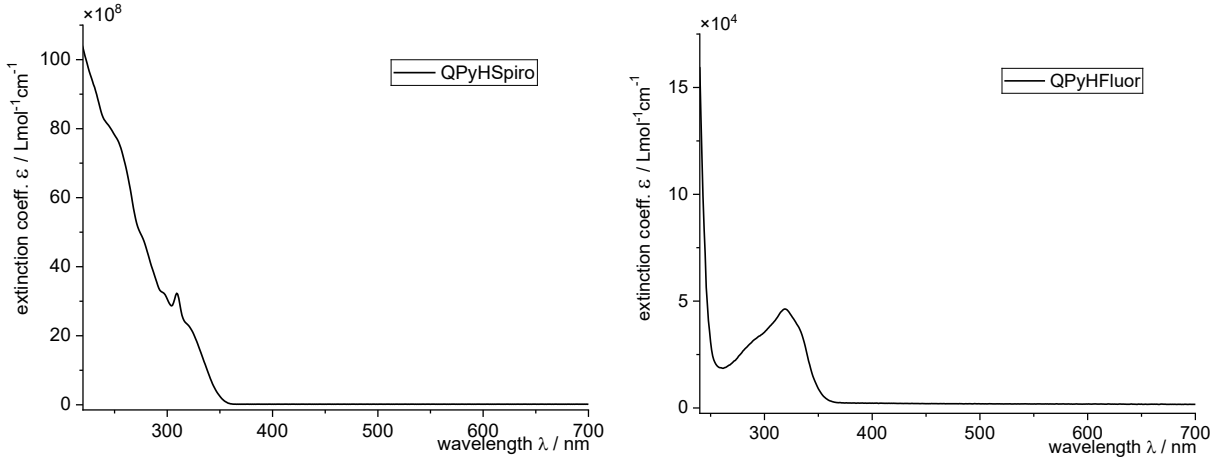

Figure 94 UV/Vis-absorption spectra of QPyHSpiro (left) and QPyHFluor (right). Measured in THF at room temperature.

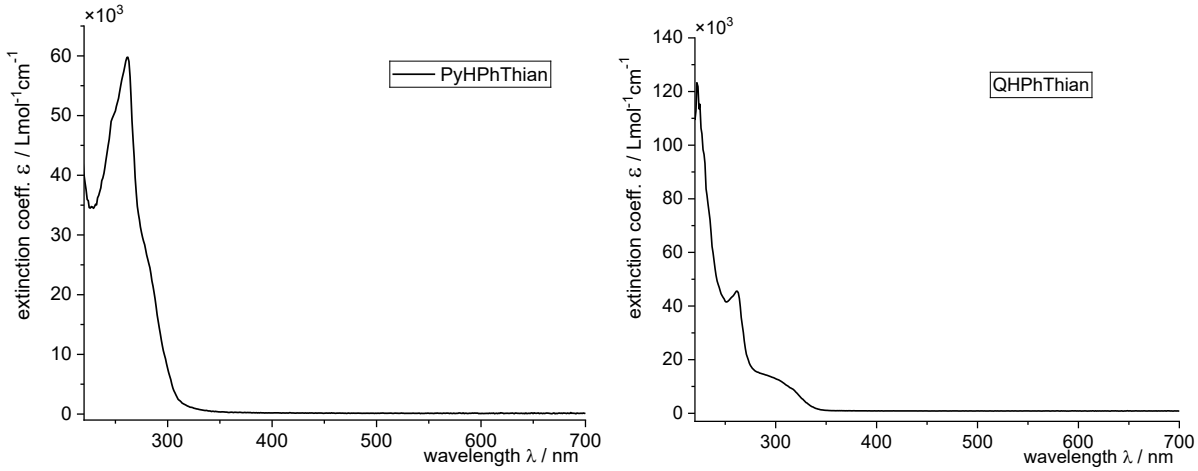

Figure 95 UV/Vis-absorption spectra of PyHPhThian (left) and QHPhThian (right). Measured in THF at room temperature.

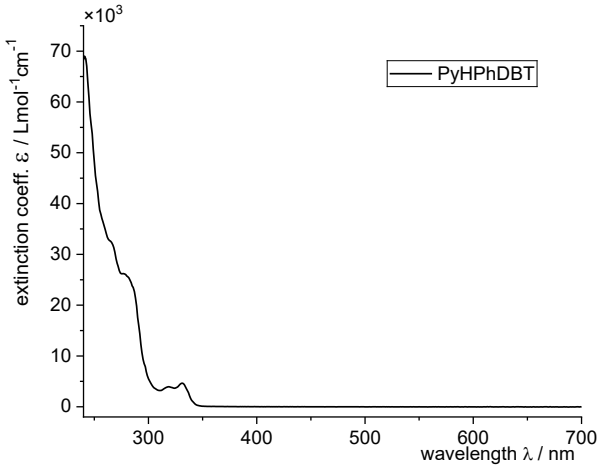

Figure 96 UV/Vis-absorption spectra of PyHPhDBT. Measured in THF at room temperature.

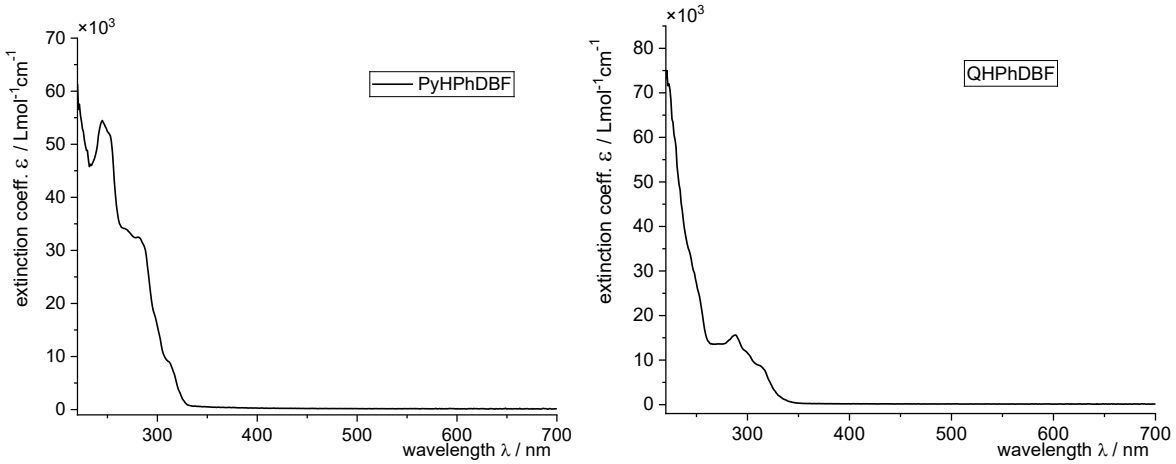

Figure 97 UV/Vis-absorption spectra of PyHPhDBF (left) and QHPhDBF (right). Measured in THF at room temperature.

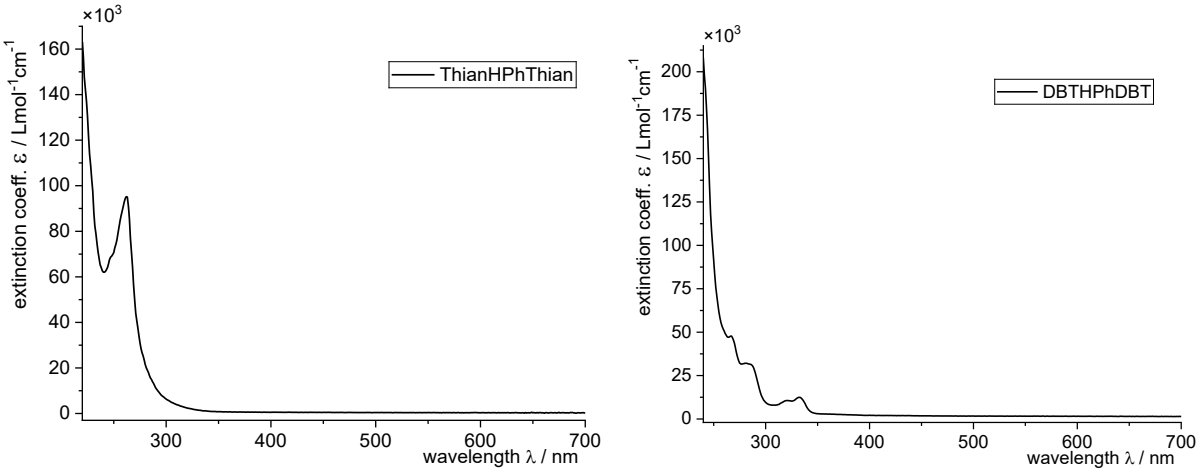

Figure 98 UV/Vis-absorption spectra of ThianHPhThian (left) and DBTHPhDBT (right). Measured in THF at room temperature.

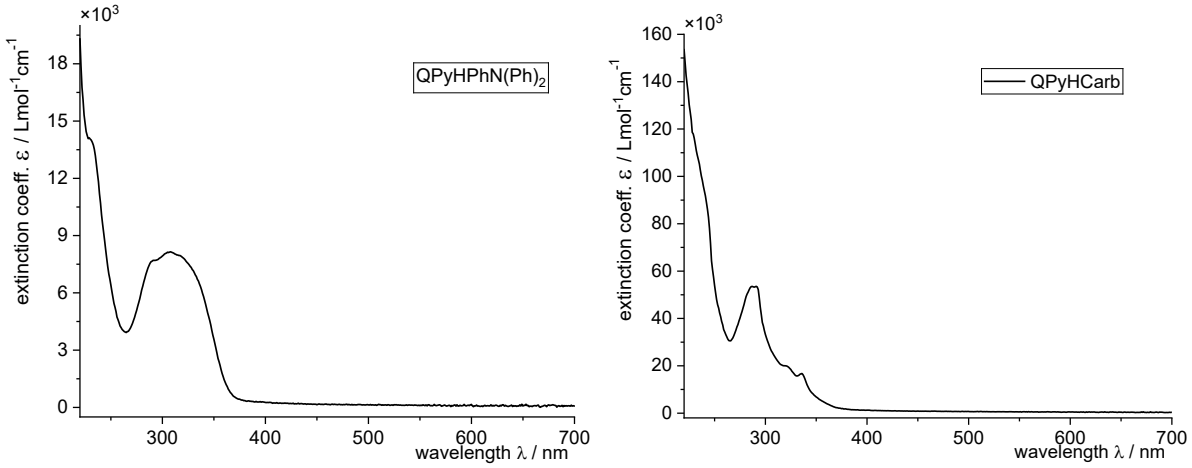

Figure 99 UV/Vis-absorption spectra of $QPyHPhN(Ph)_2$ (left) and QPyHCarb (right). Measured in THF at room temperature.

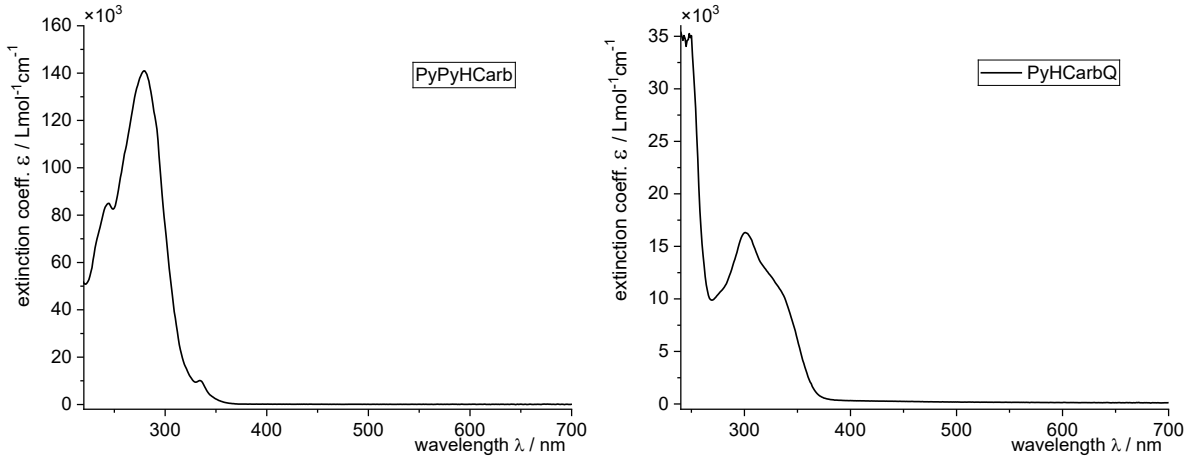

Figure 100 UV/Vis-absorption spectra of PyPyHCarb (left) and PyHCarbQ (right). Measured in THF at room temperature.

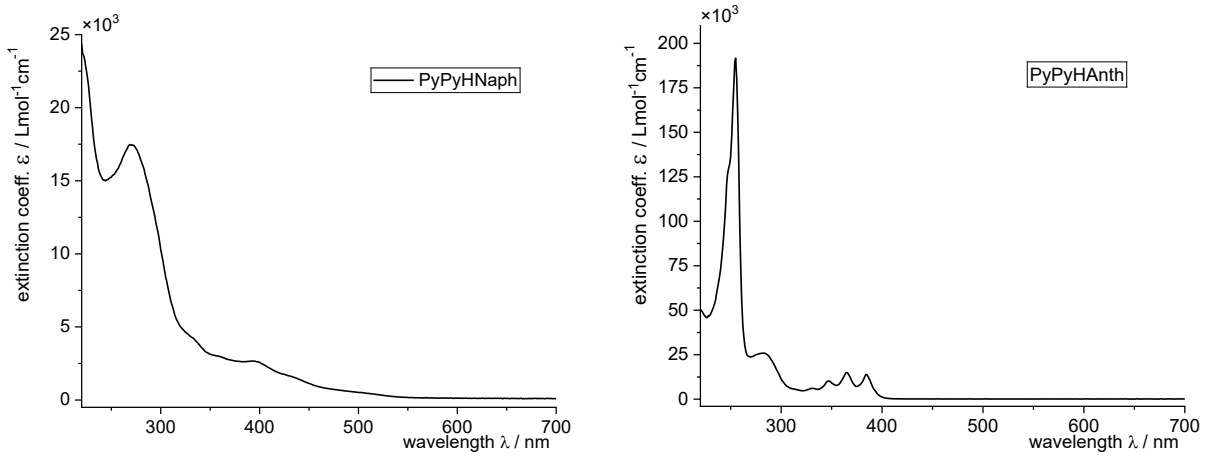

Figure 101 UV/Vis-absorption spectra of PyPyHNaph(left) and PyPyHAnth (right). Measured in THF at room temperature.

8.1.2 UV/Vis Absorption Spectra of Complexes

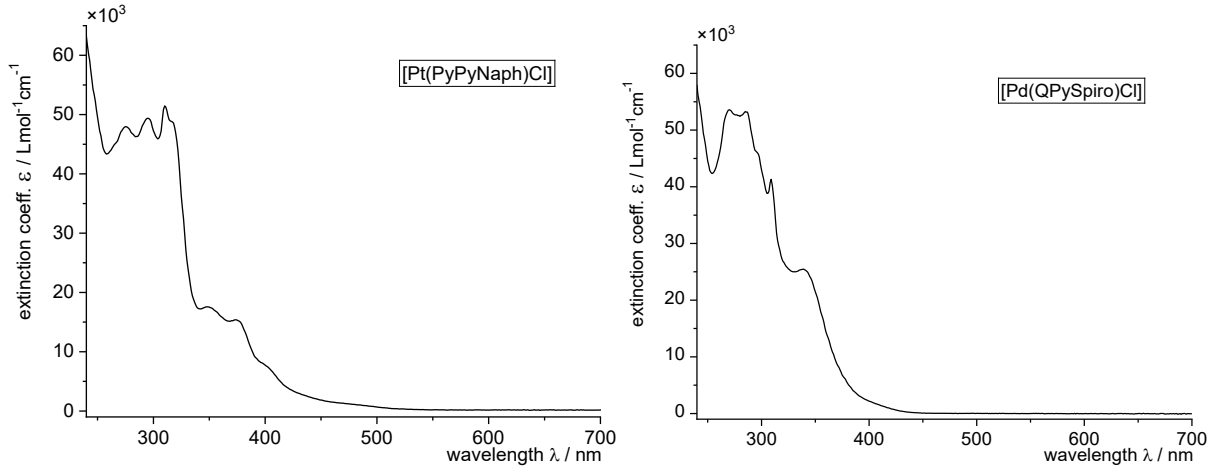

Figure 102 UV/Vis-absorption spectra of [Pt(QPySpiro)Cl] (left) and [Pd(QPySpiro)Cl] (right). Measured in THF at room temperature.

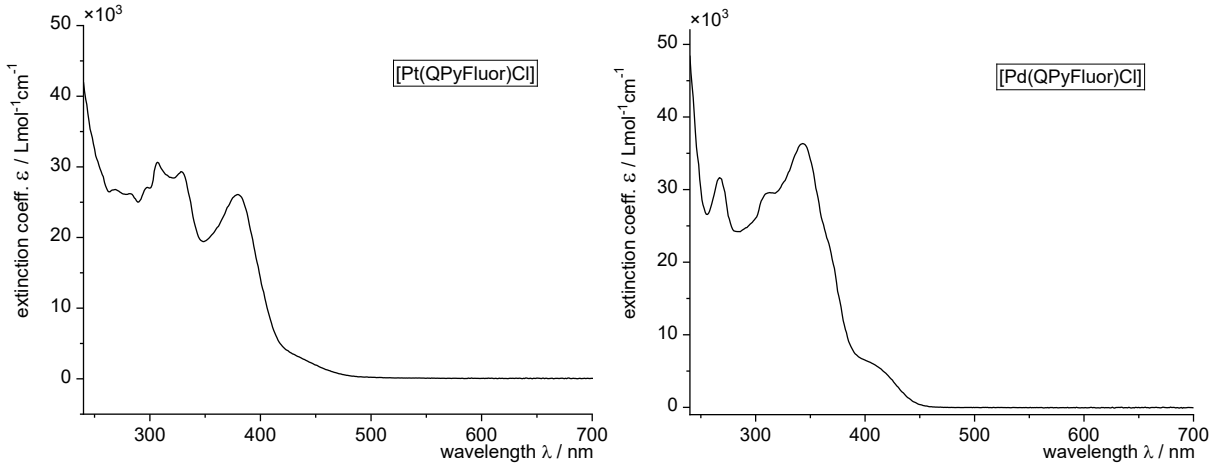

Figure 103 UV/Vis-absorption spectra of [Pt(QPyFluor)Cl] (left) and [Pd(QPyFluor)Cl] (right). Measured in THF at room temperature.

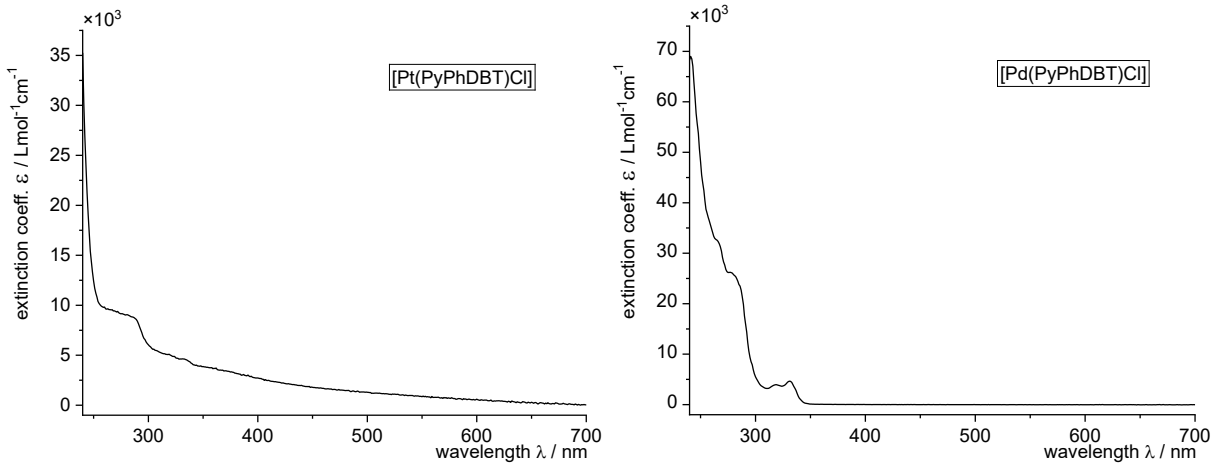

Figure 104 UV/Vis-absorption spectra of [Pt(PyPhDBT)Cl] (left) and [Pd(PyPhDBT)Cl] (right). Measured in THF at room temperature.

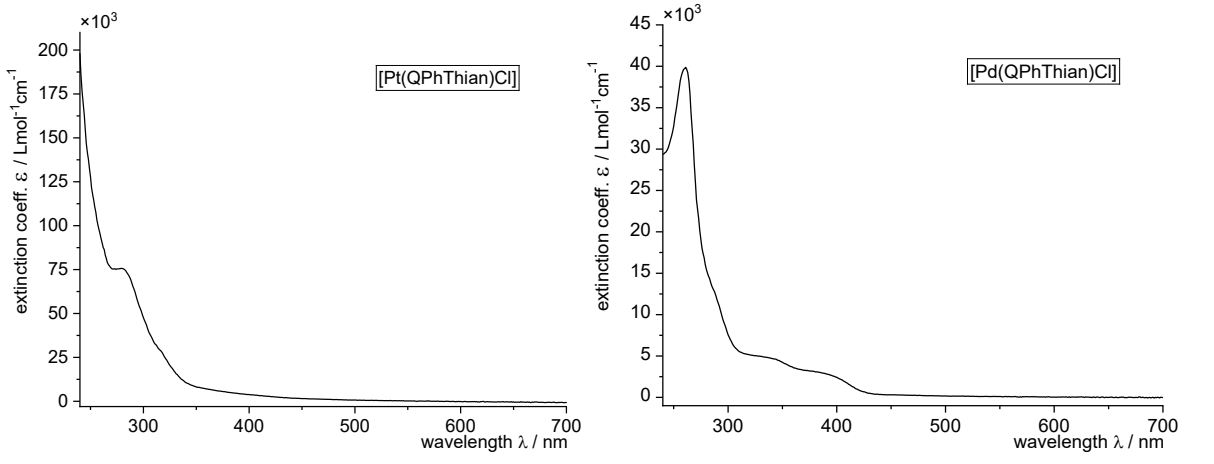

Figure 105 UV/Vis-absorption spectra of [Pt(QPhThian)Cl] (left) and [Pd(QPhThian)Cl] (right). Measured in THF at room temperature.

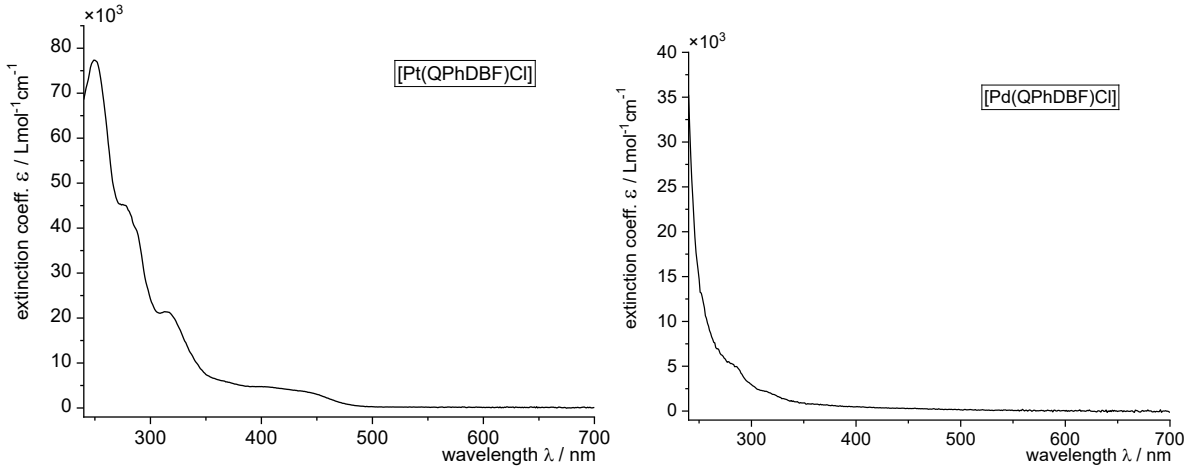

Figure 106 UV/Vis-absorption spectra of [Pt(QPhDBF)Cl] (left) and [Pd(QPhDBF)Cl] (right). Measured in THF at room temperature.

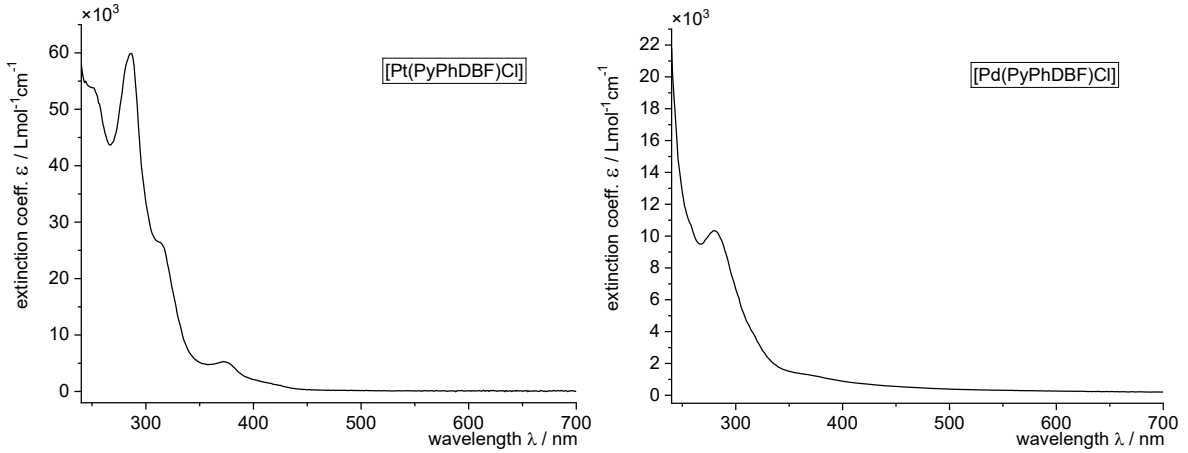

Figure 107 UV/Vis-absorption spectra of [Pt(PyPhDBF)Cl] (left) and [Pd(PyPhDBF)Cl] (right). Measured in THF at room temperature.

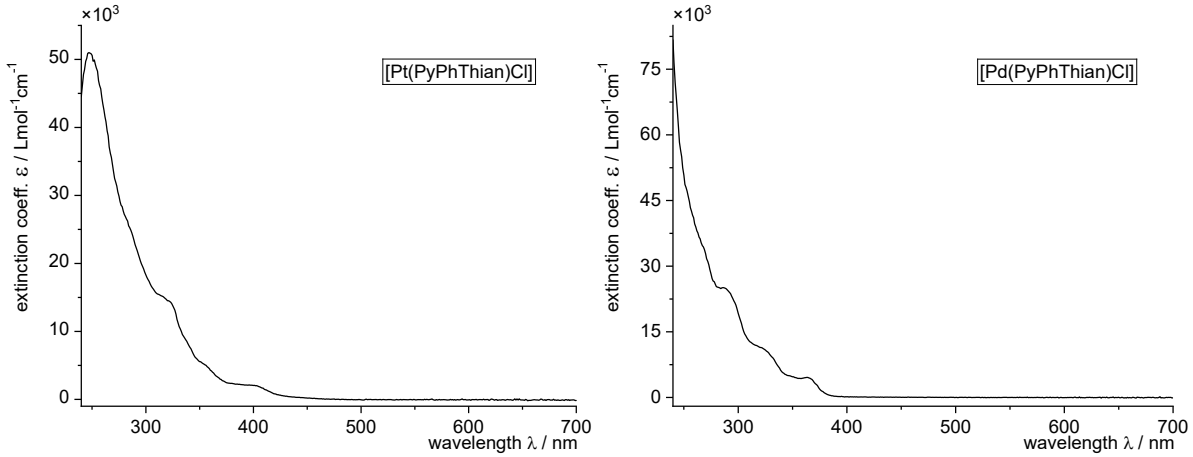

Figure 108 UV/Vis-absorption spectra of [Pt(PyPhThian)Cl] (left) and [Pd(PyPhThian)Cl] (right). Measured in THF at room temperature.

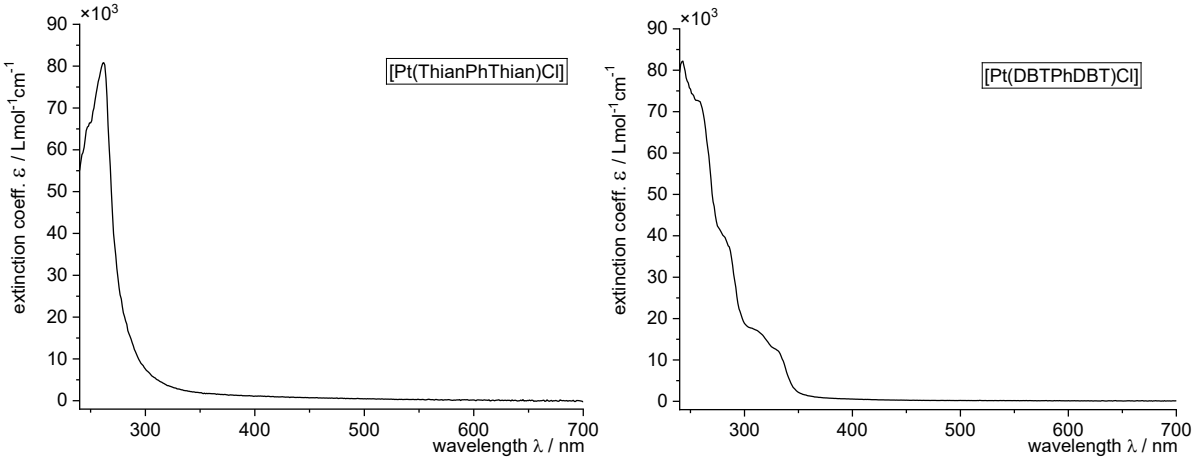

Figure 109 UV/Vis-absorption spectra of [Pt(ThianPhThian)Cl] (left) and [Pt(DBTPhDBT)Cl] (right). Measured in THF at room temperature.

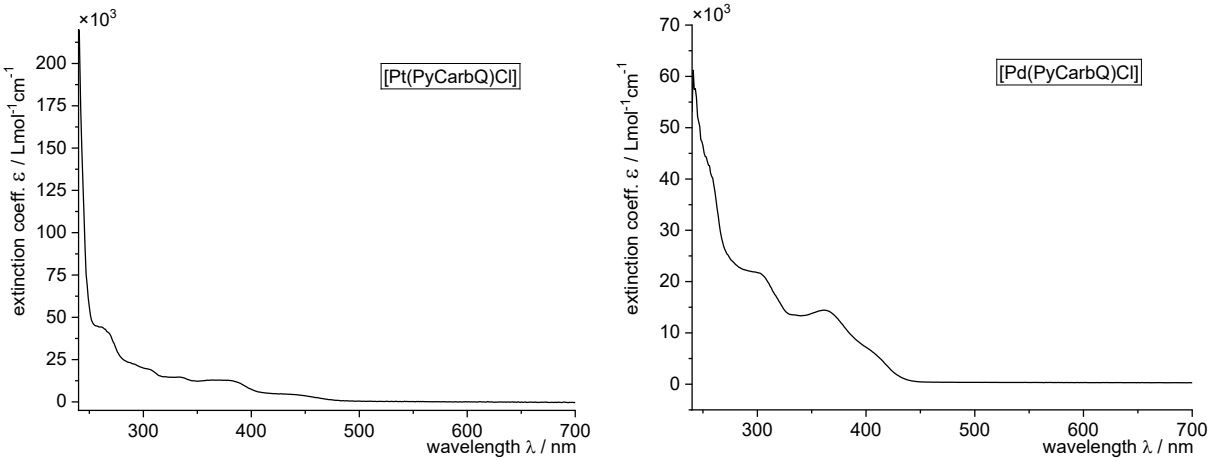

Figure 110 UV/Vis-absorption spectra of [Pt(PyCarbQ)Cl] (left) and [Pd(PyCarbQ)Cl] (right). Measured in THF at room temperature.

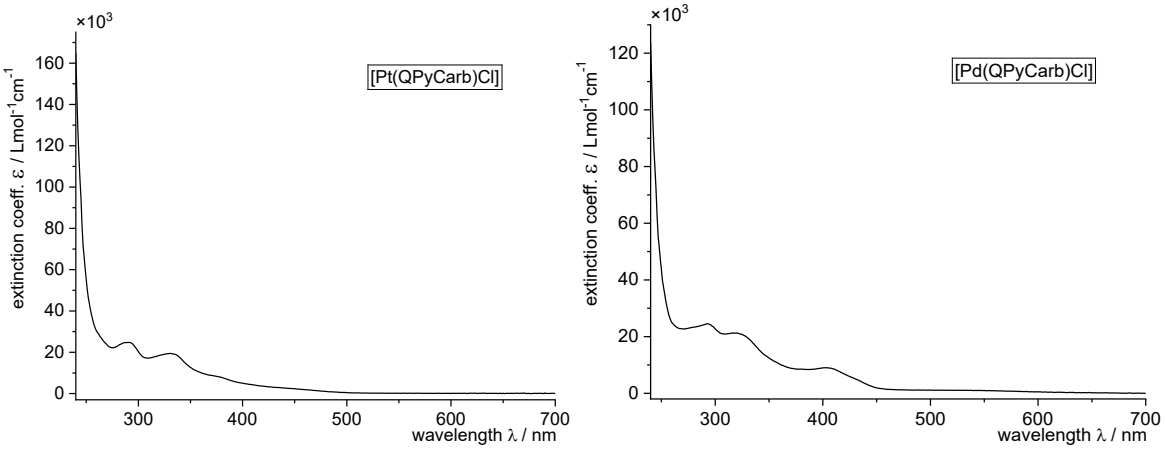

Figure 111 UV/Vis-absorption spectra of [Pt(QPyCarb)Cl] (left) and [Pd(QPyCarb)Cl] (right). Measured in THF at room temperature.

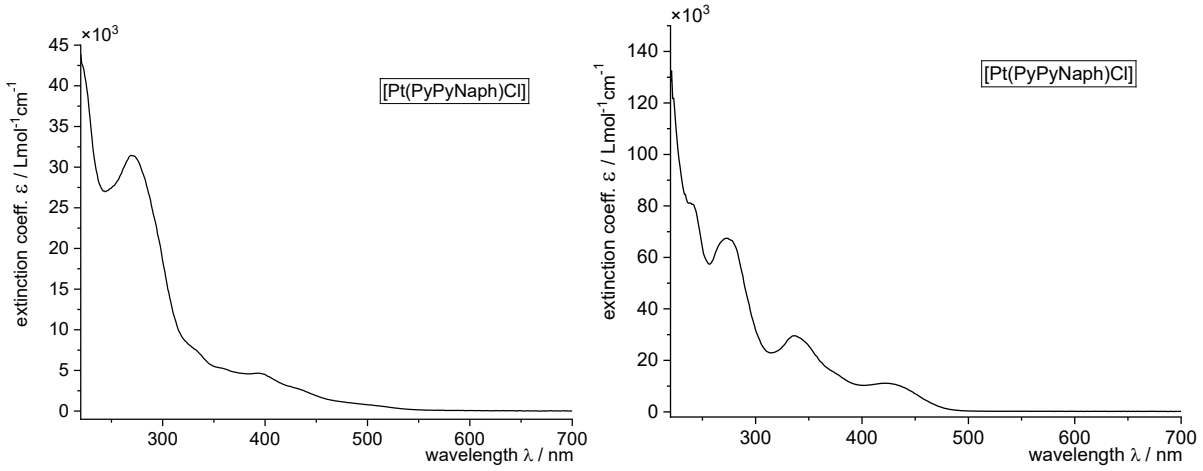

Figure 112 UV/Vis-absorption spectra of [Pt(PyPyNaph)Cl] (left) and [Pd(PyPyNaph)Cl] (right). Measured in THF at room temperature.

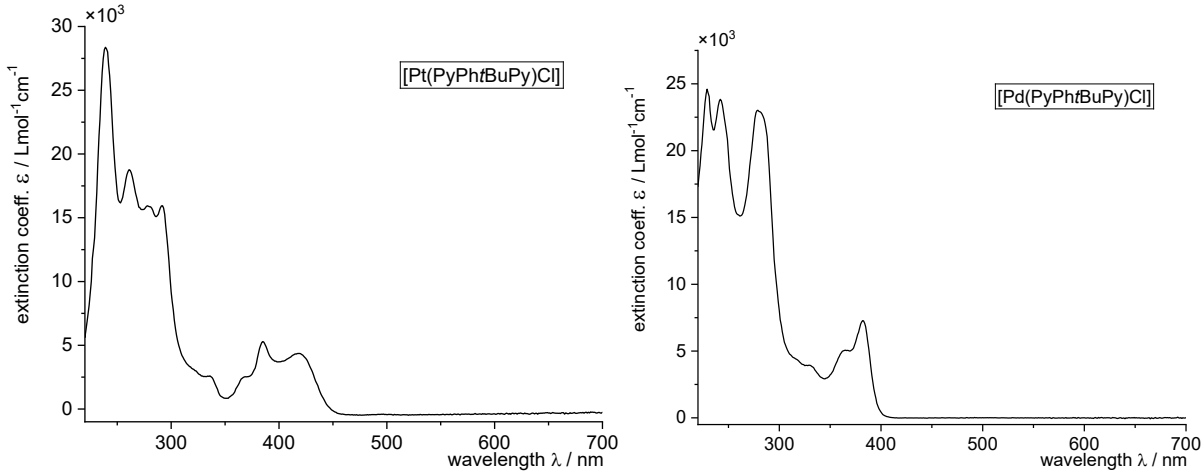

Figure 113 UV/Vis-absorption spectra of [Pt(Py*t*BuPhPy)Cl] (left) and [Pd(Py*t*BuPhPy)Cl] (right). Measured in THF at room temperature.

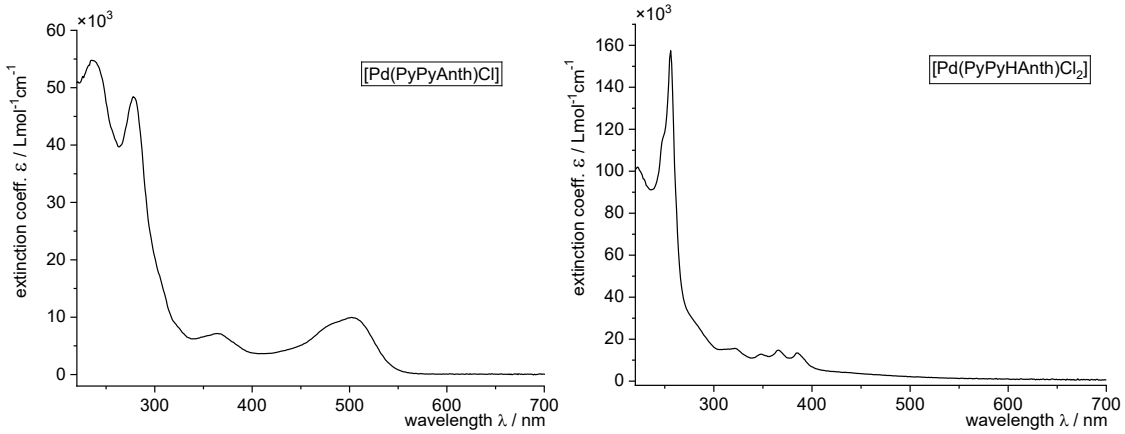

Figure 114 UV/Vis-absorption spectra of [Pd(PyPyAnth)Cl] (left) and [Pd(PyPyHAnth)Cl_2] (right). Measured in THF at room temperature.

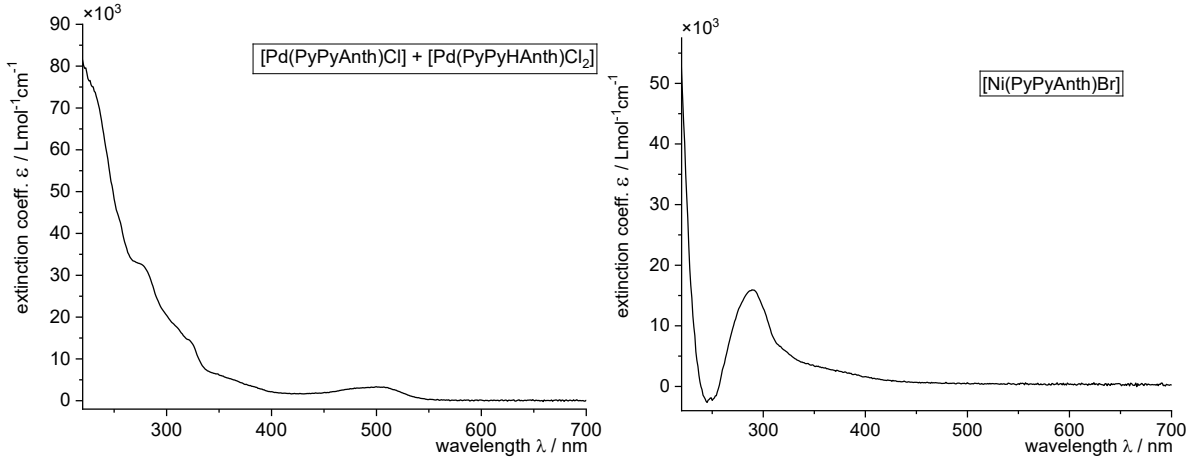

Figure 115 UV/Vis-absorption spectra of [Pd(PyPyAnth)Cl] + [Pd(PyPyHAnth)Cl_2] (left) and [Ni(PyPyAnth)Br] (right). Measured in THF at room temperature.

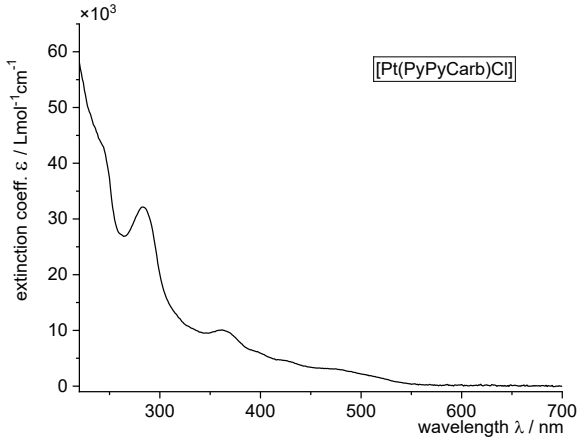

Figure 116 UV/Vis-absorption spectra of [Pt(PyPyCarb)Cl]. Measured in THF at room temperature.

8.1.3 UV/Vis Absorption Spectra of Coligand Exchange Reactions

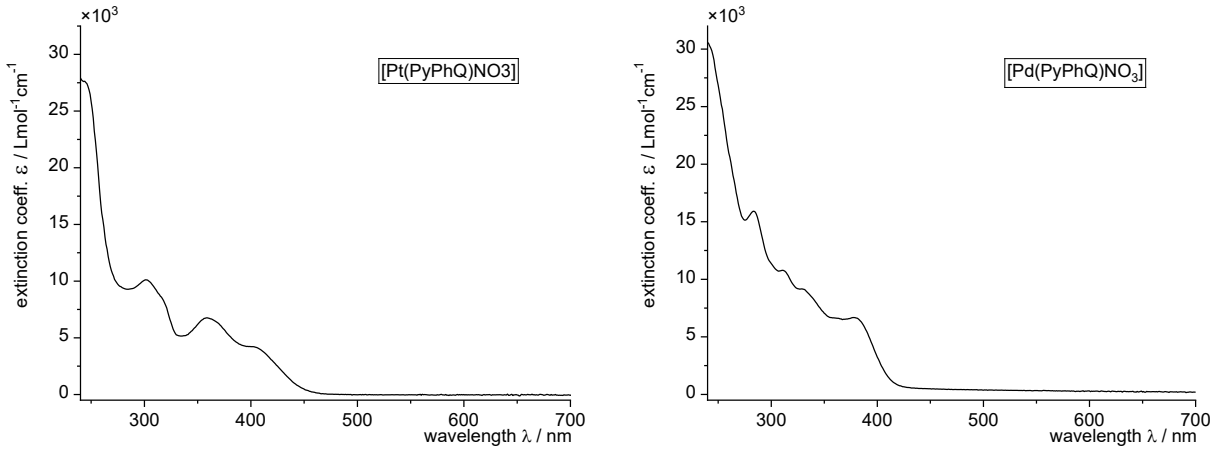

Figure 117 UV/Vis-absorption spectra of [Pt(PyPhQ)NO_3] (left) and [Pd(PyPhQ)NO_3]. Measured in THF at room temperature.

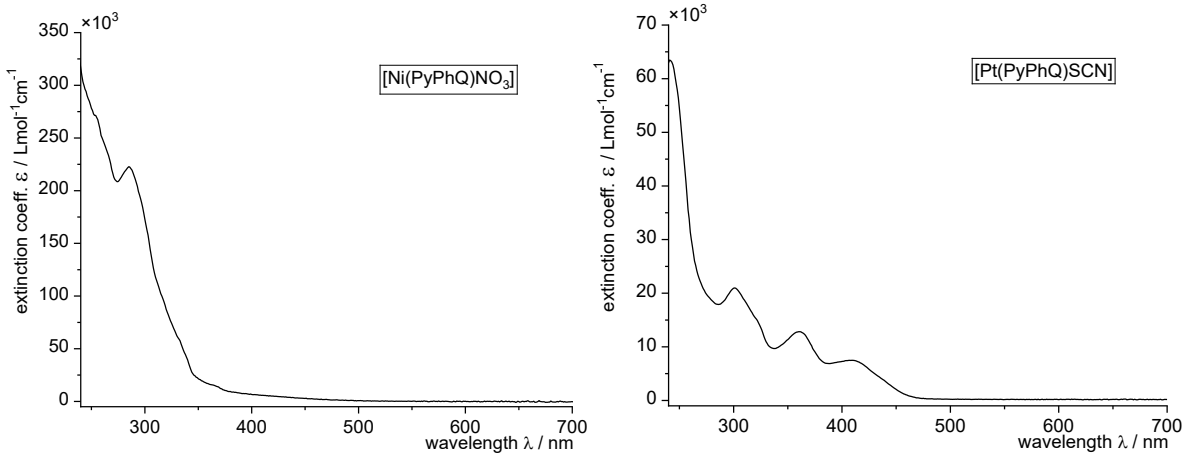

Figure 118 UV/Vis-absorption spectra of [Ni(PyPhQ)NO_3] (left) and [Pt(PyPhQ)SCN] (right). Measured in THF at room temperature.

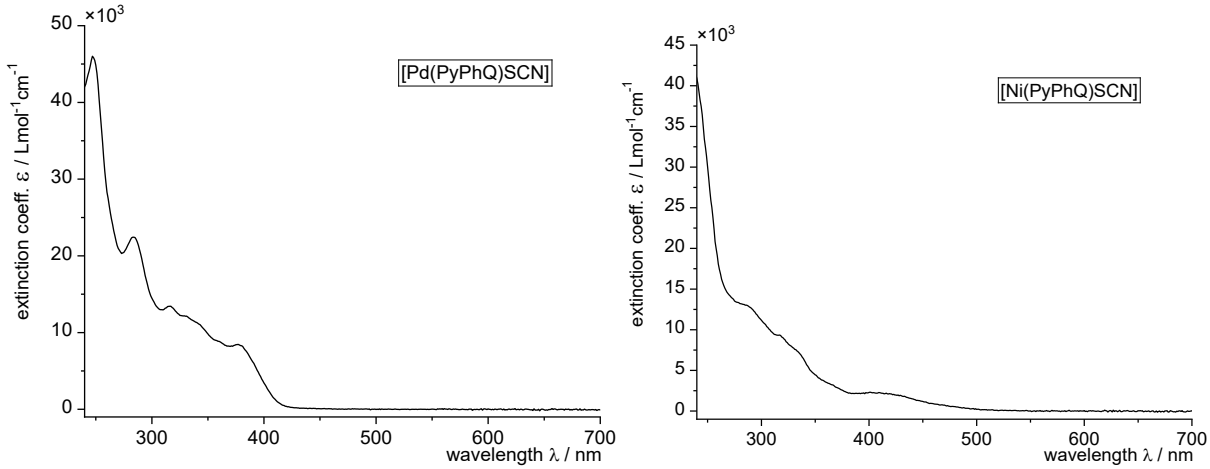

Figure 119 UV/Vis-absorption spectra of [Pd(PyPhQ)SCN] (left) and [Ni(PyPhQ)SCN]. Measured in THF at room temperature.

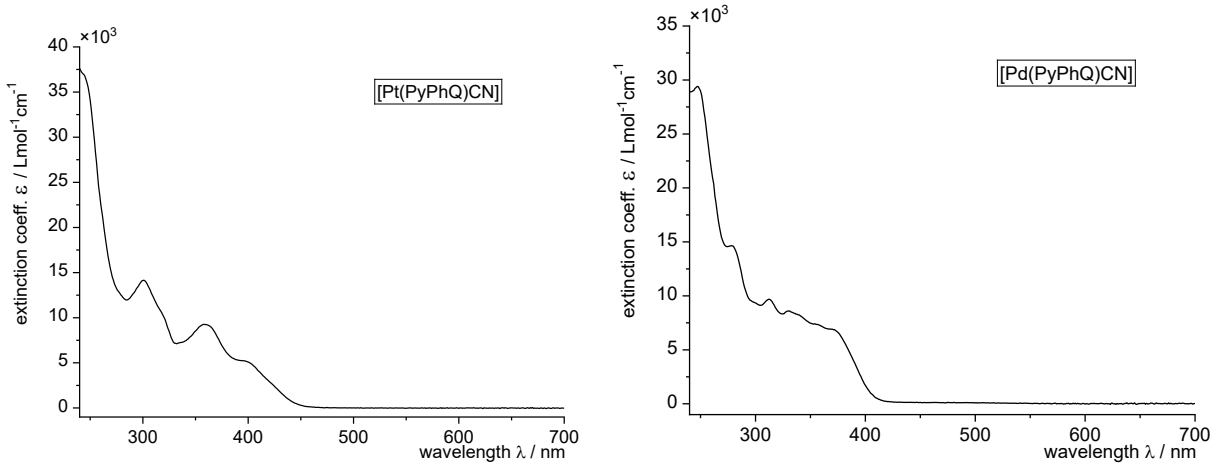

Figure 120 UV/Vis-absorption spectra of [Pt(PyPhQ)CN] (left) and [Pd(PyPhQ)CN] (right). Measured in THF at room temperature.

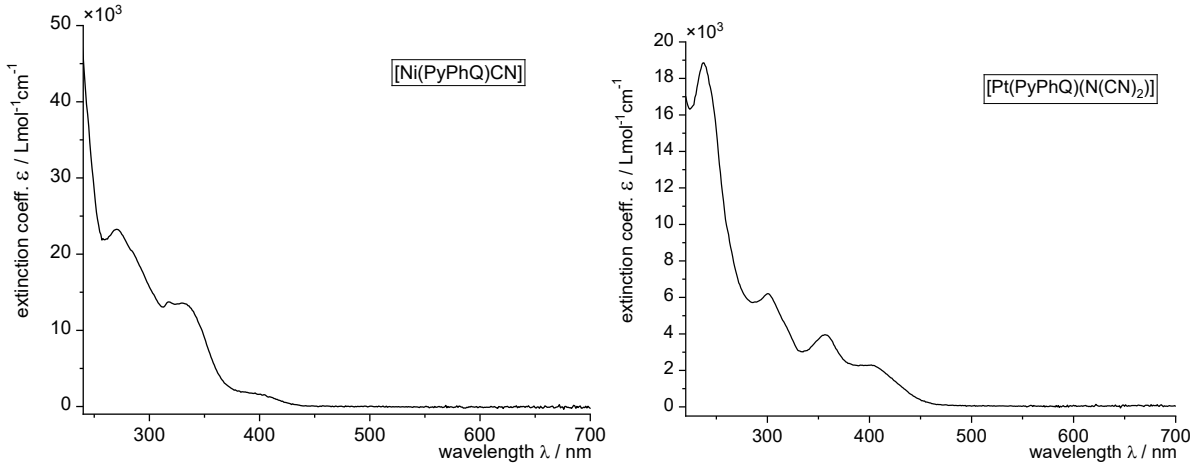

Figure 121 UV/Vis-absorption spectra of [Ni(PyPhQ)CN] (left) and [Pt(PyPhQ)(N(CN))$_2$] (right). Measured in THF at room temperature.

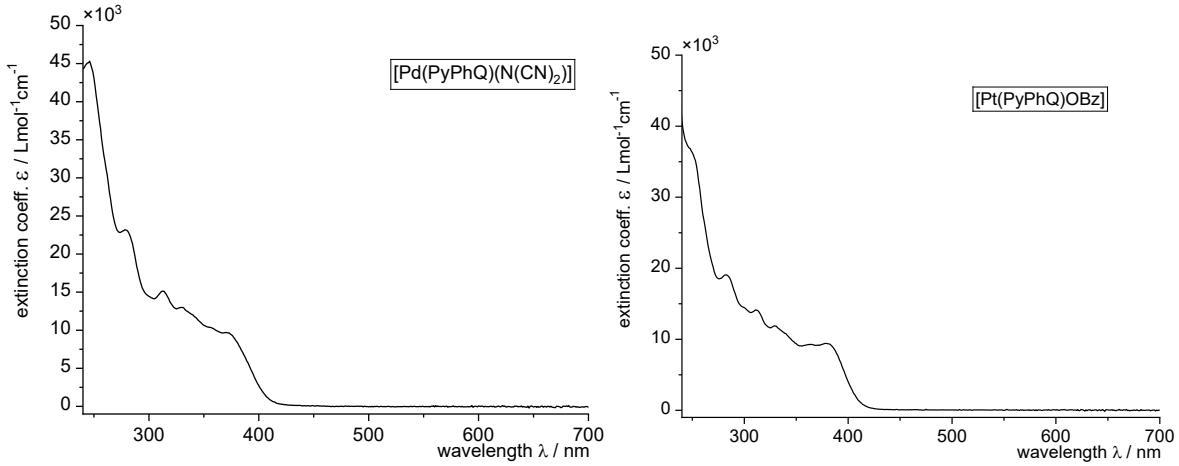

Figure 122 UV/Vis-absorption spectra of [Pd(PyPhQ)(N(CN))$_2$] (left) and [Pt(PyPhQ)OBz] (right). Measured in THF at room temperature.

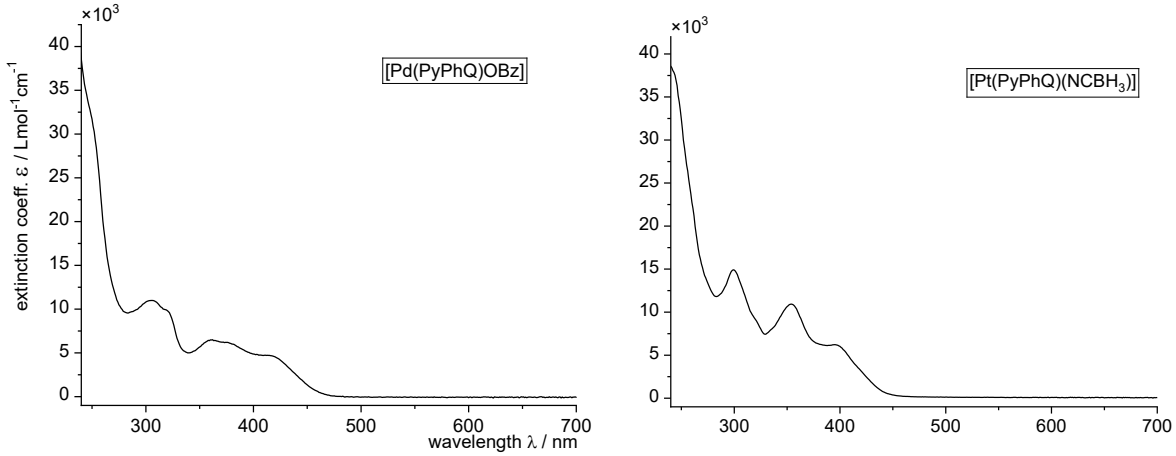

Figure 123 UV/Vis-absorption spectra of [Pd(PyPhQ)OBz] (left) and [Pt(PyPhQ)(NCBH$_3$)]. Measured in THF at room temperature.

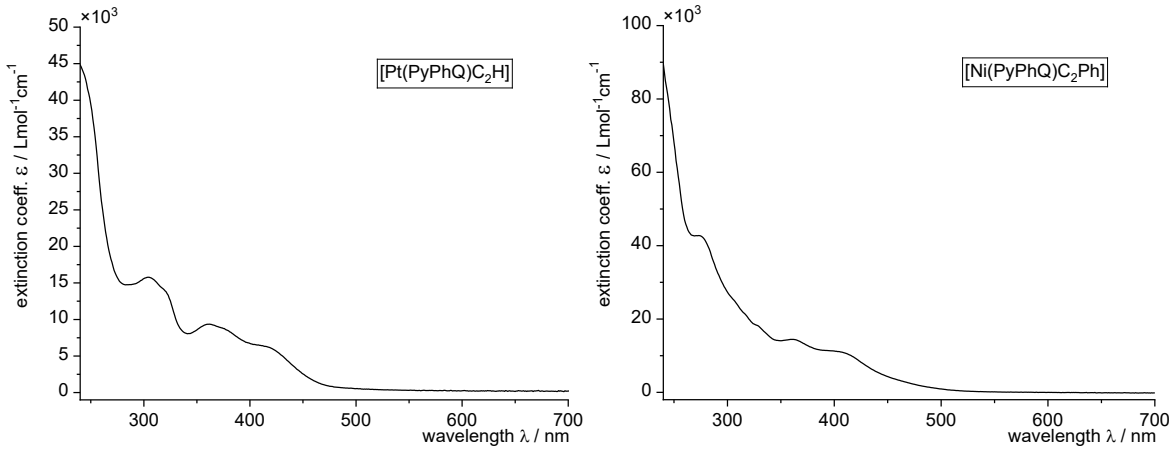

Figure 124 UV/Vis-absorption spectra of [Pt(PyPhQ)C2Ph] (left) and [Ni(PyPhQ)C2Ph] (right). Measured in THF at room temperature.

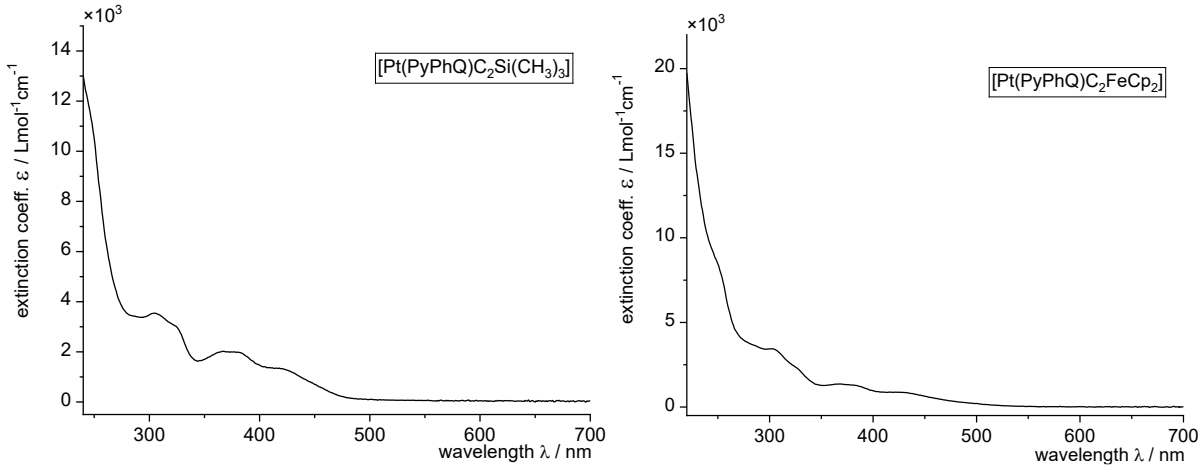

Figure 125 UV/Vis-absorption spectra of [Pt(PyPhQ)C2Si(CH3)3] (left) and [Pt(PyPhQ)CzFeCp2] (right). Measured in THF at room temperature.

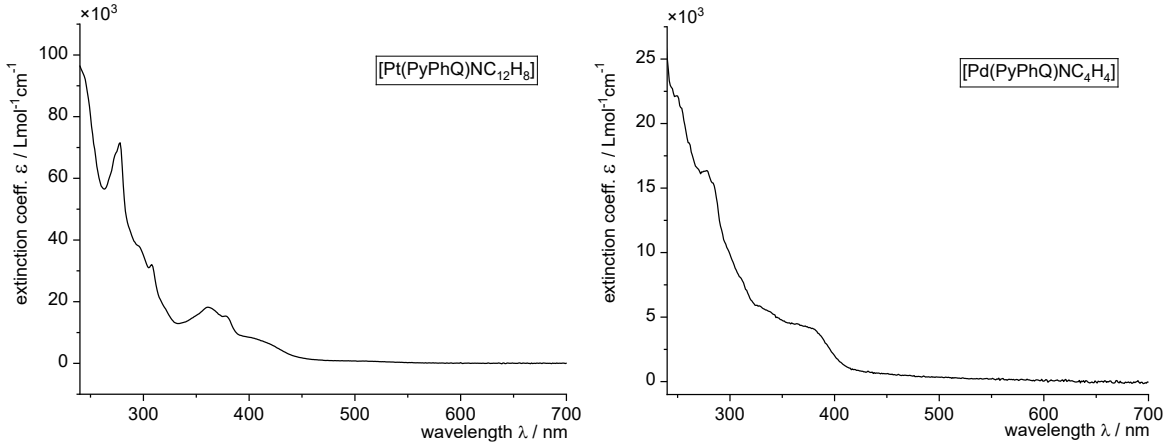

Figure 126 UV/Vis-absorption spectra of [Pt(PyPhQ)(NC4H4)] (left) and [Pt(PyPhQ)(NC4H4)] (right). Measured in THF at room temperature.

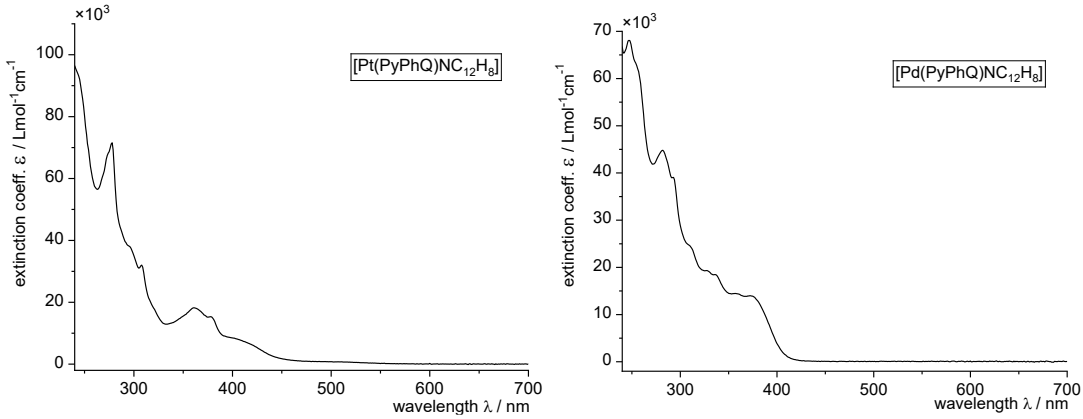

Figure 127 UV/Vis-absorption spectra of [Pt(PyPhQ)($NC_{12}H_8$)] (left) and [Pt(PyPhQ)($NC_{12}H_8$)] (right). Measured in THF at room temperature.

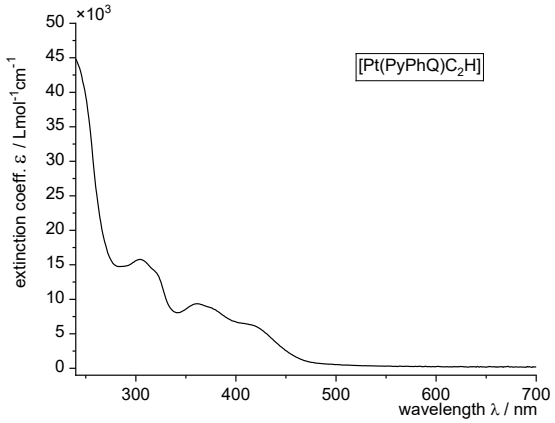

Figure 128 UV/Vis-absorption spectra of [Pt(PyPhQ)C_2H], measured in THF at room temperature.

8.2 Cyclovoltammograms

8.2.1 Cyclovoltammograms of Protoligands

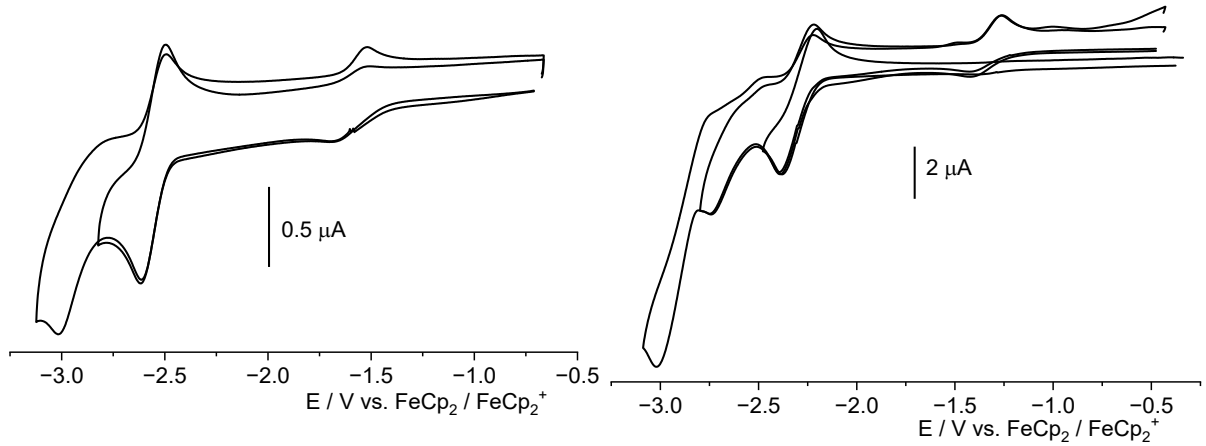

Figure 129 Cyclic voltammograms of QPyHSpiro (left) and QPyHFluor (right), in 0.1 M NBu_4NPF_6 solution in THF at room temperature at a scan rate of 100 mV/s.

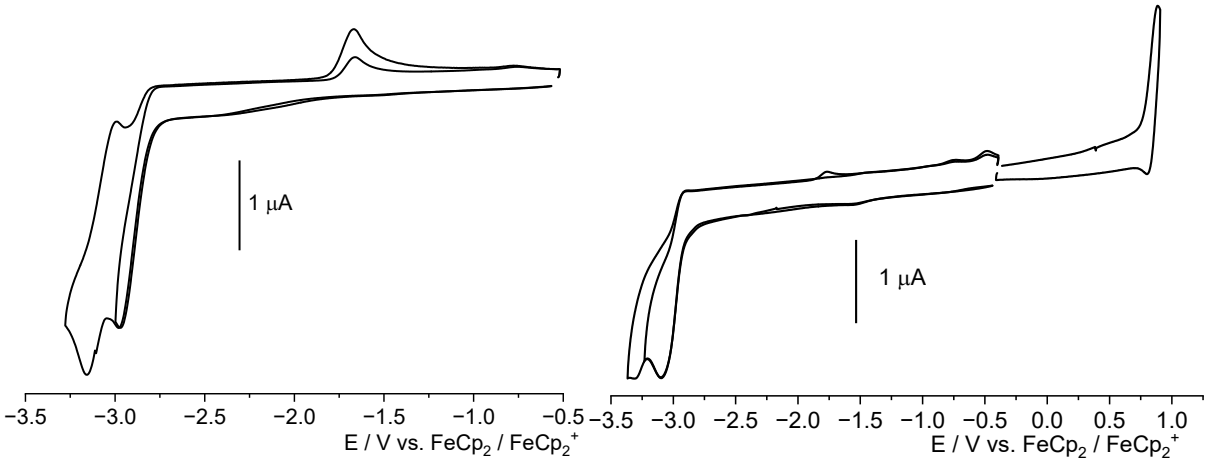

Figure 130 Cyclic voltammograms of DBTHPhDBT (left) and ThianHPhThian (right), in 0.1 M NBu_4NPF_6 solution in THF at room temperature at a scan rate of 100 mV/s.

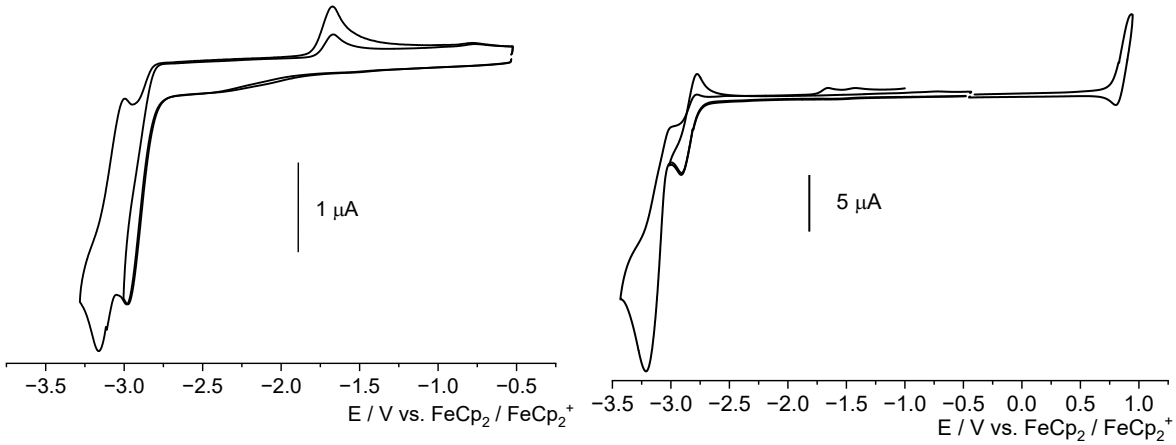

Figure 131 Cyclic voltammograms of PyHPhDBT (left) and PyHPhThian (right), in 0.1 M NBu_4NPF_6 solution in THF at room temperature at a scan rate of 100 mV/s.

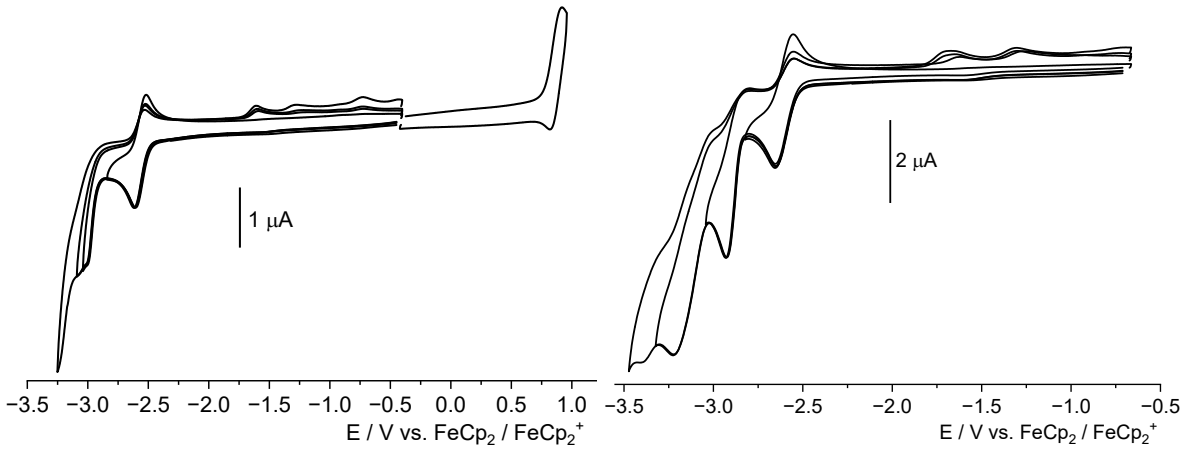

Figure 132 Cyclic voltammograms of QHPhThian (left) and QHPhDBF(right), in 0.1 M NBu_4NPF_6 solution in THF at room temperature at a scan rate of 100 mV/s.

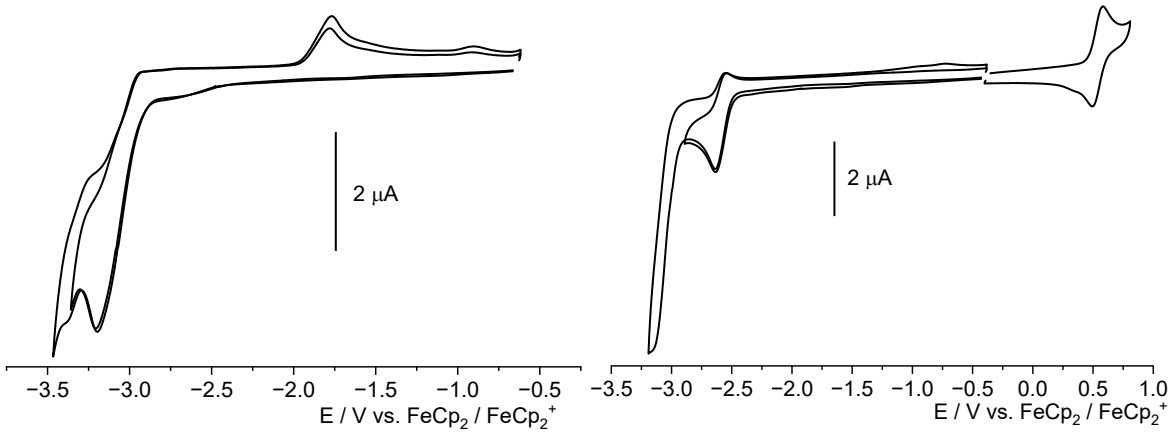

Figure 133 Cyclic voltammograms of PyHPhDBF (left) and QPyHPh(N(Ph)2) (right), in 0.1 M NBu_4NPF_6 solution in THF at room temperature at a scan rate of 100 mV/s.

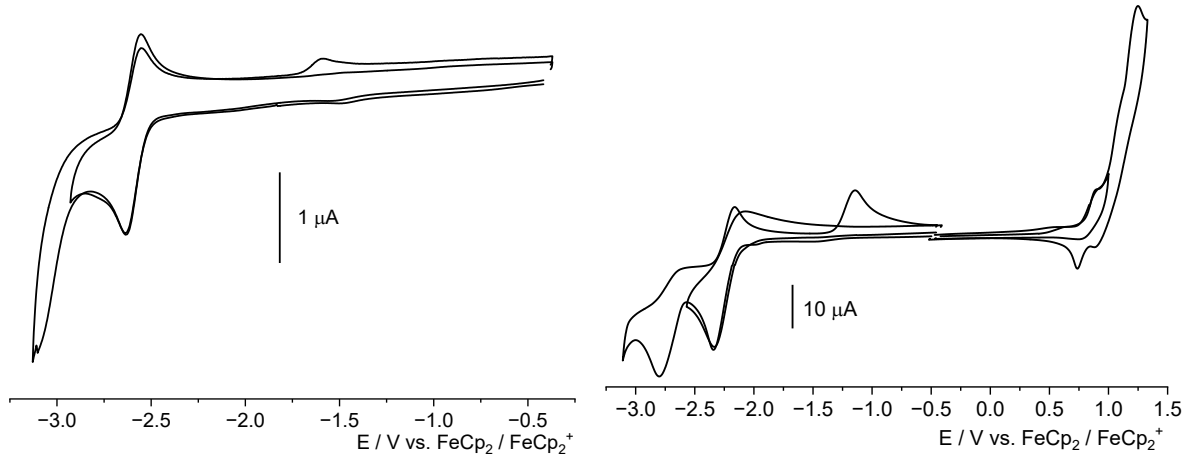

Figure 134 Cyclic voltammograms of PyPyHCarb (left) and QPyHCarb (right), in 0.1 M NBu_4NPF_6 solution in THF at room temperature at a scan rate of 100 mV/s.

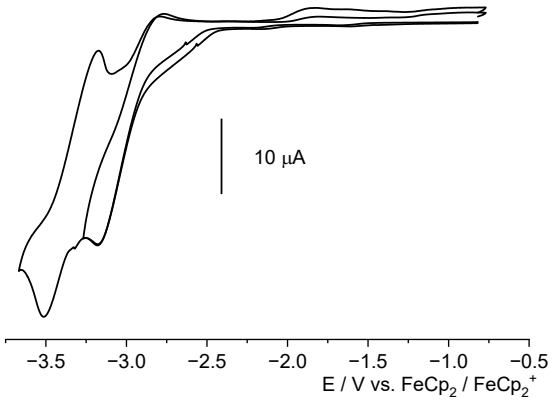

Figure 135 Cyclic voltammograms of PyPyHAnth (left) in 0.1 M NBu_4NPF_6 solution in THF at room temperature at a scan rate of 100 mV/s.

8.2.2 Cyclovoltammograms of Complexes

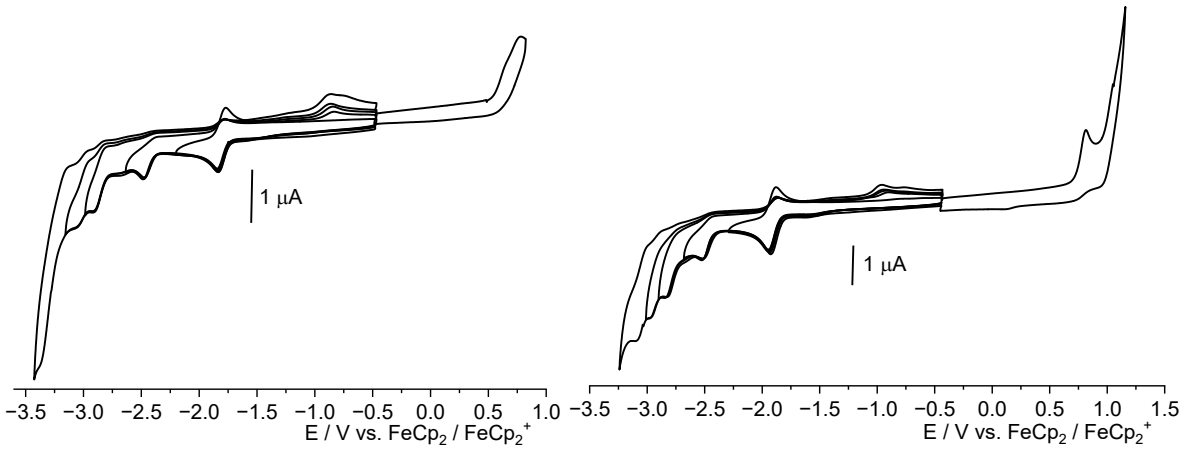

Figure 136 Cyclic voltammograms of [Pt(QPySpiro)Cl] (left) and [Pd(QPySpiro)Cl] (right) in 0.1 M NBu_4NPF_6 solution in THF at room temperature at a scan rate of 100 mV/s.

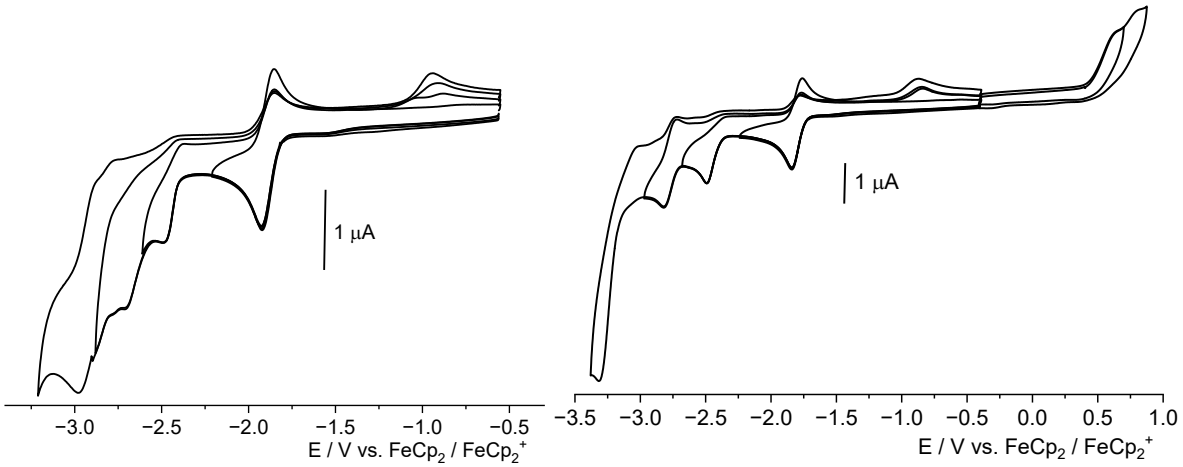

Figure 137 Cyclic voltammograms of [Pt(QPyFluor)Cl] (left) and [Pd(QPyFluor)Cl] (right) in 0.1 M NBu_4NPF_6 solution in THF at room temperature at a scan rate of 100 mV/s.

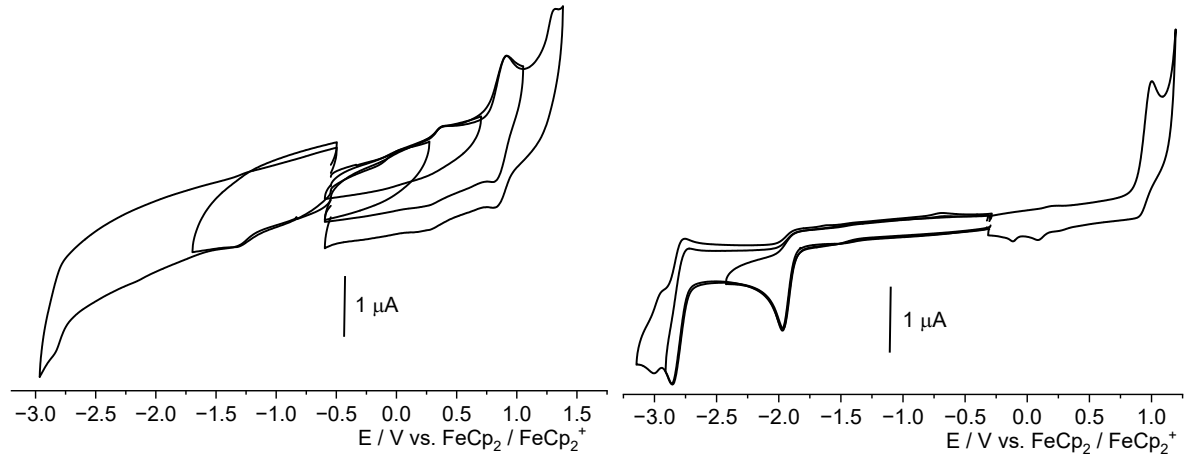

Figure 138 Cyclic voltammograms of [Pt(ThianPhThian)Cl] (left) and [Pt(DBTPhDBT)Cl] (right) in 0.1 M NBu_4NPF_6 solution in THF at room temperature at a scan rate of 100 mV/s.

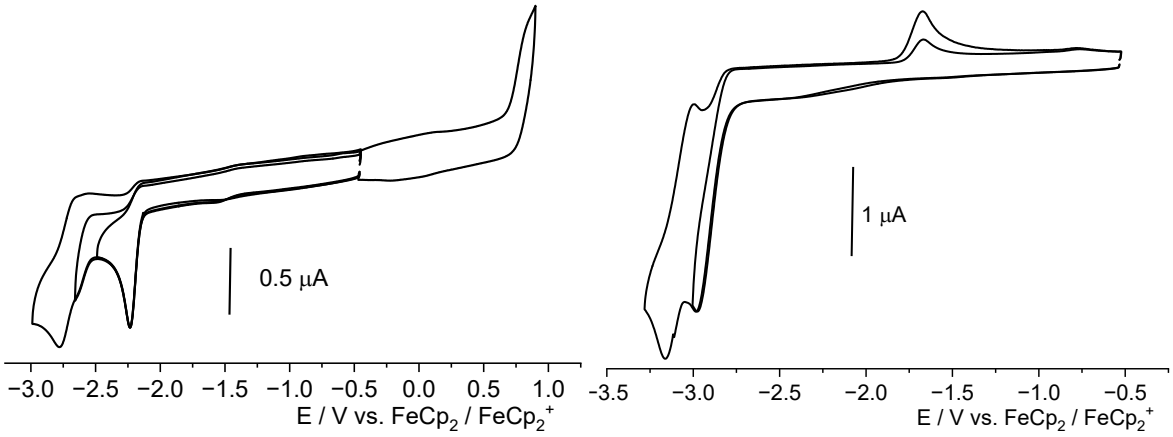

Figure 139 Cyclic voltammograms of [Pt(PyPhDBT)Cl] (left) and [Pd(PyPhDBT)Cl] (right) in 0.1 M NBu_4NPF_6 solution in THF at room temperature at a scan rate of 100 mV/s.

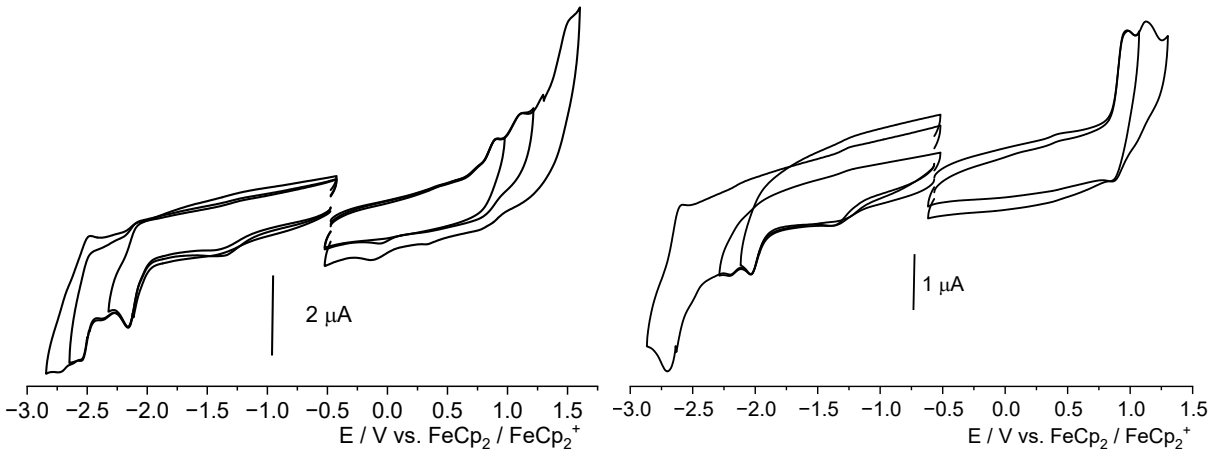

Figure 140 Cyclic voltammograms of [Pt(PyPhThian)Cl] (left) and [Pd(PyPhThian)Cl] (right) in 0.1 M NBu_4NPF_6 solution in THF at room temperature at a scan rate of 100 mV/s.

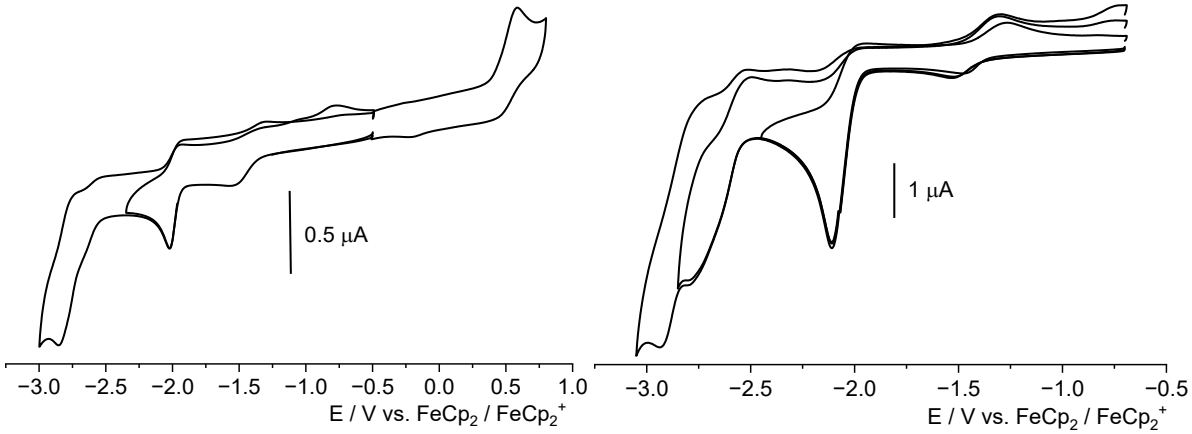

Figure 141 Cyclic voltammograms of [Pt(PyCarbQ)Cl] (left) and [Pd(PyCarbQ)Cl] (right) in 0.1 M NBu_4NPF_6 solution in THF at room temperature at a scan rate of 100 mV/s.

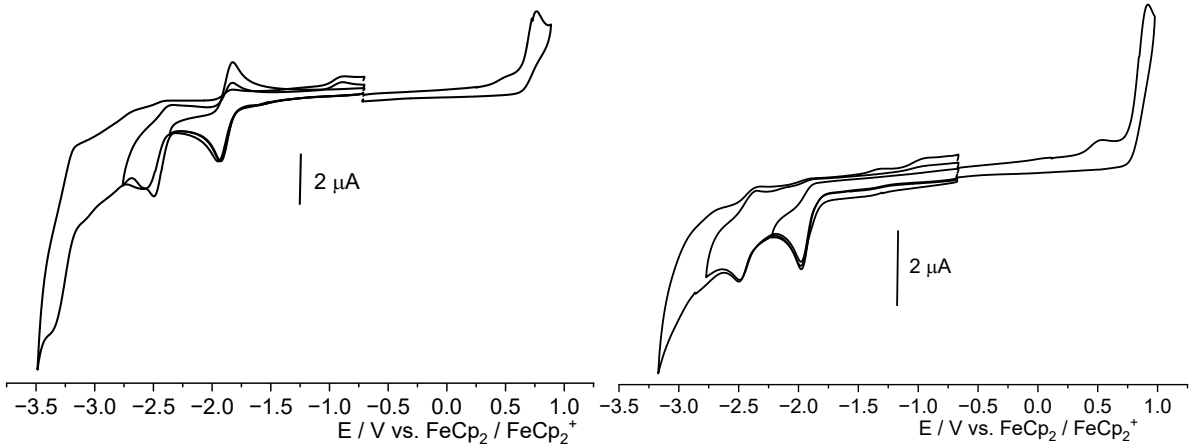

Figure 142 Cyclic voltammograms of [Pt(QPyCarb)Cl] (left) and [Pd(QPyCarb)Cl] (right) in 0.1 M NBu_4NPF_6 solution in THF at room temperature at a scan rate of 100 mV/s.

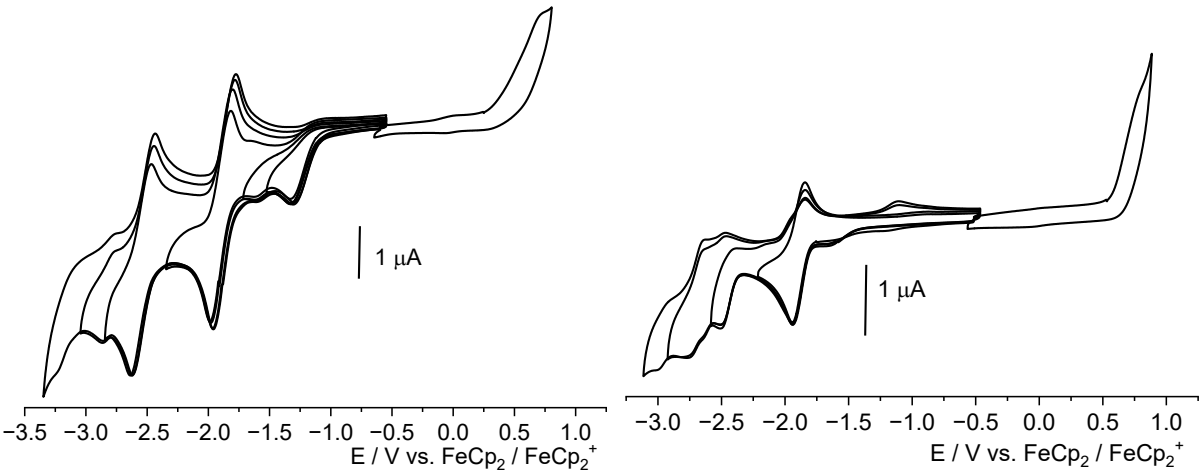

Figure 143 Cyclic voltammograms of [Pt(PyPyNaph)Cl] (left) and [Pd(PyPyNaph)Cl] (right) in 0.1 M NBu_4NPF_6 solution in THF at room temperature at a scan rate of 100 mV/s.

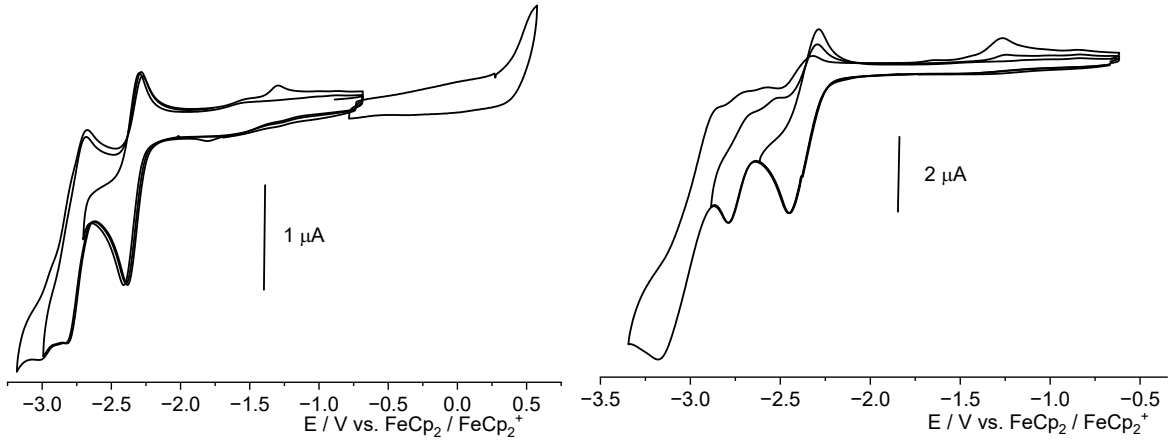

Figure 144 Cyclic voltammograms of [Pt(Py*t*BuPhPy)Cl] (left) and [Pd(Py*t*BuPhPy)Cl] (right) in 0.1 M NBu_4NPF_6 solution in THF at room temperature at a scan rate of 100 mV/s.

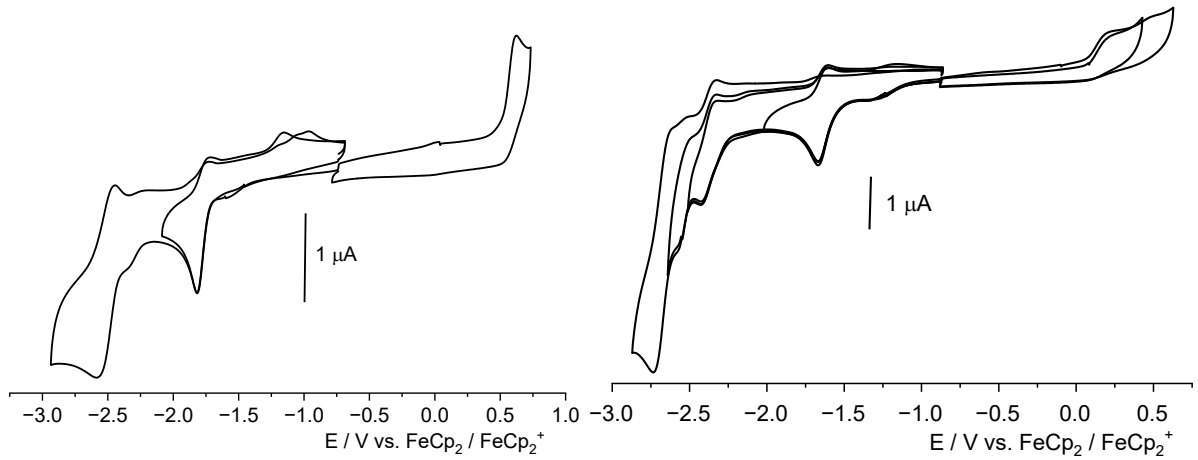

Figure 145 Cyclic voltammograms of [Pd(PyPyAnth)Cl] (left) and [Ni(PyPyAnth)Br] (right) in 0.1 M NBu_4NPF_6 solution in THF at room temperature at a scan rate of 100 mV/s.

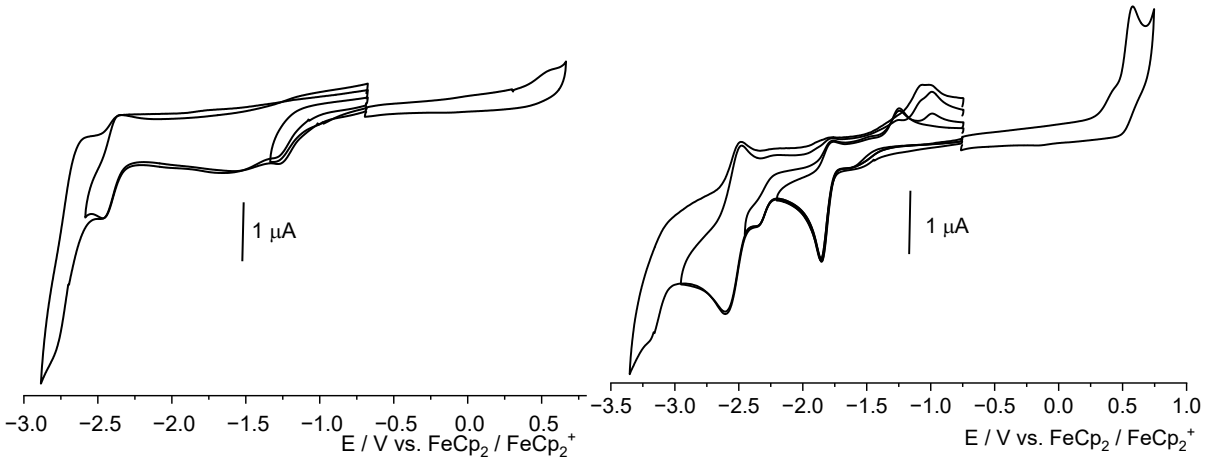

Figure 146 Cyclic voltammograms of [Pd(PyPyHAnth)Cl_2] (left) and mixture of [Pd(PyPyHAnth)Cl_2] + [Pd(PyPyAnth)Cl] (right) in 0.1 M NBu_4NPF_6 solution in THF at room temperature at a scan rate of 100 mV/s.

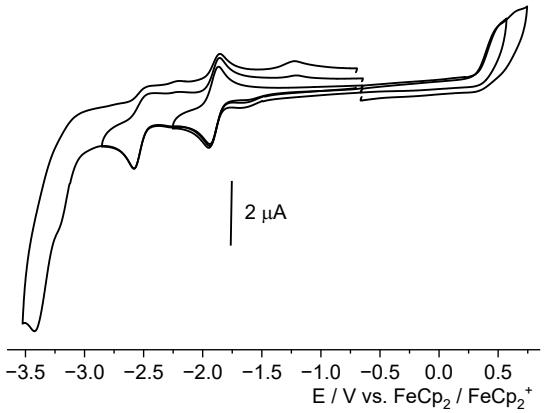

Figure 147 Cyclic voltammograms of [Pt(PyPyCarb)Cl] in 0.1 M NBu_4NPF_6 solution in THF at room temperature at a scan rate of 100 mV/s.

8.2.3 Cyclovoltammograms of Coligand Exchange Reactions

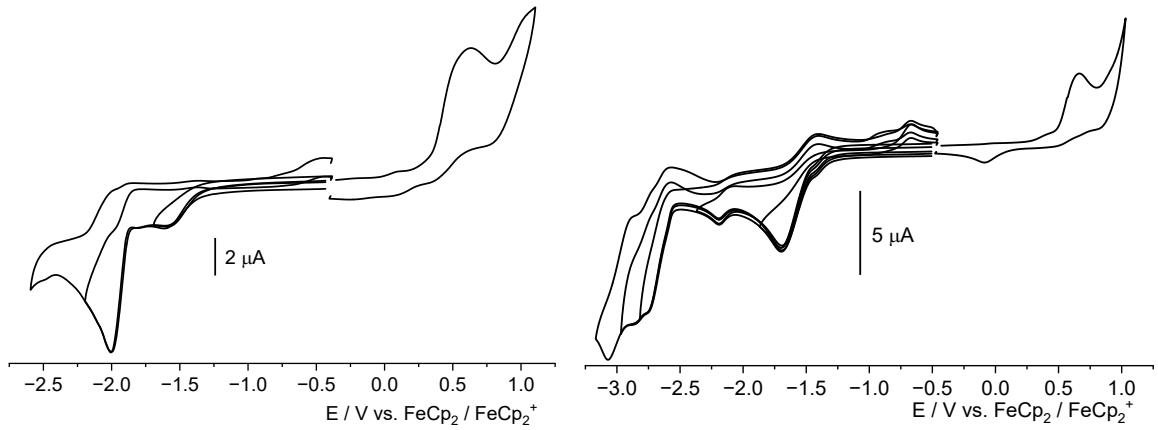

Figure 148 Cyclic voltammograms of [Pt(PyPhQ)NO_3] (left) and [Pd(PyPhQ)NO_3] (right) in 0.1 M NBu_4NPF_6 solution in THF at room temperature at a scan rate of 100 mV/s.

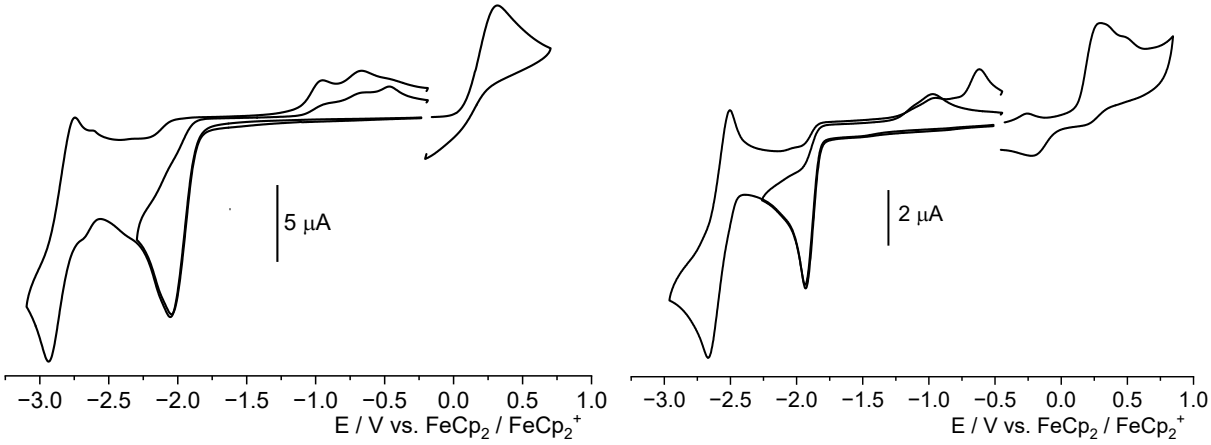

Figure 149 Cyclic voltammograms of [Ni(PyPhQ)NO_3] (left) and [Pt(PyPhQ)SCN] (right) in 0.1 M NBu_4NPF_6 solution in THF at room temperature at a scan rate of 100 mV/s.

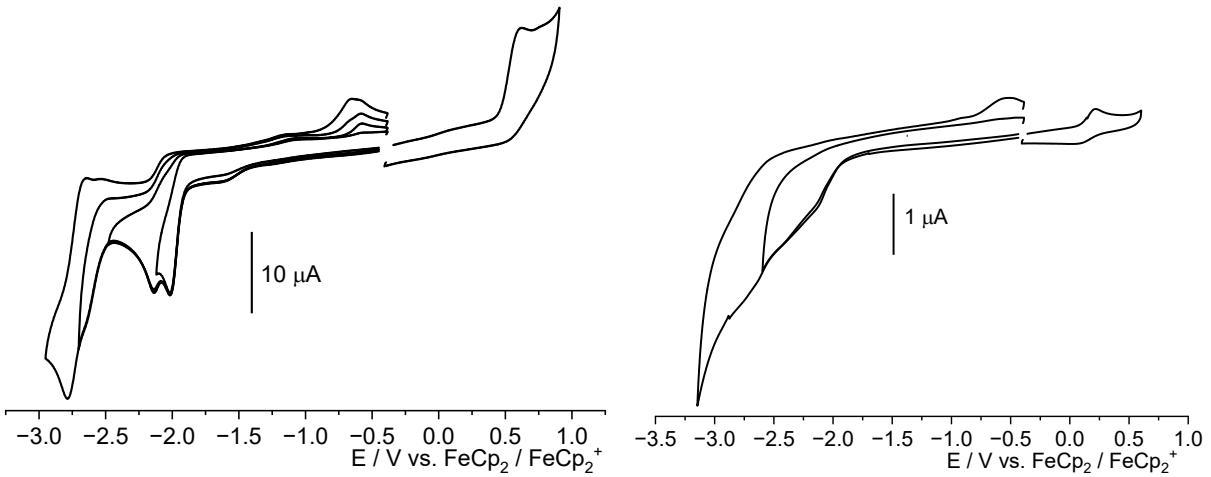

Figure 150 Cyclic voltammograms of [Pd(PyPhQ)SCN] (left) and [Ni(PyPhQ)SCN] (right) in 0.1 M NBu_4NPF_6 solution in THF at room temperature at a scan rate of 100 mV/s.

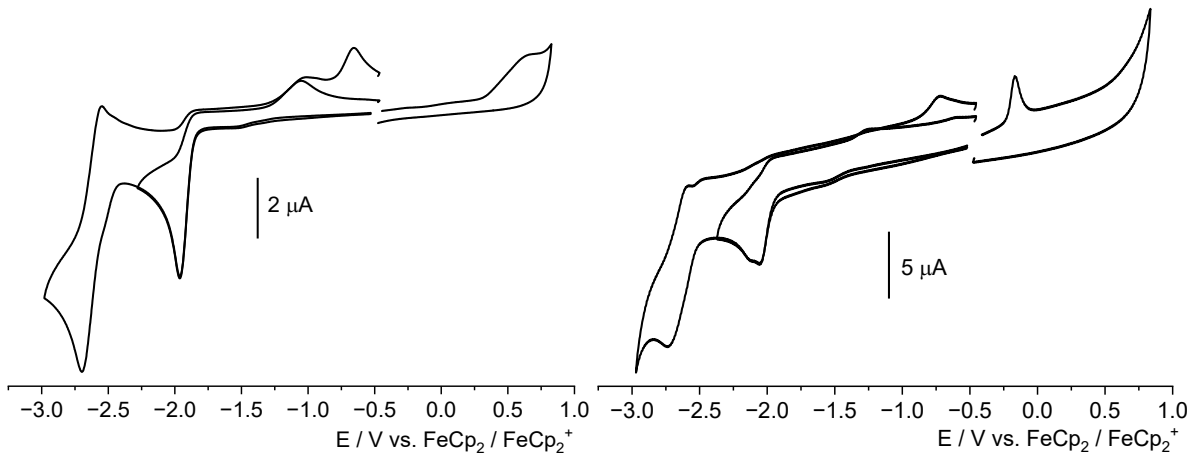

Figure 151 Cyclic voltammograms of [Pt(PyPhQ)CN] (left) and [Pd(PyPhQ)CN] (right) in 0.1 M NBu_4NPF_6 solution in THF at room temperature at a scan rate of 100 mV/s.

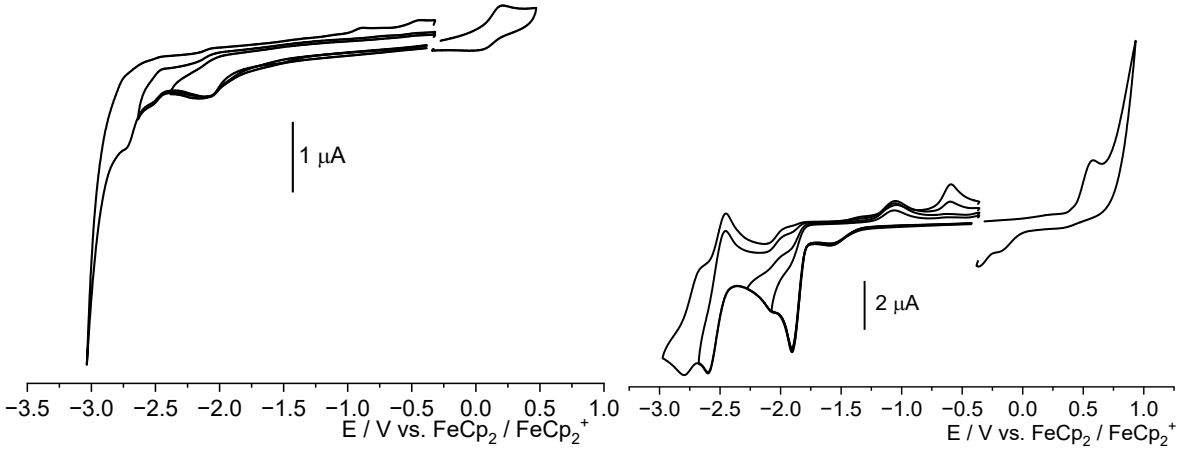

Figure 152 Cyclic voltammograms of [Ni(PyPhQ)CN] (left) and [Pt(PyPhQ)($N(CN)_2$)] (right) in 0.1 M NBu_4NPF_6 solution in THF at room temperature at a scan rate of 100 mV/s.

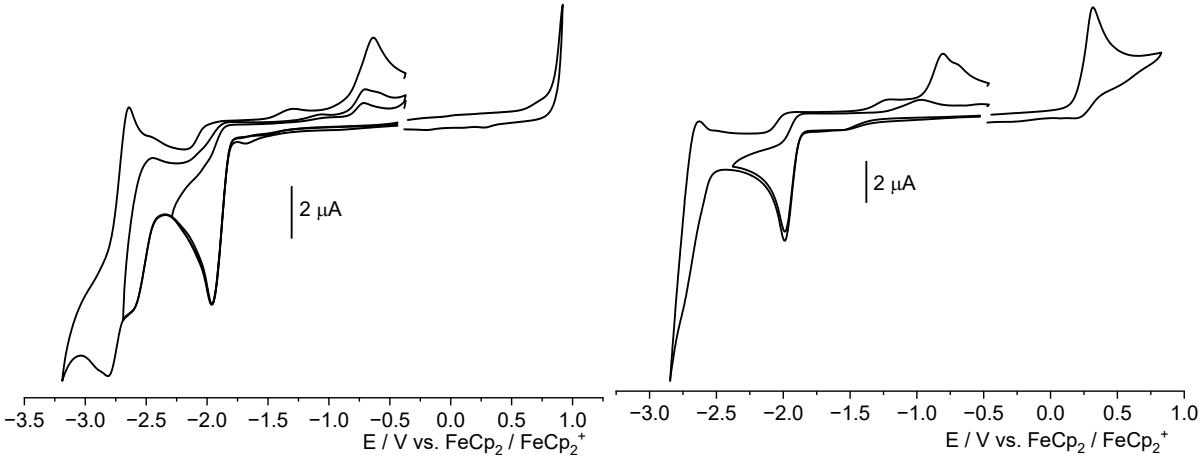

Figure 153 Cyclic voltammograms of [Pd(PyPhQ)($N(CN)_2$)] (left) and [Pt(PyPhQ)OBz] (right) in 0.1 M NBu_4NPF_6 solution in THF at room temperature at a scan rate of 100 mV/s.

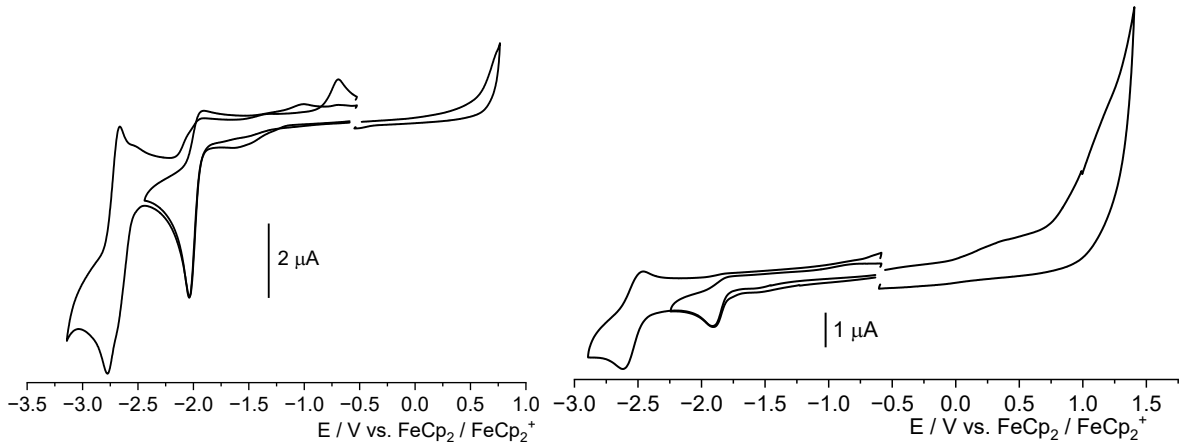

Figure 154 Cyclic voltammograms of [Pd(PyPhQ)OBz] (left) and [Pt(PyPhQ)(NCBH$_3$)] (right) in 0.1 M NBu$_4$NPF$_6$ solution in THF at room temperature at a scan rate of 100 mV/s.

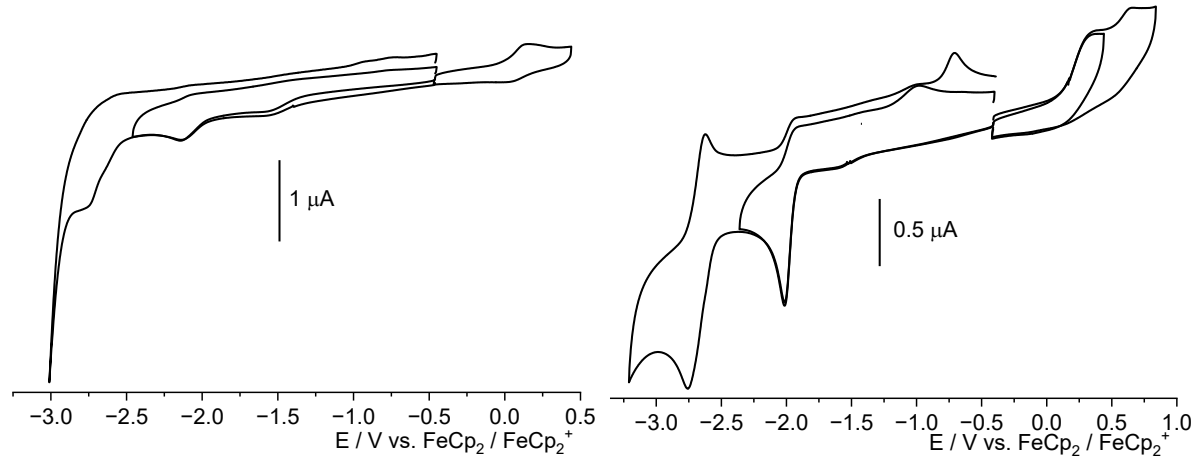

Figure 155 Cyclic voltammograms of [Ni(PyPhQ)C$_2$Ph] (left) and [Pt(PyPhQ)C$_2$Ph] (right) in 0.1 M NBu$_4$NPF$_6$ solution in THF at room temperature at a scan rate of 100 mV/s.

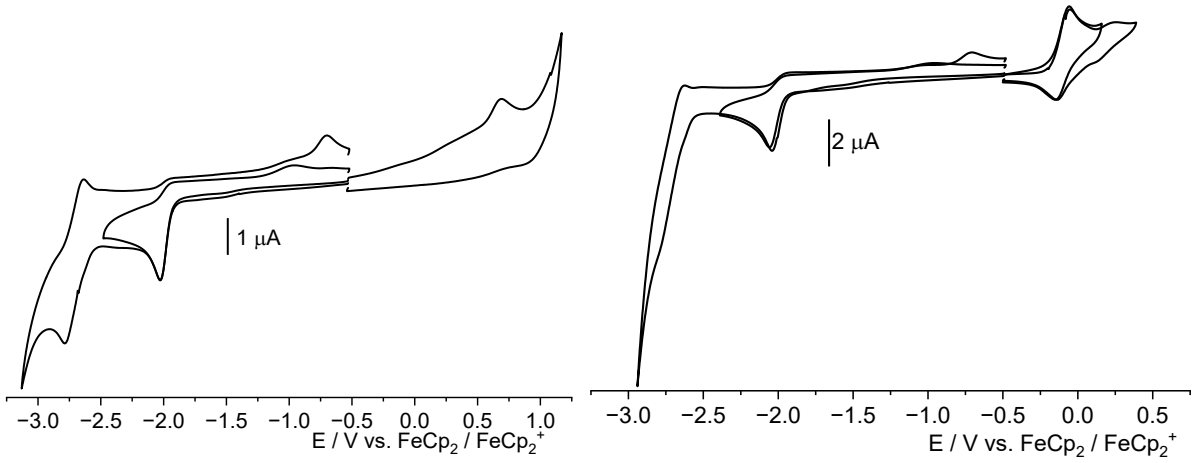

Figure 156 Cyclic voltammograms of [Pt(PyPhQ)C$_2$Si(CH$_3$)$_3$] (left) and [Pt(PyPhQ)C$_2$FeCp$_2$] (right) in 0.1 M NBu$_4$NPF$_6$ solution in THF at room temperature at a scan rate of 100 mV/s.

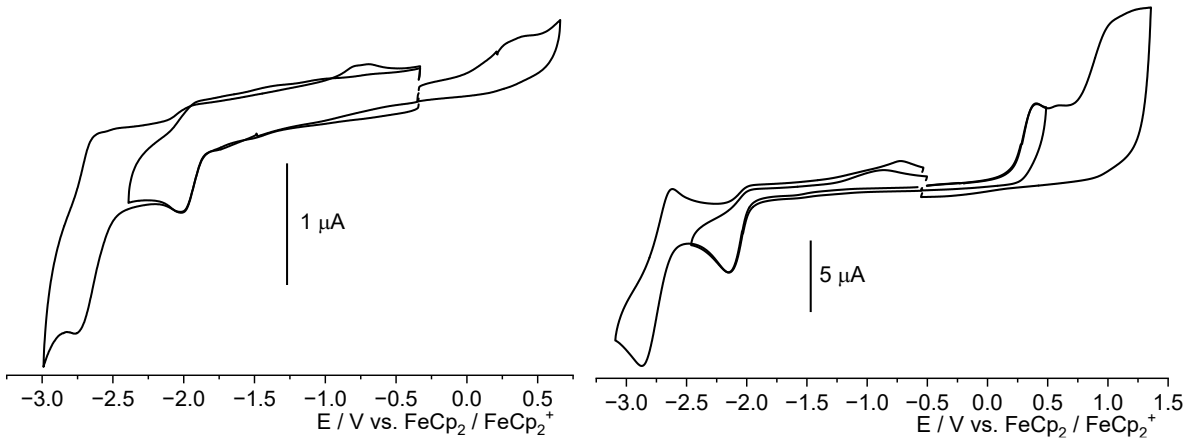

Figure 157 Cyclic voltammograms of [Pt(PyPhQ)C_2H] (left) and [Pt(PyPhQ)(NC_4H_4)] (right) in 0.1 M NBu_4NPF_6 solution in THF at room temperature at a scan rate of 100 mV/s.

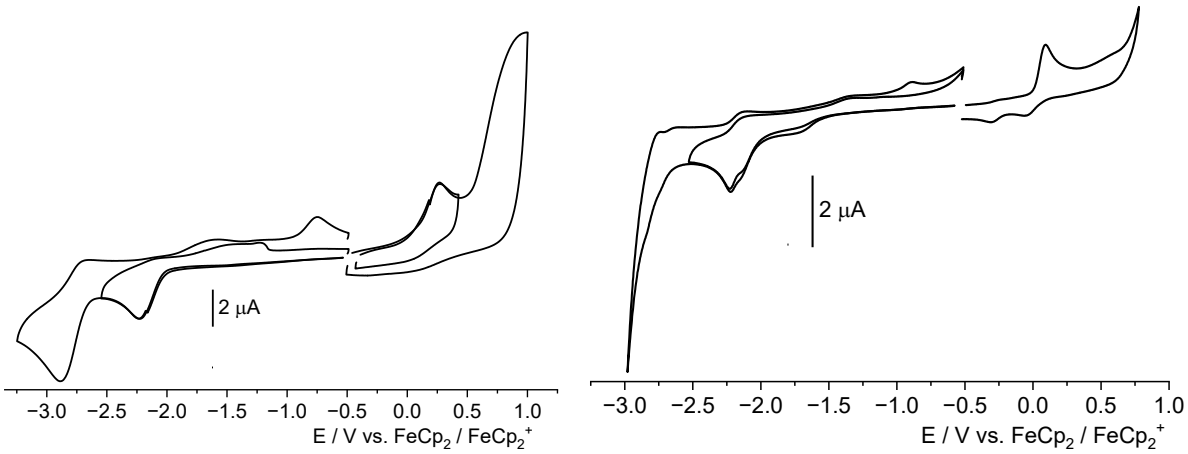

Figure 158 Cyclic voltammograms of [Pd(PyPhQ)(NC_4H_4)] (left) and [Pt(PyPhQ)($NC_{12}H_8$)] (right) in 0.1 M NBu_4NPF_6 solution in THF at room temperature at a scan rate of 100 mV/s.

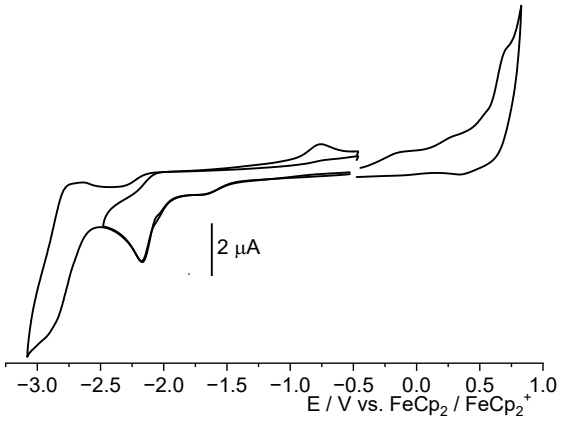

Figure 159 Cyclic voltammograms of [Pd(PyPhQ)($NC_{12}H_8$)] in 0.1 M NBu_4NPF_6 solution in THF at room temperature at a scan rate of 100 mV/s.

8.3 Crystallographic Data

8.3.1 Crystallographic Data of Complexes

Table 38 Crystal data and structure refinement for the complexes [Pd(QPyCarb)Cl], [Pd(PyCarbQ)Cl] and [Pt(QPyFluor)Cl].[a]

	[Pd(QPyCarb)Cl]	[Pd(PyCarbQ)Cl]	[Pt(QPyFluor)Cl]
CCDC			
Empirical formula	$C_{32}H_{27}ClN_3O_{1.5}Pd$	$C_{26}H_{16}ClN_3Pd$	$C_{29}H_{21}ClN_2Pt$
Formula weight (g mol^{-1})	619.41	512.27	628.02
Temperature (K) / wavelength (Å)	100 / 0.71073	100 / 0.71073	100 / 0.71073
Crystal System	monoclinic	monoclinic	monoclinic
Space group	*C*2/*c*	*C*2/*c*	$P2_1/n$
Unit cell dimensions			
a (Å)	23.7358(9)	24.099(2)	9.5553(4)
b (Å)	12.0571(4)	7.3951(5)	18.8865(8)
c (Å)	21.7073(1)	23.6398(2)	12.6657(5)
α (°)	90	90	90
β (°)	119.1980(1)	111.237(2)	93.7290(1)
γ (°)	90	90	90
Volume (Å^3) / Z	5423.0(4) / 8	3927.0(5) / 8	2280.9(2) / 4
δ_{calc} (g/cm^3) / μ(mm^{-1})	1.517 / 0.816	1733 / 1.101	1.829 / 6.289
F (000)	2520.0	2048.0	1216.0
Crystal size (mm^3)	0.16 × 0.06 × 0.04	0.07 × 0.04 × 0.04	0.36 × 0.09 × 0.08
2θ range for data collection (°)	3.908 to 56.582	5.8 to 52.746	3.878 to 55.752
Index ranges	–31 ≤ h ≤ 31	–30 ≤ h ≤ 28	–12 ≤ h ≤ 12
	–15 ≤ k ≤ 16	–9 ≤ k ≤ 9	–24≤ k ≤ 24
	–28 ≤ l ≤ 28	–28 ≤ l ≤ 29	–16 ≤ l ≤ 16
Reflections collected / Independent	67105 / 6724	25514 / 4005	60905/ 5404
R_{int}	0.0881	0.0890	0.0378
Completeness to θ / angle (°)	0.997 / 25.24	0.995 / 25.24	0.998 / 25.24
Absorption correction	Multi-Scan	Multi-Scan	Multi-Scan
Data / restraints / parameters	6724 / 0 / 348	4005 / 0 / 281	5404 / 0 / 300
GOOF on F^2	1.080	1.212	1.062
Final *R* indices [I>2σ(I)][a]	R_1 = 0.0469, wR_2 = 0.1185	R_1 = 0.0688, wR_2 = 0.1279	R_1 = 0.0151, wR_2 = 0.0328
R indices (all data)	R_1 = 0.0628, wR_2 = 0.1284	R_1 = 0.0847, wR_2 = 0.1348	R_1 = 0.0163, wR_2 = 0.0333
Largest diff. peak / hole (e ×Å^{-3})	0.87 / –0.80	1.12 / –1.25	0.48 / –0.71

[a] From single crystal X-ray diffraction. $R_1 = \Sigma||F_o| - |F_c||/\Sigma|F_o||$; $wR_2 = \left[\Sigma\left[w\left(F_o^2 - F_c^2\right)^2\right]/\Sigma\left[w\left(F_o^2\right)^2\right]\right]^{1/2}$

Table 39 Crystal data and structure refinement for the complexes [Pd(QPyFluor)Cl] and [Pt(QPySpiro)Cl].[a]

	[Pd(QPyFluor)Cl]	[Pt(QPySpiro)Cl]
CCDC		
Empirical formula	$C_{29}H_{21}ClN_2Pd$	$C_{39}H_{23}ClN_2Pt$
Formula weight (g mol^{-1})	539.33	750.02
Temperature (K) / wavelength (Å)	100 / 0.71073	100 / 0.71073
Crystal System	monoclinic	Orthorhombic
Space group	$P2_1/n$	*Pbca*
Unit cell dimensions		
a (Å)	9.5690(3)	23.7574(2)
b (Å)	18.8990(6)	14.0964(1)
c (Å)	12.5953(4)	36.236(3)
α (°)	90	90
β (°)	93.7490(1)	90
γ (°)	90	90
Volume (Å^3) / Z	2272.9(1) / 4	12135.3(2) / 16
δ_{calc} (g/cm^3) / μ(mm^{-1})	1.576/ 0.955	1.642 / 4.741
F (000)	1088.0	5856.0
Crystal size (mm^3)	0.35 × 0.11 × 0.03	0.06 × 0.07 × 0.05
2θ range for data collection (°)	3.892 to 56.608	4.042 to 50.7
Index ranges	–12 ≤ h ≤ 12	–28 ≤ h ≤ 28
	–25 ≤ k ≤ 25	–14 ≤ k ≤ 16
	–14 ≤ l ≤ 16	–43 ≤ l ≤ 43
Reflections collected / Independent	75270 / 5657	71937 / 11078
R_{int}	0.0655	0.0689
Completeness to θ / angle (°)	0.994 / 25.24	0.998 / 25.24
Absorption correction	Multi-Scan	Multi-Scan
Data / restraints / parameters	5657/ 0 / 300	11078 / 0 / 775
GOOF on F^2	1.088	1.120
Final *R* indices [I>2σ(I)][a]	R_1 = 0.0339, wR_2 = 0.0804	R_1 = 0.0753, wR_2 = 0.1405
R indices (all data)	R_1 = 0.0403, wR_2 = 0.0849	R_1 = 0.0989, wR_2 = 0.1554
Largest diff. peak / hole (e ×Å^{-3})	0.87 / –0.93	2.30 / –1.15

[a] From single crystal X-ray diffraction. $R_1 = \Sigma||F_o| - |F_c||/\Sigma|F_o|$; $wR_2 = \left[\Sigma\left[w\left(F_o^2 - F_c^2\right)^2\right]/\Sigma\left[w\left(F_o^2\right)^2\right]\right]^{1/2}$

Table 40 Crystal data and structure refinement for the complexes [Pt(PyPhThian)Cl], [Pd(PyPhThian)Cl] and [Pt(PyPhDBT)Cl].[a]

	[Pt(PyPhThian)Cl]	[Pd(PyPhThian)Cl]	[Pt(PyPhDBT)Cl].
Empirical formula	$C_{23}H_{14}ClNPtS_2$	$C_{23}H_{14}ClNPdS_2$	$C_{23}H_{14}ClNPtS$
Formula weight (g mol^{-1})	599.01	510.32	1133.90
Temperature (K) / wavelength (Å)	100 / 0.71073	100/ 0.71073	100 / 0.71073

Crystal System	monoclinic	monoclinic	monoclinic
Space group	$P2_1/n$	$C2/c$	$P2_1/c$
Unit cell dimensions			
a (Å)	12.0138(5)	14.8716(4)	18.3211(7)
b (Å)	14.6963(5)	11.1642(6)	10.8298(5)
c (Å)	12.8261(5)	25.0118(8)	19.5878(9)
α (°)	90	90	90
β (°)	105.7150(10)	93.2250(2)	94.934(2)
γ (°)	90	90	90
Volume (Å^3) / Z	2179.9(2) / 4	4146.1(2) / 8	3872.1(3) / 8
δ_{calc} (g/cm^3) / μ(mm^{-1})	1.825 / 6.759	1.635 / 1.234	1.945 / 7.500
F (000)	1144.0	2032.0	2160.0
Crystal size (mm^3)	0.2 × 0.09 × 0.08	0.13 × 0.07 × 0.02	0.08 × 0.04 × 0.01
2θ range for data collection (°)	4.308 to 55.754	4.564 to 56.582	4.174 to 56.626
Index ranges	–15 ≤ h ≤ 15	–19 ≤ h ≤ 19	–24 ≤ h ≤ 23
	–19 ≤ k ≤ 19	–14 ≤ k ≤ 14	–14 ≤ k ≤ 14
	–16 ≤ l ≤ 16	–33 ≤ l ≤ 33	–26 ≤ l ≤ 26
Reflections collected / Independent	69192 / 5157	64107 / 5151	99082/ 9627
R_{int}	0.0402	0.0718	0.0728
Completeness to θ / angle (°)	0.993 / 25.24	0.997 / 25.24	0.999 / 28.31
Absorption correction	Multi-Scan	Multi-Scan	Multi-Scan
Data / restraints / parameters	5157 / 0 / 253	5151 / 0 / 253	9627 / 0 / 487
GOOF on F^2	1.068	1.015	1.062
Final *R* indices [I>2σ(I)][a]	R_1 = 0.0166, wR_2 = 0.0369	R_1 = 0.0242, wR_2 = 0.0595	R_1 = 0.0525, wR_2 = 0.1038
R indices (all data)	R_1 = 0.0172, wR_2 = 0.0372	R_1 = 0.0275, wR_2 = 0.0621	R_1 = 0.0652, wR_2 = 0.1120
Largest diff. peak / hole (e ×Å^{-3})	1.04 / –0.46	0.45 / –0.53	1.45 / –1.87

[a] From single crystal X-ray diffraction. $R_1 = \Sigma||F_o| - |F_c||/\Sigma|F_o||$; $wR_2 = \left[\Sigma\left[w\left(F_o^2 - F_c^2\right)^2\right]/\Sigma\left[w\left(F_o^2\right)^2\right]\right]^{1/2}$

Table 41 Crystal data and structure refinement for the complexes [Pd(PyPyHAnth)Cl$_2$] and [Pd(PyPyAnthO$_2$)Cl].[a]

	[Pd(PyPyHAnth)Cl$_2$]	[Pd(PyPyAnthO$_2$)Cl]
CCDC		
Empirical formula	$C_{48}H_{32}Cl_4N_4Pd_2$	$C_{24}H_{15}ClN_2O_2Pd$
Formula weight (g mol^{-1})	1019.37	502.23
Temperature (K) / wavelength (Å)	100 / 0.71073	100 / 0.71073
Crystal System	monoclinic	monoclinic
Space group	$P2_1$	$C2/c$
Unit cell dimensions		
a (Å)	9.1211(2)	20.42(2)
b (Å)	13.3968(3)	7.468(9)

c (Å)	16.0617(4)	29.12(4)
α (°)	90	90
β (°)	96.6380(1)	107.69(3)
γ (°)	90	90
Volume (Å^3) / Z	1949.48(8) / 2	4230(1) / 8
δ_{calc} (g/cm^3) / μ(mm^{-1})	1.737 / 10.299	1.587 / 1.026
F (000)	1016.0	2016.0
Crystal size (mm^3)	0.07 × 0.01 × 0.01	0.12 × 0.02 × 0.02
2θ range for data collection (°)	5.540 to 144.08	4.322 to 50.696
Index ranges	–11 ≤ h ≤ 10	–20 ≤ h ≤ 24
	–16 ≤ k ≤ 16	–8 ≤ k ≤ 0
	–19 ≤ l ≤ 19	–20 ≤ l ≤ 35
Reflections collected / Independent	44423 / 7546	3446 / 3446
R_{int}	0.0867	0.1045
Completeness to θ / angle (°)	0.986 / 67.68	0.955 / 24.71
Absorption correction	Multi-Scan	Multi-Scan
Data / restraints / parameters	7546 / 1 / 523	3535 / 48 / 271
GOOF on F^2	0.700	1.127
Final *R* indices [I>2σ(I)][a]	R_1 = 0.0297, wR_2 = 0.0853	R_1 = 0.1354, wR_2 = 0.2512
R indices (all data)	R_1 = 0.0316, wR_2 = 0.0866	R_1 = 0.1756 wR_2 = 0.2779
Largest diff. peak / hole (e ×Å^{-3})	0.56/ –0.64	1.57 / –1.20

[a] From single crystal X-ray diffraction. $R_1 = \Sigma||F_o| - |F_c||/\Sigma|F_o||$; $wR_2 = \left[\Sigma\left[w\left(F_o^2 - F_c^2\right)^2\right]/\Sigma\left[w\left(F_o^2\right)^2\right]\right]^{1/2}$

8.3.2 Crystallographic Data of Coligand Exchange Reactions

Table 42 Crystal data and structure refinement for the complexes [Pt(PyPhQ)CN], [Ni(PyPhQ)NO$_3$] and [Pt(PyPhQ)NO$_3$][a]

	[Pt(PyPhQ)CN]	[Ni(PyPhQ)NO$_3$]	[Pt(PyPhQ)NO$_3$]
CCDC			
Empirical formula	$C_{21}H_{13}N_3Pt$	$C_{20}H_{13}N_3O_3Ni$	$C_{20}H_{13}N_3O_3Pt$
Formula weight (g mol^{-1})	502.43	402.04	538.42
Temp. (K) / wavelength (Å)	100 / 0.71073	100 / 0.71073	100 / 0.71073
Crystal System	monoclinic	triclinic	monoclinic
Space group	$P2_1/c$	$P\bar{1}$	$P2_1/n$
Unit cell dimensions			
a (Å)	9.6532(5)	7.3073(4)	7.2377(2)
b (Å)	11.7129(6)	9.1449(5)	22.3117(8)
c (Å)	14.0695(7)	12.4297(6)	9.7253(4)
α (°)	90	103.192(2)	90
β (°)	96.371(2)	98.795(2)	91.036(1)
γ (°)	90	91.582(2)	90
Volume (Å^3) / Z	1581.0(1) / 4	797.49(7) / 2	1570.2(1) / 4
δ_{calc} (g/cm^3) / μ(mm^{-1})	2.111 / 8.883	1.674 / 1.245	2.278 / 8.695
F (000)	952.0	412.0	1024.0

Crystal size (mm^3)	0.07 × 0.01 × 0.01	0.08 × 0.04 × 0.03	0.11 × 0.02 × 0.02
2θ range for data collection (°)	4.536 to 50.694	4.584 to 56.608	4.57 to 50.696
Index ranges	–11 ≤ h ≤ 11	–9 ≤ h ≤ 9	–8 ≤ h ≤ 8
	–14 ≤ k ≤ 14	–12 ≤ k ≤ 12	–26 ≤ k ≤ 26
	–16 ≤ l ≤ 16	–16 ≤ l ≤ 16	–11 ≤ l ≤ 11
Ref. collected / Indep.	22637 / 2876	60282 / 3959	24781 / 2880
R_{int}	0.0348	0.0425	0.0683
Completeness to θ / angle (°)	0.992 / 25.242	0.998 / 25.242	1 / 25.242
Absorption correction	Multi-Scan	Multi-Scan	Multi-Scan
Data / restraints / parameters	2876 / 0 / 226	3959 / 0 / 244	2880 / 235 / 244
GOOF on F^2	1.075	1.076	1.103
Final *R* indices [I>2σ(I)][a]	R_1 = 0.0247, wR_2 = 0.0601	R_1 = 0.0287, wR_2 = 0.0706	R_1 = 0.0282, wR_2 = 0.0566
R indices (all data)	R_1 = 0.0268, wR_2 = 0.0613	R_1 = 0.0314 wR_2 = 0.0730	R_1 = 0.0342 wR_2 = 0.0591
Largest diff. peak / hole (e ×$Å^{-3}$)	2.29/ –0.67	0.65/ –0.28	0.97/ –2.34

[a] From single crystal X-ray diffraction. $R_1 = \Sigma||F_o| - |F_c||/\Sigma|F_o||$; $wR_2 = \left[\Sigma\left[w\left(F_o^2 - F_c^2\right)^2\right]/\Sigma\left[w\left(F_o^2\right)^2\right]\right]^{1/2}$

Table 43 Crystal data and structure refinement for the complexes [Pt(PyPhQ)C_2Ph], [Pt(PyPhQ)C_2FeCp_2]and[Pt(PyPhQ)CNBH_3].[a]

	[Pt(PyPhQ)C_2Ph]	[Pt(PyPhQ)C_2FeCp_2]	[Pt(PyPhQ)CNBH_3]
CCDC			
Empirical formula	$C_{28}H_{18}N_2Pt$	$C_{32}H_{22}FeN_2Pt$	$C_{45.5}H_{36}B_2N_6Pt_2$
Formula weight (g mol^{-1})	577.53	685.45	1078.60
Temp. (K) / wavelength (Å)	100 / 0.71073	109 / 0.71073	100 / 0.71073
Crystal System	monoclinic	triclinic	triclinic
Space group	$P2_1/c$	$P\bar{1}$	$P\bar{1}$
Unit cell dimensions			
a (Å)	14.6904(9)	7.5921(6)	7.0462(5)
b (Å)	10.1649(5)	10.7789(9)	13.069(2)
c (Å)	16.0805(9)	13.8544(1)	21.417(2)
α (°)	90	85.215(3)	72.456(4)
β (°)	110.560(2)	86.562(3)	89.491(3)
γ (°)	90	88.917(3)	84.736(3)
Volume ($Å^3$) / Z	2248.3(2) / 4	1127.7(2) / 2	1872.3(3) / 2
δ_{calc} (g/cm^3) / μ(mm^{-1})	1.706 / 6.258	2.019 / 6.866	1.913/ 7.507
F (000)	1112.0	664.0	1034.0
Crystal size (mm^3)	0.05 × 0.04 × 0.01	0.06 × 0.03 × 0.01	0.15 × 0.04 × 0.01
2θ range for data collection (°)	4.836 to 50.696	3.792 to 50.698	3.99 to 50.694
Index ranges	–17 ≤ h ≤ 17	–9 ≤ h ≤ 9	-8 ≤ h ≤ 8
	–12 ≤ k ≤ 12	–12 ≤ k ≤ 12	-15 ≤ k ≤ 15
	–19 ≤ l ≤ 19	0 ≤ l ≤ 16	-25 ≤ l ≤ 25
Ref. collected / Indep.	85095 / 4115	4106 / 4106	55833 / 6867

R_{int}	0.0722	0.0616	0.0478
Completeness to θ / angle (°)	1.0 / 25.348	0.996 / 25.242	0.997 / 25.24
Absorption correction	Multi-Scan	Multi-Scan	Multi-Scan
Data / restraints / parameters	4115 / 0 / 280	4106 / 0 / 320	6867/136/535
GOOF on F^2	1.069	1.156	1.100
Final *R* indices [I>2σ(I)][a]	R_1 = 0.0253, wR_2 = 0.0601	R_1 = 0.0485, wR_2 = 0.1284	R_1 = 0.0372, wR_2 = 0.0881
R indices (all data)	R_1 = 0.0328, wR_2 = 0.0630	R_1 = 0.0518, wR_2 = 0.1312	R_1 = 0.0428, wR_2 = 0.0913
Largest diff. peak / hole (e ×Å^{-3})	1.04/ –1.12	5.48/ –1.92	3.91/-1.82

[a] From single crystal X-ray diffraction. $R_1 = \Sigma||F_o| - |F_c||/\Sigma|F_o||$; $wR_2 = \left[\Sigma\left[w\left(F_o{}^2 - F_c{}^2\right)^2\right]/\Sigma\left[w\left(F_o{}^2\right)^2\right]\right]^{1/2}$

Table 44 Crystal data and structure refinement for the complexes [Pt(PyPhQ)($NC_{12}H_8$)].[a]

	[Pt(PyPhQ)($NC_{12}H_8$)]
CCDC	
Empirical formula	$C_{32}H_{21}N_3Pt$
Formula weight (g mol^{-1})	642.21
Temp. (K) / wavelength (Å)	103
Crystal System	triclinic
Space group	$P\bar{1}$
Unit cell dimensions	
a (Å)	9.2421(6)
b (Å)	12.9189(7)
c (Å)	12.9535(8)
α (°)	87.787(2)
β (°)	79.812(2)
γ (°)	89.144(2)
Volume (Å^3) / Z	1521.05(16) / 2
δ_{calc} (g/cm^3) / μ(mm^{-1})	1.402 / 4.622
F (000)	624.0
Crystal size (mm^3)	0.15 × 0.1 × 0.03
2θ range for data collection (°)	4.41 to 50.694
Index ranges	-11 ≤ h ≤ 11
	-15 ≤ k ≤ 15
	-15 ≤ l ≤ 15
Ref. collected / Indep.	66004
R_{int}	0.0584
Completeness to θ / angle (°)	0.999 / 25.347
Absorption correction	Multi-Scan
Data / restraints / parameters	5573/0/325
GOOF on F^2	1.062
Final *R* indices [I>2σ(I)][a]	R_1 = 0.0203, wR_2 = 0.0478

R indices (all data)	R_1 = 0.0222, wR_2 = 0.0488
Largest diff. peak / hole (e ×Å^{-3})	0.80/0.90

[a] From single crystal X-ray diffraction. $R_1 = \Sigma||F_o| - |F_c||/\Sigma|F_o|$; $wR_2 = \left[\Sigma\left[w\left(F_o^2 - F_c^2\right)^2\right]/\Sigma\left[w\left(F_o^2\right)^2\right]\right]^{1/2}$

8.4 DFT-Calculated Coordinates of Optimized Ground State S_0 Complex Structures

Table 45 Calculated coordinates of the optimized singlet ground state S_0 structures of the complexes [Pt(PyPhThian)Cl] and [Pd(PyPhThian)Cl]. [a]

[Pt(PyPhThian)Cl].				[Pd(PyPhThian)Cl]			
	coordinates (Å)				coordinates (Å)		
	X	Y	Z		X	Y	Z
Pt	0.8498910	-0.5418470	-0.3158020	Pd	0.9469570	-0.6211060	-0.3675100
Cl	0.5902540	-2.8425270	-1.0844490	Cl	0.6756850	-2.8624530	-1.2535350
S	-1.3206760	-0.2491450	-0.7669400	S	-1.2297240	-0.2720900	-0.8248410
S	-4.3119920	0.1230940	-0.9819140	S	-4.2424080	0.1261160	-0.9340750
N	2.8563270	-0.7452360	0.0499200	N	2.9465560	-0.8581360	0.0278370
C	3.1632000	2.8838800	0.4057180	C	3.2929890	2.7713010	0.2932950
C	2.6339450	1.5993010	0.2954600	C	2.7449380	1.4899720	0.2305750
C	1.2385530	1.3630140	0.1272960	C	1.3455500	1.2782080	0.0877930
C	0.3709740	2.4800530	0.1528270	C	0.4947450	2.4028340	0.0985610
C	0.9525180	3.7666660	0.1895980	C	1.0928250	3.6832320	0.0869320
C	2.3150570	3.9755630	0.3164010	C	2.4602810	3.8727910	0.1820790
C	3.4957150	0.4214080	0.3232910	C	3.5949790	0.3024910	0.2890690
C	-1.1209180	2.4348960	0.1280140	C	-0.9972170	2.3815620	0.1173080
C	4.8607490	0.4108280	0.6133830	C	4.9558940	0.2845390	0.5988870
C	5.5560040	-0.7877350	0.6248550	C	5.6357330	-0.9230810	0.6395770
C	4.8780150	-1.9707710	0.3460320	C	4.9483530	-2.1026030	0.3711740
C	3.5255330	-1.9095830	0.0618800	C	3.5990400	-2.0278940	0.0674990
C	-1.9250890	1.3564300	-0.2952210	C	-1.8229370	1.3194570	-0.3001950
C	-3.3215140	1.4767030	-0.3977070	C	-3.2199070	1.4557120	-0.3526870
C	-3.9688920	2.6522310	-0.0374390	C	-3.8405620	2.6320190	0.0523050
C	-3.2054470	3.7018290	0.4529480	C	-3.0504210	3.6665770	0.5319990
C	-1.8286230	3.5832640	0.5410020	C	-1.6721130	3.5327890	0.5704650
C	-2.3440370	-1.2646490	0.3001720	C	-2.2354860	-1.3159590	0.2274850
C	-3.7204840	-1.1323500	0.1120820	C	-3.6169770	-1.1643830	0.0982630
C	-1.8378900	-2.1784180	1.2200830	C	-1.7050620	-2.2681260	1.0933970
C	-2.7210850	-3.0042450	1.9076370	C	-2.5687870	-3.1083320	1.7879620
C	-4.0948780	-2.9058970	1.6926140	C	-3.9487290	-2.9864990	1.6338680
C	-4.6012510	-1.9570850	0.8120990	C	-4.4780790	-2.0033030	0.8062420
H	4.2296590	3.0362190	0.5200250	H	4.3634940	2.9103410	0.3853130
H	0.3238910	4.6399160	0.0865050	H	0.4707230	4.5600280	-0.0296060

H	2.7080900	4.9847160	0.3379020	H	2.8701180	4.8753730	0.1640220
H	5.3708320	1.3374220	0.8373770	H	5.4742980	1.2080780	0.8169670
H	6.6150860	-0.7991740	0.8521210	H	6.6913380	-0.9435030	0.8823690
H	5.3810380	-2.9284380	0.3457050	H	5.4406570	-3.0656710	0.3940530
H	2.9374190	-2.7861650	-0.1747770	H	3.0037320	-2.9012400	-0.1647370
H	-5.0470180	2.7205730	-0.1077940	H	-4.9197030	2.7129320	0.0206330
H	-3.6860390	4.6135990	0.7869780	H	-3.5103790	4.5775410	0.8958680
H	-1.2830290	4.4107750	0.9697290	H	-1.0986000	4.3461640	0.9908500
H	-0.7705170	-2.2561820	1.3721070	H	-0.6328510	-2.3660860	1.1943680
H	-2.3316200	-3.7272050	2.6143150	H	-2.1594970	-3.8600850	2.4520750
H	-4.7767760	-3.5540670	2.2302620	H	-4.6165450	-3.6443220	2.1774290
H	-5.6693740	-1.8434930	0.6718340	H	-5.5495300	-1.8742200	0.7126030

[a] DFT calculations on TPSSh/def2-TZVP/CPCM(THF) level of theory.

Table 46 Calculated coordinates of the optimized singlet ground state S_0 structures of the complexes [Pt(PyPhDBT)Cl] and [Pd(PyPhDBT)Cl]. [a]

[Pt(PyPhDBT)Cl].				[Pd(PyPhDBT)Cl]			
	coordinates (Å)				coordinates (Å)		
	X	Y	Z		X	Y	Z
Pt	0.6377680	-0.6587590	0.0712660	Pd	0.7139890	-0.7570970	0.0177510
Cl	0.2164210	-3.0471340	0.0302850	Cl	0.2051010	-3.1050890	-0.1627520
S	-1.4041430	-0.1584030	0.8715190	S	-1.3074930	-0.2097050	0.8892390
N	2.6378810	-0.8542070	-0.3158040	N	2.7280350	-0.9821930	-0.3114110
C	3.1539300	2.6923520	0.5042500	C	3.2634160	2.5437490	0.5735910
C	2.5705880	1.4528440	0.2314850	C	2.6697220	1.3115050	0.2848170
C	1.1614590	1.2812250	0.1797020	C	1.2622730	1.1737190	0.1838230
C	0.3605620	2.4457920	0.2745870	C	0.4765080	2.3456300	0.2562420
C	0.9715640	3.6741790	0.5827450	C	1.0979020	3.5669170	0.5761400
C	2.3463610	3.7988000	0.7217150	C	2.4692400	3.6658510	0.7567100
C	3.3674760	0.2722830	-0.0890690	C	3.4632230	0.1209220	-0.0160710
C	-1.0872840	2.4547540	-0.0364310	C	-0.9660940	2.3738180	-0.0754180
C	4.7555030	0.2351060	-0.2268680	C	4.8566290	0.0601740	-0.0690340
C	5.3831630	-0.9397570	-0.6084480	C	5.4822410	-1.1209390	-0.4370570
C	4.6137240	-2.0730920	-0.8542110	C	4.7079380	-2.2330560	-0.7516500
C	3.2421020	-1.9928940	-0.6926710	C	3.3294250	-2.1245360	-0.6706460
C	-1.9099330	1.3382380	0.1134800	C	-1.8033960	1.2741440	0.1068290
C	-3.2416170	1.2775140	-0.3229860	C	-3.1378830	1.2225810	-0.3230560
C	-3.8189200	2.4212600	-0.8774800	C	-3.6945770	2.3586760	-0.9148200
C	-3.0416190	3.5661230	-1.0009900	C	-2.8986450	3.4856710	-1.0760340
C	-1.7036360	3.5783040	-0.6084180	C	-1.5605630	3.4900350	-0.6801920
C	-2.9007410	-0.9732990	0.3865310	C	-2.8290850	-1.0030160	0.4688870
C	-3.8126700	-0.0525040	-0.1593340	C	-3.7312150	-0.0885570	-0.1053170
C	-3.2336180	-2.3005360	0.6272000	C	-3.1829060	-2.3138240	0.7657380

C	-4.5134580	-2.7219070	0.2821690	C	-4.4746040	-2.7242720	0.4554600
C	-5.4376920	-1.8259120	-0.2639240	C	-5.3890480	-1.8345370	-0.1177810
C	-5.0987710	-0.4970840	-0.4810110	C	-5.0285640	-0.5228720	-0.3950330
H	4.2313350	2.7959780	0.5558130	H	4.3403670	2.6309190	0.6557010
H	0.3492470	4.5495940	0.7277860	H	0.4853350	4.4527430	0.6978640
H	2.7835800	4.7572840	0.9740180	H	2.9165770	4.6181290	1.0150320
H	5.3363990	1.1284400	-0.0433600	H	5.4447910	0.9353460	0.1705390
H	6.4604150	-0.9698400	-0.7179690	H	6.5635010	-1.1716770	-0.4810140
H	5.0608110	-3.0087590	-1.1621450	H	5.1551510	-3.1719900	-1.0496580
H	2.5861250	-2.8394330	-0.8444690	H	2.6663270	-2.9544710	-0.8773380
H	-4.8448530	2.4119400	-1.2252160	H	-4.7215080	2.3564270	-1.2599390
H	-3.4684800	4.4586230	-1.4432460	H	-3.3112150	4.3699790	-1.5472910
H	-1.1152370	4.4686760	-0.7917420	H	-0.9575460	4.3661040	-0.8848630
H	-2.5110850	-2.9858990	1.0487720	H	-2.4676730	-2.9957820	1.2050210
H	-4.7939050	-3.7563570	0.4408550	H	-4.7724820	-3.7454100	0.6615530
H	-6.4319950	-2.1727390	-0.5196270	H	-6.3926520	-2.1731450	-0.3467360
H	-5.8251630	0.1901250	-0.8988410	H	-5.7471930	0.1597270	-0.8333770

[a] DFT calculations on TPSSh/def2-TZVP/CPCM(THF) level of theory.